DGK Veröffentlichungen der DGK

Ausschuss Geodäsie der Bayerischen Akademie der Wissenschaften

Reihe C | Dissertationen | Heft Nr. 838

Kyriakos Balidakis

On the development and impact of propagation delay and geophysical loading on space geodetic technique data analysis

München 2019

Verlag der Bayerischen Akademie der Wissenschaften

ISSN 0065-5325 ISBN 978-3-7696-5250-5

Diese Arbeit ist gleichzeitig veröffentlicht in:
Universitätsbibliothek der Technischen Universität Berlin
DOI: 10.14279/depositonce-9125, Berlin 2019

Veröffentlichungen der DGK

Ausschuss Geodäsie der Bayerischen Akademie der Wissenschaften

Reihe C | Dissertationen | Heft Nr. 838

On the development and impact of propagation delay and geophysical loading on space geodetic technique data analysis

Von der Fakultät VI – Planen Bauen Umwelt

der Technischen Universität Berlin

zur Erlangung des Grades

Doktor-Ingenieur (Dr.-Ing.)

genehmigte Dissertation

Vorgelegt von

Dipl.-Ing. Kyriakos Balidakis

Geboren am 12.10.1991 in Thessaloniki Griechenland

München 2019

Verlag der Bayerischen Akademie der Wissenschaften

ISSN 0065-5325 ISBN 978-3-7696-5250-5

Diese Arbeit ist gleichzeitig veröffentlicht in:
Universitätsbibliothek der Technischen Universität Berlin
DOI: 10.14279/depositonce-9125, Berlin 2019

Adresse der DGK:



Ausschuss Geodäsie der Bayerischen Akademie der Wissenschaften (DGK)

Alfons-Goppel-Straße 11 ● D – 80 539 München

Telefon +49 – 331 – 288 1685 ● Telefax +49 – 331 – 288 1759

E-Mail post@dgk.badw.de ● http://www.dgk.badw.de

Prüfungskommission:

Vorsitzender: Prof. Dr.-Ing. Frank Neitzel

Referent: Prof. Dr.-Ing. Dr. h.c. Harald Schuh

Korreferenten: Prof. Dr.-Ing. Rüdiger Haas (Chalmers University of Technology)
Dr.-Ing. Daniela Thaller (Bundesamt für Kartographie und Geodäsie)

Tag der mündlichen Prüfung: 26.02.2019

© 2019 Bayerische Akademie der Wissenschaften, München

Alle Rechte vorbehalten. Ohne Genehmigung der Herausgeber ist es auch nicht gestattet,
die Veröffentlichung oder Teile daraus auf photomechanischem Wege (Photokopie, Mikrokopie) zu vervielfältigen

ISSN 0065-5325 ISBN 978-3-7696-5250-5

Acknowledgements

The eagle has landed. After a couple of hundred pages in 3rd person and passive voice, *I* finally have the chance to express my gratitude to those instrumental for this achievement.

First and foremost, I am deeply grateful to my supervisor Prof. Dr.-Ing. Dr. h.c. Harald Schuh for offering me the opportunity to carry out my doctoral studies as a member of the VLBI group at GFZ Potsdam, for providing guidance throughout the course of my work, for securing the necessary means for my doing solid research, and for the freedom he allowed on my investigations. My gratitude extends to Dr.-Ing. Daniela Thaller and Prof. Dr.-Ing. Rüdiger Haas for agreeing to evaluate this thesis. I thank Rüdiger Haas in particular, for suggestions to the manuscript that greatly improved its arc of content.

My working at GFZ gave me access to the geoscientific elite and exposed me to a host of stimulating ideas, some of which were developed further upon in the framework of my dissertation. I would like to thank my current roommates James M. Anderson, Sadegh Modiri, and Minghui Xu for innumerable fruitful discussions, as well as my former roommates Benedikt Soja (JPL), Santiago Belda (University of Valencia), and Maria Karbon (Universität Bonn) for supporting my first research steps. I would also like to acknowledge Susanne Glaser, Tobias Nilsson (Lantmäteriet), Georg Beyerle, and our group leader Robert Heinkelmann for several fascinating ideas as well as constructive comments during group meetings and coffee breaks in the office of Franz Kuglitsch. Collaboration with colleagues stationed at GFZ but not affiliated with the VLBI group, especially Florian Zus, Fadwa Alshawaf, Zhiguo Deng, Henryk Dobslaw, Robert Dill, Benjamin Männel, and Max Semmling led to the sharpening of my understanding, and to a number of publications. My thanks also go to Rolf König and Hans Neumayer, for my stay at GFZ in DLR Oberpfaffenhofen related to atmospheric delay modelling in SLR. I want to thank, Sylvia Magnussen (IT specialist) for providing solutions to several technical issues, instantaneously. In particular, I am deeply grateful to (i) Florian for sharing his deep understanding of atmospheric refraction, and for trusting me with the `FORTRAN` source code of his ray-tracing routines, (ii) Susanne for her insight in space geodesy and multi-technique combination that was immensely helpful in my developing the FGST simulator as well as for providing solutions to everyday problems, and (iii) Benedikt for the initial ignition and the unforgettable road trip in South Africa.

My interest in research was started in Greece. I would like to thank all those who introduced me to geodesy from the Aristotle University of Thessaloniki, and in particular Prof. Christos Pikridas, Prof. Christopher Kotsakis, and Prof. Ilias Tziavos, for additionally supporting my "scientific migration". I would also like to thank my colleagues, Thalia Nikolaidou (University of New Brunswick) and Athina Peidou (York University), for their support during the last years.

Last but not least, I would like to thank all my friends, and especially Filippos Evagelou and Katerina Rapti for their support during the last four years. I want to say a heartfelt "thank you" to my parents Despina and Konstantinos, and my brother Thanasis for their unconditional love and valuable advice for without which this accomplishment would be impossible. Beyond all, I want to thank my Susanne for her love, support, direction, trust, and unwavering patience for the last quadrennium. I could not have done it without you.

More than 500 TB of data were processed in the framework of this dissertation. I would like to acknowledge all services from which I retrieved data, and especially ECMWF and GMAO/NASA for making them publicly available. I would like to acknowledge the continuous work of all the IVS, IGS, ILRS and IDS components over many years for providing data of high quality.

The research I carried out since my coming to Germany was supported by the Deutsches GeoForschungsZentrum Potsdam, the Deutsche Forschungsgemeinschaft project "ECORAS" (Extension of the coordinate parameterization of radio sources observed by VLBI, HE 5937/2-1), and the Helmholtz Association of German Research Centers project "ADVANTAGE" (Advanced Technologies for Navigation and Geodesy, ZT-0007). Unrelated to the thesis, but still very helpful was working for project "BeRTISS" (Balkan-Meditteranean Real Time Severe weather Service).

Abstract

This study contributes to the effort of space geodesy to reach the 1 mm accuracy level on a global scale. This stringent requirement is vital to realize a global reference system upon which phenomena such as sea-level rise can be reliably monitored. The study deals with two interrelated challenges: modeling geophysical loads imposed on the crust of the Earth and quantifying the atmospheric propagation delay of signals employed by space geodetic techniques, namely VLBI, SLR, GNSS, and DORIS. If not adequately modeled, both geophysical loading and propagation delay corrupt space geodetic data analysis results, thus distorting the implied reference frame and compromising the physical interpretation of other parameters. The explicit purpose of this work is to understand how these effects propagate into the parameters estimated within the geodetic adjustment, and to develop models that alleviate geodetic results from these effects. To achieve this goal, the scientific framework was divided into two contributions to be understood and enhanced: the theory governing the effects of geophysical loading and atmospheric propagation, and the space geodetic technique data analysis pipeline, largely using VLBI as a test-bed. In essence, the research conducted here includes: (i) the development of software capable of realistically simulating VLBI, SLR, GNSS, and DORIS observations within a Monte Carlo framework, (ii) the homogenization of in situ meteorological data recorded at VLBI and SLR stations, (iii) the development of ray-traced delays, mapping functions and higher-order gradients for all four space geodetic techniques, (iv) the comprehensive investigation of inter-frequency and inter-system atmospheric ties, (v) the development of models to describe the displacement induced by mass redistribution within Earth's fluid envelope including the atmosphere, the ocean, and the continental hydrology, (vi) the development of empirical models to describe the signal propagation delay (GFZ-PT) and the non-tidal geophysical loading displacement (EGLM), and (vii) the study of the impact of the atmospheric refraction and non-tidal geophysical loading models in space geodetic data analysis on station coordinates, the terrestrial reference frame, the Earth orientation, and the integrated water vapour trends. A number of developments were carried out herein for the first time, for example, the simulation of space geodetic measurements based on ray-traced delays, the study of systematic errors on the reference frame induced by not properly accounting for the orbital altitude of the satellites in the calculation of atmospheric refraction corrections, and the assessment of the probability of successful laser ranges based on integrated cloud fraction along the ray path. It was found that microwave and optical atmospheric gradients are starkly different both spatially and temporally, and cannot be scaled to fit each other. Failing to account for non-tidal geophysical loading and atmospheric asymmetries induces a scale bias in the SLR reference frame as well as a spurious geocenter motion predominantly along the Z-axis. Employing a VLBI-tailored atmospheric refraction model to reduce DORIS observations displaces stations in the radial component thus inducing a large scale bias in the implied frame. Employing homogeneous in lieu of raw meteorological data in VLBI data analysis reduces the scatter of station coordinates and improves the baseline length repeatability. Employing the mapping functions developed herein in lieu of VMF1 yields an overall improvement in VLBI data analysis. Applying the geophysical loading models developed herein reduces the response of almost all station coordinate and baseline length series at seasonal and synoptic timescales. Based on the investigations carried out herein, differences in Earth orientation induced by the quality of the atmospheric refraction and geophysical loading models — or their very application for the latter — are not statistically significant in the framework of the modern VLBI system. Nevertheless, to fulfill the 1 mm requirement, proper treatment of geophysical loading and atmospheric refraction is a necessity.

Zusammenfassung

Diese Arbeit trägt zu den Bestrebungen der Geodäsie bei, im globalen Maßstab eine Genauigkeit von 1 mm zu erreichen. Diese Anforderung ist für die Realisierung eines globalen Referenzsystems, das für eine zuverlässige Bestimmung von Phänomenen wie dem Meeresspiegelanstieg verwendet werden kann, zwingend erforderlich. Diese Arbeit beschäftigt sich mit zwei miteinander zusammenhängenden Herausforderungen: die Modellierung geophysikalischer Auflastdeformationen der Erdoberfläche, sowie die Quantifizierung der atmosphärischen Laufzeitverzögerungen von Signalen, die von den geodätischen Weltraumverfahren VLBI, SLR, GNSS und DORIS verwendet werden. Eine unzureichende Modellierung, sowohl der geophysikalische Auflastdeformationen als auch der atmosphärischen Laufzeitverzögerungen, wirkt sich negativ auf die Analyseergebnisse der geodätischen Weltraumverfahren aus, wodurch sich Unsicherheiten im impliziten Referenzrahmen ergeben und die physikalische Interpretation anderer Parameter beeinträchtigt wird. Der explizite Zweck dieser Arbeit ist es zu verstehen, wie sich diese Effekte innerhalb der geodätischen Auswertung auf die geschätzten Parameter verteilen, und welche Modelle entwickelt werden können, die den Einfluss dieser Effekte auf die geschätzten geodätischen Parameter reduzieren. Um dieses Ziel zu erreichen, wurde diese Arbeit in zwei Bereiche, die verstanden und verbessert werden sollen, gegliedert: die Theorie für die Behandlung von Auswirkungen geophysikalischer Auflastdeformationen und atmosphärischer Signalausbreitung, sowie die Datenanalyse für die geodätischen Weltraumverfahren, wobei der Fokus weitestgehend auf VLBI liegt. Im Wesentlichen umfassen die hier durchgeführten Arbeiten: (i) die Entwicklung von Software für realistische Monte-Carlo-Simulationen von VLBI-, SLR-, GNSS- und DORIS-Beobachtungen, (ii) die Homogenisierung der an VLBI- und SLR-Stationen aufgezeichneten meteorologischen Daten, (iii) die Entwicklung von Korrekturen auf der Grundlage von Signalstrahlverfolgung (engl. *ray-traced delays*), Abbildungsfunktionen (engl. *mapping functions*) und Gradienten höherer Ordnung für alle vier geodätischen Weltraumtechniken, (iv) die umfangreiche Untersuchung von atmosphärischen Verbindungsvektoren (engl. *atmospheric ties*) zwischen verschiedenen Signalfrequenzen und Beobachtungsverfahren, (v) die Entwicklung von Modellen zur Beschreibung der Auflastdeformationen durch Massenumverteilung in der Atmosphäre, des Ozeans, und der kontinentalen Hydrologie, (vi) die Entwicklung empirischer Modelle für Signallaufzeitverzögerungen (GFZ-PT) und für gezeitenunabhängige Auflastdeformationen (EGLM) sowie (vii) die Untersuchung, wie sich die Modelle der atmosphärischen Refraktion und der gezeitenunabhängigen Auflastdeformation auf die Stationskoordinaten, den terrestrischen Referenzrahmen, die Erdorientierung und den Trend des integrierten Wasserdampfgehaltes innerhalb der geodätische Datenanalyse auswirken. Hier wurden zum ersten Mal eine Reihe von Entwicklungen durchgeführt, beispielsweise die Simulation von Beobachtungen geodätischer Weltraumverfahren auf der Grundlage von Laufzeitverzögerungen mittels Strahlverfolgung, die Untersuchung von systematischen Unsicherheiten im Referenzrahmen, die durch inkorrekte Berücksichtigung der Satellitenbahnhöhe bei der Korrekturberechnung der atmosphärischen Laufzeitverzögerung verursacht wurden, und die Beurteilung der Wahrscheinlichkeit erfolgreicher Laserentfernungen basierend auf dem integrierten Wolkenanteil entlang des Strahlenwegs. Es wurde festgestellt, dass atmosphärische Gradienten für Mikrowellen- und optische Frequenzen räumlich und zeitlich stark voneinander abweichen und nicht durch Skalierung in Übereinstimmung gebracht werden können. Falls gezeitenunabhängige Auflastdeformationen und atmosphärische Asymmetrien nicht berücksichtigt werden, kommt es zu einer Abweichung im Maßstab des SLR-Referenzrahmens sowie zu einer verfälschten Geozentrumsbewegung vor allem entlang der Z-Achse. Die Verwendung eines auf VLBI zugeschnittenen atmosphärischen Refraktionsmodells zur Modellierung von DORIS-Beobachtungen führt zu Stationsverschiebungen in der radialen Komponente und somit zu einer Maßstabsabweichung des Referenzrahmens. Werden anstelle von meteorologischen Rohdaten,

homogene Daten in der VLBI-Datenanalyse verwendet, reduziert sich die Streuung der Stationskoordinaten und die Wiederholbarkeit der Basislinienlängen verbessert sich. Die Verwendung der im Rahmen dieser Arbeit entwickelten Abbildungsfunktionen anstelle von VMF1 führt zu einer allgemeinen Verbesserung in der VLBI-Datenanalyse. Die Anwendung der hier entwickelten geophysikalischen Auflastmodelle verringert Signale in den Zeitreihen der Stationskoordinaten und Basislinienlängen für saisonale und synoptische Zeitskalen. Basierend auf den hier durchgeführten Untersuchungen sind Unterschiede in der Erdorientierung, die durch die Qualität der atmosphärischen Refraktions- und geophysikalischen Auflastmodelle — oder gerade deren Anwendung auf diese — induziert werden, im Rahmen des modernen VLBI-Systems statistisch nicht signifikant. Um jedoch die Anforderung von 1 mm zu erfüllen, ist eine geeignete Berücksichtigung geophysikalischer Auflastdeformationen und atmosphärischer Refraktion notwendig.

Contents

List of Figures iii

List of Tables xv

List of Abbreviations, Symbols and Nomenclature xix

1 Introduction 1
- 1.1 Overview . . . 1
- 1.2 Motivation and research objective . . . 2
- 1.3 Thesis outline . . . 4

2 Space geodetic techniques 7
- 2.1 Very long baseline interferometry . . . 7
- 2.2 Satellite laser ranging . . . 13
- 2.3 Global navigation satellite systems . . . 19
- 2.4 Doppler Orbitography and Radiopositioning Integrated by Satellite . . . 22
- 2.5 Space geodetic data analysis . . . 24
- 2.6 Monte Carlo simulation of VLBI, SLR, GNSS, and DORIS observations . . . 30

3 Background on atmospheric signal propagation 41
- 3.1 Wave propagation through Earth's atmosphere . . . 42
  - 3.1.1 Maxwell's equations . . . 42
  - 3.1.2 The eikonal equation . . . 44
  - 3.1.3 Propagation through the electrically neutral atmosphere . . . 45
- 3.2 Ray-tracing . . . 49
- 3.3 Homogenization of meteorological series . . . 51
  - 3.3.1 Reference meteorological series . . . 52
  - 3.3.2 Homogenized in situ VLBI and SLR meteorological records . . . 62

4 Development of atmospheric delay models 71
- 4.1 Atmospheric delay perturbations . . . 72
  - 4.1.1 Radius of curvature . . . 72
  - 4.1.2 Orbital altitude . . . 73
  - 4.1.3 Observation geometry . . . 75
  - 4.1.4 Numerical weather model . . . 80
  - 4.1.5 Ionosphere . . . 82
- 4.2 Estimation of mapping functions and gradients . . . 86
  - 4.2.1 Previous mapping function developments . . . 86
  - 4.2.2 Gradient component models . . . 88
  - 4.2.3 Gradient mapping functions . . . 90
  - 4.2.4 Potsdam mapping functions . . . 94

4.2.5 Berlin mapping functions . . . 99
4.3 Development of the empirical atmospheric model GFZ-PT . . . 101
4.4 Atmospheric ties . . . 107
4.4.1 Intra-technique atmospheric ties . . . 108
4.4.2 Inter-technique atmospheric ties . . . 111

5 Development of geophysical loading models 123
5.1 Simulation of geophysical loading deformations . . . 124
5.1.1 Impact of the elastic Earth model . . . 127
5.1.2 Impact of the ocean response to pressure and wind . . . 129
5.1.3 Impact of the spatio-temporal resolution . . . 133
5.2 Simulation of atmospheric pressure loading . . . 135
5.2.1 Tidal atmospheric pressure loading . . . 136
5.2.2 Non-tidal atmospheric pressure loading . . . 138
5.3 Simulation of non-tidal ocean loading . . . 142
5.4 Simulation of continental water storage loading . . . 147
5.5 Development of the empirical geophysical loading model EGLM . . . 152

6 Application of propagation delay models to space geodetic data analysis 157
6.1 Atmospheric refraction treatment in SLR analysis . . . 158
6.2 Impact on station coordinates . . . 165
6.3 Impact on station network . . . 172
6.4 Impact on Earth orientation parameters . . . 174
6.5 Impact on integrated water vapour trends . . . 178

7 Application of geophysical loading models to space geodetic data analysis 187
7.1 Impact on station coordinates . . . 188
7.2 Impact on the station network . . . 199
7.3 Impact on Earth orientation parameters . . . 204
7.4 Impact on satellite orbits . . . 211

8 Summary, conclusions and outlook 213
8.1 Recapitulation . . . 213
8.2 Conclusions and recommendations . . . 215
8.2.1 Recommendations to relevant IAG services . . . 220
8.3 Future research . . . 222

Bibliography 225

A Components of EGLM 247

B Impact of loading displacements on TRFs 250

List of Figures

2.1.1 Polar motion helix drifting away from the CIO ($x_p = y_p = 0\,\mathrm{m}$). Shown are series with respect to the IAU 2006/2000A precession-nutation model and consistent with ITRF2014, EOP 14 C04. 11

2.1.2 The occurrence of baseline-dependent clocks in VLBI data analysis with `Solve` (`./Solve/BaselineClockSetup.nc` in the `vgosDB` directory structure) for the 20 baselines that have the largest number of observations in the IVS archive (1979–2019). 13

2.1.3 The network of all radio telescopes that contributed to ITRF2014 (upper row). The baselines (lower left) and stations (lower right) that as of fall 2018 have successfully participated in most observations carried out in the framework of IVS and QUASAR, based on `vgosDB` and `NGS` data (right). The description for the two- and eight-letter station codes are in `ns-codes.txt`. 14

2.2.1 On the upper left shown are the CDP codes of the stations that have observed most satellite arcs, on the upper right shown are the stations that carried out most of the normal point observations (geodetic observable), and on the lower row shown are the satellites to which most ranges have been achieved, over the last decade; 19 % of the ranges stem from Yarragadee (7090), and 10 % of the ranges were towards Ajisai (2nd best). Both graphs were generated based on ILRS normal point data. . 15

2.2.2 The network of all laser ranging stations that contributed to ITRF2014. Only 37 stations (26 %) are still active. 17

2.2.3 The relative number of laser ranges per SLR station (2008–2018) as a function of local hour of day (HoD). The graph was generated based on ILRS normal point data. 18

2.3.1 The network of all GNSS stations that contributed to ITRF2014. 20

2.4.1 The network of all DORIS stations that contributed to ITRF2014. 22

2.4.2 Data availability from satellites equipped with DORIS receivers, based on DORIS 2.2 format files and DORIS/`RINEX` 3.0. 23

2.4.3 The DORIS beacons (left), and satellites equipped with DORIS receivers (right) that contribute with the largest amount of observations. The graphs were created based on DORIS 2.2 format files and DORIS/`RINEX` 3.0. 23

2.5.1 The celestial atlas of the extragalactic radio sources observed in the framework of IVS that have been considered in this study, in an equatorial system. Shown are the sources that participate in the NNR condition equations (red), the sources the coordinates of which have been estimated as global parameters (blue), the special handling sources (green), and others the positions of which were estimated from experiments such as the VLBA calibrator survey (black). The ecliptic is shown in orange, and the galactic plane is shown in brown. Note the uneven distribution near the ecliptic. 27

2.6.1 The probability of at least one clock break per station being detected, based on a complete reanalysis of the IVS and QUASAR archive (1979–2019) with VieVS@GFZ. 31

2.6.2 The driving white noise simulated based on Table 2.6.1 for 2018/04/01. 33

2.6.3 Low (1st column), medium (2nd column), and high (3rd column) cloud cover from ERA5 fields. Shown are the 2000–2018 average (upper row) fields, and the instantaneous fields on 2017/01/01 00:00 (lower row). 35
2.6.4 Scatterograms between simulated radial component displacements due to non-tidal atmospheric pressure loading (cf. Sec. 5.2) and cloud cover, from ERA5 fields at Arequipa, Peru (left), and Papeete, Tahiti (right). 36
2.6.5 The spatial correlation (SC) between ERA5-derived TCC time series at some SLR stations (active or planned) and virtual stations (ERA5 grid nodes) over summer (red) and winter (blue). ξ_s and ξ_w denote the correlation length from the covariance model of Hirvonen (4.3.5) for summer and winter, respectively. 37
2.6.6 The temporal auto-correlation (TC) of ERA5-derived TCC time series at some SLR stations (active or planned) over summer (red) and winter (blue). ξ_s and ξ_w denote the correlation time lag from the covariance model of Hirvonen (4.3.5) for summer and winter, respectively. 37
2.6.7 The correlation matrix of the adjustment carried out for the GNSS simulations, at Wettzell, where different parameters are set up as unknowns. 38

3.3.1 Compressibility factor calculated following (3.3.6), employing ERA Interim at 2017/04/24 00 UTC. 54
3.3.2 Compressibility factor (unitless) as a function of temperature and pressure for the extreme cases of dry air (left) and water-vapor-saturated air (right) 55
3.3.3 Barometric pressure series from the surface fields of ECMWFop, ERAin, NCEPre2, MERRA, MERRA2 and JRA-55 at Badary, Russia (left) and Zelenchukskaya, Russia (right). The temporal resolution is 6 h for all models except for MERRA2 (1 h). 59
3.3.4 Barometric pressure series from the model levels (ML) and the surface fields (SFC) of ECMWFop and ERAin at Badary, Russia (left) and Zelenchukskaya, Russia (right). 59
3.3.5 Barometric pressure (left), air temperature (middle) and relative humidity (right) bias stemming from the extraction approach: from the surface fields (ERAin) and exactly at the reference height of the each VLBI station, from the model levels (VLBI). 60
3.3.6 Orography (left) and surface pressure (right) differences between ECMWFop and ERAin at 2000-01-01, 2006-02-01, 2010-01-26, and 2015-05-12. 61
3.3.7 Differences between in situ meteorological data recorded at SLR stations and ERAinML. The differences at Simosato, Japan (left), and Borowiec, Poland (right) are shown. The colors indicate the data source; black for full-rate, blue for normal point, and red for consolidated normal point ILRS data. 64
3.3.8 Barometric pressure difference between raw and homogenized pressure series recorded at SLR stations, with respect to ERAinML. The differences shown are for two stations in Simeiz, Crimea (upper row), Arequipa, Peru (lower left), and Wettzell, Germany (lower right). 65
3.3.9 Differences between meteorological observations recorded in the vicinity of the some VLBI stations, and reference series constructed employing ERA Interim model level data (blue). In red illustrated are these differences after the homogenization process. Shown session-wise are the differences at Kokee Park, Matera, Green Bank, Noto, Ny-Ålesund, Onsala, Parkes, Sejong, Svetloe, Tsukuba, Wettzell, and Zelenchukskaya. The scatter of the meteorological parameter anomalies during the course of a session is illustrated in gray. 68

3.3.10 Differences between meteorological observations recorded in the vicinity of the stations constituting the VLBA in the USA, and reference series constructed employing ERA Interim model level data (blue). In red illustrated are these differences after the homogenization process. Shown are the session-wise differences at Brewster (WA), Los Alamos (NM), Pie Town (NM), Ft. Davis (TX), Mauna Kea (HI), St. Croix (VI), Hancock (NH), North Liberty (IA), Kitt Peak (AZ), and Owens Valley (CA). The scatter of the meteorological parameter anomalies during the course of a session is illustrated in gray. 69

4.1.1 Radii against φ for WGS84. Illustrated are the radii of curvature in meridian R_M and in prime vertical R_N, as well as the Gaussian radius of curvature R_G, and the geocentric radius R. 74

4.1.2 Orbital altitude dependence. The ddifferences $\tau_{trop}^{\text{P-R}}(3°,0°)$ (left), and $\tau_{trop}^{\text{P-R}}(3°,90°)$ (right) are illustrated. Note that delays calculated assuming the average GPS orbital altitude are always larger from delays assuming a quasar target. 75

4.1.3 Orbital altitude dependence. Shown are the differences $\tau_{trop}^{\text{P-R}}$ as a function of elevation angle (left), height (middle), and zenith non-hydrostatic delay (right). 75

4.1.4 Skyplots of the radio sources observed by `WETTZELL` in a single VLBI session under a regular rapid turnaround network configuration (left), CONT14 (middle), and simulated 32-station VGOS (right). 77

4.1.5 The ground track of the GPS (blue), GLONASS (red), Galileo (green), BeiDou (black) and QZSS (magenta) constellations on 2017/01/03. 78

4.1.6 Satellite visibility diagrams for MGEX at Ny-Ålesund (Svalbard), Wettzell (Germany), Fortaleza (Brazil) and Hobart (Tasmania) on 2016/05/18. Shown are the GPS (blue), GLONASS (red), Galileo (green), BeiDou (black) and QZSS (magenta) constellations. 78

4.1.7 Satellite visibility diagrams for LAGEOS-1 (cyan), LAGEOS-2 (blue), Etalon-1 (magenta) and Etalon-2 (red) orbits from Ny-Ålesund (Svalbard), Wettzell (Germany), Fortaleza (Brazil) and Hobart (Tasmania) on 2016/05/18. 79

4.1.8 The ground tracks of LAGEOS-1 (cyan), LAGEOS-2 (blue), Etalon-1 (magenta) and Etalon-2 (red) orbits, on 2016/05/18, are on the left. The ground tracks of Ajisai (red), LARES (black), Larets (green), Starlette (blue), and Stella (cyan) orbits on 2016/05/18 are on the right. 79

4.1.9 Total cloud cover atlas (left) and its scatter (right) at the orography of ERA5, calculated from hourly ERA5 fields (2000.0–2018.0). 80

4.1.10 Satellite visibility diagrams for CryoSat-2 (black), Envisat (blue), HY-2A (red), Jason-2 (green) and Jason-3 (magenta) orbits from Ny-Ålesund (Svalbard), Wettzell (Germany), Fortaleza (Brazil) and Hobart (Tasmania) on 2018/01/01. 80

4.1.11 The ground track of the CryoSat-2 (black), Envisat (blue), HY-2A (red), Jason-2 (green) and Jason-3 (magenta) missions on 2018/01/01. 81

4.1.12 The impact of alternating the underlying NWM between ERA5 and ERA Interim (upper row), and ECMWF's operational model and ERA-Interim (lower row), on ray-tracing products (2014/05/05 00:00). The differences between the equivalent height errors δH, d_{nh}^{z}, G_{NS}, and G_{EW} are presented. 82

4.1.13 The differences $\int(1+10^{-6}N)\,ds_i - \int(1+10^{-6}N)\,ds_\infty$ for the most commonly used frequencies in GNSS (left), DORIS (middle), and VLBI (right) for $\varepsilon = 3°$ and $\alpha = 0°$, 2012/04/15 12:00. The frequencies the results refer to are 1.57542, 1.22760, 2.03625, 0.40125, 8.4, 2.3 GHz. Note while the spatial pattern remains, the colorbar is scaled as a function of frequency. 85

4.2.1 The mf_h at 2017/01/01 00 UTC, employing ERA5. 87

4.2.2 Cases of strong asymmetries in Tsukuba, at 1996-07-10 18 UTC (upper left), 2000-08-12 00 UTC (upper right), 2003-08-15 06 UTC (lower left), and 2003-08-16 00 UTC (lower right). Slant hydrostatic (blue) and non-hydrostatic (red) delays at $\varepsilon = 3°$ by different modelling approaches: mapping functions (solid line), mapping functions and linear horizontal gradients (dotted line), mapping functions and high-order gradients (dashed line), and ray-traced delays (asterisks) calculated employing ERA Interim. 89

4.2.3 Spatial average of the WRMS of the post-fit residuals (azimuthal fit to ray-traced delays) per ε for the two gradient mapping functions under consideration. O^0 indicates no gradients, O^1 indicates a linear gradient model, whereas O^2 indicates 2nd order components as well. Evidently CH97 outperforms BS98, and retaining 2nd order components is advantageous for $\varepsilon < 10°$. 90

4.2.4 The WRMS of the post-fit residuals of gradient estimation (azimuthal fit to ray-traced delays) for the BS98 O^1 (1st column), CH97 O^1 (2nd column), and CH97 O^1+O^2 (3rd column). The rows correspond to elevation angles of 3, 5, 7, 10, 15, and 20 degrees, respectively. 92

4.2.5 Differences in the average (upper row) and S_a amplitude (lower row) between gradient components (G_{NS} left and G_{EW} right) estimated employing the BS98 or CH97 mf_g, from ERA5 refractivity tensors. 93

4.2.6 Gradient mapping function coefficients employing the CH97 ansatz truncated to the 1st order. The 38-year average fields of the total C_t, hydrostatic C_d and non-hydrostatic C_v gradient mapping function coefficient are illustrated in the upper left, middle, and right panel, respectively, as well as the dispersion thereof: σ_{C_t}, σ_{C_d}, and σ_{C_v} (lower row). The spatiotemporal mean is indicated by white. 94

4.2.7 Uncertainties of pressure (left), temperature (middle), and relative humidity (right) from a 10-member ensemble of ERA5 data assimilations (2018/01/01 00:00). 97

4.2.8 Average formal error of basic surface fields of ECMWF's operational analysis. The graphs show the fields of pressure (left), temperature (middle), and specific humidity (right). 98

4.2.9 The PMF products at 00:00 UTC January 1st 2017, employing ERA Interim: d_h^z (upper left) and d_{nh}^z (upper-right), the mapping function coefficients (2nd and 3rd row), linear horizontal gradient components (4th row), and 2nd order gradients (last row). 98

4.3.1 IWV rates (1st row) and S_a amplitudes (2nd row) estimated employing ERA Interim fields (left), ERA5 fields (middle), and the differences thereof (right), for the period 1979.0–2019.0. 103

4.3.2 IWV trends (left) and IWV annual amplitudes (right) at Algonquin Park (Canada), estimated employing ERA5 data. For the estimation thereof the length of the time series as well as the first and last epoch were varied. 104

4.3.3 The amplitudes of low-frequency harmonics of pressure (1st column), temperature (2nd column), and relative humidity (3rd column), employing ERA Interim. The graphs present the amplitudes of the S_a (1st row), S_{sa} (2nd row), S_{ta} (3rd row), and S_{11} (4th row) harmonics, as well as the scatter of the post-fit residuals thereof (5th row). Note the different color scales. 105

4.3.4 The amplitude of high-frequency harmonics of pressure (1st column), temperature (2nd column), and relative humidity (3rd column), employing ERA5. The graphs present the amplitudes of the S_1 (1st row), S_2 (2nd row), and S_3 (3rd row) harmonics, as well as the scatter of the post-fit residuals thereof (4th row). Note the different color scales. 106

4.3.5 Zenith total delay (left), G_{NS} (middle), and G_{EW} (right) rates for microwaves (upper row) and lasers at 532 nm (lower row) from 39 years of ERA Interim. 107

4.4.1 Zenith hydrostatic delay ties. The differences between ray-traced d_n^z at the orography of ERA5 and virtual orographies 25 m (left), 100 m (middle), and 500 m (right) above are illustrated. In the upper row shown are the δd_h^z averaged over a month (2018/01), whereas in the lower row shown are the ties at the epoch 2018/01/01 00:00. Note the different color scales. 110

4.4.2 Zenith non-hydrostatic delay ties. Shown are the differences between ray-traced d_n^z at the orography of ERA5 and virtual orographies 25 m (left), 100 m (middle), and 500 m (right) above. In the upper row shown are the δd_h^z averaged over a month (2018/01), whereas in the lower row shown are the ties at the epoch 2018/01/01 00:00. Note the different color scales. 111

4.4.3 Hydrostatic mapping factor differences. Shown are the differences between ray-traced mf_h (7°) at the orography of ERA5 and virtual orographies 25 m (left), 100 m (middle), and 500 m (right) above. In the upper row shown are the δmf_h (7°) averaged over a month (2018/01), whereas in the lower row shown are the ties at the epoch 2018/01/01 00:00. Note the different color scales. 112

4.4.4 Non-hydrostatic mapping factor differences. Shown are the differences between ray-traced mf_{nh} (7°) at the orography of ERA5 and virtual orographies 25 m (left), 100 m (middle), and 500 m (right) above. In the upper row shown are the δmf_{nh} (7°) averaged over a month (2018/01), whereas in the lower row shown are the ties at the epoch 2018/01/01 00:00. Note the different color scales. 113

4.4.5 North-South tropospheric gradient component ties. Shown are the differences between ray-traced G_{NS} at the orography of ERA5 and virtual orographies 25 m (left), 100 m (middle), and 500 m (right) above. In the upper row shown are the δG_{NS} averaged over a month (2018/01), whereas in the lower row shown are the ties at the epoch 2018/01/01 00:00. Note the different color scales. 113

4.4.6 East-West tropospheric gradient component ties. Shown are the differences between ray-traced G_{EW} at the orography of ERA5 and virtual orographies 25 m (left), 100 m (middle), and 500 m (right) above. In the upper row shown are the δG_{EW} averaged over a month (2018/01), whereas in the lower row shown are the ties at the epoch 2018/01/01 00:00. Note the different color scales. 114

4.4.7 Inter-system d_h^z ties. Shown are the d_h^z for VLBI (left), and SLR (middle), calculated at the orography of ERA5. In the right column the amount the d_h^z is amplified from VLBI (R) to SLR (L) is illustrated. In the upper row shown are the results averaged over a month (2018/01), whereas in the lower row shown are results at the epoch 2018/01/01 00:00. Note the different color scales. 115

4.4.8 Inter-system d^z_{nh} ties. Shown are the d^z_{nh} for VLBI (left), and SLR (middle), calculated at the orography of ERA5. In the right column the d^z_{nh} ratio of VLBI (R) to SLR (L) is illustrated. In the upper row shown are the results averaged over a month (2018/01), whereas in the lower row shown are results at the epoch 2018/01/01 00:00. Note the different color scales. 115

4.4.9 The long-term average G_{NS} (left), averaged over a month (2018/01) G_{NS} (middle), and G_{NS} at the epoch 2018/01/01 00:00 (right). Displayed are GNSS (upper), and SLR (lower) results. 116

4.4.10 The long-term average G_{EW} (left), averaged over a month (2018/01) G_{EW} (middle), and G_{EW} at the epoch 2018/01/01 00:00 (right). Displayed are GNSS (upper), and SLR (lower) results. 117

4.4.11 The S_a amplitude of GNSS-based (upper), and SLR-based (lower) G_{NS} (left), and G_{EW} (right) from GFZ-PT (cf. 4.3). 117

4.4.12 The spatial correlation between gradient amplitude (upper row) and phase (lower row) time series from ray-tracing in ERA5-derived microwave (left) and optical at 532 nm (right) refractivity fields at Yarragadee (in the middle of the figures) and the neighbouring grid nodes. 118

4.4.13 Shown are the long-term discrepancies between G_{NS} tailored for the different microwave-based techniques. Shown are the differences between GNSS and VLBI (left), DORIS and GNSS (middle), and DORIS and VLBI (right), averaged over a month (upper row) and at the epoch 2018/01/01 00:00 (lower row). 120

4.4.14 Shown are the long-term discrepancies between G_{EW} tailored for the different microwave-based techniques. Shown are the differences between GNSS and VLBI (left), DORIS and GNSS (middle), and DORIS and VLBI (right), averaged over a month (upper row) and at the epoch 2018/01/01 00:00 (lower row). 120

4.4.15 Error in the atmospheric delay corrections for laser ranges towards GRACE-FO induced by not accounting for the orbital altitude (left), or the atmospheric asymmetries (right). Shown are the results from ray-tracing in ERA5 fields, at 532 nm, for 0° azimuth and 10° elevation. 120

4.4.16 The differences in slant symmetric delays at 7° between GNSS-VLBI (left), and DORIS-VLBI (right), stemming from the orbital altitude dependence are presented. The results averaged over a month (2018/01) are in the upper row, whereas the results at the epoch 2018/01/01 00:00 are illustrated in the lower row. Note the different color scales. 121

5.1.1 Spectral power of the orography-discrepancy-adjusted surface pressure fields of ERA5 (upper left), the EWH from Mog2D-G ocean bottom pressure anomalies (upper right), and the EWH from the hydrological mass variations from ERA5 (lower left), at a trimmed spectral range, as a function of spherical harmonic degree. The spherical harmonic degree variance of the mass anomalies for the individual loading contributions at one epoch are shown in the second row for the radial (left), North-South (middle), and East-West (right) coordinate component. Note the different color scales. 126

5.1.2 Load Green's functions for the radial (upper) and the tangential (lower) displacement component. The global Green's functions from Earth models (PREM, `iasp91`, and `ak135`) with varying crustal structures are illustrated, as well as local Green's functions (`Crust 1.0` and `TEA12`), averaged for the sake of illustration, in the center-of-mass isomorphic reference frame (left). For `ak135`, the displacements are presented in the center of mass of the solid Earth (CE), the center of mass of the entire Earth system (CM), the center of surface figure (CF), the center of surface lateral figure (CL), and the center of surface of height figure (CH). 128

5.1.3 Differences between simulated NTAL displacements employing hourly ERA5 fields alternating the Earth model, with respect to PREM. The differences presented are for the radial (left), North-South (middle), and East-West (EW) component, for Algonquin park, Canada (upper) and Zelenchuskaya, Russia (lower). 129

5.1.4 Degree-one surface deformation due to NTAL (upper row), NTOL (middle row), and CWSL (lower row) on 2017/10/22 12:00, in the radial (left column), North-South (middle row), and East-West (right row) coordinate component. 130

5.1.5 Degree-one surface deformation from ERA Interim (NTAL and CWSL), and ECCO (NTOL). The displacements in the radial (blue), North-South (black), and East-West (red) component are presented for Algonquin Park, Canada (up) and Hartebeesthoek, South Africa (bottom). 130

5.1.6 The average (upper) and RMS (lower) of surface pressure (left) 10 m wind speed amplitude (middle), and dynamic atmospheric correction (right) for 2016, from ERA5 and Mog2D-G data. 132

5.1.7 The dynamic atmospheric correction (left), the modified inverted barometer correction (middle), and the difference thereof (right) on 2016/01/01 00 UTC, employing ERA5 near surface model levels. 132

5.1.8 Atmospheric loading displacements employing hourly ERA5 fields (blue) and MIB, and ERA5 and Mog2D-G fields (red) at Badary (upper) and Onsala (lower). The differences in the radial (left), North-South (middle), and East-West (EW) component are shown in green. 133

5.2.1 Barometric pressure anomalies (blue) and simulated NTAL radial displacements (red) at Wettzell (upper left), Hartebeesthoek (upper right), Fortaleza (lower left), and Kokee Park (lower right). 136

5.2.2 The amplitude of the simulated displacements induced by S_1 (upper row) and S_2 (lower row) atmospheric tides at the vertical (left), North-South (middle) and East-West (right) coordinate component. Note the different color scales. 138

5.2.3 The amplitude of the combined tidal atmospheric loading effect stemming from K_1, L_2, M_2, N_2, P_1, R_2 and T_2 (ERA Interim, GFZ Section 1.3) and S_3 (ERA5, this study) (upper row). The lower row shows the fraction of the signal due to the combined S_1 and S_2 with respect to the accumulated signal (10 waves). The columns refer to the radial (left), North-South (middle), and East-West (right) coordinate component. 139

5.2.4 The amplitude of the simulated displacements induced by NTAL at S_a (1st column), S_{sa} (2nd column), and S_{ta} (3rd column) frequencies, at the radial (1st row), North-South (2nd row) and East-West (3rd row) coordinate component. The 4th column shows the RMS of the post-fit residuals. Note the different color scales. 140

5.2.5 The differences between simulated NTAL displacements of EOST, GFZ, and IMLS, with respect to GGFC, at Algonquin Park (upper row) and Kokee Park (lower row), in the radial (left), East-West (middle), and North-South (right) coordinate component. The loading signal from GFZ is shown in gray. 140
5.3.1 The amplitude of the simulated displacements induced by NTOL at S_a (1st column), S_{sa} (2nd column), and S_{ta} (3rd column) frequencies, at the radial (1st row), North-South (2nd row) and East-West (3rd row) coordinate component. The 4th column shows the RMS of the post-fit residuals. Note the different color scales. 143
5.3.2 The differences between simulated NTOL displacements of EOST, GFZ, and IMLS, with respect to GGFC, at Algonquin Park (upper row) and Kokee Park (lower row), in the radial (left), East-West (middle), and North-South (right) coordinate component. The loading signal from GFZ is in gray. 145
5.3.3 Variability of equivalent water height anomalies induced by monthly ocean bottom pressure variations observed by GRACE. 146
5.3.4 The degree variance of the ocean bottom pressure simulated by OMCT05 (left), and MPIOM (right) trimmed at degree 100. 147
5.4.1 Dispersion of the hydrological mass in mm of equivalent water height from CPCv2 (upper left), GLDAS/Noah_v3.3 (upper middle), ERA5 (upper right), GRACE (lower left), and WaterGAP 2.2a (lower right). 148
5.4.2 The amplitude of the simulated displacements induced by CWSL at S_a (1st column), S_{sa} (2nd column), and S_{ta} (3rd column) frequencies, at the radial (1st row), North-South (2nd row) and East-West (3rd row) coordinate component. The 4th column shows the RMS of the post-fit residuals. Note the different color scales. 149
5.4.3 Radial component of simulated CWSL displacements at Badary (upper left), Fortaleza (upper middle), Gilmore Creek (upper right), Hartebeesthoek (lower left), Westford (lower middle), and Wettzell (lower right). 151
5.4.4 The differences between simulated CWSL displacements of EOST, GFZ, and IMLS, with respect to GGFC, at Algonquin Park (upper row) and Kokee Park (lower row), in the radial (left), East-West (middle), and North-South (right) coordinate component. The loading signal from GFZ is in gray. 151
5.5.1 The portion of the radial (upper), North-South (middle), and East-West (lower) component of the NTAL (left), NTOL (middle), and CWSL (right) signal captured by a sinusoid at the dominant frequency, expressed in terms of normalized PSD. . . 153
5.5.2 The linear EGLM trends of displacements in the CM frame estimated from a least-squares adjustment together with seasonal and inter-annual harmonics. Shown are the rates in the radial (left), North-South (middle), and East-West (right) coordinate component from NTAL (1st row), NTOL (2nd row), and CWSL (3rd row). 154
5.5.3 EGLM's power spectral density (PSD) or the so-called variance rate of the underlying white noise process from simulated displacements induced by NTAL (1st column), NTOL (2nd column), CWSL (3rd column), and the total non-tidal loading (4th column), in the radial (1st row), North-South (2nd row), and East-West (3rd row) coordinate component. Note the different color scales. 155

6.1.3 The datum perturbation parameters from a 7-parameter Helmert transformation between solutions where the atmospheric asymmetry was modelled, or was neglected at the observation equation level. The offset and scatter of the related time series are shown in the legend. 160

6.1.1 The coordinate bias in a topocentric system (radial, East-West, and North-South) for some of the high-performing SLR stations, induced by neglecting to model the tropospheric asymmetry. In the graph, the scenarios of expanding the parameter space of the geodetic adjustment are shown. In all solutions, the mapping function is assumed to be known within the precision of the underlying NWM (ERA5). SLR solutions where a 2 hPa bias was introduced in the a priori zenith delay are denoted with # (gray bar frame). L1L2 and ALL9 denote solutions where only LAGEOS-1 and 2 were used, and all aforementioned spherical satellites, respectively. 161

6.1.2 The spurious bias in d_{NS} induced in SLR data analysis if atmospheric asymmetry is not treated. The values shown stem from a 10-year-long simulation with 9 spherical satellites, accounting for the clouds, and assuming no other systematic errors. The circle size is indicative of the related uncertainty. 162

6.1.4 The WRMS of the post-fit residuals from a least-squares adjustment of coordinate time series in a topocentric system (radial, East-West, and North-South), for some of the high-performing SLR stations, induced by neglecting to model the tropospheric asymmetry. See the description of Fig. 6.1.1. 163

6.1.5 The S_a amplitude of coordinate time series in a topocentric system (radial, East-West, and North-South), for some of the high-performing SLR stations, induced by neglecting to model the tropospheric asymmetry. See the description of Fig. 6.1.1. 166

6.2.2 The number of space vehicles that constitute the GNSS constellation for which simulations were carried out with FGST. The related `sp3` files were prepared by Zhiguo Deng (GFZ Potsdam). 167

6.2.1 The S_a (1st row), S_{sa} (2nd row), and S_{ta} (3rd row) amplitudes of station displacements in the radial coordinate component, as well as the WRMS of the post-fit residuals, after applying PMF (blue), the VMF1 (red), and GFZ-PT (green) mapping functions, at the observation equation level, in the analysis of all IVS rapid turnaround sessions during the period 2002–2014. 168

6.2.3 The average displacement bias (upper left), the spurious linear velocity (upper right), the S_a amplitude (lower left), and the WRMS (lower right) of the radial station coordinate relative errors stemming from alternating the mapping functions to GFZ-PT. 170

6.2.4 The average displacement bias (upper left), the spurious linear velocity (upper right), the S_a amplitude (lower left), and the WRMS (lower right) of the radial station coordinate relative errors stemming from alternating the meteorological to GFZ-PT. 170

6.2.5 The average displacement bias (upper left), the spurious linear velocity (upper right), the S_a amplitude (lower left), and the WRMS (lower right) of the radial station coordinate relative errors stemming from alternating both the mapping functions and meteorological data to GFZ-PT. 171

6.2.6 Topocentric coordinate differences between a DORIS solution where a DORIS-tailored PMF was used, and a DORIS solutions where a GPS-tailored PMF was used. The stations shown are Belgrano (left), Ny-Ålesund (middle), and Thule (right). 172

6.3.1 The time series of a 7-parameter similarity transformation between the ensemble mean of the solution where GFZ-PT served as mapping functions (left), the solution where GFZ-PT was used to calculate the d_h^z (middle), and the solution where GFZ-PT was used for mf_h, mf_{nh}, and d_h^z (right), with respect to the GNSS solution where no systematic errors where simulated. In the legend of these graphs, the average offset appears, as well as the WRMS of a straight-line fit, enclosed in parenthesis. . 173

6.3.2 The datum perturbation parameters from a 7-parameter Helmert transformation between DORIS solutions where a VLBI-, and a DORIS-tailored mapping function was used to model the delay decay with increasing elevation angle. The offset and scatter of the related time series are shown in the legend. 174

6.4.2 The differences in the EOPs estimated in VLBI data analysis employing the PMF developed herein and VMF1. The differences are shown in red, and the running median in black. 175

6.4.1 The correlation between EOPs and station coordinates in least-squares adjustments with `VieVS@GFZ` (all IVS-R1 and IVS-R4 spanning the period 2002–2018), where EOPs and station coordinates are set up as single offsets per station. 176

6.4.3 The differences in the EOPs estimated in VLBI data analysis employing the homogenized in situ meteorological data and ERAinML. The differences are painted red, and the running median in black. 178

6.4.4 The differences in the EOPs estimated in VLBI data analysis employing the homogenized and raw in situ meteorological data. The differences are in red and the running median in black. 179

6.5.1 IWV trends estimated from real VLBI and GPS observations employing `VieVS@GFZ`, `EPOS.P8`, and ray-tracing. For the trend estimation, the three different time series (for every station) were synchronized. 180

6.5.3 Zenith non-hydrostatic delay estimated from simulated GNSS observation with FGST at `POTS`. The d_{nh}^z from numerical integration in the model levels of ERA Interim is displayed in black, the estimates from the individual ensemble members are shown in gray, and the ensemble mean is shown in red. On the left shown is a series of solutions where no systematic errors were introduced, and only GPS observations were utilized. The solutions from multi-GNSS observations are in the middle, and on the right are GPS solutions where the a priori d_h^z stem from GFZ-PT. 181

6.5.2 Linear atmospheric gradients estimated from simulated GNSS observation with FGST at `POTS`. Gradients from ray-tracing are displayed in black, the estimates from the individual ensemble members are shown in gray, and the ensemble mean is shown in red. On the left, the G_{NS} are presented, and on the right lie the G_{EW}. On the upper row are the GPS-only solutions, and on the lower row are the multi-GNSS solutions. 181

6.5.4 Deviations of linear IWV rates from simulated VLBI observations with respect to IWV from numerical integration in ERA Interim, for stations with more than 10 years of observations. The upper panel shows the trends estimated by converting the d_{nh}^z output of FGST directly to IWV, and the lower panel shows the trends estimated after correcting for the erroneous d_h^z. In the legend, first appears the name of the model for the a priori delay and then the mapping function. 182

6.5.5 Deviations of linear G_{NS} and G_{EW} rates from simulated VLBI observations (FGST) with respect to ray-traced gradients in ERA Interim, for stations with more than 10 years of observations. 183

6.5.6 From left to right, the observation geometry during 2002 (upper row), and 2012 (lower row), for HARTRAO, HOBART26, TIGOCONC, and TSUKUB32 is presented. Note the improvement of the azimuthally uneven observation distribution over one decade. 183

6.5.7 Deviations of linear G_{NS} and G_{EW} rates from simulated VLBI observations (FGST) with respect to ray-traced gradients in ERA Interim, for stations with more than 10 years of observations. In this simulation run, no noise was applied to **b**. 184

6.5.8 IWV (1st row) and gradient component (2nd and 3rd row) trends estimated from simulated VLBI and GNSS observations employing FGST, and ray-tracing. For the trend estimation, the three different time series (for every station) were synchronized. 185

7.1.1 The S_a (1st row), S_{sa} (2nd row), and S_{ta} (3rd row) amplitudes of station displacements in the radial coordinate component after applying no non-tidal displacement models (blue), the fully fledged EGLM (red), and the discrete series of detrended accumulated geophysical loading (green), at the observation equation level. 193

7.1.2 The normalized PSD at the S_a (1st row), S_{sa} (2nd row), and S_{ta} (3rd row) frequency of radial station displacements after applying no non-tidal displacement models (blue), the fully fledged EGLM (red), and the discrete series of detrended accumulated geophysical loading (green), at the observation equation level. 194

7.1.3 The station height repeatability (seasonals removed) after applying no non-tidal displacement models (blue), the fully fledged EGLM (red), and the discrete series of detrended accumulated geophysical loading (green), at the observation equation level. 195

7.1.4 The portion of WRMS (upper panel) and S_a amplitude (lower panel) in the VLBI station coordinates that is solely attributed to neglecting to model non-tidal loading deformation at the observation equation level, based on simulated observations (cf. Sec. 2.6). The scatter in the radial, North-South, and East-West coordinate component is shown in blue, red, and green, respectively. 196

7.1.5 The coordinate bias in the radial (1st column), East-West (2nd column), and North-South (3rd column) component, induced by neglecting to model NTAL at the observation equation level in SLR data analysis, for all stations that are part of ITRF2014. The 1st row shows the bias when only noise is injected in the observations and NTAL is not modelled. The 2nd row shows the bias when in addition to noise, the atmospheric asymmetry is not modelled nor estimated either. Rows 3rd and 4th display the difference between the solutions on the first two rows and the respective ones where the correct NTAL model was applied at the observation level. In the legend, LCC, MCC, HCC, and TCC denote the low, medium, high, and total cloud cover aloft the stations. 197

7.1.6 The coordinate bias in the radial (1st column), East-West (2nd column), and North-South (3rd column) component, induced by neglecting to model NTAL (1st row) or ANGL (2nd row) at the observation equation level in SLR data analysis, for all stations whose data were assimilated into ITRF2014. For the simulation of the related observations, hourly cloud tensors from ERA5 have been utilized. In the legend, LCC, MCC, HCC, and TCC denote the low, medium, high, and total cloud cover aloft the stations. 198

7.1.7 Station coordinate residuals (from simulated observations) obtained when non-tidal geophysical loading displacements at Wettzell are not modelled. The displacements due to NTAL (left) and ANGL (right) are shown in red. In black shown is the three-month moving median. The long-term average and scatter are shown in the legend. 199

7.2.1 The impact of the combined effect of non-tidal atmospheric pressure loading, non-tidal ocean loading and continental water storage loading on the scale of the implied reference frame of the networks of IVS (upper-left), ILRS (upper-right), IGS (lower-left) and IDS (lower-right). The colorbars indicate the number of stations. 201

7.2.2 The annual amplitude and phase of T_Z and the differential scale factor from the application of loading models at the parameter level, as well as the scatter of the post-fit residuals. Note the varying vertical axis limits. 202

7.2.3 The differential scale factor between VLBI station coordinates estimated employing `VieVS@GFZ`. Shown from left to right are the scale for (i) no non-tidal vs. discrete, (ii) no non-tidal vs. EGLM, and (iii) EGLM vs. discrete loading model. 203

7.2.4 The impact of not applying NTAL (left) and ANGL (right) on the implied reference frame realized by SLR observations, expressed in terms of Helmert transformation parameters. Laser ranges were simulated based on the *temporal average* of the cloud cover atop each station. In the legend, the long-term average and the scatter of the related series is illustrated. 204

7.2.5 The impact of not applying NTAL (left) and ANGL (right) on the implied reference frame realized by SLR observations, expressed in terms of Helmert transformation parameters. Laser ranges were simulated based on *hourly* cloud cover tensors. In the legend, the long-term average and the scatter of the related series is shown. . . 205

7.3.1 The impact of the *combined effect of NTAL, NTOL and CWSL* on EOPs estimated in VLBI data analysis. The differences between the EOPs obtained employing non-tidal loading and those obtained applying no non-tidal loading models (red), the formal errors thereof (gray), and the 60-day running median (black). 206

7.3.2 The impact of *EGLM* on EOPs estimated in VLBI data analysis. The differences between the EOPs obtained employing EGLM and those obtained applying no non-tidal loading models (red), the formal errors thereof (gray), and the 60-day running median (black). 207

7.3.3 The differences in the EOPs estimated in VLBI data analysis employing discretized loading series developed herein and EGLM. The differences (red), the formal errors thereof (gray), and the 60-day running median (black). 207

7.3.4 VLBI stations that participated in most IVS and QUASAR Intensive VLBI sessions. In the upper row, stations that appear in larger font have participated in more Intensives; baselines drawn employing wider lines have been observed more during Intensives. Shown are the stations (lower left) and baselines (lower right) that have the largest number of observations. 209

7.3.5 Tidal atmospheric pressure loading at Wettzell (upper left), Kokee Park (upper middle), Tsukuba (upper right), Ny-Ålesund (lower left), Badary (lower middle), and Zelenchukskaya (lower right), on 2019-01-01. The displacements shown have been simulated by GFZ (solid line), and GGFC (dashed line), for the radial (blue), North-South (black), and East-West (red) coordinate component, in the CM frame. 210

A.0.1 The period at which the PSD from simulated displacements induced by NTAL (left), NTOL (middle), CWSL (right), in the radial (1st row), North-South (2nd row), and East-West (3rd row) coordinate component is maximized. Note the different color scales. 248
A.0.2 The phase of the simulated displacements induced by NTAL at S_a (1st column), S_{sa} (2nd column), and S_{ta} (3rd column) frequencies, at the radial (1st row), North-South (2nd row) and East-West (3rd row) coordinate component. 248
A.0.3 The phase of the simulated displacements induced by NTOL at S_a (1st column), S_{sa} (2nd column), and S_{ta} (3rd column) frequencies, at the radial (1st row), North-South (2nd row) and East-West (3rd row) coordinate component. 249
A.0.4 The phase of the simulated displacements induced by CWSL at S_a (1st column), S_{sa} (2nd column), and S_{ta} (3rd column) frequencies, at the radial (1st row), North-South (2nd row) and East-West (3rd row) coordinate component. 249

B.0.1 The impact of non-tidal atmospheric pressure loading effects on the scale of the implied reference frame of the networks of IVS (upper-left), ILRS (upper-right), IGS (lower-left) and IDS (lower-right). The colorbars indicate the number of stations. 250
B.0.2 The impact of non-tidal ocean loading effects on the scale of the implied reference frame of the networks of IVS (upper-left), ILRS (upper-right), IGS (lower-left) and IDS (lower-right). The colorbars indicate the number of stations. 251
B.0.3 The impact of continental water storage loading effects on the scale of the implied reference frame of the networks of IVS (upper-left), ILRS (upper-right), IGS (lower-left) and IDS (lower-right). The colorbars indicate the number of stations. 251
B.0.4 The impact of the combined effect of non-tidal atmospheric pressure loading and continental water storage loading on the scale of the implied reference frame of the networks of IVS (upper-left), ILRS (upper-right), IGS (lower-left) and IDS (lower-right). The colorbars indicate the number of stations. 252

List of Tables

2.6.1 Elevation-dependent noise parameters injected in the Monte Carlo simulations of the different GNSS constellations. The ansatz employed is $\sigma_w = \alpha \csc(\varepsilon)$, and the input data are post-fit residuals of the operational multi-GNSS processing at GFZ Potsdam. 32

3.1.1 Optical refractivity constants (Ciddor, 1996; Ciddor and Hill, 1999). 49
3.3.1 Constants for the moist air compressibility factor expression. 56

4.1.1 Orbital altitude (average) of some satellite systems and individual satellites, of interest to space geodesy. 76
4.2.1 The impact of employing inconsistent gradient mapping function and gradient components. The graphs present the discrepancies between assembled asymmetric delays employing CH97, and BS98 with the hydrostatic (left) and non-hydrostatic mapping functions (right), at 3°, 5°, 7° and 10°, respectively. 91
4.2.2 Gradient mapping function coefficients estimated from ray-traced delays in ERA Interim. 93

5.2.1 The most widely used NTAL services along with their basic characteristics. For the abbreviations, see text. 141
5.3.1 The most widely used NTOL services along with their basic characteristics. For the abbreviations, see text. 144
5.4.1 The most widely used CWSL services along with their basic characteristics. For the abbreviations, see text. 152

6.4.1 Seasonal amplitudes and WRMS of the post-fit residuals of the EOP differences stemming from alternating the mapping functions (PMF, VMF1, and GFZ-PT), and the meteorological data used for the computation of d_h^z (raw in situ, GFZ-PT, ERAinML, and homogenized in situ), at the observation equation level in VLBI data analysis (IVS non-intensive sessions spanning the period 1979–2018). 177
6.5.1 The portion [%] of the VLBI (R) and GNSS (P) station networks where the gradient component linear temporal rates show statistically significant deviations with respect to ray-traced gradients. In the description row, first appears the a priori zenith delay source, and then the mapping function name. 184

7.1.1 The percentage of VLBI stations that contributed to ITRF2014 where there is a statistically significant seasonal amplitude (S_a, S_{sa}, S_{ta}) and a WRMS reduction (improvement) upon applying discrete loading models (NTAL, NTOL, and CWSL) developed in Chapter 5 using ERA Interim data. R, EW, and NS denote the radial, East-West, and North-South topocentric coordinate component, respectively. 190

7.1.2 The percentage of SLR stations that contributed to ITRF2014 where there is a statistically significant seasonal amplitude (S_a, S_{sa}, S_{ta}) and a WRMS reduction (improvement) upon applying discrete loading models (NTAL, NTOL, and CWSL) developed in Chapter 5 using ERA Interim data. R, EW, and NS denote the radial, East-West, and North-South topocentric coordinate component, respectively. 190

7.1.3 The percentage of DORIS stations that contributed to ITRF2014 where there is a statistically significant seasonal amplitude (S_a, S_{sa}, S_{ta}) and a WRMS reduction (improvement) upon applying discrete loading models (NTAL, NTOL, and CWSL) developed in Chapter 5 using ERA Interim data. R, EW, and NS denote the radial, East-West, and North-South topocentric coordinate component, respectively. 191

7.1.4 The percentage of GNSS stations that contributed to ITRF2014 where there is a statistically significant seasonal amplitude (S_a, S_{sa}, S_{ta}) and a WRMS reduction (improvement) upon applying discrete loading models (NTAL, NTOL, and CWSL) developed in Chapter 5 using ERA Interim data. R, EW, and NS denote the radial, East-West, and North-South topocentric coordinate component, respectively. 191

7.2.1 WRMS of the session-wise Helmert transformation parameters between VLBI solutions obtained employing `VieVS@GFZ` to analyze all the IVS rapid turnaround sessions, where no non-tidal loading, the EGLM, and the discrete loading model was applied at the observation equation level. 203

7.3.1 Seasonal amplitudes and WRMS of the post-fit residuals of the EOP differences between applying the discrete loading model or EGLM, and not applying any non-tidal loading model, at the observation equation level in VLBI data analysis (IVS rapid turnaround sessions spanning the period 2002–2018). 208

7.3.2 Seasonal amplitudes and WRMS of the post-fit residuals of the dUT1 differences [µs] between applying the discrete loading model or EGLM, and not applying any non-tidal loading model, at the observation equation level in VLBI data analysis of Intensive sessions. 211

B.0.1 The bias, temporal rate, scatter, annual amplitude and phase, as well as the WRMS of the post-fit residuals from the estimates of the 7- and 14-parameter similarity transformations employing the *NTAL* model developed in Chapter 5, and the station coordinates and the covariance matrices thereof assimilated into ITRF2014. Standard SINEX notation was used: R for VLBI, L for SLR, P for GNSS, and D for DORIS. 253

B.0.2 The bias, temporal rate, scatter, annual amplitude and phase, as well as the WRMS of the post-fit residuals from the estimates of the 7- and 14-parameter similarity transformations employing the *NTOL* model developed in Chapter 5, and the station coordinates and the covariance matrices thereof assimilated into ITRF2014. Standard SINEX notation was used: R for VLBI, L for SLR, P for GNSS, and D for DORIS. 254

B.0.3 The bias, temporal rate, scatter, annual amplitude and phase, as well as the WRMS of the post-fit residuals from the estimates of the 7- and 14-parameter similarity transformations employing the *CWSL* model developed in Chapter 5, and the station coordinates and the covariance matrices thereof assimilated into ITRF2014. Standard SINEX notation was used: R for VLBI, L for SLR, P for GNSS, and D for DORIS. 255

B.0.4 The bias, temporal rate, scatter, annual amplitude and phase, as well as the WRMS of the post-fit residuals from the estimates of the 7- and 14-parameter similarity transformations employing the *NTAL and CWSL* models developed in Chapter 5, and the station coordinates and the covariance matrices thereof assimilated into ITRF2014. Standard SINEX notation was used: R for VLBI, L for SLR, P for GNSS, and D for DORIS. 256

B.0.5 The bias, temporal rate, scatter, annual amplitude and phase, as well as the WRMS of the post-fit residuals from the estimates of the 7- and 14-parameter similarity transformations employing the *NTAL, NTOL, and CWSL* models developed in Chapter 5, and the station coordinates and the covariance matrices thereof assimilated into ITRF2014. Standard SINEX notation was used: R for VLBI, L for SLR, P for GNSS, and D for DORIS. 257

List of Abbreviations, Symbols and Nomenclature

ADVANTAGE	Advanced Technologies for Navigation and Geodesy
AGN	Active Galactic Nucleus
ANGL	accumulated non-tidal geophysical loading
ASD	Allan standard deviation
BMF	Berlin mapping functions
CRF	celestial reference frame
CWSL	continental water storage loading
DAC	dynamic atmospheric correction
DORIS	Doppler Orbitography and Radiopositioning Integrated by Satellite
ECMWF	European Centre for Medium Range Weather Forecasts
EGLM	empirical geophysical loading model
EOP	Earth orientation parameter
ERAinML	ERA Interim model levels
ERP	Earth rotation parameter
FGST	fast geodetic simulation tool
GFZ	GeoForschungsZentrum
GFZ-PT	GeoForschungsZentrum pressure temperature
GGFC	global geophysical fluid center
GGOS	global geodetic observing system
GMAO	global modeling and assimilation office
GLONASS	Globalnaya Navigazionnaya Sputnikovaya Sistema
GNSS	global navigation satellite systems
GPS	Global Positioning System
GRACE	gravity recovery and climate experiment
GSFC	Goddard space flight center
HCC	high cloud cover
IDS	international DORIS service
IERS	international Earth rotation and reference system serivce
IFS	integrated forecast system
IGS	international GNSS service
ILRS	international laser ranging service
ITRF	international terrestrial reference frame

ITRS	international terrestrial reference system
IVS	international VLBI service for geodesy and astrometry
IWV	integrated water vapour
LAGEOS	laser geodynamics satellite
LCC	low cloud cover
LGF	load Green's functions
LLN	load Love number
MCC	medium cloud cover
MGEX	multi-GNSS experiment
NASA	National Aeronautics and Space Administration
NEQ	normal equation system
NNR	no net rotation
NNT	no net translation
NTAL	non-tidal atmospheric pressure loading
NTOL	non-tidal ocean loading
NWM	numerical weather model
PMF	Potsdam mapping functions
PSD	power spectral density
PWLF	piecewise-linear function
QZSS	Quasi-Zenith Satellite System
SLR	satellite laser ranging
TCC	total cloud cover
TRF	terrestrial reference frame
VieVS@GFZ	GFZ version of the Vienna VLBI software
VGOS	VLBI global observing system
VLBI	very long baseline interferometry
VMF	Vienna mapping functions
WRMS	weighted root mean square
$d^z_{h(nh)}$	zenith hydrostatic (non-hydrostatic) delay
$G_{NS(EW)}$	North-South (East-West) gradient component
$mf_{h(nh)}$	hydrostatic (non-hydrostatic) mapping function
$S_{a(sa)}$	annual (semi-annual) frequency
$S_{1(2)}$	diurnal (semi-diurnal) frequency

1 Introduction

1.1 Overview

The study of the dynamics of the solid Earth and its fluid envelope (e.g., atmosphere, hydrosphere, and cryosphere) has been accommodated by the space geodetic data explosion raging for over two decades now. Studying the evolution of Earth's shape, orientation, and gravity field allows an indirect observation of climate evolution as the variable concentration of greenhouse gases affects them in addition to atmospheric temperature. Observing bedrock uplift in Greenland, length of the day shortening, gravity field signal weakening over West Antarctica, mean sea level rise, and integrated water vapour content increase (on average), are but a few climate change indicators made possible thanks to the prolific growth of geodetic research and infrastructure. However, there is a number of effects such as non-gravitational accelerations acting upon satellites, turbulent atmospheric refraction variations, finite stability of state-of-the-art frequency standards, and non-linear crustal deformation, that hinder drawing inferences from the available data. Some of these effects induce spurious systematic and/or random variations in the parameters of interest, for example, ground station and satellite coordinates, Earth orientation parameters (EOP), and gravity field spherical harmonics. The efficient treatment of such intricacies that typically involves their modelling based upon independent data sets and/or their estimation based on the relevant geodetic observations, has occupied the interest of geodesists, astronomers, and geophysicists over several decades.

To date, least-squares is the most popular estimator employed in geodesy, as it has charming properties in the context of statistical inference. Nevertheless, the urge for practical results often overshadows several theoretical aspects; being not robust, least-squares — among else — demands the reduced observations participating in the adjustment be solely subject to zero-mean random errors, which is rarely the case. Not accounting for the full spectrum of systematic effects in individual observing systems, yields results that may be precise but lack in accuracy when compared with results stemming from other observing systems. While more observations do not facilitate the reduction of systematics, they frequently provide the commodity of enabling the estimation of parameters that to an extent are capable of describing the effects that induce these errors. Nonetheless, these "nuisance" parameters often correlate with the parameters of interest (e.g., residual atmospheric delay and station height), thus obstructing the estimation of the latter.

To be able to harness the space geodetic data explosion, efficacious treatment of the identified error sources is a necessity; otherwise, this advantage remains latent. In this work, two error sources are studied: atmospheric refraction; and geophysical loading. In essence, atmospheric refraction is mainly induced by the varying atmospheric density, and causes signals that traverse Earth's atmosphere to do so along bent paths, at a slightly lower speed — that holds accepting the premise of geometric optics. Geophysical loading is generated by the mass redistribution within Earth's fluid envelope, and is mainly responsible for transient crustal displacements and gravity field perturbations, at a multitude of spatial and temporal scales. If not properly accounted, these effects compromise the integrity of geodetic products. The need to improve geodetic products in this regard has fueled an exciting area of interdisciplinary research with numerous implications in geodesy, geophysics, and meteorology.

1.2 Motivation and research objective

One application for space geodesy is the realization of the Global Geodetic Reference Frame (GGRF), that underpins, among else, Earth- and climate-related research; the importance of GGRF has been recognized by the United Nations General Assembly, on February 26th 2015 (A/RES/69/266). Therefore, efforts should be made to improve the GGRF further upon, with a goal to meet the Global Geodetic Observing System (GGOS) requirements; 1 mm in accuracy, and 1 mm dec^{-1} in stability (e.g., Gross et al., 2009). For instance, the geodetic community is in a quandary over the exact nature of the scale bias between very long baseline interferometry (VLBI) and satellite laser ranging (SLR), of almost 8 mm at the equator (distances measured by SLR are slightly smaller than distances measured by VLBI).

Atmospheric refraction and geophysical loading have been identified as major error sources since the dawn of space geodesy (e.g., Veis, 1960). Most developments in these fields build upon the seminal works of Marini and Murray (1973); Saastamoinen (1973); Gardner (1976) and Farrell (1972), who described the underlying theoretical concepts. Both effects are relevant in terms of reference system realization; to reduce the uncertainties of rates deduced from geodetic time series, the logging interval, the data span and the modulated noise are critical. To reduce the length of the time series necessary to obtain meaningful trends, the underlying noise must be reduced, thus atmospheric refraction effects and geophysical loading effects need to be well understood.

In modern geodesy, the treatment of atmospheric refraction is carried out at the observation equation level, that is, approximate corrections are applied to the observations directly. Prior to that, manifestations of space weather (ionosphere, plasmasphere, and thermosphere) are removed from the observations usually by means of multi-frequency combinations (e.g., Guier and Weiffenbach, 1960). The latter applies only to microwave-based techniques, for which the ionosphere is a dispersive (frequency-dependent) medium; lasers are only marginally affected. Notwithstanding the measurement noise amplification, such an approach removes ionospheric effects almost completely. Higher-order ionospheric corrections (e.g., Fritsche et al., 2005; Zus et al., 2017b) are applied based on models, as the combination of more than two frequencies considerably degrades the quality of observations. The electrically neutral atmospheric is a non-dispersive medium for microwave signals, but dispersive for lasers. Therefore, it is theoretically possible to considerably reduce the tropospheric delay effects from SLR and lunar laser ranging (LLR) measurements by combining simultaneous ranges at different frequencies (e.g., Wijaya and Brunner, 2011). However, low return rates and satellite signature effects render employing this attribute impractical in the framework of GGOS, for to obtain an improvement the precision of the normal points needs to improve by two orders of magnitude. Ergo, atmospheric delay effects for both microwaves and lasers should be mitigated in terms of modelling. In brief, the atmospheric delay may be decomposed into a contribution from dry gasses, and a contribution from water vapour. Variations of the former are mostly well understood, whereas the variations of the latter are very volatile both in space and time, are thus difficult to predict. State-of-the-art numerical weather models (NWM) are very accurate in describing dry gasses, but are still not accurate enough to provide reliable water-vapour-related corrections. While the propagation of signals in the optical band is not appreciably affected by water vapour (zenith delays rarely larger than 20 ps), accurate geodetic results from microwave-based techniques (e.g., VLBI, global navigation satellite systems GNSS, and Doppler Orbitography and Radiopositioning Integrated by Satellite DORIS) can only be obtained should a successful mitigation of water-vapour-induced effects be achieved (zenith delays typically exceed 1 ns). To achieve the highest accuracy in the data analysis of microwave-based systems, the estimation of corrections to the values obtained

by the models, from the observations themselves, is mandatory. No tropospheric parameters are typically estimated in SLR analysis. Thus, atmospheric delay corrections in SLR processing must be of the highest quality and void of any systematic errors, as the latter would propagate predominantly into the station position. For microwave techniques, in addition to an accurate a priori model, appropriate parameters need to be set up during the geodetic adjustment so that corrections may be estimated. In situ meteorological data of high quality are necessary for the former, a combination of good observation geometry and apt functional model is essential for the latter, and accurate mapping functions are necessary for both.

To meet the GGOS requirements, several aspects of the current method of accounting for atmospheric refraction in space geodesy, need to be revised and improved: the quality of in situ meteorological measurements; accurate alternatives in the absence of in situ observations; accurate ray-traced delays and mapping functions (corrections necessary to account for the increasing atmospheric delay with decreasing elevation angle, typically based on NWMs); and sensible atmospheric delay parameterization. In addition to these, there is a number of points that are not treated whatsoever, for example: atmospheric delay variations induced by the varying orbital altitude between different systems, or within a satellite pass; atmospheric asymmetries for lasers; frequency-dependence of optical mapping functions; and frequency-dependent atmospheric delay variations induced by the ionosphere altering the ray-path. Moreover, the relations between the atmospheric refraction effects of the four techniques that currently contribute to the realization of international terrestrial reference frame (ITRF), the so-called "atmospheric ties", should be better understood, to allow the combination of tropospheric parameters in addition to station coordinates and Earth rotation parameters in the framework of multi-technique combination. All aforementioned issues are addressed in this work.

Earth's deformation driven by geophysical loading is caused by masses largely external to the solid Earth applying pressure to the surface; not being perfectly rigid, the Earth deforms under the weight of the loads in a manner governed by its interior structural composition. The mass redistribution within the atmosphere, the oceans, and the continental hydrology, all spheres in constant flux, occurs at a broad spatio-temporal scale, thus exciting station displacement at a rich spectrum of responses. Tidal effects, predominantly oceanic, are modeled accurately as their detection is fairly easy; however, non-tidal effects, mainly atmospheric and hydrological, are more difficult to monitor for they largely depend on accurate monitoring and prediction of weather conditions and the hydrological cycle. However, as space geodetic accuracy improved, these subtle effects began to gain more prominence. In spite of non-tidal effects being recognized several decades ago (e.g., Schuh, 1987; Rabbel and Schuh, 1986; van Dam et al., 1994; van Dam and Herring, 1994), debates are still vigorous concerning the treatment thereof, with no consensus reached at the time of writing. This indecision is often attributed to the fact that no model yields an 100 % improvement in geodetic data analysis, and that differences between modelling approaches can be quite large (especially for hydrological loading). Furthermore, a number of issues are still unclear, for example: the isomorphic reference frame that should be used for each technique; the derivation of the load Love numbers; and the ocean response to atmospheric forcing.

Mass loading signals are ubiquitous in all space geodetic measurements; therefore, to effectively distinguish loading-induced deformation from signals induced by other geophysical processes, such as tectonic deformation, it is paramount that both tidal and non-tidal mass loading is accurately understood. This is one of the cases where more observations do not necessarily pave the way towards the solution. For example, the fact that daytime tracking of high-altitude satellites poses a challenge to modern SLR systems — thus yielding an imbalance in the ratio of observations during day and night, underlines the need for accurate models to describe effects

like tidal atmospheric loading. Moreover, differences between geophysical loading displacement predictions based on mass anomalies from atmospheric, oceanic, and hydrological loading models, and station displacements obtained by space geodetic measurements are immensely helpful as they reflect potential deficiencies in the mass anomaly fields, the geodetic analysis, and the assumed Earth structure. Modelling non-tidal effects is also important for chronometric leveling that utilizes optical atomic clocks (current relative clock stability uncertainty is 10^{-18}) to measure gravity potential differences (Leßmann and Möller, 2018). This work aspires to clarify some of these issues and to contribute to a decision in favor of applying non-tidal loading models at the observation equation level, by providing proof for an improvement attained by analyzing real and simulated geodetic observations of several space geodetic systems.

Despite the very high accuracy of space geodetic measurements, there is still a number of effects that are not completely understood; this is evident from discrepancies between parameters that can be estimated from more than one space geodetic sensor (e.g., Earth rotation variations, station displacements, and water vapor distribution aloft stations). To thoroughly investigate atmospheric refraction and geophysical loading on space geodetic observations, it is necessary to isolate them from others that are not understood and could potentially mask their influence on the geodetic measurement. To this end, software should be developed capable of realistically and consistently simulating VLBI, GNSS, SLR, and DORIS observations.

1.3 Thesis outline

This section outlines the structure of a series of efforts toward the improvement of space geodesy by refining atmospheric refraction and geophysical loading modelling, and by assessing these models in the analysis of real and simulated geodetic measurements.

Chapter 2 is dedicated to the concise description of the space geodetic techniques that currently contribute to realization of the terrestrial and celestial reference system. The observing systems and the related analysis of VLBI, SLR, GNSS, and DORIS observations are presented. The basic observation equations and the adjustment of space geodetic measurements employing batch least-squares and a Kalman filter coupled with a Rauch-Tung-Striebel smoother is presented. Since the state-of-the-art geodetic analysis features a high level of complexity that renders the attribution of incompatibilities across the techniques futile, a Monte Carlo simulator was developed to facilitate the comprehension of the sensitivity of the adjustment to the observation geometry and to the modelling of weather-induced variations. To study technique-specific intricacies as well as vexing issues in the inter-technique combination, simulations are crucial as they furnish results free of unknown errors, so long as they are carried out consistently.

Chapter 3 introduces the basic principles underlying wave propagation through Earth's atmosphere relevant to the subsequent chapter. A Maxwellian derivation of the eikonal equation is presented, followed by the ray-tracing method (variational approach). The calculation of the refractivity tensor as well as the position operator in a state-of-the-art NWM on account of a non-ideal equation of state is presented as well. The process to acquire homogenized in situ meteorological observations, pertinent to the modelling of atmospheric refraction (applicable to VLBI, SLR, GNSS, and DORIS) and thermal expansion (applicable only to VLBI) is presented. Special emphasis is placed on the computation of the relevant time series from state-of-the-art NWMs. The complete meteorological archive of VLBI and SLR/LLR has been homogenized. All breakpoints detected have been confirmed with multiple NWMs, and some of them have also been confirmed by metadata, for example, a pressure bias at all 10 telescopes comprising the very long baseline array (VLBA) and a significant jump in the pressure log of the SLR station at Wettzell.

Chapter 4 deals with the development of ray-traced delays, mapping functions and gradients for GNSS, SLR, VLBI, and DORIS, as well as inter- and intra-technique atmospheric ties. A number of atmospheric delay perturbations are treated therein such as the impact of varying the radiation frequency, considering the ionosphere, and altering the orbital altitude. The description of the estimation of the Potsdam and Berlin mapping functions and gradients falls under this chapter. The development of a new analytical model for meteorological parameters of geodetic interest, GFZ-PT (pressure, temperature), is carried out herein. Moreover, new developments have been achieved in the area of inter- and intra-technique atmospheric ties, thereby laying the framework of multi-technique combination employing tropospheric estimates in addition to local and global ties.

Chapter 5 describes the development of models to simulate the displacement of an elastic half-space subjected to concentrated load induced by mass transport within Earth's fluid envelop. The development of tidal and non-tidal atmospheric, non-tidal ocean, and continental hydrological loading is carried out herein. The impact of the elastic Earth model based on which the related load Love numbers are derived, the ocean response to atmospheric (pressure and wind) forcing, as well as the spatio-temporal resolution of the underlying mass anomaly fields is studied. Furthermore, a new model featuring long-wavelength simulated geophysical loading displacements and the process noise induced by high-frequency displacements, the empirical geophysical loading model EGLM, is introduced in this chapter.

Chapter 6 is devoted to a comprehensive treatment of atmospheric refraction in space geodetic data analysis. Investigations were carried out on the expansion of the SLR parameter space to account for uncalibrated meteorological sensors, as well as mismodelling atmospheric asymmetries. The impact of alternating mapping functions, and the meteorological data source on station coordinates, baseline lengths, datum perturbation parameters, EOPs, as well as the integrated water vapour trends, was assessed by analyzing real and simulated VLBI and GNSS observations. The impact of not accounting for the lower orbital altitude in the derivation of atmospheric corrections for DORIS is demonstrated on the station coordinates and the implied reference frame. The quality of some of the atmospheric refraction models developed in Chapter 4 is evaluated.

Chapter 7 presents the impact of applying some of the geophysical loading models developed in Chapter 5 in the analysis of real (VLBI), and simulated (VLBI, SLR, GNSS, and DORIS) observations, at both the parameter and observation equation level, on station coordinates, the implied station network, and Earth orientation in inertial space. In a geodetic adjustment where the celestial component (radio source coordinates, satellite orbits), the terrestrial component (station coordinates), and Earth's orientation, is estimated, non-tidal loading affects mainly the station height. Nevertheless, applying the same loading models to different space geodetic techniques yields different seasonal variations in the station coordinates and the datum perturbation parameters.

Finally, a recapitulation of the most important results obtained herein, some conclusions, recommendations for the international geodetic services, and ideas for further research work are given in Chapter 8.

2 Space geodetic techniques

The main purpose of this chapter is to provide an overview of the space geodetic techniques that as of 2018 contribute to the realization of the international terrestrial reference frame (ITRF), that is, very long baseline interferometry (VLBI, cf. Sec. 2.1), satellite laser ranging (SLR, cf. Sec. 2.2), global navigation satellite systems (GNSS, cf. Sec. 2.3), and Doppler orbitography and radiopositioning integrated by satellite (DORIS, cf. Sec. 2.4). Real and simulated data from these techniques are used in Chapter 6 and Chapter 7 to assess the models developed in Chapter 4 and Chapter 5. A concise description of the concepts behind each technique as well as the observation equations underlying the estimation of parameters of geodetic interest is presented to elucidate the characteristics shared across the techniques, and to identify the points of contrast. Section 2.5 provides the fundamental setting for the geodetic adjustment as well as the application of the models developed in Chapter 4 and Chapter 5, at the different analysis levels, that is, the observation equation, the normal equation, and the estimated parameter level. Section 2.6 describes the rigorous simulation of geodetic observations with the Monte Carlo method, employing the related observation equations, and respecting the technique-specific issues such as the fact that laser ranging is hindered in the presence of clouds. This is the first time, the simulation of geodetic observations considers ray-traced delays taylored for the different observing systems. The consideration of clouds is deliberate for it aims at emphasizing the fact that the scale bias between a reference frame realized employing solely laser observations (SLR/LLR) and another employing solely microwave observations (e.g., VLBI) is made worse by the fact that no observations in the presence of thick cloud cover are assimilated to the former.

2.1 Very long baseline interferometry

For a comprehensive end-to-end review of the VLBI technique (Matveenko et al., 1965; Hinteregger et al., 1972), the interested reader is referred to Sovers et al. (1998); Schuh and Behrend (2012); Heinkelmann (2013); Schuh and Böhm (2013); Nothnagel (2019) as well as the numerous references therein, that served as the main material for compiling this section.

Synchrotron radiation produced by relativistic jets driven by the gravitation of supermassive black holes is detected by VLBI for more than half a century. The angular position of these cosmological (redshift ranging between zero and five), point-like and radio-loud sources, also known as active galactic nuclei (AGN) usually features neither proper motion nor parallax, thus rendering AGN suitable for the realization of a reference system upon which positioning on Earth as well as navigation in space is conducted. Without loss of generality, the triangle formed by the trajectory of a signal emitted from the oscillator onboard a GPS satellite to the stations at the ends of a single baseline ($\mathbf{x_B} - \mathbf{x_A}$) degenerates to a rectangular, should an AGN be considered; AGN that constitute the space segment of VLBI are so distant that the assumption of a planar wavefront is sound.

Resuming the single baseline paradigm, let a radio signal emitted from an AGN be recorded at both stations. Since the structure of the signal is unknown and the desired accuracy for the baseline length is at the mm-level, very accurate time-tagging of the quasar signal (in

essence white noise) is necessary. A high accuracy level is achieved by utilizing among else (cf. Sec. 4.1.3) very stable low-phase-noise frequency standards — active hydrogen masers (AHM), ASD = 10^{-14}@50 min (e.g., Herring et al., 1990) — to provide a reference signal that allows the acquisition of time-tagged signal information. To measure the influence of Earth's ionosphere and the ionized interstellar medium on signal propagation, the AGN's radiation is recorded (inescapably together with artificial noise induced by the receiver itself and other man-made sources in the vicinity of the telescope) in at least two widely separated frequencies, in particular several channels (or sub-bands) within each band; in the current so-called legacy observations these are usually 6 for S-band (2.2–2.4 GHz) and 8 for X-band (8.2–8.9 GHz). While the vast majority of geodetic VLBI observations have been carried out in the S/X system, higher frequencies are now available (K-, Ka-, and Q-band) that potentially offer benefits over the old system such as resilience to source structure effects. Dual frequency observations are motivated from the dependence of the ionospheric delay upon frequency, thus rendering a combination capable of mitigating the plasma effect, at the expense of amplified noise. In the state-of-the-art VLBI Global Observing System (VGOS) (e.g., Petrachenko et al., 2009; Niell et al., 2018) four bands (16 sub-bands) are utilized, in the frequency range of 2–14 GHz. Past these signals being recorded, they are subjected to cross-correlation (in parallel) and within the bandwidth synthesis process, the estimates of group (τ_g) and phase (τ_p) delays are obtained as well as the time derivatives thereof ($\dot{\tau}_g$ and $\dot{\tau}_p$) from fringe-fitting by maximizing the delay resolution function (post–phase-rotation summed power of cross spectrum, e.g., Takahashi et al. (2000)).

In geodetic VLBI analysis, the main observables are the ionosphere-free delays that are related to the delays within each band as follows

$$\tau_{[g/p][S/X]} = \tau^{if} + \tau_{ion}(f_{[S/X]}) + \tau_{ins}, \tag{2.1.1}$$

where τ_{ion} is the propagation delay difference induced by the ionosphere (4.1.9), a function of the ionospheric effective frequencies that differ for the group and the phase, and τ_{ins} is the instrumental delay difference. The mitigation of the plasma effects is carried out by the so-called ionosphere-free linear combinations

$$\begin{aligned} \tau^{if}_{gXgS} &= \frac{f^2_{gX}\tau_{gX} - f^2_{gS}\tau_{gS}}{f^2_{gX} - f^2_{gS}}, \quad \tau^{if}_{pXpS} = \frac{f^2_{pX}\tau_{pX} - f^2_{pS}\tau_{pS}}{f^2_{pX} - f^2_{pS}}, \\ \tau^{if}_{pXgS} &= \frac{f^2_{pX}\tau_{pX} - f^2_{gS}\tau_{gS}}{f^2_{pX} - f^2_{gS}}, \quad \tau^{if}_{gXpS} = \frac{f^2_{gX}\tau_{gX} - f^2_{pS}\tau_{pS}}{f^2_{gX} - f^2_{pS}}, \end{aligned} \tag{2.1.2}$$

among which the so-called bandwidth synthesis[1] delay τ^{if}_{gXgS}, is the most common. Despite the fact that the precision of the pure phase delays is much higher (at least an order of magnitude), their use is precluded by challenging issues stemming from the ambiguity resolution over long baselines. Combining delays as in (2.1.2) inescapably combines the τ_{ins} thereof, which is of no concern as this is absorbed by the constant term of the clock function. Mitigating the ionospheric delay in such a fashion requires higher SNR — SNR is inversely proportional to the group delay uncertainty — during observations compared to obtaining the ionospheric delay corrections externally, e.g., from global maps of ionospheric total electron content[2]. For instance, in experiment `IVS-R1888`, 99.5 % of X-Band group delay observations have smaller uncertainties

[1] Bandwidth synthesis is a technique where a wide effective bandwidth is obtained from the combination of widely-separated narrow-band channels. This is necessary because the group delay accuracy improves with increasing bandwidth, and recording capabilities are finite (e.g., Rogers, 1970; Kondo and Takefuji, 2016).

[2] For example, see https://sideshow.jpl.nasa.gov/pub/iono_daily/gim_for_research/.

compared to the respective S-Band observations, which is related to the fact that in 79.9 % of the observations the SNR in X-band is larger compared to the SNR in S-Band. Performing error propagation in (2.1.2) shows the uncertainty of τ^{if}_{gXgS} is larger in 100 % of the observations, compared to X-Band, and smaller in 99.4 % of the observations, compared to S-Band.

Simply put, accounting only for the geometric delay and neglecting other propagation delay effects, the time-of-arrival difference ($\tau \geq 0$ by convention) of the wavefront emitted by an AGN to an antenna pair is the cathetus of the right triangle built by the two stations (hypotenuse) and the projection thereof in the direction of $\hat{\mathbf{k}}$. It reads (e.g., Schuh, 1987; Sovers and Jacobs, 1994)

$$c\tau = (\mathbf{x_B} - \mathbf{x_A}) \cdot \hat{\mathbf{k}}, \tag{2.1.3}$$

where the radio source unit vector is $\hat{\mathbf{k}} = -\begin{bmatrix}\cos(\alpha)\cos(\delta) & \sin(\alpha)\cos(\delta) & \sin(\delta)\end{bmatrix}^\top$, with the coordinates (α, δ) denoting the right ascension and declination of the radio source in a CRF. Nevertheless, (2.1.3) fails to describe a number of effects that act upon the signal during its journey across the interstellar medium (gravitational and ionizing effects), the Solar system, Earth's atmosphere, as well as the receiving system of the radio telescopes. As VLBI is a differential technique, many effects that are common to all stations constituting the radio interferometer, cannot be detected and are thus mutually exclusive. Other effects such as the fact that AGN are not always point-like[3] are dependent upon the observation geometry and must be modelled (e.g., Charlot, 1990; Anderson and Xu, 2018). Accounting for a number of geophysical and instrumental effects, the basic delay reads

$$\tau = \tau_{geom} + \tau_{rel} + \tau_{ion} + \tau_{atm} + \tau_{ins} + \tau_{ant} + \tau_{clk} + \tau_{tide} + \tau_{load} + \epsilon. \tag{2.1.4}$$

The geometric delay in the Solar system barycentric (SSB) frame is

$$\tau_{geom} = -\frac{\hat{\mathbf{k}} \cdot (\mathbf{Q}(t_A)\mathbf{R}(t_A)\mathbf{W}(t_A)\left(\mathbf{x_B}(t_A) - \mathbf{x_A}(t_A) + \mathbf{x_B}(t_B) - \mathbf{x_B}(t_A)\right))}{c(1 - \hat{\mathbf{k}} \cdot \mathbf{v_2})}, \tag{2.1.5}$$

where $\mathbf{v_2}$ is the velocity of station B in SSB. This quantity τ_{geom} must be subjected to a Lorentz transformation accounting at least for yearly and daily aberration. The motion of the celestial intermediate pole (CIP) in a TRF, that is, polar motion, is described by the product of three orthogonal rotation matrices[4] adopting the non-rotating origin formalism (e.g., Petit and Luzum, 2010)

$$\mathbf{W}(y_p, x_p, s) = \mathbf{R_3}(-s)\mathbf{R_2}(x_p)\mathbf{R_1}(y_p), \tag{2.1.6}$$

where $x_p(t)$ and $y_p(t)$ are the so-called polar coordinates of the CIP, and $s(t, x_p, y_p)$ is the terrestrial intermediate origin (TIO) locator necessary to realize the instantaneous prime meridian (Capitaine, 2000; Capitaine et al., 2003). Figure 2.1.1 illustrates the evolution of polar motion

[3] Source structure must be accounted in the reduction of the related observations $\hat{\mathbf{k}}$. Ideally, it has to be accounted for the scheduling and in the correlation process as it can affect the bandwidth synthesis especially for very long baselines (M. Xu, personal communication).

[4] Given any angle θ, the relevant rotation matrices are $\mathbf{R_1}(\theta) = \begin{bmatrix}1 & 0 & 0\\ 0 & \cos(\theta) & \sin(\theta)\\ 0 & -\sin(\theta) & \cos(\theta)\end{bmatrix}$, $\mathbf{R_2}(\theta) = \begin{bmatrix}\cos(\theta) & 0 & -sin(\theta)\\ 0 & 1 & 0\\ \sin(\theta) & 0 & \cos(\theta)\end{bmatrix}$, and $\mathbf{R_3}(\theta) = \begin{bmatrix}\cos(\theta) & \sin(\theta) & 0\\ -\sin(\theta) & \cos(\theta) & 0\\ 0 & 0 & 1\end{bmatrix}$. It is $(\mathbf{R_i}(\theta))^{-1} = (\mathbf{R_i}(\theta))^\top = \mathbf{R_i}(-\theta)$.

over the past half-century.

Earth's rotation around the conventional ephemeris pole (CEP) axis is described by

$$\mathbf{R}(\theta) = \mathbf{R_3}(\theta), \tag{2.1.7}$$

where $\theta(t)$ is the Earth rotation angle between the celestial intermediate origin (CIO) and the TIO on the CIP equator. It is defined by

$$\theta = 2\pi 0.7790572732640 + 0.00273781191135448(JD - 2451545.0), \tag{2.1.8}$$

where JD is the $UT1$ Julian date fraction (θ is a linear function of $UT1$). The difference between $UT1$ and the time scale driven by atomic clocks (UTC) is $dUT1$ and can only be estimated accurately by VLBI. Satellite techniques (e.g., GNSS and SLR) are capable of measuring only the time derivative thereof, that is, the length of day LOD, provided that orbital perturbations induced by e.g., solar radiation pressure, are accurately mitigated (e.g., Rothacher et al., 1999). The LOD is the excess time in respect of the mean solar day

$$dLOD = -\frac{\partial(UT1 - UTC)}{\partial t} = LOD - 86\,400\,\mathrm{s}. \tag{2.1.9}$$

Both LOD and $dUT1$ are related to the axial component of the excitation function: $\chi_3 = -dLOD/86400 + const$. The motion of the celestial intermediate pole (CIP) in a CRF is described by

$$\mathbf{Q} = \mathbf{NP}, \tag{2.1.10}$$

that is, a composite of the nutation $\mathbf{N}$ and precession $\mathbf{P}$. $\mathbf{N}$ is a function of nutations in ecliptic longitude $\Delta\psi(t)$, mean ϵ and true obliquity $\Delta\epsilon(t)$ of the ecliptic of day

$$\mathbf{N}(\Delta\epsilon, \Delta\psi, \epsilon) = \mathbf{R_1}(-(\epsilon + \Delta\epsilon))\mathbf{R_3}(-\Delta\psi)\mathbf{R_1}(\epsilon). \tag{2.1.11}$$

The precession is calculated as follows

$$\mathbf{P}(z, \Theta, \zeta) = \mathbf{R_3}(-z)\mathbf{R_2}(\Theta)\mathbf{R_3}(\zeta), \tag{2.1.12}$$

where the Newcomb angles z, Θ, and ζ (Lieske et al., 1977) quantify the orientation of the mean equator and equinox at t in respect of the equator and equinox of J2000. Nevertheless, it is more convenient to express the rotation due to nutation and precession as follows (Capitaine, 2000)

$$\mathbf{Q} = \begin{bmatrix} 1 - aX^2 & -aXY & X \\ -aXY & 1 - aY^2 & Y \\ -X & -Y & 1 - a(X^2 + Y^2) \end{bmatrix} \mathbf{R_3}(S), \tag{2.1.13}$$

where S is the CIO locator, $a \approx 0.5 + 0.125(X^2 + Y^2)$ (at 1 µas precision level), $X = \psi \sin(\epsilon_0)$, and $Y = \epsilon$. The second term in (2.1.4), τ_{rel} accounts for a number of general and special relativistic effects, e.g., the Shapiro delay, and the space-time curvature (deflection) of a signal propagating in the neighbourhood of a massive body (e.g., Sun, Earth, and Jupiter). The sum of τ_{geom} and τ_{rel} comprise the so-called theoretical delay.

The ionospheric delay τ_{ion} is extremely small owing to the fact that the 1st order ionospheric delay describing more than 99 % of ionospheric refraction has already been mitigated by the ionosphere-free linear combination. Nevertheless, there are higher order terms not considered

in (2.1.2). For the frequencies of geodetic VLBI, the impact of higher order terms is mostly well below the 0.5 mm level and can thus be safely neglected. Hawarey et al. (2005) confirmed that the maximum change the consideration of this effect can bring is about 0.5 mm on global baselines, a difference below the noise level reported in the Goddard Mark III databases[5]. This picture will not change as the additional bands envisaged for geodetic observations will feature only higher frequencies (2–18 GHz). The excess atmospheric delay induced by ray-bending of the signals prior to their propagating in the electrically neutral atmosphere can also be neglected as

The atmospheric delay τ_{atm} (also known as tropospheric delay) is one of the most studied still least understood impactful effects in (2.1.4). Due to the fact that it is fairly easy to predict the delay induced by dry gases (90 % of the effect) based on in situ meteorological observations, for they abide to the hydrostatic equilibrium, it is convenient to decompose τ_{atm} either into a hydrostatic and a non-hydrostatic component, or a dry and a wet component. Chapter 4 provides an exhaustive discussion on the best approaches to account for this effect in geodetic data analysis. In VLBI data analysis, usually the zenith non-hydrostatic (or the wet) delay component is estimated based on the interferometric delays, as well as a first order harmonic function that describes the behaviour of the delay as a function of azimuth. There are other ways to model the non-hydrostatic delay e.g., supply corrections obtained from independent instruments such as a neighbouring GNSS station or a water vapor radiometer. However, these corrections might contain uncalibrated errors; for instance, the latter is incapable of providing delays in the event of precipitation (e.g., saturation issues) as well as at low elevation angles. Another alternative is to obtain the relevant quantities based on NWM data and a ray-tracing algorithm. Small-scale refractivity variations in the troposphere, that is, atmospheric turbulence (e.g., Tatarskiĭ, 1971; Nilsson and Haas, 2010), are not considered in the deterministic model as the current integration time (scan) is long enough so that these fluctuations dissipate. As of this writing, the best approach to mitigate τ_{atm} — adopting the assumption that the refractivity field varies linearly in space and the time variations thereof are describable by piecewise linear functions (PWLFs) i.e., linear splines — is to utilize a priori information from an accurate NWM such as ERA5 and still estimate zenith non-hydrostatic delays and gradient vector components as loosely constrained PWLFs with e.g., hourly intervals. Ideally, the stencil should be dynamic to avoid multicollinearity induced

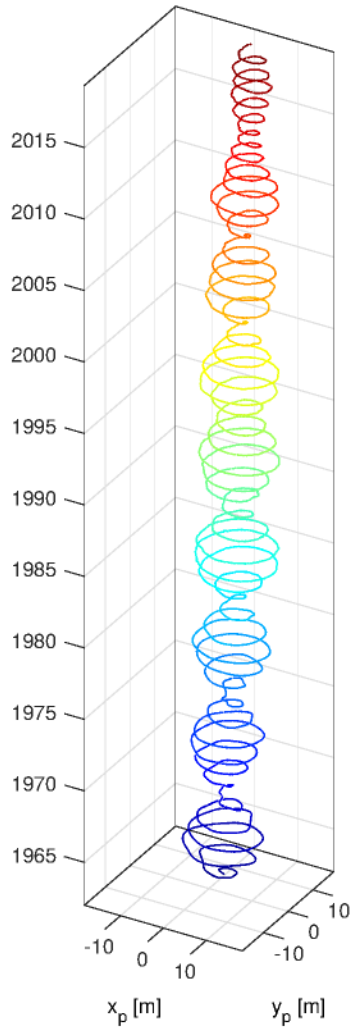


Figure 2.1.1: Polar motion helix drifting away from the CIO ($x_p = y_p = 0$ m). Shown are series with respect to the IAU 2006/2000A precession-nutation model and consistent with ITRF2014, EOP 14 C04.

[5] ftp://cddis.nasa.gov/vlbi/ivsdata/db/

by the estimated parameters being set up needlessly close. Of course, in sessions where the redundancy is not high enough, estimating tropospheric parameters will degrade the quality of the solution; not estimating tropospheric parameters and instead fixing them to NWM-derived parameters in such cases is of clear benefit.

The instrumental delay τ_{ins} is the difference between the signal propagation from the point of injection of the phase calibration impulses to the formatter (quantizes the input digital signal with precise time tagging) at the two radio telescopes. On the ideal case, τ_{ins} is provided by the phase calibration system. However, there is a number of spurious signals (also known as spurs in this context) that potentially affect τ observations by as much as 50 ps (Petrov, 2000). According to Corey (2012), the spurs stem from hydrogen-maser-locked signals, phase calibration images/intermodulation/saturation, secondary injection, polarization leakage, and others. Kiuchi et al. (1997) proposed to measure τ_{ins} with the zero baseline interferometry method. Since instrumental delays are station-dependent, they can be absorbed (to a certain extend) by the time-dependent clock offset estimate during the geodetic adjustment.

The time-tagging accuracy (thus the quality of the hydrogen maser) directly affects the coherent integration time, the correlator synchronization, and thus the accuracy of parameters estimated from analyzing a VLBI experiment, e.g., shorter integration intervals lead to more observations, that in turn provide better decorrelation between the estimated parameters (e.g., Nothnagel et al., 2018). Inaccuracies in this time-tagging together with the imperfect synchronization of the station clocks, induces the τ_{clk} term in (2.1.4). This delay is usually parameterized as the sum of two functions of time; a 2nd order linear differential equation (in practice a 2nd degree polynomial) for the entire course of the experiment, and a PWLF for the high-frequency instabilities usually resolved hourly. At a given time t the delay induced by clock mis-synchronization depends upon the individual clock functions T^A and T^B, and reads

$$\begin{aligned}\tau_{clk}(t) = &\left(T_0^B + T_1^B(t-t_0) + T_2^B(t-t_0)^2 + T^B(t_0) + T^B(t_i)\frac{t-t_{i-1}}{t_i-t_{i-1}} + T^B(t_{i-1})\frac{t_i-t}{t_i-t_{i-1}}\right)\\ &- \left(T_0^A + T_1^A(t-t_0) + T_2^A(t-t_0)^2 + T^A(t_0) + T^A(t_i)\frac{t-t_{i-1}}{t_i-t_{i-1}} + T^A(t_{i-1})\frac{t_i-t}{t_i-t_{i-1}}\right),\end{aligned} \tag{2.1.14}$$

where T_0^A is the clock offset, T_1^A is the clock frequency offset, T_2^A is clock frequency drift, and T^A is the clock function at station A. So, if in a 24-hour session no clock breaks occur and a 60-minute interval is adopted for the PWLF, $25+3$ clock parameters have to be estimated for all stations save for the one chosen to serve as the reference. Due to the fact that clock stability is related to the stability of the ambient temperature in the room where the active hydrogen maser lies (Parker, 1999), the estimation of diurnal (and semi-diurnal) harmonic terms instead of the PWLF described in (2.1.14) is a choice with physical meaning that also reduces the unknown parameters in the geodetic adjustment (J. Anderson, personal communication). Modern AHMs [6] have a sensitivity within the operating temperature range of about $1 \times 10^{-14}\,^{\circ}\mathrm{C}^{-1}$ in terms of ASD. Moreover, Plank et al. (2017) reported that clock breaks may be induced by high currents in the co-located air conditioning system compressor. Sometimes, in addition to station-dependent clock parameters, it is beneficial to estimate baseline-dependent clock offsets to absorb several uncalibrated instrumental and correlator errors in the data acquisition system (e.g., Petrov et al., 2009), including but not limited to unmodelled source structure effects and group delay ambiguity

[6] https://www.vremya-ch.com/russian/index.html

resolution artifacts[7]. Figure 2.1.2 illustrates the occurrence of baseline-dependent clock offsets in the IVS archive, for the baselines with the largest number of group delay observations.

Effects such as the thermal deformation of the radio telescopes, the antenna axis offsets, and the gravitational sag fall under τ_{ant} in (2.1.4). Thermal deformation induces an artificial annual signal (with an amplitude of $\approx 1\,\mathrm{mm}$) on the network scale of the implied reference frame (e.g., Wresnik et al., 2007). Structural deformation induced by gravitational loading, that is, sag, contributes to discrepancies detected in the inter-technique comparison. The effect of gravitational sag is dependent upon the orientation of the VLBI antenna in a topocentric frame, that is, elevation and azimuth, as well as the antenna's response to loading forces and varies the time delay between the receiver and the antenna's reference point. The axis offset induces an effect similar to the phase center variations in GNSS, which is indistinguishable from the station displacement in the radial coordinate component. Therefore, as it is difficult to infer this parameter — different for the individual stations as well as station types (azimuth-elevation, X-Y, equatorial mount) — from the analysis of a single VLBI experiment, the axis offsets may be supplied externally (e.g., local surveys). Nevertheless, there might be mm-level disagreement between the axis offsets estimated by a global solution of all VLBI observations and local surveys due to unmodelled non-linear station position variations induced by geophysical loading effects, inaccuracies in the tropospheric models (Wade, 1970; Nilsson et al., 2017a).

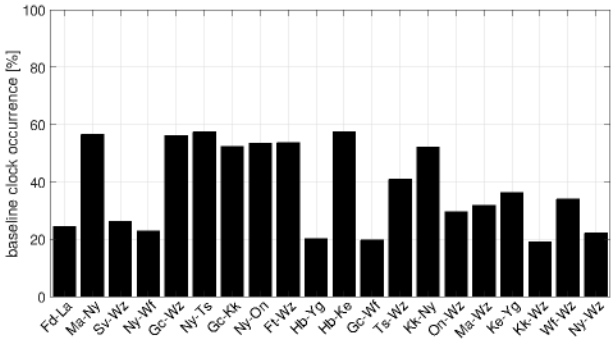


Figure 2.1.2: The occurrence of baseline-dependent clocks in VLBI data analysis with `Solve` (`./Solve/BaselineClockSetup.nc` in the `vgosDB` directory structure) for the 20 baselines that have the largest number of observations in the IVS archive (1979–2019).

The crust upon which radio telescopes are based is deforming. This deformation is a manifestation of numerous geophysical processes such as tectonic plate motion, solid Earth tides, ocean loading, solid and ocean pole tide loading, permanent tide, tidal atmospheric loading (cf. Sec. 5.2.1), non-tidal atmospheric-oceanic-hydrological loading (cf. Chapter 5), rotational deformation due to polar motion, and postglacial rebound. The tidal terms fall under τ_{tide} and the loading terms fall under τ_{load}.

Figure 2.1.3 illustrates the global network of radio telescopes that contributed to the realization of the latest terrestrial reference system. Shown in Fig. 2.1.3 is also the number of the stations that have contributed most observations in geodetic VLBI (based on data stored at the IVS and QUASAR servers).

2.2 Satellite laser ranging

A review on SLR can be found in Seeber (2003), as well as Combrinck (2010); Degnan (2013); Appleby et al. (2016); Schreiber and Kodet (2017); Exertier et al. (2018); McGarry et al. (2018), and references therein. These served as the main material for compiling the current section.

SLR differs from the other space geodetic techniques described in Chapter 2 as it is a realization of the Michelson interferometer experiment thus performing a two-way measurement

[7] http://astrogeo.org/petrov/discussion/basdep_clo/basdep_clo.html

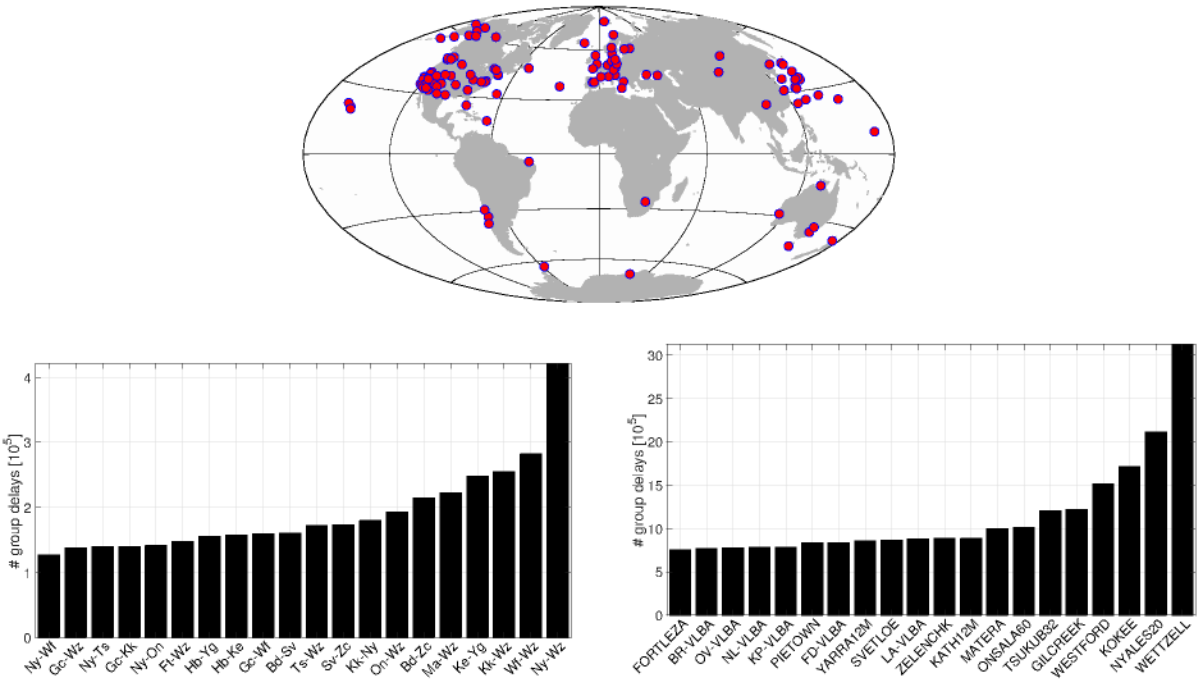


Figure 2.1.3: The network of all radio telescopes that contributed to ITRF2014 (upper row). The baselines (lower left) and stations (lower right) that as of fall 2018 have successfully participated in most observations carried out in the framework of IVS and QUASAR, based on `vgosDB` and `NGS` data (right). The description for the two- and eight-letter station codes are in `ns-codes.txt`.

(station-satellite-station) and operating in the optical regime (532 nm in most cases). The latter renders the capability of the system to perform observations dependent upon mutual visibility and in turn incapable of performing observations under cloudy weather conditions. Short high-energy mode-locked laser pulses (typically 10–200 ps, 1–2 kHz repetition rates) are emitted from ground-based stations towards corner cube reflectors (CCR) on satellites (e.g., Exertier et al., 2018). The design and the configuration of the retro-reflectors is such that the direction of the major component of the reflected wave in 3D-space is identical to that of the incident radiation. Should the retro-reflector be on the Moon (or other planets), the related processing falls under Lunar laser ranging (interplanetary laser ranging). All observations that involve active laser measurements (Maiman, 1960) to artificial satellites constitute the vast SLR archive. The first successful SLR return ever was recorded at NASA's Goddard Space Flight Center (GSFC) in Greenbelt, Maryland, employing the retro-reflectors onboard the satellite Beacon Explorer B (BE-B) in late 1964. This thesis deals only with SLR.

There is a large variety of satellite types being observed by SLR; spherical satellites such as LAGEOS (laser geodynamics satellite) -1 and -2, and spacecraft equipped with retro-reflectors of sufficient optical cross section such as Jason 2 or the GRACE-FO mission. In both cases the target is fairly inexpensive in comparison to VLBI antennas; in the former case spherical passive satellites can orbit Earth for several decades without requiring any maintenance, in the latter case, the cost installing a retro-reflector on any satellite is rather low compared to the payload cost. Figure 2.2.1 illustrates the satellites to which most ranges are aimed at, based on the normal points to 176 targets published by the ILRS (as of early 2019). These vehicles are being tracked by a network of observatories equipped with solid state lasers, most of which operate at 532 nm (maximum quantum efficiency). Some stations operate intermittently at other optical frequencies in addition (e.g., Zimmerwald). However, infrared detectors have proven to have lower accuracy

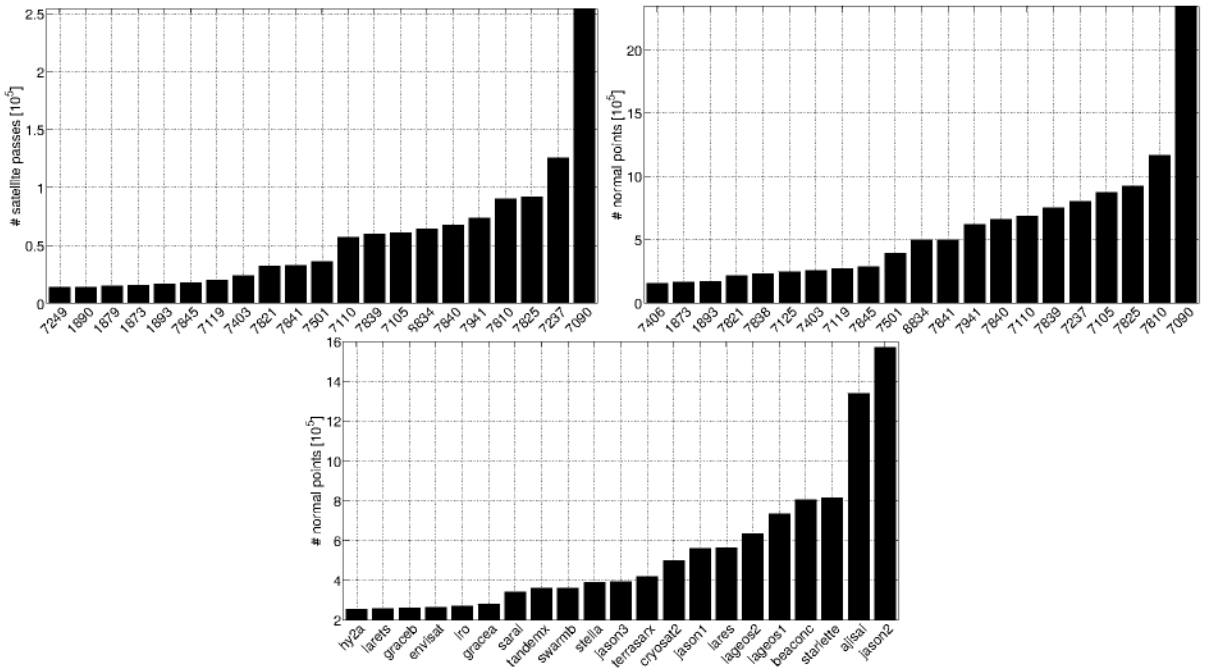


Figure 2.2.1: On the upper left shown are the CDP codes of the stations that have observed most satellite arcs, on the upper right shown are the stations that carried out most of the normal point observations (geodetic observable), and on the lower row shown are the satellites to which most ranges have been achieved, over the last decade; 19 % of the ranges stem from Yarragadee (7090), and 10 % of the ranges were towards Ajisai (2nd best). Both graphs were generated based on ILRS normal point data.

compared to those operating at 532 nm. Figure 2.2.1 depicts all stations[8] the observations of which were assimilated for the latest TRF (cf. Fig. 2.2.2). Since SLR observatories can track only one satellite at a time and several satellites are visible at any moment, the ILRS has suggested a tracking priority[9] where satellites at a low Earth orbit and a low inclination feature higher. Of course, allowances should be made occasionally for missions at a critical phase (e.g., post-launch). This list is also subject to the scientific interests of the individual stations e.g., the sole source of calibration for GLONASS system ephemeris stems from SLR, therefore Russian stations observe GLONASS space vehicles much more often than other stations.

Figure 2.2.1 also demonstrates the fact that the observations are very diverse. In total, 47 % of the observations were carried out from 5 prolific stations, namely Yarragadee (19 %), Changchun (9 %), Mount Stromlo (7 %), Zimmerwald (7 %), and Matera (7 %). Only 10 % of all ranges to Earth orbiters were aimed at the LAGEOS satellites that are usually solely utilized for geodetic processing. Should the ranges towards 9 spherical satellites (Ajisai, LAGEOS-1 and -2, Etalon-1 and -2, LARES, Larets, Stella, and Starlette) be employed for a geodetic adjustment, still about 35 % of the observations' volume would have been utilized. It should be noted that ranging stations also have to carry out tracking to targets of little potential geodetic interest, that is, space debris such as inert satellites and rocket bodies.

From the Poincaré-Einstein synchronization, the laser pulse flight-time between the start

[8]The match of CDP (Crustal Dynamics Project) codes and station locations can be found under https://ilrs.cddis.eosdis.nasa.gov/network/stations/.

[9]https://ilrs.cddis.eosdis.nasa.gov/missions/mission_operations/priorities

and the stop reads (e.g., Degnan, 2013)

$$c\tau \approx 2\left(\left\|\mathbf{Q}(t)\mathbf{R}(t)\mathbf{W}(t)\mathbf{x^j} - \mathbf{x_i}\right\|_2 + \tau_{atm} + \tau_{load} + \tau_{tide} + \tau_{rel} + \tau_{CoM} + \tau_{bias}\right) + \\ + \tau_{ins} - \tau_{ref} + \epsilon, \tag{2.2.1}$$

where t is the pulse reflection instant on the CCR, and $\mathbf{x^j}$ and $\mathbf{x_i}$ are the position vectors of the satellite and the station in the ITRS. The matrices $\mathbf{Q}$, $\mathbf{R}$, and $\mathbf{W}$ describe the transformation between a terrestrial and a celestial geocentric reference system (cf. Sec. 2.1). Traditionally, they are expressed in terms of polar motion that constitutes the two components of Earth's rotation axis trajectory projection onto the 0° meridian (x_p) and onto the 270° meridian, (y_p), Earth's rotation angle described by $UT1 - UTC$, and Earth's spin axis precession-nutation as celestial pole offsets (x_{CPO} and y_{CPO}). As the retro-reflector is not situated at the center of mass (CoM) of the spacecraft, for which the precise orbit determination (POD) is carried out, the application of the eccentricity vector τ_{CoM} is necessary. For spacecraft equipped with a propellant system that uses sloshing fuel, the magnitude of this correction changes as the fuel is being depleted. The term τ_{rel} denotes relativistic effects (Shapiro delay, Schwarzschild field, Lense-Thirring precession, Yarkovsly thermal drag and de Sitter precession) which in total do not exceed 2 cm (Combrinck, 2010). The length of the reference arm τ_{ref} is known precisely. With the exception of some isolated Cs clock drifts, that are documented by the ILRS[10], no clock-related parameters need to be introduced in the geodetic adjustment. SLR observations (time-of-flight) are unambiguous. Usually, they are grouped into the so-called normal points the bin size of which increases with increasing orbital altitude, that is, 5 s for GRACE-FO, 120 second for LAGEOS, and 300 s for Etalon or GLONASS. The normal point precision is typically better than 1–2 mm. The analysis of these observations, which are available in near-real-time, results in precise orbit determination with an accuracy of 1–2 cm for cannonball satellites such as LAGEOS, and 2–3 cm for satellites such as those constituting the GPS constellation. There are, of course, other effects that are not described in (2.2.1) such as the along-track displacement of the satellite during the two-way roundtrip time, which is at least 500 m for Etalon-1, and 200 m for LAGEOS-1.

Apart from VLBI, GNSS, and DORIS, the delay of the laser induced by atmospheric refraction (τ_{atm}) does not pose a major issue in the reduction of ranges. This is due to the fact that laser ranges are mainly affected by dry tropospheric gases, and that delay component can be fairly easily predicted based on surface meteorological observations. The contribution of water vapor is approximately 68 times smaller compared to radio techniques (cf. Sec. 4.4). Since the electrically neutral atmosphere is a dispersive medium for optical frequencies, it would be theoretically possible to mitigate τ_{atm} with proper analysis of two-color systems (e.g., Wijaya and Brunner, 2011). Nevertheless, due to very low return rates and the fact that only very few stations are capable of two-color observations, such an accomplishment remains unfulfilled as of this writing. Further details on the atmospheric refraction modelling of laser observations are provided in Chapter 4.

In the parametrization of the laser ranges, a term with no physical meaning often appears, the range and time bias, denoted by τ_{bias} (e.g., Combrinck, 2010). The magnitude of the computationally determined τ_{bias} varies with station and time to 5 mm and are correlated with the stations coordinates mainly the radial component), the elevation angle (hence SNR), as well as uncalibrated instrumental phase delays. These artifacts can be mitigated by monitoring complete satellite arcs (both ascending and descending passes).

On the grounds that the distance between a satellite and the observing station is recorded

[10] https://ilrs.dgfi.tum.de/fileadmin/data_handling/ILRS_Data_Handling_File.snx

at a high rate, several thousand observations per arc lie in the so-called full rate data. As these observations exhibit significant spatiotemporal correlations, they are grouped in the so-called normal points that are more precise per se. In modern SLR data analysis the normal points usually appear in the left part of (2.2.1).

As SLR measures distances between ground-based stations and satellites orbiting the center of mass of the Earth plus its fluid envelope, only information regarding the orientation of the station network needs to be supplied externally to estimate station and satellite coordinates. This is done by imposing NNR conditions on selected stations (2.5.5). In addition to station coordinates and Keplerian elements of the observed satellites, only Earth rotation parameters are estimated (x_p, y_p, and LOD) as well as geocenter coordinates. Satellite-based techniques (SLR, GNSS, and DORIS) are incapable of estimating simultaneously orbital parameters and $\begin{bmatrix} dUT1 & \Delta\epsilon & \Delta\psi \end{bmatrix}^\top$ because of the perfect correlation with the orbits' plane orientation in space (right ascension of the ascending node, the inclination, and the argument of latitude) (Rothacher et al., 1999). SLR is not emburdened with estimating the tropospheric parameters (residual zenith delays and gradients), clocks, or ambiguities. On account of the fact that zenith delays, clock offsets, and the coordinate height component are highly correlated, estimating all three simultaneously degrades the quality thereof (e.g., for GNSS or VLBI). Nevertheless, the occasional estimation of range biases is similar to estimating receiver clock corrections. However, unlike station clock parameters at GNSS and VLBI stations, range biasess are estimated over periods much larger than those used for station coordinates, to achieve a temporal de-correlation between them and the height coordinate component over short periods. Typically, range bias changes are related to instrumentation changes, and are therefore fairly stable over time. There are cases, however, where the estimation of arc-dependent biases is necessary[11].

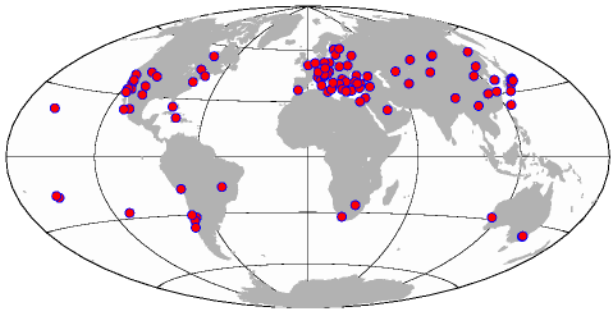


Figure 2.2.2: The network of all laser ranging stations that contributed to ITRF2014. Only 37 stations (26 %) are still active.

The estimation of station-wise parameters related to harmonic effects at frequencies equal or higher than one day is challenging as at most SLR stations the distribution of observations throughout the day in very heterogeneous due to issues pertaining to day-tracking and lacking personnel (cf. Fig. 2.2.3). Moreover, low-degree spherical harmonic coefficients of the Earth's gravity field can be estimated, that is, the principle axes of the inertia tensor expressed by coefficients (C_{21}, S_{21}, S_{22}) to the fully normalized associated Legendre functions. In point of fact, SLR-derived low-degree gravity field coefficients ($n \leq 6$) are more accurate compared to CHAMP (Challenging Minisatellite Payload), GRACE (Gravity Recovery and Climate Experiment), and GOCE (Gravity Field and Steady-State Ocean Circulation Explorer). Other parameters such as scaling factors for Earth and solar radiation, as well as empirical accelerations are also estimated (e.g., Bloßfeld et al., 2018). The contribution of SLR to the inter-technique TRF resides on the geocenter and the scale (jointly determined with VLBI). The assimilation of SLR ranges into the GNSS adjustment is beneficial for the latter as the resolution of phase center offsets of the GNSS antenna onboard the space vehicle is facilitated. Accounting for the above, SLR is the only space geodetic technique that currently links geometry, gravity and Earth rotation.

[11] See for example https://ilrs.dgfi.tum.de/fileadmin/data_handling/ILRS_Data_Handling_File.snx

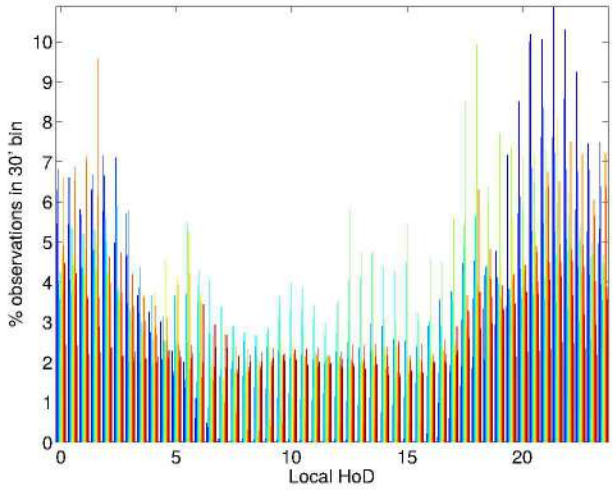


Figure 2.2.3: The relative number of laser ranges per SLR station (2008–2018) as a function of local hour of day (HoD). The graph was generated based on ILRS normal point data.

Similar to VLBI, SLR benefits from advances in technology as well as in the analysis of the laser ranges. Plans for the modernization of geodetic SLR include among else single-sensitive-photon detectors, shorter normal point intervals, and increased pass-interleaving, to allow the acquisition of more observations. The interested reader is referred to Merkowitz et al. (2018) and Pearlman et al. (2019) for further information in this regard.

The current modelling conventions to reduce laser ranges do not include non-tidal geophysical loading effects, nor asymmetric atmospheric delay modelling. In the following chapters, it will be proven for the first time via Monte Carlo simulations that the current modelling setup is at best inadequate and cannot meet the desirable accuracy level:

- ☐ Owing to the so-called blue-sky effect (e.g., Sośnica et al., 2013), laser observations are currently not carried out under cloudy conditions. While this can be mitigated by technological improvements in terms of tracking capabilities, for more than 30 years, there are very few observations through clouds. Due to the effect of atmospheric pressure loading (cf. Sec. 5.2), there is usually a positive deformation under fair weather conditions which in turn leads to a long-term height bias. As this happens to all stations, this will inescapably result in a scale effect in the underlying frame, together with a geocenter coordinate offset because of the uneven global distribution of stations. This effect creates displacements at the mm-level and is more severe at stations far from the ocean due to the inverse barometer effect.

- ☐ The fact that atmospheric thickness decreases polewards together with weather variations, gives rise to refractivity gradients that in turn cause the atmospheric delay at a station to vary as a function of azimuth. In SLR analysis these effects are not modelled. This yields a spurious poleward motion of the stations at the mm-level, which induces a scale effect and an offset along the Z axis of the underlying TRF.

The impact of these effects on the estimated SLR station coordinates and the implied reference frame is discussed in Chapter 7.

2.3 Global navigation satellite systems

The origin of GPS can be traced back to the 1960s with the United States' Department of Defense pursuing the development of a weather-independent, satellite-based navigation system that would operate in the microwave spectrum. GPS was designed in such a way that at any given time at least four satellites (currently nine) are visible from any place on Earth for $\varepsilon > 15°$. The superset known as GNSS incorporates similar systems developed by other countries such as the Russian Global Navigation Satellite System (GLONASS), the Chinese BeiDou Navigation Satellite System (BDS), the European Galileo, and the Japanese Quasi-Zenith Satellite System (QZSS). In the following a brief description of GNSS and in particular GPS is carried out. For a comprehensive end-to-end review of GNSS, the interested reader is referred to Dach et al. (2015) and Teunissen and Montenbruck (2017), as well as the numerous references therein.

The GPS constellation consists of at least 24 space vehicles orbiting almost circularly ($e < 0.02$) in 6 planes ($\delta\Omega = 60°$) inclined by $i \approx 55°$ at an altitude of 20 200 km ($a \approx 26\,560$ km). The orbital revolution period is half a sidereal day (11 h 58 min). The payload of every currently-orbiting GPS satellite includes an ensemble of atomic frequency standards (4) based on Caesium (ASD $= 10^{-13}$) and Rubidium (ASD $= 10^{-12}$). The oscillators of these clocks generate the coherent carriers L_1, L_2, and L_5 (since the Block IIR-M generation of satellites) based on the fundamental frequency $f_0 = 10.23$ MHz: $f_1 = 154 f_0$, $f_2 = 120 f_0$, and $f_5 = 115 f_0$. On these right-hand circularly polarized carriers, two pseudo-random noise codes are biphase modulated, the so-called coarse/acquisition (C/A) code on L_1, and the precision (P or Y) code on both carriers. In addition to the codes, auxiliary information (e.g., ephemeris parameters, satellite clock corrections with respect to the GPS composite clock, and ionospheric parameters), the so-called navigation message, is modulated as well. In view of the fact that the C/A-code chip length is ten times longer than the P-code chip length, the latter provides observations approximately an order of magnitude more accurate.

Positioning with GNSS is based on the multiple trilateration concept. Assuming the position of both satellite ($\mathbf{x^j}$) and receiver ($\mathbf{x_i}$) are already referred in a geocentric celestial reference system in a manner similar to (2.1.5), the single-frequency single-system code observation equation reads

$$P_i^j = \left\| \mathbf{x^j} - \mathbf{x_i} \right\|_2 + c\left(\tau^j - \tau_i\right) + \tau_{atm} + \tau_{ion} + \tau_{rel} + \tau_{mlt} + \tau_{antx} + \tau_{other} + \epsilon, \tag{2.3.1}$$

where P_i^j is the pseudo-range code observation between the satellite j and the receiver i, τ_i is the clock error of the receiver, and τ^j is the clock error of the satellite. The propagation delay in the electrically neutral atmosphere and ionosphere is denoted by τ_{atm} and τ_{ion}, respectively. Tropospheric refraction may be treated in a way similar to VLBI, should the issues stemming from the orbital altitude (cf. Sec. 4.1.2) and the frequency of the radiation (cf. Sec. 4.1.5) be ignored. The treatment of the ionosphere is identical to VLBI with the exception that the high-order ionospheric terms affect the estimated parameters considerably due to the lower frequency of the related signals (cf. Sec. 4.1.5). The relativistic effects τ_{rel} relevant for a navigation system with satellites on MEO orbits are quite different with respect to those necessary to be considered in VLBI and SLR observation modelling. In addition to the effects considered for SLR, the following must be accounted for a proper reduction of the observations collected by the receivers: time-dilation as a function of the along-track velocity, gravitational redshift and blueshift due to Earth's gravitational potential, Earth's oblateness, lunisolar tidal potential, Sagnac effect, and orbital eccentricity (Combrinck, 2010). Unlike VLBI receiving systems, GNSS antennas are omnidirectional and as such are prone to the interference between the direct and a reflected signal, also known as far-field multipath (τ_{mlt}). The phase center offsets and variations of the receiver

and the transmitter (τ_{antx}) are contingent on the direction of the signal as well as its frequency. The term τ_{other} includes effects that have already been described in (2.1.4) and (2.2.1) such as solid Earth tides, tidal and non-tidal loading, CoM corrections, satellite- and receiver-specific differential code biases, as well as effects that act upon the satellite orbit. The latter encompass gravitational perturbations such as spatiotemporal variations of Earth's gravity field due to mass transport and third-body perturbing acceleration, as well as non-gravitational forces imparted by atmospheric drag, solar radiation flux (solar radiation pressure), Earth's albedo (Earth radiation pressure), thermal dump, unbalanced thrusts, and propellant outgassing.

In addition to P_i^j, geodetic receivers observe the phase shift of the carrier wave, that is, the difference between the carrier phase of the satellite signal at the epoch of transmission (Φ^j) and the carrier phase of the reference signal generated by the quartz crystal oscillator of the receiver itself at the epoch of reception (ϕ_i). The related observation equation reads

$$\begin{aligned} L_i^j &= \lambda\left(\Phi_i - \Phi^j + N_i^j\right) \\ &= \left\|\mathbf{x^j} - \mathbf{x_i}\right\|_2 + c\left(\tau^j - \tau_i\right) + \lambda B_i^j + \tau_{atm} - \tau_{ion} + \tau_{rel} + \tau_{mlt} + \tau_{antx} + \tau_{other} + \xi, \end{aligned} \tag{2.3.2}$$

where L_i^j denotes the accumulated carrier phase, λ is the related wavelength, $N_i^j \in \mathbb{R}$ is the constant carrier phase ambiguity, and $B_i^j \in \mathbb{R}$ is the number of cycles stemming from the initial phase ambiguity. N_i^j and B_i^j remain constant throughout continuous carrier tracking arcs. In the event of the so-called "loss of lock" an additional parameter must be set up in (2.3.2) to account for the cycle slip. While most corrections in (2.3.1) hold for (2.3.2) as well, effects such as carrier phase wind-up (variations in the measured carrier phase induced by varying relative orientation of receiving and transmitting antennas, (e.g., Beyerle, 2008)) need to be introduced in the reduction of the related observations. Moreover, τ_{mlt} is quite different between L_i^j and P_i^j.

Due to the fact that modelling τ_{mlt} is a challenge that cannot be facilitated by differencing — hence is treated as white noise, τ_{mlt} is considerably smaller for L_i^j, and $\xi \lessapprox 0.01\epsilon$, integrated carrier phase measurements are preferred over pseudo-ranges.

Equations (2.3.1) and (2.3.2) can be formed for any combination of L_i^j and P_i^j. Depending on the combination one or more of the effects that require to be modelled or estimated from the related observations simply cancel out or are considerably reduced. An outline of the most important combinations follows.

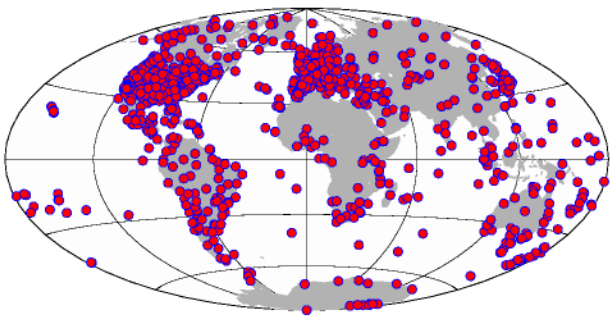


Figure 2.3.1: The network of all GNSS stations that contributed to ITRF2014.

The differences formed between the code or phase measurements of two receivers and one satellite, the so-called single differences (SD), eliminate satellite-related issues such as the hardware delays and initial phase, and considerably mitigate others such as the satellite clock offsets (provided the receiver clock corrections are known to 0.3 µs or better) and spatially-correlated effects such as ionospheric delays. Provided that the receivers participating in the formulation of the SD acquire measurements with the same accuracy, the error propagation law suggests that the noise in the single-differenced observables will be amplified by a factor of $\sqrt{2}$. In laymans' terms, VLBI corresponds to processing

only single difference GNSS observations.

The double differences (DD) are formed between a pair of receivers and a pair of satellites from the related SD, and yield observables that are in addition alleviated from receiver clock offsets, initial phases, and receiver hardware delays. The DD are the basic observable in geodetic-grade GNSS software. However, the noise of these observations is further amplified and the observations are no longer uncorrelated.

The receiver satellite-time triple differences are formed from (usually) successive DD, are utilized in the data-screening process, facilitate the integer ambiguity resolution as they are free from the latter, and are useful to make amends for cycle slips.

Given observations at three frequencies, namely L_1, L_2, and L_3, the linear combination of phase observations has the general form

$$\Phi = n_1\Phi_1 + n_2\Phi_2 + n_5\Phi_5. \tag{2.3.3}$$

The most useful combinations follow. The ionosphere-free combination

$$\lambda\Phi = \frac{f_1^2\lambda_1\Phi_1 - f_2^2\lambda_2\Phi_2}{f_1^2 - f_2^2}, \tag{2.3.4}$$

where the 1st order ionospheric effects have been eliminated, the ambiguities are not integer any longer, but the noise has been amplified. The 2nd order ionosphere-free combination

$$\begin{aligned} \lambda\Phi &= \frac{f_1^3(f_5 - f_2)}{C}\lambda_1\Phi_1 - \frac{f_2^3(f_5 - f_1)}{C}\lambda_2\Phi_2 + \frac{f_5^3(f_2 - f_1)}{C}\lambda_5\Phi_5, \\ C &= f_1^3(f_5 - f_2) - f_2^3(f_5 - f_1) + f_5^3(Jf_2 - f_1), \end{aligned} \tag{2.3.5}$$

mitigates the 2nd order ionospheric effects, but at the same time introduces noise. The geometry-free combination is formed simply by $L_4 = L_1 - L_2$. In L_4 everything other than the initial phase ambiguities and the ionospheric delay vanishes. The wide-lane combination

$$L_{WL} = \frac{f_1L_1 - f_2L_2}{f_1 - f_2}, \tag{2.3.6}$$

is used together with the DD for integer ambiguity resolution and cycle slips treatment. The Melbourne-Wübbena combination

$$L_{MW} = \frac{f_1L_1 - f_2L_2}{f_1 - f_2} - \frac{f_1P_1 - f_2P_2}{f_1 + f_2}, \tag{2.3.7}$$

eliminates the contribution of the atmosphere, the geometry and the clocks.

In the ensuing geodetic adjustment, a much larger number of parameters compared to VLBI and SLR needs to be estimated, a fact partly attributable to the vast station network (cf. Fig. 2.3.1). Unlike VLBI and SLR where no elevation-dependent weighting is mandatory, care needs to be exercised for the GNSS adjustment because of the larger susceptibility of low elevation observations to multipath (as well as atmospheric refraction). There is a large number of weighting schemes; common to all is the downweighting of low elevation observations, in particular code pseudo-ranges e.g., $w(\varepsilon) = \csc^2(\varepsilon)$ for phases, and $w(\varepsilon) = \csc^2(\varepsilon)$ for codes. Furthermore, since high-frequency observations are available, the temporal correlations should be considered in view of a more realistic estimate of the parameters' uncertainties. Some of the parameters that are usually estimated are the satellite orbital parameters together with

pseudo-stochastic pulses, phase center position increments for receiver and satellite antennas, differential code biases, clock polynomials together with PWLF for the station and satellite clocks, tropospheric parameters such as zenith delays and linear gradient components, Earth rotation parameters (x_p, y_p, LOD, $\partial\Delta\epsilon/\partial t$, and $\partial\Delta\psi/\partial t$), and station coordinates. Similar to the other satellite techniques, no-net-rotation conditions (2.5.5) must be applied to relieve the related NEQs of the inherent datum defect. Analyzing multi-year data provides the opportunity to access to other parameters such as the low-degree load deformation coefficients (e.g., Fritsche et al., 2009; Glaser et al., 2015).

Since GNSS observes satellites orbiting around the Earth's center of mass, and the observations are easily converted to distance measurements between stations and satellites, GNSS can theoretically contribute to the realization of the origin (currently done solely by SLR), and the scale (currently done by a combination of SLR and VLBI) of the global reference system. However, a number of effects hinder these contributions including but not limited to the modelling of non-gravitational accelerations such as the effect of solar radiation pressure. Fortunately, the advent of new technologies such as atom interferometry, optical inter-satellite laser links, optical clock ensembles, and the optical frequency comb technique (Nobel prize in physics 2005) potentially allow for the mitigation of some of the aforementioned effects. Such innovative concepts are explored within the framework of ADVANTAGE[12] that partly deals with the evaluation of the merits for geodesy and Earth system monitoring (Giorgi et al., 2019).

2.4 Doppler Orbitography and Radiopositioning Integrated by Satellite

DORIS is an active two-frequency one-way Doppler-tracking system that operates in the microwave domain on a number of space vehicles. A pair of fairly stable frequencies (401.25 MHz and 2036.25 MHz) is emitted continuously and omnidirectionally by ground-based beacons to satellites equipped with very stable clocks (quartz crystal resonator with Allan standard deviation ASD = 10^{-13} for $10\,\mathrm{s} < \tau < 100\,\mathrm{s}$). The Doppler shift count is carried out onboard by the involved space vehicles at intervals spanning $\approx$ 10 s. The objective of the system on its inception was the support of precise orbit determination (POD) to low Earth orbiting satellites and precise point positioning at the cm-level. The accuracy of the related range rate observations is $0.3\,\mathrm{m\,s^{-1}}$ over 10 s that corresponds to 3 mm for the range measurements. The accuracy of the time-tagging is at the 1 µs level that corresponds to 1 cm uncertainty in the along-track satellite position. Similar to GNSS, on the DORIS signal carriers is the beacon message that contains mainly station-dependent information such as the identity of the beacon, and synchronization and meteorological data. Similar to all SLR and VLBI stations, DORIS beacons are equipped with a meteorological sensor incentivized by the mitigation of the propagation delay induced by the electrically neutral atmosphere. Currently active are Sentinel-3B, Sentinel-3A, Jason-3, SARAL, HY-2A, Cryosat-2, and Jason-2. In the past, the following were tracked: STPSat-1,

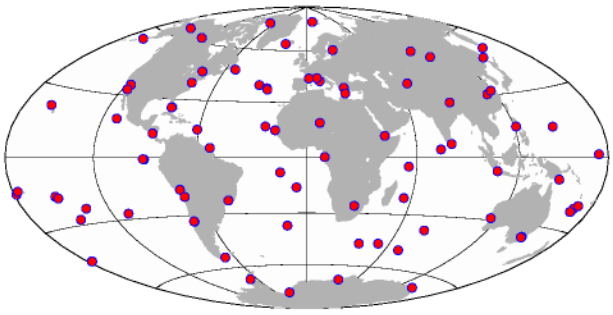


Figure 2.4.1: The network of all DORIS stations that contributed to ITRF2014.

[12] Advanced Technologies for Navigation and Geodesy, see for details https://hgf-advantage.de.

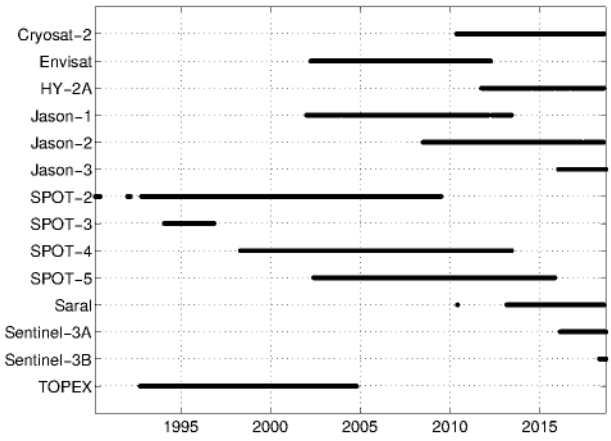


Figure 2.4.2: Data availability from satellites equipped with DORIS receivers, based on DORIS 2.2 format files and DORIS/`RINEX` 3.0.

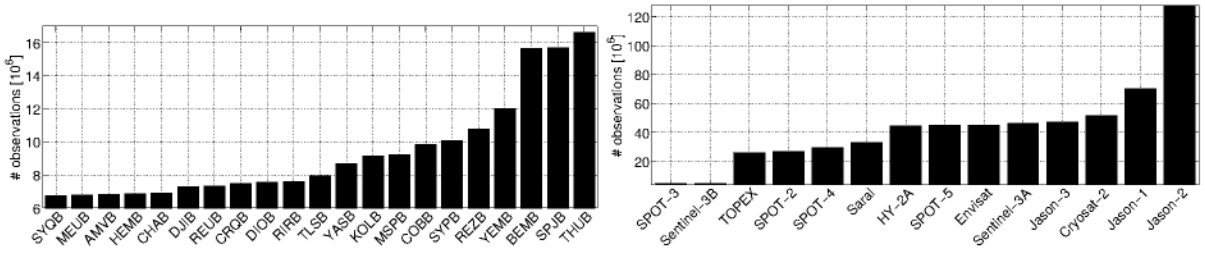


Figure 2.4.3: The DORIS beacons (left), and satellites equipped with DORIS receivers (right) that contribute with the largest amount of observations. The graphs were created based on DORIS 2.2 format files and DORIS/`RINEX` 3.0.

SPOT-5, Envisat, Jason-1, SPOT-4, SPOT-3, TOPEX/Poseidon, and SPOT-2. Figure 2.4.2 illustrates all satellites that contribute to the DORIS technique. Some of the aforementioned satellites are equipped with a corner cube retroreflectors and a GPS antenna so that the POD is assisted by the introduction of laser ranges (SLR). DORIS features the station network with the best global distribution amongst the ITRF-contributing techniques (cf. Fig. 2.4.1), given the number of stations. Figure 2.4.3 shows the number of observations per satellite and station (world top in terms of data yield) for the complete DORIS history[13] based on data in the DORIS 2.2 format, as well as in the DORIS/`RINEX` 3.0 format.

The analysis of DORIS observations reveals information about the DORIS beacons' motion, the orbits of the satellites involved, atmospheric drag, the geocenter coordinate variations, Earth's gravity field, the ERPs, and the ionosphere (as the system features dual-frequency observations). To estimate station and satellite coordinates from the DORIS data adjustment, it is necessary to impose NNR constrains on the coordinates of the observing stations, similar to GNSS.

For an introduction to DORIS as well as the other techniques already discussed in Chapter 2, the interested reader is referred to Seeber (e.g., 2003). Further details about DORIS and its contribution to space geodesy can be found in Lemoine and Schrama (2016), as well as in the International DORIS Service's (IDS[14]) webpage.

[13] ftp://cddis.gsfc.nasa.gov/doris/data/
[14] https://ids-doris.org/

2.5 Space geodetic data analysis

The adjustment of space geodetic measurements described by the observation equations laid out in the preceding sections shares many similarities across the techniques. For this reason, it was decided to concisely present the standard VLBI adjustment. Technique-specific intricacies will not be addressed as they raise a host of topic-divergent issues such as integer ambiguity resolution, and precise orbit determination. More detailed treatises may be found in the literature cited in the preceding sections.

The time delay τ described in (2.1.4) is corrupted by a number of effects that are treated with varying degrees of success during the modelling or/and the parametrization process. By and large, the impetus of a single 24-hour VLBI session adjustment is the accurate determination of station coordinates (and subsequently baseline lengths) for ITRF maintenance and refinement, the determination of AGN coordinates for ICRF (international celestial reference frame) refinement, and the monitoring of Earth's variable orientation and rotation (EOPs), which is necessary, e.g., for the transformation between terrestrial and geocentric celestial reference systems as well as for spacecraft navigation. The duration of a VLBI session, the stations that participate and the AGN observed therein as well as the scan sequence and duration, depend upon the parameters of interest[15]. In the following, the geodetic VLBI adjustment is briefly described.

The adjustment of VLBI observations is treated as a parameter estimation problem within a rank-deficient non-linear Gauss-Markov model (e.g., Koch, 1997; Kotsakis, 2013)

$$\mathbf{b} = \mathbf{A}\mathbf{x} + \mathbf{v}, \text{ and } \mathbf{v} \sim (\mathbf{0}, \mathbf{C_v}), \tag{2.5.1}$$

where $\mathbf{b} = \mathbf{y^b} - \mathbf{y^0}$ is the reduced observations vector, $\mathbf{A} = \left.\frac{\partial \mathbf{y}}{\partial \mathbf{x}}\right|_0$ is the rank-deficient Jacobian (design) matrix, $\mathbf{x} = \mathbf{x^a} - \mathbf{x^0}$ is the vector of unknown parameters, and $\mathbf{v} = \mathbf{y^b} - \mathbf{y^a}$ is the residuals' vector. $\mathbf{y^b}$ includes all the observations, $\mathbf{x^0}$ includes the initial approximation of the model parameters, $\mathbf{y^0}$ includes the approximation of the observables based on the a priori model parameters, $\mathbf{y^a}$ includes the real (thus unknown) values of the observed parameters, and $\mathbf{x^a}$ includes the real-thus-unknown values of the parameters to which the ensuing adjustment will provide an approximation. For geodetic VLBI, the parameter space is occupied by three groups (e.g., Petrov and Ma, 2003): (i) global parameters, that is, quantities that are estimated utilizing many sessions (e.g., station velocities), (ii) quantities that are estimated over the course of a single session (e.g., EOPs), and (iii) segmented (or "arc") parameters that are highly variable over time (e.g., zenith tropospheric delays). The estimation of parameters that fall under the latter group as global or local is of no benefit. Of course, some local parameters such as the station and radio source coordinates can be estimated both from the single- and multi-session solutions. Analyzing a single global VLBI session[16], the following parameters are usually estimated:

- ☐ clock parameters (per station, and occasionally for individual baselines),
- ☐ tropospheric parameters; zenith delays and gradients (per station),
- ☐ station coordinates,

[15] https://ivscc.gsfc.nasa.gov/program/descrip2011.html

[16] To the author's knowledge, there is no official definition of a "global" network. While an IVS-R4 network is definitely global and a three-station network in Australia is regional, there is no strict boundary. The length of the longest baseline, the surface area, and the volume of the polyhedron whose vertices are the VLBI stations are used as a measure (cf. Sec. 7.3). Truly global networks have Earth's center of mass lie inside their polyhedron.

- ☐ radio source coordinates[17], and
- ☐ Earth orientation parameters (pole coordinates, celestial pole offsets, and *dUT1*).

The observing schedule (when and how long will the baseline i observe the AGN j) is very important due to the fact that it to a great extend sets the upper boundary to the accuracy achievable by analyzing the related observations; the design matrix $\mathbf{A}$ and its spectral condition number mainly depend on the schedule. To define the schedule of a VLBI experiment, the unambiguous separation of the parameters of interest is of paramount importance, as well as the spatiotemporal sampling thereof. Since one of the goals of geodetic VLBI experiments is the accurate estimation of station coordinates, the observation geometry should be such that for the subsequent data analysis a wide range of elevations and azimuths are available to decorrelate as much as possible the station height from the zenith tropospheric delay corrections ($\frac{\partial \tau}{\partial d^z}\frac{\partial \tau}{\partial H} \asymp -1$), and the lateral coordinate components from the components of the tropospheric gradient vector (highly positively correlated). Moreover, except for the sessions that last longer than two hours (the vast majority of which are the so-called Intensive VLBI sessions), most geodetic sessions nowadays span 24 hours (90 % (86 %) of all non-intensive IVS (QUASAR) sessions span between 23–25 h); this is deliberate so that geophysical and astronomical effects of 1-day period can cancel out (to a large extend), as well as to observe AGN through the full range right ascension.

Should a best linear unbiased estimator (BLUE) be adopted, the optimal aforementioned parameters will be eventually estimated from the (weighted) least squares inversion of a singular consistent system of linearized normal equations, hereinafter NEQs (e.g., Koch, 1997; Kotsakis, 2013)

$$\begin{aligned} \mathbf{N}\mathbf{x} &= \mathbf{u}, \\ \mathbf{N} &= \mathbf{A}^\top \mathbf{P}\mathbf{A}, \\ \mathbf{u} &= \mathbf{A}^\top \mathbf{P}\mathbf{b}, \end{aligned} \tag{2.5.2}$$

where $\mathbf{P} = \sigma_0^{-2}\mathbf{Q}$ is the weight matrix and $\mathbf{Q} = \sigma_0^{-2}\mathbf{C_v}$ is the cofactor matrix. As of this writing, $\mathbf{P}$ is usually populated solely with the standard deviations derived from the VLBI cross-correlation process that are slightly inflated. In some cases, some baseline-dependent re-weighting takes place stemming from the estimation of variance components, and elevation-dependent weighting. Unlike GNSS, an elevation-dependent weighting $\left(\text{e.g., } \frac{\alpha}{mf_{nh}(\varepsilon)}, \alpha \geq 0\right)$ is not as necessary because VLBI is not subject to multipath (VLBI features directional antennas, hence narrow beamwidth), phase center offset/variation uncertainties, cycle slips, and severe signal-to-noise reduction with decreasing elevation angle. Nevertheless, as in satellite-based techniques, the effect of AGN coordinate errors is amplified at low elevations, and the modelling of atmospheric refraction is more difficult. On the other hand, the lower the elevation ε utilized in geodetic processing, the more stable the estimation of tropospheric gradients, thus the better the estimation of the lateral coordinate components and, the better the decorrelation between the zenith delay, the clock offset and the height coordinate component, hence the better the quality of the solution. These potential improvements are hindered by the down-weighting of

[17] Based on the VLBI data reanalysis (IVS and QUASAR) carried out in the framework of Chapter 6 and Chapter 7, 50 % of the AGN coordinate estimates (session-dependent AGN-dependent right ascension and declination offsets) are not statistically significant, and 61.5 % of the radio sources had never had either of their coordinate components estimated statistically significantly. AGN that participate in the NNR conditions are typically not estimated in the 24-hour sessions. Therefore, in many cases setting up as unknown parameters the coordinates of all AGN that are observed in a VLBI session could be avoided, if the minimization of the weighted sum of the single-session post-fit residuals is sought.

low elevation observations. Nevertheless, spatiotemporal correlations between observations that stem from small-scale highly dynamic refractivity fluctuations induced by turbulent eddies in the lower troposphere render the uncertainty of the estimates of geodetic data analysis overoptimistic (e.g., Halsig et al., 2016). These effects can be accounted for employing the well-known Kolmogorov turbulence theory (Treuhaft and Lanyi, 1987; Nilsson and Haas, 2008, 2010), but are rarely considered. Due to the fact that station and source coordinates are non-estimable quantities based on the information nested in the observations, to obtain a free network solution (Sillard and Boucher, 2001) by inverting (2.5.2) additional information must be supplied to the NEQs. For VLBI, the observations provide information only about the scale of the implied frame, therefore information about the origin and the orientation must be introduced externally. To date, the best way to do so is by imposing minimum constraints on the normal equation system (2.5.2), as they do not affect the internal network geometry. The consistent set of the linear(ized) minimum constraining equations reads

$$\mathbf{HWx} = \mathbf{c}, \tag{2.5.3}$$

where $\mathbf{H}$ is the design matrix (Jacobian) of the reduced pseudo-observation vector $\mathbf{c}$, and $\mathbf{W}$ is the associated symmetric positive-definite weight matrix, whose choice leads to different optimizations (Schaffrin, 1985; Bevis et al., 2013; Kotsakis, 2016). Using the minimum constraint matrix $(\mathbf{HWH}^\top)^{-\mathbf{1}}\mathbf{HW}$ in the implementation of (2.5.3) instead of $\mathbf{HW}$ is numerically more stable, thus preferred. In geodetic VLBI, the best treatment for the datum defect is applying no-net-translation (NNT) and no-net-rotation (NNR) to the station coordinates of a stable and reliable TRF (e.g., Altamimi et al., 2016; Seitz et al., 2016; Abbondanza et al., 2017), and NNR on the source coordinates of a stable CRF (e.g., Fey et al., 2015), thus realizing a network-intrinsic reference system (e.g., Dermanis, 2004). For the terrestrial component, the NNT (preservation of the center of mass) reads

$$\sum_{i=1}^{N} \delta X_i = 0 \wedge \sum_{i=1}^{N} \delta Y_i = 0 \wedge \sum_{i=1}^{N} \delta Z_i = 0, \tag{2.5.4}$$

where for the i station situated at (X_i, Y_i, Z_i) at the epoch of the experiment it is $\delta X_i = X_i - X_i^o$. For the NNR (elimination of relative angular momentum), it is

$$\sum_{i=1}^{N} (Y_i^o \delta Z_i - Z_i^o \delta Y_i) = 0 \wedge \sum_{i=1}^{N} (Z_i^o \delta X_i - X_i^o \delta Z_i) = 0 \wedge \sum_{i=1}^{N} (X_i^o \delta Y_i - Y_i^o \delta X_i) = 0. \tag{2.5.5}$$

There is the possibility to preserve the mean quadratic scale (no-net-scale, NNS), but as it is defined by the nature of the observations, it is inessential

$$\sum_{i=1}^{N} (X_i^o \delta X_i + Y_i^o \delta Y_i + Z_i^o \delta Z_i) = 0. \tag{2.5.6}$$

The NNR conditions for the source coordinates read

$$\begin{aligned} \alpha_j - \alpha_j^0 &= A_1 \tan(\delta_j) \cos(\alpha_j) + A_2 \tan(\delta_j) \sin(\alpha_j) - A_3 \\ \delta_j - \delta_j^0 &= -A_1 \sin(\alpha_j) + \cos(\delta_j), \end{aligned} \tag{2.5.7}$$

where (α_j, δ_j) are the coordinates of the AGN j based on the observations of the current exper-

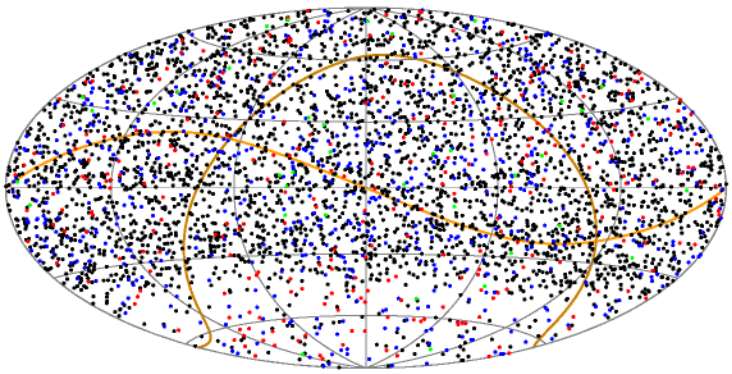


Figure 2.5.1: The celestial atlas of the extragalactic radio sources observed in the framework of IVS that have been considered in this study, in an equatorial system. Shown are the sources that participate in the NNR condition equations (red), the sources the coordinates of which have been estimated as global parameters (blue), the special handling sources (green), and others the positions of which were estimated from experiments such as the VLBA calibrator survey (black). The ecliptic is shown in orange, and the galactic plane is shown in brown. Note the uneven distribution near the ecliptic.

iment, and (α_j^0, δ_j^0) are the CRF coordinates of the j radio source. While additional parameters may be set up to account for a drift in right ascension and declination as a function of a reference declination δ_0 (D_α and D_δ, respectively) or a fictitious equator tilt in declination (B_δ),

$$\begin{aligned} \alpha_j - \alpha_j^0 &= A_1 \tan(\delta_j)\cos(\alpha_j) + A_2 \tan(\delta_j)\sin(\alpha_j) - A_3 + D_\alpha\,(\delta_j - \delta_0)\,, \\ \delta_j - \delta_j^0 &= -A_1 \sin(\alpha_j) + \cos(\delta_j) + D_\delta\,(\delta_j - \delta_0) + B_\delta, \end{aligned} \tag{2.5.8}$$

it is uncommon partly owing to the fact that the estimation thereof induces high correlation with the rotations around the CRF axes (e.g., Titov et al., 2011). For a typical rapid turnaround session where around 90 AGN are observed (since 2016), 55 % thereof are some of the 295 ICRF2 (Fey et al., 2015) "defining" sources and are thus stable enough to participate in the NNR conditions and therefore realize the implied CRS axes. The more "stable" the sources that participate in the NNR equations, the better the definition of the underlying CRF. Of course, there is a number of AGN that despite realizing a CRF, experience source structure and therefore must not be involved in the NNR (e.g., 0642+449 Xu et al., 2016; Anderson and Xu, 2018). On the other hand a great number of AGN that were unstable (structure index higher than 3) in the past are now suitable to realize a CRF. Therefore, to include as many sources as possible in the inner constraint conditions and avoid erroneous AGN, all sources should participate in the NNR but with weights proportional to their stability. In Fig. 2.5.1 shown are the radio sources employed in the VLBI-related investigations carried out herein, in an equatorial coordinate system. The defining sources are in red. The curve in orange depicts the ecliptic (apparent motion of the Sun from the Earth), and the curve in brown depicts the galactic plane.

In addition to the constraints introduced to relieve the NEQ in (2.5.2) of the datum defect, a number of pseudo-observations are incorporated to stabilize the solution — that is, render the estimation process more robust to outliers and aid to avoid singularities when estimated parameters are not supported by real observations e.g., tropospheric parameters at Wettzell in an IVS-R1 session while it participates in the INT1 session — in the form of relative or absolute constraints. These equations have a form similar to (2.5.3) and are usually imposed on all parameters. In essence, the absolute constraints read

$$\hat{x}^a - x^0 = 0 \pm \sigma, \tag{2.5.9}$$

where $\hat{x}^a$ denotes the a posteriori value of a parameter to be estimated and x^0 the a priori thereof. The relative constraints describe the relation between consecutive parameters under the Markov assumption. They read:

$$\hat{x}_i^a - \hat{x}_{i-1}^a = 0 \pm \sigma, \tag{2.5.10}$$

where the subscript i is indicative of time. For instance, the variations in the atmospheric refractive index are modelled as random walk processes ($\sigma^2 = d^2 t$) with a drift rate of $6.25\,\mathrm{mm^2\,h^{-1}}$ for the d^z, and $0.09\,\mathrm{mm^2\,h^{-1}}$ for the $\mathrm{G_{NS}}$ and $\mathrm{G_{EW}}$ (e.g., Nilsson et al., 2015b). In modern VLBI sessions, these constraints are fairly loose. The necessity to impose tight constraints on certain parameters (e.g., gradient components in sessions before 1990) is indicative of a lacking observation geometry to resolve the parameters demanded to be estimated.

Imposing the data- and datum-related constraints leads to the following NEQ

$$(\mathbf{N} + \mathbf{H}^\top \mathbf{W}\mathbf{H})(\mathbf{x} - \mathbf{x_0}) = \mathbf{u} + \mathbf{H}^\top \mathbf{W}\mathbf{c}. \tag{2.5.11}$$

While absolute and relative constraints are fairly necessary for all types of sessions, neither NNT (2.5.4) nor the NNR (also known as Tisserand) conditions (2.5.5) and (2.5.7) need to be applied for sessions where neither station, nor source coordinates are estimated, such as the so-called Intensives (1-hour long). By and large, the solution to the adjustment (2.5.11) is

$$\hat{\mathbf{x}} = \mathbf{x_0} + (\mathbf{N} + \mathbf{H}^\top \mathbf{W}\mathbf{H})^{-\mathbf{1}}\mathbf{u} + (\mathbf{N} + \mathbf{H}^\top \mathbf{W}\mathbf{H})^{-\mathbf{1}}\mathbf{H}^\top \mathbf{c}, \tag{2.5.12}$$

and the precision/accuracy thereof is described by the following variance-covariance matrix

$$\mathbf{C}_{\hat{\mathbf{x}}} = \frac{\hat{\mathbf{v}}^\top \mathbf{P}\hat{\mathbf{v}}}{dof}(\mathbf{N} + \mathbf{H}^\top \mathbf{W}\mathbf{H})^{-\mathbf{1}}\mathbf{N}(\mathbf{N} + \mathbf{H}^\top \mathbf{W}\mathbf{H})^{-\mathbf{1}}, \tag{2.5.13}$$

where the degrees of freedom *dof* is the number of observations and constraint equations minus the number of unknown parameters. If the estimation of station and radio source coordinates is not sought (e.g., analysis of Intensives), it is simply

$$\mathbf{C}_{\hat{\mathbf{x}}} = (\mathbf{A}^\top \mathbf{P}\mathbf{A})^{-\mathbf{1}}\mathbf{A}^\top \mathbf{P}\mathbf{b}. \tag{2.5.14}$$

In addition to the classical Gauss-Markov model, it is possible to perform the adjustment of VLBI observations with other methodologies such as with the least-squares collocation (e.g., Titov and Schuh, 2000) or the Kalman filter (e.g., Herring et al., 1990; Nilsson et al., 2015b). Besides the Gauss-Markov model, a Kalman filter (Kalman, 1960; Gelb, 1974) has been used in this work both for the analysis of "real" VLBI observations and for the analysis of simulated observations for all space geodetic techniques (cf. Sec. 2.6). While both least-squares and Kalman filter minimize the sum of squares of the weighted residuals, that is, $\mathrm{argmin}\left(v^\top P v\right)$, the latter is based on a slightly different concept. The Kalman filter comprises a set of equations applied recursively to estimate the state of a dynamic system excited by an independent sequence of measurements that contain relatively small normally distributed random errors. In the processing, the VLBI observations (or of any other space geodetic technique) are organized scanwise and are sorted in time. The linearized observation equations for the i scan read (Dermanis, 1987)

$$\mathbf{b_i} = \mathbf{A_i}\mathbf{x} + \mathbf{v_i}. \tag{2.5.15}$$

The Kalman filter utilized in the framework of this study builds upon the assumption that there

are not temporal correlations between successive scans. The epoch-wise NEQ reads

$$\mathbf{N_i} = \hat{\mathbf{x}}_\mathbf{i}\mathbf{u_i}. \tag{2.5.16}$$

The solution to all parameters at the i scan (state transition equation) is given by (e.g., Herring et al., 1990)

$$\hat{\mathbf{x}}_\mathbf{i} = \hat{\mathbf{x}}_{\mathbf{i-1}} + \mathbf{Q_{i-1}A_i^\top}(\mathbf{C_i} + \mathbf{A_iQ_{i-1}A_i^\top})^{-\mathbf{1}}(\mathbf{b_i} - \mathbf{A_1}\hat{\mathbf{x}}_\mathbf{i}), \tag{2.5.17}$$

where the related cofactor matrix $\mathbf{Q_i}$ reads

$$\begin{aligned}
\mathbf{Q_i} &= (\mathbf{I} - \mathbf{K_iA_i})\mathbf{Q_i}(\mathbf{I} - \mathbf{K_iA_i})^\top + \mathbf{K_iC_iK_i^\top}, \\
\mathbf{K_i} &= \mathbf{F_iD_i^{-1}}, \\
\mathbf{D_i} &= \mathbf{C_i} + \mathbf{A_iF_i}, \\
\mathbf{F_i} &= \mathbf{Q_iA_i^\top},
\end{aligned} \tag{2.5.18}$$

where $\mathbf{K_i}$ is the so-called Kalman gain. The stochastic processes that drive the parameter variations were assumed to be random walks[18] for all parameters except for the station clock whose fluctuations are modelled by the sum of a random walk and an integrated random walk. No deterministic parameters are assumed here. The underlying noise is determined empirically by analyzing the related parameter time series. For instance, the derivation of the station coordinate process noise is described in Sec. 5.5. There are, however, other options to describe the stochastic dynamics involved, e.g., a first-order Gauss-Markov process for gradient components, and a three-state model for the station clock. For further information on stochastic models for VLBI Kalman filters, the interested reader is referred to e.g., Herring et al. (1990); Nilsson et al. (2015b); Soja (2016). To obtain a stable solution it is necessary to run the discrete filter both forward and backward in time, and then apply a smoother. The final smoothed solution $\hat{\mathbf{x}}_\mathbf{i}^\mathbf{s}$ at the scan i is

$$\hat{\mathbf{x}}_\mathbf{i}^\mathbf{s} = \hat{\mathbf{P}}_\mathbf{i}^\mathbf{b}\hat{\mathbf{x}}_\mathbf{i}^\mathbf{b} + \hat{\mathbf{P}}_\mathbf{i}^\mathbf{f}\hat{\mathbf{x}}_\mathbf{i}^\mathbf{f}, \tag{2.5.19}$$

which is in essence an average of the forward solution $\hat{\mathbf{x}}_\mathbf{i}^\mathbf{f}$ and the backward solution $\hat{\mathbf{x}}_\mathbf{i}^\mathbf{b}$ weighted by the respective a posteriori weight matrices thereof ($\hat{\mathbf{P}}_\mathbf{i}^\mathbf{f}$ and $\hat{\mathbf{P}}_\mathbf{i}^\mathbf{b}$).

The solution ensuing the Kalman filtering and smoothing is in effect equivalent to a recursive least-squares solution (e.g., Mysen, 2017), with the additional feature that for every new scan (in the case of VLBI) the elements of $\mathbf{Q_i}$ that correspond to Markov parameters are increased to an extend. That extend is dictated by the PSD of the white noise process driving the related stochastic processes (e.g., random walk and integrated random walk).

Complete reanalysis of all VLBI, SLR, and DORIS observations takes a couple of hours on a modest PC, as opposed to the reanalysis of all GNSS observations that requires multiple weeks on a modern cluster.

Modeling atmospheric refraction can only take place at the observation equation level; $\mathbf{b}$ and $\mathbf{A}$ are affected. The reduced observations' vector $\mathbf{b}$ is modified upon varying the mapping functions, the a priori zenith delays (e.g., by inserting different barometric pressure), and the gradients. The Jacobian matrix $\mathbf{A}$ is only affected by changes in the non-hydrostatic mapping function.

Directly affecting the position of the stations, geophysical loading models can be applied at

[18] In practice, a random walk process may be generated by progressively adding independent and identically distributed randomly generated numbers. The integrated random walk is generated correspondingly.

all processing levels (observation equations, NEQ, estimated parameters) with varying effectiveness. Should the displacement models be used at the observation level, their quality must be ascertained for mismodelling at this level spawns errors that propagate to all estimated parameters. Moreover, the identification of outliers could be rendered erroneous. Due to the inherent correlation between different parameter groups as well as the imperfect observation geometry, accounting for the geophysical loading a posteriori does not consider the impact on e.g., *dUT1*. Nevertheless, applying loading displacements a posteriori provides an approximation of the impact on the station coordinates and therefore the implied reference frame, accepting the premise that there is no transfer of loading information to parameters other than the station coordinates.

2.6 Monte Carlo simulation of VLBI, SLR, GNSS, and DORIS observations

Thus far in Chapter 2 an introduction has been attempted regarding the modelling and parametrization of space geodetic observations that fall under the techniques of VLBI, SLR, GNSS, and DORIS. It is apparent that the physical measurements are not fully consistent, and the mathematical models to describe the various effects acting upon the related observations are incomplete. For instance, in geodetic VLBI data analysis zenith delays and gradients are usually estimated hourly. However, such a setup may result in spurious clock variations, if weather fluctuations at shorter time-scales cannot be described by that deterministic model. Moreover, while the tilted plane approximation of azimuth-dependent atmospheric delay variations is sufficient in most cases, it may fail during severe weather events (cf. Fig. 4.2.2). Besides, as the observation equations lead to a non-linear estimation process, access to a priori values of poor quality renders the estimation process less effective. While utilizing redundant measurements will reduce the former, it cannot assist in sharpening the comprehension of the underlying physical processes, ergo the improvement of the observations' parametrization. To accurately monitor effects such as global warming via indicators like decadal sea level change or long-term changes in integrated water vapour time series, an accurate parametrization needs to be ascertained. Moreover, to determine the extend to which parameters describing effects sensed across the techniques are compatible (e.g., station displacements, atmospheric refraction, and Earth rotation), hence can be combined at any processing level — observation equations, NEQs ($\mathbf{N}$,$\mathbf{u}$), or parameters ($\hat{\mathbf{x}}$, $\mathbf{C}_{\hat{\mathbf{x}}}$) — the design consistency needs to be assured.

Developed here, Fast Geodetic Simulation Tool (`FGST`) is a Monte Carlo simulation engine designed to study the impact of the observation geometry, and systematic and random effects on the estimation of ordinary parameters (e.g., residual atmospheric delays, station and satellite clocks, and residual coordinates) in the space geodetic adjustment. Since the focus of the dissertation is placed on the description of atmospheric refraction and geophysical loading effects, `FGST` assumes that these two may solely affect the related observations, and that all other effects (e.g., orbital perturbations and source structure) are perfectly understood, thus no parameters are set up in the ensuing adjustment. As the dominant stochastic error budget stems from (i) water vapor content fluctuations in the lower troposphere, (ii) the stability of the related frequency standards, and (iii) the level of Gaussian noise, the sum thereof determines the noise that drives the simulator. While the author is familiar with the fact that the noise in the geodetic observations in not only white (e.g., Williams, 2008), it was decided that investigations on the noise color digress from the main objectives of the dissertation.

For the simulation of the delays induced by propagation through the turbulent electrically neutral atmosphere, two assumptions have been adopted; the geometric optics approximation still

holds, and the ray-path remains unaffected (Nilsson et al., 2013). There are two ways to obtain the turbulent slant delays based on which the `FGST` operates, that is, apply the contribution of atmospheric turbulence on: (i) the non-hydrostatic refractivity tensor and perform ray-tracing for every simulation run, and (ii) the delays obtained by numerical integration at the different stations/epochs/directions employing non-turbulent refractivity tensors (ray-tracing performed only once per observation). It was decided to follow the latter, out of convenience. In so doing, equivalent zenith non-hydrostatic delays d^z_{nh} were employed

$$d^z_{nh} = \frac{d_{nh}}{mf_{nh}}, \tag{2.6.1}$$

where d_{nh} denotes the slant non-hydrostatic delay, and mf_{nh} is the mapping factor cf. (4.2.3). All quantities in (2.6.1) are dependent upon the direction of the ray (elevation and azimuth), and time. Utilizing symmetric mapping functions such as the Potsdam mapping functions PMF (cf. Sec. 4.2.4) is most common; nevertheless, the Berlin mapping function BMF (cf. Sec. 4.2.5) was used instead for enhanced precision. The d_{nh} series are simulated as random walk processes (simply time-integrated white noise). Further information on the turbulence simulator can be found in Treuhaft and Lanyi (1987); Nilsson et al. (2007); Nilsson and Haas (2008); Nilsson et al. (2009); Nilsson and Haas (2010); Halsig et al. (2016), as well as the references therein.

The stability of the frequency standards employed by the microwave space geodetic techniques is to an extend responsible for the high quality of the observables as well as the products of the respective geodetic adjustment. VLBI stations are equipped with hydrogen masers, GNSS satellites feature atomic Rubidium and Caesium clocks (and passive hydrogen masers for Galileo), GNSS stations are usually equipped with quartz crystal oscillators (ASD = 10^{-9}@1 s), oven-controlled quartz oscillators (ASD = 10^{-12}@100 s) — sometimes GNSS receiver clocks are locked to the frequency of a nearby AHM — and the DORIS composite clock is realized by quartz crystal ultra stable oscillators (ASD = 10^{-13}@1000 s). However, the finite stability of these oscillators is responsible for a large portion of the random errors inherent in the observations. Since clock instabilities cannot be predicted with a sufficient accuracy in reality, their influence on the observations simulated by `FGST` is described as a stochastic process. For active hydrogen masers (VLBI) it is $\mathrm{argmin}_\tau(\mathrm{ASD}) = 1 - -2\,\mathrm{h}$, which is the lowest bound. The upper bound for any τ is approximated by the superposition of a random walk and an integrated random walk, where the power spectral densities (hereinafter PSD) of the driving white noise are 0.15×10^{24} s and 0.05×10^{30} s, respectively (Herring et al., 1990). The stability of the clocks onboard the GNSS satellites is slightly worse at these timescales as they are designed for long-term stability. Due to the fact that the stability floor of Cs, Rb, and passive hydrogen maser (PHM) clocks is one to three orders of magnitude inferior to the one of the AHM, the noise level induced by instabilities of the satellite clocks is simulated accordingly. A distinction is made for the clocks of the different systems; the noise is inflated more for GPS than Galileo and QZSS, and even

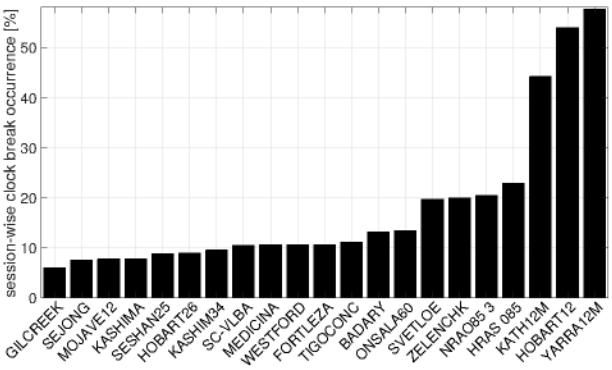


Figure 2.6.1: The probability of at least one clock break per station being detected, based on a complete reanalysis of the IVS and QUASAR archive (1979–2019) with VieVS@GFZ.

Table 2.6.1: Elevation-dependent noise parameters injected in the Monte Carlo simulations of the different GNSS constellations. The ansatz employed is $\sigma_w = \alpha \csc(\varepsilon)$, and the input data are post-fit residuals of the operational multi-GNSS processing at GFZ Potsdam.

	GPS	GLONASS	Galileo	BeiDou	QZSS	MGEX
P3 [mm]	415.46	453.37	419.11	312.33	555.93	409.34
L3 [mm]	4.23	4.61	4.27	4.28	4.50	4.31

more for BeiDou and GLONASS (Z. Deng personal communication). The proper simulation of the stability of the related clocks is crucial also in light of the fact that clock function estimates determined in the geodetic adjustment absorb effects unrelated to the stability of the frequency standards involved (station and satellite clocks). For instance, Halsig et al. (2018) found 3–6 times larger clock variations than direct AHM comparisons, by analyzing VLBI data. No clock breaks have been simulated in the framework of the current dissertation as no matter how many clock breaks occur in a modern VLBI experiment (up to 3), the redundancy of the observations is such that it can cope with the additional parameters being set up without impacting the other estimated parameter or the structure of $\mathbf{C}_{\hat{\mathbf{x}}}$. However, due to the fact that the number of clock breaks that are detected largely varies among stations, simulations would be more realistic if the station-wise of the respective AHMs is considered. Figure 2.6.1 illustrates the probability of clock break occurrence, based on a complete reanalysis of all IVS and QUASAR non-intensive sessions.

White noise should be introduced as well to account for the measurement noise of the observing system e.g., the thermal noise in the case of VLBI (bandwidth, integration time, and source equivalent flux density). The level of the white noise differs considerably across the systems, as well as a function of elevation and time. For instance, for VLBI2010 (Petrachenko et al., 2009) it is expected that the standard deviation of the white noise will be around 1.2 mm, around three times smaller that the current levels. Following Glaser et al. (2017b, 2018), the following levels of white noise may be adopted: 70 cm for code and 5 mm for phase GNSS observations, 9 mm for laser ranges to spherical satellites, 4.5 mm for VLBI group delays, and 0.035 cm s^{-1} for DORIS velocities. Nevertheless, examining the post-fit residuals with state-of-the-art geodetic software reveals that applying constant noise may not be a realistic approximation, as there is a significant dependence upon ε. To determine the elevation-dependent white noise drift rate injected in the GNSS simulations, the post-fit residuals of the dual-frequency ionosphere-free combination of codes (P3) and carrier phases (L3) of a global MGEX network form the operational processing at GFZ Potsdam (Deng et al., 2016) was employed. The noise parameters that were estimated by a least-squares adjustment with $\sigma_w = \alpha \csc(\varepsilon)$ serving as the observation equation (the elevation-dependent second central moment of the post-fit residuals served as observations), are illustrated in Tab. 2.6.1. Figure 2.6.2 illustrates the simulated driving white noise to be applied to the carrier phase GNSS observations. The uncertain interplay between the quality of the satellite clocks and the post-fit residuals is beyond the scope of this work. Accepting the premise that the contribution of the atmospheric delay and geophysical loading are the sole occupants of the observation space, the observation equation reads

$$\tau_{atm} + \tau_{load} + w = mf_h\, d_h^z + mf_{nh}\, d_{nh}^z + mf_g\, (G_{NS}\cos(\alpha) + G_{EW}\sin(\alpha)) + clk + d\mathbf{x}, \tag{2.6.2}$$

where d_{atm} denotes the ray-traced delay, the term $mf_h d_h^z$ denotes the assembled slant hydrostatic delay, $mf_{nh} d_{nh}^z$ is the slant non-hydrostatic delay, clk is the station clock function, $d\mathbf{x}$

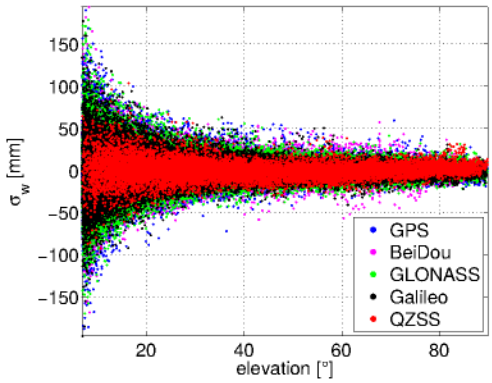


Figure 2.6.2: The driving white noise simulated based on Table 2.6.1 for 2018/04/01.

is the residual position in the topocentric frame[19], and w is the stochastic component of the observations, which is the sum of a random walk process (troposphere), a random walk and an integrated random walk (clock) and white noise. From (2.6.2) d^z_{nh}, G_{NS}, G_{EW}, $d\mathbf{x}$, and clk (similar to equation (2.1.14)) are estimated at intervals similar to those of the analysis of the actual geodetic observations, unless the Kalman filter module is employed; then all parameters are estimated observation-wise. The observation equation (2.6.2) can be taylored to account for other effects as well. Care should be exercised on the relative constrains imposed on segmented parameters. For instance, different zenith delay drift rates should be utilized between a solution where the a priori zenith delay stems from in situ meteorological data, and a solution where the a priori zenith delay stems from an empirical model. This is because in the latter case the residual zenith delays should vary more to account for the unmodelled fluctuations of the hydrostatic component. Therefore, should an empirical model be employed to model atmospheric refraction, the uncertainty of the zenith delay relative constraint equation should be amplified.

While equation (2.6.2) can be applied for modern VLBI, GNSS, and DORIS observations, it should not be applied under poor observation geometry (e.g., very early VLBI experiments, or single satellite DORIS observations). In such cases some parameters cannot be estimated accurately, unless it is at the expense of others. For instance, the analysis of laser ranges to LAGEOS-1 and LAGEOS-2 alone renders the estimation of hourly gradient components not only inaccurate but detrimental for the lateral position components. Hence, in SLR data analysis, gradients should not be estimated but modelled instead, unless the observation geometry permits it. Furthermore, instead of station clocks, range biases are occasionally estimated for SLR, and it is inessential to employ separate mapping functions for the hydrostatic and non-hydrostatic delay component.

The quality of radio-based geodetic technique observations under consideration are to a certain extend independent of weather conditions. Nevertheless, VLBI stations that are not enclosed by a protection radome do not operate under extremely high winds ($>40\,\mathrm{km\,h^{-1}}$), extreme temperatures ($>35\,^\circ\mathrm{C}$ or $<-20\,^\circ\mathrm{C}$), or heavy precipitation ($>50\,\mathrm{mm\,h^{-1}}$). The aforementioned weather conditions assure full performance for the vast majority of geodetic VLBI stations. While

[19]The transition from the ordinary geocentric is conducted at the observation equation level so as to make the corrections between the radial coordinate component estimate and the other parameters more apparent

$$\begin{bmatrix}\delta E\\ \delta N\\ \delta U\end{bmatrix} = \begin{bmatrix}-\sin(\lambda) & \cos(\lambda) & 0\\ -\cos(\lambda)\sin(\varphi) & -\sin(\lambda)\sin(\varphi) & \cos(\varphi)\\ \cos(\lambda)\cos(\varphi) & \sin(\lambda)\sin(\varphi) & \sin(\varphi)\end{bmatrix}\begin{bmatrix}\delta X\\ \delta Y\\ \delta Z\end{bmatrix}. \tag{2.6.3}$$

the loss of potential observation time for most VLBI stations does not exceed a couple of days per year (e.g., according to in situ meteorological only 15 h for `WETTZELL`, on average), there are stations such as `ONSA13SW`, `SC-VLBA`, `OHIGGINS`, and `SYOWA`, that according to ERA5 data do not meet the primary operating conditions for 10 d, 20 d, 35 d, and 60 d per year, respectively. On the other hand, laser ranges through clouds cannot yield station/satellite coordinates or ERP with geodetic accuracy. For the first time, these issues have been treated in the VLBI and SLR simulations. Given a potential observation, that is, a range to a satellite seen with $\varepsilon > 10°$, it has to be determined whether the laser observation can or cannot be carried out. Employing ERA5 cloud occurrence fields, the probability of an observation to be rejected is set proportional to the cloud cover in the vicinity of the SLR station. That is, cloud cover of 70 % translates to a 30 % chance of a successful laser observation (normal point). Four stochastic approaches were examined to represent the inability of SLR to observe under cloudy conditions:

- ☐ Fraction of cloud cover tensors (discretized on 137 levels) have been used to determine the probability of a successful laser range. The direction of each observation is considered. Given that there exist clouds at the altitude of the uppermost model level of ERA5, around 80 km above sea level (noctilucent clouds), the projection of the exit point of a ray from the upper boundary of ERA5 on Earth's surface can be as far as 450 km from the ground station ($\cot(10°)\cdot 80\,\mathrm{km}$). Therefore, given that the spatial resolution of ERA5 is 31 km, the surrounding 15 nodes in every direction are necessary instead of the four nearest nodes. Once the ray-path has been determined (cf. Sec. 3.2), the cloud cover fraction at the nodes of the ray-path is interpolated employing Lagrange polynomials, and the occurrence probability (one minus total cloud cover) is calculated as adopting the maximum-random overlap assumption (Geleyn and Hollingsworth, 1979), that is, $\prod_{j=1}^{137} \frac{1-\max(c_j,c_{j-1})}{1-c_{j-1}}$, where c_j denotes the cloud fraction at layer j.

- ☐ Based on the cloud distribution at three altitudes at a given time, the reduced cloud cover tensor is built, and it in turn serves to assess whether the ray encounters clouds from the station to the satellite. This is determined employing low ($\leq 2\,\mathrm{km}$), medium (2–6.5 km), and high (6.5–80 km) cloud cover fields (LCC, MCC, and HCC, respectively). So, the elevation and the azimuth of each observation are considered, as well as the cloud distribution as a function of time.

- ☐ The probability of a ray experiencing cloud formation is determined by the total cloud cover (TCC) aloft a station at a given time. So, the "actual" cloud distribution is considered, but the direction of the ray is disregarded.

- ☐ The probability of a ray never reaching the satellite is determined by the long-term time average of the TCC aloft a station. So, the "average" cloud distribution is somehow considered, but the direction of the ray is disregarded.

Figure 2.6.3 and Fig. 4.1.9 illustrate the 2000–2018 average LCC, MCC, HCC, and TCC calculated from ERA5. Since no steep spatial gradients are to be found in the temporal average of LCC, MCC, or HCC, it is futile to account for the actual ray-path in an average cloud cover tensor. While there are spatial patterns discernible on the temporally averaged fields, it is very difficult to distinguish them in the instantaneous fields. Note that the intuitive at first exposure $TCC = LCC + MCC + HCC$ does not hold. Still, these approaches to generate potential laser observations seems to be belied by the empirical evidence as the station performance is usually much lower than the potential determined by the cloud occurrence. There are sites such as

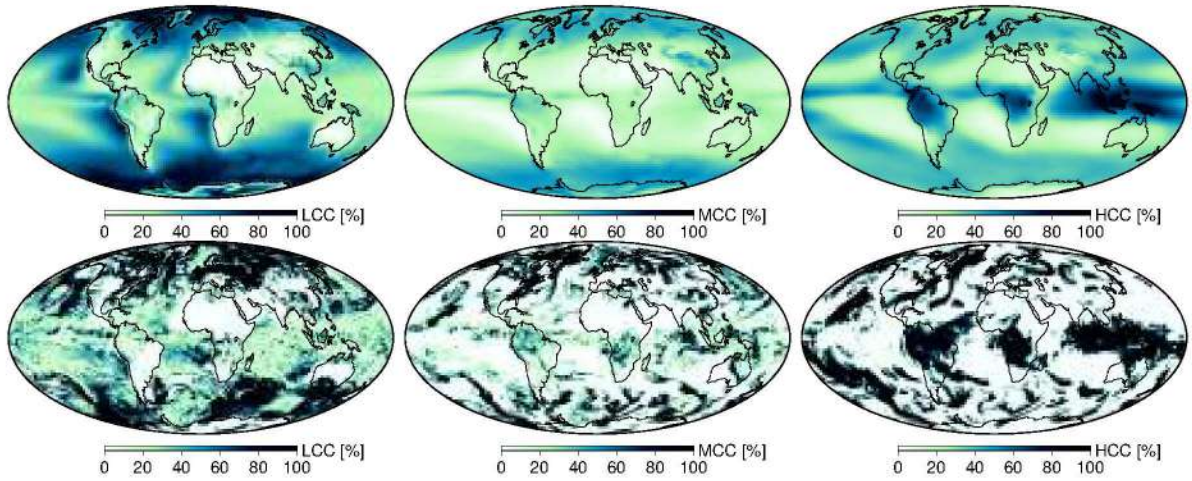


Figure 2.6.3: Low (1st column), medium (2nd column), and high (3rd column) cloud cover from ERA5 fields. Shown are the 2000–2018 average (upper row) fields, and the instantaneous fields on 2017/01/01 00:00 (lower row).

Zimmerwald and Yarragadee where the performance is higher than expected, proof that observatories with automatic operations outpace those with manual operations (Glaser et al., 2019). Further investigation on such discrepancies will feature in future research.

For the simulation of past observations conducted by existing stations, the `RINEX` GNSS and DORIS files, the log VLBI files, as well as the SLR/LLR normal point files can be utilized by just applying a proper noise function to the "computed" vector ($\mathbf{y^0}$). Nevertheless, the fact that a potential laser observation to e.g., LAGEOS-2 was not obtained may not be related to weather conditions, but to the fact that another satellite had to be observed instead or that no operator was available to carry out the observation. Thus, to fully understand the potential limitations imposed on an SLR observatory by weather and its subsequent repercussions on the parameter estimation process, it is crucial that the clouds be taken into consideration. Besides, to realistically simulate observations at a planned laser station, it is far better to account for the cloud occurrence in the simulation of the observations than to randomly set that e.g., 80 % of the potential observations (or arcs) are lost. For instance, based on the cloud occurrence fields an automatically operated laser station in South Africa will be able to perform more observations than a station in Antarctica or the Amazon rainforest. Notwithstanding the additional observations, the utility of a new station has to be rigorously assessed in the POD as well as the TRF determination (Glaser et al., 2019).

To realistically simulate VLBI, SLR, GNSS, and DORIS observations employing `FGST`, vast torrents of data were ingested; refractivity tensors to obtain ray-traced delays, cloud cover fields, satellite orbits, and VLBI schedules drive the simulator. For the ray-tracing and the degree of cloud cover utilized in simulations conducted here, hourly ERA5 fields were employed at the native resolution (31 km). Additional motivation for choosing to work with hourly 3D cloud cover fields rather than location-specific constants was provided from the fact that TCC time series show poor correlation in space and time, and thus are difficult to model analytically[20]. Figure 2.6.5 and Fig. 2.6.6 attest to that statement and also show that the spatiotemporal variations differ largely between winter and summer. The multi-GNSS and SLR satellite orbits

[20]The overlapping Allan variance calculated for the TCC time series suggests that for $\tau < 24\,\mathrm{h}$ TCC is a random walk process, and for larger averaging intervals it gradually becomes a white noise process.

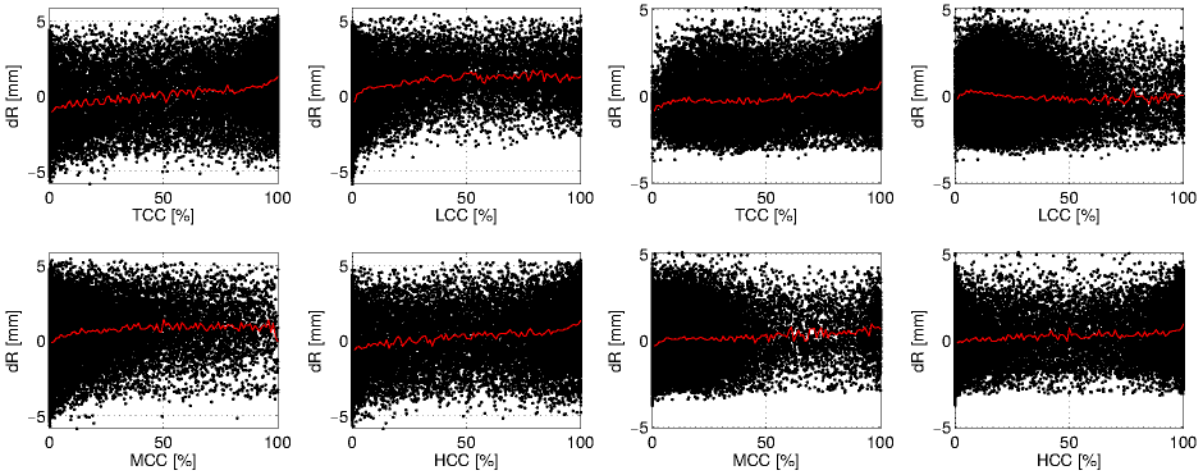


Figure 2.6.4: Scatterograms between simulated radial component displacements due to non-tidal atmospheric pressure loading (cf. Sec. 5.2) and cloud cover, from ERA5 fields at Arequipa, Peru (left), and Papeete, Tahiti (right).

were retrieved from GFZ-Potsdam[21] and GFZ-Oberpfaffenhofen[22], respectively. The orbits of satellites that are not processed by GFZ were obtained from the precise satellite ephemerides of SGF[23], Herstmonceux, UK. The DORIS orbits were obtained from CNES-SSALTO[24]. Figure 4.1.5 illustrates the ground track for the most important GNSS constellations for a single day. In Fig. 4.1.8 shown are the ground tracks of the most commonly observed satellites with SLR.

The results (e.g., station coordinates) displayed in the subsequent Chapters 6 and 7 stem from a least median of squares estimator (e.g., Rousseeuw and Leroy, 2005) over the $n = 50$ ensemble members. Given the estimates of n runs (herein observations), subsets of $n_j = u$ are formed. The least median of squares is obtained employing the objective function

$$\Omega = \min \left(\underset{j}{\text{median}} \left\{ \mathbf{v}_j^2 \right\} \right), j \in \left(1, \binom{n}{u} \right), \tag{2.6.4}$$

where $\mathbf{v_j}$ are the residuals between the $\mathbf{x_j}$ solution and all n observations. A reweighting of the observations is applied

$$w_i = \begin{cases} 1, \text{ if } |v_i| \leq k \sqrt{\dfrac{\left(1 + \dfrac{5}{n-u}\right)}{\Phi^{-1}(0.75)} \sqrt{\Omega}} \\ 0, \text{ otherwise} \end{cases}, \tag{2.6.5}$$

where j runs over permutations, i runs over observations, Ω is calculated following (2.6.4), Φ denotes the cumulative distribution function of the standard normal distribution, k denotes the statistical significance level (e.g., $k = 3$ for 99.7 %). The multiplicand (square root) in the first case of (2.6.5) denotes the robust unit weight standard deviation. The numerator of the fraction

[21] ftp://ftp.gfz-potsdam.de/GNSS/products/mgnss/
[22] ftp://edc.dgfi.tum.de/slr/products/orbits/
[23] ftp://cddis.gsfc.nasa.gov/pub/slr/cpf_predicts/*.sgf
[24] ftp://cddis.gsfc.nasa.gov/doris/products/orbits/ssa/

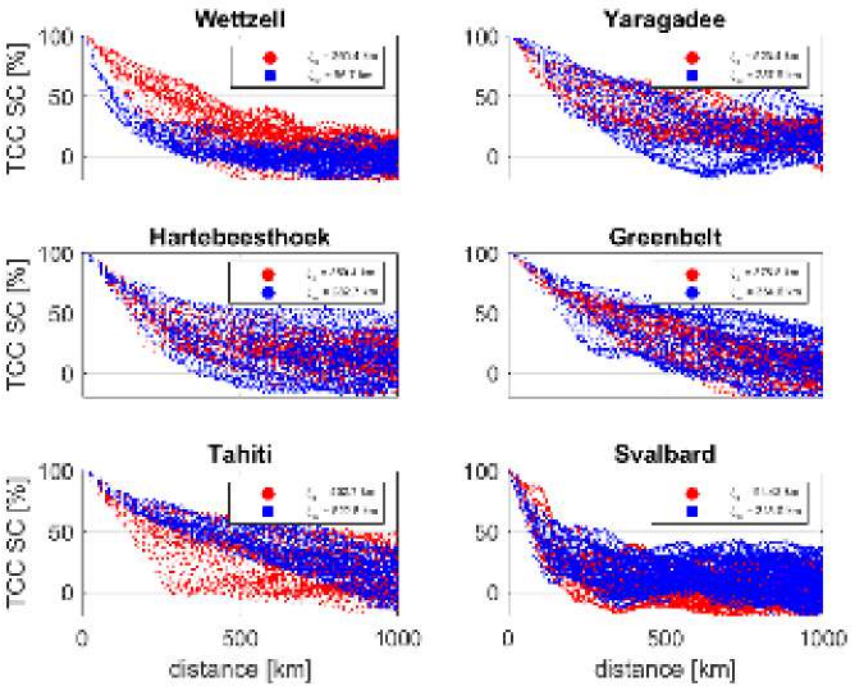


Figure 2.6.5: The spatial correlation (SC) between ERA5-derived TCC time series at some SLR stations (active or planned) and virtual stations (ERA5 grid nodes) over summer (red) and winter (blue). ξ_s and ξ_w denote the correlation length from the covariance model of Hirvonen (4.3.5) for summer and winter, respectively.

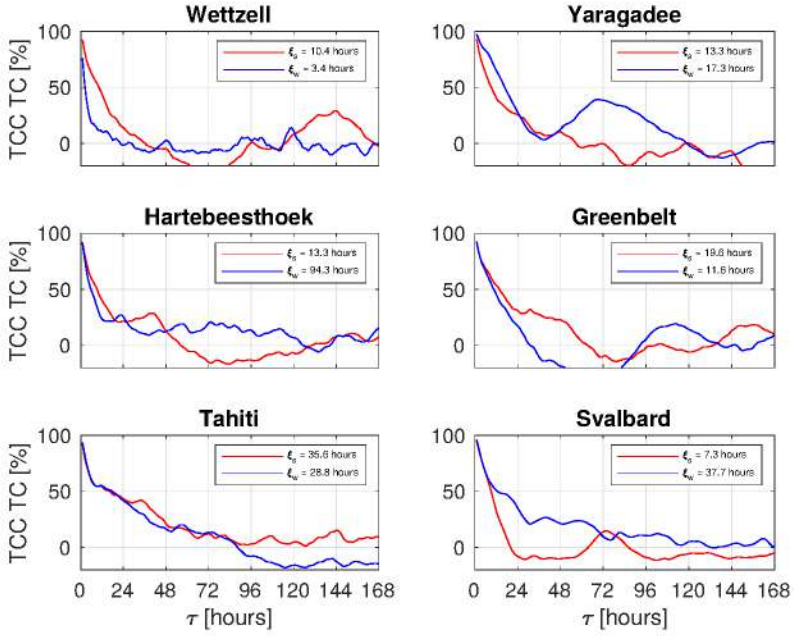


Figure 2.6.6: The temporal auto-correlation (TC) of ERA5-derived TCC time series at some SLR stations (active or planned) over summer (red) and winter (blue). ξ_s and ξ_w denote the correlation time lag from the covariance model of Hirvonen (4.3.5) for summer and winter, respectively.

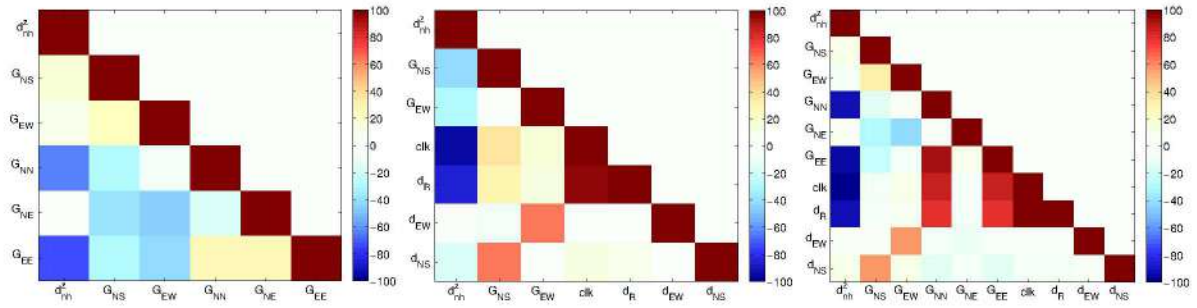


Figure 2.6.7: The correlation matrix of the adjustment carried out for the GNSS simulations, at Wettzell, where different parameters are set up as unknowns.

in (2.6.5) assures no underestimation occurs in case of small redundancy. This approach has been employed in a different context by Bachmann et al. (2016) as well as by the IVS tropospheric combination centre[25].

As no deterministic clock function is simulated nor any ground antenna motion (except for tectonics and environmental loading), the systematic and random deviation of the respective estimated parameters (station coordinates, and characteristics of the receiver clock described by a three-state temporal model (Gödel et al., 2017) including a time offset parameter, a frequency offset parameter, and a frequency drift parameter) from zero is indicative of either lacking deterministic model or observation geometry. Following Chaffee (1987); Greenhall (2011); Suess and Matsakis (2011), the clock state at epoch t is

$$\mathbf{x}(t) = \begin{bmatrix} 1 & \tau & \frac{\tau^2}{2} \\ 0 & 1 & \tau \\ 0 & 0 & 1 \end{bmatrix} \mathbf{x}(t-\tau) + \mathbf{w}(t,\tau), \tag{2.6.6}$$

where τ is the integration interval. The evolution of $\mathbf{x}(t)$ is driven by the stochastic differential equation

$$\frac{d\mathbf{x}(t)}{dt} = \begin{bmatrix} 0 & 1 & 0 \\ 0 & 0 & 1 \\ 0 & 0 & 0 \end{bmatrix} \mathbf{x}(t) + \mathbf{w}(t), \tag{2.6.7}$$

where $\mathbf{w}$ is the process noise whose covariance matrix (symmetric) reads

$$\mathbf{Q}(t,\tau) = \begin{bmatrix} q_1\tau + \frac{q_2\tau^3}{3} + \frac{q_3\tau^5}{20} & \frac{q_2\tau^2}{2} + \frac{q_3\tau^4}{8} & \frac{q_3\tau^3}{6} \\ & q_2\tau + \frac{q_3\tau^3}{3} & \frac{q_3\tau^2}{2} \\ & & q_3\tau \end{bmatrix}, \tag{2.6.8}$$

where $\begin{bmatrix} q_1 & q_2 & q_3 \end{bmatrix}^\top$ denote the time-dependent variance of the white, the random walk, and the random run frequency modulation, respectively.

The simulations are imperative as they provide a hindsight on the possible influence of different measurements and parameters estimated in the geodetic adjustment, as well as the

[25] http://media.gfz-potsdam.de/gfz/sec11/projects/tropospheric_combination_centre/Balidakis_IVS_tropo_combi.pdf

understanding of the interplay of parameters that are non-linearly related. For instance, Fig. 2.6.7 illustrates the correlation matrices calculated from the respective covariance matrices (2.5.13) of a GNSS adjustment utilizing all satellite observations available at 2018/01/01, following (6.4.1). Three different parameter setups were carried out. It is important to note the correlation between (i) clk, d^z_{nh} and d_R, (ii) G_{NS} and d_{NS}, and (iii) G_{EW} and d_{EW}, where $\begin{bmatrix} d_R & d_{EW} & d_{NS} \end{bmatrix}^\top$ is the station displacement vector in the topocentric frame (up, East-West, North-South). The correlation between G_{NS} and d_{NS} is larger than correlation between G_{EW} and d_{EW} due to the fact that in most cases the skyplot is symmetric about the North-South axis, provided no obstacles lie in the vicinity of the station. That is, the number of observations with negative and positive sine of azimuth (partial derivative for G_{EW}) are almost equal, whereas the number of observations with negative and positive cosine of azimuth (partial derivative for G_{NS}) are not equal. The latter has been confirmed by Zhou et al. (2017) by analyzing real multi-GNSS observations, however, without providing a justification for this effect.

To assess whether the software described in the preceding paragraphs, `FGST`, simulates the aforementioned random effects faithfully and provides realistic results, a number of tests were carried out. First, runs were carried out for all modules applying no noise (white noise or refraction- or clock-induced), nor systematic mismodelling (e.g., employing a weather-driven mapping function to simulate, and an empirical mapping function to reduce the simulated observations), that is, $\mathbf{b} = \mathbf{0}$ ("observed" equals "computed"). The results of these so-called "zero tests" were that $\hat{\mathbf{x}} = \mathbf{0}$ and $\hat{\mathbf{v}} = \mathbf{0}$. Of course, they slightly deviate from zero due to e.g., round-off errors. There were cases where due to extremely poor observation geometry (especially in the SLR simulations for stations under very cloudy conditions), a least-squares solution (employing singular value decomposition) could not be achieved (e.g., the number of observation equations was smaller than the number of unknown parameters being set up) or the variation of the number of observations was considerable (e.g., by more than 100 %) between the different runs within the ensemble. The latter resulted in a very large ensemble spread. To treat such issues, absolute constrains on all parameters can be applied, e.g., the difference between the coordinate estimate vector and the a priori thereof should not exceed 5 m. Doing so, it is possible to obtain a solution even if no observations are available. However, such cases are of no interest herein, as they do not allow to investigate the effects to which this thesis is dedicated (mm-level), therefore, they were identified and eliminated from further analysis. When noise was injected in the simulator, the residuals' vector $\mathbf{v}$ was assessed. Due to the fact that several effects that have a systematic impact on geodetic observations have not been considered in the geodetic adjustment (e.g., deformation due to surface thermal radiation (Haas et al., 2013)), they have not been considered in `FGST` either. Therefore, it is not possible to compare directly real and simulated observations. This limitation expands to simulators such as `VIE_SIM` of `VieVS@GFZ` (e.g., Pany et al., 2011; Glaser et al., 2017a). As an alternative, a comparison was carried out between the WRMS of the post-fit residuals from the analysis of the real observations, and the ensemble mean of the respective WRMS from the individual simulation runs. Accounting for the fact that the simulated observations heavily rely on real weather data (ERA5), the good agreement found suggests an appropriate driving noise for the different stochastic processes, as well as a suitable deterministic model. Second, comparisons were carried out between the ensemble scatter of e.g., station coordinates, and the uncertainty of station coordinates from the services' (IVS, ILRS, IGS, and IDS) contribution to the latest ITRS realization, ITRF2014. The volume of the uncertainty ellipsoid of the station coordinates from the simulated observations is typically slightly smaller since there is a host of effects that are not yet fully understood in the analysis of real observations and consequently a number of "nuisance" parameters need to be set up, which are not set up in `FGST`. Nevertheless, the comparison of VLBI simulations with the output of `VIE_SIM`

of `VieVS@GFZ` (external validation), which has been used extensively for the simulations in the framework of VGOS as well as for GGOS-SIM[26], indicates that its ensemble scatter is on par with the ensemble scatter from `FGST` — after a bug fix in clock simulation module by B. Soja (the ASD of the individual stochastic processes was larger by a factor of $\sqrt{2}$). This is an indicator that the noise added to the observations by `FGST`, as well as the weighting scheme were realistic. Moreover, the impact of e.g., erroneous meteorological observations and mapping functions on residual atmospheric delays and station coordinates has been assessed by both `VieVS@GFZ` and `FGST`, and the results were in excellent agreement.

[26] https://www.gfz-potsdam.de/en/section/space-geodetic-techniques/projects/ggos-sim/

3 Background on atmospheric signal propagation

Given a moist air packet of barometric pressure P, density ρ, thermodynamic (absolute) temperature T and water vapor mole fraction x_v, the non-ideal equation of state (EOS) may be expressed as (e.g., Picard et al., 2008)

$$\rho = \frac{PM_d}{ZRT}\left(1 - x_v\left(1 - \frac{M_v}{M_d}\right)\right), \tag{3.0.1}$$

where R is the molar gas constant, Z is the compressibility factor of moist air, and M_d and M_v are the mole fraction of dry air and water vapor, respectively. The parameters P, ρ, T, x_v, and Z participating in (3.0.1) are in constant flux. The latitudinal contrast of solar heating gives rise to poleward ρ gradients, that drive atmospheric circulation. P differences, ensuing the different expansion rates of Earth's geophysical fluids, induce atmospheric motion at a multitude of spatiotemporal scales partly in the form of winds. By and large, the temporal evolution of atmospheric conditions exerts three disturbing effects in space geodetic data analysis:

- ☐ the signals emanating from quasars, navigation, retroreflector-carrying, or beacon-receiving satellites, suffer refraction and delay that mainly depend upon the pressure, temperature and water vapor distribution in the neutral atmosphere;

- ☐ the crust of the Earth undergoes loading deformation and the gravity vector is affected following continuous mass redistribution (atmospheric and oceanic circulation, hydrological cycle); and

- ☐ the vector of Earth's rotation (spin axis direction and rotation rate) undergoes internal torques stemming from angular momentum exchange between solid Earth and the fluid envelope thereof i.e., atmosphere, oceans, and the continental hydrosphere (e.g., Schindelegger et al., 2013).

Provided the underlying driving mechanisms are well understood, these effects can be accurately reduced from geodetic observations, with the caveat that the state of the atmosphere is accurately known. The latter cannot be inferred solely from meteorological observations at the surface of the Earth owing to the highly volatile lapse rate of parameters such as water vapor density. Currently, information on global atmospheric circulation is obtained by proper manipulation of the state tensors that stem from the method of numerical weather prediction introduced almost a century ago, thus constituting the so-called numerical weather models (NWMs). In essence, NWMs are software capable of solving a number of nonlinear differential equations (the so-called primitive equations) that describe atmospheric circulation based on predefined boundary conditions, suitable model parametrization, and of course weather observations. Therefore, NWMs are an invaluable commodity for the conduct of the research carried out in the framework of the current. For a comprehensive description of how the assimilation process is carried out by

state-of-the-art NWMs, the interested reader is referred to ECMWF (2017) and the numerous references therein.

This chapter aims at providing the fundamental background on which the developments presented in Chapter 4 and Chapter 5 build upon. Emphasis is placed on the troposphere, the atmospheric layer that undergoes net radiative cooling and at the same time is being climatically balanced by water vapor fluxes from Earth's surface (Sherwood et al., 2010), because shortcomings in modelling thereof e.g., the water cycle, pose a major roadblock to the determination of geodetic parameters, owing to poor geophysical models. An introduction to NWMs is not attempted. A general background on atmospheric composition may be found in Böhm et al. (2013a) as well as the references therein. This chapter is organized as follows. Section 3.1 is dedicated to signal propagation in the atmosphere. A Maxwellian (Sec. 3.1.1) derivation of the eikonal equation (Sec. 3.1.2) is presented. The atmospheric range correction theory for radio and optical space geodetic techniques in the electrically neutral atmosphere (Sec. 3.1.3) is reviewed. Section 3.2 describes the ray-tracing algorithm utilized in this work, that is, Euler-Lagrange equations corresponding to Fermat's principle (Zus et al., 2012, 2014). Section. 3.3 describes the approach developed here to homogenize meteorological parameters recorded in situ, in the vicinity of SLR and VLBI stations, employing state-of-the-art NWMs. In Sec. 3.3.1, a detailed presentation of the reference meteorological series computation methodology takes place, introducing a non-ideal equation of state (compressibility factor included) as well as a rigorous scheme to obtain the vertical component of the position operator of the NWM tensors. The merit of the approach introduced is most apparent in the context of extracting meteorological parameters at ridged topography. The methodology presented here is particularly useful not only to simulate atmospheric refraction effects, but to compose the mass anomalies induced by atmospheric circulation (cf. Sec. 5.2). In Sec. 3.3.2 the results of the homogenization process applied to the complete historical archive of in situ VLBI and SLR/LLR meteorological parameters is presented. According to the results obtained here, a large number of meteorological sensors reported parameters that have a systematic bias, several jumps, and sometimes trends. For instance, a pressure jump of 1.3 hPa in the SLR data of Wettzell apparently introduces an erroneous velocity, and a consistent ≈ 2 hPa pressure bias across the VLBA is probably responsible for discrepancies between global parameters estimated from the analysis of the IVS and the VLBA VLBI network. Moreover, the barometric pressure time series recorded in the vicinity of several VLBA stations (see for example `KP-VLBA`, `LA-VLBA`, and `NC-VLBA`) as well as other IVS stations (see for example `MATERA`) experience positive trends. These trends are in disagreement (within confidence level 0.99) with the pressure trends derived from ECMWF (operational analysis, ERA-Interim, and ERA5), as well as GMAO models (MERRA2).

3.1 Wave propagation through Earth's atmosphere

For a comprehensive review of signal propagation in the electrically neutral atmosphere and the ionosphere from a geodetic viewpoint, the interested reader is referred to Nilsson et al. (2013) and Alizadeh et al. (2013), respectively, as well as the numerous references therein.

3.1.1 Maxwell's equations

The electromagnetic radiation field employed by space geodetic techniques to measure the distance between transmitter and receiver is distorted as it interacts with atmospheric matter. The effect of electromagnetic radiation on material objects is described by the electric vector $\mathbf{E}$, the magnetic induction $\mathbf{B}$, the electric current density $\mathbf{j}$, the electric displacement $\mathbf{D}$, and the mag-

netic vector $\mathbf{H}$. Maxwell's equations connect these vectors as well as the space-time derivatives thereof (e.g., Born and Wolf, 1999)

$$\begin{aligned} \nabla \cdot \mathbf{D} &= 4\pi\rho \quad \text{(Gauss' law for electric fields)}, \\ \nabla \cdot \mathbf{B} &= 0 \quad \text{(Gauss' law for magnetic fields)}, \\ \nabla \times \mathbf{E} + \frac{1}{c}\frac{\partial \mathbf{B}}{\partial t} &= \mathbf{0} \quad \text{(Faraday's law of induction), and} \\ \nabla \times \mathbf{H} - \frac{1}{c}\frac{\partial \mathbf{D}}{\partial t} &= \mathbf{j}\frac{4\pi}{c} \quad \text{(Ampère's law)}, \end{aligned} \tag{3.1.1}$$

where ρ is the electric charge density and $c = \frac{1}{\sqrt{\varepsilon_0 \mu_0}}$ is the speed of light in vacuum. The relations (3.1.1) are supplemented by the constitutive relations that have a simple form for an isotropic medium

$$\begin{aligned} \mathbf{j} &= \sigma \mathbf{E}, \\ \mathbf{D} &= \varepsilon_0 \mathbf{E} + \mathbf{P}, \\ \mathbf{B} &= \mu_0 \mathbf{H} + \mathbf{M}, \end{aligned} \tag{3.1.2}$$

where σ is the specific conductivity, ε_0 is the vacuum electric permitivity, $\mathbf{P}$ is the polarization, μ_0 is the vacuum magnetic permeability, and $\mathbf{M}$ describes magnetization. Due to the fact that in the atmosphere (static, linear, non-conducting and isotropic medium) $\rho = 0$, $\mathbf{M} = \mathbf{0}$, $\mathbf{P} = \mathbf{0}$ and $\mathbf{j}$ is negligibly small, employing the constitutive relations Maxwell's equations can be rewritten

$$\nabla \cdot \mathbf{E} = 0, \tag{3.1.3}$$

$$\nabla \cdot \mathbf{H} = 0, \tag{3.1.4}$$

$$\nabla \times \mathbf{E} = -\frac{\mu}{c}\frac{\partial \mathbf{H}}{\partial t}, \tag{3.1.5}$$

$$\nabla \times \mathbf{H} = \frac{\varepsilon}{c}\frac{\partial \mathbf{E}}{\partial t}, \tag{3.1.6}$$

where ε is the permitivity and μ is the permeability of the medium. To derive the wave equation, first (3.1.5) and (3.1.6) are differentiated with respect to time. The fact that $\nabla \times (\nabla \times) = \nabla(\nabla \cdot) - \Delta$ and $\nabla \varsigma \Upsilon = \varsigma \nabla \times \Upsilon + (\nabla \varsigma) \times \Upsilon$, where ς any scalar and Υ any vector, is employed. After some manipulation, and assuming a homogeneous medium (ε and μ do not vary considerably over space and time) the standard equations for electromagnetic waves being propagated with phase velocity $v = \frac{c}{\sqrt{\varepsilon\mu}}$ are obtained

$$\begin{aligned} \Delta \mathbf{E} - \frac{\varepsilon\mu}{c^2}\frac{\partial^2 \mathbf{E}}{\partial t^2} &= \mathbf{0}, \text{and} \\ \Delta \mathbf{H} - \frac{\varepsilon\mu}{c^2}\frac{\partial^2 \mathbf{H}}{\partial t^2} &= \mathbf{0}. \end{aligned} \tag{3.1.7}$$

Employing Maxwell's formula, the phase velocity is related to the light velocity in vacuum via the absolute refraction index n

$$n \equiv \frac{c}{v}. \tag{3.1.8}$$

Assuming that local dispersion is very small and linear, the group velocity is related to the phase velocity via Rayleigh's formula

$$v_g = v + k\frac{\partial v}{\partial k}, \tag{3.1.9}$$

and the group refraction index ($n_g \equiv \frac{c}{v_g}$) reads

$$n_g = v + k\frac{\partial n}{\partial \omega}, \tag{3.1.10}$$

where $\omega = \frac{2\pi}{f}$ denotes the angular frequency of the propagating wave.

Due to μ practically being unity, Maxwell's relation reduces to $n^2 = \varepsilon_r$, where $\varepsilon_r = \frac{\varepsilon}{\varepsilon_0}$ is the relative dielectric constant or permitivity. By and large, ε_r is a radiation frequency function, what constitutes the effect of dispersion. In the absence of dispersion (e.g., troposphere), the phase velocity coincides with the group velocity. Moreover, as phase velocity has no physical significance, it is possible that $v > c$ e.g., in regions of anomalous dispersion.

3.1.2 The eikonal equation

Assuming a (nearly) plane wave i.e., many λ away from the source of radiation, the general time-harmonic field is expressed (e.g., Born and Wolf, 1999)

$$\mathbf{E}(\mathbf{x}, f, t) = \mathbf{e}e^{i(k_0 S - 2\pi f t)} \quad \text{and} \quad \mathbf{H}(\mathbf{x}, f, t) = \mathbf{h}e^{i(k_0 S - 2\pi f t)}, \tag{3.1.11}$$

where $S(\mathbf{x}, f)$ denotes the so-called eikonal (or optical path length), $\mathbf{e}(\mathbf{x}, f)$ and $\mathbf{h}(\mathbf{x}, f)$ are weak functions of position $\mathbf{x}$, and k_0 is the wave number in vacuum. If monochromatic radiation is considered, as well as that ε does not vary appreciably over the radiation wavelength, the Helmholtz equation holds: $\left(\Delta + k^2\right)\mathbf{E} = 0$. Replacing the wave number (wave vector $\mathbf{k} = k\hat{\mathbf{s}}$ norm, where $\hat{\mathbf{s}}$ denotes the direction of the wave) in the medium with the respective in vacuum, $k = k_0 n$, leads to

$$\Delta\mathbf{E} + k_0^2 n^2(\mathbf{x}, f)\,\mathbf{E} = 0. \tag{3.1.12}$$

To solve the latter, (3.1.11) and (3.1.12) are combined. After simple manipulations, for the case of a high-frequency wave propagating through a slowly varying medium ($\lambda \to 0$ and $\nabla\varepsilon \to 0$) it is (e.g., Wheelon, 2001)

$$\|\nabla S\|_2^2 = n^2 \Leftrightarrow \frac{\nabla S}{n} = \frac{\nabla S}{\|\nabla S\|_2}, \tag{3.1.13}$$

and $2\nabla\mathbf{e}\nabla S + \mathbf{e}\Delta S = 0$. The relation (3.1.13) is the eikonal equation, a non-linear Hamilton-Jacobi partial differential equation, that provides the fundamental setting of geometrical optics. Rays propagate in the direction of ∇S and are normal to surfaces comprising of points of equal

eikonal (S = constant), the geometrical wavefronts. The right part of (3.1.13) is the direction of the time-averaged Poynting vector. Employing the latter, the rays in terms of the eikonal can be expressed by: $n(\mathbf{x}, f)\, d\mathbf{x} = \nabla S(\mathbf{x}, f)\, ds$, where ds is the ordinary line element in Euclidean space.

Herein the geometrical optics principle is adopted, thus, the propagation of an electromagnetic waves is described by the propagation of a ray. The geometrical optics approximation yields an approximate solution to (3.1.1) and (3.1.13), disregarding diffraction, turbulence, interference and extinction (absorption and scattering) effects. The applicability of geometrical optics is subject to the following heuristic conditions (e.g., Kravtsov and Orlov, 1981; Wijaya, 2010):

- the macroscopic parameters of the medium (such as the mass density and the refraction index) as well as the traits of the wave (phase gradient, amplitude) must not vary appreciably over the cross-section of the first Fresnel volume;
- the phase difference between rays arriving/emanating at/to the same point must exceed π; and
- the wavelength must be substantially smaller than the inner scale of turbulence, that is $\lambda \to 0$.

The ray approximations suggests that the optical path length from source to receiver is exactly the same to the OPL from receiver to the signal source (reversibility principle).

So, integrating (3.1.13) over the ray path between e.g., a satellite α and a ground receiver β yields the optical path length (hereinafter OPL) between the points

$$R = S_\beta - S_\alpha = \int_\alpha^\beta n(\mathbf{x}, f)\, ds, \tag{3.1.14}$$

which constitutes the main observable in techniques such as GNSS and SLR.

Accepting the premise of geometrical optics, light travels in straight lines only in a perfectly uniform medium, like the vacuum. In an inhomogeneous medium the ray bends towards increasing refraction index. The evolution of the ray trajectory described by the eikonal constitutes the so-called ray-tracing procedure (cf. Sec. 3.2).

3.1.3 Propagation through the electrically neutral atmosphere

In this section the method for treating the propagation effect on signals traversing the electrically neutral atmosphere in a non-turbulent framework is reviewed. The atmospheric propagation effect that consists of dispersion and refraction, delays the propagation of a signal along a bent trajectory. The related delay in a dispersive medium can theoretically be mitigated by a multi-frequency combination (e.g., Guier and Weiffenbach, 1960). All developments carried out here in this context presuppose that the response of the atmosphere as a medium to the radiation employed by space geodetic techniques is described by macroscopic parameters such as the refraction index.

Since for space geodetic techniques operating in the microwave band (e.g., VLBI, GNSS, and DORIS) the ionosphere is a dispersive medium, the ionospheric advance can be effectively eliminated (more than 99 % of the effect) by utilizing measurements at two frequencies. The combination of signals at more frequencies facilitates the treatment of higher order terms (2.3.5). Ionospheric refraction for radio waves is addressed in Sec. 4.1.5.

In the absence of dispersion ($\frac{\partial n}{\partial f} = 0$), propagation delay effects must be treated by other means (e.g., modelling or estimation). Usually, in microwave-based systems (VLBI, GNSS, and DORIS) the largest (climate-driven) portion of atmospheric delay is modelled, and weather-dependent delay fluctuations are estimated as PWLFs or random walk processes based on the geodetic measurements.

For techniques utilizing optical frequencies (e.g., SLR or LLR), the electrically neutral atmosphere is a dispersive medium. Unfortunately, owing to low return rates from high orbiting satellites (e.g., LAGEOS and Etalon), and to satellite signature effects from low Earth orbiters (e.g., GRACE and GOCE), adopting a two-color reduction methodology (e.g., Wijaya and Brunner, 2011) is not practicable to mitigate the tropospheric delay because the noise is prohibitively amplified. Since the relatively poor observation geometry hinders the estimation of atmospheric delay parameters — a standard procedure for microwave-based techniques — the delay laser ranges suffer is customarily modelled.

Therefore, as dispersion cannot be exploited to eschew modelling, the tropospheric delay is treated in a similar manner for all techniques, taking into consideration the fact that the refraction indices differ as a function of frequency. Under the assumption that the total atmospheric density is zero, that is in vacuum, and the signal under consideration is not prone to other effects e.g., induced by the ionosphere and the solar plasma, the refractive index is an all-ones tensor $\mathbf{n}(\mathbf{x}, f_i) = \mathbf{J}_{\mathbf{nlat,nlon,nlev}}$, and the relevant optical path length (OPL) is reduced to the chord distance between receiver ($\mathbf{x_i}$) and satellite ($\mathbf{x^j}$): $\rho = \int ds_o = \left\|\mathbf{x_i} - \mathbf{x^j}\right\|_2$. Nevertheless, space geodetic observations are always contingent on atmospheric and ionospheric refraction effects, hence the measurements are always larger than ρ.

Since refraction effects are largely systematic, to properly adjust space geodetic observations to estimate e.g., $\mathbf{x_i}$, $\mathbf{x^j}$, or EOPs, for the adjustment ρ is sought instead. The difference between the measured ranges and ρ constitute the atmospheric propagation delay

$$d_{atm} \equiv \int n(\mathbf{x}, f_i)\, ds_i - \int ds_o = \left(\int n(\mathbf{x}, f_i)\, ds_i - \int ds_i\right) + \left(\int ds_i - \int ds_o\right), \quad (3.1.15)$$

where $\int ds_i$ is the geometric length of the optical path, ds_i denotes the ray-trajectory's line element, and ds_o denotes the chord's line element. In essence, the variable refraction index induces delay along the OPL (1st term of (3.1.15)), and ray-bending (2nd term of (3.1.15)). Due to the fact that in Earth's electrically neutral atmosphere it is $n \to 1$ — ≈ 0.0003 (0.0003) for the hydrostatic and ≈ 0.00004 (0.0000008) for the non-hydrostatic part for microwave (optical) frequencies at the surface— the group refractivity N is used instead

$$N \equiv 10^6(n-1). \quad (3.1.16)$$

So, the effect of atmospheric refraction on ranges can be alternatively written as follows

$$d_{atm} = 10^{-6} \int N(\mathbf{x}, f_i)\, ds_i - \rho. \quad (3.1.17)$$

Since the advent of space geodesy, a large number of expressions for the refractivity of moist air at microwave frequency bands has been employed in an attempt to model atmospheric refraction. The ansatz of the vast majority thereof follows the form

$$N = \left(k_1 \frac{P_d}{T} + k_4 \frac{P_d}{T^2}\right) Z_d^{-1} + \left(k_2 \frac{P_w}{T} + k_3 \frac{P_w}{T^2}\right) Z_w^{-1}, \quad (3.1.18)$$

where T is the absolute temperature, P_d and P_w denote the partial pressures for dry air and water vapor, Z_d^{-1} and Z_w^{-1} denote the inverse of the respective compressibility factors that are calculated by virtue of (3.3.5) and (3.3.6). In almost all cases, the k_4 term is not retained. Employing the EOS (3.0.1), the refractivity may be recasted as a function of atmospheric densities in lieu of partial pressures and temperature

$$N = k_1 R_d \rho_d + k_2 R_w \rho_w + k_3 R_w \frac{P_w}{T}, \tag{3.1.19}$$

where the coefficients k_i are the so-called refractivity constants that are usually derived from experimental values and are independent of frequency.

Both (3.1.18) and (3.1.19) are implicitly decomposed to dry (terms multiplied by P_d or ρ) and wet (terms multiplied by P_w or ρ_w) refractivity (N_d and N_w, respectively). However, the distinction between hydrostatic and non-hydrostatic is advantageous for it offers a distinction between the contribution of gases the behaviour of which abides by the hydrostatic equilibrium. Therefore, assuming that the moist air behaves as an ideal gas, the refractivity is reformulated as follows

$$\begin{aligned} N &= k_1 \frac{P}{T_v} + k_2' \frac{P_w}{T} + k_3 \frac{P_w}{T^2}, \\ N &= k_1 R_d \rho_t + k_3 R_w \rho_w \left(\frac{1}{T} + k_5 \right), k_5 = k_3^{-1} \left(k_2 - k_1 \frac{R_d}{R_w} \right), \end{aligned} \tag{3.1.20}$$

where the 1st term denotes the hydrostatic component (N_h), and the sum of the 2nd and 3rd component denote the non-hydrostatic component (N_{nh}).

The expressions presented in (3.1.20) are equivalent to (3.1.18) and (3.1.19), should the total delay be used in the reduction of geodetic ranges.

The most important refractivity expressions for radio wavelengths follow:

- SW53 (Smith and Weintraub, 1953):

$$N = \frac{77.6}{T} \left(P + 4.810 \frac{P_w}{T} \right) = 77.6 \frac{P}{T} + 3.73 \cdot 10^5 \frac{P_w}{T^2} \tag{3.1.21}$$

- TH74 (Thayer, 1974):

$$N = 77.6 \frac{P_d}{T} Z_d^{-1} + 64.8 \frac{P_w}{T} Z_w^{-1} + 3.776 \cdot 10^5 \frac{P_w Z_w^{-1}}{T^2}, \tag{3.1.22}$$

  where Z_d^{-1} and Z_w^{-1} are given by (3.3.5).

- HS75 (Hasegawa and Stokesberry, 1975):

$$N = 77.6 \frac{P_d}{T} + 69.4 \frac{P_w}{T} + 3.701 \cdot 10^5 \frac{P_w}{T^2} \tag{3.1.23}$$

- BE94 (Bevis et al., 1994):

$$N = 77.6 \frac{P_d}{T} + 70.4 \frac{P_w}{T} + 3.739 \cdot 10^5 \frac{P_w}{T^2} \tag{3.1.24}$$

☐ FO99 (Foelsche, 1999):

$$N = 77.65\frac{P_d}{T} + 65.99\frac{P_w}{T} + 3.777 \cdot 10^5 \frac{P_w}{T^2} \tag{3.1.25}$$

☐ RU02 (Rüeger, 2002):

$$N = 77.6890\frac{P_d}{T} + 71.2952\frac{P_w}{T} + 3.75463 \cdot 10^5 \frac{P_w}{T^2} \tag{3.1.26}$$

☐ AL11 (Aparicio and Laroche, 2011):

$$\begin{aligned} N &= N_0 \left(1 + \frac{10^{-6}}{6} N_0\right) \\ N_o &= \left(222.682 + \frac{0.069(273.15 - T)}{T}\right)\rho_d + \left(6701.605 + \frac{6385.886(273.15 - T)}{T}\right)\rho_w, \end{aligned} \tag{3.1.27}$$

where ρ_d and ρ_w are the atmospheric densities for moistless air and water vapor, respectively.

The disadvantage of all aforementioned refractivity expressions in the fashion of (3.1.18) lies in the fact that (i) the nonlinear dependence of atmospheric densities on refractivity is overlooked (usually below $0.04\,\mathrm{mm\,km^{-1}}$), (ii) the definition of the partial pressures P_d and P_w within a non-ideal moist air mixture is ambiguous thus leading to an intrinsic error stemming from multiple representations thereof, and (iii) the non-ideal moist air behavior is either disregarded altogether or described inadequately (e.g., Aparicio and Laroche, 2011).

Conversely, for group refractivity at visible and near-infrared frequencies (SLR/LLR measurements) there is not such a large variety of models, as it is not exited by the permanent dipole moment of water vapor molecules as efficiently as by microwave radiation. The refractivity for lasers is calculated employing Ciddor (1996); Ciddor and Hill (1999), as presented in Mendes and Pavlis (2004); Hulley and Pavlis (2007)

$$N = N_h + N_{nh} \quad = \frac{K_1^L f_h(\lambda) Z_d R_d \left(P - (1-\epsilon)P_w\right)}{T} + \frac{-K_1^L \epsilon f_h(\lambda) Z_d P_w + K_2^L f_{nh}(\lambda) Z_w P_w}{ZT}, \tag{3.1.28}$$

where Z, Z_d, and Z_w are the compressibility factors for moist air, dry air, and pure water packets, respectively, P denotes the total pressure, P_w is the partial pressure of water vapor, and T is the temperature. The wavelength-dependent dispersion formulas for the hydrostatic (f_h) and non-hydrostatic (f_{nh}) component read

$$f_h(\lambda) = 10^{-2}\left(\frac{k_1^*\left(k_0 + \lambda^{-2}\right)^2}{\left(k_0 - \lambda^{-2}\right)^2} + \frac{k_3^*\left(k_2 + \lambda^{-2}\right)^2}{\left(k_2 - \lambda^{-2}\right)^2}\right) C_{CO_2}, \text{ and} \tag{3.1.29}$$

$$f_{nh}(\lambda) = 0.003101\left(w_0 + 3w_1\lambda^{-2} + 5w_2\lambda^{-4} + 7w_3\lambda^{-6}\right), \tag{3.1.30}$$

where λ is the laser pulse wavelength. All other parameters in (3.1.28), (3.1.29), and (3.1.30) are

Table 3.1.1: Optical refractivity constants (Ciddor, 1996; Ciddor and Hill, 1999).

Coefficient	Value
K_1^L	$0.823\,956\,8\ \mathrm{K\,Pa^{-1}}$
K_2^L	$0.724\,760\,0\ \mathrm{K\,Pa^{-1}}$
ϵ	0.622
k_0	$238.0185\ \mu\mathrm{m}^{-2}$
k_1^*	$19\,990.975\ \mu\mathrm{m}^{-2}$
k_2	$57.362\ \mu\mathrm{m}^{-2}$
k_3^*	$579.551\,74\ \mu\mathrm{m}^{-2}$
w_0	295.235
w_1	$2.6422\ \mu\mathrm{m}^2$
w_2	$-0.032\,380\ \mu\mathrm{m}^4$
w_3	$0.004\,028\ \mu\mathrm{m}^6$

constants that are provided in Table 3.1.1.

Having set the boundaries (receiver and transmitter), the atmospheric delay is computed by employing N from (3.1.21) to (3.1.28) to evaluate (3.1.15). Aside from the fact that the delay changes over direction and most notably over elevation, the magnitude of the delay is dependent upon the refractivity of the moist air packets constituting the ray-trajectory. Hydrostatic refractivity N_h for microwave radiation ($267\,\mathrm{mm\,km^{-1}}$ on average at Earth's surface) is always smaller than the optical N_h at the most widely used wavelength, that is $\lambda = 532\,\mathrm{nm}$. Average optical N_h range from $260\,\mathrm{mm\,km^{-1}}$ for $\lambda = 1064\,\mathrm{nm}$, to $334\,\mathrm{mm\,km^{-1}}$ for $\lambda = 355\,\mathrm{nm}$. On account of the fact that lasers fail to excite the dipole component of the water vapor refractivity to the extend that radio signals do, non-hydrostatic refractivity N_{nh} at radio frequencies ($35\,\mathrm{mm\,km^{-1}}$ on average) is much larger compared to N_{nh} at any optical wavelength (0.7–$1.2\,\mathrm{mm\,km^{-1}}$). An elaborate treatise on the relation between delays induced by the atmosphere on signals of different frequency is conducted in Sec. 4.4.

3.2 Ray-tracing

Owing to ray-bending, the elevation and azimuth angles of the signal arriving to the ground station differ from the nadir angles of the signal transmitted from the satellite or quasar. To estimate the apparent elevation and azimuth at the receiver as well as the ray trajectory of a signal traversing the atmosphere, a numerical ray-tracing algorithm is necessary. Wijaya (2010) presents a classical ray-tracing system and provides an extensive list of ray-tracing algorithms developed by others.

In this work, ray-tracing was conducted employing a variational approach as it renders it precise and efficacious, that is, well-suited for geodetic applications even with the multi-GNSS constellation. This section succinctly describes the algorithm. The approach has been presented in Zus et al. (2012, 2014) and implemented in the in-house GFZ direct numerical simulation (DNS) software.

The approach followed here to find the ray-path is a generalization of geometric optics in full rigor. It addresses the fundamental optimization problem of the calculus of variations; fastest descent curve determination (ray-trajectory) between two points. Fermat's principle of least time of descent (or equivalently the shortest optical path) is adopted. Let $(\alpha, y(\alpha), z(\alpha))$ and $(\beta, y(\beta), z(\beta))$ be the two points (e.g., receiver and satellite respectively), expressed in a local

orthonormal reference frame the direction of the x-axis of which is the chord, bounding the curve the trajectory of which is sought $(x, y(x), z(x))$. The ordinary line element of the chord (geometric path) in Euclidean space is

$$ds = \sqrt{dx^2 + dy^2 + dz^2} = \sqrt{1 + \left(\frac{dy(x)}{dx}\right)^2 + \left(\frac{dz(x)}{dx}\right)^2}\, dx, \tag{3.2.1}$$

and its product with the refractive index yields the OPL element, $d\bar{s}$. By virtue of (3.1.15), employing (3.1.14) and (3.2.1) the propagation delay induced by the components of n e.g., moist air, ionosphere, and solar plasma, is written as

$$d_{atm} = \int_{\alpha}^{\beta} n(x, y, z) \sqrt{1 + \left(\frac{dy}{dx}\right)^2 + \left(\frac{dz}{dx}\right)^2}\, dx - \beta + \alpha. \tag{3.2.2}$$

To calculate the ray-trajectory along which the travel time is minimized, the integrant must satisfy the Euler-Lagrange equation for two coordinate components[1] The system (3.2.3) may be recasted as

$$\begin{aligned} &\frac{d^2y}{dx^2} - \frac{1}{n}\left(\frac{\partial n}{\partial y} - \frac{\partial n}{\partial x}\frac{dy}{dx}\right)\left(1 + \left(\frac{dy}{dx}\right)^2 + \left(\frac{dz}{dx}\right)^2\right) = 0, \text{ and} \\ &\frac{d^2z}{dx^2} - \frac{1}{n}\left(\frac{\partial n}{\partial z} - \frac{\partial n}{\partial x}\frac{dz}{dx}\right)\left(1 + \left(\frac{dy}{dx}\right)^2 + \left(\frac{dz}{dx}\right)^2\right) = 0, \end{aligned} \tag{3.2.4}$$

corresponding to the 3D ray-tracing. The ordinary 2nd order differential equations (3.2.4) describe the optimal ray-trajectory. The posed non-linear boundary value problem is solved within an implicit finite difference framework, utilizing the coordinates of the ray-trajectory endpoints as explicit boundary conditions.

To further enhance the efficiency of the ray-tracing system by an order of magnitude, based on the fact that n is mainly a function of height is used, two assumptions are introduced:

- ☐ out-of-azimuth-plane bending are not allowed, that is, $\frac{dz}{dx} = 0$ (corresponding to the 2D case);
- ☐ refractivity variations are not induced by latitude and longitude transposition that is, $\frac{\partial N}{\partial \varphi} = \frac{\partial N}{\partial \lambda} = 0$.

These simplifications do not introduce statistically significant errors if a meso-β scale NWM such as ECMWF operational analysis, ERA-Interim, or ERA5 is considered, because the uncertainty of the underlying refractivity tensor and its position operator outweigh the uncertainty introduced

[1]
$$\frac{d}{dx}\frac{\partial f}{\partial \frac{dy}{dx}} - \frac{\partial f}{\partial y} = 0 \quad \text{and} \quad \frac{d}{dx}\frac{\partial f}{\partial \frac{dz}{dx}} - \frac{\partial f}{\partial z} = 0 \tag{3.2.3}$$

by the ray-tracing algorithm (Zus et al., 2014). Both can be lifted, of course at the expense of computation time.

3.3 Homogenization of meteorological series

Should the interest in analysing space geodetic data lie solely in station coordinates and EOPs, the signal propagation delay induced by the non-zero atmospheric density tensor in electrically neutral atmosphere (applies to VLBI, SLR, GNSS, and DORIS), and the antenna thermal deformation (applies only VLBI) induced by local temperature fluctuations, constitute nuisance effects that ought to be eliminated by means of accurate modelling at the observation equation level. Any random errors that are not described in the reduced observations' covariance matrix propagate via the adjustment method of choice (cf. Sec, 2.5) in certain estimated parameter groups (e.g., Heinkelmann et al., 2018; Balidakis et al., 2016). On the other hand, systematic errors such as biases are usually absorbed by the estimated parameters — if small enough, at the expense of estimation accuracy. In the analysis of microwave-based space geodetic observations zenith non-hydrostatic delays d^z_{nh} are estimated as corrections to a priori zenith hydrostatic delays d^z_h — and occasionally the sum total of $d^z_h + d^z_{nh}$ — calculated employing in situ meteorological data. On account of inherent correlations between the station-specific residual tropospheric delay, clock polynomial coefficients, and height coordinate component, it is imperative that any systematic errors in the a priori zenith delays be mitigated. Similarly, the deformation of VLBI telescopes under varying temperature conditions is highly correlated with the radial coordinate component. Thus, erroneous pressure, temperature, or relative humidity records (necessary for the estimation of d^z_{nh}, cf. Askne and Nordius, 1987) induce spurious signals not only in the station coordinates but in other parameters such as the ERP as well (e.g., Vey et al., 2009; Balidakis et al., 2016; Heinkelmann et al., 2018; Balidakis et al., 2018c).

This section is dedicated to the homogenization of meteorological observations obtained by dedicated sensors in the vicinity of geodetic sites. Pressure, temperature, and relative humidity records from VLBI and SLR stations have been compared to several NWMs. A large number of artificial offsets, trends, and drifts has been identified. Since a residual tropospheric delay is usually estimated in radio techniques, the impact of erroneous a priori meteorological data is ameliorated to an extend by the estimation of corresponding d^z_{nh} that in turn lose their physical meaning. Following (4.2.9), and since mf_h progressively differs from mf_{nh} as $\varepsilon \to 0°$, estimating the remaining zenith atmospheric delay (non-hydrostatic part, theoretically) cannot fully compensate impurities in the a priori d^z_h. This is the point where employing a total mapping function is of some advantage, as the geodetic results are not affected by imprecise d^z_h (Boehm et al., 2006); notwithstanding, a shortcoming of this approach is that it fails to describe variations in the atmospheric state at timescales of hours or shorter. However, in the analysis of laser ranges no zenith delays are usually estimated, thus allowing errors in $d^z_h + d^z_{nh}$ to propagate mainly into the stations' height. Thus, the treatment of inhomogeneities in SLR meteorological records is more important, in absolute terms. While there have been several attempts to homogenize VLBI meteorological data, this is the first time SLR/LLR meteorological records have been rigorously homogenized based on NWM data. VLBI and SLR related results have been presented in Balidakis et al. (2018c) and Koenig et al. (2018), respectively.

The detection of factitious systematic effects in the recorded meteorological parameter time series is a fairly difficult task as abrupt jumps e.g., in the pressure series take place on a weekly basis. To facilitate the detection of behaviour that does not stem from weather variations, differences (hereinafter anomalies) should be formed with respect to data sets the quality of which is beyond dispute. Then, spurious effects in the recursive average of the anomalies are indicative

of inhomogeneities. Usually, the data of multiple neighbouring stations are used for this task (e.g., Alexandersson, 1986). Nevertheless, this approach requires a very dense global network of well-maintained meteorological stations, and thus serves ill the homogenization of meteorological geodetic stations. To this end, in this work the anomalies were formed by differencing in situ observations with the output of state-of-the-art NWMs. This gives rise to the following issue: say that in the time series of the differences (in situ minus NWM) a jump appears; where should the jump be attributed?

To addresses this issue, several state-of-the-art NWMs were utilized in this thesis in lieu of a single, namely ECMWF's operational analysis (ECMWFop), ERA Interim, ERA5, NCEPre2, NCEP-DOE AMIP-II, MERRA, MERRA2[2] and JRA-55. Some of these models are better suited for homogenization purposes than others, that is, reanalysis models should be preferred over operational ones. For instance, the introduction of a new type of observations may introduce a bias in some or all NWM parameters. On the other hand, while reanalysis products are more robust they have a latency that is prohibitive for operational work. Therefore, for the quality check of data in the framework of the IVS tropospheric combination centre[3] ECMWFop is used, and for past observations models such as ERA Interim and MERRA2 (Balidakis et al., 2018c).

There is a large variety of approaches to detect breakpoints in time series, as well as the significance thereof. Some of the most widely used tools include: singular spectrum analysis (e.g., Alshawaf et al., 2017), the least absolute shrinkage and selection operator (Tibshirani, 1996), the penalized maximal t-test (e.g., Wang et al., 2007), and the Mann-Whitney-Wilcoxon and Pettitt-Mann-Whitney tests (e.g., Lanzante, 1996). While utilizing reference time series facilitates the detection of artificial temporal patterns, there exist methods that perform the change point detection without a reference (e.g., Killick et al., 2012). However, as such algorithms demand a uniform logging interval their applicability is fairly limited in VLBI and SLR data. From the aforementioned methods, the LASSO (Balidakis et al., 2015b; Bertin et al., 2017) and the penalized maximal t-test (Balidakis et al., 2016, 2018c) have been used in this work.

In point of fact, no matter how sophisticated the method, an experienced eyeball is the best at discerning temporal patterns (e.g., Blewitt et al., 2016). To this end, time series-specific parameters are used for the detection of inhomogeneities.

3.3.1 Reference meteorological series

This section describes the method followed here for obtaining meteorological data from NWMs, suitable for homogenizing in situ records. All physical geodesy formulas necessary to do so that are provided in this section were retrieved from Hofmann-Wellenhof and Moritz (2006); Arabelos and Tziavos (2007).

To homogenize in situ barometric pressure, air temperature, and relative humidity series, these parameters need to be extracted from the NWM of choice. To obtain the corresponding parameters from the NWM data, there are two approaches: (i) to utilize only surface NWM fields and then extrapolate at the height of interest, and (ii) to utilize 3D NWM fields to render the vertical interpolation more precise.

In the first approach, the reference series are formed based on surface fields (2D). In this case, surface pressure, 2 m temperature, 2 m dewpoint temperature, and surface geopotential are necessary. Due to the fairly gentle temperature lapse rate ($\approx 6.5\,^{\circ}\mathrm{C\,km^{-1}}$), one can safely consider that the 2 m temperature corresponds to the surface of the model. Employing the

[2] Modern-Era Retrospective Analysis for Research and Applications, version 2 (Gelaro et al., 2017).

[3] http://media.gfz-potsdam.de/gfz/sec11/projects/tropospheric_combination_centre/Balidakis_IVS_tropo_combi.pdf

skin temperature instead would be a mistake. After obtaining the relevant parameters for the horizontal position of the station of interest, a height adjustment must take place as due to the finite representativeness of any NWM, there will always be differences between the actual height of the station and the altitude to which the surface parameters of the model refer to. Past the so-called height interpolation, a horizontal interpolation takes place. Following the August-Roche-Magnus approximation, the relative humidity reads (e.g., Böhm et al., 2013a)

$$RH = 100e^{\frac{17.625T_d}{243.04+T_d}-\frac{17.625T}{243.04+T}}. \tag{3.3.1}$$

The surface data approach yields reasonable results only when the height difference between the station and the orography of the model is small (e.g., below 500 m). Should the interest lie solely in breakpoint detection, the aforementioned procedure suffices. Nevertheless, in the presence of large height discrepancies significant biases might be introduced in the derived parameters, especially in the pressure and relative humidity series.

In the second approach, the reference series are formed employing NWM parameters on several model (σ-pressure coordinates) or pressure levels. The choice to work with model levels in lieu of pressure levels was deliberate as (i) ECMWF data are originally produced on model levels and at the surface, (ii) the transformation to pressure levels introduces a deterioration in vertical resolution, and (iii) the use of model levels addresses the known issue of discontinuities (induced by surface features) by introducing atmospheric levels that follow the contours of the surface of the Earth in the lower troposphere. In particular, the tensor of temperature and specific humidity are necessary in addition to the surface pressure and surface geopotential. To enhance the computational efficiency, if there is no interest in integrated quantities such as integrated water vapor, not all levels need to be loaded (e.g., only the 20 lowermost model levels in ERA Interim). Other than the temperature tensor, pressure and relative humidity at different heights are derived quantities. For NWMs published by ECMWF, the following procedure based on Simmons and Burridge (1981); ECMWF (2017) was followed. First, the pressure tensor P is computed level-wise

$$\begin{aligned} P_k &= \frac{P_{k-\frac{1}{2}}+P_{k+\frac{1}{2}}}{2}, \qquad \text{for } 1 \leqslant k \leqslant k_{max}, \\ P_{k+\frac{1}{2}} &= A_{k+\frac{1}{2}} + B_{k+\frac{1}{2}}P_s, \quad \text{for } 0 \leqslant k \leqslant k_{max}, \end{aligned} \tag{3.3.2}$$

where the subscript k denotes parameters at full-levels, the subscript $k \pm \frac{1}{2}$ denotes parameters at layer interfaces, the subscript s denotes surface parameters, and k_{max} denotes the number of levels. The parameters $A_{k+\frac{1}{2}}$ and $B_{k+\frac{1}{2}}$ are constant coefficients defining the vertical finite-element scheme of the model.

Second, the geopotential tensor Φ is computed level-wise based on the hydrostatic equation

$$\begin{aligned} \Phi_k &= \Phi_s + \sum_{j=k+1}^{k_{max}} R_d (T_v)_j \ln\left(\frac{P_{j+\frac{1}{2}}}{P_{j-\frac{1}{2}}}\right) + \alpha_k R_d \left(T_v\right)_k, \\ \alpha_k &= \begin{cases} \ln 2, & \text{for } k = 1 \\ 1 - \dfrac{P_{k-\frac{1}{2}}}{P_{k+\frac{1}{2}}+P_{k-\frac{1}{2}}} \ln\left(\frac{P_{k+\frac{1}{2}}}{P_{k-\frac{1}{2}}}\right), & \text{for } k > 1 \end{cases}, \end{aligned} \tag{3.3.3}$$

where T_v is the virtual temperature.

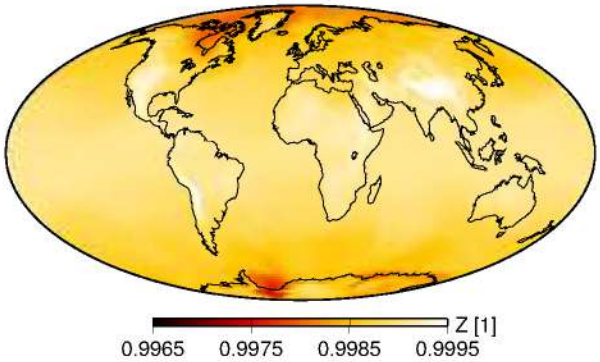


Figure 3.3.1: Compressibility factor calculated following (3.3.6), employing ERA Interim at 2017/04/24 00 UTC.

In the EOS, T_v is a thermodynamic variable that explains both the moisture and the compressibility. T_v is capable of absorbing local gas constant fluctuations that stem from the different molecular weight of moistless air and water vapor (Aparicio et al., 2009). The non-ideal virtual temperature is

$$T_v = T\left(1 + \left(\frac{R_v}{R_d} - 1\right) Q\right) Z, \tag{3.3.4}$$

where Q is the specific humidity. Utilizing such an expression for T_v, a parcel of moist air with temperature T can be safely treated as moistless with temperature T_v.

Z describes the departure of the atmospheric constituents' behaviour from that of an ideal gas ($Z = 1$) e.g., finite size of molecules and intermolecular attraction (cf. Fig. 3.3.1). Within Earth's atmosphere these corrections (Van der Waals) do not exceed 0.35 % under normal conditions (cf. Fig. 3.3.2), but have non-negligible effects since omission thereof leads to a decrease of the computed refractivity and consequently the atmospheric delays ($Z < 1$) (Aparicio et al., 2009; Healy, 2011). The most widely used expressions were presented by Owens (1967), who performed a least-squares polynomial curve fitting to thermodynamic data

$$\begin{aligned} Z_d^{-1} &= 1 + P_d\left(57.90 \times 10^{-8}\left(1 + \frac{0.52}{T}\right) - 9.4611 \times 10^{-4}\frac{t}{T^2}\right), \\ Z_w^{-1} &= 1 + 1650\frac{P_w}{T^3}\left(1 - 0.01317t + 1.75 \times 10^{-4}t^2 + 1.44 \times 10^{-6}t^3\right). \end{aligned} \tag{3.3.5}$$

Due to the fact that these formulas describe moistless air and airless water vapor deviations, and Z is related to the interactions between the mixture's molecules, Z_d^{-1} and Z_w^{-1} at least theoretically are not applicable individually to the constituents of the moist air mixture (Aparicio and Laroche, 2011). Whilst Z_d^{-1} can be safely applied to represent the dry air fraction of moist air, Z_w^{-1} is not an accurate choice as water vapor molecules in the atmosphere are most likely surrounded by dry-air molecules (Aparicio and Laroche, 2011). For this, a different expression was adopted featuring a compressibility factor derived from the virial coefficients of moist air, that treats moistless air as a pure gas and accounts for the cross interactions between air and water. Following Picard et al. (2008), the compressibility reads

$$Z = 1 - \frac{P}{T}\left(a_0 + a_1 t + a_2 t^2 + (b_0 + b_1 t)\, x_v + (c_0 + c_1 t)\, x_v^2\right) + \frac{P^2}{T^2}\left(d + e x_v^2\right) \tag{3.3.6}$$

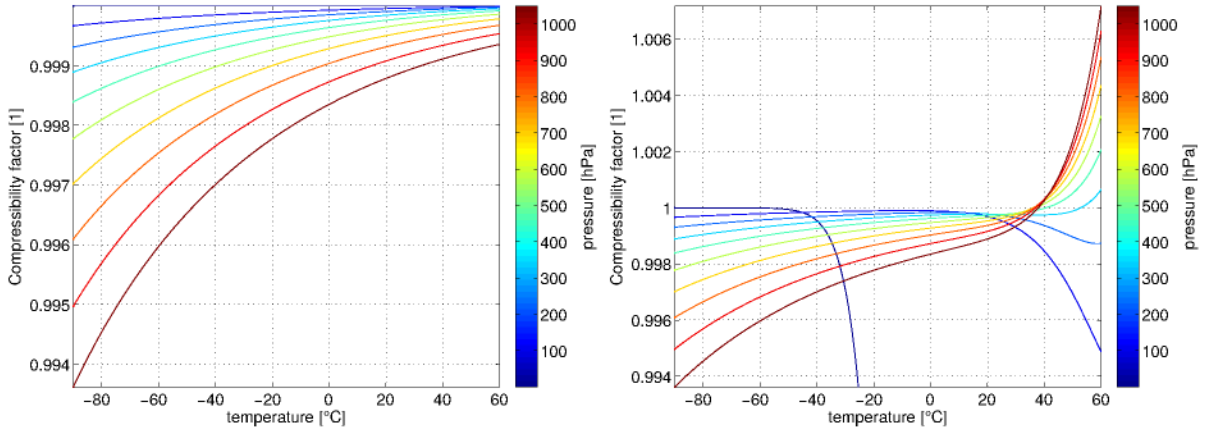


Figure 3.3.2: Compressibility factor (unitless) as a function of temperature and pressure for the extreme cases of dry air (left) and water-vapor-saturated air (right)

where the mole fraction of water vapor x_v is calculated by

$$x_v = RH \frac{f P_{sv}}{P} \tag{3.3.7}$$

where the relative humidity[4] $RH \in [0,1]$, the vapor pressure at saturation P_{sv} (using Teten's formula) and the enhancement factor (fugacity) f are obtained by

$$\begin{aligned}
RH &= \frac{PQ\dfrac{R_v}{R_d}}{\left(1+\left(\dfrac{R_v}{R_d}-1\right)Q\right)P_{sv}} \\
P_{sv} &= \begin{cases} P_{sv} = P_{sv}^w = \alpha_1 e^{\alpha_3^w \frac{T-T_3}{T-\alpha_4^w}}, & \text{for } T > T_3 \\ P_{sv} = P_{sv}^i = \alpha_1 e^{\alpha_3^i \frac{T-T_3}{T-\alpha_4^w}}, & \text{for } T < T_i \\ P_{sv} = P_{sv}^i + \left(P_{sv}^w - P_{sv}^i\right)\left(\dfrac{T-T_i}{T_3-T_i}\right)^2, & \text{for } T \in [T_i, T_3] \end{cases} \\
f &= \alpha + \beta P + \gamma t^2,
\end{aligned} \tag{3.3.8}$$

employing the coefficients tabulated in Table 3.3.1. This expression is robust and properly behaved over a broad range of conditions over the meteorologically relevant spectrum of pressure, temperature and humidity (Healy, 2011). At this point it should be noted that moist air is less ideal as it becomes colder or denser, and when it becomes moister[5], that renders polar regions and the tropical troposphere particularly prone to inaccuracies when adopting an ideal gas equation of state.

Including Z in the equation of state (EOS) reduces the height of model levels, since $Z < 1$ (cf. Fig. 3.3.2). Thus, quantities such as the zenith delay and the integrated water vapor will

[4] RH is assumed to be constant beyond the bounds of the NWM.

[5] This feature is relevant only for warm air as cold air can hold but a small amount of moisture before it gets saturated.

always appear to be slightly larger should the compressibility be neglected. Disregarding Z also introduces biases to all parameters derived from interpolation to the model levels e.g., P and T. On the other hand, if Z is applied solely to the refractivity operator, the zenith delays will always be slightly smaller. To avoid such modelling biases, compressibility should be applied to both the refractivity and the position operator.

In a generic NWM system such as those run by ECMWF and GMAO (Global Modeling and Assimilation Office), the vertical coordinate at any given node is a hybrid quantity, strongly linked to pressure. Altitude, which is of great interest in this work, is a derived quantity. NWMs provide the means to compute directly dynamic (or geopotential) heights H^d whereas for geodetic applications such as ray-tracing (cf. Sec. 3.2) either ellipsoidal or orthometric heights are necessary. H^d have purely physical meaning[6]; it is the difference in potential between the point of interest and its projection on the geoid along the plumb line, in distance units. The transformation between H^d and ellipsoidal heights h is not straightforward. Given the geopotential number Φ (the local gravity potential difference between the geoid and the point of interest), it is

$$H^d = \frac{\Phi}{\gamma_0^{45}}, \tag{3.3.9}$$

where the scale factor γ_0^{45} is the normal gravitational acceleration (3.3.12) on the surface of the ellipsoid at $\varphi = 45°$. In most NWMs, in lieu of 45° a WMO-defined constant is adopted ($g_0 = 9.806\,65\,\mathrm{m\,s^{-1}}$).The value of g_0 must not change within a vertical datum (Jekeli, 2016).

The lack of an explicit geometric interpretation in the H^d poses a problem for practical applications. To overcome this, the normal heights are employed

Table 3.3.1: Constants for the moist air compressibility factor expression.

Coefficient	Value
T_3	273.16 K
T_i	250.16 K
α_1	6.1121 Pa
α_3^w	17.505
α_4^w	32.19 K
α_3^i	22.587
α_4^i	−0.70 K
A	$1.237\,884\,7 \times 10^{-5}\,\mathrm{K^{-2}}$
B	$-1.912\,131\,6 \times 10^{-2}\,\mathrm{K^{-1}}$
C	33.93711047
D	$-6.343\,164\,5 \times 10^{-3}\,\mathrm{K}$
α	1.00062
β	$3.14 \times 10^{-8}\,\mathrm{Pa^{-1}}$
γ	$5.67 \times 10^{-5}\,\mathrm{K^{-2}}$
A	$1.237\,884\,7 \times 10^{-5}\,\mathrm{K^{-2}}$
A	$1.237\,884\,7 \times 10^{-5}\,\mathrm{K^{-2}}$
a_0	$1.581\,23 \times 10^{-6}\,\mathrm{K\,Pa^{-1}}$
a_1	$-2.9331 \times 10^{-8}\,\mathrm{Pa^{-1}}$
a_2	$1.1043 \times 10^{-10}\,\mathrm{K^{-1}\,Pa^{-1}}$
b_0	$5.707 \times 10^{-6}\,\mathrm{K\,Pa^{-1}}$
b_1	$-2.051 \times 10^{-8}\,\mathrm{Pa^{-1}}$
c_0	$1.9898 \times 10^{-4}\,\mathrm{K\,Pa^{-1}}$
c_1	$-2.376 \times 10^{-6}\,\mathrm{Pa^{-1}}$
d	$1.83 \times 10^{-11}\,\mathrm{K^2\,Pa^{-2}}$
e	$-0.765 \times 10^{-8}\,\mathrm{K^2\,Pa^{-2}}$

$$H^N = \frac{\Phi}{\bar{\gamma}}, \tag{3.3.10}$$

where $\bar{\gamma}$ denotes the average normal gravity along the normal plumb line. The connection to the ellipsoidal height system is provided by

$$h = H^N + \zeta, \tag{3.3.11}$$

where ζ is the height anomaly that can be retrieved from geopotential models. In this work,

[6]Given $H^d_{P_1} > H^d_{P_2}$, water flows from P_1 to P_2. This does not always hold for H^N.

ζ from Förste et al. (2014) was used. This expression is preferable to employing geoid undulations for no implicit assumption regarding the mass density of the orography is made. For the aforementioned expressions, the normal gravity has to be calculated accurately.

Due to Earth's dominant polar flattening and the near symmetry about the equator, any meridional section is closer to an ellipse than a circle. Assuming a normal gravity field, an ellipsoidal gravity field is composed of gravitation and centrifugal acceleration. It is based upon a level biaxial ellipsoid of revolution of total mass M, angular velocity ω, semi-major axis a, geometrical flattening factor f, and its own gravity field. According to the Stokes-Poincaré theorem, such a gravity field is uniquely defined in the space exterior to the ellipsoid employing the linearly independent parameters a, f, M and ω, and is described by the normal potential $U(\mathbf{x})$. Note that with the exception of the level ellipsoid, no other spheropotential surface ($U(\mathbf{x}) = constant$) is of ellipsoidal shape.

The relationship between the normal gravity vector and its potential is simply $\gamma = \nabla \mathbf{U}$. The component of γ perpendicular to the spheropotential surfaces, which embodies its magnitude, at the surface of the level ellipsoid ($h = 0$) is given by Somigliana (1929)

$$\gamma_0 = \frac{a\gamma_e \cos^2(\varphi) + b\gamma_p \sin^2(\varphi)}{\sqrt{a^2 \cos^2(\varphi) + b^2 \sin^2(\varphi)}}, \tag{3.3.12}$$

where γ_e and γ_p are the normal gravity at the equator and poles, respectively. They are given by

$$\gamma_e = \frac{GM}{a^2\,(1-f)} \left(1 - m - \frac{me'}{6}\frac{q_0'}{q_0}\right), \text{ and} \tag{3.3.13}$$

$$\gamma_p = \frac{GM}{a^2} \left(1 + \frac{me'}{3}\frac{q_0'}{q_0}\right), \tag{3.3.14}$$

where GM is the geocentric gravitational constant, and

$$q_0 = \frac{1}{2}\left(1 + \frac{3}{e'^2}\right) \tan^{-1}(e') - \frac{3}{2e'}, \tag{3.3.15}$$

$$q_0' = 3\left(1 + \frac{1}{e'^2}\right)\left(1 - \frac{1}{e'}\tan^{-1}(e')\right) - 1, \tag{3.3.16}$$

$$m = \omega^2 a^3 \frac{1-f}{GM}, \tag{3.3.17}$$

and the second eccentricity is given by

$$e' = \frac{\sqrt{a^2 - b^2}}{b}, \tag{3.3.18}$$

where b is the semi-minor axis. Assuming relatively small altitudes, $h \ll a$, normal gravity can be expanded into a Taylor series in terms of h

$$\gamma(\varphi, h) = \gamma_0 + \frac{\partial\gamma}{\partial h}\Big|_0 + \frac{1}{2}\frac{\partial^2\gamma}{\partial h^2}\Big|_0 h^2 + \ldots \tag{3.3.19}$$

The first partial derivative may be obtained employing Bruns' formula[7], and the second from the spherical approximation of the normal gravity field ($\gamma = GMr^{-2}$), omitting f and e'. Thus, considering both gravitation and acceleration due to the rotation of the Earth-centered, Earth-fixed terrestrial reference system, the normal gravity of an ellipsoid of revolution in equilibrium may be approximated by

$$\gamma(\varphi, h) = \gamma_0 \left(1 - \frac{2}{a}\big(1 + f + m - 2f\sin^2(\varphi)\big)\, h + \frac{3}{a^2}h^2 \right). \tag{3.3.20}$$

For enhanced accuracy and to avoid spurious systematics e.g., in the delay gradient vector orthogonal components, the gravity anomalies must be considered as well. Neglecting the inclusion of gravity anomalies at this point is responsible for spurious spatial features over regions with steep gravity anomaly gradients e.g., Marianas Trench visible in Fig. 3 & Fig. 4 of Landskron and Böhm (2018a) but not in Fig. 6 of Balidakis et al. (2018c).

While this expression holds near the surface of the ellipsoid, it is not sufficiently accurate to be applied to the entire atmosphere. Adopting it for altitudes at the spanning to e.g., the uppermost ERA5 model level (≈ 83 km), yields relative errors in the position operator at the km-level.

To treat this shortcoming in terms of accurate H^N computation, given Φ, (3.3.10) needs to hold. Performing a couple of iterations on

$$\Phi = H^N \gamma(\varphi, H^N), \tag{3.3.21}$$

commencing from $H^N = H^d = \Phi/\gamma(\varphi, H^d)$ leads to convergence at the sub-mm level. To speed up the procedure, here this process is initiated from the lower model level to the uppermost, employing the estimates for H^N and γ from the previous (lower) model level.

Ergo, the ellipsoidal height h of the geopotential Φ stemming from the dynamic height H^d of a NWM and the height anomaly ζ from a geopotential model reads (3.3.11):

$$h = -\int \left(\frac{ZRT_v}{g_0 P} \right) dP = \frac{\Phi}{\gamma(\varphi, H^N)} + \zeta, \tag{3.3.22}$$

where Φ varies in 4 dimensions (3D space and time), γ varies in 3 (3D space), and ζ only horizontally (2D).

If the aforementioned procedure is not adopted, relative height errors at the upper model levels exceed 2 km. For the investigations carried out in this work, height anomalies (and geoid undulations) as well as gravity anomalies were obtained from EIGEN-6C4 (Förste et al., 2014) via spherical harmonic synthesis of full degree and order.

In this work, the reference meteorological series were always formed employing NWM data at the model levels. While this approach is computationally expensive compared to performing extrapolations from the surface of the model, the reference series are free of the extrapolation-induced bias. Figure 3.3.5 shows the offset in the meteorological parameters of interest as a function of height difference between the orography of ERA Interim and all VLBI geodetic markers. For all points that lie within the vertical bounds of the NWM, the model level approach is more precise. Due to the fact that the vertical distance between the model levels of meso-β

[7] Bruns' formula relates the vertical gravity gradient with the mean curvature of spherodynamic surfaces. Applied to the normal gravity field, it reads: $\frac{\partial\gamma}{\partial h} = -2\gamma J_0 - 2\omega^2$, where $J_0(\varphi)$ denotes the mean curvature of the ellipsoid (e.g., Arabelos and Tziavos, 2007).

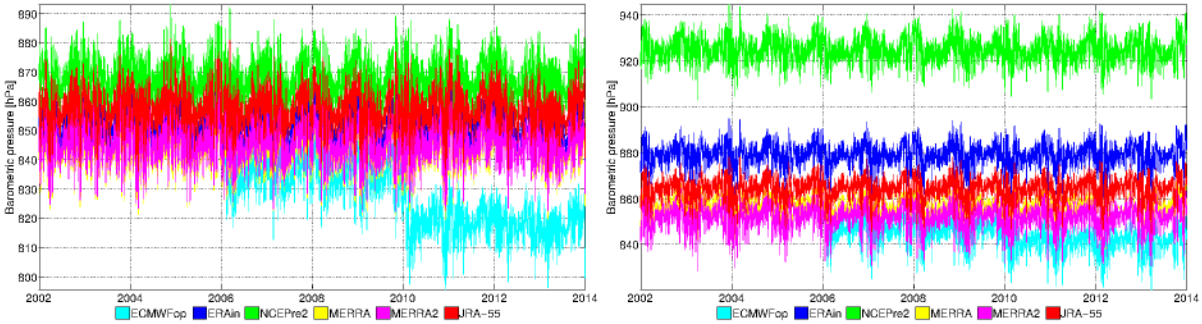


Figure 3.3.3: Barometric pressure series from the surface fields of ECMWFop, ERAin, NCEPre2, MERRA, MERRA2 and JRA-55 at Badary, Russia (left) and Zelenchukskaya, Russia (right). The temporal resolution is 6 h for all models except for MERRA2 (1 h).

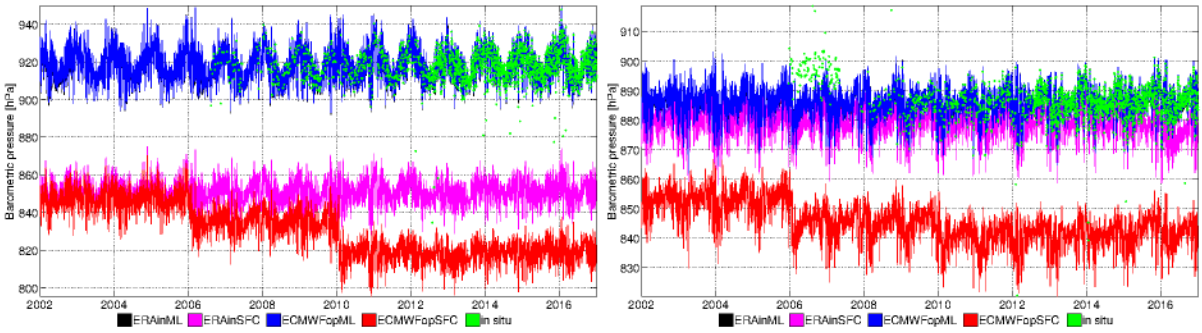


Figure 3.3.4: Barometric pressure series from the model levels (ML) and the surface fields (SFC) of ECMWFop and ERAin at Badary, Russia (left) and Zelenchukskaya, Russia (right).

NWMs such as ERA5 is below 30 m for the lowermost pair of levels and increases logarithmically to 6 km at the altitude of 80 km, it allows for an interpolation where the nodes involved are always fairly close. For instance, owing to the VLBI station at Kokee Park (Kauai) being located more than 1100 m above ERA Interim's orography, extrapolating e.g., pressure yields a bias that will subsequently manifest mainly into the height coordinate component. For stations that are below the orography of the NWM of choice e.g., Badary, Russia, employing the model level approach is not as effective but still yields considerably better results as the lapse rate of the parameter at hand is determined more accurately. However, in cases where the point of interest lies more than several hundred meters below the orography, it is better to obtain the related value by expanding the relevant meteorological field (or profile) into a B-spline function basis (Schönberg, 1946). This approach is preferable to extrapolating assuming the lapse rate between the lowermost model level and the model's orography due to the fact that the lapse rate near the surface experiences large spatio-temporal variations and it is derived by differencing values at altitudes that are typically 10–50 m. Moreover, employing a scheme involving multiple model levels to obtain meteorological parameters renders the time series not susceptible to changes stemming from the utilization of a better resolved orography during the NWM generation process (cf. Fig. 3.3.3 and Fig, 3.3.4).

The approach outlined thus far for obtaining meteorological parameters compatible with those recorded in situ is extended for the calculation of parameters that refer to an altitude more appropriate than the surface. This is instrumental in the development of a state-of-the-art atmospheric pressure loading model (cf. Sec. 5.2), and in particular for the calculation of the mass anomaly fields.

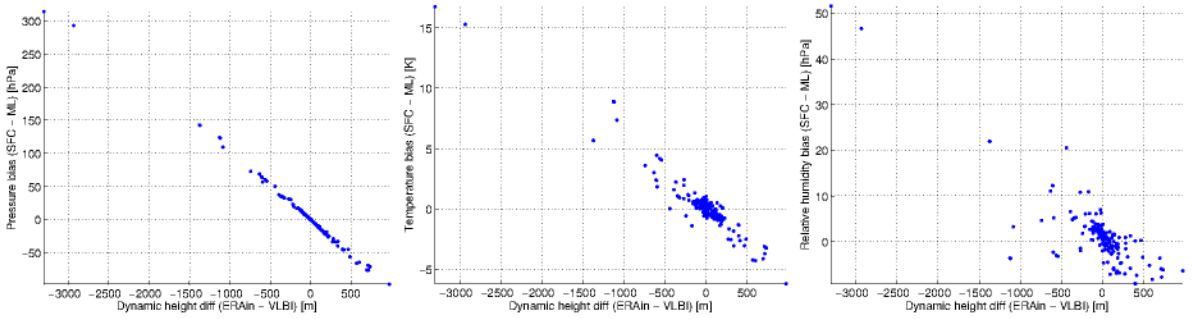


Figure 3.3.5: Barometric pressure (left), air temperature (middle) and relative humidity (right) bias stemming from the extraction approach: from the surface fields (ERAin) and exactly at the reference height of the each VLBI station, from the model levels (VLBI).

In most NWMs, geopotential numbers are archived in spectral space, similar to gravity field models, thus rendering sharp spatial orographic gradients unresolvable. For the calculation of the near-field environmental contribution to geophysical loading displacement, a grid with a granularity much higher than the one of the model is required. This necessitates to orography-adjust the related fields prior to further considerations. To this end, a new orography was generated by fusing ETOPO1 (Amante and Eakins, 2009) and the latest orography of ECMWF; the former was imposed over the land grid nodes according to an equiangular 0.125° land-sea mask[8] (ECMWF, 2016).

Projecting meteorological parameters on a time-invariant orography allows for the generation of jump-free NWM data driven models (e.g., atmospheric delay and geophysical loading), even if the data by which these models are excited experience resolution changes. For example, over the last years five major spatial resolution changes took place in the integrated forecasting system that drives ECMWF products[9]: (i) increase of horizontal resolution from T511L60 (39 km) to TL799 (25 km), and increase of vertical resolution from 60 to 91 model levels, on 2006/02/01, (ii) horizontal resolution increase to TL1279 (15 km), on 2010/01/26 (iii) vertical resolution increase to 137 model levels, on 2013/06/25, (iv) introduction of a better land-sea mask, lake mask, mean and sub-grid orography and climate fields on 2015/05/12, and (v) the introduction of the octahedral grid Q1280 (9 km), on 2016/03/08.

To assess the effectiveness of the model level interpolation on a global grid, pressure fields from ERAin and ECMWFop were projected on a common reference orography, and the differences were examined. Prior to the first major change, due to the fact that ECMWFop and ERAin share the same analysis traits (assimilation cycle), the improvement model level interpolation approach yields is moderate (7 %). Nevertheless, as the spatial resolution of ECMWF's operational model diverged significantly afterwards, so did the improvement: 28 %, 41 % and 76 %, after the first, second and third system change, respectively (cf. Fig. 3.3.6). An approach to obtain meteorological parameters similar to the developments presented herein (Balidakis et al., 2016), has been developed independently by Dobslaw (2016).

[8] The orography and land-sea mask of IFS-CY45R1 are based on Shuttle Radar Topography Mission (SRTM30), ESA's Globcover V2.2, Global Land One-kilometer Base Elevation for $|\varphi| > 60°$, as well as specialized models for Antarctica, Greenland and Iceland.

[9] https://www.ecmwf.int/en/forecasts/documentation-and-support/changes-ecmwf-model

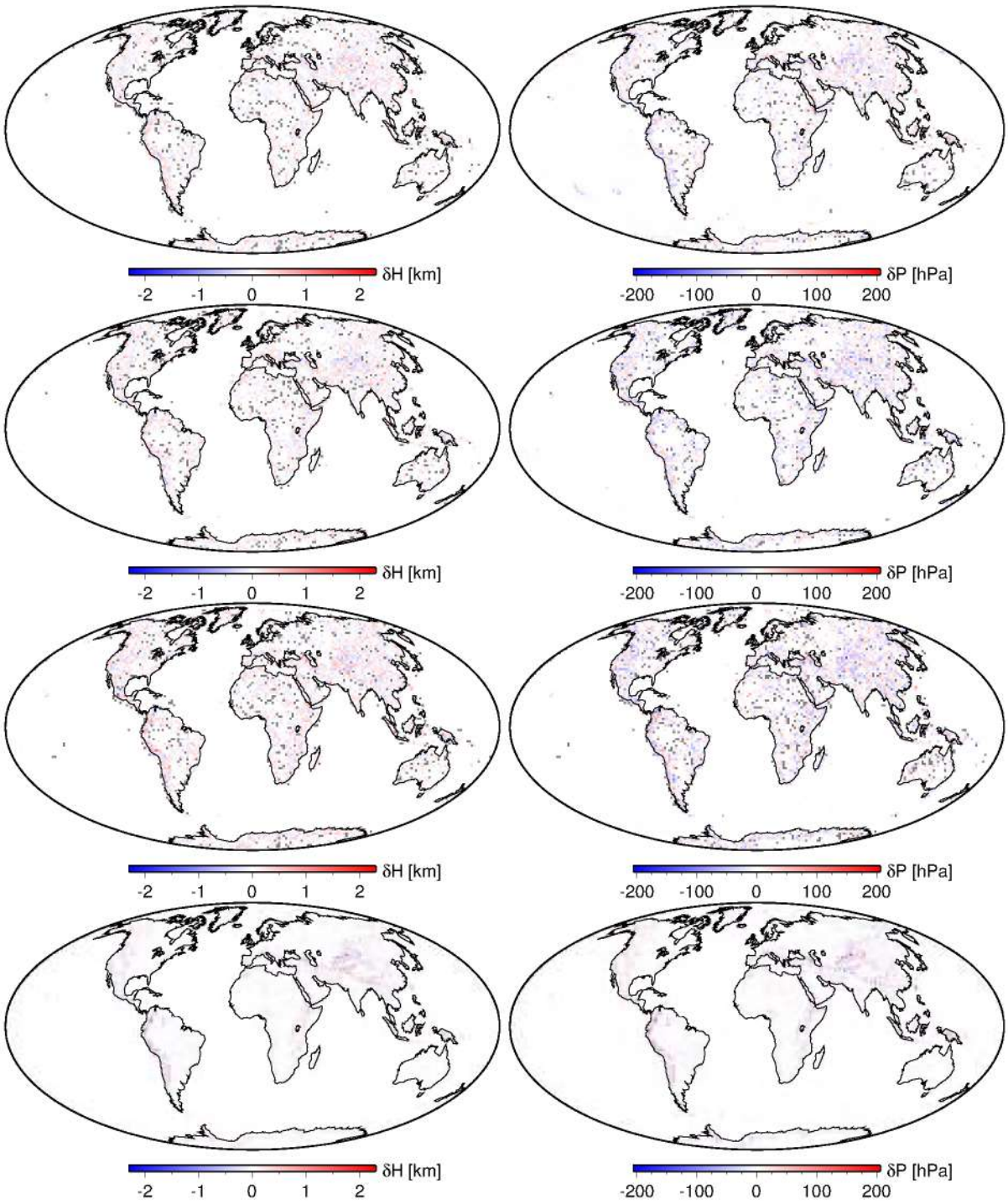


Figure 3.3.6: Orography (left) and surface pressure (right) differences between ECMWFop and ERAin at 2000-01-01, 2006-02-01, 2010-01-26, and 2015-05-12.

3.3.2 Homogenized in situ VLBI and SLR meteorological records

The homogenization process condenses into the elimination of outliers outright, the determination of breakpoints, and the estimation of analytical functions between them. In most pathological cases the anomalies, that is the difference between the values recorded in situ and the reference (cf. Sec. 3.3.1), can be segmented and modelled as piecewise linear offsets.

Past the formation of meteorological observation (pressure, temperature, and relative humidity) anomalies, they are averaged on a daily (SLR/LLR) or a session (VLBI) basis. The reason for that lies with the fact that save for individual outlier occurrences, inhomogeneities usually do not take place during the course of a session[10]. Moreover, the temporal resolution of the NWMs employed is usually 6 h, 1 h at best (ERA5), which is inferior to the logging interval of the sensors installed in the vicinity of the geodetic stations (1 s–10 min)[11]. To avoid the averaging step, a more accurate eddy-resolving meso-γ scale model capable of disentangling deterministic and random effects must be used. Such models are not publicly available on a global scale which is necessary for the quality control of globally distributed networks. To obtain meteorological parameters at higher spatiotemporal scales, effort has been recently put into running the weather research and forecasting (WRF) numerical weather prediction system (Powers et al., 2017), at GFZ Potsdam (together with F. Zus and F. Alshawaf).

The meteorological data recorded in the vicinity of VLBI stations are not directly accessible, but are reported together with the related observations. However, there is a number of stations such as `ONSALA60` and `WETTZELL` where the meteorological data recorded in the vicinity thereof are publicly available, at high temporal resolution. In this work the meteorological observations were obtained from three different sources: (i) the `log` files[12], (ii) the so-called `NGS`[13] cards, and (iii) `vgosDb`[14] files. With a few exceptions, the meteorological series retrieved are quite similar and differ only in the timestamp e.g., the meteorological observations in the `NGS` are reported in such a way that they refer to integer seconds, whereas this does not hold in the `log` or `wx` files (typically at the beginning of each scan).

As in VLBI, meteorological observations recorded in the framework of laser ranging are also not available as is from the sensor, but are reported together with the related ranges. In this work, the pressure, temperature, and relative humidity series from the ILRS archive were composed from three different sources: (i) the full-rate data[15], (ii) the normal points[16], and (iii) the consolidated normal points[17]. No differences were found amongst them save for those stemming from the temporal averaging and necessary interpolations.

The artificial systematic effects that might be found in the meteorological records are with decreasing probability jumps, trends, and drifts, all of which can be treated with calibration. The estimation of the necessary coefficients is carried out by performing a least-squares adjustment (least median squares to facilitate the identification of outliers) utilizing as weights of the

[10] With the exception of `18AUG03XQ` where erroneous temperature and relative humidity values have been recorded at `ZELENCHK` during 25 out of 471 scans, there is no other incident where reliable and unreliable meteorological records co-exist in the same session for one parameter.

[11] While most VLBI and some GNSS (e.g., `MOSE`) stations are equipped with expensive meteorological sensors capable of highly temporally resolved output, VLBI analysts rely on meteorological quantities that stem from interpolation of the original data at the reference epoch of each scan, for the data reduction. Consecutive scans for legacy S/X geodetic experiments typically several minutes apart.

[12] ftp://cddis.gsfc.nasa.gov/pub/vlbi/ivsdata/aux/????/*/*.log

[13] ftp://cddis.gsfc.nasa.gov/pub/vlbi/ivsdata/ngs/

[14] https://vlbi.gsfc.nasa.gov/output/vgosDB_IVS/

[15] ftp://edc.dgfi.tum.de/pub/slr/data/fr/

[16] ftp://edc.dgfi.tum.de/pub/slr/data/npt/

[17] ftp://edc.dgfi.tum.de/pub/slr/data/npt_crd/

session-wise average meteorological values the scatter threof with respect to the reference. The reason behind this choice lies with the fact that in sessions that span 24 hours mismodelled high-frequency variations largely cancel out, whereas in Intensives the session-wise scatter is on average much larger, exclusively for that reason. There are large segments in the meteorological parameter time series where the anomalies (observations minus weather model or properly reduced neighbouring sensor data) cannot be fit satisfyingly by any analytical function, even if they are segmented into several pieces per year. Without suspending the trust placed in the reference time series, such cases might be caused by faulty sensory systems, or frequent relocations of the meteorological sensors. The latter can explain the segmentation of the pressure time series but not the temperature since the vertical temperature gradient is on average 125 time smaller compared to pressure. For instance, `KOKEE` during the period 2001–2003 and `WESTFORD` during the period 1990–1993 are some of the cases examined herein where the homogenization process was fruitless (cf. Fig. 3.3.9). With the exception of slightly different inter-annual waves for pressure and temperature, the comparison of ECMWF- and GMAO-derived series carried out in the framework of this study did not reveal any offsets whatsoever.

Several barometers co-located with VLBI stations recorded slowly varying signals. Under this category fall several VLBA stations, as well as other IVS stations such as `MATERA` and `HRAS 085` that feature long-term statistically significant pressure trends. Comparing these series with the output of ERA Interim, ERA5, MERRA2, as well as other (e.g., WMO stations) co-located meteorological sensors (within a radius of 50 km), it is concluded that these trends are artificial; therefore they are no retained in the homogenized time series. However, it should be mentioned that smaller air pressure trends can be real (cf. Sec. 4.3). At several co-location sites, the individual geodetic systems obtain meteorological observations from separate sensors. A comparison after applying the necessary reductions (for height difference) reveals that slight deviations larger than the nonimal uncertainty of the measuring devices do exist (see for example in Onsala[18]). These differences may be ascribed to imperfect instrumentation and local features.

No falsely larger harmonic signals e.g., S_a, S_1, or S_2 are expected in the NWM (based on ERA Interim, ERA5, MERRA2, and the meteorological archive of IVS, ILRS, and IGS). On account of the latter, and due to the fact that global meso-β scale NWMs usually underestimate the amplitude of harmonic variations, the meteorological observations are averaged daily, and no seasonal signals adjustments are enforced in the homogenization process (corrections in the amplitude or the phase). At most stations the harmonic waves for pressure and temperature diurnal variations and overtones thereof are largely underestimated by ERA Interim. Due to the fact that (i) the output of weather models typically corresponds to an instant and not an averaging period, and (ii) the temporal resolution of ERA Interim (utilizing only the reanalysis products, without the reanalysis) is at the Nyquist frequency for the S_2 wave, which is the most important for the high-frequency pressure variations at most sites, cf. Fig. 4.3.4, the quality of the representation of high-frequency effects largely depends on the longitude of the site of interest and the phase of the signal of interest, even if a more sophisticated interpolation approach is adopted (e.g., van den Dool et al., 1997). The latter implies that the detection of inhomogeneities is facilitated by a uniform high temporal distribution, short or no periods of missing data streams, and time series that contain many cycles of the dominant harmonic term (year). Figure 3.3.7 illustrates the differences between the in situ records and the values extracted from the model levels of ERA Interim. Note the offsets, jumps, and trends especially in the pressure series. Since the relative humidity accuracy attained by state-of-the-art NWMs is at the level of 10 %, the larger scatter in the 3rd row of Fig. 3.3.7 is justified. This figure also shows that the resolution

[18] view-source:http://www.oso.chalmers.se/weather/plots/*.png

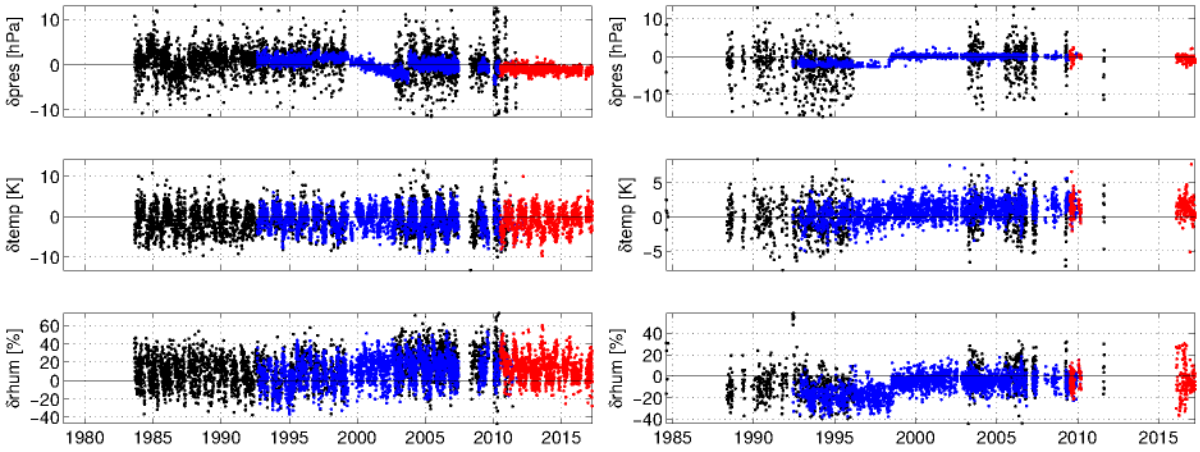


Figure 3.3.7: Differences between in situ meteorological data recorded at SLR stations and ERAinML. The differences at Simosato, Japan (left), and Borowiec, Poland (right) are shown. The colors indicate the data source; black for full-rate, blue for normal point, and red for consolidated normal point ILRS data.

of S_a signals is better at continental Europe compared to Japan, mainly stemming from the finite representativeness of the model. Placing the focus on the more recent SLR data, Fig. 3.3.8 displays the differences between ERAinML and the raw data, and the homogenization process product. It is evident that at some sites the reference point of the geodetic instrument and the co-located barometer do not coincide, but either have a height difference of e.g., 30 m for Arequipa (Peru), or the latter has not undergone proper calibration, if at all.

In Fig. 3.3.9 in situ meteorological observations recorded at VLBI sites are compared with ERAinML. In some stations the erroneous meteorological observations are easy to detect; (i) the pressure time series of Sejong (South Korea) were segmented into a part where a 50.8 hPa offset and a 4.8 hPa (after 2016.1) offset are necessary, and (ii) a constant offset of 49.5 hPa was detected at Parkes (Australia). In other sites the inhomogeneities are not as apparent but still significant. While a constant offset in either pressure or temperature may be partly absorbed by the estimated parameters (estimated residual zenith atmospheric delay, station clock offset, axis offsets, and height and subsequently network scale), jumps manifest into spurious velocities in the radial coordinate component. The latter is true at for several stations including but not limited to Green Bank (WV, USA), Ny-Ålesund (Svalbard), Svetloe (Russia), and Zelenchukskaya (Russia), cf. Fig. 3.3.9. Furthermore, large undetected pressure offsets result in the flagging of "good" observations as outliers simply because the "computed" vector $\mathbf{y^0}$ is erroneous, thus resulting in the reduction of observations for the stations where the large pressure biases are found. Moreover, there is a worryingly large number of isolated sessions scattered accross the IVS archive where while the temporal variations of the meteorological parameters is highly correlated with the output of weather models, neighbouring WMO (World Meteorological Organization) stations, or neighbouring geodetic stations (e.g., SLR or GNSS), the time series have a huge bias wrt the reference series. These cases are treated by simly reducing the bias to the one provided by the reference series, while retaining the temporal variations.

Such pressure jumps give rise to large inconsistencies in the multi-technique TRF generation process should co-motion constraints be imposed between VLBI and the markers of techniques that use surrogate (climatology) modelling (e.g., GNSS) or the meteorological data thereof experience no such jumps. To provide proof for this statement, an experiment is carried out. A VLBI-SLR co-location at Wettzell is considered (baseline length: 77.36 m). The stations ob-

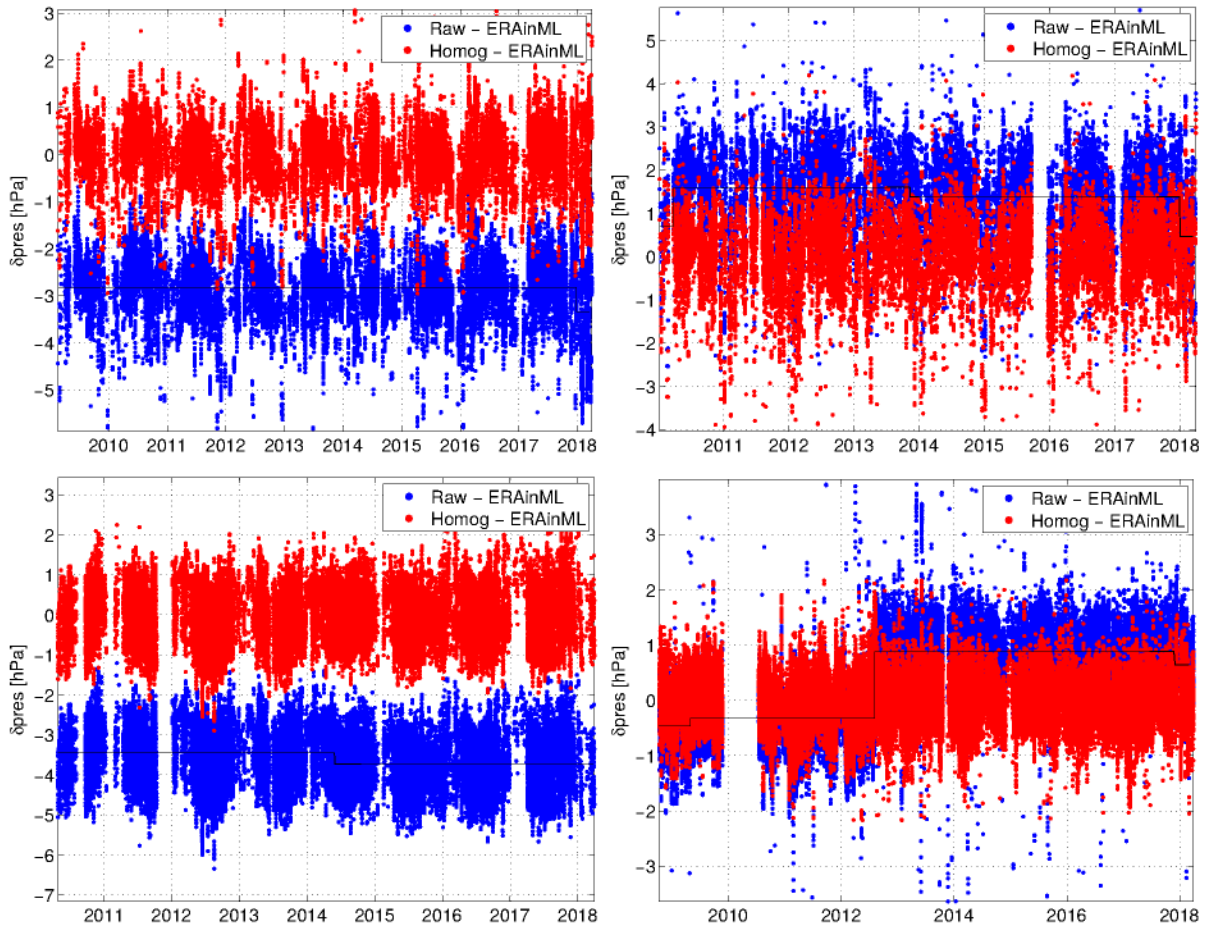


Figure 3.3.8: Barometric pressure difference between raw and homogenized pressure series recorded at SLR stations, with respect to ERAinML. The differences shown are for two stations in Simeiz, Crimea (upper row), Arequipa, Peru (lower left), and Wettzell, Germany (lower right).

serve in parallel for 10 years. If all technique-specific systematics are perfectly understood, and the VLBI and SLR networks do not change appreciably, the single-technique velocities should be identical within the bounds defined by the uncertainty of the underlying observations. A high-accuracy calibrated barometer is installed on the site and provides observations to both stations. After 5 years of observations, the barometer is slightly displaced resulting in a 2 hPa difference with respect to what it used to record. In the first scenario, during the data analysis of the VLBI sessions that took place after the barometer displacement, the change in the height difference between the barometer and the antenna reference point is not taken into account, resulting into approximately 1 mm height error (see next paragraph). In the SLR analysis the pressure difference was considered, so no relative height bias occurs. The site's height velocity according to the VLBI observations will be erroneously larger by 1.5 mm dec^{-1}. This error is not statistically significant adopting a 99.9 % confidence level, since the height velocity uncertainty provided by ITRF2014 at `WETTZELL` is 0.6 mm dec^{-1}. Moreover, comparing the velocities in X, Y, and Z direction, the differences appear to be even smaller (at the 1–σ level). However, such an error is too large to ignore, with a view to meet the GGOS goal of 1.0 mm dec^{-1}. In the second scenario, the barometer displacement is considered in the VLBI data analysis, but not in the SLR analysis. Unlike VLBI, in SLR processing, no residual zenith delays are typically estimated nor clock coefficients; therefore, the bias will be absorbed mainly by the radial coordinate component correction. In Sec. 6.1, it is proven that a 2 hPa bias results in a 10–15 mm height error, depending on the altitude of the station, as well as the observation geometry (more severe if observations at elevation angles below 20° are utilized). Therefore, in this case the SLR velocity will incorrectly larger by 22.4 mm dec^{-1}, which is several times larger than 1.0 mm dec^{-1} (radial coordinate velocity component uncertainty of `8834` according to ITRF2014). In this particular scenario, the identification of this issue is trivial because there is a large redundancy in co-located geodetic sensors. In such cases, further complications may be avoided by segmenting the time series at the epoch of the barometer relocation; of course more appropriate would be to correct for the pressure bias. Such a workaround is not preferable is observations are sparse. In the third scenario, the pressure bias is not taken into consideration by neither the VLBI nor the SLR data analysis. Applying equal weights to the VLBI and the SLR solutions and imposing co-motion constraints, the site's height velocity will be falsely larger by 3.1 mm dec^{-1} (VLBI's velocity is 3.5 times more precise).

Examining the quality of meteorological observations collected by the very long baseline array (VLBA), a fairly consistent systematic $\approx$ 2 hPa pressure bias became evident (cf. Fig. 3.3.10). This bias has been confirmed to be true based on the relevant documentation of the VLBA weather stations[19], as well as examining any of the antenna design documents (e.g., Napier et al., 1994) where the elevation axis (close to the geodetic reference point) is 13.66 m above the azimuth track, which is 1 m above ground level, thus yielding a height difference around 15 m that justifies the pressure bias detected (J M. Anderson, personal communication). Such a bias may introduce a scale factor as well as a geocenter offset in the implied TRF. At the session level, this artefact may propagate into global parameters estimated by the VLBA network thus inducing a systematic disagreement with estimates from other networks (e.g., quasar positions and EOPs). To assess whether this presumption is true, some simulations were carried out based on pressure from the model levels of ERA5 to obtain the "observed" vector $\mathbf{y^b}$, and applying a 2 hPa bias to obtain the "computed" vector $\mathbf{y^0}$. From the geodetic adjustment, it was found that for sessions where only the 10 VLBA stations participate, the height bias is on average 1 mm. However, this figure changes as a function of (i) the observation geometry, that is, it becomes slightly larger

[19] http://library.nrao.edu/public/memos/vlba/tech/VLBATR_47.pdf

if there is a large number of low-elevation observations, and (ii) observation weighting, that is, it becomes moderately larger if no elevation-dependent weighting scheme is employed. These are in agreement with Tregoning and Herring (2006). For these solutions, no baseline offsets were set up as unknowns, and all stations participate in the NNT/NNR conditions. Performing a 7-parameter Helmert transformation (cf. (7.2.1)) yields negligible translations and rotations, however, it yields a scale bias of 1 mm. If such a consistent bias is applied to other non-global (regional) networks such as the Russian (`BADARY`, `SVETLOE`, and `ZELENCHK`) or the Australian (`HOBART12`, `HOBART26`, `KATH12M`, and `YARRA12M`), the results are similar; 1 mm scale bias. These conclusions are valid for global networks as well; based on the fact that a consistent height bias of about 1 mm is to be expected for an erroneous (consistent) 2 hPa offset, a Helmert transformation was performed including hundreds of radio telescopes[20], only to reconfirm the 1 mm scale bias. Accounting for this bias may shed light onto reducing the aforementioned effects. As the contribution of thermal deformation to the reduced group delay typically does not exceed 15 ps, discrepancies in the temperature series are not as harmful to the geodetic products as pressure errors.

To check whether the spurious effects identified are not ascribed to systematics in the reference time series, alternating the reference data set source was also investigated. All breakpoints identified employing ERA Interim have been confirmed by ECMWF operational analysis (only past 1994 due to availability at GFZ) and ERA5 (only past 2000 due to partial product release) reanalysis. Nonetheless, due to the possibility of a systematic error consistent in all ECMWF products, a reference independent of ECMWF was deployed, MERRA2. Employing MERRA2 as a reference reconfirmed all breakpoint detected using ECMWF products, thus providing a higher confidence in the homogenization process. While there is a confidence concerning the breakpoint events, the analytical function coefficients estimated for the treatment thereof may vary slightly at the sub-hPa or sub-Kelvin level, alternating the NWM. Due to that fact, smaller biases are more difficult to detect e.g., a pressure bias of 0.7 hPa in Badary after 2010.8.

[20] ftp://ftp.gfz-potsdam.de/pub/home/kg/kyriakos/internal/VLBI_coords_ngs+vgosdb+pet+nrao+lof.xyzllhH

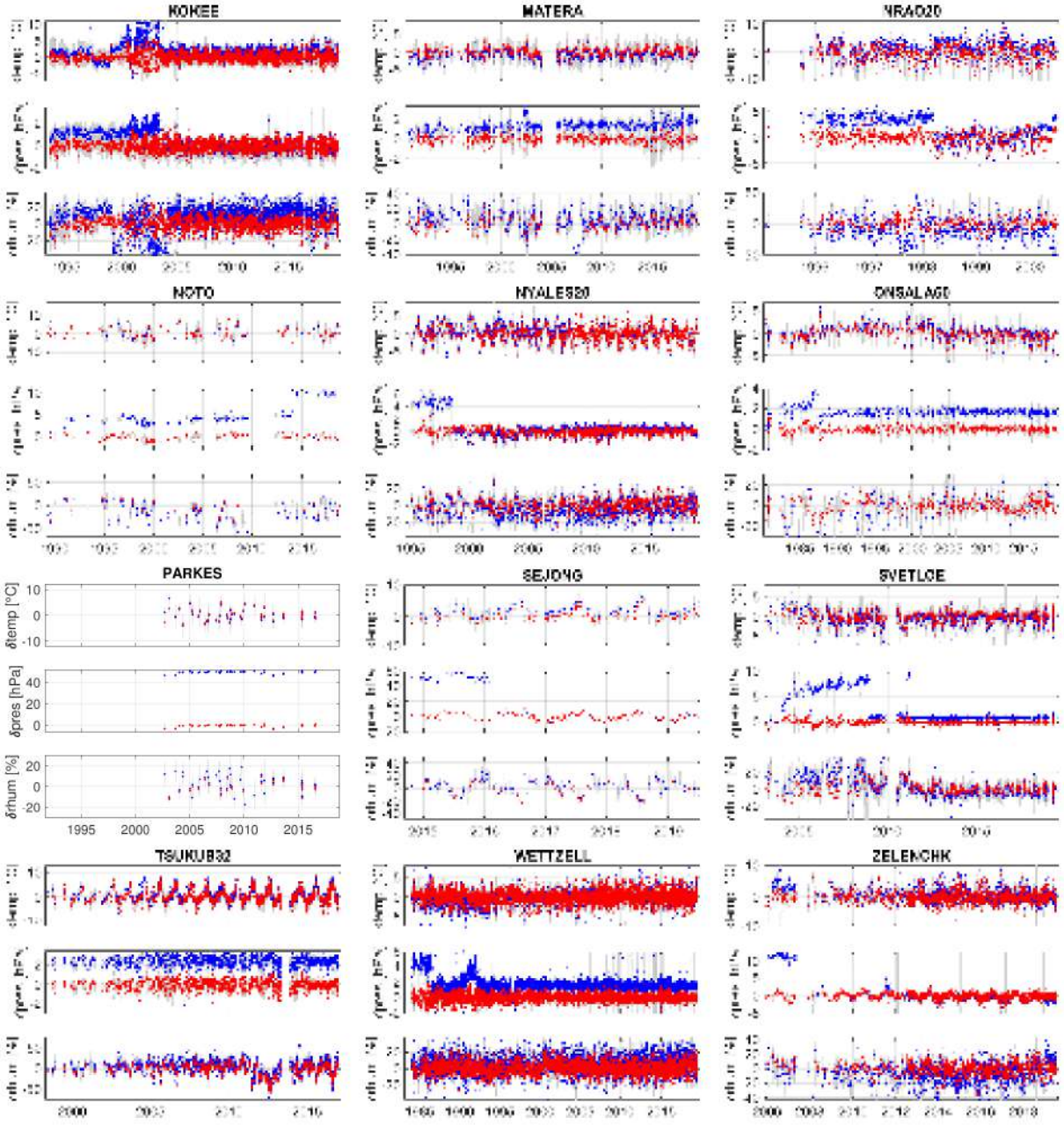


Figure 3.3.9: Differences between meteorological observations recorded in the vicinity of the some VLBI stations, and reference series constructed employing ERA Interim model level data (blue). In red illustrated are these differences after the homogenization process. Shown session-wise are the differences at Kokee Park, Matera, Green Bank, Noto, Ny-Ålesund, Onsala, Parkes, Sejong, Svetloe, Tsukuba, Wettzell, and Zelenchukskaya. The scatter of the meteorological parameter anomalies during the course of a session is illustrated in gray.

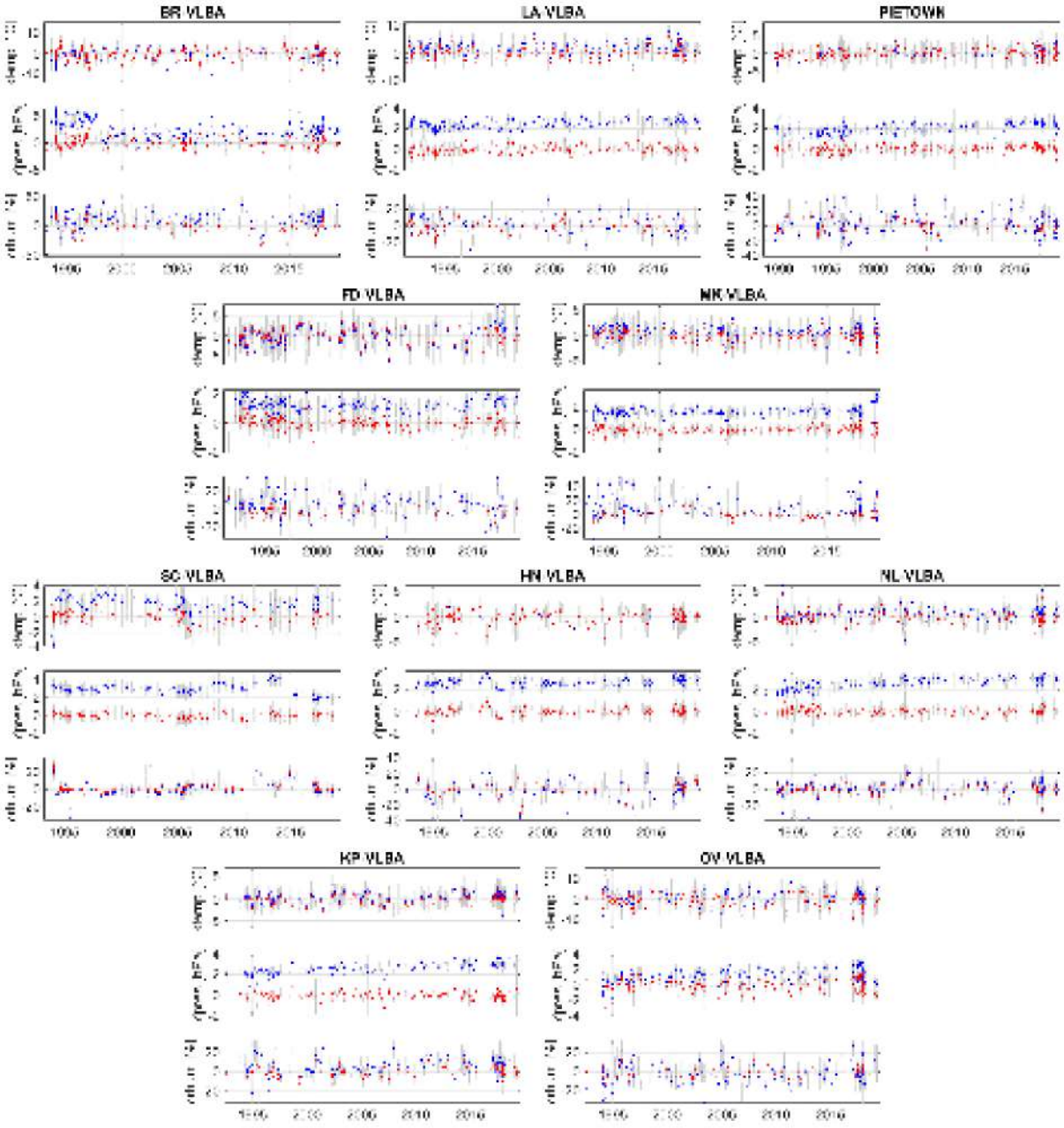


Figure 3.3.10: Differences between meteorological observations recorded in the vicinity of the stations constituting the VLBA in the USA, and reference series constructed employing ERA Interim model level data (blue). In red illustrated are these differences after the homogenization process. Shown are the session-wise differences at Brewster (WA), Los Alamos (NM), Pie Town (NM), Ft. Davis (TX), Mauna Kea (HI), St. Croix (VI), Hancock (NH), North Liberty (IA), Kitt Peak (AZ), and Owens Valley (CA). The scatter of the meteorological parameter anomalies during the course of a session is illustrated in gray.

4 Development of atmospheric delay models

In this chapter ray-tracing, as well as the development of mapping functions and gradients for all four space geodetic techniques (namely GNSS, SLR, VLBI, and DORIS) is conducted. The impact of the radius of curvature, the orbital altitude, the refractivity expression, the ionospheric contribution, and the underlying NWM is rigorously assessed.

To date, there are only VLBI-tailored time-dependent atmospheric delay corrections publicly available. They have been adopted by all other microwave space geodetic techniques, regardless of the fact that they are unsuitable more often than not (especially adopting atmospheric range corrections for VLBI in DORIS data analysis) for a number of reasons, such as the orbital altitude dependence and the ionosphere-induced ray-bending.

In Sec. 4.1 several atmospheric delay perturbations are investigated. The impact of the radius of curvature (Sec. 4.1.1), the orbital altitude of the target (Sec. 4.1.2), the observation geometry (Sec. 4.1.3), and the ionosphere (Sec. 4.1.5) on ray-traced delays, mapping functions and gradients is studied. The impact of the underlying NWM is assessed as well (Sec. 4.1.4).

Section 4.2 addresses the issue of parameterizing the tropospheric delays as a function of elevation and azimuth. A concise review of state-of-the-art symmetric and asymmetric mapping functions is presented in Sec. 4.2.1 and Sec. 4.2.3, respectively. Modelling approaches for tropospheric asymmetries are explored in Sec. 4.2.2. Section. 4.2.4 and Sec. 4.2.5 outline the development of the Potsdam and Berlin mapping functions, respectively.

Section 4.3 describes the development of the state-of-the-art empirical model GFZ-PT (Balidakis et al., 2018c) that features bias, trend, S_{11}, S_a, S_{sa}, S_{ta}, S_1, S_2, and S_3 coefficients for a number of parameters, namely pressure, temperature, relative humidity, zenith delays, mapping function coefficients, and gradient vector components of the 1st and 2nd order, water vapour-weighted mean temperature and integrated water vapour. GFZ-PT is driven from 39 years of 6-hourly ERA Interim fields, and 10 years of hourly ERA5 fields.

Section 4.4 deals with atmospheric ties. As of this writing, only corrections to zenith delays and the hydrostatic mapping factor have been considered. Herein, in addition to these parameters, the non-hydrostatic mapping factor, as well as linear and non-linear gradient components are treated as well. A previously-ignored height dependence of the non-hydrostatic mapping factor is demonstrated. It is proven that linear and non-linear gradients diminish with height, in an absolute sense. In the optical domain, it is shown that not applying frequency-specific mapping functions and gradients results in systematic errors larger that 1 mm in the height coordinate component, thus introducing a scale bias to the implied TRF (e.g., mapping functions and gradients for 532 nm to 366 nm). The orbital altitude dependence of mapping factors and gradients is assessed. It is shown that employing mapping functions tailored for VLBI to reduce DORIS observations introduces a height bias of 1 mm. The fact that atmospheric ties are dependent upon time is also discussed. All developments in this section are based on rigorous ray-tracing in ERA5 fields.

4.1 Atmospheric delay perturbations

Wave propagation through a medium of variable index of refraction is bent. Adopting the geometrical optics approximation (Sec. 3.1), the wave reduces to a ray whose delay and bending is dictated by the gradient of the refraction index field (Sec. 3.2). The contribution of the ray-bending to the total atmospheric delay is dependent upon the several factors, mainly the elevation angle, the underlying refractivity field, the orbital altitude (cf. Sec. 4.1.2), and the frequency of the signal at hand. By and large, ray-bending increases exponentially with increasing atmospheric delay and of course with decreasing ε. Ray-bending is important only for $\varepsilon < 30°$ because for higher ε this effect is well below 1 mm. Based on ray-tracing in ERA5 refractivity tensors, it was found that at elevations as low as 3° ray-bending amounts 0.8–2.1 % of the total delay, that is as much as 0.5 m for sites at sea level. There are a number of parameters that affect the total delay induced by transatmospheric and transionospheric propagation. The direction of the ray in a topocentric reference system with the station of interest in its center is the most important.

The computation of the atmospheric delay based on ray-tracing and the subsequent numerical integration is but a "simulation" of the delay the actual signal experiences on its way from e.g., phase center of a GPS satellite to the phase center of receiver. To make this simulation more realistic, a number of effects should be taken into account. Some effects whose treatment is not as rigorous as it should in terms of meeting the so-desired GGOS goals are remedied within the framework of this section. As of this writing, the slant delays' accuracy obtainable by state-of-the-art NWMs is $\sigma_{\tau_{atm}} \approx 10\csc(\varepsilon)$ [mm]. Of course, that figure is much higher under humid conditions, under severe weather events, or epochs/regions with sparse meteorological observations that were assimilated into the NWM. The effect of atmospheric turbulence on the refractivity tensor is not considered within the ray-tracing, but at the later stage of analyzing the related observations within the geodetic adjustment (stochastic model). To account for turbulence at the ray-tracing level, an eddy-resoling NWM must be employed. The latter is beyond the intended scope of this work. All developments carried out herein (meso-β NWMs) apply to NWMs at meso-γ spatiotemporal scales in the exactly the same way. Following Fujita (1986), the spatial resolution of meso-β (meso-γ) models is about 20–200 km (2–20 km) half-wavelength, and the temporal resolution thereof ranges between 30 min (3 min) and 6 h (30 min).

4.1.1 Radius of curvature

Due to the rotational symmetry governing the ellipsoid, all radii considered herein are independent of longitude.

The curvature of the normal section with normal section azimuth α, is calculated using Euler's theorem as a function of the principal radii of curvature R_M and R_N (e.g., Hofmann-Wellenhof and Moritz, 2006)

$$R_E(\varphi, \alpha) = \frac{R_M R_N}{R_M \sin^2(\alpha) + R_N \cos^2(\alpha)}, \tag{4.1.1}$$

where R_N is the radius of curvature of the prime vertical normal section at the point of the

ellipsoid normal, and R_M is the radius of curvature of the meridian ellipse

$$\begin{aligned} R_N &= \frac{a}{\sqrt{1 - e^2 \sin^2(\varphi)}}, \\ R_M &= \frac{a(1-e^2)}{(1 - e^2 \sin^2(\varphi))^{\frac{3}{2}}}, \end{aligned} \tag{4.1.2}$$

where a and e denote the semi-major axis and first eccentricity of the ellipsoid, respectively. To locally approximate the ellipsoid by an osculating sphere, the average of R_E over all α, termed as Gaussian mean radius, is employed

$$R_G(\varphi) = \sqrt{R_M R_N} \tag{4.1.3}$$

It is $R_N \geq R_G \geq R_M$ (cf. Fig. 4.1.1), and R_E ranges from R_N (for north-south directions) to R_M (for east-west directions). Atmospheric delays determined employing R_G differ (incorrectly) from those determined using R_E up to 25 mm at elevation angles as low as 3°, as a function of decreasing $|\varphi|$. The differences exceed the 1 mm level for $\varepsilon < 15°$ (e.g., 15 mm@10°). Given elevation-angle-fixed delays at a site, the differences between R_G and R_E are positive in the positive intervals of the function $\cos(2\varphi)$, that is, the differences maximize for $\alpha = j90°$ (for $j = [0, 3]$), whereas they are zero for $\alpha = 45° + j90°$. Mapping factors estimated from ray-traced delays where R_G was utilized are erroneously larger than those for which R_E was employed. The latter stems from the declaration of $\alpha = 0°$ for ray-tracing in the refractivity profile above a given site (e.g., PMF, cf. Sec. 4.2.4). Should an approach akin to BMF (cf. Sec. 4.2.5) be used to estimate the mapping function coefficients, the effect in most cases diminishes considerably. This bias increases with decreasing $|\varphi|$ and can be as large a 25 mm at 3°. The orthogonal gradient components are systematically affected but to a much lesser extend, up to 4 µm (that is less than 1 mm@3°) in the tropics; for instance if $G_{NS} > 0$, it is $G_{NS}^{R_G} < G_{NS}^{R_E}$. Provided an observation geometry where for every ray there is another at a supplementary azimuth, the estimation of 1st order gradient components is independent of the radius of curvature employed during ray-tracing. The latter may be proven by closed-form expressions (e.g., Zus et al., 2018). However, higher-order gradient components are affected due to the fact that the partial derivatives thereof do not oscillate around zero, given a constant azimuthal granularity[1]. Euler's radius of curvature is the most elaborate approach and hence is adopted for all ray-tracing work carried out in this dissertation (either determination of mapping functions and gradients or application of ray-traced delays directly to space geodetic data analysis).

4.1.2 Orbital altitude

Let $\mathbf{r^i}$ and $\mathbf{r_j}$ denote the position of the emitter and receiver, respectively, in an Earth-centered, Earth-fixed system. The source unit vector in the direction of signal propagation (emitter-receiver) is given by

$$\hat{\boldsymbol{\varrho}} = \frac{\mathbf{r^i} - \mathbf{r_j}}{\|\mathbf{r^i} - \mathbf{r_j}\|_2} \tag{4.1.4}$$

[1] It is: $\int_0^{2\pi} \cos^2(\alpha)\, d\alpha = \int_0^{2\pi} \sin^2(\alpha)\, d\alpha = \pi$.

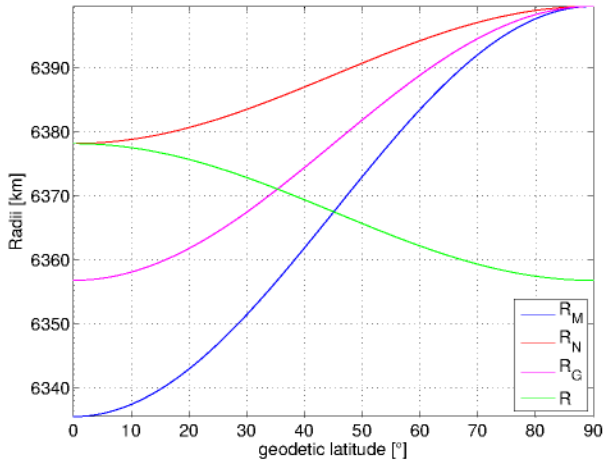


Figure 4.1.1: Radii against φ for WGS84. Illustrated are the radii of curvature in meridian R_M and in prime vertical R_N, as well as the Gaussian radius of curvature R_G, and the geocentric radius R.

The free-of-refraction elevation ε and azimuth α are given by (e.g., Leick et al., 2015)

$$\begin{aligned}
\varepsilon &= \sin^{-1}\left(\langle \hat{\boldsymbol{\varrho}}, \hat{\boldsymbol{u}} \rangle\right) \\
&= \sin^{-1}\left(\frac{\cos(\varphi)\sin(\lambda)(x_j - x_i) + \cos(\varphi)\sin(\lambda)(y_j - y_i) + \sin(\varphi)(z_j - z_i)}{\sqrt{(x_j - x_i)^2 + (y_j - y_i)^2 + (z_j - z_i)^2}}\right) \\
\alpha &= \tan^{-1}\left(\frac{\langle \hat{\boldsymbol{\varrho}}, \hat{\boldsymbol{e}} \rangle}{\langle \hat{\boldsymbol{\varrho}}, \hat{\boldsymbol{n}} \rangle}\right) \\
&= \tan^{-1}\left(\frac{\cos(\lambda)(y_j - y_i) - \sin(\lambda)(x_j - x_i)}{-\sin(\varphi)\cos(\lambda)(x_j - x_i) - \sin(\varphi)\sin(\lambda)(y_j - y_i) + \cos(\varphi)(z_j - z_i)}\right)
\end{aligned} \tag{4.1.5}$$

where $\hat{\boldsymbol{n}}$, $\hat{\boldsymbol{e}}$ and $\hat{\boldsymbol{u}}$ are the defining unit vectors in the local north-east-up coordinate system. The calculation observation directions of VLBI observations is slightly more complicated as information pertinent to Earth rotation has to be parsed as well. For further details, the interested reader is referred to e.g., `iau_atco13.for` from the software routines from the IAU standards of fundamental astronomy (SOFA) collection[2].

Given a geometric direction (ε, α), the ray path from emitter and receiver (and vice versa) is bent more with decreasing distance (e.g., Yan, 1996). This fact has two implications for atmospheric delay modelling:

- ☐ First, given the receiver, slant delays for LEOs (e.g., CryoSat-2) are slightly larger than slant delays for MEOs (e.g., GPS), and the latter are marginally larger than slant delays for quasars.

- ☐ Second, the distance between a given receiver and emitter changes usually as a function of ε, thus affecting the ray-bending in addition to refractivity. Usually rising and setting satellites ($\varepsilon \to 0$) are more far away from a receiver than when they are on the zenith so, the ray-bending is slightly smaller. These distance variations are 35 % for GPS, 30 % for GLONASS, 87 % for Galileo, 95 % for BeiDou, and 38 % for QZSS. For laser ranging the differences are similar; 24 % for LAGEOS-1, 27 % for LAGEOS-2, and 57 % for Etalon-1

[2] http://www.iausofa.org/

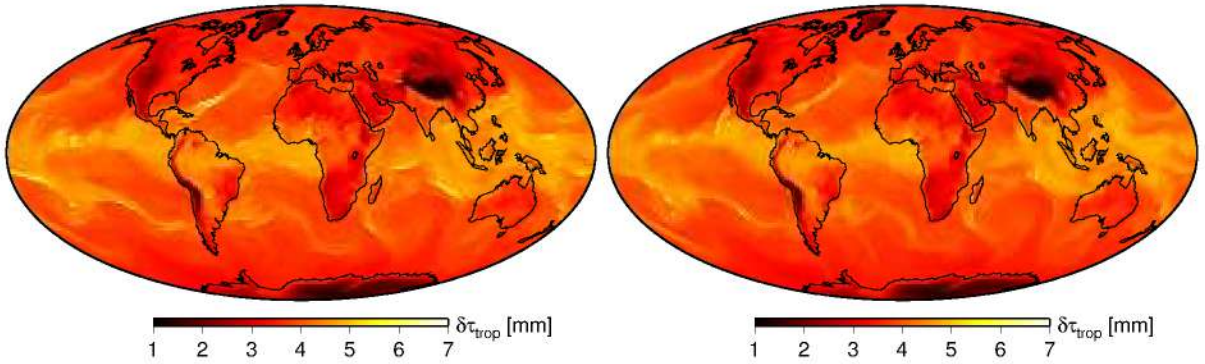


Figure 4.1.2: Orbital altitude dependence. The ddifferences $\tau_{trop}^{\text{P-R}}$ (3°,0°) (left), and $\tau_{trop}^{\text{P-R}}$ (3°,90°) (right) are illustrated. Note that delays calculated assuming the average GPS orbital altitude are always larger from delays assuming a quasar target.

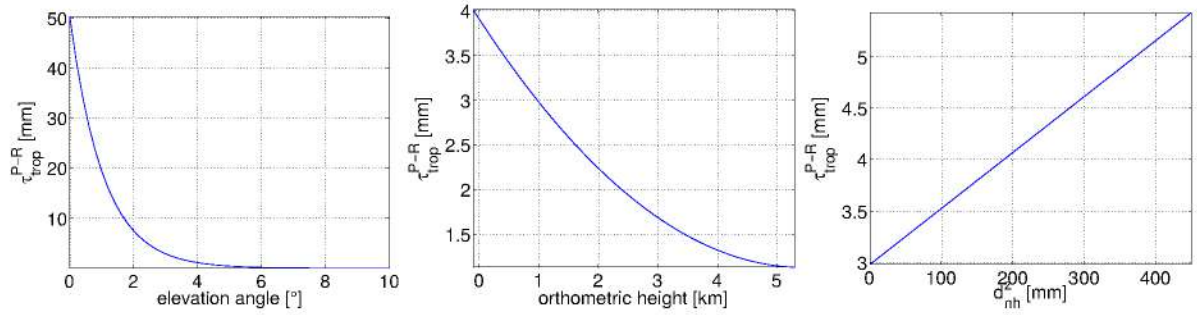


Figure 4.1.3: Orbital altitude dependence. Shown are the differences $\tau_{trop}^{\text{P-R}}$ as a function of elevation angle (left), height (middle), and zenith non-hydrostatic delay (right).

and Etalon-2. Table 4.1.1 displays the average orbital altitude of some satellites observed by the space geodetic techniques, where some contribute to the realization of ITRF.

The fact that "the lower the target, the larger the ray-bending" is indicated by Fig. 4.1.2 where ray-traced delays at a very low ε in two perpendicular directions (0°, 90°) are shown. The differences can be as large as 7 mm, and depend on the orography and the total atmospheric density across the ray-path (cf. Fig. 4.1.3).

The mapping functions recommended by the latest IERS conventions, that is VMF1 (Boehm et al., 2006), assume no orbital altitude dependence of τ_{trop}. This implies that e.g., ray-traced delays for VLBI, GNSS and DORIS should be identical. Despite the fact that τ_{trop} is insensitive to orbital altitude perturbations of ±1000 km that correspond to the different navigation satellite constellations, should a different space geodetic technique be considered e.g., VLBI (∞) or DORIS ($\leqslant$ 1400 km), $\delta\tau_{trop}$ is no longer inconsequential. While this presumption holds for e.g., $\varepsilon > 7°$ between GPS and VLBI, employing VLBI-tailored tropospheric products in DORIS analysis results in height estimates biased by at least 1 mm.

4.1.3 Observation geometry

The space segment plays a pivotal role in the ability of space geodetic techniques to decorrelate effects induced by tropospheric refraction (and clocks) from actual crustal motion, as well as to probe atmospheric density variations. Ideally, the skyplot at every point on Earth would feature evenly distributed observations across azimuth and elevation (ranging from the zenith to the

Table 4.1.1: Orbital altitude (average) of some satellite systems and individual satellites, of interest to space geodesy.

Satellite(s)	Orbital altitude	Satellite(s)	Orbital altitude
GPS	20 180 km	Larets	691 km
GLONASS	19 140 km	Starlette	812 km
Galileo	23 222 km	Stella	815 km
BeiDou	21 150 km	TOPEX	1330 km
QZSS	32 000 km	Jason-1/2/3	1336 km
LAGEOS-1	5850 km	Envisat	782 km
LAGEOS-2	5625 km	SPOT-2/3/4/5	832 km
Etalon-1	19 105 km	CryoSat-2	717 km
Etalon-2	19 135 km	HY-2A	971 km
Ajisai	1485 km	SARAL	800 km
LARES	1450 km	GRACE-FO	500 km

lowest elevation angle permitted by the local landscape) such that no patch of sky would be unobserved within 1 h (the usual estimation interval of zenith delays and gradients). While this is achievable during simulating observations (or ray-tracing), in reality it is not feasible.

VLBI observations are carried out employing large directional antennas. While this offers advantages (from a geodetic perspective) such as that unlike GNSS, VLBI does not suffer from multipath, the number of radio sources that may be observed is restricted. The main limiting factors are the telescope's slewing rates, the data recording rates, and the strength of the sources available, F, as fainter radio sources require larger integration time spans to achieve a sufficiently large SNR. The following formula gives approximately the minimum scan length t necessary for a source detection by a two-element interferometer

$$\begin{aligned} t &= \left(\frac{1.75\,SNR}{F}\right)^2 \left(\frac{SEFD_1\,SEFD_2}{2BN_c}\right), \\ SEFD &= \frac{8kT_s}{\pi D^2 \eta 10^{-26}}, \end{aligned} \tag{4.1.6}$$

where SNR denotes the minimum signal-to-noise ratio, $SEFD$ is the system equivalent flux density, the product $2BN_c$ indicates the recording rate, k denotes Boltzmann's constant, T_s denotes the system temperature, D denotes the diameter of the antenna, and η is the VLBI processing factor. Slewing rates and antenna sensitivity are in conflict as on the one hand larger (thus more sensitive) telescopes can detect radio sources ($SNR > 7$) much faster than smaller ones (shorter scan length), and on the other hand larger telescopes require more time to move from observing one source to the next. Moreover, the larger the number of stations participating in a VLBI experiment, the shorter the time spent switching. Figure 4.1.4 illustrates the direction of all observations that would take place within a 24-hour session at Wettzell, with three different configurations: rapid turnaround, CONT14, and VGOS. The observations are not evenly distributed across elevation — they usually increase with decreasing ε — and besides, the antennas are subject to the keyhole problem. Keyholes constitute of a set of directions (in the topocentric frame) where coordinate singularities exist, that is, the antenna may be able to point to one of these directions, tracking is difficult because infinite rotation speed is required (Salzberg, 1967). Keyholes depend upon the antenna mount; the most common antenna mount amongst

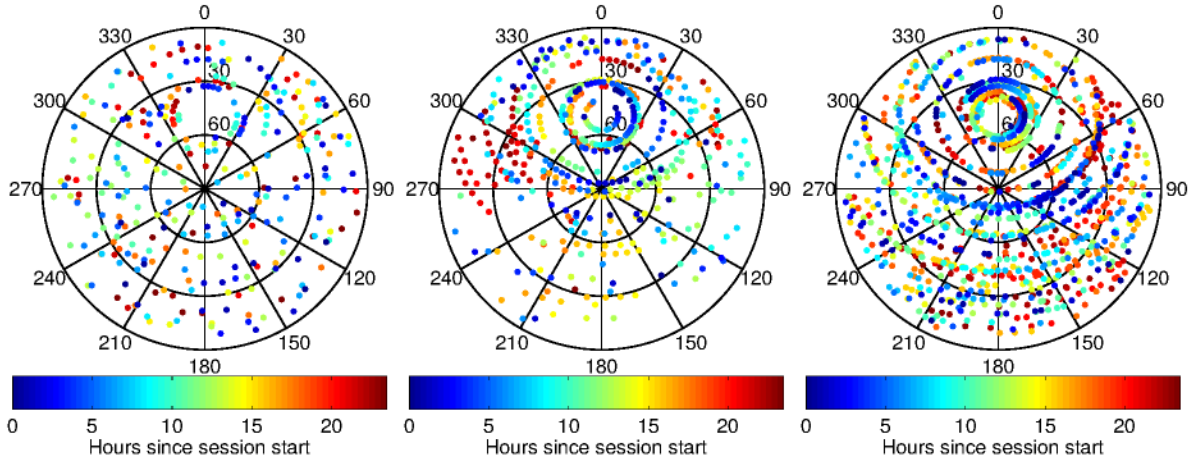


Figure 4.1.4: Skyplots of the radio sources observed by WETTZELL in a single VLBI session under a regular rapid turnaround network configuration (left), CONT14 (middle), and simulated 32-station VGOS (right).

modern VLBI radio telescopes is the altitude-azimuth due to the fact that it is symmetric thus it can support heavy antennas — exceptions do exist, e.g., HARTRAO (hour angle-declination) and HOBART26 (X-Y). AZEL antennas. Altitude-azimuth antennas cannot track continuously objects near the local zenith, whereas they keyhole of hour angle-declination antennas depends upon the station's latitude. The benefits stemming from the VGOS configuration, that is faster slewing, higher recording rates, and larger station network, are apparent. The optimal resolution of such issues is treated by scheduling software packages e.g., SKED or VIE_SCHED, and is still subject of scientific debate (e.g., Sun, 2013).

GNSS antennas are omnidirectional which implies that if the channel capacity of the related hardware is sufficient, they can record many signals concurrently. This feature renders GNSS estimates prone to multipath, one of the reasons a relatively high elevation mask ($\varepsilon > 7°$) is utilized in addition to an elevation-dependent strategy to weight the observations. Utilizing the current multi-GNSS constellation, geodetic sites are capable of receiving signals from 20–57 different satellites per day. Figure 4.1.5 was created employing the final orbits of the MGEX constellation (GPS, GLONASS, Galileo, BeiDou and QZSS) estimated at GFZ (Deng et al., 2016), and illustrates the ground track for the most important GNSS constellations for a single day. Assuming uninterrupted view ($\varepsilon \geq 7°$), the number of satellites is variable throughout a single day (minimum plus 9–23 satellites pet site) and depends on the site's geographic location, as well as the orbital elements of the individual satellites. Observing more satellites improves the skyplot and therefore the dilution of precision, the phase ambiguity resolution, and the accuracy, but at the same time increases the number of parameters in the subsequent adjustment e.g., ambiguities, satellite orbits and inter-system bias. Studying the satellite coverage of MGEX (cf. Fig. 4.1.6), a blank patch of sky is apparent; it is located around the zenith direction at sites near the North (South) pole and it moves towards the North (South) with decreasing $|\varphi|$, also reducing its radius (e.g., 34° at Alert, Nunavut). This feature is induced by the inclination of the orbits —thus it is different for GPS and GLONASS— and it is proven later in this thesis that it affects the estimation of G_{NS} in the presence of nonlinearities. Furthermore, the number of observations increases with decreasing ε, at all sites; if the elevation mask is set at 5° in lieu of 7°, there is an average increase of 5 % in the number of observations.

As of this writing, the estimation of tropospheric parameters (e.g., d^z_{nh}, G_{NS}, G_{EW}) dur-

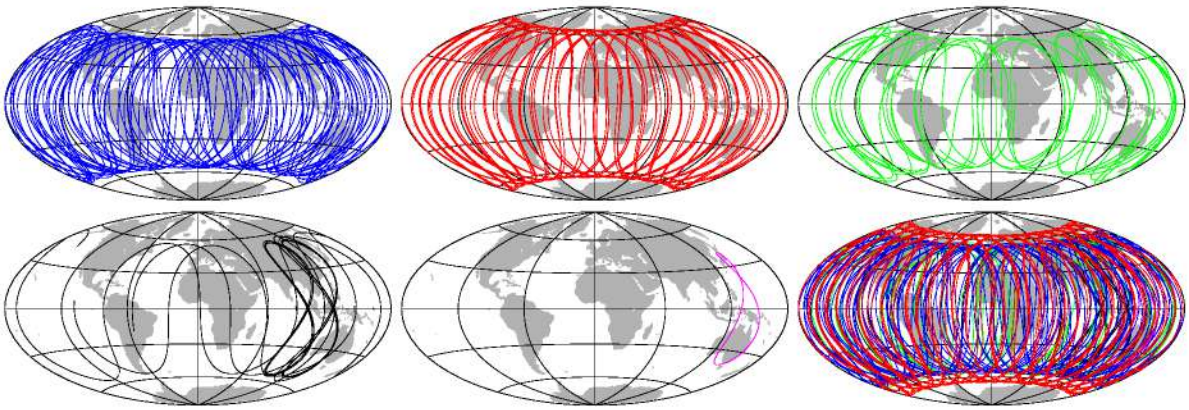


Figure 4.1.5: The ground track of the GPS (blue), GLONASS (red), Galileo (green), BeiDou (black) and QZSS (magenta) constellations on 2017/01/03.

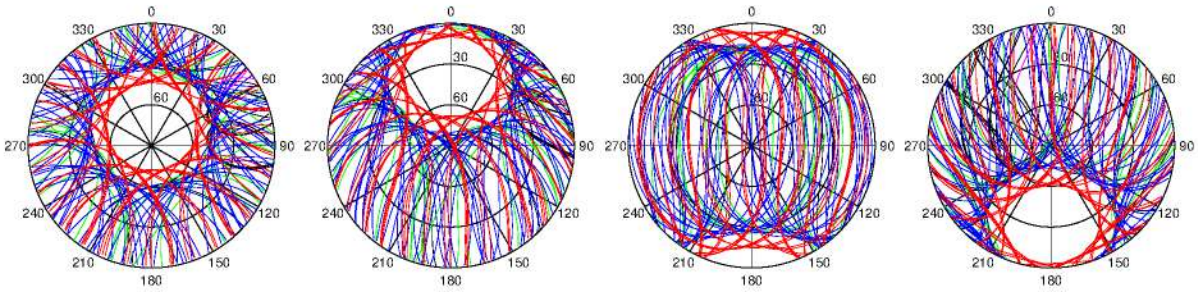


Figure 4.1.6: Satellite visibility diagrams for MGEX at Ny-Ålesund (Svalbard), Wettzell (Germany), Fortaleza (Brazil) and Hobart (Tasmania) on 2016/05/18. Shown are the GPS (blue), GLONASS (red), Galileo (green), BeiDou (black) and QZSS (magenta) constellations.

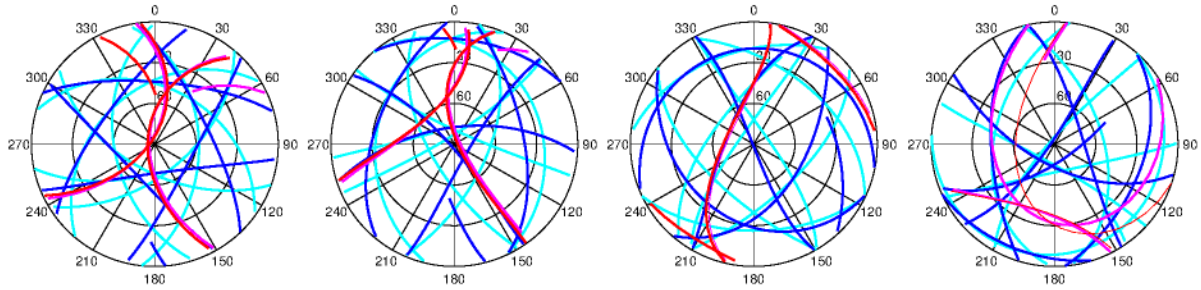


Figure 4.1.7: Satellite visibility diagrams for LAGEOS-1 (cyan), LAGEOS-2 (blue), Etalon-1 (magenta) and Etalon-2 (red) orbits from Ny-Ålesund (Svalbard), Wettzell (Germany), Fortaleza (Brazil) and Hobart (Tasmania) on 2016/05/18.

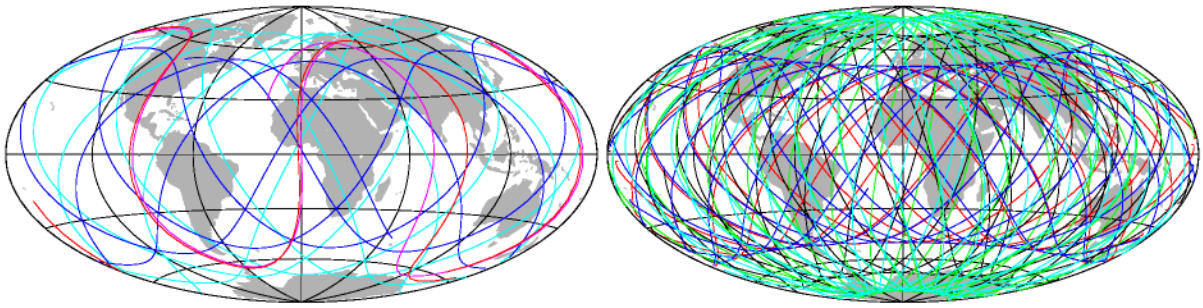


Figure 4.1.8: The ground tracks of LAGEOS-1 (cyan), LAGEOS-2 (blue), Etalon-1 (magenta) and Etalon-2 (red) orbits, on 2016/05/18, are on the left. The ground tracks of Ajisai (red), LARES (black), Larets (green), Starlette (blue), and Stella (cyan) orbits on 2016/05/18 are on the right.

ing the analysis of laser observations is not recommended by the latest IERS conventions (Petit and Luzum, 2010). This situation was established owing to the fact that optical d^z_{nh} are 66 times smaller than microwave (cf. Sec. 4.4) and therefore any errors stemming from approximating d^z_{nh} analytically based on surface measurements would be too small to affect the estimated parameters. This presumption is true to a certain extend. Nevertheless, as demonstrated in Fig. 4.4.9, the impact of refractivity gradients on ranges near the horizon (10°) can exceed 5 cm at mid-latitudes. One of the reasons gradients are not estimated in SLR data analysis is the relatively poor observation geometry at the common intervals of gradient estimation for microwave space geodetic techniques. Figure 4.1.7 displays satellite visibility diagrams for four common stations tracking the satellites that are most commonly used for geodetic applications; LAGEOS-1, LAGEOS-2, Etalon-1, and Etalon-2. SLR analysis benefits from the addition of more satellites in a manner similar to GNSS. Figure 4.1.8 illustrates the ground tracks of the most commonly observed satellites with SLR. Notwithstanding the relatively good sky coverage, not all of these tracks can be observed; a number of satellites (27) rank higher in the tracking priority list of ILRS, and laser observations cannot be carried out under cloudy conditions. Calculated herein, an atlas illustrating the stacked hourly total cloud cover (TCC) fields from ERA5 (2008.0–2018.0) is shown in Fig. 4.1.9. The higher the TCC, the lower the number of potential observations. Figure. 4.1.9 also presents the variability of TCC. In addition, most laser tracking facilities are still operated manually so, not all possible observations (weather-wise) are currently carried out.

On account of the low orbital altitude of DORIS satellites, hence high along-track velocity component, they are visible very shortly per pass, and these observations are sparsely distributed over the course of the day. For instance, it is $\max(\partial\varepsilon/\partial t) = 0.5\,^\circ\,\mathrm{s}^{-1}$, and $\max(\partial\alpha/\partial t) = 7.5\,^\circ\,\mathrm{s}^{-1}$

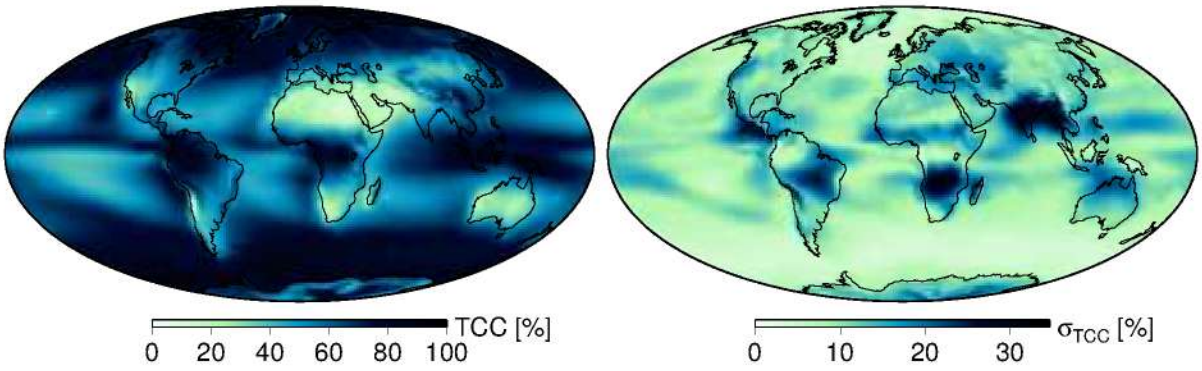


Figure 4.1.9: Total cloud cover atlas (left) and its scatter (right) at the orography of ERA5, calculated from hourly ERA5 fields (2000.0–2018.0).

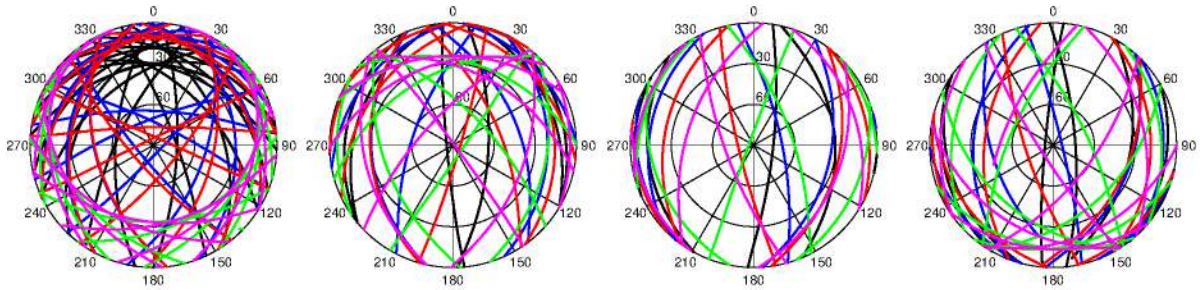


Figure 4.1.10: Satellite visibility diagrams for CryoSat-2 (black), Envisat (blue), HY-2A (red), Jason-2 (green) and Jason-3 (magenta) orbits from Ny-Ålesund (Svalbard), Wettzell (Germany), Fortaleza (Brazil) and Hobart (Tasmania) on 2018/01/01.

for CryoSat-2 from Wettzell on 2018/01/01. Such an observation geometry hinders the precise estimation of tropospheric parameters and especially gradient components, at least at the level of GNSS or VLBI. Figure 4.1.11 displays the ground track of the most commonly used DORIS satellites. Similar to the other space geodetic techniques, for DORIS also applies that the lower the elevation mask, the more the potential observations. Figure 4.1.10 attests to the latter. A hole in the skyplot of polar sites does exist (cf. Ny-Ålesund in Fig. 4.1.10), it is of the same origin as in the related GPS skyplots (or in the skyplots of other navigation MEOs), but its radius is considerably smaller.

Figure 4.1.6, Fig. 4.1.7, and Fig. 4.1.10 were generated based on the station positions of the VLBI stations `NYALES20`, `WETTZELL`, `FORTLEZA`, and `HOBART26`, and the satellite orbits of GNSS, SLR, and DORIS. These figures differ from those based on real observations due to the fact that there may be physical obstacles. The rational behind presenting these figures is to illustrate the varying observation distribution for different observing systems, as well as for station locations.

4.1.4 Numerical weather model

Perhaps the most crucial aspect of calculating the atmospheric delays utilizing NWMs (or radiosonde profiles) and a ray-tracing algorithm is the quality thereof. In this work the NWMs' spatiotemporal resolution is valued together with their ability to predict severe weather events and to maintain a long-term stability. The capacity of accurately representing cloud formation, moist convection, coupling between atmospheric water and circulation, and heating (e.g., Oueslati and Bellon, 2013) also influenced the current choices. A large number of models has

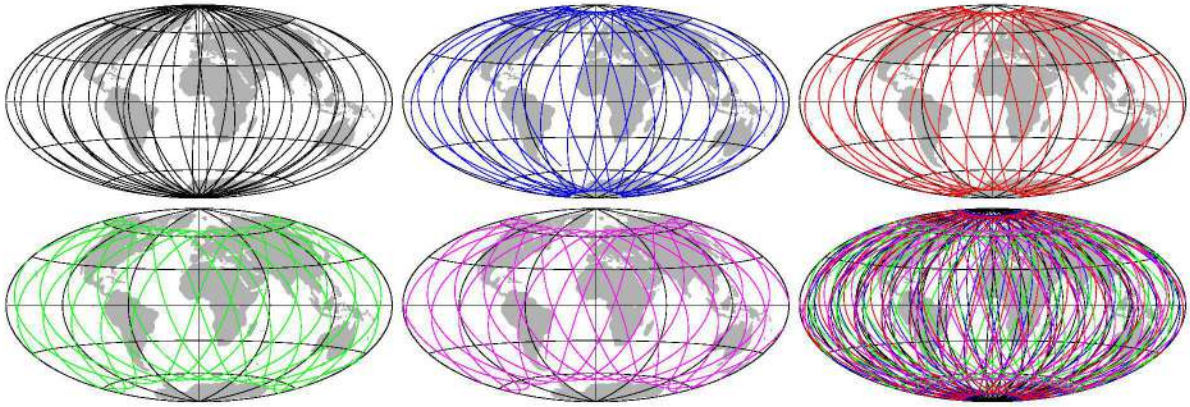


Figure 4.1.11: The ground track of the CryoSat-2 (black), Envisat (blue), HY-2A (red), Jason-2 (green) and Jason-3 (magenta) missions on 2018/01/01.

been tested herein, namely ECMWF's operational model, ERA Interim, ERA5, NCEP-DOE AMIP-II, JRA-55, MERRA, and MERRA2. While it is definitely interesting to study in depth the differences thereof, it is beyond the intended scope of this work. Nevertheless, some comparisons have been carried out in an effort to obtain reliable pressure, temperature, and relative humidity series, at the earlier stage of this study (cf. Sec. 3.3).

Since the atmospheric parametrization carried out herein is intended for the reduction of series of microwave and optical observations that span several decades, the stability is crucial. Inconsistencies will lead to spurious rates in the estimated parameters such as the d^z_{nh}, and the velocity of the height coordinate component. Accordingly, while ECMWF's operational model benefits from the frequent updates in the assimilation system and upgrades in the horizontal and vertical resolution, ERA Interim is more suitable for reanalysis purposes. ERA5, the successor of ERA Interim, is even more suitable than its predecessor for it was designed for climate analysis and does not suffer from e.g., inconsistencies in the sea surface temperature.

Data sets with known issues were avoided. For instance ray-tracing in NCEP-DOE AMIP-II Reanalysis fields (Kanamitsu et al., 2002) yields slightly larger zenith and slant non-hydrostatic delays compared to ECMWF-based models as well as VLBI and GNSS estimates.

The native spatiotemporal resolution of the fields used to compute refractivity prior to ray-tracing is pivotal. Lumps and bumps in pressure, temperature, specific humidity, and of course orography smaller than the half-wavelength of native resolution of the NWM employed for ray-tracing cannot be resolved, especially in view of the fact that prognostic variables such as surface pressure and temperature are stored as spherical harmonic coefficients. Consequently there is no benefit in employing meso-β NWMs at meso-γ spatial scales. On the other hand, interpolating to a coarser spatiotemporal resolution could cause aliasing to the related data sets and therefore was avoided. Of course, to better perform the numerical integrations some interpolations are necessary in any case. The ray-tracing results will be marginally different between e.g., ERA Interim at 0.25° and ERA Interim at 0.125°. From a parameter-oriented viewpoint, the higher the native resolution of the NWM employed in ray-tracing the sharper the atmospheric gradients. That is, ray-tracing in a 0.25°-resolved ERA Interim and ERA5 fields yields sizable differences in linear and non-linear gradient components, as well as in the assembled delays (mapping factor times zenith delay). Following the rule of thumb, employing ERA5 in lieu of ERA Interim will have an impact on the estimated heights. Studying Fig. 4.1.12 one notices that the d^z_h (d^z_{nh}) differences between ECMWF's operational model, ERA Interim and ERA5 are normally distributed about zero with a scatter around 1 mm (1 cm). Moreover, in more than 94 % of the

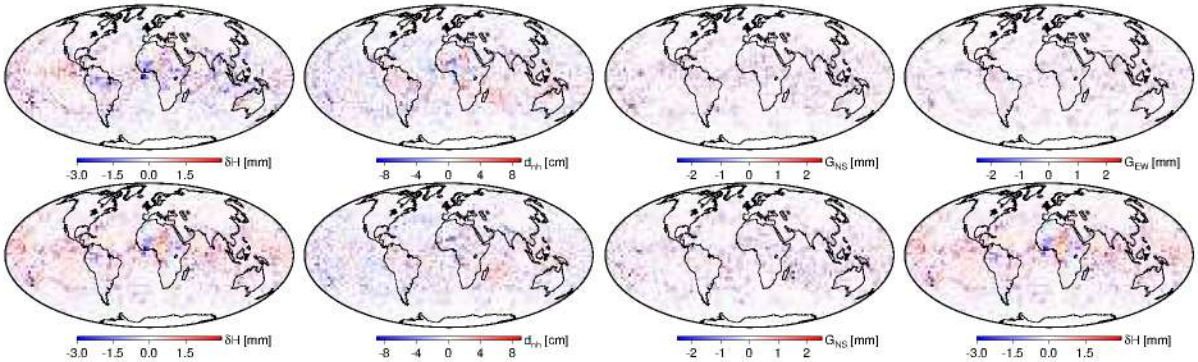


Figure 4.1.12: The impact of alternating the underlying NWM between ERA5 and ERA Interim (upper row), and ECMWF's operational model and ERA-Interim (lower row), on ray-tracing products (2014/05/05 00:00). The differences between the equivalent height errors δH, d_{nh}^z, G_{NS}, and G_{EW} are presented.

cases the equivalent height errors are below 1 mm, in 75 % of the cases the asymmetric delay differences are below 1 cm, and have a scatter below 1 cm at 7°.

Every NWM node represents a spatial average around its nominal coordinates. In contrast to this fact, it expresses an instantaneous value (in the temporal domain). Due to the fact that geodetic observations are arbitrarily distributed in time, an interpolation scheme is necessary. For all temporal interpolations carried out in this work, Lagrange interpolating polynomials were employed (six points on either side). Given this interpolation method (or simply spline), a site, a target, and an epoch, two strategies are possible:

- ☐ Calculate the slant total delay by performing ray-tracing only once, at a refractivity field that is obtained by temporal interpolation of either (i) the 3D fields of pressure, temperature, specific humidity, and height, or (ii) the 3D refractivity fields at the epochs provided by the NWM of choice.

- ☐ Calculate the slant total delay by performing ray-tracing on the related epochs provided by the NWM of choice, and perform the temporal interpolations on the parameter level.

For state-of-the-art models such as ERA5 or MERRA2 the differences between the two methods are well below the accuracy the models claim (e.g., from a N-member ensemble of data assimilations). The first approach has been followed by Eriksson et al. (2014). Nevertheless, the first approach is inefficient as the ray-tracing and the subsequent numerical integrations are much faster — the ray-tracer employed herein works out 10^5 rays per second — for a reasonable amount of rays than loading huge fields into RAM (2GB per epoch for ERA5) and preparing them for ray-tracing. Hence, the second strategy was selected.

4.1.5 Ionosphere

The propagation of optical waves is marginally affected by the ionosphere. For microwave radiation, the electrically neutral atmosphere is a non-dispersive medium thus the delay it induces is independent of frequency. This statement holds true under the assumption that no charged particles exist between transmitter and receiver. While the refractivity tensor therein $N(\varphi, \lambda, H, t)$ is independent of frequency, the ray-path is not. The deviations are ascribable to the curvature effects induced by the ionosphere which depend upon frequency. The higher the frequency,

the smaller the deviation of the actual ray-path from the chord (geometric) vector, that is because microwave propagation effects in the ionddosphere are roughly proportional to the carrier wavelength. These ray-path deviations that increase with decreasing ε, are insignificant for X-/K-/Ka-/Q-/W-band (VLBI), but within L-band reach hundreds of metres at low ε. For instance, employing ERA5 the slant total delay differences between channels L_1 and L_2 are as large as 2 mm at 10°. These differences increase with more finely resolved NWMs, that is, transitioning to meso-γ spatial scales (e.g., regional COSMIC-DE at 2.5 km, or global IBM's GRAF at 3 km).

For the signals employed by space geodetic techniques that operate in the microwave frequency spectrum (e.g., GNSS, VLBI, and DORIS) propagation effects through a medium composed of plasma (charged particles) are dispersive. Adopting the quasi-longitudinal approximation in the Appleton-Hertee-Lassen formula (e.g., Budden, 1985), the phase refractive index for an ordinary signal at frequency f_i at a given point in collisionless plasma reads (e.g., Bassiri and Hajj, 1993; Brunner and Gu, 1991)

$$\begin{aligned} n_p\left(f_i,\mathbf{x}\right) &= 1-\frac{C_X}{2f_i^2}N_e\left(\mathbf{x}\right) \\ &\quad+\frac{C_XC_Y}{2f_i^3}N_e\left(\mathbf{x}\right)B\left(\mathbf{x}\right)\cos\left(\vartheta\right)-\frac{C_X^2}{8f_i^4}N_e\left(\mathbf{x}\right)^2 \\ &\quad-\frac{C_XC_Y^2}{4f_i^4}N_e\left(\mathbf{x}\right)B\left(\mathbf{x}\right)^2\left(1+\cos\left(\vartheta\right)^2\right), \\ C_X &= \frac{e^2}{4\pi^2\varepsilon m_e}\approx 80.62\,\mathrm{C^2\,m\,F^{-1}\,kg^{-1}}, \\ C_Y &= \frac{\mu e}{2\pi m_e}\approx 606826c\mathrm{H\,C\,m^{-1}\,kg^{-1}}, \end{aligned} \tag{4.1.7}$$

where c denotes the speed of light ($\mathrm{m\,s^{-1}}$), ϑ is the angle between the wave normal vector and the ambient magnetic field vector $\mathbf{B}$, $N_e\left(\mathbf{x}\right)$ is the electron density field, e is the charge of the electron (C), m_e is the mass of the electron (kg), ε is the vacuum electric permitivity ($\mathrm{F\,m^{-1}}$), and μ_0 is the vacuum magnetic permeability ($\mathrm{H\,m^{-1}}$). The group refractive index is (e.g., Bassiri and Hajj, 1993)

$$\begin{aligned} n_g\left(f_i,\mathbf{x}\right) = n_p\left(f_i,\mathbf{x}\right)+f_i\frac{\partial n_p\left(f_i,\mathbf{x}\right)}{\partial f_i} &= 1+\frac{C_X}{2f_i^2}N_e\left(\mathbf{x}\right) \\ &\quad+\frac{C_XC_Y}{f_i^3}N_e\left(\mathbf{x}\right)B\left(\mathbf{x}\right)\cos\left(\vartheta\right)+\frac{3C_X^2}{8f_i^4}N_e\left(\mathbf{x}\right)^2 \\ &\quad+\frac{3C_XC_Y^2}{4f_i^4}N_e\left(\mathbf{x}\right)B\left(\mathbf{x}\right)^2\left(1+\cos\left(\vartheta\right)^2\right). \end{aligned} \tag{4.1.8}$$

Combining the propagation effects of the electrically neutral atmosphere and the ionosphere, and adopting the quasi-isotropic approximation (cf. Sec. 3.2), the optical path length for e.g., the phase carrier is

$$O_i=\int\left(1+10^{-6}N-\frac{40.311}{f_i^2}N_e-\frac{7527cB\cos\left(\vartheta\right)N_e}{2f_i^3}-\frac{812.48N_e^2}{3f_i^4}\right)ds_i, \tag{4.1.9}$$

where ds_i denotes the frequency-dependent (f_i) ordinary line element in Euclidean space. It should be noted that while the optical path of the group wave and the carrier phase are identical (e.g., Born and Wolf, 1999), the optical path lengths differ for the respective numerical integration takes place employing different refractivity fields; (4.1.7) or (4.1.8). From these formulae it is apparent that the carrier phase is advanced whereas the wave group (or modulated code) is delayed. Thus, the ionospheric "delay" for the carrier phase reads

$$I_i = \int \left(1 + 10^{-6} N\right)\, ds_\infty - \int \left(1 + 10^{-6} N - \frac{40.311}{f_i^2} N_e - \frac{7527 c B \cos(\vartheta)\, N_e}{2 f_i^3} - \frac{812.48 N_e^2}{3 f_i^4}\right) ds_i, \tag{4.1.10}$$

modelling the impact of the ionosphere on signal propagation is a rather complicated task as it required precise knowledge of N_e and $\mathbf{B}$. Nevertheless, the ionosphere is a dispersive medium at microwave wavelengths, thus the related propagation effects can be mitigated (to the kth order) by performing observations at $k+1$ frequencies and subsequently forming a standard linear combination of the observables. Should such an approach not be followed, large residuals are expected in the geodetic adjustment due to the solar stimulation of the atmosphere of the Earth at several frequencies (S_1, S_a, S_{11}). Let f_1 and f_2 denote the carrier frequencies[3]: both in L-band for GNSS, X- and S-band for VLBI, and S- and P-band for DORIS. The quasi ionosphere-free (IF) linear combination e.g., for phase ranges reads (e.g., Guier and Weiffenbach, 1960; Fritsche et al., 2005)

$$L_3 = \left(\frac{f_2^2}{f_1^2 - f_2^2} + 1\right) L_1 - \frac{f_2^2}{f_1^2 - f_2^2} L_2 = \rho + \delta I + \lambda_N \left(N_{L_1} + \frac{\lambda_W}{\lambda_{L_2}(N_{L_1} - N_{L_2})}\right) + \omega, \tag{4.1.11}$$

where ρ is the geometric distance, $\lambda_N = c/(f_1 + f_2)$ and $\lambda_W = c/(f_1 - f_2)$ denote the narrow- and wide-lane wavelengths respectively, N_{L_1} and N_{L_2} denote the phase ambiguity for respective wavelengths, ω is the phase windup effect, and δI denotes the ionospheric residual

$$\begin{aligned}\delta I =& \frac{7527 c}{f_1^2 - f_2^2}\left(\frac{1}{f_1}\int B\cos(\vartheta)\, N_e\, ds_1 - \frac{1}{f_2}\int B\cos(\vartheta)\, N_e\, ds_2\right) \\ &+ \frac{40.311}{f_1^2 - f_2^2}\left(\int N_e\, ds_1 - \int N_e\, ds_2\right) \\ &+ \int \left(1 + 10^6 N\right)\, ds_\infty - \left(\frac{f_1^2}{f_1^2 - f_2^2}\int \left(1 + 10^6 N\right)\, ds_1 - \frac{f_2^2}{f_1^2 - f_2^2}\int \left(1 + 10^6 N\right)\, ds_2\right),\end{aligned} \tag{4.1.12}$$

where the 1st term is induced by Earth's magnetic field $\mathbf{B}$, the 2nd term stems from the fact that the ray-bending is a function of frequency, and the 3rd term is due to ray-bending (Hoque and Jakowski, 2007; Kashcheyev et al., 2012; Zus et al., 2017a,b). The contribution of δI to the total ionospheric effect is at the level of 0.1 %.

[3] It is:
$[f_1 \quad f_2]^\top = [1.57542 \quad 1.22760]^\top$ GHz for GPS,
$[f_1 \quad f_2]^\top = [8.4 \quad 2.3]^\top$ GHz for VLBI, and
$[f_1 \quad f_2]^\top = [2.03625 \quad 0.40125]^\top$ GHz for DORIS.

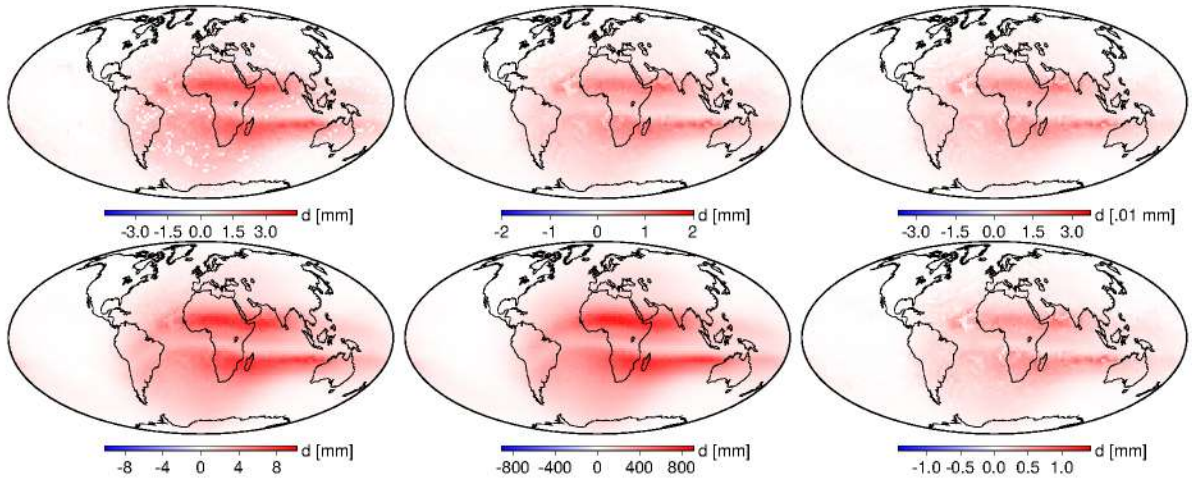


Figure 4.1.13: The differences $\int(1+10^{-6}N)\,ds_i - \int(1+10^{-6}N)\,ds_\infty$ for the most commonly used frequencies in GNSS (left), DORIS (middle), and VLBI (right) for $\varepsilon = 3°$ and $\alpha = 0°$, 2012/04/15 12:00. The frequencies the results refer to are 1.57542, 1.22760, 2.03625, 0.40125, 8.4, 2.3 GHz. Note while the spatial pattern remains, the colorbar is scaled as a function of frequency.

For the investigations conducted herein, the refraction induced by the neutral atmosphere was generated based on the model levels of ERA5, and the refraction induced by the electron density in the ionosphere and plasmatosphere by International Reference Ionosphere 2016 (IRI-2016[4]) (Bilitza et al., 2017). Information regarding the magnetic field vector (Earth's magnetic induction) was retrieved from the spherical harmonic coefficients of the International Geomagnetic Reference Field 12 (IGRF-12[5]) (Thébault et al., 2015).

The difference between the atmospheric delay (sum of the optical path length and the delay along the path) under the assumption that the signal did or did not propagate through the ionosphere, is given by

$$\int(1+10^{-6}N)\,ds_i - \int(1+10^{-6}N)\,ds_\infty, \tag{4.1.13}$$

and is illustrated in Fig. 4.1.13. For the S-/X-band VLBI system, the impact of the ionosphere is barely detectable on the atmospheric delays. On the other hand, the ionosphere-induced ray-bending is not negligible for GNSS and DORIS (UHF_1 at 0.401 25 GHz and UHF_2 at 2.036 25 GHz), that operate at lower frequencies. Galileo's C-band (5.020 GHz), as well as the less commonly used VLBI frequencies K- (24 GHz), K_a- (32 GHz), Q- (43 GHz), and W-band (86 GHz) are not affected whatsoever. Within the radio band, the lower the frequency the larger the ray-bending. Of course, in addition to frequency, the magnitude of the perturbation introduced by the ionosphere varies with time (space weather), location, and ray-direction.

The direct calibration of plasma effects from Earth's ionosphere and the solar plasma on the microwave observations, with methods such as the ionosphere-free linear combination (4.1.11) or even with acceptable modelling of higher-order ionospheric effects does not treat the atmospheric delay perturbations.

[4] http://irimodel.org/IRI-2016/
[5] https://www.ngdc.noaa.gov/IAGA/vmod/igrf12coeffs.txt

4.2 Estimation of mapping functions and gradients

4.2.1 Previous mapping function developments

To describe the elevation angle dependence of the atmospheric delay a signal suffers at an oblique direction on the delay at the zenith, the mapping function concept was devised

$$d(\varepsilon) = mf(\varepsilon)d^z, \tag{4.2.1}$$

where ε is the vacuum elevation angle, mf is the mapping function, and d^z is the zenith total delay. Assuming a flat Earth ($R = \infty$) with an azimuthally symmetric ($\partial\rho/\partial\alpha = 0$) and evenly stratified ($\partial^2\rho/\partial h^2 = 0$) atmosphere, the mapping function reduces to $\csc(\varepsilon)$. Whilst this approximation yields relative errors not larger than 1 cm for $\varepsilon > 36°(17°)$ for the microwave hydrostatic (non-hydrostatic) slant delay and for $\varepsilon > 37°(6°)$ for the optical hydrostatic (non-hydrostatic) slant delay, it is inadequate at lower ε for it does not consider the curvature of the Earth nor the spatio-temporal changes of atmospheric density ρ. An asymptotic expansion of $\sin(\varepsilon)$ leading to a rational fraction approximation (Marini, 1972; Marini and Murray, 1973) is a more precise ansatz, provided the related coefficients stem from a reliable source (fits to ray-traced delays from NWMs, radiosondes or climatology)

$$mf = \cfrac{1}{\sin(\varepsilon) + \cfrac{a}{\sin(\varepsilon) + \cfrac{b}{\sin(\varepsilon) + \cdots}}} \tag{4.2.2}$$

Normalized to yield unity at zenith (Herring, 1992) and truncated at the c coefficient, the mapping function ansatz reads

$$mf = \cfrac{1 + \cfrac{a}{1 + \cfrac{b}{1 + c}}}{\sin(\varepsilon) + \cfrac{a}{\sin(\varepsilon) + \cfrac{b}{\sin(\varepsilon) + c}}}. \tag{4.2.3}$$

Geodetic literature on mapping function developments for microwave techniques (mainly GNSS and VLBI) surpasses in both volume and depth the corresponding literature dedicated to optical techniques (mainly SLR). This is justified by the fact that the choice of mapping functions for SLR is less crucial compared to GNSS or VLBI owing to the fact that satellites are usually not tracked at $\varepsilon < 10°$ (because of eye-safety concerns)[6]. Ranging at low ε is vital for the decorrelation of range bias errors and station height errors. Nevertheless, on account of not estimating residual atmospheric delays - rather than range biases, parameters without physical meaning - any mf inaccuracies contaminate the rest of the estimated parameters. Regarding microwave techniques, unlike low-elevation GNSS observations, the VLBI observations are impervious to the effects of multi-path scattering and phase center variations. Thus the adoption of an elevation dependent weighting strategy as well as an elevation mask angle (e.g., 7°) is not as critical. However, to avoid ground-noise pickup elevation dependent weighting as well as elevation mask should be

[6] An exception to this is Tidbinbilla, Australia for $0° < \alpha < 36°$ during 1995/07-1995/09

considered (e.g., Tahmoush and Rogers, 2000). This allows VLBI analysis to benefit from fully utilizing low-elevation observations. However, as ε decrease, σ_{mf} rapidly increase, degrading the positioning precision. Therefore, it is imperative that accurate mf are applied and that their uncertainties are described stochastically in the adjustment. This explains the fact that the major atmospheric correction developments were first established in VLBI.

In geodetic data analysis, unlike the partial derivatives of the observed group delay $\partial\tau/\partial h = \sin(\varepsilon)$ and $\partial\tau/\partial\tau_{clk} = 1$ that are known, $\partial\tau/\partial d^z = mf$ is subject to errors that inescapably propagate primarily in the height and clock function estimates. The mf is inversely proportional to the estimated residual zenith delay. Niell et al. (2001) suggested that $\sigma_{d(7°)} = 3\sigma_h$, whereas Böhm (2004) refined the rule of thumb to $\sigma_{d(5°)} = 5\sigma_h$.

Due to the curvature of the Earth and the smaller scale height of the non-hydrostatic atmospheric component (≈ 1.7 km) with respect to the hydrostatic (≈ 6.5 km), it is $mf_{nh} > mf_h$. Nevertheless, when $\varepsilon \to 0°$ the ray-bending effect prevails occasionally yielding $mf_h > mf_{nh}$. The quality of mf_{nh} is more crucial with decreasing $|\varphi|$, due to very small moisture content of air at polar regions.

Due to Earth's rotation and poleward density gradients, the atmosphere is thicker at the equator so, given any ε mapping functions increase with decreasing $|\varphi|$. The atmosphere gets flatter ($mf \to \csc(\varepsilon)$) with increasing altitude, hence the mf increases (Fig. 4.2.1).

Hitherto one of the most accurate and definitely the most popular mf are the VMF1 (Boehm et al., 2006). Their reliability stems from a precise formalism and an underlying NWM of very high quality (ECMWF's operational analysis). VMF1 are realized by time series of 6-hourly a_h and a_{nh} on a global grid as well as at fundamental geodetic sites. Due to the fact that VMF1 are tuned for $\varepsilon = 30°$, large relative errors with respect to ray-traced delays appear around $\varepsilon = (5, 10)°$, which is devastating because e.g., in VLBI data analysis observations at low elevations improve the decorrelation of the estimated position height from the estimates of the residual zenith delay and the clock parameters, hence enhancing the precision of these parameters as well as the overall stability of the adjustment.

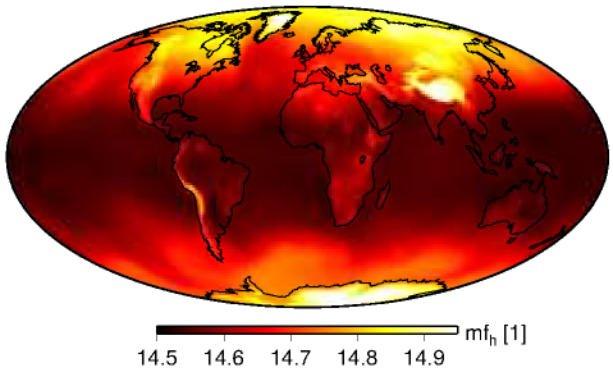


Figure 4.2.1: The mf_h at 2017/01/01 00 UTC, employing ERA5.

An attempt to depart from the azimuthal symmetry resulted in VMF2 (Böhm et al., 2005) where the mapping function depends additionally on the azimuth. It was determined not based on the refractivity profiles aloft the station of interest alone, but employed the refractivity profiles of the surrounding nodes. 3D ray-tracing was performed with a granularity of 30° in the refractivity fields of ECMWF's operational analysis. Such an approach renders the estimation of gradients unnecessary and more accurately represents the azimuthal variability, but was abandoned due to high computational burden in spite of its superior performance.

Another effort to model the azimuthal anisotropy of the atmosphere, labeled the adaptive mapping functions (Gegout et al., 2011), involved a Fourier expansion of coefficients of the continued fraction form. Truncating the continued fraction at the 3rd term and the azimuthal harmonic series at the 4th (27 coefficients) yields relative errors at the 1 mm-level under non-severe meteorological situations. A noteworthy feature of this approach is the truncation changes to adapt to perturbed weather events.

As far as SLR is concerned, the FCUL (mapping Function Commonly Used for Laser data) family of mf (Mendes et al., 2002) is the most popular, as of now. They feature a total isotropic mf, because the contribution of the orientation polarization of water vapour molecules to atmospheric refraction at optical frequencies is inconsiderable. They were determined based on ray-tracing in radiosonde refractivity profiles of fairly limited spatio-temporal range, the vertical discretization of which was conducted employing the observed quantities, at 22 elevations and are tuned for $\lambda = 532\,\text{nm}$. They claim to be valid for $355\,\text{nm} < \lambda < 1064\,\text{nm}$ and as all mf mentioned herein apply for $\varepsilon > 3°$. FCULa depends on latitude, height and temperature, and FCULb does not depend on the latter as it adopts the formalism suggested by Niell (1996).

A comprehensive review of mapping functions can be found in Mendes (1999) and Nilsson et al. (2013).

4.2.2 Gradient component models

In the data analysis of space geodetic techniques utilizing microwave radiation, the azimuthally symmetric delay component is separated into hydrostatic and non-hydrostatic, and are mapped onto the zenith employing different elevation-only-dependent mapping functions (Sec. 4.2.1).

To account for the disregarded horizontal heterogeneities of the tropospheric delay, the most popular approach as of now, suggests a planar troposphere with the zenith delay experiencing only linear lateral changes, which in essence condenses to the estimation of linear horizontal delay gradient components in two orthogonal directions, namely the North-South (G_{NS}) and the East-West (G_{EW}) components. Thus, the atmospheric delay can be expanded to the following expression

$$d_{atm}(\varepsilon,\alpha) = mf_h\, d_h^z + mf_{nh}\, d_{nh}^z + mf_g(G_{NS}\cos(\alpha) + G_{EW}\sin(\alpha)), \tag{4.2.4}$$

where the last addend is the asymmetric delay, and mf_g is the gradient mapping function that will be discussed in Sec. 4.2.3. This approach assumes the index of refraction varies linearly towards supplementary azimuth angles ($\partial^2 n/\partial x^2 = 0$). In substance, the index of refraction field surrounding a given site is considered as a tilted plane. This assumption holds to a great extend in normal atmospheric conditions.

Abnormal weather situations involving delay gradients in isolated directions caused by e.g., topography-induced atmospheric gravity waves, render the planar assumption prone to failure (Fig. 4.2.2). To account for non-linear spatial variations in refractivity the aforementioned approach must to be adapted appropriately. To date, there are a fairly limited number of studies that has addressed this issue. Exemplarily, Landskron et al. (2017) and Balidakis et al. (2018c) have explored employing higher order terms in the asymmetric delay expansion

$$d_{atm}^{asm}(\varepsilon,\alpha) = mf_g(\varepsilon)\begin{cases} G_{NS}\cos(\alpha) + G_{EW}\sin(\alpha) + G_{NN}\cos^2(\alpha) \\ \qquad + G_{NE}\cos(\alpha)\sin(\alpha) + G_{EE}\sin^2(\alpha) \\ \sum_{j=1}^{N} G_{nj}\cos(j\alpha) + G_{ej}\sin(j\alpha), \end{cases}, \tag{4.2.5}$$

respectively. Masoumi et al. (2017) suggested a directional model that reads

$$d_{atm}^{asm}(\varepsilon,\alpha) = mf_g(\varepsilon)\sum_{j=1}^{N} G_j\, m_{pw}^j(\alpha), \tag{4.2.6}$$

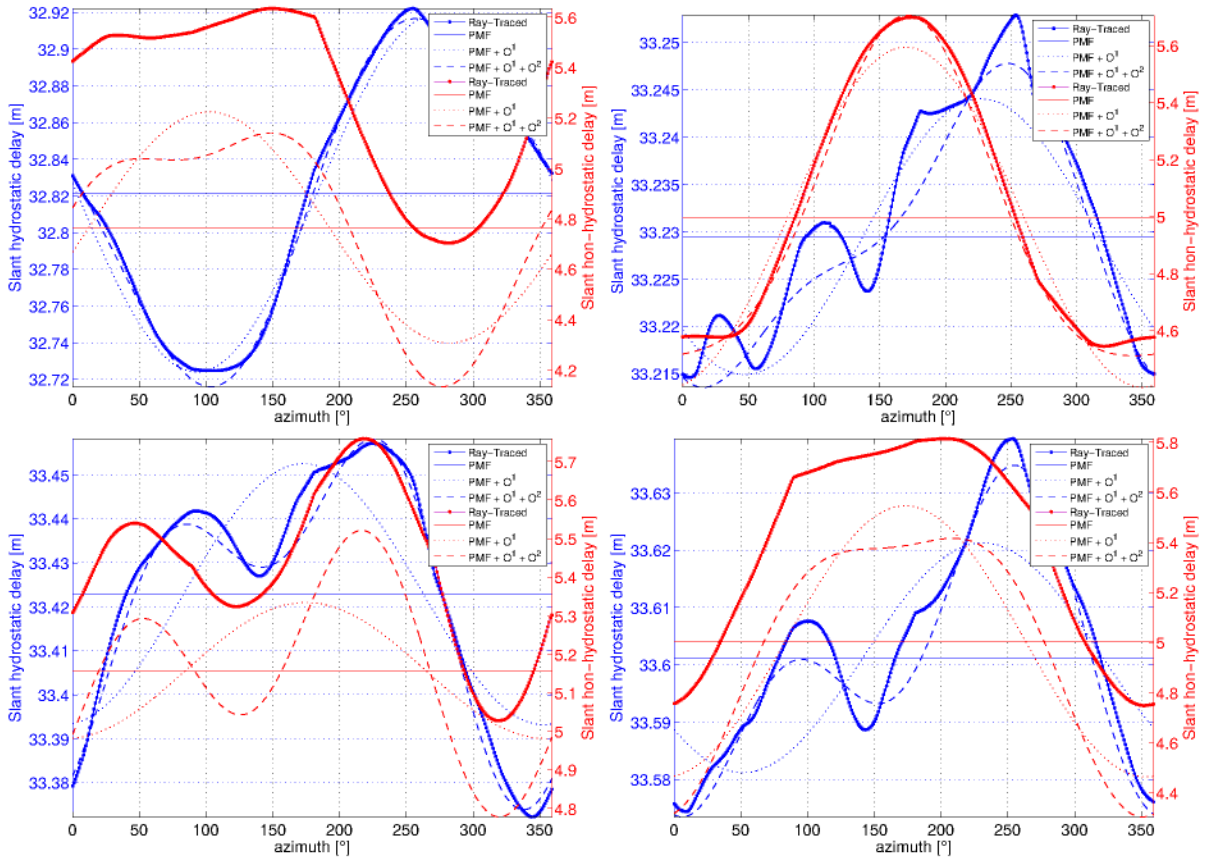


Figure 4.2.2: Cases of strong asymmetries in Tsukuba, at 1996-07-10 18 UTC (upper left), 2000-08-12 00 UTC (upper right), 2003-08-15 06 UTC (lower left), and 2003-08-16 00 UTC (lower right). Slant hydrostatic (blue) and non-hydrostatic (red) delays at $\varepsilon = 3^\circ$ by different modelling approaches: mapping functions (solid line), mapping functions and linear horizontal gradients (dotted line), mapping functions and high-order gradients (dashed line), and ray-traced delays (asterisks) calculated employing ERA Interim.

where the piecewise function $m_{pw}^{j}(\alpha)$ that relates the neighbouring nodes is given by

$$m_{pw}^{j}(\alpha) = \begin{cases} \dfrac{\alpha - (2\pi - \delta\alpha)}{\delta\alpha}, & \text{for } j = 1 \wedge \alpha > 2\pi - \delta\alpha \\ \dfrac{\delta\alpha - \alpha}{\delta\alpha}, & \text{for } j = 1 \wedge \alpha < \delta\alpha \\ \dfrac{\alpha - (j-2)\delta\alpha}{\delta\alpha}, & \text{for } 2 \leq j \leq N \wedge (j-2)\delta\alpha < \alpha \leq (j-1)\delta\alpha \\ \dfrac{j\delta\alpha - \alpha}{j\delta\alpha}, & \text{for } 2 \leq j \leq N \wedge (j-1)\delta\alpha < \alpha \leq j\delta\alpha \\ 0, & \text{otherwise} \end{cases}, \tag{4.2.7}$$

where $\delta\alpha = 2\pi/N$ is the azimuthal granularity of the estimated gradients.

Regarding the geodetic analysis, adopting gradient models more elaborate than the planar in the least-squares inversion scheme assists only in cases of acute nonlinearities, especially in the estimation of the height coordinate component and the residual zenith atmospheric delay, when low-elevation observations are considered.

In the absence of spatial nonlinearities in the refractivity field surrounding a geodetic site, the estimation of additional gradient components causes an unnecessary increase in the computational overhead, and slightly degrades the solution as there is high correlation between the related columns of the design matrix. Hence more sophisticated gradient parametrization models should not be applied invariably.

In this study, the gradient ansatz adopted is the first case of (4.2.5).

4.2.3 Gradient mapping functions

To model the azimuthal asymmetry under the assumption of a "tilted" atmosphere, the formalism proposed by Gardner (1976) is followed. To model the asymmetric delay d_{atm}^{asm} dependence on ε, two approaches have prevailed

$$d_{atm}^{asm}(\varepsilon,\alpha) = (G_{NS}\cos(\alpha) + G_{EW}\sin(\alpha)) \begin{cases} mf_{nh}(\varepsilon)\cot(\varepsilon), & \text{BS98} \\ \dfrac{1}{\sin(\varepsilon)\tan(\varepsilon)+C}, & \text{CH97} \end{cases}. \tag{4.2.8}$$

A comprehensive description of which can be found in Davis et al. (1993), MacMillan (1995a), and Bar-Sever et al. (1998) for the former, and Chen and Herring (1997) for the latter. The tilting of the mapping function is another corollary from the linear horizontal gradient model. The tilt amounts approximately to $\sqrt{G_{NS}^2 + G_{EW}^2}/d_h^z$, and its axis of symmetry is rotated by $\tan^{-1}(G_{EW}/G_{NS})$.

At this point the importance of mf_g ansatzes in the space geodetic data analysis is stressed for not only it does affect the gradient components (e.g., G_{NS} and G_{EW}) participating in the calculation of the partial derivatives thereof, but the "assembled" asymmetric delays (4.2.8) as well. This is of great importance in the context of comparing gradients from different software packages, as well as from different space geodetic techniques.

To demonstrate this issue, ray-tracing was performed on a spatially smooth meteorological data set obtained from averaging over January 2017, for all surface nodes of the underlying orography with a granularity of 0.5°. Horizontal gradients were estimated from a sufficiently dense cloud of virtual sources (240), employing the BS98 and CH97. The spatial average of the WRMS of the post-fit residuals per ε is shown in Fig. 4.2.3. It is markedly clear that CH97 outperforms BS98, even when the O^1 terms alone are retained. For $\varepsilon = \begin{bmatrix}3 & 5 & 7 & 10 & 15 & 20\end{bmatrix}^\circ$ the precision improvement is $\begin{bmatrix}27.6 & 19.4 & 36.0 & 38.3 & 33.9 & 31.9 & 30.7\end{bmatrix}$ % and $\begin{bmatrix}54.2 & 70.4 & 64.4 & 58.7 & 47.8 & 43.8 & 41.1\end{bmatrix}$ % when 2nd order terms are considered. The fact that BS98 approaches ∞ for $\varepsilon \to 0$, yielding un-

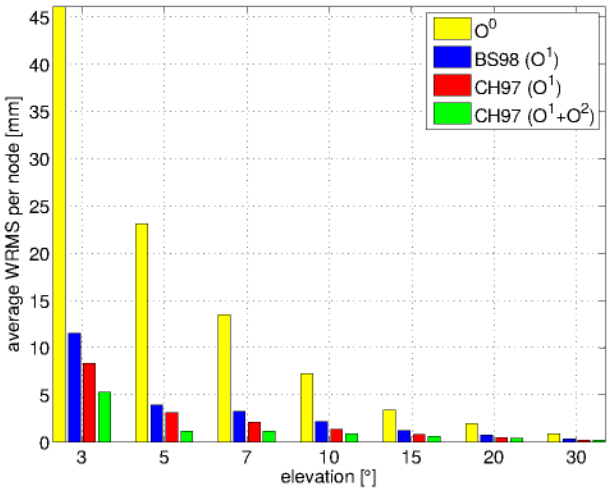


Figure 4.2.3: Spatial average of the WRMS of the post-fit residuals (azimuthal fit to ray-traced delays) per ε for the two gradient mapping functions under consideration. O^0 indicates no gradients, O^1 indicates a linear gradient model, whereas O^2 indicates 2nd order components as well. Evidently CH97 outperforms BS98, and retaining 2nd order components is advantageous for $\varepsilon < 10°$.

reliable results at low elevations, attests to that. Fig. 4.2.4 illustrates the spatial behaviour of the WRMS at various ε for BS98 and CH97 gradient mapping function models.

Mapping asymmetric delays erroneously, i.e., employing a gradient mapping function different to the one used for the gradient component estimation, causes non-negligible errors. For instance, the WRMS of the differences between assembled asymmetric delays with BS98 and CH97 over all nodes on Earth's surface with a granularity of 0.5°, for $\varepsilon = \begin{bmatrix}3 & 5 & 7 & 10 & 15 & 20\end{bmatrix}^\circ$ is $\begin{bmatrix}17.3 & 6.3 & 5.0 & 3.1 & 1.6 & 0.9\end{bmatrix}$ mm for $\alpha = 0^\circ$, and $\begin{bmatrix}11.2 & 5.2 & 3.4 & 1.9 & 0.9 & 0.5\end{bmatrix}$ mm for $\alpha = 90^\circ$, respectively. Retaining only the CH97 results, the differences between the assembled asymmetric delays and the ones composed employing the product of the symmetric mapping functions with $\cot(\varepsilon)$ are illustrated in Tab. 4.2.1. Note that while the error appears to be random in the East-West direction, it manifests into a bias in the North-South direction.

To determine whether employing BS98 or CH97 yields systematic effects in the estimated gradient components, ray-tracing was carried out in ERA5 refractivity tensors composed of monthly means of daily means spanning the period 2000.0–2018.0. All parameters that GFZ-PT (cf. Sec. 4.3) features were estimated. Figure 4.2.5 illustrates the bias and the S_a amplitude of the differences (BS98 minus CH97). The asymmetric delay predicted by CH97 will be larger (in an absolute sense) compared to the BS98 because part of the signal has already been described by the mf_{nh}. For instance, in the Northern hemisphere G_{NS} is negative on average; Fig. 4.2.5 demonstrates that the CH97 is "more negative" in the Northern hemisphere, and "more positive" in the Southern hemisphere. The bias in G_{NS} manifests in an artificial antipoleward displacement of the North-South coordinate component thus introducing a spurious scale offset to the underlying reference frame. An offset in T_Z is also to be expected because of the uneven station distribution between North and South hemisphere.

The hydrostatic and non-hydrostatic delay as a function of azimuth are not always in phase (cf. Fig. 4.2.2 upper left). A 2nd order gradient model is a more appropriate ansatz compared to the tilted plane formula. Retaining 2nd order terms in the gradient expansion yields a precision improvement of $\begin{bmatrix}36.7 & 63.2 & 44.3 & 33.1 & 21.1 & 17.5 & 15.1\end{bmatrix}$ mm for $\varepsilon = \begin{bmatrix}3 & 5 & 7 & 10 & 15 & 20\end{bmatrix}^\circ$.

Table 4.2.1: The impact of employing inconsistent gradient mapping function and gradient components. The graphs present the discrepancies between assembled asymmetric delays employing CH97, and BS98 with the hydrostatic (left) and non-hydrostatic mapping functions (right), at 3°, 5°, 7° and 10°, respectively.

[mm]	$mf_h \cot(\varepsilon)$								$mf_{nh} \cot(\varepsilon)$							
	$\alpha = 0^\circ$				$\alpha = 90^\circ$				$\alpha = 0^\circ$				$\alpha = 90^\circ$			
mean	-3.1	-0.6	-0.2	-0.1	-0.0	-0.0	-0.0	-0.0	-4.0	-0.8	-0.3	-0.1	-0.0	-0.0	-0.0	-0.0
min	-145.7	-30.0	-9.2	-2.4	-176.8	-36.4	-11.1	-2.9	-194.5	-40.3	-12.4	-3.3	-239.7	-49.5	-15.2	-4.0
max	183.8	37.9	11.6	3.0	202.1	41.6	12.7	3.3	240.5	49.9	15.4	4.1	260.4	54.1	16.7	4.4

In this study, the gradient mapping function ansatz adopted is the one proposed by Chen and Herring (1997). Nevertheless, the scale height exerts strong control on the parameter C in (4.2.8) thus rendering the latter dependent upon space and time, as well as variable between the hydrostatic and non-hydrostatic delay component. To this end, for the first time, C was estimated from the analysis of ray-traced delays in a consistent adjustment together with the gradient vector components, separately for the hydrostatic and non-hydrostatic delay components, as well as for the total delay. Based on 38 years of ERA Interim, Fig. 4.2.6 illustrates the estimated C_i and the uncertainties thereof. Due to the fact that the estimation of C_i is highly unstable in the absence of atmospheric asymmetries and that C_i does not display notable seasonal variability — the relative power spectral density is in most cases well below 1 % — the

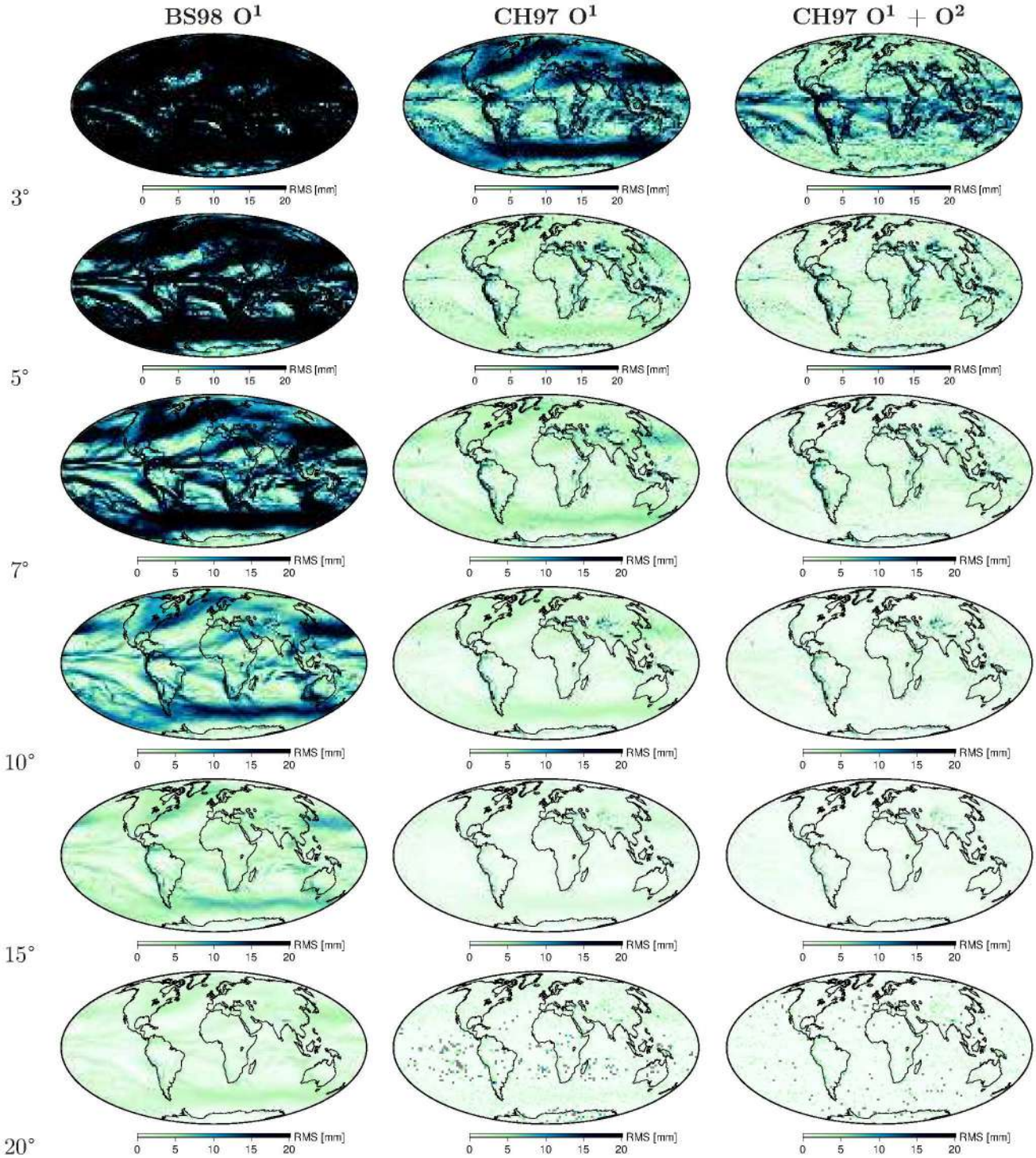


Figure 4.2.4: The WRMS of the post-fit residuals of gradient estimation (azimuthal fit to ray-traced delays) for the BS98 O^1 (1st column), CH97 O^1 (2nd column), and CH97 O^1+O^2 (3rd column). The rows correspond to elevation angles of 3, 5, 7, 10, 15, and 20 degrees, respectively.

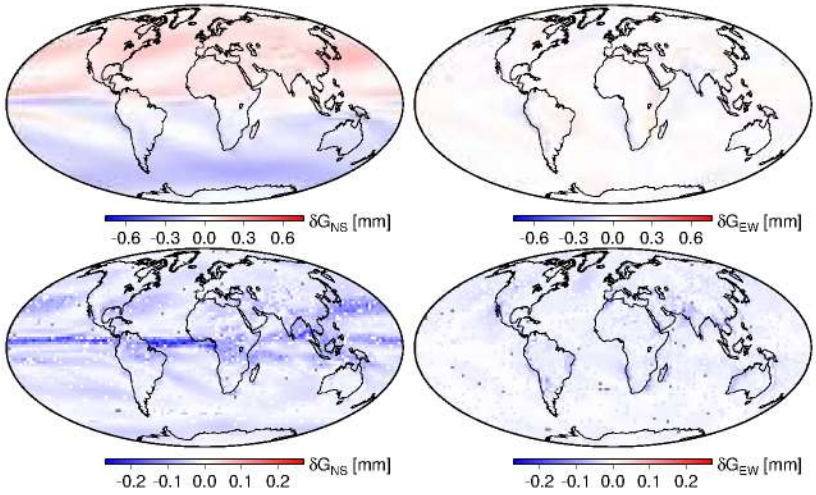


Figure 4.2.5: Differences in the average (upper row) and S_a amplitude (lower row) between gradient components (G_{NS} left and G_{EW} right) estimated employing the BS98 or CH97 mf_g, from ERA5 refractivity tensors.

hydrostatic C_h, the non-hydrostatic C_{nh}, and the total C_t were estimated as "global parameters" over time by employing the Helmert-Wolf blocking method. Prior to the least-squares adjustment observations with no atmospheric asymmetry were filtered out for they are irrelevant to the parameter of interest. To estimate the C_i as a global parameter over time and space, the area each grid node represents was factored in as a weight. Table 4.2.2 displays the C_i coefficients over land, ocean, and both. C_i was also estimated epoch-wise by imposing inequality constraints around the spatiotemporal average and a Tikhonov regularization.

Table 4.2.2: Gradient mapping function coefficients estimated from ray-traced delays in ERA Interim.

	C_h [1]	C_{nh} [1]	C_t [1]
land	0.00304	0.00081	0.00302
ocean	0.00314	0.00072	0.00310
land+ocean	0.00309	0.00075	0.00306

Nevertheless, a more faithful representation of the physical effects, that is a custom C_h and C_{nh} in lieu of a constant 0.0032 yields a precision improvement of maximum 3 mm for rays at 3° (Balidakis et al., 2018c). Due to the fact that such an improvement is overshadowed by the accuracy of the NWMs, and that comparing gradient components estimated as such becomes very complicated, for the remainder of this work, a constant C is used.

Recapitulating, to properly account for the tropospheric delay of observations near the horizon, the choice of mapping function is crucial. In this section, it has been demonstrated that:

- ☐ the gradients components estimated employing different gradient mapping functions are not comparable whatsoever,
- ☐ the asymmetric delays assembled employing different gradient mapping functions (same as the one employed for the estimation of the components thereof) can deviate largely at low elevation angles,
- ☐ the WRMS of the post-fit residuals employing CH97 are always smaller that those employing BS98 gradient mapping functions, that indicates the supremacy of the former,

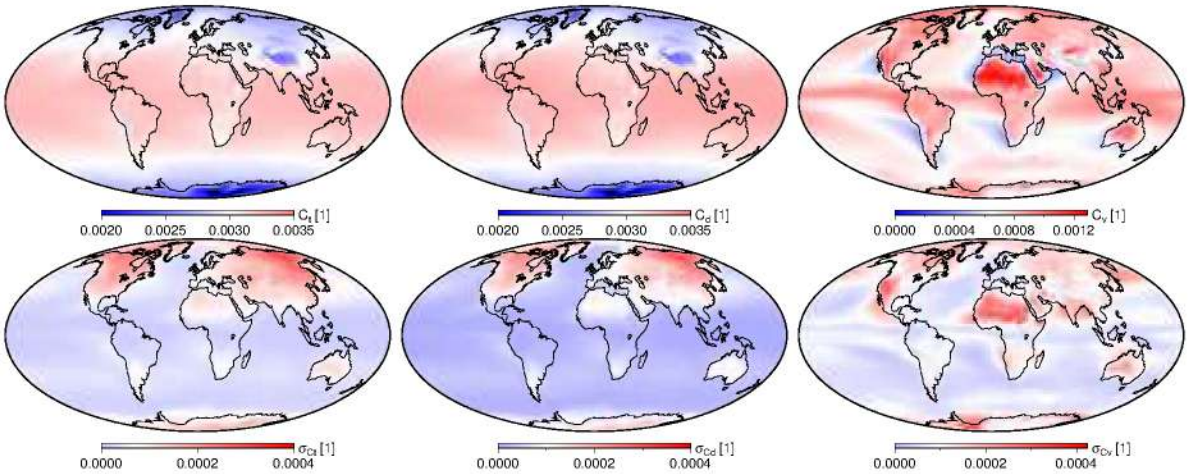


Figure 4.2.6: Gradient mapping function coefficients employing the CH97 ansatz truncated to the 1st order. The 38-year average fields of the total C_t, hydrostatic C_d and non-hydrostatic C_v gradient mapping function coefficient are illustrated in the upper left, middle, and right panel, respectively, as well as the dispersion thereof: σ_{C_t}, σ_{C_d}, and σ_{C_v} (lower row). The spatiotemporal mean is indicated by white.

and

- the choice of the gradient mapping function coefficient C (estimated or fixed value) should the CH97 ansatz be adopted, does not impact on the asymmetric delays appreciably.

4.2.4 Potsdam mapping functions

The development of the Potsdam mapping functions (hereinafter PMF) in the framework of this thesis is motivated from a number of shortcomings identified in existing mapping functions. Some of these are outlined in the following:

- Employing a constant radius of curvature in lieu of an Eulerian or even Gaussian (cf. Sec. 4.1.1) introduces a spurious scaling of all ranges as a function of $\sin(2\varphi - 45°)$, thus introducing latitude-dependent height offsets as large as 5 mm at the equator and the poles.
- Calculating the a_h and a_{nh} coefficients alone does not yield optimal mapping factors in terms of precision. The a_h and a_{nh} estimated together with the related b and c coefficients following the PMF concept are more precise than those calculated employing the VMF3 concept.
- VMF1/VMF3 products are based on ray-tracing on refractivity fields at 37 pressure levels that are poorly resolved (1°), whereas PMF's underlying model has a better horizontal (0.25°) and vertical (137 model levels) resolution.
- The orbital altitude dependence is completely ignored since all VMF1/VMF3 products are tailored for VLBI. Employing such mapping functions in DORIS data analysis introduce a constant height bias.
- The additional ray-bending induced by the ionosphere is not accounted in any of the previous considerations.
- No NWM-driven mapping functions are available for optical frequencies, as of this writing.

The PMF were originally conceived by Florian Zus.

PMF is driven by atmospheric delays calculated from a rigorous ray-tracing algorithm (Zus et al., 2012, 2014) based on the Euler-Lagrange equation derived from Fermat's principle (cf. Sec. 3.2). To enhance the computational efficiency of the algorithm, the "no out-of-plane bending" assumption is adopted implying that the direction of the refractivity gradient is always towards the center of the osculating sphere ($\partial n\left(\mathbf{x}\right)/\partial\varphi = \partial n\left(\mathbf{x}\right)/\partial\lambda = \mathbf{0}$). This simplification induces relative errors only at very low elevations ($\varepsilon < 7°$), that are below the accuracy level of state-of-the-art meso-β NWM fields (e.g., 1 cm at 3°). Such a setup allows processing 10^5 rays per second in an open multiprocessing environment (omp) employing an off-the-shelf PC. Since the time complexity decreases almost linearly with the increasing number of threads, much higher figures are to be expected should DNS be run in a cluster.

For the construction of the time-dependent atmospheric density field, ERA Interim, ERA5, and ECMWF's operational model have been utilized depending on the task in need of addressing; ERA Interim and ERA5 have been utilized to generate PMFs for the VLBI and SLR reprocessing (starting from the 80'), whereas ECMWF's operational model is utilized in the framework of the processing for the IVS combination.

The slant hydrostatic and non-hydrostatic delays between emitter (e.g., quasar, satellite, or DORIS beacon) and receiver at a given epoch, at a given direction (ε, α) are computed separately by numerical integration of the frequency-dependent refractivity field along the optical path that has been determined via ray-tracing. Since the impact of the numerical integration method adopted dissipates with more finely sampled rays, Simpson's rule is adopted instead of the trapezoidal rule, the Gauss-Lobatto quadrature, or the 1D Gauss-Legendre quadrature — the 2D Gauss-Legendre quadrature is adopted for the evaluation of loading displacements (cf.(5.1.3)).

The fitting ansatz selected for the PMF reads

$$\begin{aligned} d_{atm} = {} & mf_h\, d_h^z + mf_{nh}\, d_{nh}^z \\ & + mf_g\big(\, G_{NS}\cos(\alpha) + G_{EW}\sin(\alpha) \\ & + G_{NN}\cos^2(\alpha) + G_{NE}\sin(\alpha)\cos(\alpha) + G_{EE}\sin^2(\alpha)\big), \end{aligned} \tag{4.2.9}$$

where d_{atm} denotes the ray-traced delays in the NWM. The factors mf_i and mf_g describe the dependence of the symmetric and the asymmetric delays (Herring, 1992; Chen and Herring, 1997) on ε, respectively. The continued fraction form has been adopted (Marini, 1972) expanded to third and first order for $\sin(\varepsilon)$ and $\sin(\varepsilon)\tan(\varepsilon)$, respectively

$$mf_i = \begin{cases} \cfrac{1 + \cfrac{a_i}{1 + \cfrac{b_i}{1 + c_i}}}{\sin(\varepsilon) + \cfrac{a_i}{\sin(\varepsilon) + \cfrac{b_i}{\sin(\varepsilon) + c_i}}}, & \text{for } i = h \vee nh \\ \cfrac{1}{\sin(\varepsilon)\tan(\varepsilon) + C}, & \text{for } i = g \end{cases}, \tag{4.2.10}$$

Further expansions, hence more coefficients marginally improve the precision (below 1 mm at $\varepsilon = 3°$) at a number of extraordinary cases. Nevertheless, the additionally estimated coefficients e.g., d_i, e_i, etc. fail the tests of statistical significance (e.g., 0.001 %).

To ensure a well-posed adjustment problem, the directions are carefully chosen. To avoid multicollinearity and to expedite the ray-tracing process, rays should not have a granularity as low as $\delta\varepsilon = \delta\alpha = 1°$, especially for meso-β NWMs. To allow for the description of features such as non-linearities in the asymmetric delays, adopting $\delta\alpha = 15°$ suffices. The optimal ε vector is such that $|(mf_j - mf_i)/(\varepsilon_j - \varepsilon_i)|$, is constantly decreasing with increasing ε. The number of azimuth points with constant elevation can also be reduced with increasing elevation angle in a fashion similar to the reduced Gaussian grid concept adopted for the geophysical loading simulations (cf. Sec. 5.1.3). Nevertheless, $\varepsilon = \begin{bmatrix} 3 & 5 & 7 & 10 & 15 & 20 & 30 & 50 & 70 & 90 \end{bmatrix}°$ has been found sufficient (e.g., Boehm and Schuh, 2004; Nilsson et al., 2017b).

For PMF, the mapping function coefficients a_i, b_i, and c_i are estimated separately for the hydrostatic and the non-hydrostatic delay component based on ray-traced delays on the profile aloft the site of interest. For previous realizations (e.g., VMF1/3) only a_i is a discrete function of time and is not estimated rather than calculated following

$$a_i = \frac{1 - mf_i(\varepsilon)\sin(\varepsilon)}{\dfrac{mf_i(\varepsilon)}{\sin(\varepsilon) + \dfrac{b}{\sin(\varepsilon)+c}} - \dfrac{1}{1 + \dfrac{b}{1+c}}}, \tag{4.2.11}$$

for $\varepsilon = 3°$. The observation equations consist of the first case of (4.2.10) where $mf_i = d_i(\varepsilon)/d_i^z$. To describe the NWM-related uncertainties of low elevation atmospheric delays, a weighting scheme is applied (Zus et al., 2015b)

$$P_{ij} = \delta_{ij}\sin(\varepsilon_i)\sin(\varepsilon_j), \tag{4.2.12}$$

where δ_{ij} denotes Kronecker's delta. The design (Jacobian) matrix reads

$$J = \begin{bmatrix} \dfrac{\partial mf}{\partial a} & \dfrac{\partial mf}{\partial b} & \dfrac{\partial mf}{\partial c} \end{bmatrix}^\top, \tag{4.2.13}$$

where the partial derivatives read

$$\begin{aligned} \frac{\partial mf}{\partial a} &= \frac{1}{\left(1 + \frac{b}{1+c}\right) D} - \frac{N}{\left(\frac{b}{c+\sin(\varepsilon)} + \sin(\varepsilon)\right) D^2}, \\ \frac{\partial mf}{\partial b} &= \frac{aN}{(c + \sin(\varepsilon))\left(\frac{b}{c+\sin(\varepsilon)} + \sin(\varepsilon)\right)^2 D^2} - \frac{a}{(1+c)\left(1 + \frac{b}{1+c}\right)^2 D}, \text{and} \\ \frac{\partial mf}{\partial c} &= \frac{ab}{(1+c)^2\left(1 + \frac{b}{1+c}\right)^2 D} - \frac{abN}{(c + \sin(\varepsilon))^2\left(\sin(\varepsilon) + \frac{b}{c+\sin(\varepsilon)}\right)^2 D^2}, \end{aligned} \tag{4.2.14}$$

where N and D are the numerator and the denominator of (4.2.10), respectively. The non-linear least-squares adjustment converges to the sub-mm level within a couple of iterations. In most cases fitting non-hydrostatic mapping function coefficients requires more iterations.

A priori mapping function coefficients are obtained from relevant component of GFZ-PT (cf. Sec. 4.3). In most cases, a couple of iterations yield precision better than 1 mm at 3°. Should an identity matrix be adopted for the aforementioned least-squares adjustment in lieu of (4.2.12), in the presence of strong inversions there will be no convergence, even employing a damped least-

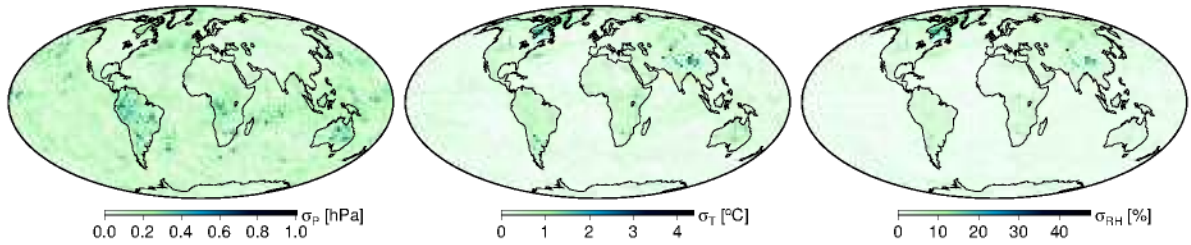


Figure 4.2.7: Uncertainties of pressure (left), temperature (middle), and relative humidity (right) from a 10-member ensemble of ERA5 data assimilations (2018/01/01 00:00).

squares estimator (Levenberg-Marquardt method). Such cases (usually on the non-hydrostatic component) are treated by imposing absolute constraints on the estimation of b_i and c_i, that is, introducing additional equations for these parameters with relatively large weights, what might be equivalent to fixing those parameters to the values obtained from GFZ-PT. Adopting (4.2.12) renders such an elaborate scheme inessential.

To estimate the gradients, (4.2.9) serve as the observation equations where mf_i and mf_g stem from ray-tracing in the refractivity profile. That is for the i component:

$$d_i(\varepsilon,\alpha) - mf_i d_i^z = d_i^{asm}(\varepsilon,\alpha), \tag{4.2.15}$$

where d_i^{asm} follows the first case of (4.2.5). Unlike the least-squares fitting of mapping functions' coefficients, gradient estimation is a linear problem hence no a priori values are necessary. A distinction between hydrostatic and non-hydrostatic gradients is not possible from space geodetic observations alone, a fact that would suggest estimating total gradient components instead of separated. Nevertheless, while such a strategy is computationally more efficient there are a number of cases (upper left of Fig. 4.2.2) where the asymmetric delays are not in phase thus giving rise to non-linear gradients with no physical meaning (resonances). If a sufficient number of observations is utilized (e.g., more than 12 per elevation) the estimating 2nd order gradients has no practical impact on the estimation of G_{NS} and G_{EW}. Moreover, this fitting benefits by applying (4.2.12) as well.

State-of-the-art NWMs such as ERA5 provide uncertainties of the meteorological fields involved in the process of calculating atmospheric delays with ray-tracing. For instance, Fig. 4.2.7 illustrates the uncertainties for pressure, temperature and relative humidity from a 10-member ensemble of ERA5 data assimilations resolved at 63 km. Figure 4.2.8 displays the average formal error of the lowermost level of the meteorological tensors necessary to calculate atmospheric refraction effects. Note the systematically larger uncertainty of humidity in the tropics, as well as the larger uncertainty of pressure and temperature in regions with fairly sparce data e.g., Antarctica and Central Africa. Nevertheless, due to the fact that as of 2018 these estimates are too optimistic and that meteorological quantities at neighbouring voxels are heavily correlated, no claims for accuracy can be made employing the simulated NWM data alone. Notwithstanding these limitation, the fact that the scatter of the post fit residuals at 3° is below 1 mm renders PMF very precise.

Estimating b, c, C, G_{NN}, G_{NE} and G_{EE} causes a negligible increase in the computational overhead but results in a closer fit to the ray-traced delays (cf. Fig. 4.2.2). Figure 4.2.9 displays the PMF products for the VLBI setup for a single epoch.

The coefficients estimated above are suitable only for the space geodetic technique for which the ray-tracing was performed. Since this thesis deals with all four space geodetic techniques, dedicated ray-tracing was carried out and therefore separate PMFs were estimated. In the

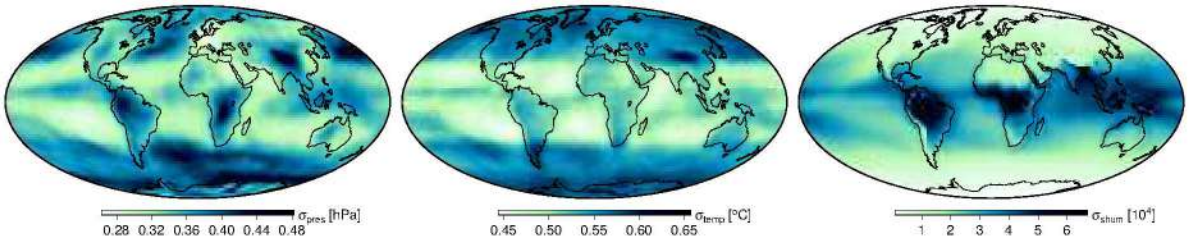


Figure 4.2.8: Average formal error of basic surface fields of ECMWF's operational analysis. The graphs show the fields of pressure (left), temperature (middle), and specific humidity (right).

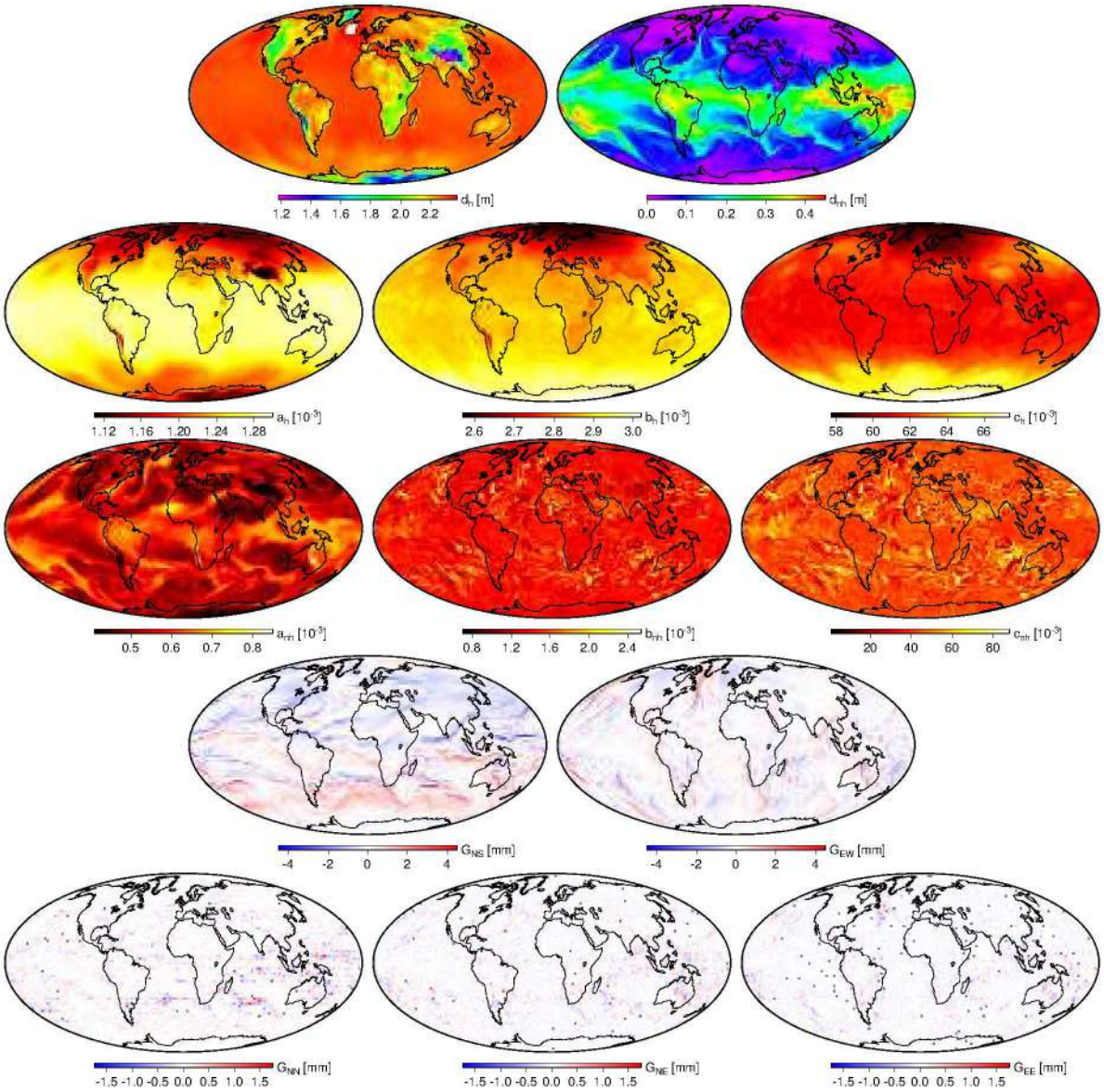


Figure 4.2.9: The PMF products at 00:00 UTC January 1st 2017, employing ERA Interim: d_h^z (upper left) and d_{nh}^z (upper-right), the mapping function coefficients (2nd and 3rd row), linear horizontal gradient components (4th row), and 2nd order gradients (last row).

framework of Balidakis et al. (tted), 6-hourly mapping functions and gradients estimated in the PMF fashion were uploaded for GNSS, SLR, VLBI, and DORIS, for all stations with a contribution to the latest ITRF: ftp://ftp.gfz-potsdam.de/pub/home/kg/kyriakos/PMF/. As of this writing, a number of scientists have used the PMF such as Krzysztof Sośnica (Bernese), and Rolf König (EPOS-OC).

4.2.5 Berlin mapping functions

The fully-fledged Potsdam mapping functions, that is symmetric and asymmetric component (4.2.9), are capable of a very precise description of the atmospheric delay. Nevertheless, due to the fact that even the accuracy of state-of-the-art NWMs is not satisfactory for high-precision geodetic applications, a number of tropospheric parameters has to be estimated in the adjustment of — as of this writing — microwave space geodetic observations. In these cases the role of the tropospheric model is dual:

- ☐ first to reduce the related observations (e.g., interferometric group delays, ionosphere-free pseudorange and carrier phase observations, laser ranges); and
- ☐ second to form the partial derivatives for d^z_{nh}, as well as the gradient components should the BS98 mf_g be adopted.

The PMF, as well as other state-of-the-art operational mapping functions such as VMF3 (Landskron and Böhm, 2018b) and UNB-VMF1 (Nikolaidou et al., 2018a) treat rigorously only the first point, when complemented by gradients. The only possibility to address the 2nd point in a manner that the tropospheric asymmetry is considered in the related partial derivatives, is to apply ray-traced delays in the geodetic analysis employing the ratio d_{atm}/d^z_{nh} as a mapping factor. While such an implementation does not encompass a heavy computational burden for VLBI, it is fairly impractical for a multi-GNSS high-rate reprocessing campaign spanning two decades and hundreds of stations, as there is no such service. To this end, developed here, the Berlin Mapping Functions (hereinafter BMF) addresses these shortcomings by featuring a precise parameterized ansatz — thus eliminating the need for performing ray-tracing — where the anisotropy is mostly embedded in the mapping function coefficients. Following the BMF concept, the assembled atmospheric delay is calculated by

$$d_{atm}(\varepsilon,\alpha) = mf_h(\varepsilon,\alpha)\, d^z_h + mf_{nh}(\varepsilon,\alpha)\, d^z_{nh}, \tag{4.2.16}$$

where the mapping functions (mf_i) are dependent upon elevation and azimuth

$$mf_i(\varepsilon,\alpha) = \frac{1+\dfrac{a_i(\alpha)}{1+\dfrac{b_i(\alpha)}{1+c_i(\alpha)}}}{\sin(\varepsilon)+\dfrac{a_i(\alpha)}{\sin(\varepsilon)+\dfrac{b_i(\alpha)}{\sin(\varepsilon)+c_i(\alpha)}}}, \tag{4.2.17}$$

and the related coefficients are given by

$$a_i(\alpha) = a_i^0 + a_i^{NS}\cos(\alpha) + a_i^{EW}\cos(\alpha) + a_i^{NN}\cos^2(\alpha) + a_i^{NE}\cos(\alpha)\sin(\alpha) + a_i^{EE}\sin^2(\alpha). \tag{4.2.18}$$

Higher harmonic expansions in (4.2.18) are possible but do not offer a statistically significant precision improvement. Note that unlike Gegout et al. (2011), (4.2.16) does not feature a separate term for asymmetric delays, as it has already been described in (4.2.17).

In terms of assembled delays, PMF and BMF yield almost identical results. PMF and BMF deviate only under conditions where strong non-linear gradients exist e.g., Fig. 4.2.2. These differences can be abridged should a site- and time-dependent gradient mapping function coefficient C_i be estimated.

To determine whether PMF or BMF are more suitable for geodetic analysis, let us make a thought experiment. Suppose the underlying NWM utilized to generate the ray-traced delays that are in turn employed as observations to estimate PMF and BMF is perfect. The observation equation in a typical PPP-like adjustment (Zumberge et al., 1997) — where the ambiguity term has been dropped for the sake of simplicity — adopting the PMF concept reads

$$\begin{aligned} d_{atm} - (&mf_h(\varepsilon)\, d_h^z + mf_g(\, G_{NS}\cos(\alpha) + G_{EW}\sin(\alpha) \\ &+ G_{NN}\cos^2(\alpha) + G_{NE}\cos(\alpha)\sin(\alpha) + G_{EE}\sin^2(\alpha))) + w \\ &= mf_{nh}(\varepsilon)\, d_{nh}^z + mf_g(\delta G_{NS}\cos(\alpha) + \delta G_{EW}\sin(\alpha) + clk + \delta\mathbf{x}, \end{aligned} \tag{4.2.19}$$

where d_{atm} are ray-traced delays, and w is the system-dependent observations' noise. The parameter space is comprized by $\begin{bmatrix} d_{nh}^z & \delta G_{NS} & \delta G_{EW} & clk & \delta\mathbf{x} \end{bmatrix}^\top$. Adopting the BMF concept, (4.2.19) turns into the following

$$d_{atm} - mf_h(\varepsilon, \alpha)\, d_h^z + w = mf_{nh}(\varepsilon, \alpha)\, d_{nh}^z + clk + \delta\mathbf{x}, \tag{4.2.20}$$

thus reducing the number of troposphere-related parameters to a third: $\begin{bmatrix} d_{nh}^z & clk & \delta\mathbf{x} \end{bmatrix}^\top$, should they be set up at identical intervals. While gradient components can be estimated in (4.2.20) the physical interpretation thereof would be just a correction to the asymmetric delays. The BMF and PMF parameters are related with the following

$$\left(mf_{nh}^{BMF} - mf_{nh}^{PMF}\right) d_{nh}^z \approx mf_g\left(\left(G_{NS}^{BMF} - G_{NS}^{PMF}\right)\cos(\alpha) + \left(G_{EW}^{BMF} - G_{EW}^{PMF}\right)\sin(\alpha)\right). \tag{4.2.21}$$

Hence, BMF should be preferred in studies where there is no interest in gradient component estimates (e.g., TRF-related work, IWV trend estimation) and the underlying NWM is very accurate. On the other hand, PMF should be favoured if for instance the task is the assimilation of GNSS-derived gradients into NWMs, or if the underlying NWM is not accurate enough. From the developer's viewpoint, BMF does not require ray-tracing in the profil aloft the site of interest — hence 9 rays fewer to process per station per epoch — but requires the estimation of more parameters in the post-ray-tracing phase. Let n denote the fraction truncation, and m denote the number of harmonic terms; for the (non-)hydrostatic component, PMF's ansatz requires the estimation of $n+m$ parameters, whereas BMS's ansatz requires $n(m+1)$. For standard geodetic processing the estimation of gradients is easily handled provided a good observation geometry, without inducing a significant computational overhead. Moreover, estimating additional parameters from geodetic observations allows to compensate shortcomings in the NWMs' atmospheric state simulations, should a satisfactory observation geometry be available. Nevertheless, when a reduced parameter space is sought, to analyze data sets such as the Intensive VLBI sessions the BMF is a reasonable choice for the omission of estimating gradients has a much smaller impact on the other quantities comprizing the parameter space.

4.3 Development of the empirical atmospheric model GFZ-PT

Developed here, GFZ-PT serves the description of meteorological parameters (in the broad sense) that are essential for geodetic and climate applications as harmonic expansions in lieu of discrete series, cf. Sec. 4 of Balidakis et al. (2018c). There are a number of applications for empirical meteorological models, that is, sets of coefficients estimated from the adjustment of meteorological observations or NWMs. Empirical models are useful — among others — for real-time applications (e.g., real-time GPS tracking), for identifying erroneous data points (e.g., homogenization), and most commonly as a back-up for systems in the event of failure (e.g., replacement of missing pressure values in VLBI processing). However, it is expected that the ever-improving publicly available short-range weather forecasting will eventually eclipse the usage of empirical models. There has been a large number of such models with varying popularity: UNB3m (Leandro et al., 2006), GPT (Boehm et al., 2007), GPT2 (Lagler et al., 2013), TropGrid2 (Schüler, 2014), GPT2w (Böhm et al., 2015), and GPT3 (Landskron and Böhm, 2018b), to name a few.

The development of GFZ-PT is motivated from the lack of a number of important features in the aforementioned models. For the first time GFZ-PT features (i) high-frequency harmonic terms (e.g., S_1 and two overtones thereof), (ii) robustly estimated rates, (iii) a precise harmonic description of gradient vector components, and (iv) additional coefficients tailored for optical observations, all estimated rigorously from ray-traced delays. In particular it has harmonic coefficients at annual (S_a), semi-annual (S_{sa}), ter-annual (S_{ta}), 11-year (S_{11}), diurnal (S_1), semi-diurnal (S_2) and ter-diurnal (S_3) frequencies. GFZ-PT considers the following ensemble of parameters:

- pressure, temperature, relative humidity,
- zenith delays, mapping function coefficients, and gradient vector components of the 1st and 2nd order,
- water vapour-weighted mean temperature and integrated water vapour,

determined at the nodes of an equi-angular 0.25°×0.25° ECMWF orography. Parameters at overtones of frequencies at which variations dominate (typically annual) have been set up, to improve the WRMS of the post-fit residuals. The effects that GFZ-PT describes are partly caused by the differential heating of Earth's atmosphere. However, due to the fact that the processes of perpetual heating and cooling do not take the same time, it is not possible to describe such harmonic variations by a single sinusoid (G. Beyerle, personal communication). Hence, to describe the 2nd order effects, harmonic terms at twice the initial frequency are set up. While this process can continue up to the point where the Nyquist frequency has been reached, or the signal has been developed to an infinite number of harmonic terms, from a statistical viewpoint it is inessential and does not serve the initial purpose of this endeavour. The coefficients for zenith delays (d_h^z and d_{nh}^z), mapping function coefficients (a_h, b_h, c_h, a_{nh}, b_{nh}, and c_{nh}), and gradient vector components (G_{NS}, G_{EW}, G_{NN}, G_{NE}, G_{EE}) stem from rigorous ray-tracing employing DNS (Zus et al., 2012, 2014). The water vapour-weighted mean temperature (T_m) and the integrated water vapour (IWV) are determined from numerical integration in the model levels

$$T_m = \frac{\int \frac{P_w}{T} Z^{-1}\, dh}{\int \frac{P_w}{T^2} Z^{-1}\, dh}, \tag{4.3.1}$$

where P_w is the partial pressure of water vapour, T is the temperature, Z^{-1} is the inverse compressibility factor (3.3.6), and h is the geodetic height, and

$$IWV = \frac{1}{g}\int Q\frac{\partial P}{\partial h}dh, \tag{4.3.2}$$

where g denotes the WMO-defined gravity acceleration (9.806 65 m s^{-2}), Q is the specific humidity and P is the total pressure.

Let y denote any of the aforementioned parameters. Given the location GFZ-PT's ansatz y is a function of the day of year (DoY) and the hour of day (HoD), and consists of the following

$$\begin{aligned} y(t) = \alpha + \alpha_0 + \beta(t - t_0) + \sum_{i=1}^{3} C_i \cos\left(2\pi i\frac{DoY}{365.25}\right) + S_i \sin\left(2\pi i\frac{DoY}{365.25}\right) \\ + \sum_{j=1}^{3} c_j \cos\left(2\pi j\frac{HoD}{24}\right) + s_j \sin\left(2\pi j\frac{HoD}{24}\right). \end{aligned} \tag{4.3.3}$$

The term α is the long-term average of y. The linear trend of y, β, is robustly estimated employing a variant of the Theil-Sen estimator

$$\beta = \text{median}\left(\frac{y_l - y_m}{t_l - t_m}\right), \forall l > m \text{ and } |t_l - t_m - \text{argmax}(\text{PSD}(y, \sigma_y))| \leq \tau, \tag{4.3.4}$$

where the signal y_l is sampled at the epoch t_l, PSD denotes the power spectral density estimator operator, σ_y represents the uncertainties of y, and τ is the relaxation coefficient. The incentive behind inserting τ in (4.3.4) is computational efficiency. MIDAS (Median Interannual Difference Adjusted for Skewness) was introduced by Blewitt et al. (2016) and slightly modified by Balidakis et al. (2018c) to better consider site-specific seasonal variations. The coefficients C_i and S_i refer to long-wavelength harmonics (S_a, S_{sa}, and S_{ta}) and are estimated employing ERA Interim reanalysis fields (0.5°×0.5° on 60 model levels) spanning the period 1979.0–2018.0. The coefficient c_j and s_j correspond to the high-frequency harmonics (S_1, S_2, and S_3) estimated from hourly ERA5 reanalysis fields (0.25°×0.25° on 137 model levels) spanning the period 2008.0–2018.0.

Harmonics at longer periods e.g., around the 5-year mark (for phenomena such as El Niño), or around the 11-year mark (for the solar activity Schwabe cycle), have also been investigated. Frequencies lower than 1 cpy yield no statistically significant improvement on the expansion of (4.3.3) for any of the parameters studied herein, hence they were dropped. The 11-year sunspot cycle slightly affects the amplitude of the both low- and high-frequency terms; the S_1 amplitude of temperature and pressure variations differ up to 1.8 °C and 0.5 hPa, respectively. Nevertheless, due to the fact that only 10 years of ERA5 being released as of this writing, and that the S_{11} terms are fairly small (cf. Fig. 4.3.3), the 11-year harmonics are not retained at the official version of GFZ-PT (Balidakis et al., 2018c), but are kept herein for the sake of completeness.

Prior to the least-squares fitting, a high-pass 3rd order Butterworth filter with a cut-off frequency of 72 h was applied for the estimation of the high-frequency harmonics (e.g., Dobslaw et al., 2017b) utilizing ERA5 data. To account for the correlation between neighbouring (in the temporal domain) observations in the estimation of the low-frequency harmonics, the generalized covariance model of Hirvonen was utilized in the least-squares adjustment (e.g.,

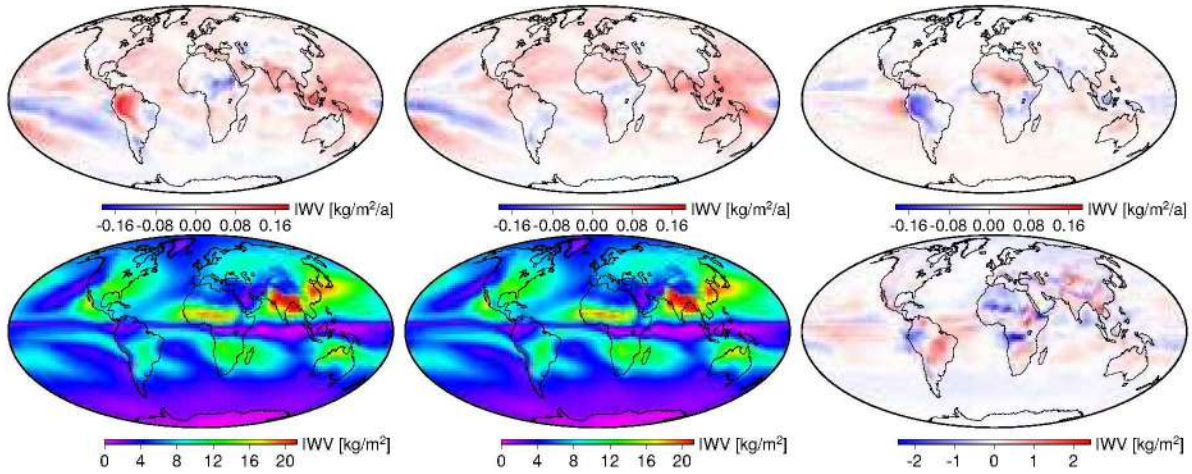


Figure 4.3.1: IWV rates (1st row) and S_a amplitudes (2nd row) estimated employing ERA Interim fields (left), ERA5 fields (middle), and the differences thereof (right), for the period 1979.0–2019.0.

Hirvonen, 1962; Kotsakis, 2007)

$$C(dt) = \frac{C_0}{1 + \left(\frac{dt}{\xi}\right)^2}, \tag{4.3.5}$$

where the signal variance C_0 and the correction time lag ξ are site- and parameter-specific.

Although ERA Interim and ERA5 (its successor) are similar in many aspects (e.g., S_a harmonics), they display differences in some of the trends. This statement is illustrated in Fig. 4.3.1 where the IWV trends from ERA5 and ERA Interim are calculated on an O320 grid, as well as the differences thereof. Positive IWV trends are underestimated in 40 % of the cases by ERA Interim, whereas negative trends are underestimated in 3 % of the cases. These differences cannot be attributed to orographic discrepancies solely. For periods well below a climate norm, the differences are amplified stemming from the fact that IWV trends are to a certain extend non-linear (cf. Fig. 4.3.2). To elaborate on the source of these differences other than ascribing them to the assimilation systems (IFS c31r2 (2006) for ERA Interim, and IFS c41r2 (2016) for ERA5) and the data ingested therein is beyond the intended scope of this work. The author plans to recalculate all GFZ-PT parameters upon the release of ERA5 fields spanning at least 30 years.

In the context of propagation delay corrections, pressure, temperature, and relative humidity, are essential to calculate a priori zenith delays for both microwave- and optical-frequency-based techniques. Most important are the low-frequency waves mainly because the amplitudes are significantly larger. Another reason is that a number of parameters such as stations coordinates and EOPs is estimated within a 24-hour long batch adjustment, ergo assuming a normal observations' distribution in time and quality all effects with an integer number of cycles within one day will probably dissipate to an extend. Figure 4.3.3 illustrates the low-frequency harmonic terms for P, T, and RH. The last column of Fig. 4.3.3 displays the scatter of the post-fit residuals that suggests the regions where (4.3.3) is successful in the signal description. For instance, for pressure, this is not the case for parts of the Arctic Ocean, the north part of the Atlantic Ocean, the North Pacific Ocean, and the Southern Ocean (especially across the ACC and in the area around Drake Passage). The pressure variability in these regions is strongly non-harmonic with

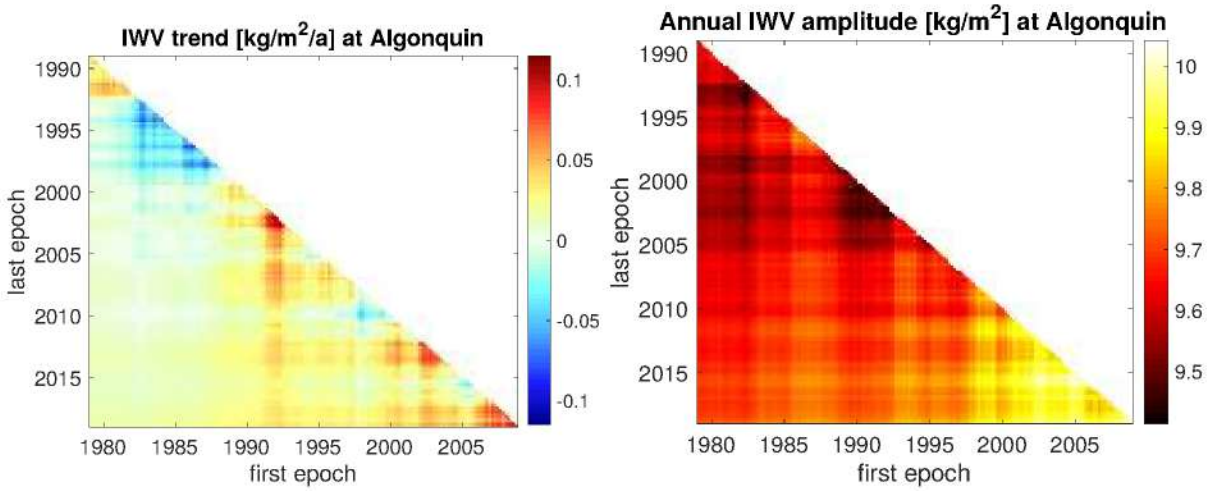


Figure 4.3.2: IWV trends (left) and IWV annual amplitudes (right) at Algonquin Park (Canada), estimated employing ERA5 data. For the estimation thereof the length of the time series as well as the first and last epoch were varied.

the maximum PSD being well below 10 %. Non-harmonic signals are the reason an analytic function cannot suffice for the description of temperature series in the poles, and of RH series in southern and east Africa, Australia, or Iran.

For VLBI, temperature observations are necessary to account for the thermal deformation of the antennas. If this effect is not properly considered, it manifests into several parameters such as station coordinates and the scale of the implied frame, thus increasing the PSD thereof at S_a (mainly) frequencies. Wresnik et al. (2007) have shown that thermal expansion introduces an S_a signal with an amplitude of 1 mm. Additionally, it has been shown recently employing advanced spectral methods that a significant portion of the baseline length variability is of thermal origin (Ghaderpour and Pagiatakis, 2017). Moreover, in the torrid zone as well as elsewhere, the S_1 variations are larger than the S_a variations, rendering the latter necessary to accurately describe the temperature series analytically. Figure 4.3.4 illustrates the high frequency waves for P, T, and RH, predicted by GFZ-PT. As for the high-frequency P variations, the contribution of atmospheric tides (cf. Sec. 5.2.1) to d_h^z induces systematic variations as large as 13 mm, thus prompting that the high-frequency parameters in GFZ-PT's expansion are crucial. The estimation of harmonic coefficients for more waves (for barometric pressure) at frequencies higher or equal than three, and lower or equal than one cycle per day has been investigated in the framework of tidal atmospheric pressure loading (cf. Sec. 5.2.1). Pressure anomalies from waves other than S_1 and S_2 have a contribution to the zenith delay that is smaller compared to the uncertainty of the underlying weather model. For the estimation thereof, Doodson's fundamental arguments need to be parsed additionally (e.g., Doodson, 1921; Wilhelm and Zürn, 1984).

The reference temperature of GFZ-PT has been assessed as well. Alternating the reference temperature between GFZ-PT and the current standard, GPT, a virtual displacement no larger than 0.2 mm (e.g., for `HOBART26` and `BADARY`) is introduced in the radial coordinate component. Due to the fact that GFZ-PT is derived from 39 years of 0.5°-resolved ERA Interim and GPT is derived from only 3 years of monthly-mean 15°-resolved ERA40 (the predecessor of ERA Interim) data, one can postulate that the reference temperature from GFZ-PT is more precise. Save for S_a and S_1 the contribution of all other temperature waves, individually, is moderate and does not exceed 1 mm (transformed to thermal expansion) at most VLBI sites.

Another novelty of GFZ-PT is its featuring harmonics for linear and non-linear gradient

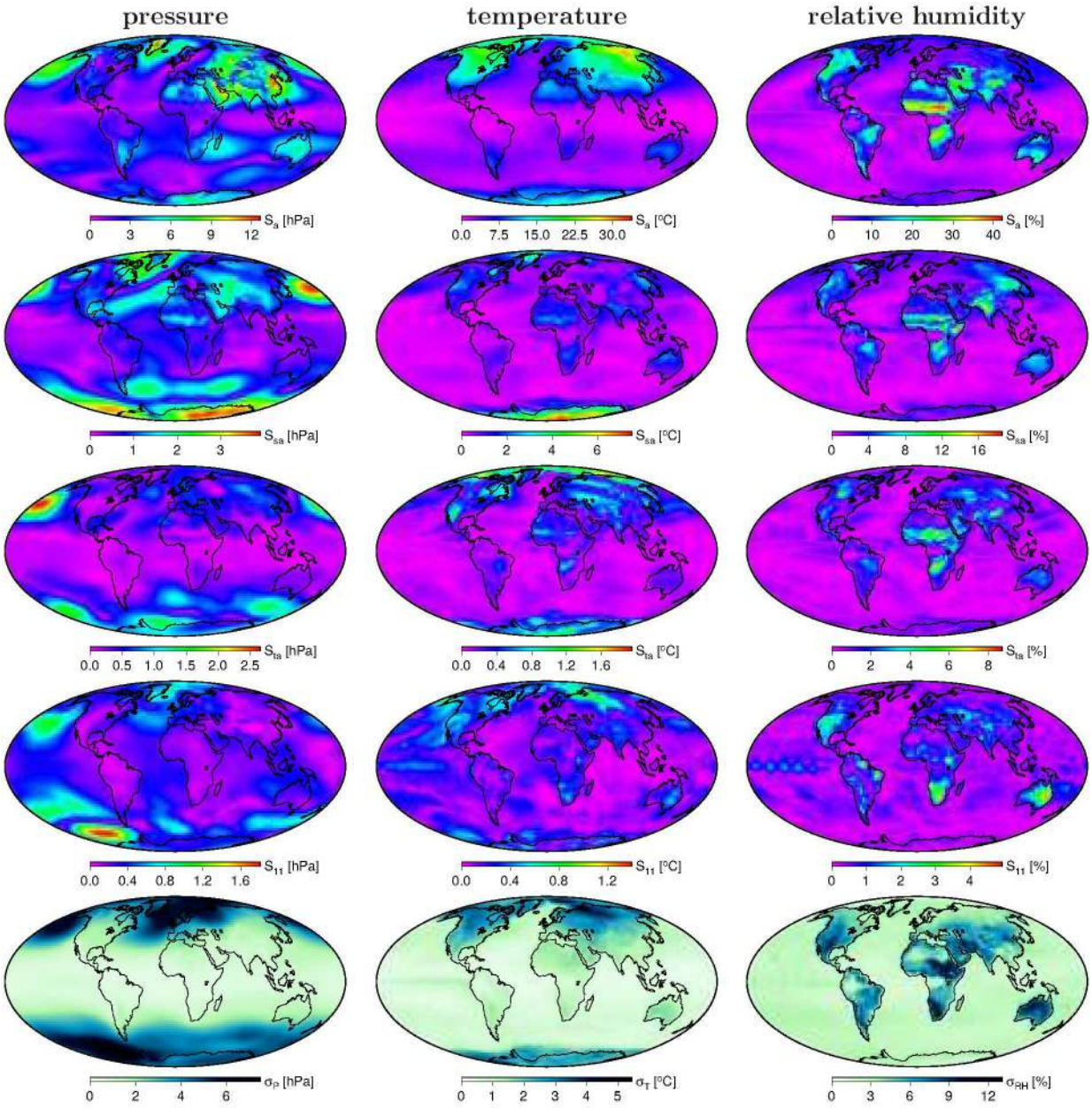


Figure 4.3.3: The amplitudes of low-frequency harmonics of pressure (1st column), temperature (2nd column), and relative humidity (3rd column), employing ERA Interim. The graphs present the amplitudes of the S_a (1st row), S_{sa} (2nd row), S_{ta} (3rd row), and S_{11} (4th row) harmonics, as well as the scatter of the post-fit residuals thereof (5th row). Note the different color scales.

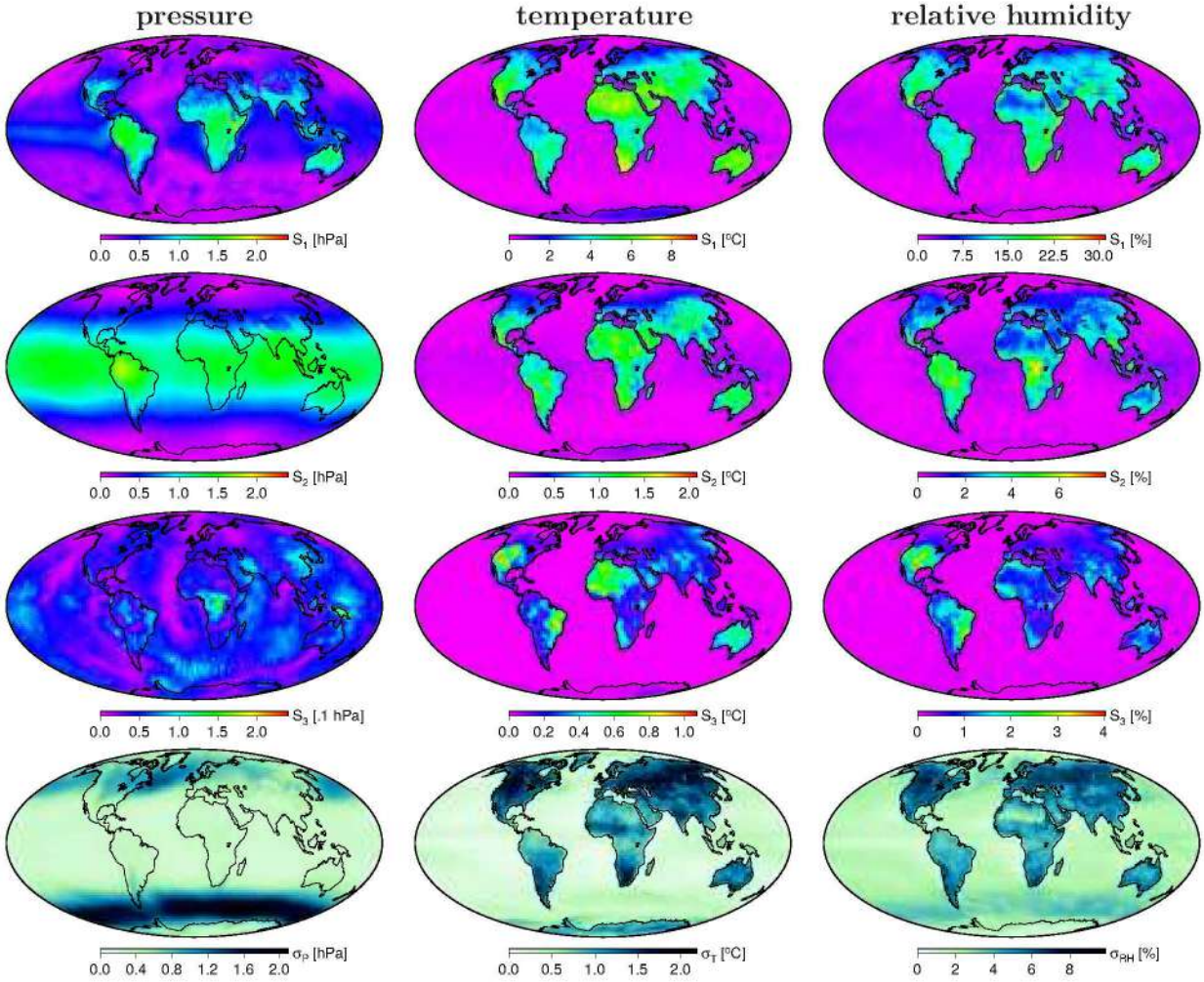


Figure 4.3.4: The amplitude of high-frequency harmonics of pressure (1st column), temperature (2nd column), and relative humidity (3rd column), employing ERA5. The graphs present the amplitudes of the S_1 (1st row), S_2 (2nd row), and S_3 (3rd row) harmonics, as well as the scatter of the post-fit residuals thereof (4th row). Note the different color scales.

components for both microwave and optical frequencies. To the author's knowledge no study has estimated gradients for optical frequencies, nor the seasonal and high-frequency harmonics thereof. Previous studies that attempted to model the gradients provided only gridded offsets in a fairly low spherical harmonic expansion, that is 9 for Böhm et al. (2013b), or site-specific offsets at a few VLBI sites (MacMillan, 1995b; MacMillan and Ma, 1997). Employing a priori information to constrain the gradient estimates from VLBI or GNSS analysis yields small differences unless the observation geometry is very poor or/and heavy weights have been applied to the relevant observation equations (Nilsson et al., 2017b). Such cases include but are not limited to early VLBI sessions and the Intensives. Examining the gradient series, it is apparent that they have a large scatter from which several harmonics emerge. S_a is the most important harmonic for all gradients considered herein, at both microwave and optical frequencies. For microwaves, S_a induces systematic variations in the tropospheric delay as large as e.g., 40 mm at 7° in the tropics. As water vapour redistribution does not affect the propagation of lasers appreciably, the signal amplitude of the related gradients is largely diminished. Figure 4.4.11 displays that for lasers

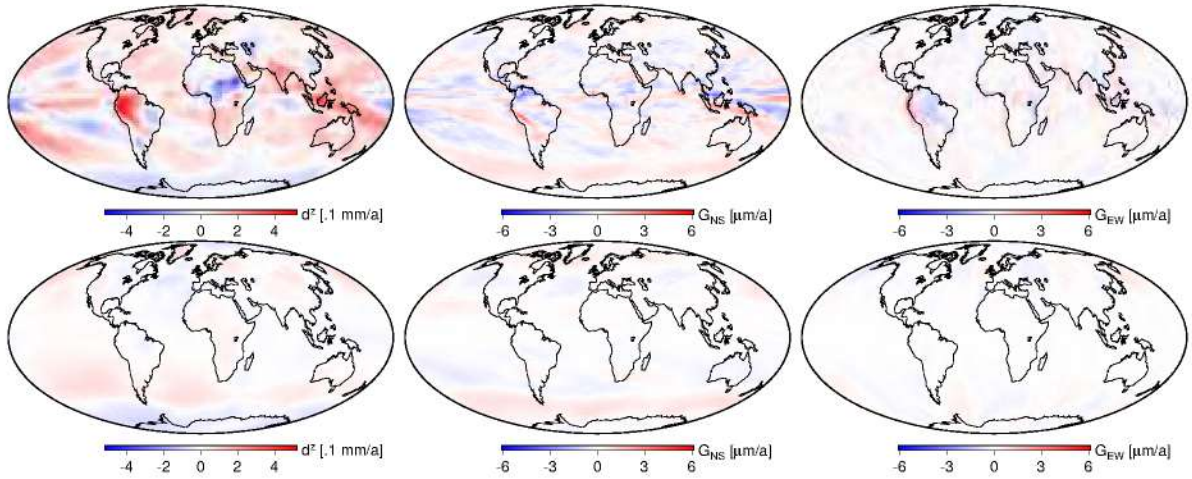


Figure 4.3.5: Zenith total delay (left), G_{NS} (middle), and G_{EW} (right) rates for microwaves (upper row) and lasers at 532 nm (lower row) from 39 years of ERA Interim.

the S_a amplitude of the asymmetric delay in the tropics is at the 1 mm level for 10°, whereas at middle latitudes (North Pacific Ocean) it can reach 9 mm for 10°. The seasonal amplitudes of G_{EW} are much smaller as their variability is mainly driven by weather. Nevertheless, decent S_a amplitudes are discerned in the vicinity of mountain ridges (e.g., Andes, Himalayas, and Pacific coast ranges of North America) and coastal areas (e.g., south Atlantic coast of Morocco, coast of Red Sea, coast of South Africa, and Andaman Sea coast). Notwithstanding the absence of the aforementioned features in optical S_a for G_{EW}, both microwave and optical G_{EW} have coherent S_a amplitudes for $|\varphi| > 30°$. Due to the small contribution of water vapour in the optical gradients, they are more suitable for a seasonal fit than the microwave gradients.

The long-term trends especially in the IWV and temperature time series have been repeatedly confirmed not to be spurious employing independent data sets such as meteorological sensors, NWMs, GPS, and VLBI (e.g., Heinkelmann et al., 2007; Nilsson and Elgered, 2008; Haas et al., 2010; Alshawaf et al., 2017). Due to the fact that (i) the IWV trends (consequently the d^z_{nh} trends too) display non-uniform spatial patterns (cf. Fig. 4.3.1), and (ii) G_{NS} and G_{EW} to an extend describe the change of the zenith delay along the meridian and parallel, respectively, gradient trends are a fact. Figure 4.3.5 attests to that by illustrating microwave and optical zenith delay and gradient trends. The agreement is excellent for both microwave and optical delays.

The software accompanying the coefficients (bias, trend, S_{11}, S_a, S_{sa}, S_{ta}, S_1, S_2, S_3) allows the extraction of all the aforementioned parameters specifically tailored for microwave or optical frequencies (366 nm $\leq \lambda \leq$ 1064 nm), any orbital altitude (150 km $\leq H_o \leq \infty$), and any station height. Further details on these reductions are provided in Sec. 4.4.

4.4 Atmospheric ties

Atmospheric (or tropospheric) ties are understood as corrections for parameters such as the zenith delays, the gradient vector components, and the mapping factors, that refer to neighbouring geodetic observing systems. The differences may lie solely in the spatial component (intra-technique atmospheric ties, cf. Sec. 4.4.1), in the technique (inter-technique atmospheric ties, cf. Sec. 4.4.2), or in time. While atmospheric ties (like local ties) could be considered by applying a constant offset or factor, due to their varying considerably with time, such an approach would

be but a first order approximation. The foremost contribution to the atmospheric tie vector between systems observing at the same frequency stems from the height difference thereof due to the fact that lateral refractivity gradients are much smaller compared to the vertical. Regarding atmospheric ties there are a number of unresolved issues such as the definition of "neighbouring" (that is, which should the maximum height difference and horizontal distance be). Similar topics are subject of a working group of IAG Commission 1 (JWG 1.3: Tropospheric Ties, chaired by R. Heinkelmann), where the author of the current dissertation is participating.

To the author's knowledge, only δd_h^z, δd_{nh}^z, and δmf_h stemming from height differences are considered, and are carried out by employing analytical expressions. Inter-technique tropospheric ties have never been considered either. Tropospheric gradient ties have not been considered thus far, save for Krügel et al. (2007) where a VLBI-GPS combination was performed. The study thereof is important for a large variety of topics such as using gradient estimates from GNSS data analysis to improve the a priori tropospheric modelling of VLBI intensive sessions (e.g., Nilsson et al., 2017b), estimating common zenith delays and gradient components at co-located sites (e.g., Nilsson et al., 2015a), and combining radio-based space geodetic techniques (e.g., Krügel et al., 2007; Thaller, 2008; Pollet et al., 2014).

4.4.1 Intra-technique atmospheric ties

In this section, besides zenith delay ties, the ties between the gradient vector components as well as the differences between the mapping function coefficients are discussed.

Following Brunner and Rüeger (1992), the d_h^z difference between two stations that operate in the microwave spectrum is given by

$$\delta d_h^z = \frac{0.0022768\,(P - P_0)}{1 - 0.00266\cos(2\varphi) - 0.00000028 H_0}, \tag{4.4.1}$$

where P denotes the (total) barometric pressure, φ denotes the geodetic latitude, and H denotes the orthometric height — the denominator is the acceleration due to gravity at the center of mass of the vertical column, divided by a constant acceleration due to gravity at the surface of the Earth at mid-latitudes. The subscript 0 corresponds to the reference point. Application of covariance propagation to (4.4.1) suggests δd_h^z has low sensitivity to H_0. Compared to forming the difference between the d_h^z at the two stations, (4.4.1) marginally underestimates the d_h^z tie, that is, by 1 mm for $\delta H > 2$ km. Moreover, (4.4.1) implies that dry air and water vapour share identical thermodynamic properties, which is not a safe assumption for meeting the intended accuracy. In essence, it is $\delta d_h^z \approx 27$ mm for $\delta H = 100$ m. For this particular height difference, the use of (4.4.1) yields an expected equivalent relative height error — compared to ray-traced delays — of $\sigma_h \leq 1$ mm in 57 % of the cases (hourly ERA5 0.25°-spaced grid nodes over land), and $\sigma_h \leq 5$ mm in 95 % of the cases.

The analytical equation for δd_{nh}^z is given by Saastamoinen (1972); Brunner and Rüeger (1992)

$$\delta d_{nh}^z = -\frac{2.789 P_{w0}}{T_0^2}\left(\frac{5.383}{T_0} - 0.7803\right)\beta\,(H - H_0)\,, \tag{4.4.2}$$

where P_w is the water vapour pressure, T is the temperature, and β is the temperature lapse rate. The expressions (4.4.1) and (4.4.2) assume that (Brunner and Rüeger, 1992; Rothacher et al.,

2011)

$$p = p_0 \left(1 - \frac{\beta\,(H - H_0)}{T_0}\right)^{\frac{g_0}{\beta R}} \approx p_0 - \frac{0.03416\,(H - H_0)\,p_0}{T_0}, \tag{4.4.3}$$

$$T = T_0 - \beta\,(H - H_0)\,, \text{and} \tag{4.4.4}$$

$$P_w = \frac{RH}{100} e^{\,2.3026\left(0.7858 + \frac{7.5\,(T - 273.15)}{T - 35.85}\right)}, \tag{4.4.5}$$

where the temperature lapse rate $\beta = 0.009\,77\,^{\circ}\mathrm{C\,m^{-1}}$, and the relative humidity $RH = 90\,\%$ are held constant[7]. For instance, for $\delta H = 100\,\mathrm{m}$, δd^z_{nh} ranges between sub-mm (polar regions) to 18 mm (tropical regions). The expected height error from the use of (4.4.2) is $\sigma_h \leq 1\,\mathrm{mm}$ in only 25 % of the cases, and $\sigma_h \leq 5\,\mathrm{mm}$ in 64 % of the cases. For this particular height difference (4.4.2) overestimates δd^z_{nh} exponentially with increasing temperature by an amount as large as 12 mm. It is therefore apparent that while d^z_h ties can be approximated analytically, the efficacy of d^z_{nh} ties diminishes in non-polar regions, where the vast majority of stations lie. Furthermore, the aforementioned expressions account only for the vertical displacement, disregarding the contribution of the horizontal displacement, which is impossible to model in such a fashion due to its being associated with weather patterns and the local landscape. Ergo, atmospheric ties in this thesis are not determined by analytical expressions but by the difference between ray-traced parameters.

Figure 4.4.1 illustrates the δd^z_h from ray-traced delays between the orography of ERA5 and virtual orographies with $\delta H = \begin{bmatrix}25 & 100 & 500\end{bmatrix}^\top\,\mathrm{m}$. δd^z_h displays spatial stability for all height differences as well as for both "snapshot" and "monthly-mean" data — save for mountainous regions.

On the contrary, Fig. 4.4.2 delineates the strong dependence of δd^z_{nh} to temperature and water vapour concentration. As expected, the monthly averaged data portray spatially smoother fields. While the long-wavelength spatial patterns persist for all δH assessed, anomalies appear for large δH in high altitude and high latitude areas due to inversions.

In addition to the zenith delays being subject to spatial change, other ray-traced delay derivatives are dependent upon spatial change. Mapping function coefficients and tropospheric delay gradient components (cf. Sec. 4.2) fall under this set as they can differ significantly over the baselines of the current local ties.

Given the mapping function coefficients at mean sea level a_0, b_0, and c_0, to account for the

[7]Nevertheless, the facts that β varies over space and time, and RH is highly volatile at meso-γ spatio-temporal scales, render the use of constants a generalized rough approximation and by transitivity the relations (4.4.3), (4.4.4), and (4.4.5). For instance, according to ERA5 (2013/05/01 00:00 UTC) β can vary from $-0.021\,47\,^{\circ}\mathrm{C\,m^{-1}}$ to $0.088\,52\,^{\circ}\mathrm{C\,m^{-1}}$ for the first 1000 m above the orography of the model, mainly as a function of co-latitude

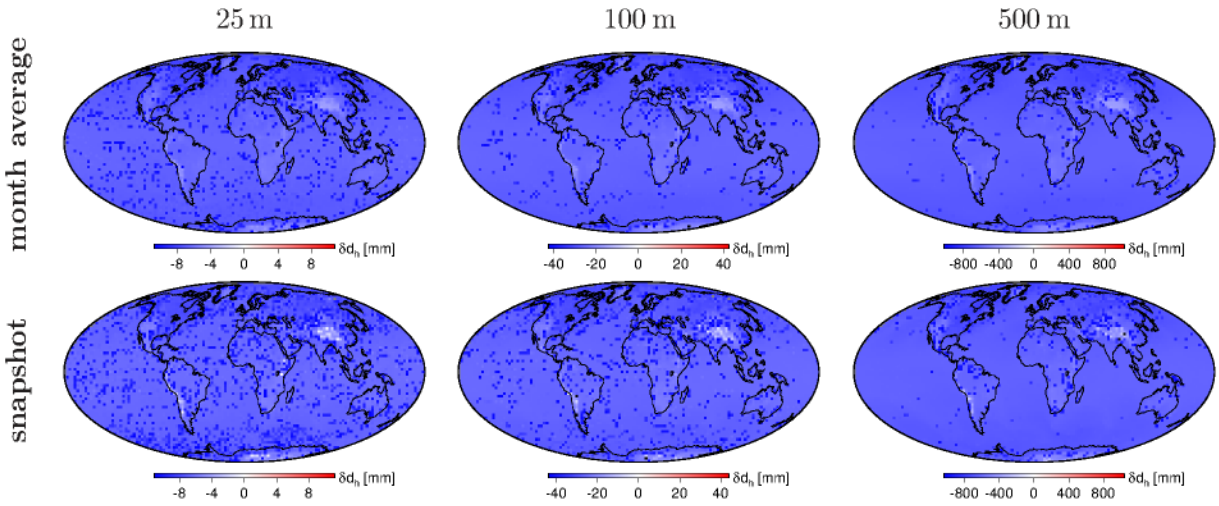


Figure 4.4.1: Zenith hydrostatic delay ties. The differences between ray-traced d_n^z at the orography of ERA5 and virtual orographies 25 m (left), 100 m (middle), and 500 m (right) above are illustrated. In the upper row shown are the δd_h^z averaged over a month (2018/01), whereas in the lower row shown are the ties at the epoch 2018/01/01 00:00. Note the different color scales.

dependence of mf_h on height, the following expression is used (Niell, 1996)

$$mf = \frac{1 + \dfrac{a_0}{1 + \dfrac{b_0}{1 + c_0}}}{\sin(\varepsilon) + \dfrac{a_0}{\sin(\varepsilon) + \dfrac{b_0}{\sin(\varepsilon) + c_0}}} + H \left(\frac{1}{\sin(\varepsilon)} \frac{1 + \dfrac{a_{ht}}{1 + \dfrac{b_{ht}}{1 + c_{ht}}}}{\sin(\varepsilon) + \dfrac{a_{ht}}{\sin(\varepsilon) + \dfrac{b_{ht}}{\sin(\varepsilon) + c_{ht}}}} \right), \qquad (4.4.6)$$

where the coefficients a_{ht}, b_{ht}, and c_{ht} are determined from climatology by Niell (1996), and H denotes the orthometric height of the station. While this analytical expression is valid for most cases, it fails at mountainous regions as well as in the presence of inversions. Figure 4.4.3 illustrates this point showing the $\delta mf_h\,(7°)$ for different altitudes. As expected, the mapping function differences' fields are more uniform for the monthly-averaged data.

Currently, it is assumed that mf_{nh} is independent of the station height. The investigations carried out herein prove the contrary (cf. Fig. 4.4.4). Owing to the inhomogenious distribution of water vapour both horizontally and vertically, the effectiveness of expressions such as (4.4.6) is very limited. The limited spatial coherence between δmf_{nh} for different δH, as exhibited in Fig. 4.4.4, attests to that statement. The error in the modelled non-hydrostatic delay can be as large as 15 mm at an elevation angle of 7° for $\delta H = 500\,\text{m}$. Such an imperfection in modelling cannot vanish by iterating the geodetic adjustment (observation equations method) for it affects the partial derivatives of estimable parameters (d_{nh}^z). For smaller height differences (e.g., 25 m) the relative error is smaller and more spatially unstable.

It is a fact that should a proper elevation-dependent weighting strategy for observations near the horizon be adopted, the lower the cutoff mask the better the estimation of tropospheric gradients and coordinate height component. The differences between mapping factors increase with decreasing elevation angle ε following $\csc(\varepsilon)$. Therefore, employing appropriate mapping factors is crucial for accurate positioning.

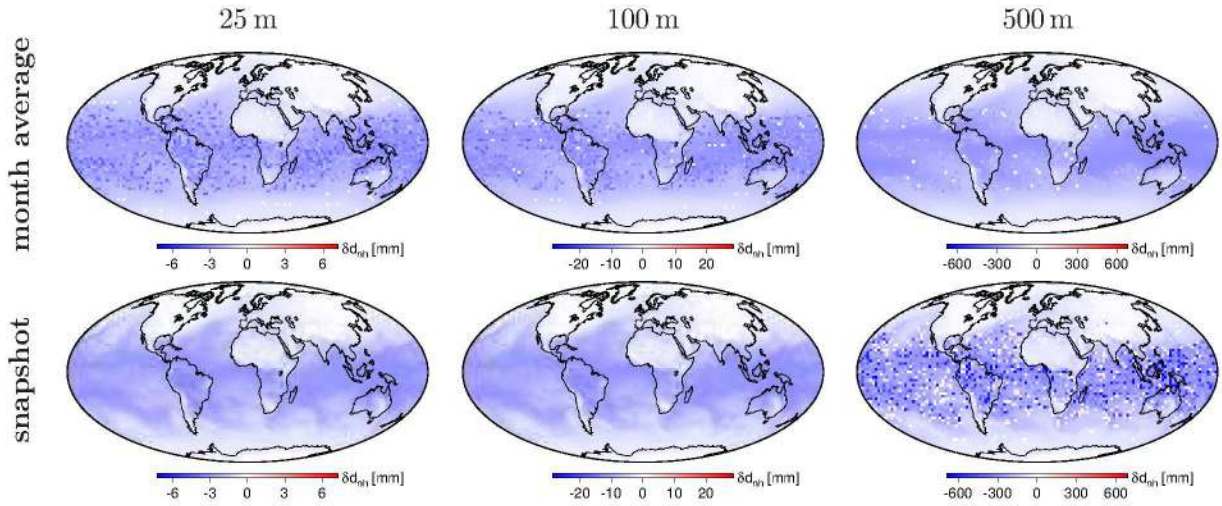


Figure 4.4.2: Zenith non-hydrostatic delay ties. Shown are the differences between ray-traced d_n^z at the orography of ERA5 and virtual orographies 25 m (left), 100 m (middle), and 500 m (right) above. In the upper row shown are the δd_h^z averaged over a month (2018/01), whereas in the lower row shown are the ties at the epoch 2018/01/01 00:00. Note the different color scales.

The differences between gradient components stemming solely from the height difference displays a consistent behaviour over δH. As demonstrated in Fig. 4.4.5 and Fig. 4.4.6, given a 2D position, that is latitude and longitude, the gradients' intensity decreases with altitude consistently. It is

$$|G_j(H)| > |G_j(H+\epsilon)|, \tag{4.4.7}$$

where $\epsilon > 0$ and $j = \begin{bmatrix} NS & EW & NN & NE & EE \end{bmatrix}^\top$. To validate (4.4.7), ray-tracing at the native horizontal resolution of ERA5 (31 km) for δH up to 1000 m with a step of 25 m was carried out on hourly refractivity fields for 2017 (365×24×421120 points, on an octahedral quasi-regular Gaussian grid O320). The results prove that this statement holds for both linear and non-linear gradient components; 98.5 % for G_{NS}, 97.8 % for G_{EW}, 96.2 % for G_{NN}, 96.7 % for G_{NE}, and 96.7 % for G_{EE}. For $\delta H < 500$ m that is of particular interest for the practical applications, the success rate is 99.8 % for G_{NS}, 99.6 % for G_{EW}, 99.4 % for G_{NN}, 99.5 % for G_{NE}, and 99.5 % for G_{EE}. The rare cases where (4.4.7) does not hold are isolated, are not related to steep orography, and take place at some of the nodes where there is almost no refractive asymmetry (very small gradient components). Similar results have been obtained employing monthly-mean ERA5 fields.

Neglecting the gradient ties impacts the modelled atmospheric delays increasingly with increasing δH — the tilting of the atmosphere decreases with increasing altitude — and decreasing ε. In essence, not accounting for δG_j yields $\delta d_{atm}(7°)$ as large as 2 mm for $\delta H = 25$ m, 10 mm for $\delta H = 100$ m, and 40 mm for $\delta H = 500$ m.

Therefore, it is possible to describe the gradient decay with altitude with analytical expressions such as 2nd degree polynomials. Further details in this regard are provided by Balidakis et al. (tted).

4.4.2 Inter-technique atmospheric ties

In this section, the compatibility of tropospheric models across space geodetic techniques (GNSS, VLBI, SLR, and DORIS) is assessed. The differences induced by employing different frequency

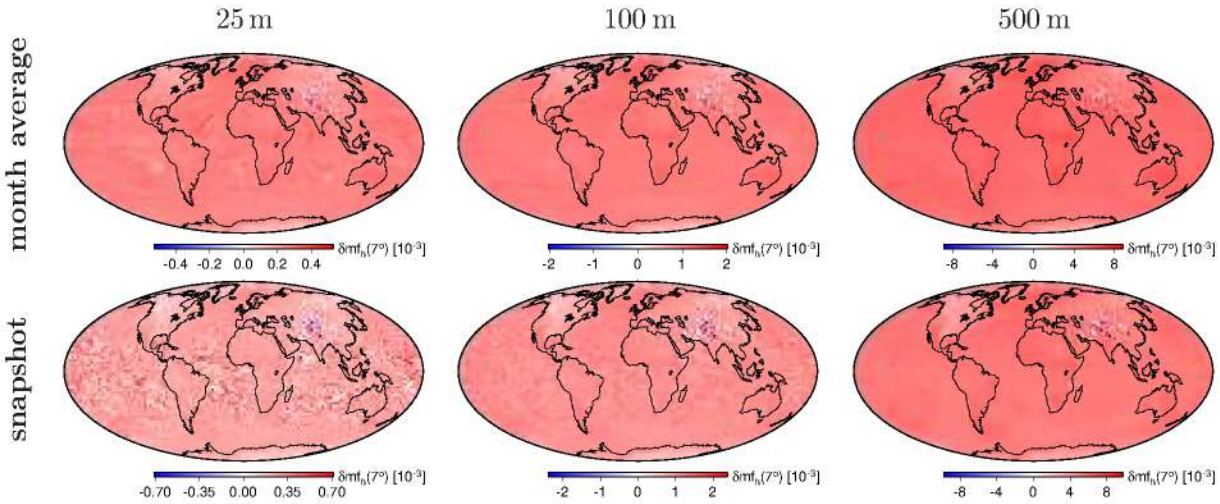


Figure 4.4.3: Hydrostatic mapping factor differences. Shown are the differences between ray-traced mf_h (7°) at the orography of ERA5 and virtual orographies 25 m (left), 100 m (middle), and 500 m (right) above. In the upper row shown are the δmf_h (7°) averaged over a month (2018/01), whereas in the lower row shown are the ties at the epoch 2018/01/01 00:00. Note the different color scales.

(microwave vs. optical, and within the optical spectrum) is studied. Furthermore, the impact of the orbital altitude is assessed. As of 2018, with the exception of Zus et al. (2015a), there has been no work where this issue is discussed.

First, unlike microwaves for which the lower atmosphere is a non-dispersive medium, the propagation delay and ray-bending optical signals experience is a function of the frequency thereof (e.g., Mendes and Pavlis, 2004). The higher the frequency, the larger the delay, both zenith and slant. For instance, at sea level d_h^z@366 nm is 32 cm larger than d_h^z@1064 nm. The corresponding difference for d_{nh}^z ranges to 2 mm in the tropics, that is around $^1/_3$ of the amplitude of the signal. As far as the mapping functions are concerned, neither FCULa nor FCULb (Function Commonly Used for laser data) consider the frequency dependence (Mendes et al., 2002). Although the contribution of the mapping function's frequency dependence to the slant delay in comparison to the zenith delay's is fairly small (0.3 %), it induces a height-dependent ($\log(H_s)$) systematic bias. To quantify this point, some examples follow:

$$\text{Utilizing mapping functions tailored for } \begin{bmatrix} 532 \\ 532 \\ 366 \\ 1064 \end{bmatrix} \text{ nm to reduce laser ranges at } \begin{bmatrix} 1064 \\ 366 \\ 1064 \\ 366 \end{bmatrix} \text{ nm}$$

$$\text{biases the modelled observations at } 10^\circ \text{ by as much as } \begin{bmatrix} -2.8 \\ 6.3 \\ -7.9 \\ 10.0 \end{bmatrix} \text{ mm.}$$

The rule of thumb proposed by Böhm (2004) suggests that the estimated heights will be biased by 2 mm for the last case. As far as the gradient components are concerned, they are frequency-dependent too. It is:

$$|G_j@f_1| > |G_j@f_2|\,, \text{where } f_1 < f_2 \tag{4.4.8}$$

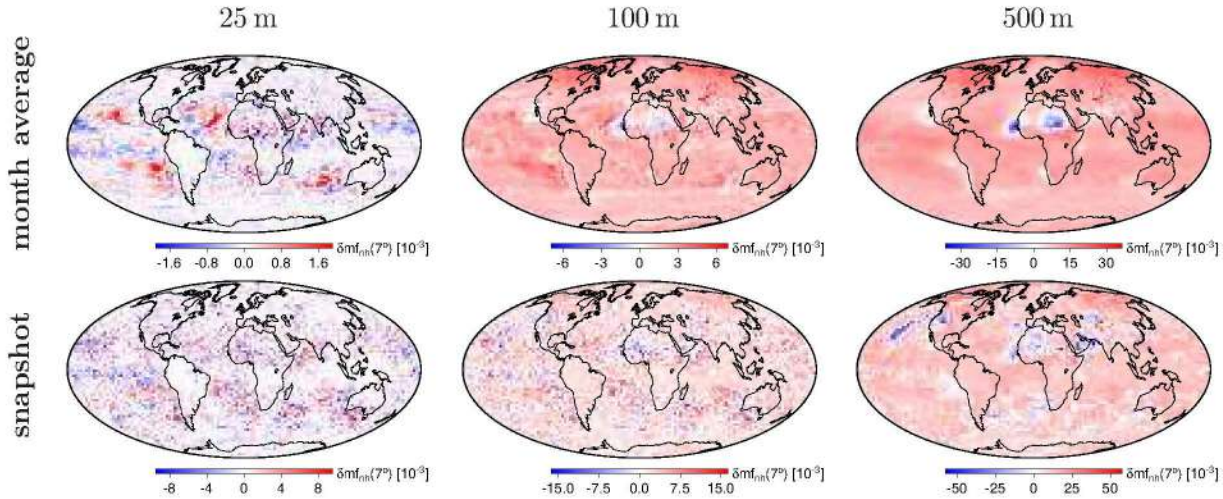


Figure 4.4.4: Non-hydrostatic mapping factor differences. Shown are the differences between ray-traced $mf_{nh}\,(7°)$ at the orography of ERA5 and virtual orographies 25 m (left), 100 m (middle), and 500 m (right) above. In the upper row shown are the $\delta mf_{nh}\,(7°)$ averaged over a month (2018/01), whereas in the lower row shown are the ties at the epoch 2018/01/01 00:00. Note the different color scales.

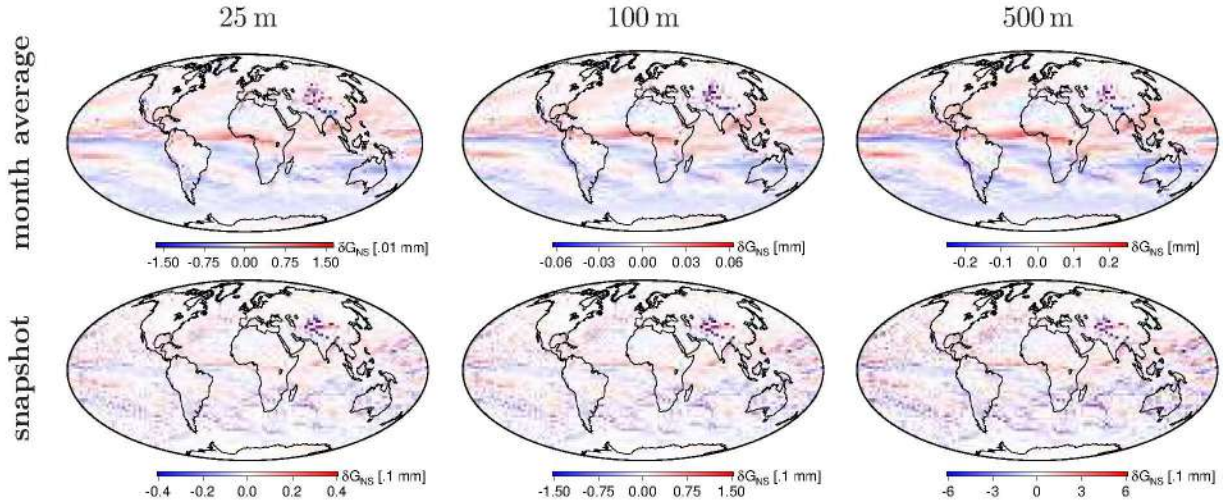


Figure 4.4.5: North-South tropospheric gradient component ties. Shown are the differences between ray-traced G_{NS} at the orography of ERA5 and virtual orographies 25 m (left), 100 m (middle), and 500 m (right) above. In the upper row shown are the δG_{NS} averaged over a month (2018/01), whereas in the lower row shown are the ties at the epoch 2018/01/01 00:00. Note the different color scales.

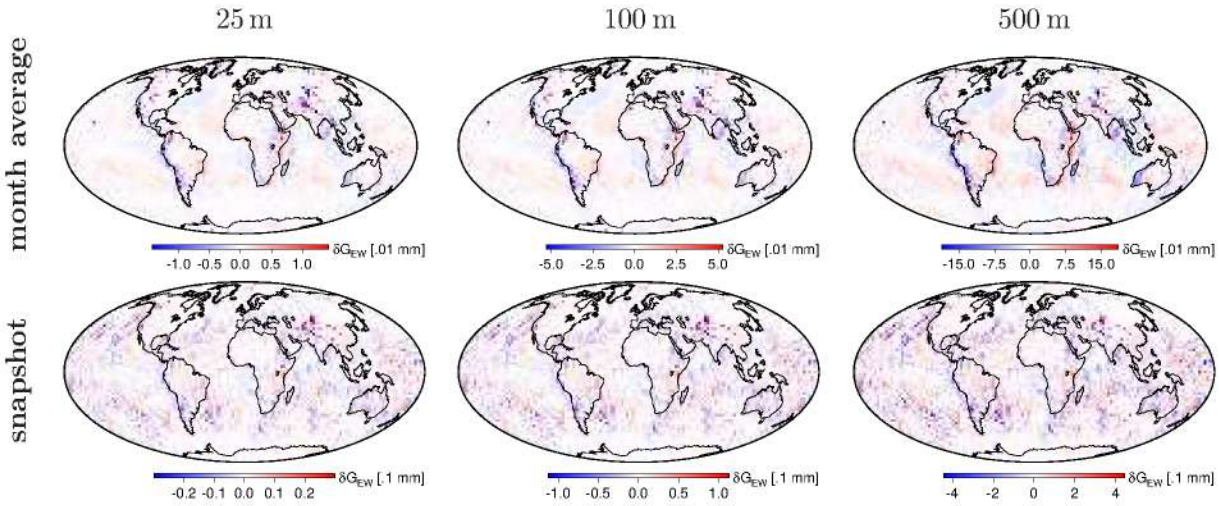


Figure 4.4.6: East-West tropospheric gradient component ties. Shown are the differences between ray-traced G_{EW} at the orography of ERA5 and virtual orographies 25 m (left), 100 m (middle), and 500 m (right) above. In the upper row shown are the δG_{EW} averaged over a month (2018/01), whereas in the lower row shown are the ties at the epoch 2018/01/01 00:00. Note the different color scales.

and j is as in (4.4.7). To illustrate this point, some examples follow:

$$\text{Utilizing gradients estimated for } \begin{bmatrix} 532 \\ 532 \\ 366 \\ 1064 \end{bmatrix} \text{ nm to correct laser ranges at } \begin{bmatrix} 1064 \\ 366 \\ 1064 \\ 366 \end{bmatrix} \text{ nm}$$

$$\text{biases the modelled observations at } 10^\circ \text{ by as much as } \begin{bmatrix} 3.1 \\ -5.4 \\ 8.5 \\ -8.5 \end{bmatrix} \text{ mm.}$$

Such modelling shortcomings potentially introduce a scale bias in the implied TRF. To overcome this issue, Balidakis et al. (tted) has developed analytical expressions that relate optical-based ray-tracing products (zenith delays, mapping functions, and gradients) at 532 nm to any other frequency in the optical spectrum.

Due to the fact that the vast majority of SLR observatories operate at 532 nm, this particular frequency is adopted for the remainder of this section.

By and large, optical d_h^z are on average 6 % larger than microwave, whereas optical d_{nh}^z are 66 times smaller than microwave. The latter stems from the fact that effects from the orientation polarization of the polar molecule of water vapour are negligible at optical frequencies. The two first columns of Fig. 4.4.7 and Fig. 4.4.8 illustrate the d_h^z and d_{nh}^z (respectively) from microwave and optical (532 nm) frequencies. Therefore, optical slant hydrostatic delays are always larger than the corresponding microwave-based delays, and optical slant non-hydrostatic delays are always smaller than the corresponding microwave-based delays. Nevertheless, microwave-based slant total delays are smaller than optical-based slant total delays only in dry conditions. At epochs/regions where the microwave d_{nh}^z is larger than 15 cm, the microwave-based slant delays are larger than the optical-based delays.

While the discrepancies between microwave and optical zenith delays are well understood

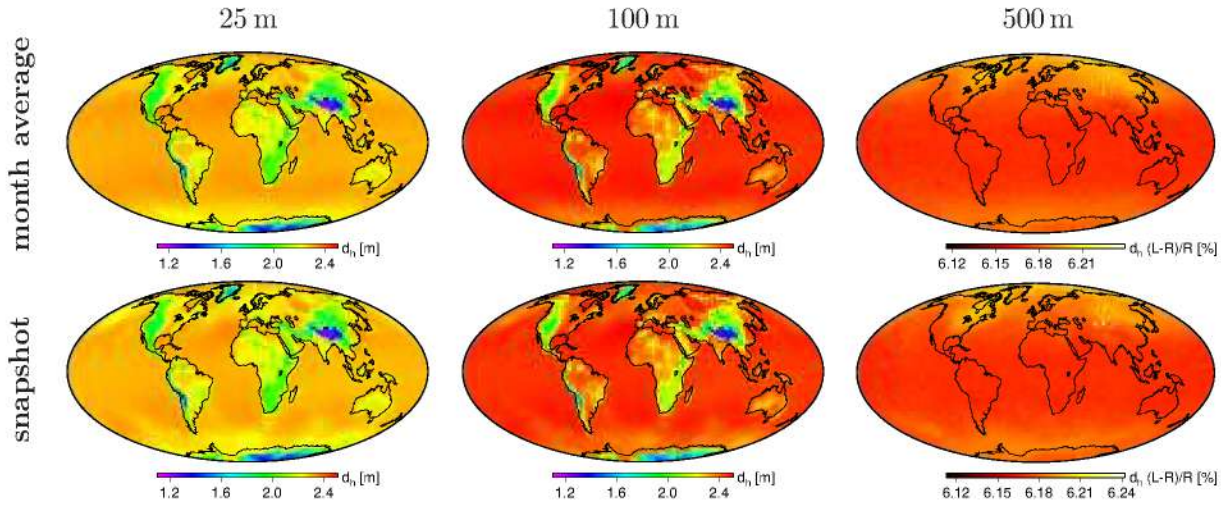


Figure 4.4.7: Inter-system d_h^z ties. Shown are the d_h^z for VLBI (left), and SLR (middle), calculated at the orography of ERA5. In the right column the amount the d_h^z is amplified from VLBI (R) to SLR (L) is illustrated. In the upper row shown are the results averaged over a month (2018/01), whereas in the lower row shown are results at the epoch 2018/01/01 00:00. Note the different color scales.

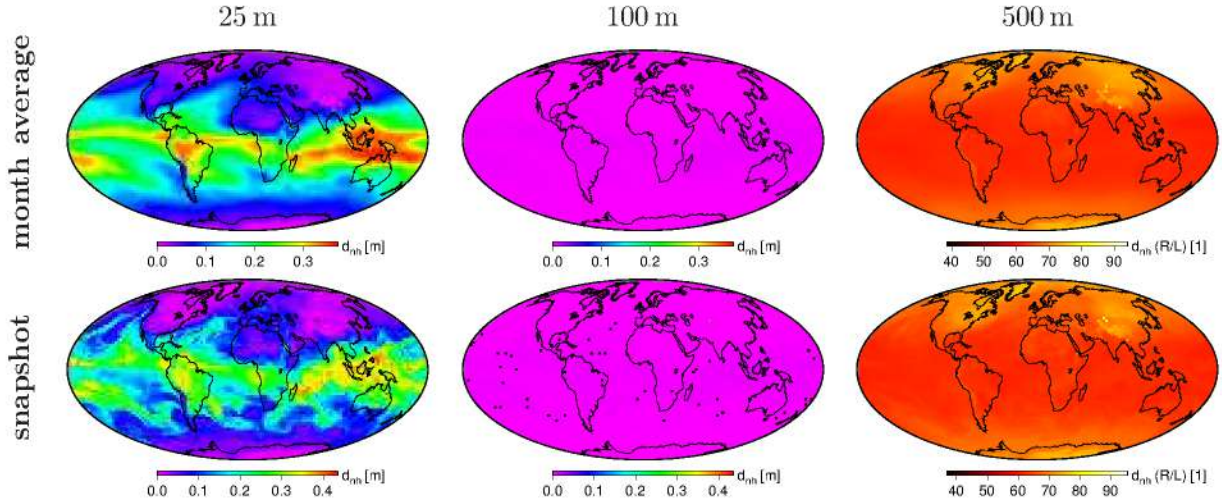


Figure 4.4.8: Inter-system d_{nh}^z ties. Shown are the d_{nh}^z for VLBI (left), and SLR (middle), calculated at the orography of ERA5. In the right column the d_{nh}^z ratio of VLBI (R) to SLR (L) is illustrated. In the upper row shown are the results averaged over a month (2018/01), whereas in the lower row shown are results at the epoch 2018/01/01 00:00. Note the different color scales.

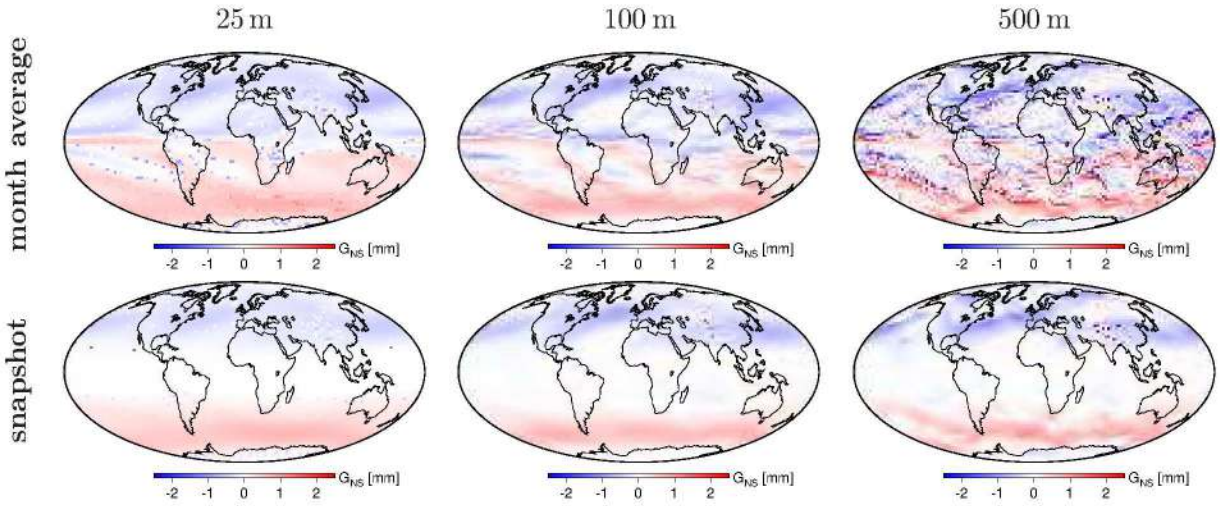


Figure 4.4.9: The long-term average G_{NS} (left), averaged over a month (2018/01) G_{NS} (middle), and G_{NS} at the epoch 2018/01/01 00:00 (right). Displayed are GNSS (upper), and SLR (lower) results.

and appropriately modelled, such a statement does not hold for the atmospheric delay gradients. There are surprisingly few studies dealing with tropospheric asymmetries in SLR (e.g., Hulley and Pavlis, 2007) especially in view of the fact that the SLR observation geometry hinders the independent (without heavy absolute constraints) gradient estimation, and that the gradient concept was proposed for satellite ranging in the first place (Gardner, 1976).

Gradients estimated from the analysis of microwave-based space geodetic techniques such as GNSS cannot be used in SLR/LLR data processing, in general. Unlike zenith delays, the tie of which is describable by a single scaling factor, such an approach is inapplicable to gradient components mainly due to the lack of wet refractivity gradients that minimizes ray-bending. In Fig. 4.4.9 and Fig. 4.4.10 G_{NS} and G_{NS} estimates are presented, respectively, from ray-tracing in ERA5. The first observation to make is lack of tropospheric asymmetries for SLR-derived gradients for $|\varphi| < 30°$, a fact associated to the water vapour not affecting considerably the propagation delay. Second, thrice the long-term averaged, the monthly averaged, and the "snapshot" SLR-derived gradients do not display differences as large as the microwave gradients. Figure 4.4.11 attests to that statement by displaying the annual amplitudes. Spatial coherence between the GNSS-derived and the SLR-derived gradients is achieved only in polar, sub-polar regions, as well as in dry regions in the warm temperate zone, whereas in the Torrid zone the largest differences are found. There lie the largest systematic GNSS-derived gradient variations alternating a slant delay at 7° by as much as 4 cm with an annual cycle. While there is some theoretical merit in relating dry (or hydrostatic) gradients from ray-tracing in the GNSS configuration to the corresponding thereof from the SLR configuration with e.g., a scaling scheme, such a feat can find no practical application for estimating dry and wet gradients from the analysis of GNSS observations is impossible without additional information from weather models (e.g., scale heights). Figure 4.4.12 illustrates the spatial correlation between gradient amplitudes and phases derived from ray-tracing in hourly ERA5 fields at Yarragadee and the neighbouring nodes of ERA5. It is apparent that the decorrelation distance is much smaller for microwave than optical gradients. The latter further supports that employing GNSS-derived gradients to reduce SLR observations is a poor choice.

Second, the systematic differences in slant atmospheric delays at low elevation angles between VLBI, GNSS, and DORIS, stem from ray-bending (Zus et al., 2015a). For a station observing at

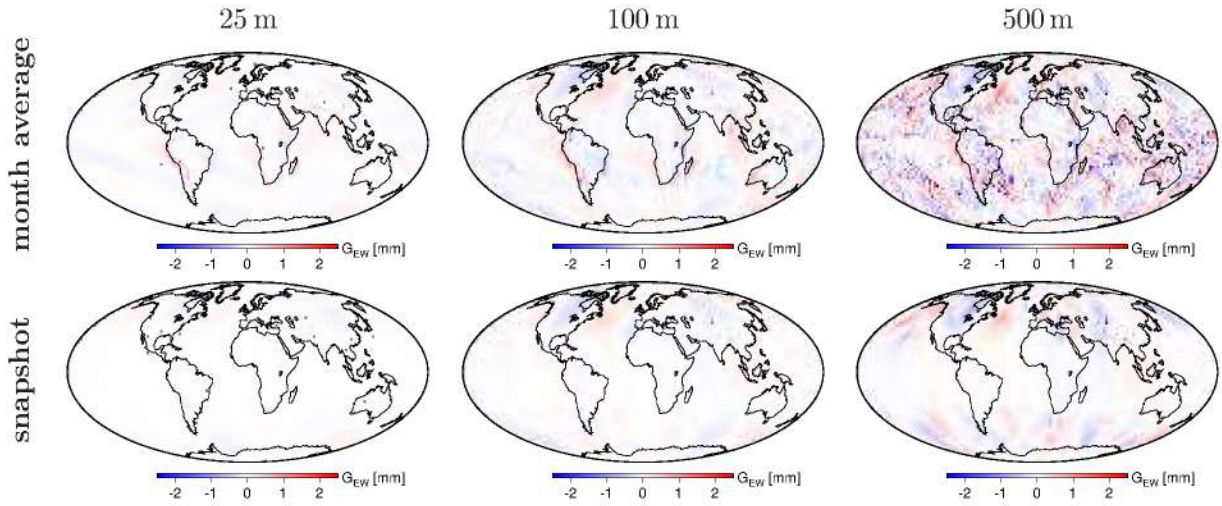


Figure 4.4.10: The long-term average G_{EW} (left), averaged over a month (2018/01) G_{EW} (middle), and G_{EW} at the epoch 2018/01/01 00:00 (right). Displayed are GNSS (upper), and SLR (lower) results.

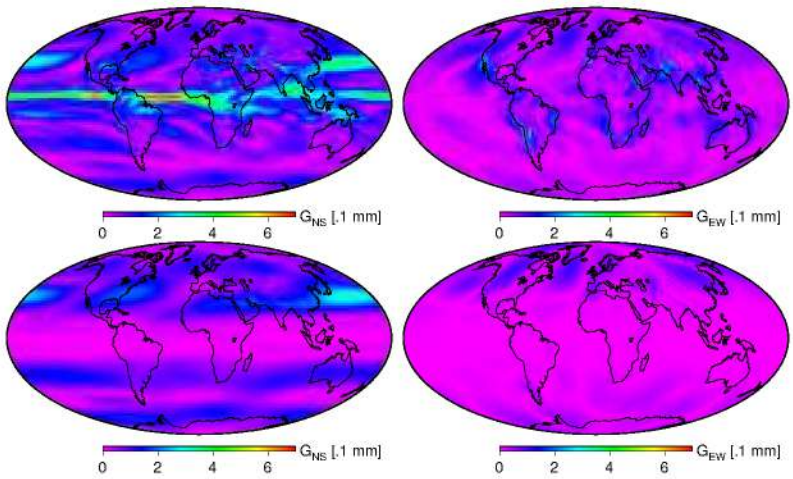


Figure 4.4.11: The S_a amplitude of GNSS-based (upper), and SLR-based (lower) G_{NS} (left), and G_{EW} (right) from GFZ-PT (cf. 4.3).

a given elevation angle, the lower the orbital altitude of the target, the larger the ray-bending, and therefore the larger the atmospheric delay. Zenith delays are in essence insensitive to the actual target orbital altitude, provided the latter is higher than the upper limit of the atmospheric density tensors employed in ray-tracing (usually 150 km). Nevertheless, gradient components and mapping function coefficients are affected.

Comparing tropospheric gradients estimated from ray-tracing to targets at different orbital altitudes (e.g, infinity for VLBI, 20 180 km for GPS, and 1000 km for DORIS) yields a small bias; the closer the target is to Earth's surface, the larger the larger asymmetries in an absolute sense. The impact of the gradient differences between GNSS and VLBI on the slant delay is as large as 0.1 mm at 3°. Nevertheless, the gradient differences between DORIS and VLBI are one order of magnitude larger, ranging to 1 mm at 5°. For current geodetic applications, these systematic effects are at least an order of magnitude below the noise level of the observations. Therefore, they can be ignored for present-day applications.

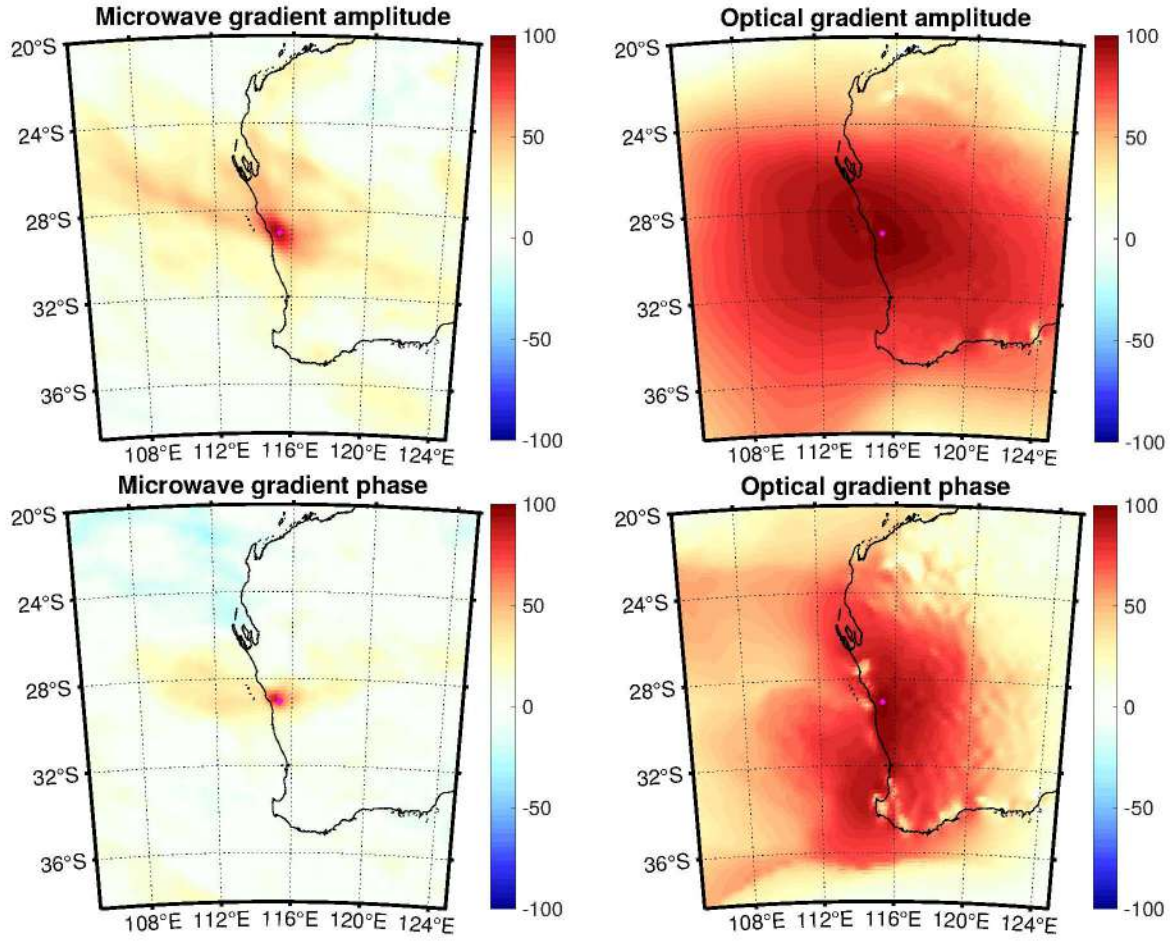


Figure 4.4.12: The spatial correlation between gradient amplitude (upper row) and phase (lower row) time series from ray-tracing in ERA5-derived microwave (left) and optical at 532 nm (right) refractivity fields at Yarragadee (in the middle of the figures) and the neighbouring grid nodes.

While the orbital altitude has a fairly small impact on the tropospheric gradients, it does affect the mapping factors considerably. This systematic error potentially manifests into a scale bias in reference frames determined employing erroneous mapping functions. As the zenith delays do not change as a function of orbital altitude but the ray-bending increases with decreasing orbital altitude, the relationship for mapping functions in the microwave domain is:

$$mf^{D}_{h,nh} \gg mf^{P}_{h,nh} > mf^{R}_{h,nh} \gg mf^{L}_{h,nh} \tag{4.4.9}$$

where for DORIS (D) Envisat was assumed, for GNSS (P) GPS was assumed, for VLBI (R) a quasar was assumed, and for SLR (L) LAGEOS-1 was assumed.

Figure 4.4.16 displays the differences in slant total delays between GNSS-VLBI, and DORIS-VLBI. The latter are one order of magnitude larger than the former. Due to GNSS observations with $\varepsilon < 7°$ usually not being considered for geodetic applications, the maximum systematic height error of utilizing mapping functions tailored for VLBI in GNSS processing would be 0.1 mm. Nevertheless, should VLBI-tailored mapping functions be used to analyze DORIS observations, the corresponding height error exceeds the 1 mm level, and therefore should be considered. Unlike GNSS satellites that orbit on similar altitudes — with the exception of QZSS –

DORIS and especially SLR targets do not share this attribute; for instance, laser ranging can be performed from LEOs such as GRACE-FO to targets on the moon (LLR). Moreover, there are a number of studies where LEO navigation satellites are utilized to augment the positioning accuracy e.g., in the framework of the project ADVANTAGE[8] (Advanced Technologies for Navigation and Geodesy). This implies the necessity for different mapping functions for different targets. Nevertheless, such a endeavour is impractical for operational use. To relate the mapping factors corresponding to different orbital altitudes, an analytical expression has been developed herein:

$$
\begin{aligned}
mf_i\left(H_o, H_s\right) &= ae^{-b\log(H_o)} + mf_i^R \\
a\left(H_s\right) &= \begin{cases} 0.75 + -5.3 \times 10^{-5}\,\mathrm{H}_s, & \text{for } i = h \\ 2.23e^{-1.2\times10^{-4}\,\mathrm{H}_s} + 6\times10^{-3}\,\mathrm{e}^{7\times10^{-4}\,\mathrm{H}_s}, & \text{for } i = nh \end{cases} \\
b\left(H_s\right) &= \begin{cases} 0.62 + 2.8\times10^{-6}\,\mathrm{H}_s, & \text{for } i = h \\ 0.62, & \text{for } i = nh. \end{cases}
\end{aligned}
\tag{4.4.10}
$$

The a and b coefficients in (4.4.10) have been estimated by a least-squares adjustment of ray-traced delays at several orbital altitudes ($H_o = \begin{bmatrix}0.15 & 0.2 & 0.25 & 0.5 & 1 & 5 & 10 & 20 & 50 & 385\end{bmatrix}^\top 1000\,\mathrm{km}$) . These coefficients could be approximated to the first order by constants; for the hydrostatic mapping factor it is $a = 0.74$ (0.04) and $b = 0.62$ (0.002), and for the non-hydrostatic mapping factor it is $a = 2.20$ (0.08) and $b = 0.62$ (0.005) — the variability is enclosed in parentheses.

Comparing DORIS-derived, GNSS-derived, and VLBI-derived tropospheric gradient components from consistent ray-tracing, no difference large enough to make an impact on the geodetic data analysis was found. Figure 4.4.13 and Fig. 4.4.14 attest to that statement illustrating that the differences although being systematic and spatially correlated with the signal, are at the 1 mm level for elevations as low as 5°. Certainly these differences are amplified at even lower elevations, but at elevation angles as low as that, the assumptions under which the ray-tracing software used in this work operates cease to hold. Hence, if there is no height difference between two differenct microwave instruments, gradient components can be stacked without the application of relevant atmospheric ties.

The orbital altitude dependence in SLR could have implications in precise orbit determination (POD) as the altitude of the targets varies from 200 km (e.g., GOCE), to 19 140 km (e.g., GLONASS), to 385 000 km (Moon). For instance, Fig. 4.4.15 illustrates the modelling errors in laser observations towards GRACE-FO induced by adopting the latest IERS standards. Nevertheless, due to the fact that SLR and LLR do not range close to the horizon (typically it is $\varepsilon > 10°$), in essence, the optical mapping functions are marginally affected whatsoever.

Since ray-bending is induced by refractivity gradients, the discrepancies between mapping functions for LEOs and VLBI are larger while ray-tracing in 3D mode employing meso-γ NWMs.

[8] https://hgf-advantage.de/

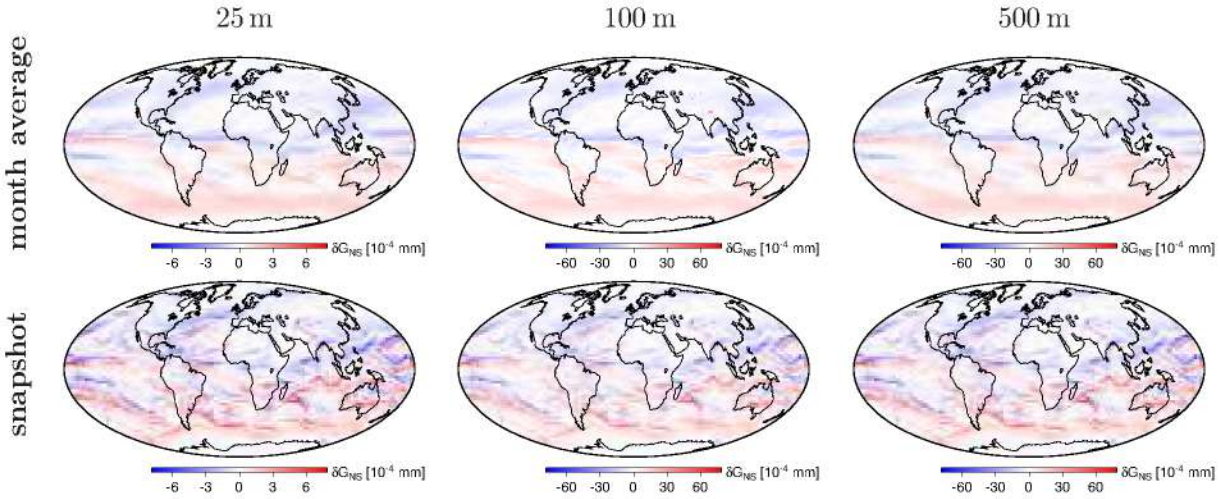


Figure 4.4.13: Shown are the long-term discrepancies between G_{NS} tailored for the different microwave-based techniques. Shown are the differences between GNSS and VLBI (left), DORIS and GNSS (middle), and DORIS and VLBI (right), averaged over a month (upper row) and at the epoch 2018/01/01 00:00 (lower row).

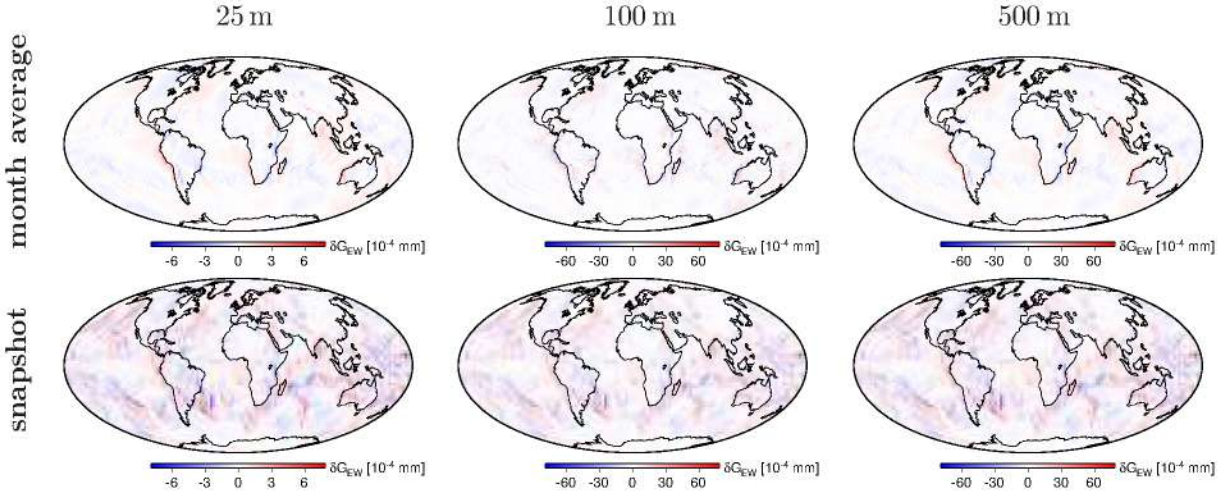


Figure 4.4.14: Shown are the long-term discrepancies between G_{EW} tailored for the different microwave-based techniques. Shown are the differences between GNSS and VLBI (left), DORIS and GNSS (middle), and DORIS and VLBI (right), averaged over a month (upper row) and at the epoch 2018/01/01 00:00 (lower row).

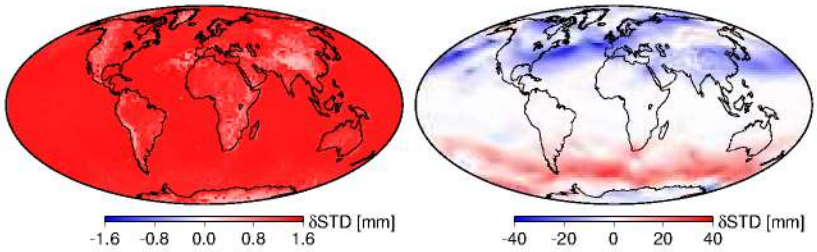


Figure 4.4.15: Error in the atmospheric delay corrections for laser ranges towards GRACE-FO induced by not accounting for the orbital altitude (left), or the atmospheric asymmetries (right). Shown are the results from ray-tracing in ERA5 fields, at 532 nm, for 0° azimuth and 10° elevation.

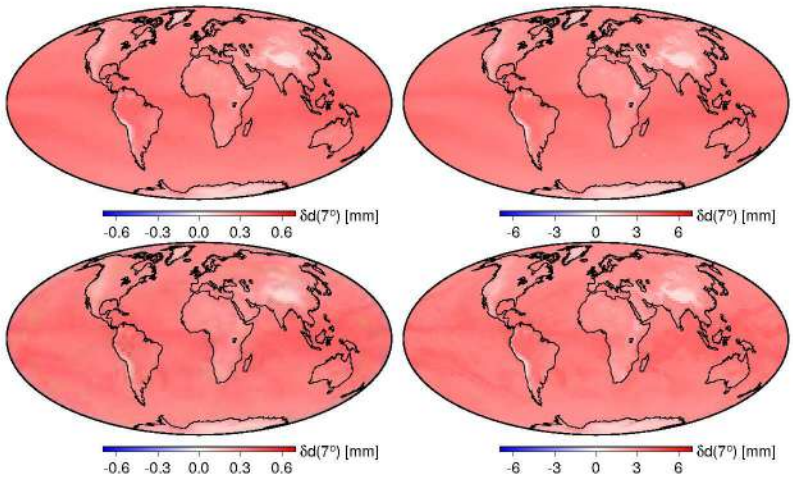


Figure 4.4.16: The differences in slant symmetric delays at 7° between GNSS-VLBI (left), and DORIS-VLBI (right), stemming from the orbital altitude dependence are presented. The results averaged over a month (2018/01) are in the upper row, whereas the results at the epoch 2018/01/01 00:00 are illustrated in the lower row. Note the different color scales.

5 Development of geophysical loading models

Gravity field variations, Earth orientation alterations and deformations at the surface of the Earth are a manifestation of numerous geophysical processes that involve the atmospheric and oceanic circulation, as well as the hydrological cycle (e.g., Wu et al., 2012). Crustal motion at a multitude of spatial and temporal scales is partly driven by mass redistribution occurring within the fluid envelope of the Earth, including the atmosphere, the oceans and the continental water storage. Unlike tidal-induced mass redistribution, which is governed by ocean processes, non-tidal mass variations are mainly due to barometric pressure anomalies and horizontal transport of hydrological mass. The site position displacement due to geophysical loads imposed on the crust of the Earth can be monitored by space geodetic techniques such as VLBI (e.g., Petrov and Boy, 2004; Boehm et al., 2009), GNSS (e.g., Tregoning and van Dam, 2005a,b; Fritsche et al., 2012; Dach et al., 2011; Männel et al., 2019) and SLR (e.g. Bock et al., 2005; Sośnica et al., 2013). Although geophysical loading is not the major error source for parameters estimated from geodetic analysis (e.g., compared to the propagation delay induced by the refractive index of moist air in the electrically neutral atmosphere), it is of paramount importance not to be left unaccounted. Some implications that may arise from such an omission are related to the scale of the realized terrestrial reference frame, strong modulated signals at synoptic and seasonal periods especially in the estimated station coordinates and EOPs, and the estimated satellite orbits.

Geophysical non-tidal loading effects can displace geodetic monuments as much as 100 mm in the radial component and 20 mm on the lateral plane, based on calculations carried out herein. At seasonal timescales, continental water storage loading (CWSL) dominates the total loading signal, whereas non-tidal atmospheric pressure loading (NTAL) and non-tidal ocean loading (NTOL) are responsible for synoptic displacements instead (Boy and Lyard, 2008; Dill and Dobslaw, 2013). For VLBI the differential nature of observations together with the No-Net-Rotation and No-Net-Translation constraints imposed on station positions and velocities, introduce the propagation of the effect of neglected geophysical loading corrections at a station to all others (e.g., Boehm et al., 2009). While a similar scenario applies to GNSS, the fact that the global VLBI network geometry is relatively poor highlights all network effects resulting in spurious motion of the stations. Today's goal of 1 mm measurement accuracy on global baselines in the framework of VLBI Global Observing System (VGOS), has rendered the employment of a priori models that describe the crustal deformation with sub-mm accuracy essential (Petrachenko et al., 2009).

In this chapter, the approach employed to simulate displacements of Earth's crust in the presence of geophysical loads imposed by the atmosphere, the oceans and terrestrially stored water is outlined in Sec. 5.1, where the impact of several possibilities of the calculation process are assessed (e.g., ocean response to atmospheric forcing and Green's kernels). Fluid-specific intricacies are analyzed separately; Sec. 5.2 for the atmosphere, Sec. 5.3 for the oceans, and Sec. 5.4 for the continental hydrology. With the exception of the atmosphere, tidal effects are not discussed herein. The models developed here are compared with state-of-the-art models of several institutes that employ a large variety of data sets forcing the mass anomalies, e.g., ERA Interim, ECMWF's operational analysis, ECCO, ECCO2, MPIOM, GLDAS, MERRA,

MERRA2, LSDM, and GRACE. Simply by differencing two geophysical loading models it is impossible to infer whether the former outperforms the latter or otherwise. However, for several models tested herein the differences between them in the spatial as well as in the frequency domain warrant an assessment anew. Developed here, a grid-based function conceptually similar to GFZ-PT (Sec. 4.3) that returns displacements due to the accumulated loading and the components thereof, the empirical geophysical loading model (EGLM) is introduced in Sec. 5.5.

Detailed study of gravitational consistency and mass conservation on surface loads— still a subject of scientific debade—(Clarke et al., 2005; Fritsche et al., 2012) is beyond the intended scope of this work.

5.1 Simulation of geophysical loading deformations

To mass variations at synoptic (barometric pressure anomalies and circulatory changes in ocean bottom pressure) and seasonal timescales (terrestrial water storage), assuming a solely elastic response of the crust of the Earth is a sound approximation (e.g., Dill et al., 2015). This is due to the Maxwell's viscoelastic relaxation time of the crust of the Earth ranging from several decades to thousands of years. For geophysical processes such as glacial isostatic adjustment and post-seismic deformation that take place on longer timescales (thousands of years and decades, respectively), viscoelasticity and anelasticity must be considered. Since this work is concerned with short-periodic mass redistribution, the yield of Earth's crust is assumed instantaneous, thus the superposition principle can be safely adopted (e.g., Dill et al., 2015).

In the past, displacements induced by pressure anomalies (atmospheric pressure loading effects) were mitigated employing a transfer function between the locally measured pressure and the estimated vertical deformation (barometric admittance or pressure loading coefficient) (e.g., MacMillan and Gipson, 1994). Due to not accounting (among else) for the long wavelength synoptic pressure systems (e.g., tropical cyclones[1] and continental anticyclones[2]) that are responsible for the largest pressure fluctuations, this approach was abandoned.

To date, the most accurate approach to model elastic surface loading deformations was introduced by Farrell (1972). Under the assumption that all disturbing masses are condensed into an infinitesimally thin layer on the surface of the Earth, for a spherically symmetric, non-rotating, isotropic, self-gravitating, linear viscoelastic Earth model (SNREI), the response to surface loads can be simulated by performing a global convolution sum between mass anomalies (atmospheric pressure, ocean bottom pressure and terrestrial water storage) and either elastic load Love numbers, LLN (spectral domain), or load Green's function kernels, LGF (spatial domain).

Being a square-integrable function, the mass anomaly field $\delta\mathbf{P}$ can be represented by an infinite series of solid spherical harmonics, as the general solution to the Laplace's field equation, $\nabla^2(\delta P) = 0$, that is,

$$\begin{aligned} \delta P(\vartheta,\lambda) &= \sum_{n=0}^{\infty}\sum_{m=-n}^{n} \psi_{nm}\bar{Y}_{nm}(\theta,\lambda), \\ \bar{Y}_{nm}(\vartheta,\lambda) &= \bar{P}_{n|m|}(\cos(\vartheta))e^{im\lambda}, \end{aligned} \tag{5.1.1}$$

where ψ_{nm} is the dimensionless Stokes' coefficient of degree n and order m, $\bar{Y}_{nm}$ is the corre-

[1] A storm or a system of winds that rotates around a center of low atmospheric pressure (indicators of clouds, rain, and in general bad weather). It comprises of counterclockwise winds on the Northern hemisphere.

[2] A system of winds that rotates around a center of high atmospheric pressure (predictors of fair weather).

sponding harmonic, $\bar{P}_{nm}$ is the fully normalized associated Legendre's function, and $\vartheta = \pi/2 - \varphi$ is the polar angle. The time dependent degree variance (spectral power) of a field, defined as

$$\sigma_n^2(t) = \sum_{m=-n}^{n} \psi_{nm}^2(t), \tag{5.1.2}$$

denotes the total signal power at a certain degree n. The smallest representable feature (half-wavelength) resolvable by $(n+1)^2$ parameters could be approximated by $\lambda(n) \approx \pi R_\oplus/n$, with $R_\oplus$ denoting the mean radius of the Earth. Submitting the mass anomaly fields to global spherical harmonic analysis indicates that unlike atmospheric pressure anomalies, that are dominated by large structures ($\lambda > 4.000\,\mathrm{km}$ with $\mathrm{S_a}$ periods, cf. Fig. 5.1.1), non-tidal variations arising from mass exchange within the oceans and the continental hydrology are dominated by high-degree Stokes' coefficients (e.g., in the vicinity of semi-enclosed bays and large river basins, respectively). The global spherical harmonic analysis was carried out following Sneeuw (1994); Fukushima (2012). Although fields from ERA5 (a reanalysis product) have been used to build the mass anomaly fields illustrated in Fig. 5.1.1, an inconsistency is discernible at epoch 2015.0. This feature was not detected in the ERA5-Land dataset[3]. Theoretically, convolving the spatial redistribution of surface loads with either the LLNs or the LGFs corresponding to an elastic homogeneous half-space is supposed to yield identical results. Nevertheless, to resolve high-degree features, global spherical harmonic analysis to a very high degree is necessary, which renders the LLN approach computationally inefficient.

In most models (atmospheric, oceanic and hydrological) for the representation of the surface and of the model physics a grid point system is utilized instead of a spectral formulation. In point of fact, with increased resolution and the introduction of the semi-lagrangian technique (e.g., for ECMWF-based models) there is no longer any significant difference in accuracy between the spectral and grid point representations. Nevertheless, due to the fact that explicit dynamics, semi-Lagrangian advection and physical parametrizations are estimated in grid point space, and that mass anomalies display features not resolvable by the number of Stokes' coefficients employed for the original model, herein it is decided to conduct the investigations in grid point space. The latter further attests to the selection of the LGF approach.

For the LGF case, the elastic displacements due to geophysical loading (atmosphere, ocean or hydrology) at a point in the topocentric coordinate system (radial u_R, North-South u_{NS}, and East-West u_{EW} displacement) are calculated as follows (e.g., Farrell, 1972)

$$\begin{aligned} u_R(\mathbf{r},t) &= \iint \delta P(\mathbf{r}',t)\mathcal{G}_{\mathcal{R}}(\psi)\cos(\phi')\,d\phi'\,d\lambda', \\ u_{NS}(\mathbf{r},t) &= \iint \delta P(\mathbf{r}',t)\cos(\alpha)\mathcal{G}_{\mathcal{L}}(\psi)\cos(\phi')\,d\phi'\,d\lambda', \\ u_{EW}(\mathbf{r},t) &= \iint \delta P(\mathbf{r}',t)\sin(\alpha)\mathcal{G}_{\mathcal{L}}(\psi)\cos(\phi')\,d\phi'\,d\lambda', \end{aligned} \tag{5.1.3}$$

where ψ and α are the angular distance[4] and the azimuth between the point of interest $\mathbf{r}$ and point to which each mass anomaly δP refers to $\mathbf{r}'$, respectively, The LGFs $\mathcal{G}_{\mathcal{R},\mathcal{L}}$, that are non-

[3] ERA5-Land is a dedicated simulation pertinent only to surface and near surface variables, stems from ERA5 atmospheric forcing, and features a higher spatial resolution (9 km) and a thermodynamic orographic adjustment (https://confluence.ecmwf.int/display/CKB/ERA5-Land+data+documentation). In general the "Land" versions of ERA Interim or ERA5 are to be preferred should the focus of the study be placed on hydrological parameters such as soil moisure and snow (H. Dobslaw, personal communication).

[4] $\psi = \cos^{-1}\left(\cos(\vartheta_{\mathbf{r}})\cos(\vartheta_{\mathbf{r}'}) + \sin(\vartheta_{\mathbf{r}})\sin(\vartheta_{\mathbf{r}'})\cos(\lambda_{\mathbf{r}} - \lambda_{\mathbf{r}'})\right)$

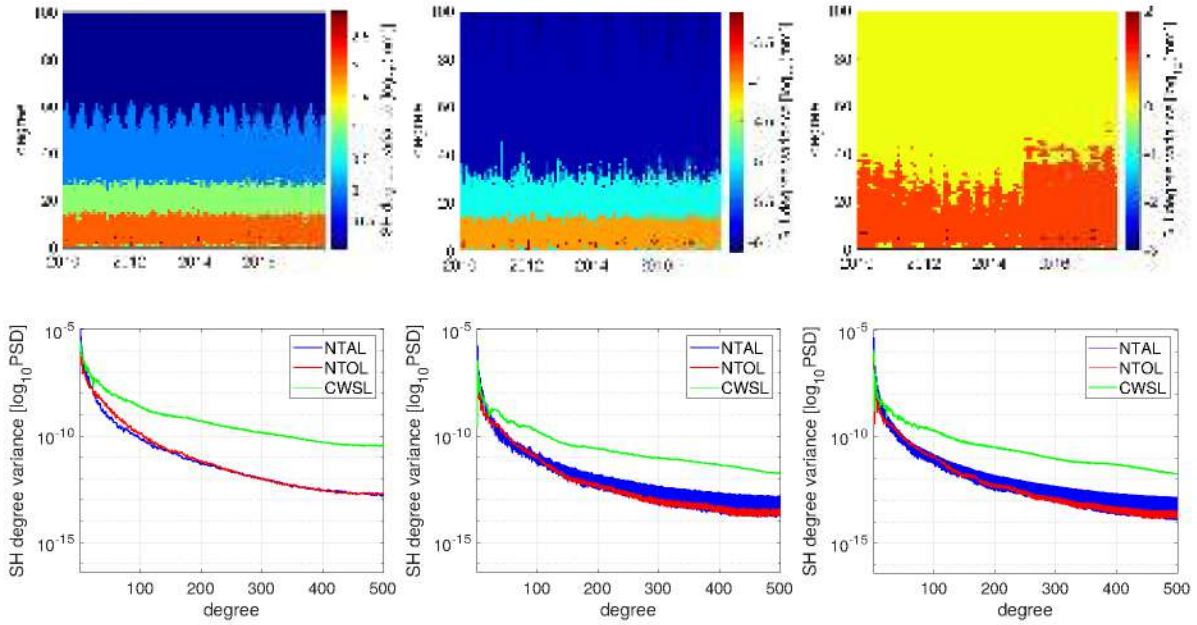


Figure 5.1.1: Spectral power of the orography-discrepancy-adjusted surface pressure fields of ERA5 (upper left), the EWH from Mog2D-G ocean bottom pressure anomalies (upper right), and the EWH from the hydrological mass variations from ERA5 (lower left), at a trimmed spectral range, as a function of spherical harmonic degree. The spherical harmonic degree variance of the mass anomalies for the individual loading contributions at one epoch are shown in the second row for the radial (left), North-South (middle), and East-West (right) coordinate component. Note the different color scales.

dimensional factors between a source (mass anomaly induced by altering gravitational potential) and its associated consequences (e.g., displacement of geodetic monuments) stem from the LLNs

$$\begin{aligned} \mathcal{G}_{\mathcal{R}} &= \frac{R_\oplus}{M_\oplus}\sum_{n=0}^{\infty} h_n P_n(\cos\psi), \\ \mathcal{G}_{\mathcal{L}} &= \frac{R_\oplus}{M_\oplus}\sum_{n=0}^{\infty} l_n \frac{\partial P_n(\cos\psi)}{\partial\psi}, \end{aligned} \tag{5.1.4}$$

where $R_\oplus$ and $M_\oplus$ denote the average Earth radius (6371 km) and mass ($5.972{\cdot}10^{24}$ kg), respectively. The harmonic coefficients of the radial h_n and the tangential l_n displacement component are the LLNs. The Legendre's functions of degree n, P_n, are calculated with the well known recurrence relations (e.g., Holmes and Featherstone, 2002). In this study, Kummer's transformation method was adopted to perform the related calculations

$$\begin{aligned} \mathcal{G}_{\mathcal{R}} &= \frac{R_\oplus h_\infty(1-2\sin\frac{\psi}{2})}{2M_\oplus\sin\frac{\psi}{2}} + \frac{R_\oplus}{M_\oplus}\sum_{n=1}^{n}(h_n-h_\infty)P_n(\cos\psi), \\ \mathcal{G}_{\mathcal{L}} &= \frac{R_\oplus l_\infty\cos\frac{\psi}{2}(1+2\sin\frac{\psi}{2})}{2M_\oplus\sin\frac{\psi}{2}(1+\sin\frac{\psi}{2})} + \frac{R_\oplus}{M_\oplus}\sum_{n=1}^{n}\frac{nl_n-l_\infty}{n}\frac{\partial P_n(\cos\psi)}{\partial\psi}. \end{aligned} \tag{5.1.5}$$

The sums in (5.1.5) have to be evaluated to a very high degree, usually $n \geq 9000$, for only when $n \to \infty$ does approximating Earth by a homogenious half-sphere holds. Herein the

sums were evaluated up to $n = 50000$ (below 1 km wavelength), to improve the precision. In similar fashion, quantities such as gravity anomalies and strain tensor components are calculated, alternating the LGF. Unlike tilts and gravity anomalies that require decomposing the impact of loading to a direct effect excerted by the gravitational attraction of the load (Newtonian attractive force), and an indirect effect stemming from the deformation of the surface of the Earth, only the latter is of interest here. Hence, the attraction excerted by the overlying air masses that requires to account for the 3D air density redistribution is not treated here. To enforce the conservation of the total mass, the degree-zero term in the LGF expansion is not retained.

To evaluate (5.1.3) lie a number of possibilities that significantly alter the estimated displacements: the mass anomalies themselves, the Earth model on which the LLNs are based, the land-sea mask, the ocean response to atmospheric forcing, and the spatial and temporal resolution of all the above. In the sequel, the state-of-the-art is reviewed and enhanced.

5.1.1 Impact of the elastic Earth model

For an Earth model, a field of elastic gravitational ordinary-differential equations, that relates the deformability to seismic S- and P-wave velocities and density, is solved for a spherical, compressible, elastic, self-gravitating Earth employing e.g., Runge-Kutta or Chebyshev-collocation methods (e.g., Guo et al., 2004). The solution of this six-equation-system yields parameters necessary for the computation of the elastic or viscoelastic LLN and thereupon the computation of LGF for radial stress and displacement, tangential stress and displacement, and gravitational potential. Differences in the properties of the crust of different models mainly affect LLNs of high-degree thus influencing LGFs at small ψ (usually, below 3°).

The LLNs and LGFs that are convolved with the mass anomaly fields to simulate geophysical loading displacements are usually computed for the preliminary reference Earth model PREM (Dziewonski and Anderson, 1981). Despite refined elastic Earth models such as the `iasp91` (Kennett and Engdahl, 1991), the `ak135` (Kennett et al., 1995), the `STW105` (Kustowski et al., 2008), `Crust 2.0` (Laske et al., 2012), `Crust 1.0` (Laske et al., 2013), and `TEA12` (Tesauro et al., 2012) having been released subsequently, PREM is still the most widely utilized Earth model.

Herein, the impact of the Earth model from which the LLNs and LGFs are estimated has been assessed. Employing the related load deformation coefficients (e.g., reported in Wang et al., 2012) and Kummer's transformation (5.1.5), the LGF were calculated for all aforementioned Earth models, as well as for "soft" and "hard" sediment scenarios for the outermost layers of PREM, `iasp91` and `ak135`, from the global average of `Crust 2.0` (Laske et al., 2012). The left panels of Fig. 5.1.2 illustrate the globally averaged LGFs for radial and tangential displacement coordinate components. Comparing the upper to the lower row, it is obvious that the radial displacement is expected to be larger compared to the tangential displacement.

The impact of the elastic Earth model on the geophysical loading signal was assessed based on mass anomalies from NWM data. Injecting hourly ERA5 fields to the geophysical loading simulator developed here, NTAL displacements were generated alternating the Earth model between those shown in Fig. 5.1.2. Figure 5.1.3 illustrates the differences between simulated NTAL displacements at two inland sites alternating the Earth model between modified crustal rheologies of PREM, `ak135`, and `iasp91`, with respect to PREM. The elastic Earth model employed to calculate the LLN and subsequently the LGF does not introduce a long term bias (well below 0.04 mm for all grid nodes) in the simulated NTAL displacements, as expected. Nevertheless, the amplitude of the S_a signal can change up to 0.2 mm, and occasionally the differences exceed 0.5 mm. For sites far from the coast the RMS between series of displacements simulated with

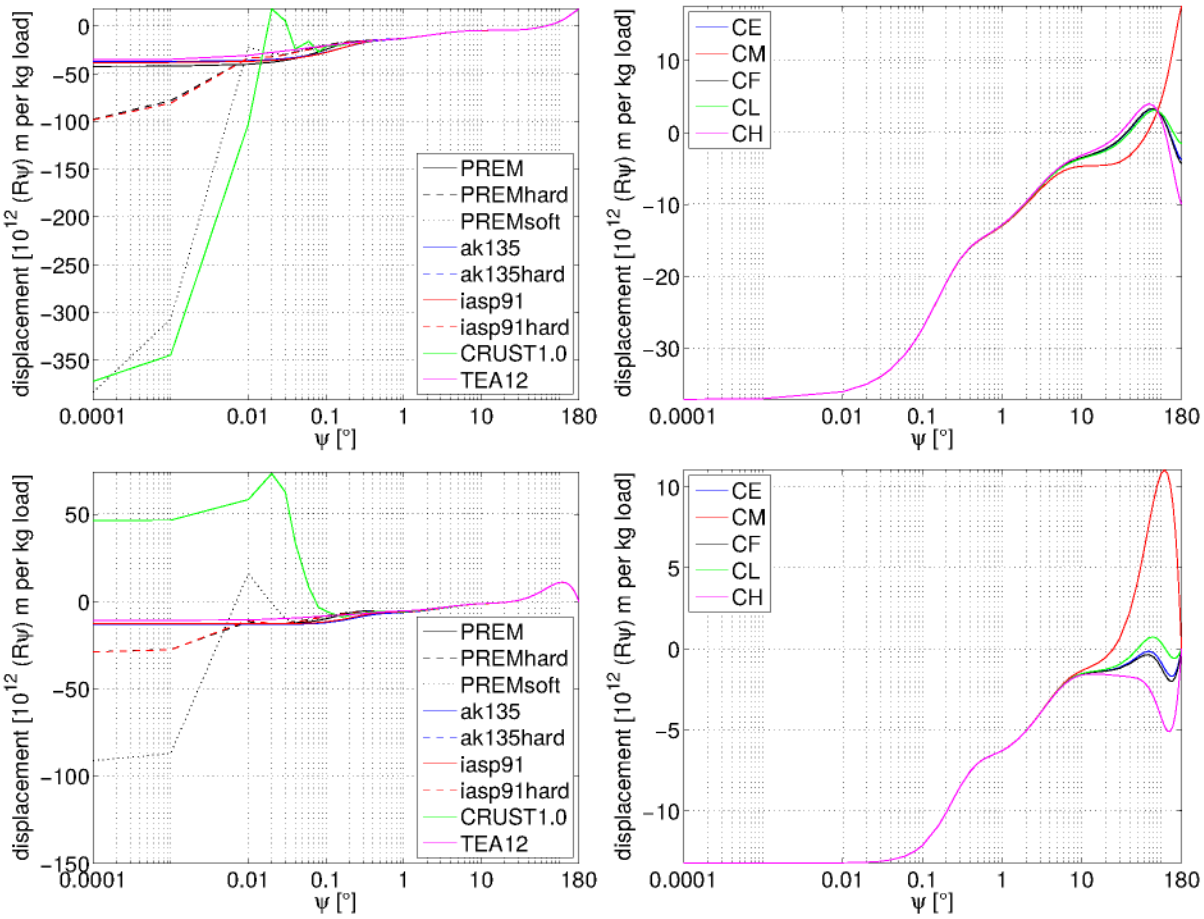


Figure 5.1.2: Load Green's functions for the radial (upper) and the tangential (lower) displacement component. The global Green's functions from Earth models (PREM, `iasp91`, and `ak135`) with varying crustal structures are illustrated, as well as local Green's functions (`Crust 1.0` and `TEA12`), averaged for the sake of illustration, in the center-of-mass isomorphic reference frame (left). For `ak135`, the displacements are presented in the center of mass of the solid Earth (CE), the center of mass of the entire Earth system (CM), the center of surface figure (CF), the center of surface lateral figure (CL), and the center of surface of height figure (CH).

different Earth models is as large as 0.3 mm. The impact of the LGF are more prominent in the radial components, where the signal is larger. The accuracy of state-of-the-art geodetic observations does not allow an independent evaluation of the performance of the aforementioned Earth models because both the uncertainty of the related observations as well as the scatter of the post-fit residuals of the geodetic adjustment are larger compared to the differences between the models presented herein.

In addition to the elastic Earth model, the LLNs and LGFs are also dependent upon the ever-changing relation between the origin of the frame and the surface of the Earth. The latter is driven by Earth's crust response to the degree-one spherical harmonic component of the mass load imposed on its surface. The degree-one spherical harmonic mode expands one hemisphere and compresses the opposite so that the net shape of the Earth is not deformed but its surface is strained (Blewitt et al., 2001). Figure 5.1.4 shows the spatial behaviour of the degree-one deformation due to NTAL, NTOL, and CWSL, at a global scale. The load moment results feature strong annual oscillations mainly between the North and South Hemisphere due to the

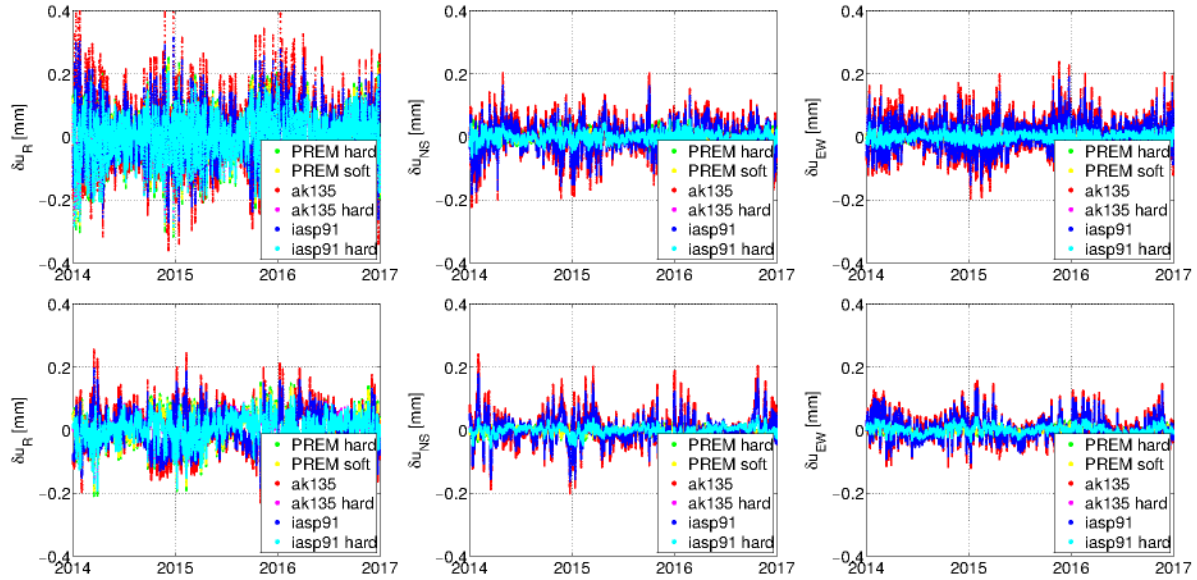


Figure 5.1.3: Differences between simulated NTAL displacements employing hourly ERA5 fields alternating the Earth model, with respect to PREM. The differences presented are for the radial (left), North-South (middle), and East-West (EW) component, for Algonquin park, Canada (upper) and Zelenchuskaya, Russia (lower).

related mass transport. Figure 5.1.5 shows the temporal behaviour of the degree-one deformation due to NTAL, NTOL, and CWSL. The S_a amplitudes can be as large as 4 mm for CWSL and 2 mm for NTAL and NTOL.

Blewitt (2003) identified five isomorphic reference frames that can be used for a large variety of applications across the field of geodesy: the center of mass of the solid Earth (CE), the center of mass of the entire Earth system (CM), the center of surface figure (CF), the center of surface lateral figure (CL), and the center of surface of height figure. The right panels of Fig. 5.1.2 show Earth's response to mass loads in different isomorphic frames. For both radial and tangential components, the weighting factors for the mass anomalies residing in the far-field is much larger compared to all other frames. The interested reader is referred to Blewitt (2003) and Wu et al. (2012) for a comprehensive discussion on this topic.

For the investigations herein, the loading displacements generated will always refer to the center of mass of the entire Earth system isomorphic reference frame (CM), and will always be generated adopting the `ak135` elastic Earth model. The reason for the former lies with the fact that deformations described in the CM frame are more appropriate for the current study on account of ITRFyy being a product of combination of space geodetic techniques some of which can very accurately sense the center of mass of the entire Earth system, e.g., SLR. The reason for the latter is that the displacements predicted by `ak135` are much closer to the average of local[5] models (e.g., `Crust 2.0`) compared to the other global[6] models (Dill et al., 2015).

5.1.2 Impact of the ocean response to pressure and wind

In the context of calculating non-tidal geophysical loading effects, the sea topography variations induced by atmospheric forcing depend on the oceanic response. From simple to more elaborate, the most widely used assumptions are (e.g., Boy and Lyard, 2008):

[5]Displacements are dependent upon the location and the spherical distance to each point load.
[6]Displacements depend only on ψ.

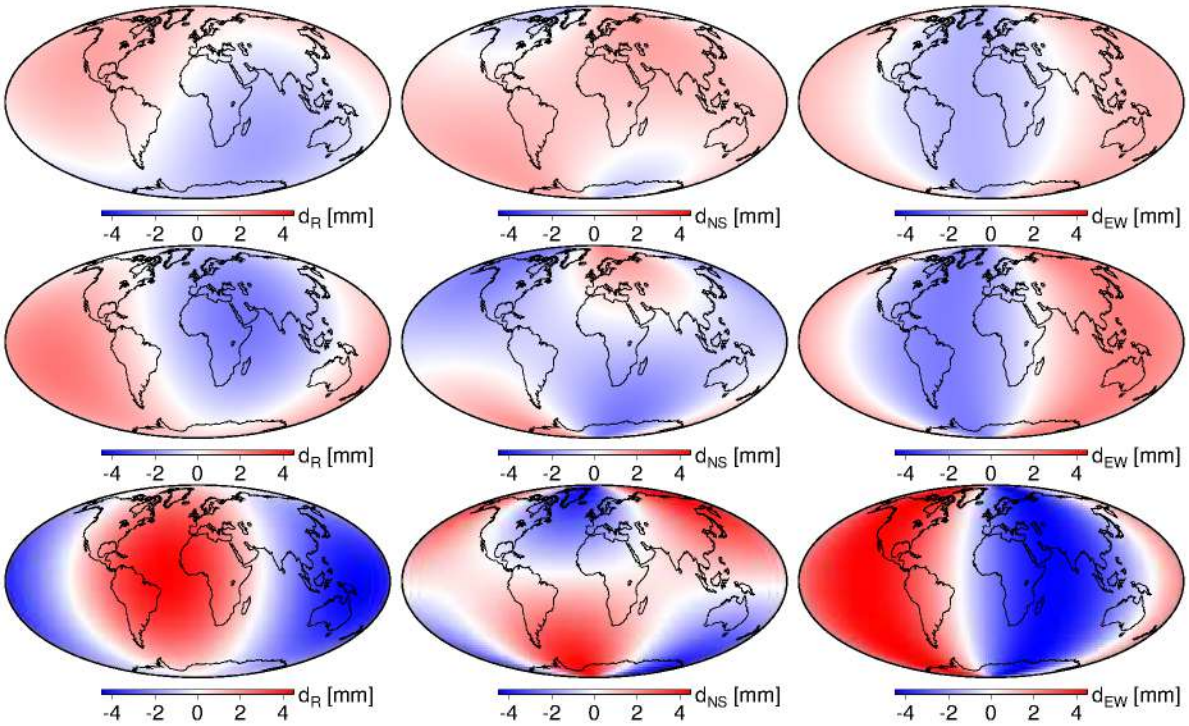


Figure 5.1.4: Degree-one surface deformation due to NTAL (upper row), NTOL (middle row), and CWSL (lower row) on 2017/10/22 12:00, in the radial (left column), North-South (middle row), and East-West (right row) coordinate component.

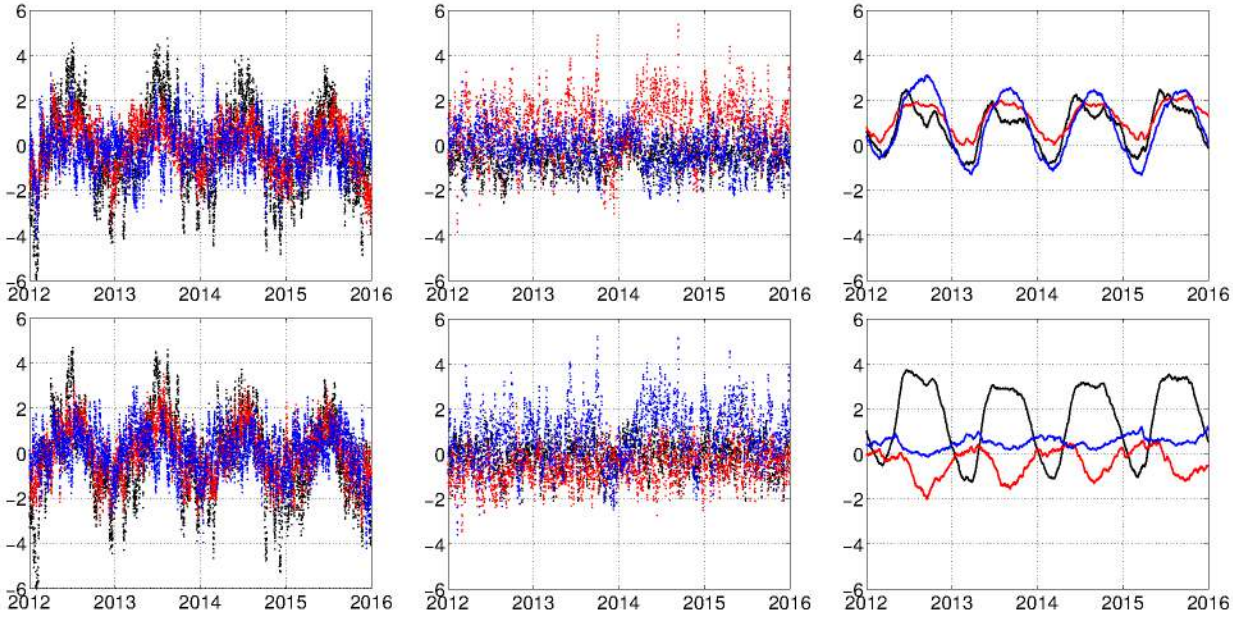


Figure 5.1.5: Degree-one surface deformation from ERA Interim (NTAL and CWSL), and ECCO (NTOL). The displacements in the radial (blue), North-South (black), and East-West (red) component are presented for Algonquin Park, Canada (up) and Hartebeesthoek, South Africa (bottom).

- ☐ non-inverted barometer (NIB);
- ☐ inverted barometer (IB);
- ☐ modified inverted barometer (MIB); and
- ☐ dynamic atmospheric correction (DAC),

which additionally depend on the ocean-continent function (or land-sea mask), defined as follows

$$O(\varphi,\lambda) = \begin{cases} 1 & \text{if } (\varphi,\lambda) \in \text{land} \\ 0 & \text{if } (\varphi,\lambda) \in \text{ocean} \end{cases}. \tag{5.1.6}$$

Finer sampling allows a more accurate representation of the coastline, which is crucial to the computation of geophysical loading effects at coastal sites. Herein, land-sea masks stemming from ETOPO1 were used.

The NIB hypothesis, that is, pressure anomalies are fully transmitted to the bottom of the ocean and the response of the sea floor is exactly the same to the solid Earth's (the convolution domain is the entire surface of the Earth), was proven not to be accurate (e.g., Boy et al., 2002), especially for stations with close proximity to large bodies of water, and at high frequencies (less than 2-3 weeks). For NIB, the sea height variations are $\delta h(\varphi,\lambda,t) = 0$.

The IB hypothesis, that is, the oceanic response to barometric pressure variations δP is considered isostatic, implies an instantaneous local deformation of the sea surface topography

$$\delta h = -\frac{\delta P}{\rho g}, \tag{5.1.7}$$

where g is the gravity and ρ is the seawater (or freshwater) density. For instance, a pressure increase of 1 hPa corresponds to a sea surface decrease of approximately 1 cm, hence the term inverted barometer effect. In this case, the convolution domain is restricted to continental regions. Adopting the IB hypothesis, implies that spatial pressure gradients that give rise to winds have no impact on the ocean height nor to the ocean dynamics triggered by the isostatic compensation. For details, the interested reader is referred to Wunsch and Stammer (1997).

The MIB hypothesis suggests that to conserve mass over very large bodies of water (primarily the oceans as well as very big lakes) the variation of the aggregate local atmospheric and ocean bottom pressure is equal to the average barometric pressure over the surface of the water body. That is, pressure forcing fluctuations at the bottom of the ocean (or lake) are set to zero (e.g., van Dam and Wahr, 1987). At a given epoch, at a certain point over water it is

$$\delta h = -\frac{P - \iint\limits_S P\, dS}{\rho g}, \tag{5.1.8}$$

where the integration is performed over the surface S of the basin the point of interest lies in. For the first time in this dissertation, MIB was applied separately for the world's oceans and every big lake e.g., Caspian Sea, Victoria, Huron, Superior, Baikal, 37 basins in total.

However, the response of large bodies of water to atmospheric forcing deviates from the inverted barometer hypothesis, especially at high frequencies (periods below 20 days). At frequencies higher than 72 hours, the response of the ocean to atmospheric forcing is certainly dynamic especially at high latitudes. Wind forcing dominates the sea surface variability signal at the 10-day period (e.g., Fukumori et al., 1998). The departure from the IB/MIB hypothesis

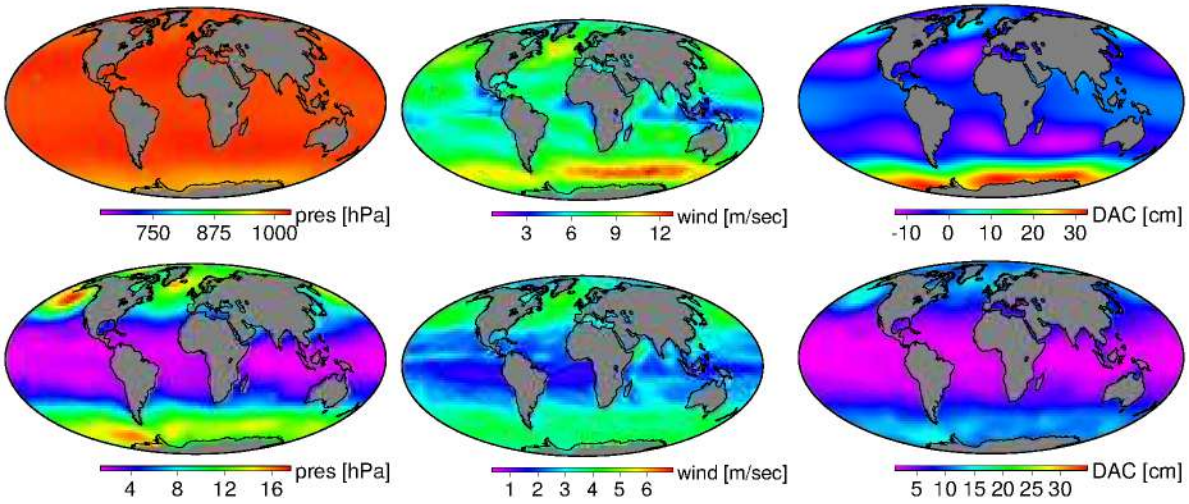


Figure 5.1.6: The average (upper) and RMS (lower) of surface pressure (left) 10 m wind speed amplitude (middle), and dynamic atmospheric correction (right) for 2016, from ERA5 and Mog2D-G data.

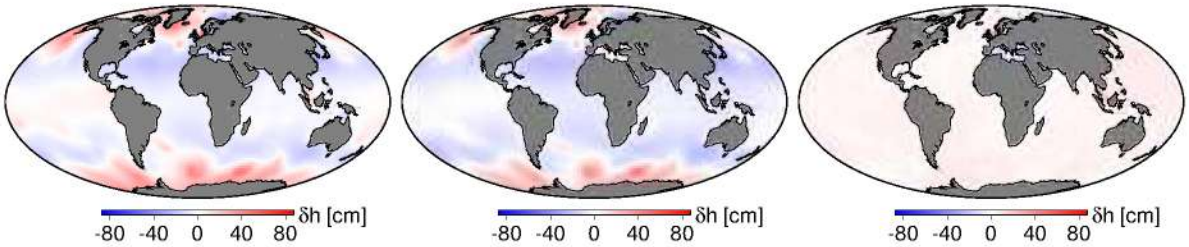


Figure 5.1.7: The dynamic atmospheric correction (left), the modified inverted barometer correction (middle), and the difference thereof (right) on 2016/01/01 00 UTC, employing ERA5 near surface model levels.

is more pronounced in shallow seas, the Southern Ocean, regions periodically covered with ice (e.g., Antarctic and Greenland), as well as in other regions (e.g., Bering Sea, Yellow Sea, North Sea, Persian Gulf and Gulf of St. Lawrence) (cf. Fig. 5.1.6). Figure 5.1.7 illustrates the ocean response to atmospheric forcing with the MIB approximation, the DAC as well as the difference thereof. In this case, the relative error induced by the MIB simulation is larger over the Hudson Bay, the North Sea and the Gulf of Thailand.

To overcome these shortcomings, the treatment attempted herein involves employing the sea surface topography after all tidal effects have been filtered out. The high-frequency ocean response to atmospheric density changes cannot be inferred by altimeter measurements owing to the long repeat cycle of the relevant satellites (e.g., 10 days for Jason-1 and Jason-2, and 35 days for SARAL/AltiKa and ENVISAT). This can only be retrieved from the output of ocean models. By and large, ocean models are divided in baroclinic and barotropic. Baroclinic models such as the ocean model for circulation and tides, OMCT[7] (Thomas, 2002; Dobslaw and Thomas, 2007), are forced by barometric pressure, wind stress, solar radiation, and freshwater fluxes (precipitation, evaporation and continental runoff). Barotropic models such as Mog2D-G/TUGO-m (Carrère and Lyard, 2003) are forced only by wind stress (near-surface fields, 10 m) and surface pressure. More sophisticated models such as MPI-OM (Max-Planck-Institute global ocean/sea-ice model, Jungclaus et al. (2013)) are additionally forced by near-surface temperature and dew

[7] ftp://isdcftp.gfz-potsdam.de/grace/Level-1B/GFZ/AOD/RL06/

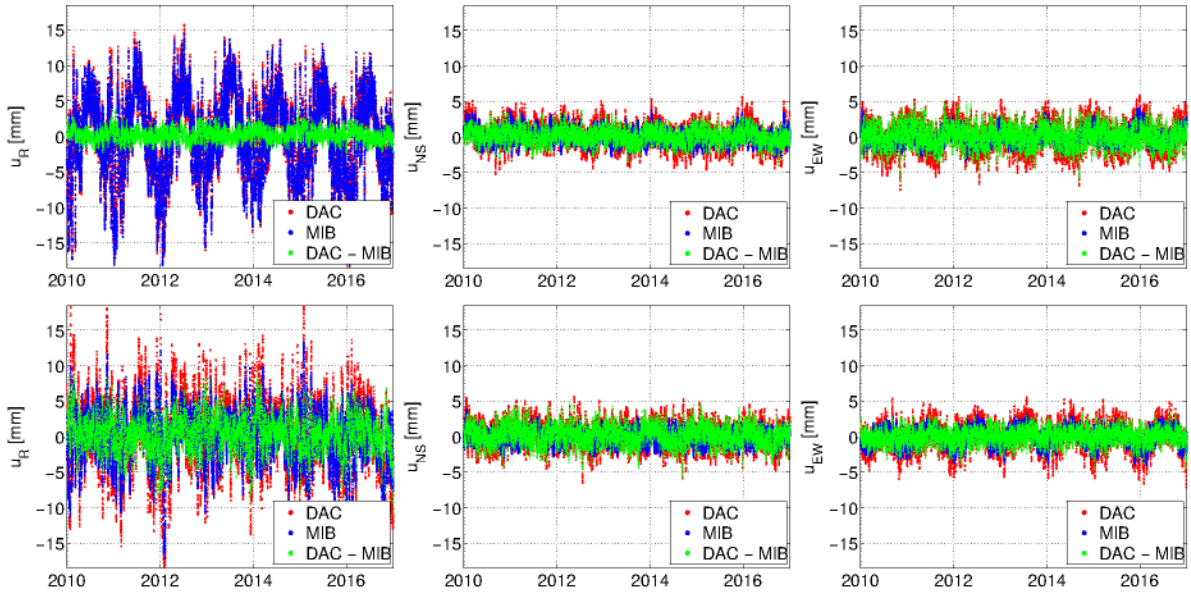


Figure 5.1.8: Atmospheric loading displacements employing hourly ERA5 fields (blue) and MIB, and ERA5 and Mog2D-G fields (red) at Badary (upper) and Onsala (lower). The differences in the radial (left), North-South (middle), and East-West (EW) component are shown in green.

point temperature (2 m), total cloud cover, total precipitation and solar (shortwave) radiation. The difference between baroclinic and barotropic models lies with the depth-dependent part of the flow; baroclinic models describe the density redistribution in the body of water as a response to the sea surface flow, whereas barotropic models assume the same water density throughout the entire water column. Due to baroclinic phenomena such as El Niño being fairly slow, the advantage of baroclinic over barotropic models cannot be exploited in the current investigations since the IB/MIB hypothesis is valid for such timescales, hence, only barotropic models will be assessed herein.

Employing ERA5ML and the state-of-the-art high frequency barotropic ocean model Mog2D-G[8], atmospheric pressure loading displacements were simulated and compared. Figure 5.1.8 depicts the differences alternating the ocean response to atmospheric forcing between MIB and DAC. The impact of this change is fairly small for inland stations such as Badary significantly affecting less than 10 % of the cases in the radial component and 50 % in the tangential component. For stations residing close to the coast such as Onsala, where the NTAL signal is attenuated, the respective figures can exceed 60 % in all components. The dynamic ocean response does not differ from the static IB approximation at low frequencies.

5.1.3 Impact of the spatio-temporal resolution

Most geophysical loading services provide displacements and gravitational changes due to loading on a grid as well as at important geodetic sites — usually those considered for the latest ITRF. If these corrections are intended for application in the analysis of space geodetic techniques (or e.g., the reduction of superconducting gravimeter measurements), site-specific series should be preferred over those interpolated from a grid. The reason behind that stems from the fairly steep gradient of the Green's functions at small distances (cf. 5.1.2). For instance, for `ak135` the $\partial \mathcal{G}_{\mathcal{R}(\mathcal{L})}/\partial\psi$ is only 3.8(1.0) $10^{12} \mathrm{R}_\oplus \mathrm{m\,kg}^{-1}$ at $\psi = 1°$, but increases rapidly to

[8] ftp.aviso.altimetry.fr/auxiliary/dac/dac_delayed_global/

8.8(5.0) $10^{12}\mathrm{R}_{\oplus}\mathrm{m\,kg}^{-1}$ at $\psi = 0.5°$ and 39.0(7.9) $10^{12}\mathrm{R}_{\oplus}\mathrm{m\,kg}^{-1}$ at $\psi = 0.25°$. In the event that site-specific corrections are not applied, non-linear interpolation methods (e.g., bi-cubic) should be preferred for while they induce an increase to the computational overhead, on average they yield more precise corrections compared to bi-linear interpolation.

The spatial resolution (or spherical harmonic expansion) of the underlying mass anomaly field employed to do the global convolution sum is even more crucial. The coarser the spatial resolution of the mass anomaly field, the more localization of sharp spatial gradients is reduced and thus the smaller the amplitude of the simulated deformations. The steep spatial gradients in the barometric pressure field are mainly due to the formulation of the orography, and are not retained in the pressure anomaly field where the spatial gradients rarely exceed 5 hPa in a typical 0.25° resolved field. On the contrary, ocean bottom pressure and hydrological mass spatial gradients reach very large values at shallow seas (e.g., during storm surge events at the North Sea), and in the vicinity of major river channels (e.g., Amazon river), respectively.

The representation of such features requires employing atmospheric, oceanic, and hydrological models of a sufficiently high spatial resolution. This does not only apply for the anomaly field utilized for the convolution, but the horizontal discretization of the observations/estimates of the assimilation algorithm. For instance, soil moisture at a certain resolution from ERA5 should be preferred over soil moisture from ERA Interim as put aside the more sophisticated assimilation system the grid step is much smaller (31 km and 79 km, respectively).

The most accurate loading results are obtained when calculating the displacements exactly at the point of interest employing a high resolution model at a high resolution. While utilizing high resolution fields is more sound from a scientific viewpoint, it is very expensive from the computational efficiency. In fact, calculating displacements for a sufficiently dense grid (e.g., 0.5°) over the entire space geodesy era (since 1976 for SLR, 1979 for VLBI and 1993 for GPS) is a time-consuming task even for state-of-the-art clusters that imposes prohibitive constrains on experimentations.

In this study, to expedite the calculation of geophysical loading displacements on a sufficiently dense grid, three simplification — practical tricks — have been employed:

- ☐ octahedral quasi-regular Gaussian grids in lieu of equi-angular;
- ☐ coarser sampling of the calculation nodes over far offshore oceanic regions for NTAL and CWSL (the opposite for NTOL); and
- ☐ the patched Green's function approach (Dill and Dobslaw, 2013; Dill et al., 2018).

Conducting the calculations on a regular Gaussian grid (the number of nodes is identical for all parallels) suffers from the decreasing distance between the nodes of the same parallel polewards, hence introducing unnecessary calculations. Performing the calculations for the nodes of an octahedral quasi-regular Gaussian grid instead of a regular Gaussian grid reduces the number of global convolution sums by 31 %. In this work, all loading displacements generated on a grid were on a Q200 grid, corresponding to a 0.45°×0.45° regular grid. The displacement fields are hardly distinct.

The global convolution sum is performed employing the patched Green's function approach (Dill and Dobslaw, 2013). That is, the calculation of the global deformation field is separated into the near-field contribution (innermost zone) where a high resolution mass anomaly field is employed, and a far-field contribution where a less finely resolved mass redistribution field is utilized. For a 2° global grid the displacements are calculated utilizing a 1° grid for $\psi > 4°$. For every node of a 0.5° grid the displacements are calculated utilizing a 0.125° mass anomaly field for $\psi \leq 4°$. Subsequently, the far-field contribution to the displacement field is upgridded to match

the spatial resolution of the near-field. Thereupon, the far-field and the near-field contributions are added to yield the final displacement for every node, and compose the deformation field.

The deformation fields calculated with the LGF approach and the patched LGF approach are almost interchangeable at the sub-mm level. The benefit from applying the patched LGF approach with the aforementioned setup lies with the fact that the number of calculations is reduced to 0.003 %. To this end the patched LGF approach is to be preferred if the calculation of point on a dense grid is intended (180,000 nodes). If the displacements only at geodetic sites are desired (1896 stations for the techniques' contribution to ITRF14) the acceleration of the calculation process is very small in absolute terms.

The same principle can be applied with more coarse spatial sampling for the far-field contribution, thus enhancing the computational efficiency further upon.

Last but not least, as the spatial gradients of both the mass redistribution fields as well as the displacements are fairly small over oceanic regions far from land (for NTAL and CWSL), it was decided that the neighbouring grid nodes of far offshore areas be further apart compared to those over land. The opposite was applied to the calculation of NTOL. For the former case, loading displacements over oceanic blocks 200 km offshore were calculated on a 2° grid. Subsequently, the displacements at the nodes, that were skipped, were computed by bi-cubic interpolation. Thus, the computational burden is reduced to 3.6 % for NTAL and CWSL over the ocean (54.8 % in total), and 3.0 % over land for NTOL (67.2 %).

5.2 Simulation of atmospheric pressure loading

To a certain extend, the series of barometric pressure and simulated NTAL radial displacement are anticorrelated. This is mainly dictated by the proximity of the site to the ocean. For non-coastal sites such as Wettzell and Hartebeesthoek, this feature is very clear as the anticorrelation exceeds 85 % and 91 %, respectively. Nevertheless, at sites by the coast (Fortaleza) and on islands (Kokee), the anticorrelation is uncertain (67 % and 18 %, respectively). A repercussion stemming from this fact, illustrated by Fig. 5.2.1, is the so-called "Blue-Sky effect". It is related to the weather-dependency of optical observations (e.g., SLR and LLR) that can be carried out only under cloudless sky conditions — typically under high barometric pressure conditions — thus biasing the related products (e.g., Sośnica et al., 2013).

As all models employ the same loading Green's kernels and the same strategy to obtain the reference pressure, the divergences arize predominantly from differences in the pressure fields extracted from the NWM (which emerge from differences in the data assimilation procedure and the spectral resolution) and the ocean-continent function.

Herein, the NWM of choice are the latest reanalyses from ECMWF, ERA Interim and ERA5. This lies with the fact that for the entire re-analysis period (from 1979 onwards) aspects such as the data assimilation system (IFS-Cy31r2 and IFS-Cy41r2) and the physical model remain unmodified. Additionally, ERA Interim performs favorably well, in particular with respect to confirming physical constraints related to e.g., mass conservation which are of special interest here (e.g. Berrisford et al., 2011).

The finite spatial representativeness of any NWM, ERA Interim and ERA5 included, render unresolvable steep orographic gradients as well as features smaller than the half-wavelength of the model. The discrepancy between the orographies of these models and the actual altitude of a geodetic station can exceed 2 km. Therefore, the surface pressure fields — that refer to the orography — could represent the air mass hundereds of metres aloft or below the point of interest. While the bias in the mass load time series does not propagate to the mass anomalies should a consistent "reference pressure" be adopted, the temporal variations can differ considerably

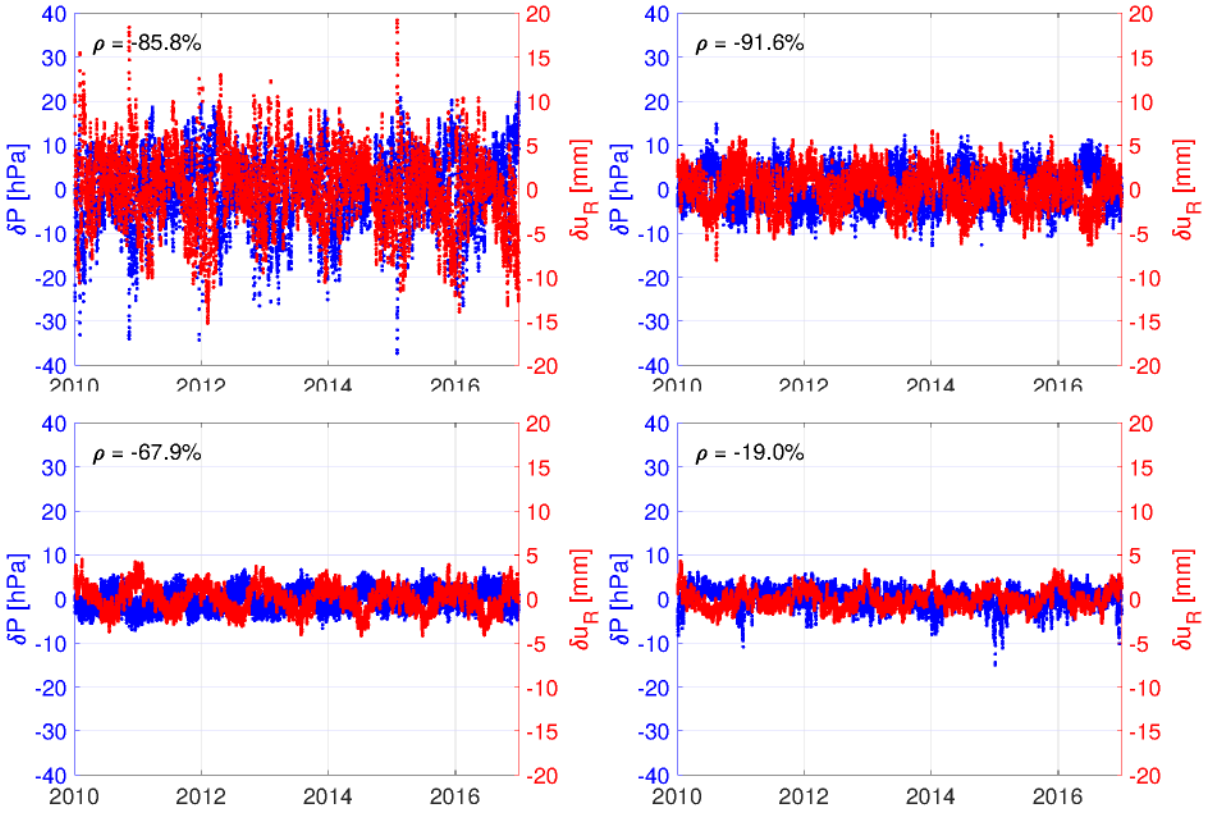


Figure 5.2.1: Barometric pressure anomalies (blue) and simulated NTAL radial displacements (red) at Wettzell (upper left), Hartebeesthoek (upper right), Fortaleza (lower left), and Kokee Park (lower right).

because temporal pressure anomalies are sensitive to varying altitude. For instance, the S_a pressure amplitude differs between series extracted from the surface fields and exactly at the altitude of a station by up to 4 hPa at some VLBI stations. These differences show neither spatial pattern nor altitude dependence, thus they cannot be modelled a posteriori. To this end, for all atmospheric loading models developed herein, the pressure fields from which the mass anomalies are built stems from the model levels and not from the surface fields (van Dam et al., 2010). The algorithm to calculate the orography-reduced pressure anomalies (Balidakis et al., 2016) is described in Sec. 3.3.

5.2.1 Tidal atmospheric pressure loading

Solar radiative heating gives rise to pressure, temperature, and wind stress oscillations predominantly at periods of one tropical year and one solar day, that in turn induce periodic elastic deformation at the same frequencies. In this section focus is placed on the high-frequency variations (cf. pressure tide model from GFZ-PT based on ERA5 fields developed here, Sec. 4.3). The excitation mechanisms governing atmospheric tides have thermal and gravitational origins that are well understood. Water (H_2O) and ozon (O_3), as well as O_2 and N_2 in the thermosphere, absorbing solar radiation (UV and IR, respectively) induce regular temperature oscillations in atmospheric regions where their concentration culminates (the lower troposphere and the middle of the stratosphere, respectively), thus causing long-wavelength patterns in the spatial domain of the vertically integrated fluid mass, that is, the pressure at the surface of the Earth. The timescales of these pressure oscillations are driven by solar irradiance, which displays seasonal

variations due to the relative position of the Earth and the Sun, as well as synoptic changes in the atmospheric density. The fact that solar heating follows a square wave function - with the duty cycle changing throughout the year - produces overtones to the S_a and S_1 frequencies. Noteworthy is that the S_2 barometric tide is stronger than the S_1. Gravitational attraction excerted by the Sun and the Moon to the masses comprising the atmosphere, as well as the displacement of its lower boundary induced by tidal motion of the crust of the Earth and the ocean surface due to both solid Earth and ocean tides, contributes fairly moderately to the barometric tides.

A common decomposition of the barometric tides is to migrating and non-migrating tidal components (e.g., Siebert, 1961; Chapman and Lindzen, 1969). The waves coherent with the apparent motion of the Sun across the sky (westward propagation) are labeled as migrating. Non-migrating are the long-wavelength waves induced by heating processes mainly related to the absorption of solar radiation by the inhomogeniously distributed water vapor in the lower troposphere, the vertical eddy heat transport at the surface, and convective heating. The S_1 wave displays largely non-migrating features, as well as migrating over the oceans in the tropics. The S_2 tide is primarily migrating, and the S_3 is the product of interaction between S_2 and gravity waves induced by tropospheric disturbances.

The spatial resolution of the pressure tide coefficients estimated in this study is 0.125°. Employing elastic LGF in lieu of the seemingly more appropriate frequency-dependent viscoelastic Green's functions yields a negligible relative error in the order of 1.5 % that projects to displacement discrepancies below 0.05 mm for the radial component of the most prominent atmospheric tide the S_2 (Petit and Luzum, 2010).

Unlike the computation of non-tidal geophysical loading effects, invoking the NIB hypothesis is sound for the simulation of atmospheric tides owing to the fact that equilibrium within the various water basins cannot be accomplished at timescales of several hours. The tidal atmospheric loading (TAL) coefficients are determined by convolving all pressure anomaly harmonic terms corresponding to frequencies equal or higher than 24 hours, that have been estimated in Sec. 4.3, with LGF (Sec. 5.1.1) from `ak135`. Displacements were generated in all aforementioned isomorphic reference frames, but only the ones corresponding to the CM were used in the geodetic analysis (cf. Chapter 7).

Figure 5.2.2 illustrates the amplitude of simulated displacements induced by S_1 and S_2 atmospheric tides, calculated employing 3-hourly[9] ERA Interim reanalysis data. Employing 3-hourly or hourly (e.g., from ERA5) data renders the interpolation scheme by van den Dool et al. (1997) or Ray and Ponte (2003) unnecessary, thus enabling to consider both migrating and non-migrating tidal components, as well as to properly estimate harmonics up to 2 hours. The selection of ERA Interim and ERA5 for the estimation of atmospheric tide components is intentional as in addition to being very accurate, the upper boundary thereof lies well above the layer with maximum O_3 (Ozon in the stratosphere absorbs UV radiation thus exciting the S_2 tide) concentration (e.g., Berrisford et al., 2011; Sakazaki and Hamilton, 2017).

TAL effects owing to waves other than S_1 and S_2 have also been assessed in this study, 10 waves in total. Figure 5.2.3 illustrates the displacement effect of S_3, K_1, L_2, M_2, N_2, P_1, R_2 and T_2 partial tides, as well as the portion of accumulated TAL signal attributed to S_1 and S_2. Retaining only the S_1 and S_2 waves induces relative errors well below 0.5 mm. While this figure is relatively small, aspiring to achieve positioning accuracy below 1 mm suggests that all models employed for observations' reduction are an order of magnitude more accurate — especially those for which no parameters are estimated in the geodetic adjustment. Hence, expanding the

[9]The meteorological fields at the epochs not coinciding with [00 06 12 18] UTC stem from the forecasts commencing at 00 and 12; the 03 fields are +3 hours from 00, the 09 fields are +9 hours from 00, the 15 fields are +3 hours from 12, and the 21 fields are +9 hours from 12.

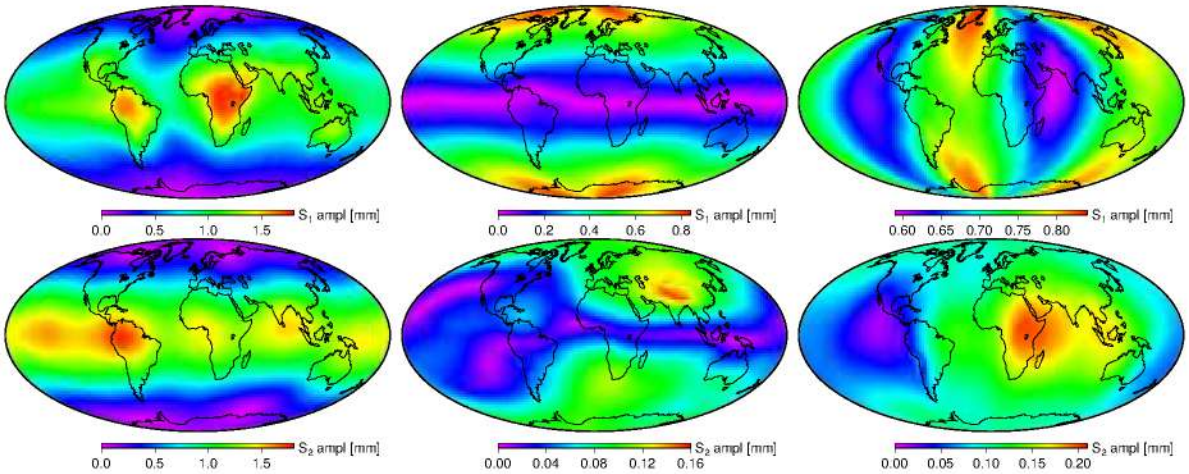


Figure 5.2.2: The amplitude of the simulated displacements induced by S_1 (upper row) and S_2 (lower row) atmospheric tides at the vertical (left), North-South (middle) and East-West (right) coordinate component. Note the different color scales.

harmonic expansion of tidal atmospheric loading to 10 instead of 2 waves is a necessity rather than a redundancy. For the remainder of this study, accounting for tidal loading effects is to be understood as applying for the aforementioned 10 waves.

Section 1.3 of GFZ Potsdam[10], and Leonid Petrov[11] also provide diurnal and subdiurnal harmonic displacement terms due to atmospheric tides.

5.2.2 Non-tidal atmospheric pressure loading

Due to the seasonal modulation of barometric tides being disregarded in the estimation of TAL, as described in Sec. 5.2.1, and the total atmospheric loading signal being the aggregate of TAL and non-tidal atmospheric loading (NTAL), employing unfiltered pressure fields to perform the global convolution sum (5.1.3) is the most rigorous approach. Nevertheless, as of this writing, the latest IERS Conventions (Petit and Luzum, 2010) recommend the application of TAL, but not yet the inclusion of NTAL corrections for operational space geodetic techniques' data analysis. Hence, a separation scheme is necessary. The most common approach is filtering the barometric pressure anomaly fields for S_1 and S_2 and applying (5.1.3) to the residuals. Another possibility lies with estimating the S_1 and S_2 harmonic terms from the loading displacements estimated employing the unfiltered pressure fields and then removing them from the related time series. While NTAL signals usually have strong S_a waves, S_{sa} periodicities are not uncommon (e.g., Algonquin Park, Ny-Ålesund, and Antarctica). Unlike NTOL and CWSL, the contribution of low frequencies (less than one cycle per year) to the total signal is insignificant. The capability of a S_a wave to describe the NTAL signal varies largely. It can be as large as 45 % for the radial displacement component of Badary and Kokee Park, or even larger (e.g., 61.6 % for Kagoshima). There are cases where harmonic waves fail to capture the NTAL signal (e.g., 3.9 % for the radial component in Fairbanks).

NTAL are predominantly associated with long wavelength synoptic pressure systems (e.g., tropical cyclones and continental anticyclones). Based on calculations carried out herein, NTAL induces displacements as large as 34 mm in the radial coordinate component and 8 mm in the

[10] ftp://ig2-dmz.gfz-potsdam.de/
[11] http://massloading.net/

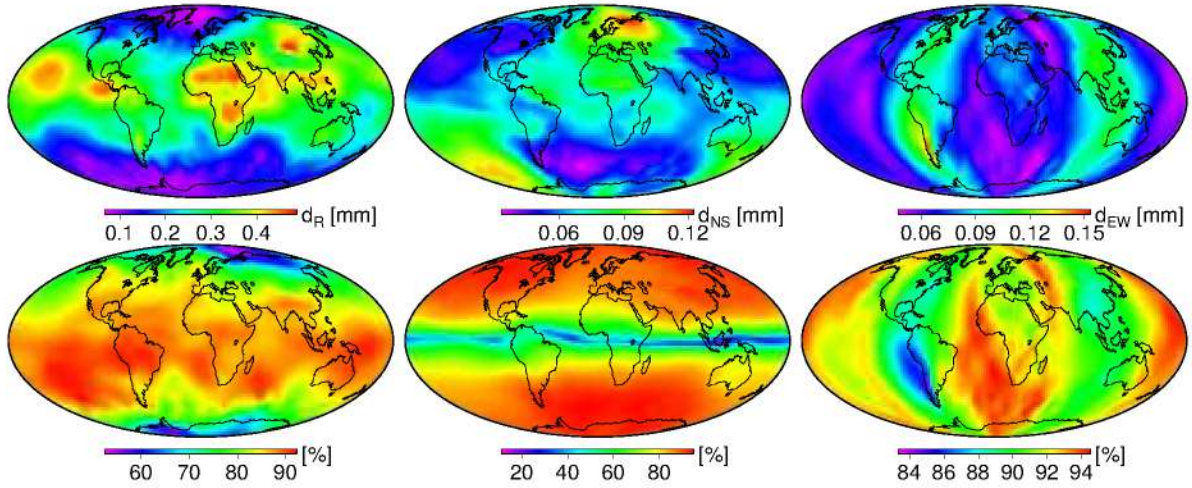


Figure 5.2.3: The amplitude of the combined tidal atmospheric loading effect stemming from K_1, L_2, M_2, N_2, P_1, R_2 and T_2 (ERA Interim, GFZ Section 1.3) and S_3 (ERA5, this study) (upper row). The lower row shows the fraction of the signal due to the combined S_1 and S_2 with respect to the accumulated signal (10 waves). The columns refer to the radial (left), North-South (middle), and East-West (right) coordinate component.

tangential component. On average, radial displacements are 166 % larger compared to tangential displacements.

Figure 5.2.4 and Fig. A.0.2 illustrate the amplitude and the phase, respectively, of NTAL-induced displacements at S_a, S_{sa}, and S_{ta} frequencies. The amplitude of the NTAL signal is largest at great distances from the ocean i.e., over Russia and Kazakhstan, whereas it is close to zero over the oceans. Nevertheless, this does not hold for the tangential displacements; the spatial distribution of NS amplitudes shows a degree-one pattern, and longitudinal features are prominent in the EW amplitudes.

As of today, there is a large number of services that provide displacements and gravity anomalies induced by NTAL. Table 5.2.1 lists the most popular along with their basic characteristics.

Most NTAL providers perform the global convolution sum in the spatial domain, provide 6-hourly displacement series in both specific stations and global grids, and adopt the MIB assumption. The displacements are usually made available in the CM and CE or CF isomorphic frames. The operational product of Global Geophysical Fluids Center (GGFC[12]), a service established by the IERS (van Dam et al., 2003), is provided on a grid (2.5°×2.5°) and is based on the NCEP reanalysis surface data (Kalnay et al., 1996).

Employing these loading displacement series in geodetic data analysis should be done with caution as there is no consensus amongst providers regarding the frequencies that should be filtered out. That is, the International Mass Loading Service (IMLS, Petrov, 2017) removes all harmonic variations occurring at frequencies higher than 36 hours, GFZ 1.3 removes all frequencies higher than 72 hours, GGFC, GSFC, and Technische Universität Wien (TUV) removes only S_1 and S_2, and the École et Observatoire des Sciences de la Terre (EOST) provides the sum of TAL and NTAL for the time series, but NTAL only for the gridded displacements.

There is a fairly good agreement between the NTAL models for the calculation of which a form of the IB hypothesis was adopted. Figure 5.2.5 illustrates the differences between simulated NTAL displacements by some services at Algonquin Park (inland) and Kokee Park (island). For

[12] http://geophy.uni.lu/ and http://loading.u-strasbg.fr/GGFC/

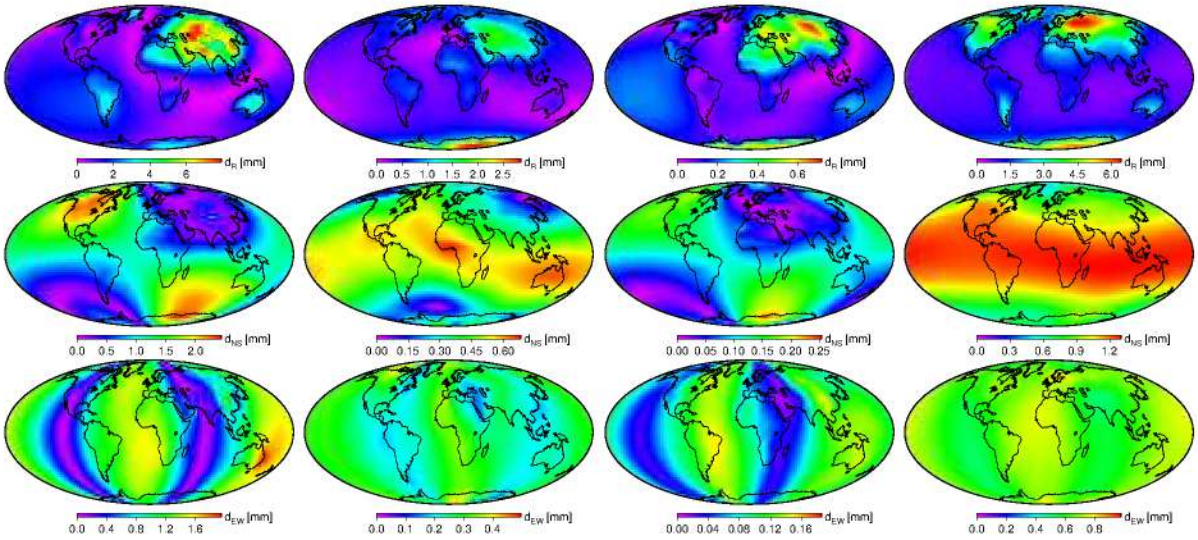


Figure 5.2.4: The amplitude of the simulated displacements induced by NTAL at S_a (1st column), S_{sa} (2nd column), and S_{ta} (3rd column) frequencies, at the radial (1st row), North-South (2nd row) and East-West (3rd row) coordinate component. The 4th column shows the RMS of the post-fit residuals. Note the different color scales.

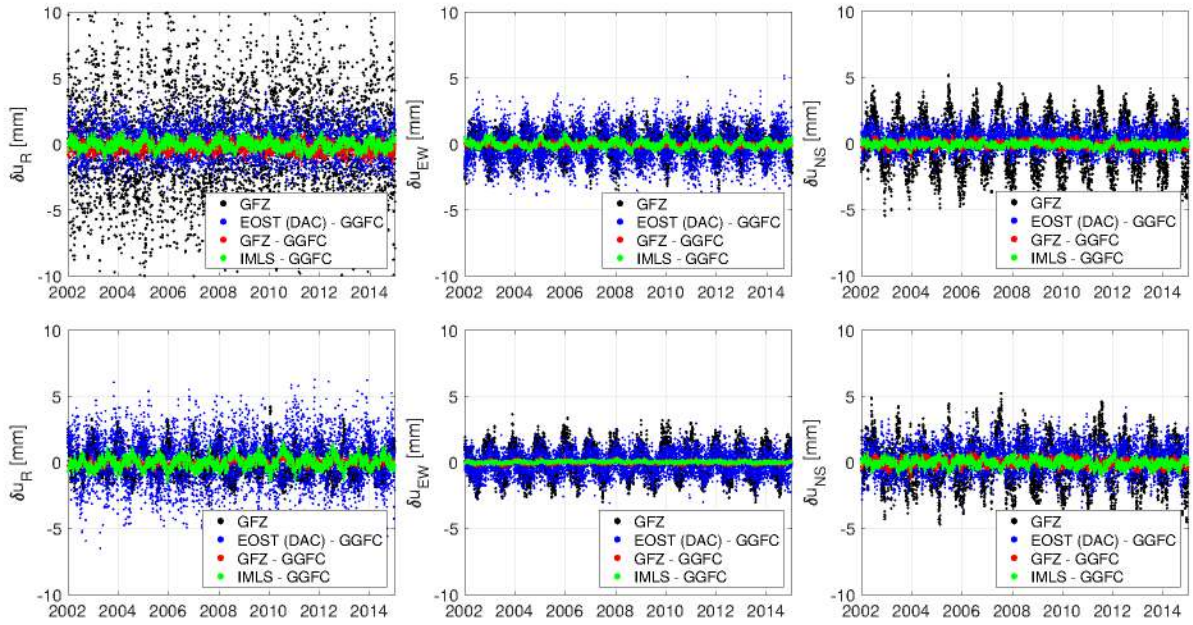


Figure 5.2.5: The differences between simulated NTAL displacements of EOST, GFZ, and IMLS, with respect to GGFC, at Algonquin Park (upper row) and Kokee Park (lower row), in the radial (left), East-West (middle), and North-South (right) coordinate component. The loading signal from GFZ is shown in gray.

Table 5.2.1: The most widely used NTAL services along with their basic characteristics. For the abbreviations, see text.

service	conv	ocean response	underlying NWM	temporal resolution	spatial resolution	sites	time span
EOST	LGF	MIB	ECMWFop	3h	0.5°×0.5°	✓	2000.8–2017.8
EOST	LGF	MIB	ERA Interim	6h	0.5°×0.5°	✓	1979.0–2017.8
EOST	LGF	DAC	ECMWFop TUGOm ERA-40	3h	0.5°×0.5°	✓	2002.0–2017.0
GFZ 1.3	LGF	MIB	ERA Interim ECMWFop	3h	0.5°×0.5°	✓	1976.0–RT
GGFC	LGF	MIB	NCEP/NCAR Reanalysis 1	6h	2.5°×2.5°	x	1980.0–2015.0
GSFC	LGF	MIB	NCEP/NCAR Reanalysis 1	6h	2.5°×2.5°	✓	1976.0–NRT
IMLS	LLN	MIB	GEOS-FPIT	3h	2.0′×2.0′	✓	2000.0–RT
IMLS	LLN	MIB	MERRA2	6h	2.0′×2.0′	✓	1980.0–NRT
TUV	LGF	MIB	ECMWFop	6h	1.0°×1.0°	✓	1979.0–NRT

the comparison to be fair, series from EOST were low-pass filtered (36 hours). Significant differences are smaller and less frequent over and areas covered with water, hence the predicted displacements in inland sites deviate further.

To assess the agreement, since the NTAL signals fluctuate a few mm around zero a rather simple quantitative metric used here is the number of grid nodes where the differences between the simulated displacements do not exceed the loading signal[13]. Comparing the product developed herein (ERA5, MIB) to the operational IERS product (University of Luxembourg), a good agreement is found. Over land, in 10.2 % (R), 13.1 % (NS), and 11.0 % (EW) of the cases the differences are larger than the signal. Over the oceans, the respective figures are 10.6 %, 11.8 %, and 8.0 %. The average[14] RMS over land is 0.6 mm, and over the oceans it is 0.3 mm. To practically quantify the differences between the models, the percentage of cases where the differences between the simulations exceed the 1 mm level was determined; over land 20.4 % (R), 1.1 % (NS), and 10.5 % (EW), and over water 1.3 % (R), 0.5 % (NS), and 0.5 % (EW). The displacements from the simulation runs with ERA5, where MIB and DAC (Mog2D-G) was adopted, differ considerably; over land the average RMS is 2.0 mm whereas over the oceans it is 4.2 mm. The deformation differences exceed the 1 mm in 57.3 mm (R), 48.1 % (NS), and 46.3 % (EW) over land, and 73.9 % (R), 47.7 % (NS), and 48.0 % (EW) over water. The largest discrepancies lie across the ACC, the Arctic Ocean, and in the regions where the NTOL signal is not negligible (cf. 5.3.1). Thus, the ocean response to atmospheric forcing is the major source

[13]The meridian convergence is taken into account.

[14]On forming the average, the grid ondes are weighted by the area of ellipsoidal trapezoid limited by meridians $\varphi_1 < \varphi_2$, and parallels λ_1 and λ_2 is evaluated by:

$$E = b^2 (\lambda_2 - \lambda_1) \int_{\varphi_1}^{\varphi_2} \frac{\cos\varphi}{\left(1 - e^2 \sin^2\varphi\right)^2} d\varphi. \tag{5.2.1}$$

where e denotes the first eccentricity of the ellipsoid.

of discrepancy between NTAL models.

Comparing all models listed in Table 5.2.1 with GGFC, the differences between the simulated displacements exceed the loading signal in 11.7 % (R), 13.9 % (NS), and 14.7 % (EW) of the grid nodes over land. These results are similar to those obtained comparing the model developed here. The IMLS provides GEOS-FPIT (Rienecker et al., 2008) and MERRA2 (Gelaro et al., 2017). The EOST loading service provides a large variety of models driven by pressure anomalies from ECMWF's operational model and ERA Interim reanalysis. The loading service of GeoForschungsZentrum Potsdam (GFZ, Dill and Dobslaw, 2013) provides displacements from a fusion of ERA-40, ERA Interim, and ECMWF's operational analysis. TUV employs ECMWF's operational analysis. GGFC employs NCEP/NCAR Reanalysis 1 (Kalnay et al., 1996). In these statistics the ECMWF+TUGOm model from EOST is not included as the largest differences, that stem from the treatment of the ocean response to pressure and wind forcing, are found here. The average RMS over land is 0.7 mm (R), and over water is 0.3 mm (R). The RMS in the tangential direction ranges around 2 mm.

Assimilating in situ barometric pressure observations (in the vicinity of VLBI stations) with a logging interval on the scale of several minutes into the pressure anomaly fields extracted from global NWMs allows to account for high-frequency short-scale (near-field) fluctuations that NWMs cannot capture. The orography-adjusted pressure fields from ERA Interim were first interpolated at the reference epoch of each scan. Then, each field was modified in such a way that bilinear interpolation at the VLBI stations returns the pressure observation introduced. This approach has been successfully tested in Balidakis et al. (2015a) employing homogenized in situ pressure records at VLBI sites with promising results for the CONT14 campaign[15]. Nevertheless, due to the large computational burden stemming from the convolution being performed every few minutes, this approach is ill-suited for long reanalysis campaigns and hence no further investigations have been carried out in this regard in the current framework.

5.3 Simulation of non-tidal ocean loading

Lunar and solar tides excluded, the redistribution of the oceanic mass is induced mainly by atmospheric circulation, freshwater fluxes, and changes in the integrated atmospheric mass above the oceans (e.g., van Dam et al., 2012). Atmospheric circulation, mainly winds, excites the dynamic oceanic circulation. The global freshwater flux regulates salinity which together with temperature drive water density and therefore deep circulation; sea ice formation and evaporation enhance it, and ice melt, precipitation, and runoff decrease it. This mass redistribution is perceived as ocean bottom pressure anomalies that in turn load Earth's surface. Based on calculations carried out herein, the extend of the related displacements ranges between -48 to 52 mm in the radial, -10 to 11 mm in the NS, and -11 to 10 mm in the EW coordinate component. The main frequency nested in the NTOL signals is found around 1 cpy, with some cases around 2 cpy. Due to phenomena such as the El Niño-southern oscillation (ENSO) cycle (El Niño and La Niña) there are several locations where the related PSD peaks at much lower frequencies (5 years). In all cases where the main frequency stongly deviates from 1 cpy, the maximum normalized PSD is well below 5 %. At locations where the main frequency is annual, the maximum normalized PSD can vary largely (e.g., for the radial components of Wettzell and Fortaleza it is 25.3 % and 6.1 % respectively).

[15] The number of baselines the WRMS (repeatability) of which improves (reduces) with respect to not applying non-tidal atmospheric pressure loading is 7 % larger for the solution where in situ pressure observations were used to calculate the displacement model, compared to the solution where the atmospheric loading model of GSFC was utilized. The VLBI data analysis was carried out employing the Kalman filter module of `VieVS@GFZ`

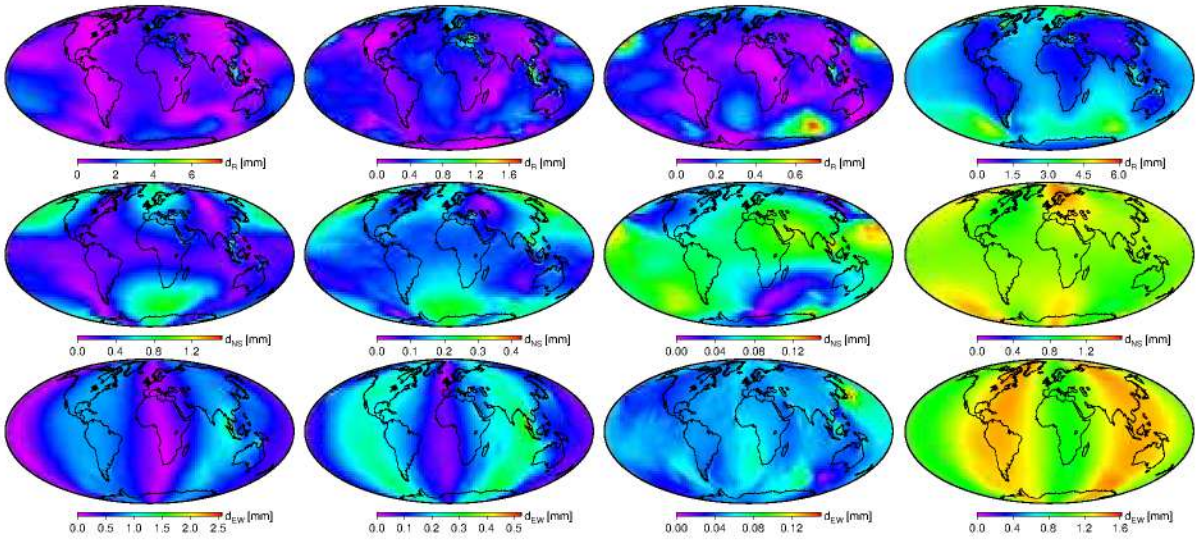


Figure 5.3.1: The amplitude of the simulated displacements induced by NTOL at S_a (1st column), S_{sa} (2nd column), and S_{ta} (3rd column) frequencies, at the radial (1st row), North-South (2nd row) and East-West (3rd row) coordinate component. The 4th column shows the RMS of the post-fit residuals. Note the different color scales.

After reducing the offset, the linear trend, the S_a, S_{sa}, and S_{ta} harmonics (cf. EGLM Sec. 5.5), the time series display a scatter as large as 5.9 mm in the radial and 1.6 mm in the tangential coordinate component (cf. Fig. 5.3.1). The largest RMS values are found in Bering Sea, East Siberian Sea, Kara Sea, Hudson Bay, North Sea, Gulf of Thailand, and the South Antarctic circumpolar current front. Over land, in areas not sharing a coastline with the aforementioned regions, the RMS of the NTOL signals does not exceed 1.0 mm. Figure 5.3.1 and Fig. A.0.3 illustrate the amplitudes and phases, respectively, of EGLM. The largest S_a amplitudes are found in the Gulf of Thailand. At S_{sa}, and S_{ta} frequencies large amplitudes appear in the Black Sea and in the southern Indian Ocean.

The barotropic case i.e., the dynamic sea level equals the equivalent sea level due to dynamic ocean bottom pressure anomalies, was adopted for the calculations herein. The ocean bottom pressure p_o was calculated employing the sea surface height anomalies ζ (dynamic or adjusted sea level) from Mog2D-G (Lynch and Gray, 1979; Carrère and Lyard, 2003)

$$p_o = g_s \left(\rho_s \zeta + \int_H^0 \rho \, dh \right) + \iint_S P \, dS, \tag{5.3.1}$$

where ρ_s is the sea surface density (density of the uppermost layer of the resting ocean), g_s is the acceleration due to gravity at the sea surface, and H is the bottom depth. The last term is the spatial average of atmospheric pressure over the global ocean. Note that under the assumptions that ρ is constant and $\zeta = 0$, there is an isostatic responce of the ocean to atmospheric forcing, viz., sea level gradients fully compensate for the applied loading, hence p_o is constant across the ocean floor and of course equal to the spatial average of atmospheric pressure over the global ocean. To obtain the dynamic ocean bottom pressure, the last term of (5.3.1) must be subtracted from p_o.

Notable long-term trends do exist in the NTOL and CWSL series partly due to the Boussi-

Table 5.3.1: The most widely used NTOL services along with their basic characteristics. For the abbreviations, see text.

service	conv	underlying NOM	temporal resolution	spatial resolution	sites	time span
EOST	LGF	ECCO	12h	1.0°×1.0°	✓	1993.0–2017.5
EOST	LGF	ECCO2	24h	0.25°×0.25°	✓	1992.0–2017.2
EOST	LGF	GLORYS2v3	24h	0.25°×0.25°	✓	1992.0–2014.0
GGFC	LGF	ECCO	12h	2.5°×2.5°	x	1993.0–2017.5
GFZ 1.3	LGF	MPIOM	3h	0.5°×0.5°	✓	1976.0–RT
GSFC	LGF	ECCO	12h	1.0°×1.0°	✓	1993.0–2014.3
IMLS	LLN	OMCT	6h	2.0′×2.0′	✓	1980.0–NRT

nesq approximation[16] adopted in the related models, i.e., the time derivative of the volume and not the mass of the respective fluid is implicitly constrained to zero (conserved). Of course, real trends do exist in the NTOL and CWSL series (e.g., trends in freshwater fluxes, atmospheric forcing, large scale circulation) but it is very difficult to discern them from the spurious. A rather practical approach to mitigate that is to reduce the mass anomalies prior to the convolution by the instantaneous global ocean bottom pressure average (Greatbatch, 1994). Thereupon, for the calculation of the global convolution sum (5.1.3), mass changes expressed in terms of ocean bottom pressure anomalies are masked over land. In the calculations carried out herein, for the sake of consistency, the same land-sea mask was employed for all geophysical loading simulations.

The shallow water hydrodynamic model Mog2D-G (2 Dimensions Gravity waves model) was a deliberate choice as it has been extensively tested against tide and bottom pressure gauge data as well as altimeter data. Moreover, Mog2D-G is forced by a very high quality NWM (operational model of ECMWF), it has acceptable latency (3 weeks), it is available since 1992, and it is successfully used e.g., for the removal of the barotropic signal from the observations of GRACE. Figure 5.3.2 illustrates the differences between simulated NTOL displacements at some sites, by some services listed in Table 5.3.1.

Estimation of the circulation & climate of the ocean (ECCO[17]) products are usually employed for NTOL calculations. Although there are several releases, ECCO-JPL (Fukumori, 2002; Wunsch et al., 2009) and ECCO2 (Menemenlis et al., 2005) are the most popular due to their high quality and near real-time availability. Of the two, most common is ECCO-JPL that is forced by NCEP reanalysis and operational data, commences in 1993, and spans at $-78.5° < \varphi < 79.5°$. Unlike other numerical oceanic models (NOM) such as OMCT05, MPIOM, and Mog2D-G that are forced solely by NWM data, ECCO additionally assimilates in situ data, as well as products of altimetry and scatterometry. ECCO products are provided on an 1° grid except for the tropic belt (0.3°), on 46 levels, at 12-hourly intervals. For the comparisons carried out below, the fact that data from ECCO represent an average over time rather than a snapshot, is considered.

The baroclinic ocean model for circulation and tides (OMCT[18], Thomas, 2002;

[16] Under the Boussinesq approximation the magnitude of $\frac{\partial \rho}{\partial t}$ is rather small in comparison to the magnitude of the velocity gradients $\nabla \cdot \mathbf{v}$ in a given geophysical fluid model. Hence, the continuity equation in most ocean or hydrological models takes its incompressible form $\nabla \cdot \mathbf{v} = 0$ (volume conservation) instead of $\frac{1}{\rho}\frac{\partial \rho}{\partial t} + \nabla \cdot \mathbf{v} = 0$ (mass conservation).

[17] http://www.ecco-group.org/

[18] www.gfz-potsdam.de/en/section/earth-system-modelling/topics/

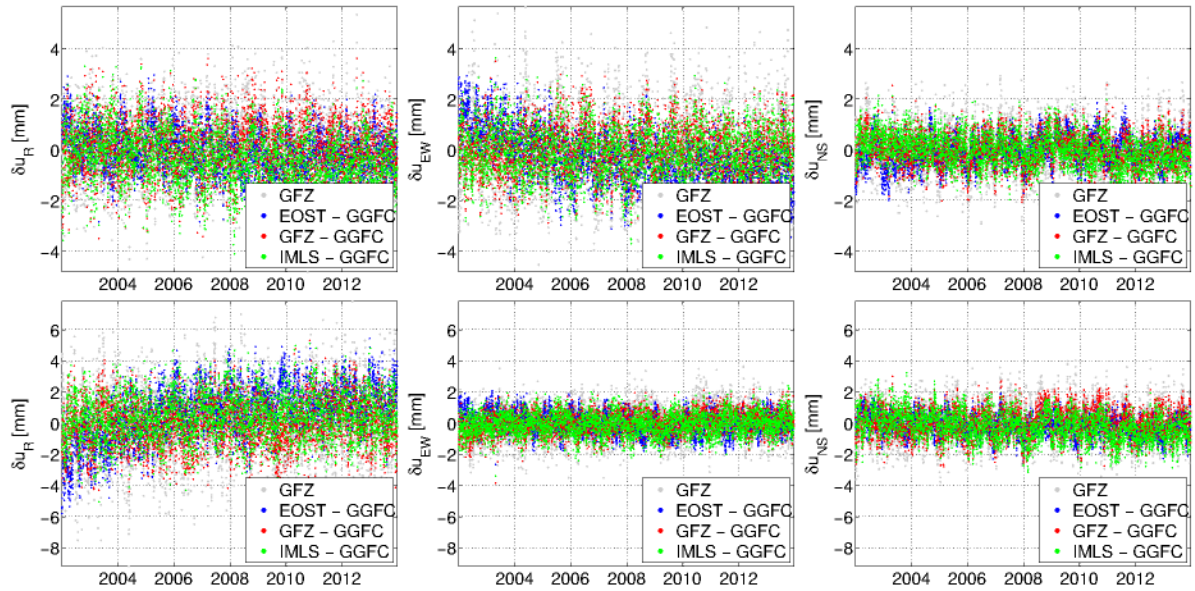


Figure 5.3.2: The differences between simulated NTOL displacements of EOST, GFZ, and IMLS, with respect to GGFC, at Algonquin Park (upper row) and Kokee Park (lower row), in the radial (left), East-West (middle), and North-South (right) coordinate component. The loading signal from GFZ is in gray.

Dobslaw and Thomas, 2007) uses nonlinear balance equations for momentum, the continuity equation, and conservation equations for salt and heat. As with most state-of-the-art NOMs, the Boussinesq and hydrostatic approximations have been employed. The latest version of OMCT, OMCT05, is forced by wind speed, surface pressure, temperature, specific humidity, heat and freshwater fluxes fields, and Charnock's parameters (relate the sea surface roughness length to wind-induced stress) from ECMWF's operational analysis. The ocean mass is artificially conserved by removing a homogeneous layer of mass at each epoch. The horizontal resolution of OMCT is 1.875° on 13 levels, and the time step is set to 30 min. Low-frequency variability does exist in the ocean bottom pressure output of OMCT and is assumed to be largely artificial, hence reduced in the investigations herein. They are primarily related to the heating of water masses at intermediate depths, and the effects thereof on the thermohaline circulation. A simple comparison with the Max-Planck-Institute for Meteorology Ocean Model (MPIOM) in the spectral domain attests to this feature (Fig. 5.3.4). OMCT has been widely used for the GRACE Level-1B atmosphere and ocean de-aliasing products up to release AOD1B_RL05 (Dobslaw et al., 2013).

The MPIOM[19] (Jungclaus et al., 2013) simulation is a primitive equation baroclinic model. The MPIOM output GFZ employs stems from an own run of the model routines that have been slightly modified. The output is given on a regular 1° grid on 40 levels, with a time step of 90 min. MPIOM (TP10L40) is driven by data from ERA-40 (1970–1978), ERA Interim (1979–2006), and ECMWF's operational analysis (2007–present). In particular, to calculate the atmospheric forcing, the following fields have been utilized: surface pressure, 2m temperature, 2m dew point temperature, total cloud cover, total precipitation, surface short-wave incoming radiation, 10 m wind speed components, as well as the Charnock parameter. To conserve the total ocean mass in time and to alleviate of spurious rates stemming from the Boussinesq approximation employed in the MPIOM momentum equations, the epoch-wise average ocean bottom pressure over the

dynamics-of-atmosphere-and-hydrosphere/omct-model/

[19] www.mpimet.mpg.de/en/science/models/mpi-esm/mpiom/

oceans is reduced. The mass anomalies are calculated by subtracting the time-average ocean bottom pressure field, and by applying the necessary inverse barometer corrections. MPIOM run by GFZ has been extensively tested as it is utilized for AOD1B_RL06 (Dobslaw et al., 2017b). Further details are provided in Dobslaw et al. (2017a).

Ocean bottom pressure can also be deduced from GRACE observations (e.g., Chambers and Bonin, 2012) monthly, at a spatial resolution of 1°. Figure 5.3.3 illustrates the variability of the equivalent water height (EWH) anomalies induced by monthly ocean bottom pressure variations observed by GRACE, calculated at the GFZ. Comparison between ocean bottom pressure estimated from GRACE (and its successor GRACE-FO) and NOMs will shed light on detecting spurious low-frequency variability, and will be part of future studies.

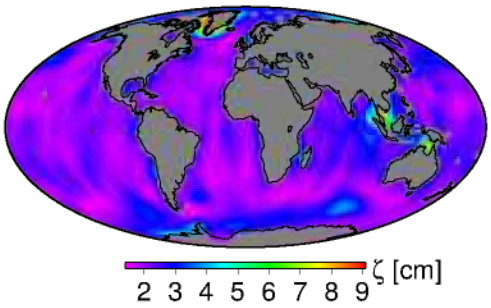


Figure 5.3.3: Variability of equivalent water height anomalies induced by monthly ocean bottom pressure variations observed by GRACE.

There is a number of studies where regional NOMs such as POLSSM (Proudman Oceanographic Laboratory Storm Surge Model) have been employed and it was proven that they outperform global ones (e.g., Williams and Penna, 2011). While this is very promising, it s not as practical, in terms of the consistensy of analyzing global networks.

The agreement between different NTOL models available (cf. Table 5.3.1) is rather poor in comparison to the agreement between NTAL models. To assess the agreement, the same metrics as for NTAL were employed. Comparing the product developed herein to the operational IERS product[20] (University of Luxembourg) after removing trends and jumps in the ECCO data, it is found that the agreement over land is better compared to the agreement over water. In particular, 26.9 %, 23.4 %, and 26.3 % of the grid nodes over land for the radial, NS and EW component, respectively, over the period 1993–2014. Over the oceans, the respective numbers are 26.1 %, 25.3 %, and 23.9 %. For the period 1993-2014, after removing long-term trends, the average RMS over land is 1.2 mm, and over the oceans 1.9 mm. On 40.4 % and 33.3 % of the grid nodes the displacement differences exceed the 1 mm level for the radial and tangential components, respectively.

A comparison with other services reveals similar discrepancies; over land the RMS is around 1 mm, and over the oceans up to 2 mm. Nevertheless, better agreement is found when comparing OMCT05 (IMLS), MPIOM (GFZ), and Mog2D-G (this study), where the RMS of the differences is reduced by 50 %. The closer agreement is to be expected as all three are forced from ECMWF operational analysis. However, in 30 % (radial) and 10 % (lateral) of the cases the differences exceed the mm-level. The RMS of the differences in the radial component can be as large as 5 mm in regions such as the Gulf of Thailand, the Chukchi Sea, and the Arctic Ocean. In general, the discrepancies are larger over semi-enclosed seas (e.g., Hudson Bay and Black Sea), whereas the agreement over land is on average below 0.6 mm in RMS. When the same NOM is employed (e.g., ECCO-JPL) the RMS differences between the different providers are on average well below 0.5 mm over land and below 0.3 mm over the oceans.

[20]Products from the GGFC were provided upon request from Prof. van Dam.

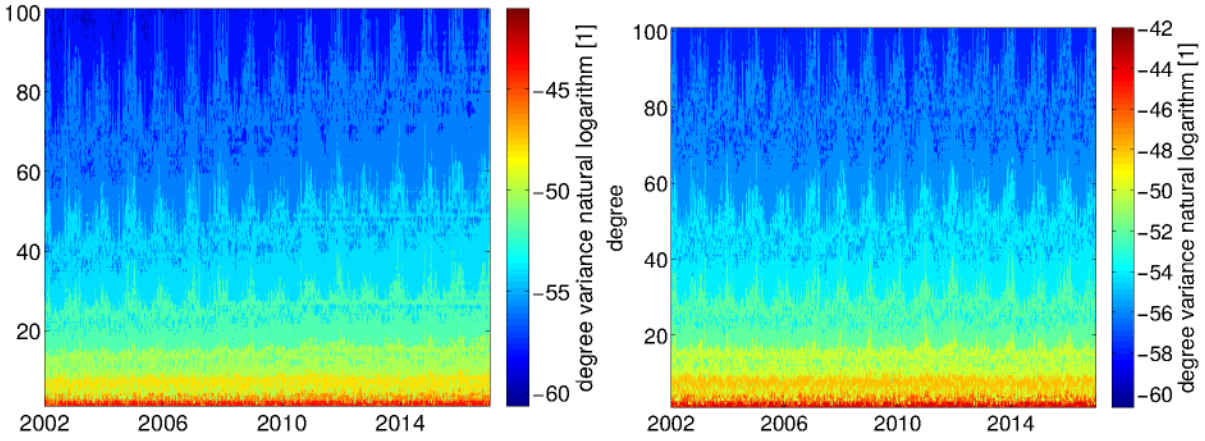


Figure 5.3.4: The degree variance of the ocean bottom pressure simulated by OMCT05 (left), and MPIOM (right) trimmed at degree 100.

5.4 Simulation of continental water storage loading

The mass redistribution within Earth's continental hydrosphere is perceived herein as anomalies in the total water W of each local catchment, in practice a grid node

$$W = W_i + W_s + W_g + W_r, \tag{5.4.1}$$

where W_i is the glacier-ice store, W_s is the snowpack store, W_g is the groundwater store, and W_r is the root-zone store (e.g., Milly and Shmakin, 2002). Therefore, the hydrological mass balance is given by

$$\frac{\partial W}{\partial t} = \frac{\partial W_i}{\partial t} + \frac{\partial W_s}{\partial t} + \frac{\partial W_g}{\partial t} + \frac{\partial W_r}{\partial t}. \tag{5.4.2}$$

For glaciated cells melt and sublimation deplete the glacier ice contributing to $\partial W_i/\partial t$. For such regions W_g and W_r are always zero. For non-glaciated cells $\partial W_s/\partial t$ is represented as the aggregate contribution from the rate of frozen precipitation, snowpack, and sublimation. The $\partial W_r/\partial t$ comprises of the sum of rainfall and snowmelt minus the sum of evaporotranspiration and drainage that is found between the surface and the effective depth of rooting (that is 2.89 m for ERA5). The $\partial W_g/\partial t$ is given by the difference between the total discharge and the discharge to the surface water network (e.g., rivers, wetlands, lakes, and man-made reservoirs).

In essence, the terrestrial component of the hydrological cycle can be expressed by

$$\frac{\partial W}{\partial t} = P - E - Y, \tag{5.4.3}$$

where the forcing stems from the sum of the rate of frozen precipitation and rainfall P, the sum of evaporation, transpiration, and sublimation E (the rate of water vapor transfer from the ground to the atmosphere), and the sum of the rate of discharge to the surface water network (surface runoff), and to groundwater (drainage), Y. The amount of the net water flux into the surface ($P-E$) that is converted either to deep percolation or surface runoff is determined by the transitory ratio of the saturation to the capacity of soil layers to hold water (e.g., Dobslaw et al., 2010). In practice, (5.4.3) is decomposed into the radial and lateral components that are connected via water fluxes: runoff, drainage, infiltration, and interflow (e.g., Dill, 2008).

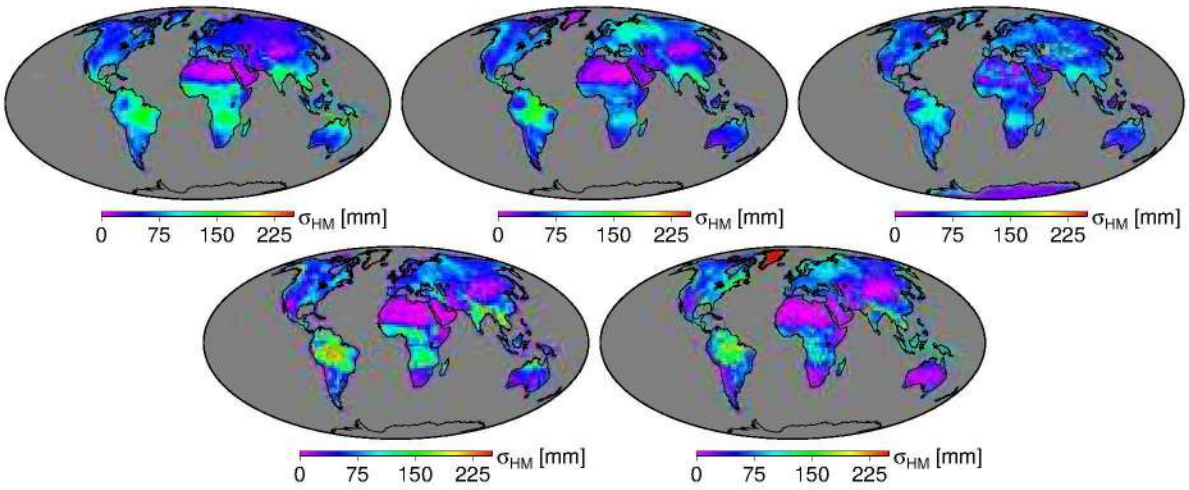


Figure 5.4.1: Dispersion of the hydrological mass in mm of equivalent water height from CPCv2 (upper left), GLDAS/Noah_v3.3 (upper middle), ERA5 (upper right), GRACE (lower left), and WaterGAP 2.2a (lower right).

The accurate simulation of global water storage variations is an intricate task owing to lacking knowledge of the individual aforementioned components of the water balance equation directly from NWMs (e.g., groundwater storage, water in river channels and other reservoirs). For the investigations carried out herein, the hydrological mass was calculated employing (i) soil moisture, snow accumulation, and plant canopy water, (ii) convective and stratiform precipitation, water lost from the soil through deep soil drainage and surface runoff, and moisture flux from the soil into the atmosphere, and (iii) mass anomalies from GRACE (cf. Fig. 5.4.1). The development of a new hydrological model is beyond the intended scope of this work.

Calculations carried out herein indicate that the CWSL signal is the strongest over land, ranging from -420 to 164 mm in the radial, -57 to 60 mm in the EW, and -58 to 54 mm in the NS coordinate component. The largest signal amplitudes are found along major river channels such as Amazon, Paraná, Orinoco, Mississippi, Nile, Niger, Congo, Yangtze, Brahmaputra, Mekong, Irrawaddy, Ob, as well as lake Nasser and the Pacific Coast Ranges of North America. Figure 5.4.2 and Fig. A.0.4 illustrate the amplitudes and phases of EGLM, respectively.

Unlike NTAL and NTOL, usually CWSL signals do not display prominent synoptic features regularly — save for major precipitation events or river floods — hence more often than not are discretized at monthly intervals. S_a is the principal harmonic nested in the CWSL signals, being able to describe more than 80 % of the signal in all cases where the magnitude of the CWSL signal renders its omission harmful for the quality of the estimates stemming from the analysis of space geodetic observations. Moreover, due to reasons similar to NTOL the amplitude of harmonics near the 5-year mark are prominent as well (e.g., lake Nasser), and range to 2 cm in the radial component, and below 0.1 mm on the lateral plane. Applying a deterministic model such as EGLM (cf. Sec. 5.5) the residual time series are left with an RMS lower than 1 mm on average. Nevertheless, the RMS can be as large as 8 cm in the radial component, but no more than 1 cm on the lateral plane.

CWSL is far more complicated to model and less understood compared to NTAL and NTOL. The CWSL displacements are computed in a manner similar to NTAL (1 Pa equals 1 mm EWH divided by 0.10197), that is by convolving load Green's kernels (5.1.5) with mass anomalies from NWMs or GRACE (cf. Fig. 5.4.1) employing (5.1.3). For CWSL, the total hydrological mass is conserved by applying a uniform thin layer to surfaces covered by oceans. The big

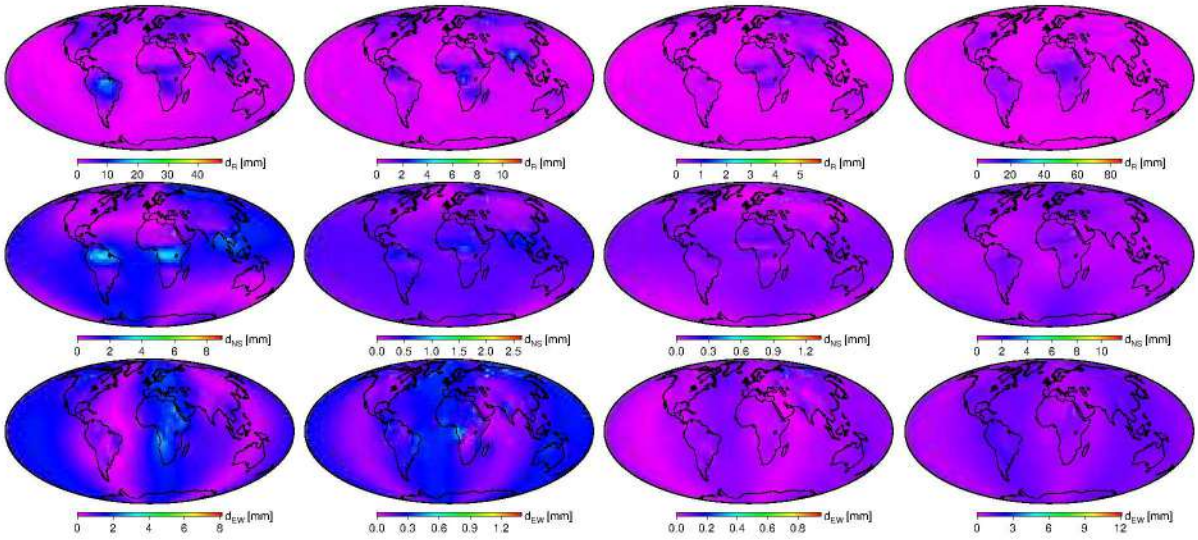


Figure 5.4.2: The amplitude of the simulated displacements induced by CWSL at S_a (1st column), S_{sa} (2nd column), and S_{ta} (3rd column) frequencies, at the radial (1st row), North-South (2nd row) and East-West (3rd row) coordinate component. The 4th column shows the RMS of the post-fit residuals. Note the different color scales.

difference between NTAL/NTOL and CWSL calculations lies with the fact that while for the former the composition of mass anomalies is fairly straightforward (that is air pressure variations and dynamic atmospheric corrections, and ocean bottom pressure anomalies, respectively), the latter features a potentially long list of contributors. Usually, only the mass from plant canopy water, snow accumulation, and soil moisure up to the effective depth of rooting is considered. While this is a reasonable approximation, variations in the groundwater store as well as in e.g., river channels and lakes, or due to streamflow from upstream cells, are usually disregarded. Moreover, unreliable forcing data and the lack of a dynamic ice sheet model result in the masking of mass anomalies in glaciated cells (e.g., for GLDAS/Noah_v3.3) in the convolution, thus rendering CWSL computations in the vicinity thereof inaccurate.

Employing GRACE data provides a workaround regarding the poorly understood groundwater depletion. GRACE captures mass transport in general; notwithstanding, GRACE is incapable of resolving small scale spatio-temporal variability (half wavelength of 200 000 km by the equator and 90 000 km by the poles). Thus far, mass flux anomalies (and subsequently EWH) from GRACE can be resolved to 10 days and and equiangular grid of 4° — GRACE mascon solution (Rowlands et al., 2005; Watkins et al., 2015). Monthly-averaged solutions have a better resolution (1°) but a smoothing kernel has to be applied nonetheless (e.g., 400 km Gaussian) mainly owing to the artificial longitudinal striping features related to the orbital configuration, as well as the fact that GRACE's products suffer from spatially correlated errors. Recently, Pagiatakis and Peidou (2019) proved that the stripes are spatially non-stationary (eastward drift), and are highly coherent with the ground tracks thus creating constructive and destructive Moiré fringes. Such a resolution is too coarse compared to the one provided by global NWMs such as ERA5 and MERRA2 (hourly, 30 km and 50 km respectively), but has proven to be sufficient for the intended application (e.g., Eriksson and MacMillan, 2014).

The parameters considered to construct the mass anomaly fileds have a huge impact on CWSL calculations. There is a number of models that provide information about the redis-

tribution of hydrological mass. Relevant Global Land Data Assimilation System (GLDAS[21]) products, that is canopy water, snow accumulation, soil moisture up to 2 m, are very often employed to compose the mass anomaly fields. Similar information can be extracted by NWMs such as ERA Interim, ERA5, MERRA2, and NOAA's Climate Prediction Center model (CPC[22]) (cf. Fig. 5.4.1). The contribution of plant canopy surface water to the total hydrological mass signal variation is marginal. For instance, only in 0.6 % of the grid nodes of GLDAS/Noah_v3.3 does the signal exhibit 0.5 % of the total signal. The soil moisture has the largest contribution to the hydrological mass as it exceeds 75 % of the signal in 77.6 % of the pixels. Liquid water equivalent thickness due to groundwater, rivers and lakes are not provided by ERA5, CPC, nor GLDAS. To the author's knowledge, only the global freshwater model WaterGAP[23] (Water Global Assessment and Prognosis global hydrology model WGHM) provides information about the net groundwater abstraction (Döll et al., 2014). Based on calculations carried out herein, due to the cooling during the winter season the ratio of the groundwater store to the total water store decreases to and average of 4 %. In the summer, this figure is 20 % of the signal, on average. On the other hand, one of the advantages of global hydrospheric models lies with the fact that they are capable of providing small scale spatio-temporal variability not resolvable by GRACE's signals that are integrated over space and time e.g., major precipitation events, floods along river channels (Dill and Dobslaw, 2013; Dill et al., 2018). Neither short-wavelength nor high-frequency variabilities are resolvable by GRACE; sharp spatio-temporal mass anomaly gradients are lost.

Mainly due to the aforementioned reasons, there is a fairly large discrepancy between the different CWSL models available (cf. Table 5.4.1) in comparison to NTAL and NTOL models. The agreement was assessed employing the same metrics as for NTAL and NTOL. The radial displacements due to CWSL from GLDAS/Noah_v3.3[24], ERA5, and GRACE are presented in Fig. 5.4.3. The displacement series of GLDAS and ERA5 were averaged over the periods to which the GRACE solutions refer to. CWSL differences stemming from mass anomaly differences between the NWMs and GRACE (cf. Fig. 5.4.3) can be attributed to errors in the underlying models and observations, respectively.

For consistency with the NTAL and NTOL simulations, CWSL displacements from ERA Interim were simulated as well. Comparing this product to the operational IERS product (University of Luxembourg, GLDAS) after removing the trends in the GLDAS data, it is found that 36.0 % (R), 35.2 % (NS), and 25.4 % (EW) of the grid nodes assigned to land experience differences larger than the signal itself. After removing long-term trends, the average RMS over land in the time span 1979–2012 is 1.2 mm. On 37.4 % and 4.2 % of the grid nodes the displacement differences exceed the 1 mm level for the radial and tangential components, respectively. Nevertheless, in regions such as the Amazon basin, the Pacific Coast Ranges of North America, and the central Siberian plateau the RMS of the differences in the radial component can be as large as 5 mm. A comparison with other services reveals similar discrepancies; over land, the spatial average of the RMS over land is above 1 mm. The comparison between GGFC and GFZ revealed that the spatial average of the RMS is 1.3 mm, and exceeds 10 mm for several catchments (e.g., Amazon, Congo, Lena, and Nasser). Figure 5.4.4 confirms the result of the simulations carried out herein, that is that the differences between different CWSL providers easily exceed the amplitude of the signal itself.

[21] https://ldas.gsfc.nasa.gov/gldas/
[22] https://esrl.noaa.gov/psd/
[23] http://www.watergap.de/
[24] Following Rodell et al. (2004), in GLDAS/Noah_v3.3 few points at Arctic regions that are permanently ice-covered are masked owing to unreliable forcing data and the lack of a dynamic ice sheet model.

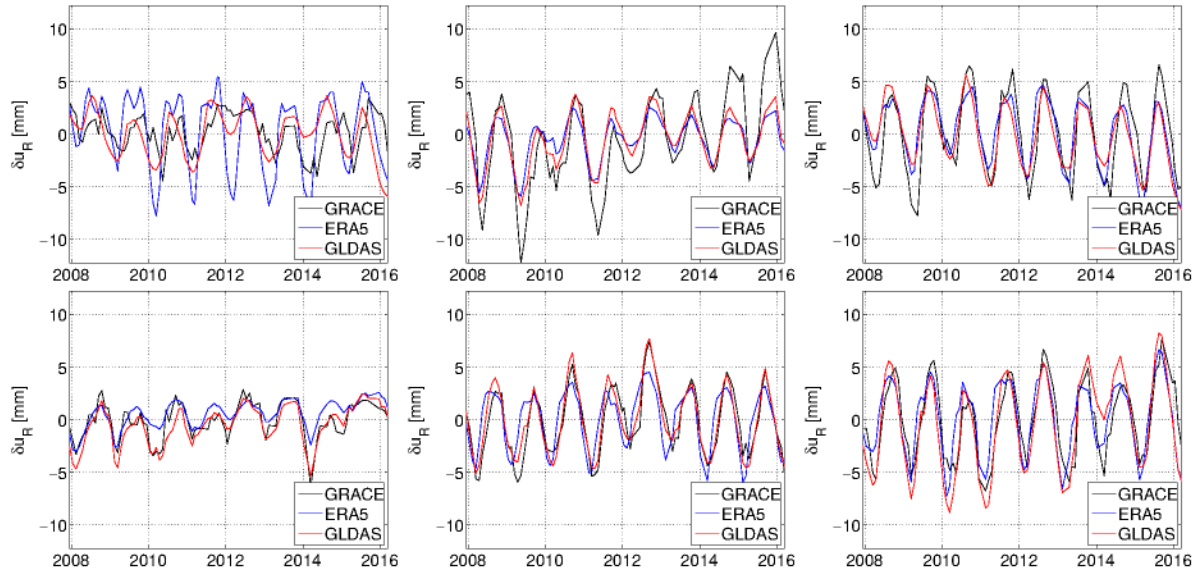


Figure 5.4.3: Radial component of simulated CWSL displacements at Badary (upper left), Fortaleza (upper middle), Gilmore Creek (upper right), Hartebeesthoek (lower left), Westford (lower middle), and Wettzell (lower right).

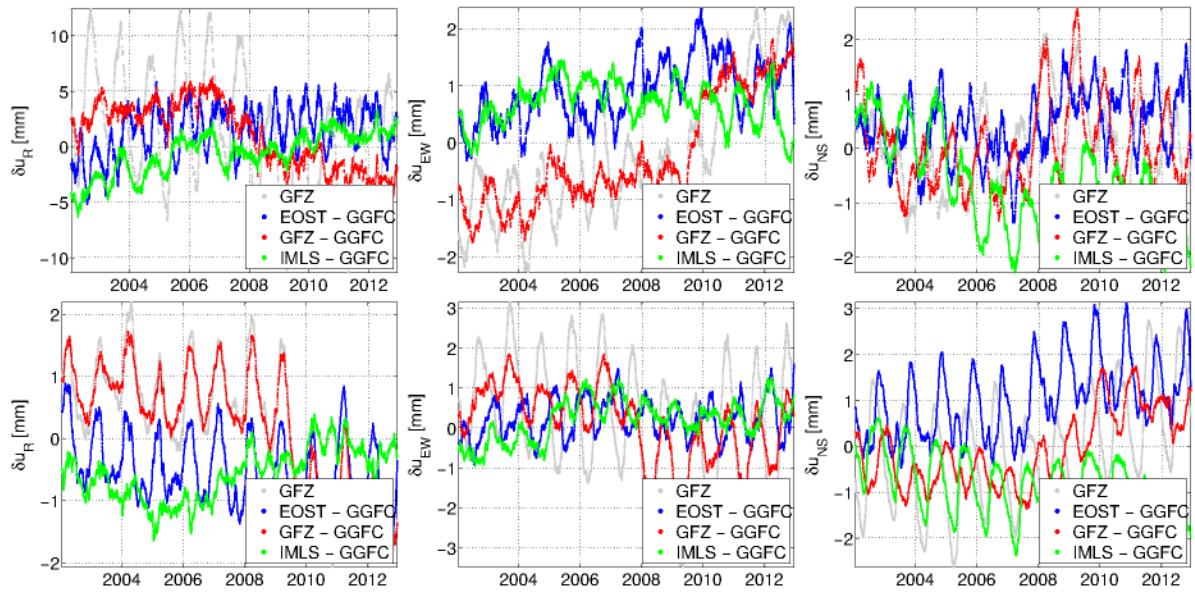


Figure 5.4.4: The differences between simulated CWSL displacements of EOST, GFZ, and IMLS, with respect to GGFC, at Algonquin Park (upper row) and Kokee Park (lower row), in the radial (left), East-West (middle), and North-South (right) coordinate component. The loading signal from GFZ is in gray.

Table 5.4.1: The most widely used CWSL services along with their basic characteristics. For the abbreviations, see text.

service	conv	ocean response	underlying NWM	temporal resolution	spatial resolution	sites	time span
EOST	LGF	MIB	GLDAS/Noah v1.0	3h	0.25°×0.25°	✓	2000.2–2017.8
EOST	LGF	MIB	ERA Interim	6h	0.5°×0.5°	✓	1979.0–2016.7
EOST	LGF	MIB	MERRA2	1h	0.5°×0.625°	✓	1980.0–2017.7
EOST	LGF	MIB	MERRA-land	1h	0.5°×0.67°	✓	1980.0–2016.2
EOST	LGF	MIB	GRACE	1m	0.5°×0.625°	✓	2003.0–2016.2
GFZ 1.3	LGF	MIB	LSDM	24h	0.5°×0.5°	✓	1976.0–RT
GGFC	LGF	MIB	GLDAS	1m	2.5°×2.5°	x	1979.0–2013.0
GSFC	LGF	MIB	GLDAS	1m	1.0°×1.0°	✓	1979.0–2016.5
IMLS	LLN	MIB	GEOS-FPIT	1h	2.0′×2.0′	✓	2000.0–RT
IMLS	LLN	MIB	MERRA2	1h	2.0′×2.0′	✓	1979.0–NRT

5.5 Development of the empirical geophysical loading model EGLM

Inspired by the fact that a large portion of the individual geophysical loading signals is distinctly harmonic, the empirical geophysical loading model (EGLM) has been developed in this work. Figure 5.5.1 illustrates the segment of the signal that can be reconstructed utilizing a single harmonic function at the dominant frequency. In the vast majority of cases the most prominent peak in the periodogram appears in the annual mark and sometimes in overtones thereof. For NTOL and CWSL signals, there is a number of nodes where the dominant frequency was found to be close to 5-years. Nevertheless, in such cases the loading signal is fairly weak and the location of the peak itself is not always statistically significant. Figure 5.5.1 demonstrates that EGLM's concept is more effective for CWSL owing to the general lack of synoptic features — with the exception of events associated with heavy precipitation and river floods — in the time series of the related signals, for instance, an S_a sinusoid captures more than 85 % of the CWSL signal in Amazon's basin, whereas the associated sinusoid describing NTAL and NTOL capture 80 % and 15 %, respectively.

In essence, EGLM is a function conceptually similar to GFZ-PT (Sec. 4.3) that returns displacements due to NTAL, NTOL, CWSL, and the accumulated loading based on a global regular lattice of 0.5° degrees spacing, given time and location. Harmonic coefficients at S_a, S_{sa}, S_{ta}, and S_{5a}, an offset and a linear rate have been estimated based on GFZ's loading models (Dill and Dobslaw, 2013) spanning the period 1979–2018. To concentrate on low-frequency variability a 3rd order Butterworth filter with 72-hour cutoff was applied to NTAL and NTOL time series, prior to the least-squares adjustment. The choice of the source data is deliberate for the three components are consistently forced, and the total mass is conserved to the extend allowed by the accuracy of the forcing data. The fitting ansatz of every grid node of EGLM reads

$$\hat{x}(\phi,\lambda,t) = x_0 + v_x\,(t-t_0) + \sum_{i=1}^{4} C_i \cos\left(\frac{2\pi t}{T_i}\right) + S_i \sin\left(\frac{2\pi t}{T_i}\right), \tag{5.5.1}$$

where x_0 is the offset, v_x is the linear trend, and C and S are the harmonic coefficients for periods $T = \begin{bmatrix} 5 & 1 & {}^1/_2 & {}^1/_3 \end{bmatrix}$ years. A T determined recursively by argmax(PSD(x)) was tested, but not

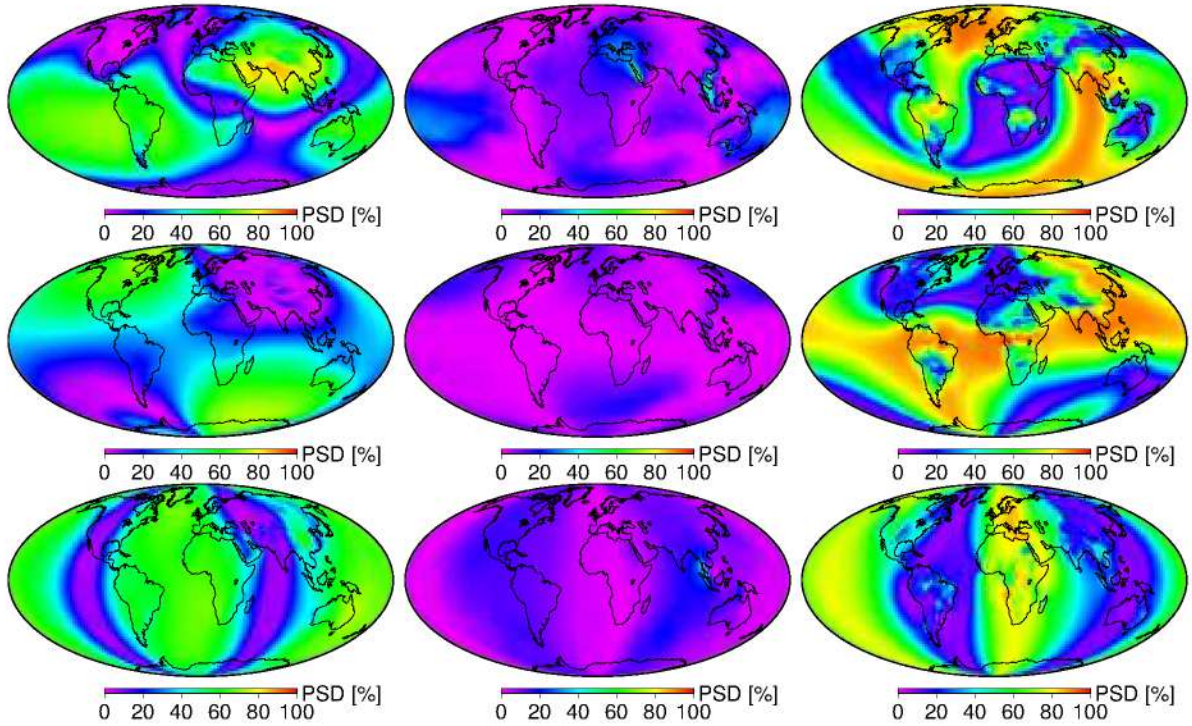


Figure 5.5.1: The portion of the radial (upper), North-South (middle), and East-West (lower) component of the NTAL (left), NTOL (middle), and CWSL (right) signal captured by a sinusoid at the dominant frequency, expressed in terms of normalized PSD.

a statistically significant improvement was found; hence the current T was retained for simplicity. Figure A.0.1 illustrates the periodicity of the dominant signal of each node, where in the vast majority of cases that is S_a. At regions where there are sharp spatial gradients in the phase of the S_a signal — usually very weak signals — the dominant peaks can take values such as 0.5 or 5 years.

An important feature of EGLM is its linear rates. Figure 5.5.2 shows that while NTAL and NTOL rates could result to a maximum displacement of 2 mm over 50 years, in certain catchments CWSL rates reach this figure in a single year. The radial component of the CWSL-related results presented in Fig. 5.5.2 is consistent with Rodell et al. (2018). Due to the total water mass stored in the atmosphere being very small, difference between evaporation and precipitation over the oceans should equal the difference between precipitation and evaporation over land. Not satisfying the latter gives rise to trends in freshwater fluxes that will inescapably lead to trends in the simulated loading series. These trends could reflect reality. The formation of deep and large groundwater depression cones in the vicinity of aquifers used for irrigation, the decreasing water levels in several major lakes, the construction of dams resulting in large artificial reservoirs, and true trends in freshwater fluxes (precipitation, evaporation, etc.), are some of the reasons. Nevertheless, some of them are largely artificial and stem from parametrizations such as the Boussinesq approximation, imperfections in the melting scheme, and inaccuracies in the soil holding capacities.

The treatment of these trends can be conducted in a number of approaches. For the geodetic investigations herein all time series are relieved of a linear trend that was estimated together with several harmonic terms employing 39 years of data. In doing so, it is implicitly assumed that either the trends are spurious, or that they are real and the station velocities estimated

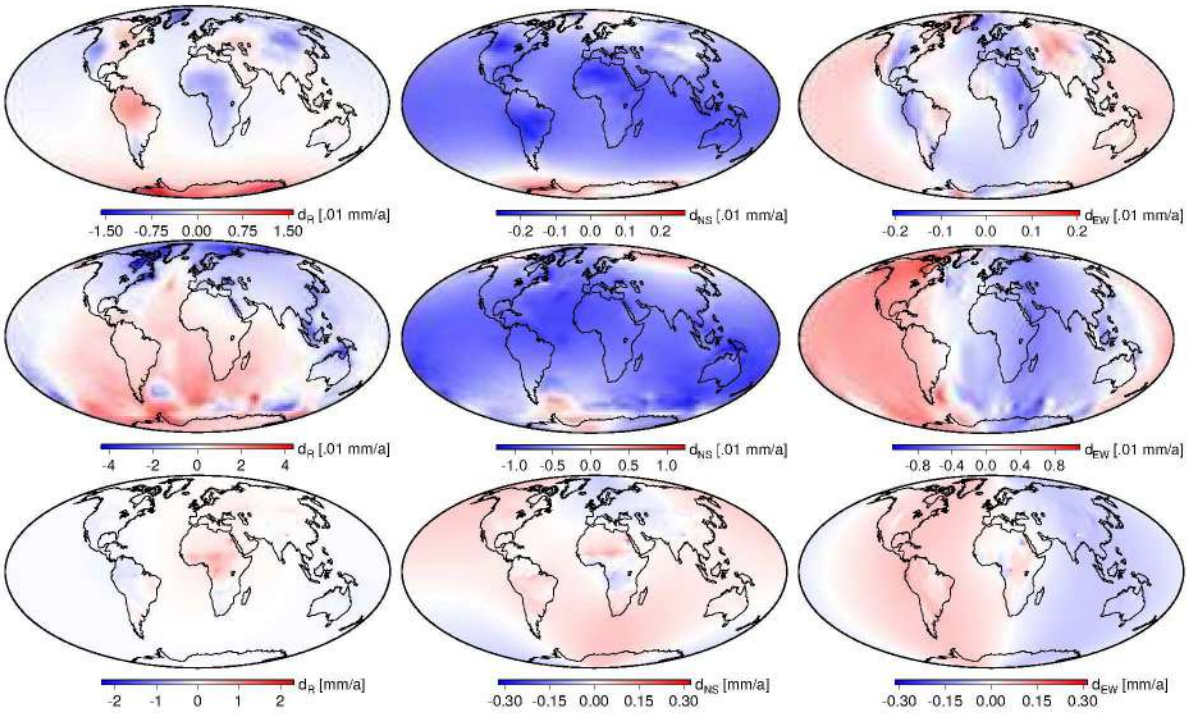


Figure 5.5.2: The linear EGLM trends of displacements in the CM frame estimated from a least-squares adjustment together with seasonal and inter-annual harmonics. Shown are the rates in the radial (left), North-South (middle), and East-West (right) coordinate component from NTAL (1st row), NTOL (2nd row), and CWSL (3rd row).

from the geodetic time series (e.g., I/D/JTRFyy) are capable of accurately capturing them. Another reasonable workaround is to merge intra-annual variations from hydrological models forced from NWMs with inter-annual variations from GRACE (R. Dill, personal communication). Yet another approach involves the fusion of long-wavelength mass anomalies from GRACE with short-wavelength mass anomalies from hydrological models, in the spectral domain. The two latter approaches suggest that the portion of the station velocity attributed to geophysical motion is resolved. The validation of these trends remains.

The noise nested in the post-fit residuals of the different components of EGLM, $\hat{v} = x - \hat{x}$, is also provided by the function as it is useful for selecting a proper noise level in estimating station coordinates utilizing Kalman-type filters. Nevertheless, more useful than just a WRMS is the provision of noise characterisation by the two-sample Allan standard deviation, assuming that the displacements vary as random walk processes (e.g., Soja et al., 2016)

$$\mathrm{ASD}\,(\tau) = \langle v^2(t+\tau) - 2v(t+\tau)v(t) + v^2(t)\rangle \tau^{-2}, \tag{5.5.2}$$

where $\tau < 96$ hours denotes the time shift. The length of the time series is crucial as the PSD can vary considerably (e.g., 40 % for Wettzell) for series shorter than 5 years. Figure 5.5.3 illustrates the slope of $\log(\mathrm{ASD})$ over $\log(\tau)$ for the displacements induced by the different geophysical fluids as well as for the accumulated loading effect. Figure 5.5.3 demonstrates that while the main contribution to station displacements at seasonal timescales stems from CWSL, NTAL provides the main contribution to the noise component. As expected, the contribution of NTOL to the process noise is very small over land. This component of EGLM has been successfully tested in the framework of Soja et al. (2018).

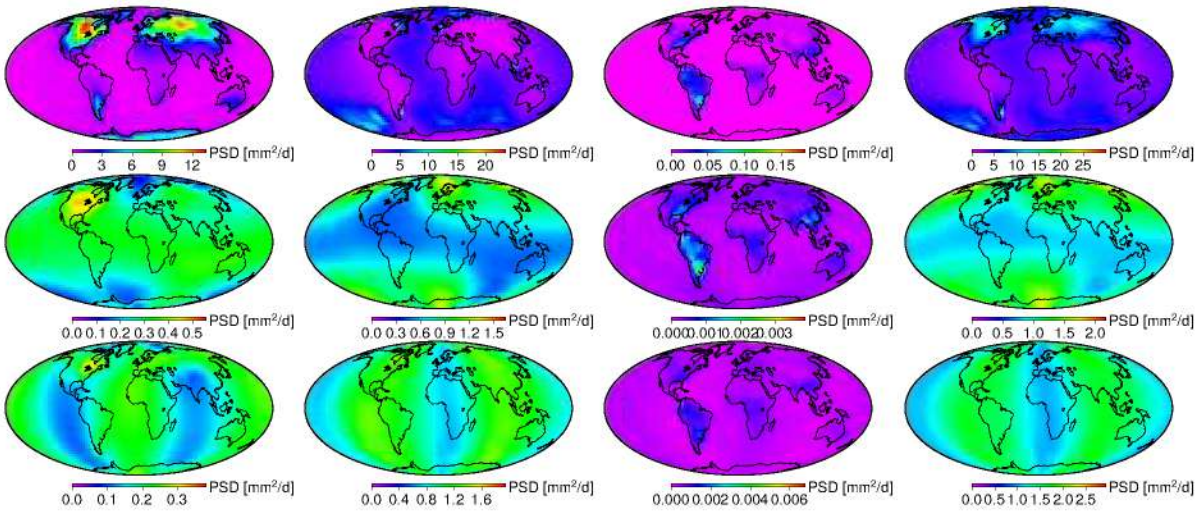


Figure 5.5.3: EGLM's power spectral density (PSD) or the so-called variance rate of the underlying white noise process from simulated displacements induced by NTAL (1st column), NTOL (2nd column), CWSL (3rd column), and the total non-tidal loading (4th column), in the radial (1st row), North-South (2nd row), and East-West (3rd row) coordinate component. Note the different color scales.

6 Application of propagation delay models to space geodetic data analysis

In this chapter, some approaches to model atmospheric refraction suggested in Chapter 4 are assessed by analyzing real (VLBI) and simulated (VLBI, GNSS, SLR, and DORIS) space geodetic technique measurements (cf. Sec. 2.6). Unlike non-tidal geophysical loading displacements that typically do not feature very rapid or very large variations within the course of a day and could be applied at the parameter level (conditional upon the assumptions outlined in Chapter 7), atmospheric refraction corrections must be applied directly at the raw (or differenced) observations (e.g., the group delays in VLBI data analysis) or the NEQ level, but certainly prior to the least-squares inversion. In the following pages, the impact of varying the a priori atmospheric delay quality in microwave space geodetic technique is assessed. In particular, two sets of solutions were produced: those dealing with the a priori zenith delay, and those dealing with the related mapping functions.

In this work, special emphasis is placed on the atmospheric refraction treatment in SLR analysis, as it is still immature (cf. Sec. 6.1). Section 6.2 deals with the changes in the station coordinates and the baseline lengths induced by alternating the mapping functions between VMF1 (IERS 2010 standard) and the PMF and GFZ-PT that were developed herein. The differences induced by the a priori zenith delays, in essence the barometric pressure, are studied as well. In particular, the quality of solutions where raw in situ (standard), homogenized in situ, data from the model levels of ERA Interim, and GFZ-PT were employed to compute d_h^z were assessed. The implications on the station network induced by shortcomings in atmospheric refraction modelling are described in Sec. 6.3, where an analysis of real VLBI observations as well as simulated GNSS observations takes place. It is shown that unlike zenith delay errors, mapping function imperfections cannot be compensated by the estimation of tropospheric parameters. In Sec. 6.4 the impact of varying the a priori zenith delays and the mapping functions on Earth orientation parameters is presented. Therein, the focus is placed on the analysis of real group delays from the complete IVS and QUASAR session history (Nothnagel et al., 2015). Section 6.5 presents a comprehensive analysis of the impact of the meteorological data and mapping functions quality on integrated water vapour trends from real and simulated VLBI and GNSS observations. It is proven that the varying observation geometry in VLBI — mainly due to station network expansion — affects the fidelity of long-term rates, especially in the asymmetric delay.

In this work, VLBI analysis of real observations refers to the batch least-squares or Kalman Filter and Smoother adjustment of the group delays found in the database 4 (or higher) files (also known as NGS files), where the ambiguities have already been resolved and the first order ionospheric refraction effects have already been removed. All necessary procedures prior to that (scheduling, experiment, correlation, and fringe-fitting) are not studied whatsoever.

To reduce atmospheric refraction effects at the observation equation level in microwave space geodetic techniques, usually three components are necessary: (i) an approximation of the zenith delay, (ii) a function to project delays aloft the stations to any other elevation angle, and (iii) a function to approximate the azimuthal delay variations. In `VieVS@GFZ`, by default the a priori tropospheric delay at a station consists of the product of the time-dependent zenith hydrostatic

delay (d_h^z), and the elevation- and time-dependent hydrostatic mapping factor (mf_h), plus the product of the elevation-dependent gradient mapping function (mf_g) and the a priori gradient components that feature a time-invariant bias. The implementation of the latter was motivated by the spurious station displacement (usually polewards) in the event that atmospheric delay asymmetries are not treated either by modelling or appropriate parameter set up. Such an approach is not necessary for modern global geodetic VLBI sessions. In the analysis carried out herein, the treatment was slightly different. In modern VLBI sessions, no a priori gradients were applied because (i) linear horizontal gradients are resolvable by post-2002 sessions due to a good sky coverage — in the vast majority of cases, (ii) single offset gradient models are partly counter-intuitive since in addition to the average atmospheric tilt, the modelling of atmospheric delay fluctuations that vary at short (mainly G_{EW}) and seasonal timescales (e.g., MacMillan, 1995b; Böhm et al., 2013b) is sought, and (iii) there is no information regarding the uncertainty thereof so that it is properly introduced in the stochastic model of the VLBI adjustment. Moreover, the slant non-hydrostatic delay ($mf_{nh}\, d_{nh}^z$) was added to the slant hydrostatic delay because then the residual zenith delays are much smaller. However, a statistically significant improvement in the estimated coordinates and the uncertainties thereof (99.9 % level) is achieved in less than 4 % of the cases in the post-2000 era. These results were obtained from iterative least-squares adjustments until all estimated parameters converge numerically. Nevertheless, should the non-linear least-squares adjustment be carried out only once (not fully rigorous, but efficient), the importance of the a priori values is highlighted, and a slightly larger improvement is found, especially in the analysis of Intensive sessions.

6.1 Atmospheric refraction treatment in SLR analysis

In this section, the treatment of atmospheric refraction in SLR data analysis takes place. Due to the fact that d_{nh}^z at $\lambda = 532$ nm is 66 times smaller compared to the non-hydrostatic delay that microwaves experience, it is usually assumed that the errors stemming from approximating d_{nh}^z employing surface meteorological observations (pressure, temperature, and relative humidity) is negligible in absolute terms. Therefore, conventionally in SLR (as well as LLR) data analysis, the a priori atmospheric delay consists of the symmetric delay induced by the hydrostatic and non-hydrostatic atmospheric components. Since d_{nh}^z is small in absolute terms (maximum 6 mm in the tropics, cf. Fig. 4.4.8), there is no utility in using a mapping function tailored for the non-hydrostatic component. Given an observation geometry (station and satellite location), the differences between the symmetric non-hydrostatic ray-traced delay component, the product of the zenith delay (typically smaller than 6 mm) and the non-hydrostatic mapping factor (stemming from the parameterized form), and the product of the cosecant and the very same zenith delay are well below 0.5 mm at elevations of 10° (the current lowest bound for laser observations). However, given a station, laser ranges at the same elevation but varying azimuth are subject to the latitude-dependent atmospheric thickness and passing weather systems, that induce azimuth- and time-dependent atmospheric delay fluctuations. There are three approaches to account for azimuth-dependent variations, none of which is used operationally as of this writing:

- ☐ modelling at the observation equation level employing slant delays or gradients derived from ray-tracing in NWMs,
- ☐ estimation of station-wise, segmented parameters in the geodetic adjustment, and
- ☐ combining the two aforementioned approaches.

Opting for the first approach requires trust in the data from the NWM, the refractivity expressions, as well as the ray-tracing algorithm. Choosing the second implies confidence in the accuracy of the related ranges as well as a uniform distribution over elevation and azimuth. Nonetheless, none of the above hold; NWMs are not perfect, and the SLR observation geometry renders the estimation of gradients a difficult task, especially when only observations from the LAGEOS satellites are used. Should none of the aforementioned approaches be adopted, parameters with no clearly-defined physical meaning such as the station- or satellite-dependent range biases need to be estimated to reduce the residuals, and if not, atmospheric asymmetry manifests into spurious station displacements in the lateral plane (particularly in the meridional direction). State-of-the-art SLR analysis suggests not considering atmospheric asymmetry and not estimating residual zenith atmospheric delays.

To improve SLR data analysis, in the following it is assessed — based on simulated laser ranges with FGST (cf. Sec. 2.6) — whether the estimation of residual zenith delays and linear horizontal gradient components is possible and beneficial in SLR data analysis, and under which conditions. To this end, twelve SLR solutions were run (50 times each), spanning 10 years, and 143 stations (all that contributed to ITRF2014). In all scenarios, clouds, and geophysical loading were simulated, and the mapping functions were assumed to be known within the uncertainties suggested by the spread of the 10-member ensemble of ERA5. In all SLR solutions, atmospheric asymmetry was not modelled, deliberately. First the observation geometry was varied: (i) tracking of LAGEOS passes only (if permitted by clouds), and (ii) tracking of 9 spherical satellites, namely Ajisai, LAGEOS-1 and -2, Etalon-1 and -2, LARES, Larets, Stella, and Starlette (if permitted by clouds). Afterwards, two sets of solutions were produced with additional parameters being set up, as opposed to not estimating residual tropospheric effects (standard): (i) d^z_{nh} estimated, and (ii) d^z_{nh}, G_{NS}, and G_{EW} estimated. Then, another set of solutions was calculated to assess the potential benefit of a better constellation or a more complete functional model in the presence of a bias in the a priori zenith delay. Following from the investigations carried out in Sec. 3.3.2 regarding the quality of meteorological measurements in the vicinity of SLR stations, a bias in the recorded barometric pressure at the range of 2 hPa is not uncommon, and was thus introduced.

Failing to account for tropospheric asymmetry in SLR analysis has severe effects on the estimated station coordinates, the uncertainty thereof, as well as the implied reference frame. Figure 6.1.1 shows the average displacements over 10 years of continuous observations for some of the high-performing SLR stations. Without knowing where the stations are, it should be apparent that Yarragadee and Mount Stromlo lie in the Southern Hemisphere because the North-South gradient G_{NS} there is on average positive (due to the latitude-dependent atmospheric thickness) thus rendering range delays towards the North (South) larger than delay ranges towards the South (North). Not accounting for this effect, forces stations to move away from the equator (polewards) so that the L_2-norm condition is satisfied in the SLR adjustment. Figure 6.1.2 illustrates the average d_{NS} displacement from processing 10 years of the 9 aforementioned satellites. Therefore, neglecting to account for the atmospheric asymmetry cannot be ameliorated by processing more satellites. It is apparent that such a systematic deformation is equivalent to the introduction of a spurious scale factor in the implied TRF (−1.1 mm), as well as geocenter coordinate bias stemming from the uneven distribution of the global SLR network (1.5 mm). In essence, a non-negligible translation along the Z axis is certain. Figure 6.1.3 displays series of the datum perturbation parameters from Helmert transformations (7.2.1), that display a bias of $\begin{bmatrix}-0.2 & 0.0 & 1.5 & -0.4 & 0.4 & -0.3 & -1.1\end{bmatrix}^\top$ mm on the translations, rotations, and scale, respectively. The seasonal variations are below the 1 mm level. However, as the number of SLR stations contributing to a single solution is typically below 30 (cf. 2nd colorbar of Fig. 7.2.1),

the expected scatter will be larger, but the bias will remain. On account of the fact that until non-gravitational accelerations acting on non-spherical satellites are sufficiently understood, TRF origin stems solely from SLR, and should therefore be free of systematics when employed to transfer the datum to other techniques (e.g.

Unless a priori gradients from ray-tracing are supplied at the observation equation level, the only approach to circumvent the host of issues outlined above is to estimate gradient components based on the laser ranges. Owing to the very poor observation geometry, as well as that the most ranges from SLR stations are not towards spherical satellites (main data source of interest in the TRF framework), estimating gradients is not as easy as in GNSS data analysis. However, it is not impossible either (Drożdżewski and Sośnica, 2018). This is the first time, optical gradients are estimated in a realistic simulation without absolute constraints (loose relative constraints between consecutive gradient components are necessary for the stabilization of the solution).

To commence the expansion of the parameter space, first d^z_{nh} were set up. This is deliberate as regardless of the quality of the meteorological observations recorded in situ, the calculated d^z_{nh} will be flawed (to some extent) due to the fact that the vertical gradient of water vapour cannot be predicted accurately based on surface observations alone. To verify this statement, employing ERA5 data and the optical refractivity expressions summarized in Mendes and Pavlis (2004), d^z_h and d^z_{nh} were calculated following two approaches; for the point of interest: (i) total and water vapour pressure were extracted (cf. Sec. 3.3), and then the delays were evaluated, and (ii) the delays were determined by numerical integration in the model levels. While the differences between zenith hydrostatic delays from the surface and the model levels are within the nominal accuracy of ERA5, the differences between the non-hydrostatic delays are much larger – often exceeding the signal itself, especially in the presence of inversions. Therefore, if it is allowed by the observation geometry, there should be some benefit from estimating residual zenith delays.

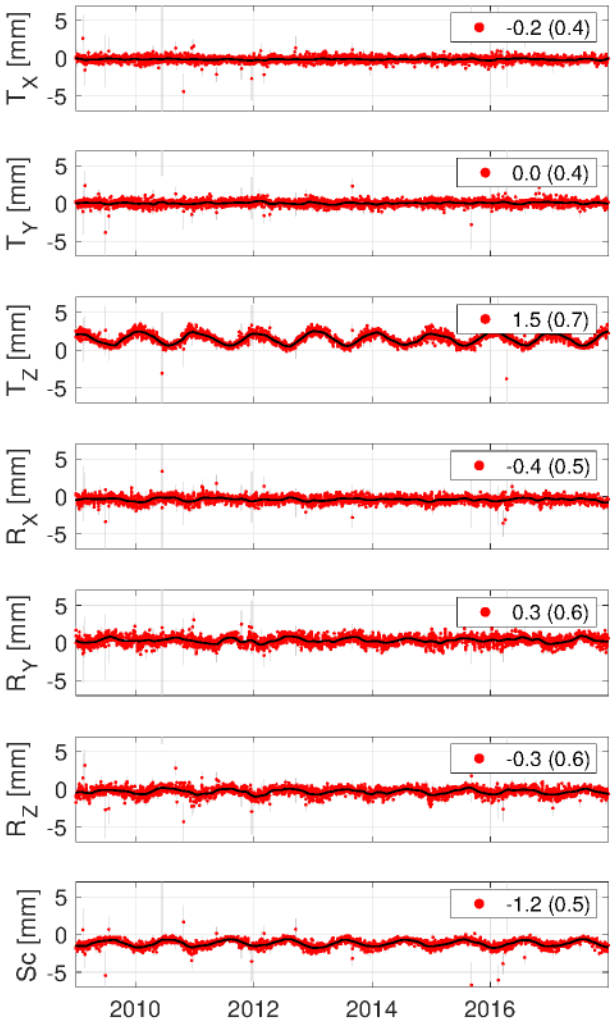


Figure 6.1.3: The datum perturbation parameters from a 7-parameter Helmert transformation between solutions where the atmospheric asymmetry was modelled, or was neglected at the observation equation level. The offset and scatter of the related time series are shown in the legend.

To demonstrate the advantage of estimating residual zenith delays in SLR data analysis, a pressure bias was introduced in some stations. If this offset is not detected prior to the SLR analysis, the height component of the station where the bias lies will experience a spurious vertical jump. Figure 6.1.1 provides proof that if a +2 hPa bias is present in the series of barometric

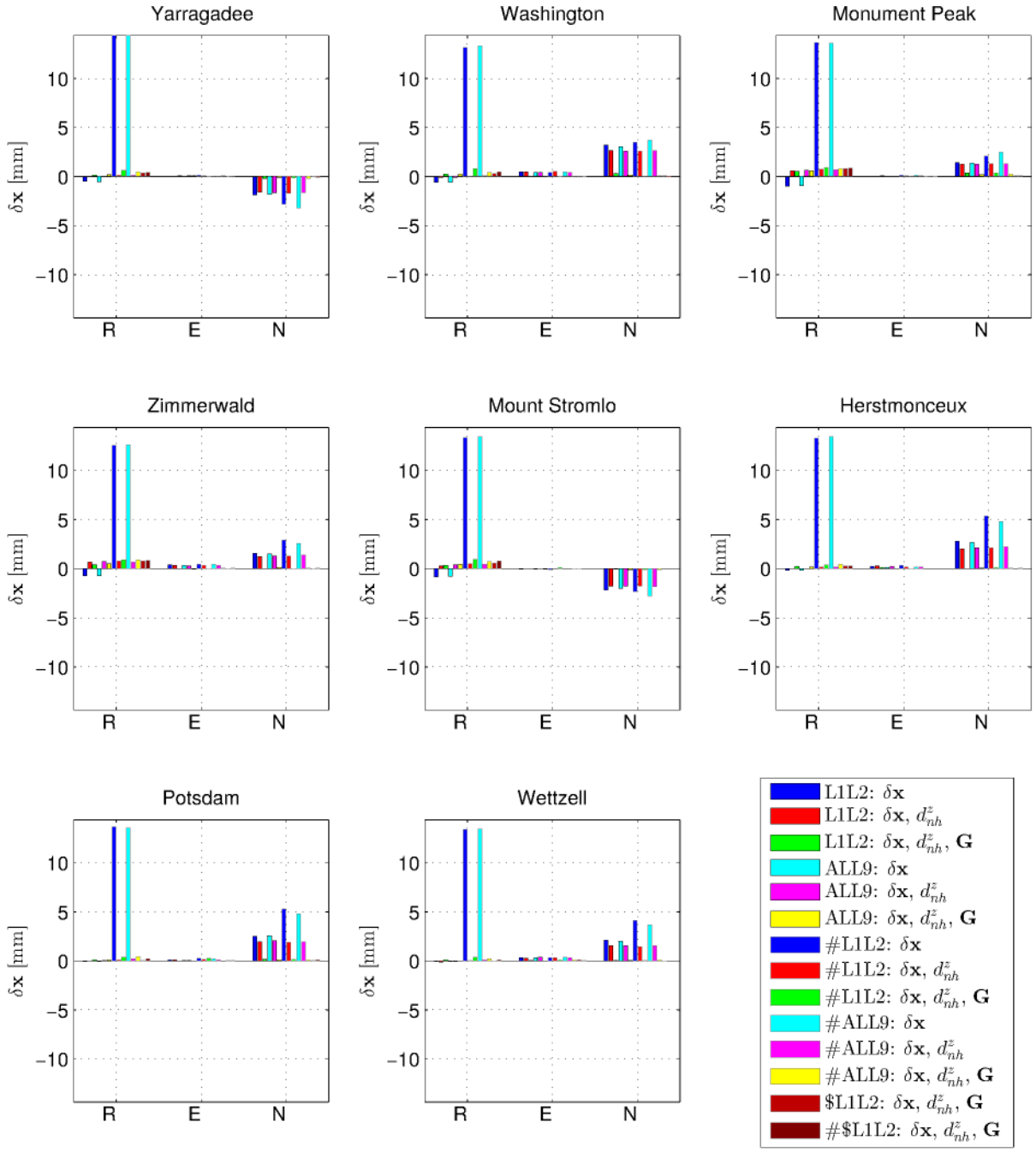


Figure 6.1.1: The coordinate bias in a topocentric system (radial, East-West, and North-South) for some of the high-performing SLR stations, induced by neglecting to model the tropospheric asymmetry. In the graph, the scenarios of expanding the parameter space of the geodetic adjustment are shown. In all solutions, the mapping function is assumed to be known within the precision of the underlying NWM (ERA5). SLR solutions where a 2 hPa bias was introduced in the a priori zenith delay are denoted with # (gray bar frame). L1L2 and ALL9 denote solutions where only LAGEOS-1 and 2 were used, and all aforementioned spherical satellites, respectively.

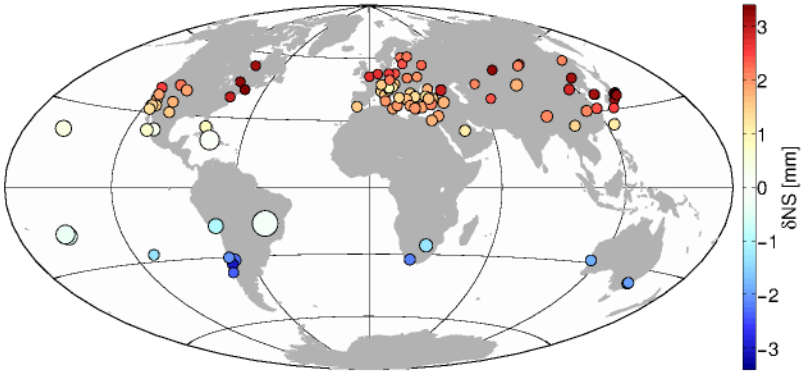


Figure 6.1.2: The spurious bias in d_{NS} induced in SLR data analysis if atmospheric asymmetry is not treated. The values shown stem from a 10-year-long simulation with 9 spherical satellites, accounting for the clouds, and assuming no other systematic errors. The circle size is indicative of the related uncertainty.

pressure and no residual zenith delays are estimated, the radial coordinate component will experience a long-term bias in the range of 10–15 mm, depending on the altitude and latitude of the station. Estimating d^z_{nh} absorbs the height bias almost completely, and at the same time slightly improves the lateral coordinate components (at the level of 40 %). This is expected because unlike microwave techniques where different mapping functions are used for the hydrostatic and non-hydrostatic delay component, only one mapping function is used at optical frequencies, thus allowing to account for a relatively small error in a priori zenith delay within a couple of iterations. In point of fact, comparing the solution where no pressure bias was introduced and no residual d^z_{nh} were estimated, to the solution where a pressure bias was introduced and residual d^z_{nh} were estimated, reveals that the latter yields height estimates closer to the truth, for 75 % of the stations. However, should one opt for estimating d^z_{nh} without absolute constraints in SLR analysis, the noise in the height time series is amplified which in turn leads to a 60 % larger WRMS, on average, after reducing the main seasonal signals (cf. Fig. 6.1.4). This is expected, as a larger number of additional parameters is estimated, and unlike microwave techniques no low-elevation observations can assist in improving the observation geometry. To ameliorate the scatter amplification, since SLR d^z_{nh} may be set up at longer intervals (e.g., 6-hourly), but then the physical meaning of d^z_{nh} is lost. Therefore, it is apparent that estimating d^z_{nh}, when possible, is capable of compensating errors in the a priori zenith tropospheric delay — as well as absorbing other unmodelled effects acting on the radial coordinate component — with the caveat that the scatter in the position time series increases.

To avoid long-term polewards (mainly) station coordinate offsets, gradients must be set up as unknown parameters, if the atmospheric asymmetry is not considered in the so-called "reduced observations vector". As higher order asymmetries stem mainly from water vapour transport in the lower troposphere, there is no utility in estimating 2nd order terms because lasers are largely insensitive to them. So, similar to microwave-based space geodetic data analysis, linear horizontal gradient components are set up as unknowns, without absolute constraints, and with very loose relative constraints, at hourly intervals. Again, 10 years of simulated data were processed with the aforementioned scenarios. Comparing the long-term North-South coordinate offset, between the solution where linear gradients were not estimated, and the solution where gradients were estimated hourly (when allowed by the observation geometry), reveals that in all 143 stations the bias induced by neglecting the atmospheric asymmetry is reduced by 93 %, on average. For instance, at Yarragadee d_{NS} is suppressed from 3.2 mm (asymmetry neglected) to only 0.3 mm

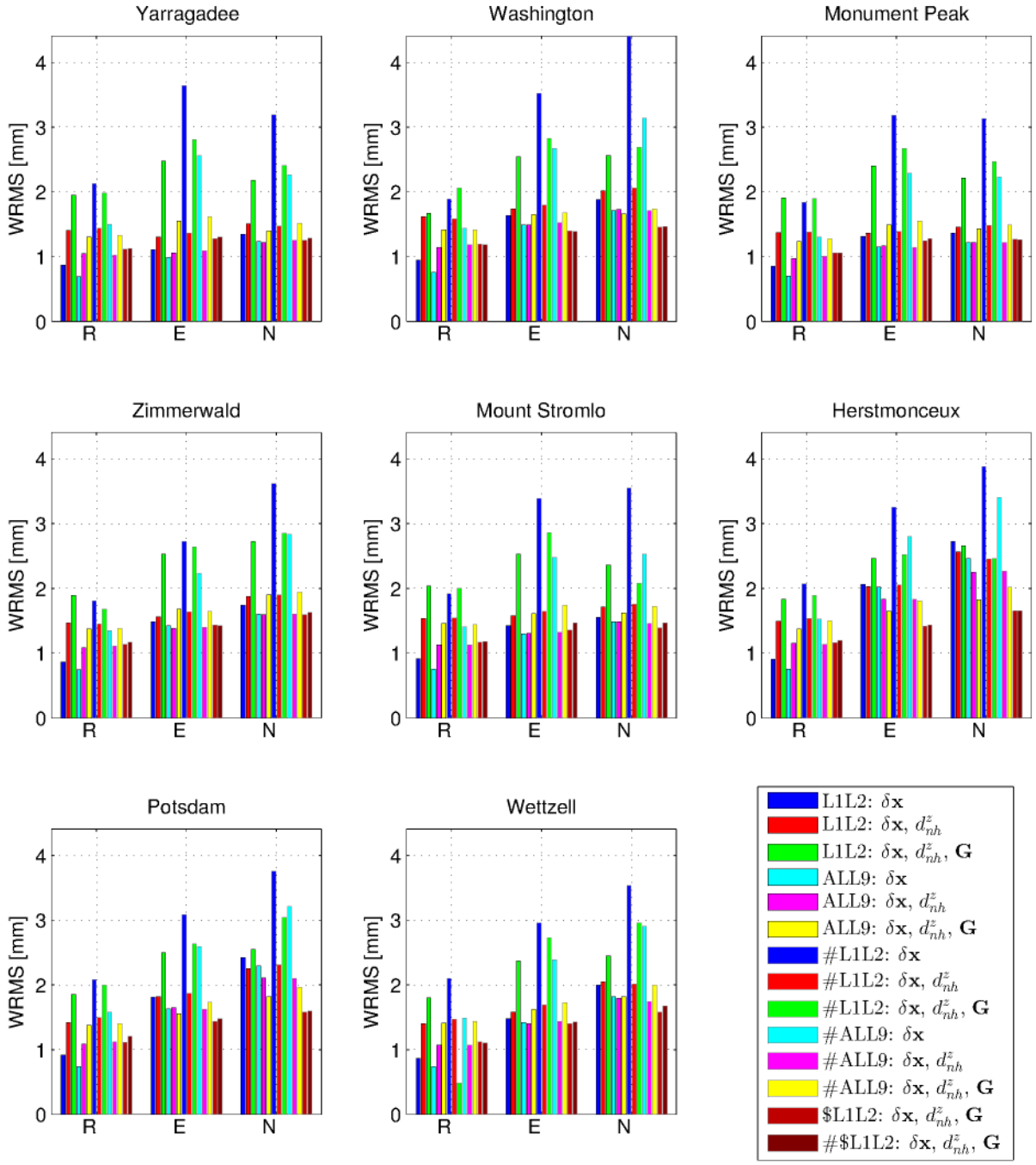


Figure 6.1.4: The WRMS of the post-fit residuals from a least-squares adjustment of coordinate time series in a topocentric system (radial, East-West, and North-South), for some of the high-performing SLR stations, induced by neglecting to model the tropospheric asymmetry. See the description of Fig. 6.1.1.

(gradients estimated). While the bias in the both lateral coordinate components is practically eliminated, the scatter in the time series thereof is inflated; estimating hourly gradients increases the WRMS (after filtering the main seasonal signals) in all stations by 60 % (East-West), and 30 % (North-South). This should come as no surprise since up to 50 additional parameters are set up per day — usually much less because in FGST no segmented parameters are set up at intervals with no observations. So, similar to estimating d^z_{nh} in addition to the other parameters in the SLR adjustment, estimating linear gradient components is capable of reducing the impact of unmodelled effects that are correlated with the lateral coordinate components with the drawback of inflating the scatter in the position time series.

Due to the fact that unlike gradient components estimated from microwave space geodetic techniques (VLBI, GNSS, and DORIS), (i) optical gradients do not experience so rapid fluctuations, and (ii) the observation geometry of SLR cannot support high temporal resolution of atmospheric gradients, it is investigated whether dilating the gradient estimation intervals in SLR data analysis can reduce the systematic offsets induced by ignoring the atmospheric asymmetry, and at the same time reduce the scatter increase expected from the additional unknown parameters. This is motivated from (i) the decay and effective correlation delay of a Hirvonen covariance model (cf. (4.3.5)) for microwave gradients' series being much steeper and shorter, respectively, compared to a similar model based on optical gradient time series, and (ii) the correlation stemming from the SLR adjustment covariance matrix between consecutive gradient component estimates is very high. To this end, another set of solutions was produced featuring the estimation of a single piece-wise linear segment per day for the linear gradient components. Comparing the solutions where gradients were estimated hourly to a daily estimation, the bias reduction remains; the difference in long-term average in all coordinate components estimated in the adjustment where gradients were set up hourly and daily, is for all stations below 0.2 mm. Moreover, the scatter — in essence the WRMS of the differences between the coordinate series estimated by FGST and the coordinates employed to simulate the related observations free of systematic and random errors — in the time series is reduced by 45 % on average in all coordinate components, as opposed to a large increase when hourly gradients are estimated (cf. Fig. 6.1.4). The latter is an indication that setting up atmospheric delay corrections in SLR data analysis leads to an overparameterized problem. A detailed discussion on coping with such formulations in the least-squares framework is presented in Kotsakis (2005). In the presence of a consistent error in the a priori zenith delay, the results do not change considerably; the height bias is again almost completely absorbed by d^z_{nh} (32 % improvement of daily d^z_{nh} over hourly d^z_{nh}, by as much as 0.5 mm), the lateral bias induced by atmospheric asymmetry is compensated by the gradients (improvement in 90 % of the stations by as much as 0.5 mm), the height WRMS decreases in 95 % of the stations by 41 % (on average), and the horizontal coordinate WRMS decreases in all stations by 48 % (on average). While the improvement in the bias is not statistically significant, the noise deflation in the coordinate time series is.

Based on the aforementioned SLR solutions, it is also found that even if d^z_{nh} and linear gradient components are estimated daily, the combined effect of an uncalibrated barometer and neglecting to model the atmospheric asymmetry will induce no systematic nor random errors in the estimated coordinates. In fact, the maximum long-term difference between a solution that all reduced-observation vectors consist solely of the noise component, and a solution where the reduced-observation vectors include systematics in the horizontal and vertical components, is 0.1 mm (below the noise floor). There is no notable increase in the noise of the coordinate time series, nor the type thereof.

For all aforementioned solutions — atmospheric asymmetries are not accounted at the observation equation level — two sets of solutions were generated varying the satellites taken into

consideration. Processing simulated data from 9 satellites in lieu of only LAGEOS-1 and -2, yields a statistically significant improvement in recovering the correct station coordinates in only 46 % (R), 67 % (EW), and 84 % (NS) of the cases. The S_a amplitudes reduce in 38 % (R), 63 % (EW), and 71 % (NS) of the cases (cf. Fig. 6.1.5). As far as the WRMS of the post-fit residuals from the seasonal fit on the coordinate time series is concerned, employing more satellites reduces the scatter in all stations. The true station velocity is facilitated by employing more satellites in all stations. However, the improvement in the uncertainty of the estimated parameters is not in all cases equivalent to the increase in the number of normal points. This issue is related to the scheduling of laser ranges, and will be addressed in a separate study.

6.2 Impact on station coordinates

It is known that observations at low elevation angles facilitate the decorrelation between the station height, the residual zenith delay, and the constant term of the clock function (e.g., MacMillan and Ma, 1997; Rothacher et al., 1997; Böhm, 2004; Niell, 2001; Nilsson et al., 2013) in VLBI and GNSS data analysis. Therefore, observing at low elevations is pertinent in obtaining accurate information about refractivity fluctuations aloft a station, as well as its actual height. However, due to the fact that incoming low-elevation signals spend more time in a highly turbulent medium (lower troposphere), the usefulness of these measurements in the geodetic adjustment is dependent upon the quality of the related atmospheric delay corrections. Therefore, stations that observe at low elevation angles are most affected by the mapping function quality.

Based on the data analyzed in this work, in geodetic VLBI, only 6 % of the observations are scheduled below 10° (less than 0.3 % below 5°). On average, 34 % of the observations are scheduled at elevations between 10° and 30°. For elevations above 30° simply employing the cosecant in lieu of a sophisticated mapping functions will yield sub-mm differences in the related symmetric atmospheric delay correction. Non-negligible differences between the PMF, the VMF1, and GFZ-PT start becoming prominent at elevations below 10°–15°. There are a number of stations that do not typically observe below 10° (e.g., `BADARY`, `SVETLOE`, and `ZELENCHK`) so, any variations in station-wise parameters occurring at such stations are network effects. As far as the azimuthal distribution is concerned, in modern VLBI operations, the North-South imbalance in the station-wise skyplots is not as pronounced as in the early VLBI years. On average, there are 30 % more radio sources towards the North or South, depending on the station location and the observing network.

Contrary to mapping function errors, that influence only low elevation observations, errors in the a priori zenith delay influence all observations, to an extent scaled by the cosecant (first approximation), or the related hydrostatic mapping factor (rigorously). Thus, treating these errors (mainly due to erroneous pressure measurements) is crucial in obtaining accurate parameter corrections in all four space geodetic techniques, and particularly in SLR data analysis where no residual atmospheric delay estimates can absorb spurious a priori zenith delay features.

In the following, the temporal variations of the station coordinates (in a topocentric coordinate system) are assessed, as well as the baseline lengths. At first exposure, the baseline length is a quantity derivative from the station coordinates, and therefore should not offer additional information. However, this is untrue because while station coordinates heavily depend on the approach adopted to impose the datum (e.g., no-net conditions, or fixed coordinates), baseline lengths are independent of that. Since the VLBI network changes considerably over time, portion of the temporal variations can be ascribed to network effects. This is the main reason why station coordinate time series from co-located GNSS stations (obtained from the analysis of a global network featuring hundreds of stations) are considerably less noisy than VLBI time series.

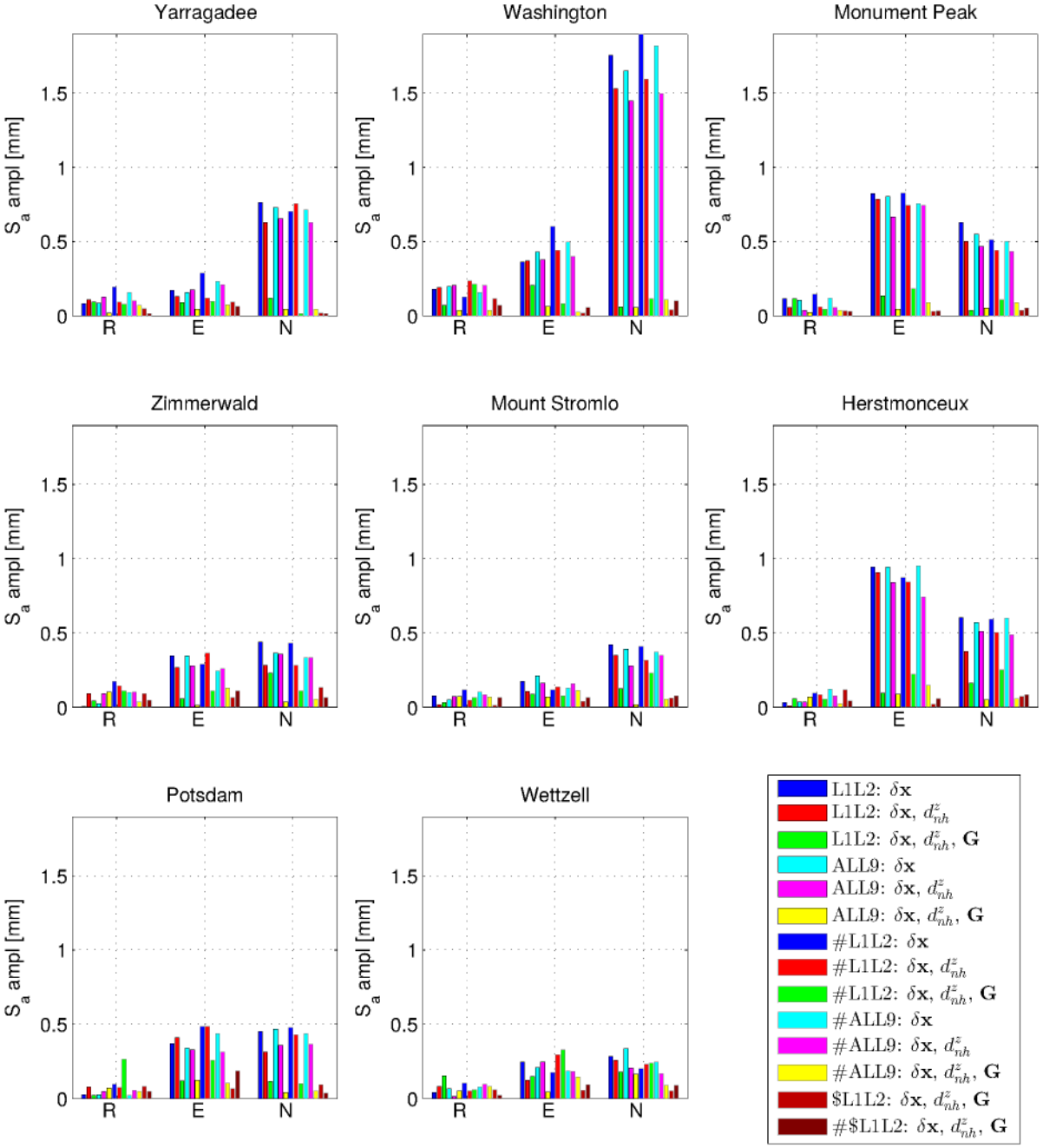


Figure 6.1.5: The S_a amplitude of coordinate time series in a topocentric system (radial, East-West, and North-South), for some of the high-performing SLR stations, induced by neglecting to model the tropospheric asymmetry. See the description of Fig. 6.1.1.

Therefore, there is a merit in studying the baseline lengths, in addition to the station coordinates.

Based on the investigations carried out herein, changing the mapping functions does not seem to affect considerably the seasonal variations of the radial coordinate component. Figure 6.2.1 attests to this statement. There are no significant differences in the signal response at the S_a, S_{sa}, and S_{ta} frequency bands. However, opting to use empirical mapping functions (GFZ-PT) in lieu of discrete series of mapping function coefficients slightly amplifies the WRMS of the post-fit residuals, on average. No significant differences were identified between PMF and VMF1.

The impact of alternating the mapping functions and the a priori zenith delays on the estimated station coordinates was also assessed in the framework of multi-GNSS observations simulated with FGST. Twenty years of observations were simulated, based on the space vehicles constituting the constellation made available[1] by GFZ Potsdam, and a ground network of 130 globally distributed stations (cf. Fig. 6.2.2). The assumptions based on which this Monte Carlo simulation was run are outlined in Sec. 2.6. In brief, all stations can track all satellites above 7°, all stations operate continuously, the data loss is 5 % per station daily, elevation- and system-dependent white noise was applied in the observations together with noise stemming from the clocks and atmospheric turbulence, phase ambiguities are known and all observations are simulated based on GNSS-tailored ray-traced delays in ERA Interim reanalysis. Four scenarios were considered: (i) correct atmospheric delay model, that is $\mathbf{b} = \mathbf{0}$ plus noise, (ii) slightly incorrect mapping functions compared to the ray-traced delays (GFZ-PT), (iii) slightly incorrect pressure compared to the discrete series (GFZ-PT), and (iv) a combination of the previous two scenarios. The purpose of these simulations was to assess the importance of pressure and mapping functions in the analysis of microwave space geodetic observations in a controlled environment. To mitigate the influence of the observation geometry on the interpretation of the results, the coordinate corrections were not compared to the a priori values, but with the parameters estimated in a GNSS solution were no systematic errors were simulated (i).

The artificial offset in station coordinates induced by erroneous mapping functions, and pressure, is in most cases relatively small (cf. Fig. 6.2.3, Fig. 6.2.4, and Fig. 6.2.5). In 32 % (12 %) of the GNSS stations employing GFZ-PT in lieu of ray-traced mapping factors (GFZ-PT instead of ERAinML series) yields uncertainties larger than 1 mm. The combination thereof introduces a bias larger than 1 mm in 36 % of the stations. The reduced sensitivity to "wrong" pressures, in comparison with "wrong" mapping functions, is due to the fact that the residual atmospheric delay compensates almost completely any mismodelling in the a priori zenith delay. Therefore, in this regard, GGOS requirements cannot be satisfied by analytical approximations of "correct" atmospheric refraction models. The fact that statistically significant biases do exist in these simulation scenarios spanning 20 years, is proof that not all atmospheric refraction modelling shortcomings can be compensated by the tropospheric parameter estimation.

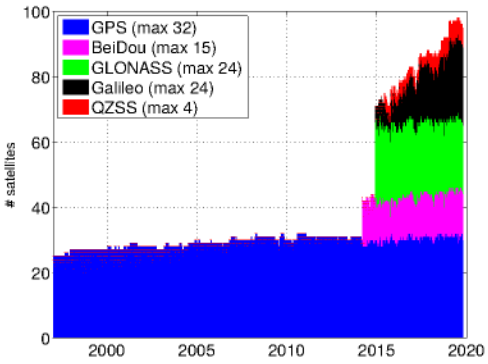


Figure 6.2.2: The number of space vehicles that constitute the GNSS constellation for which simulations were carried out with FGST. The related `sp3` files were prepared by Zhiguo Deng (GFZ Potsdam).

Based on the simulations carried out herein, it is found that the velocities of the station coordinates are marginally affected by alternating either the mapping function or the a priori

[1] ftp://ftp.gfz-potsdam.de/GNSS/products/mgex/

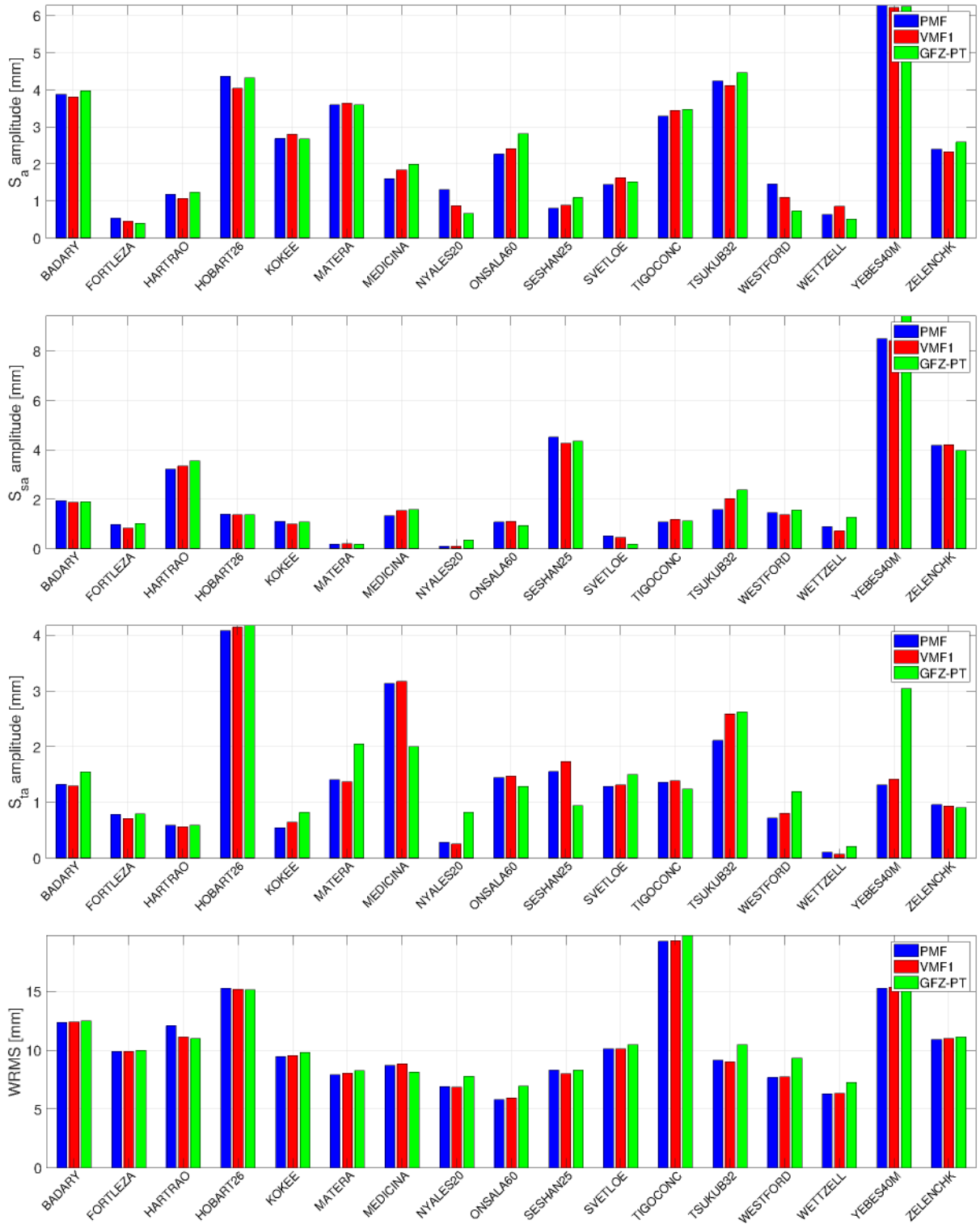


Figure 6.2.1: The S_a (1st row), S_{sa} (2nd row), and S_{ta} (3rd row) amplitudes of station displacements in the radial coordinate component, as well as the WRMS of the post-fit residuals, after applying PMF (blue), the VMF1 (red), and GFZ-PT (green) mapping functions, at the observation equation level, in the analysis of all IVS rapid turnaround sessions during the period 2002–2014.

zenith delay. The largest discrepancies (in the radial coordinate component, as expected) were at the level of 0.5 mm dec^{-1} (cf. Fig. 6.2.3, Fig. 6.2.4, and Fig. 6.2.5) in the cases where the empirical mapping functions were used, which is well below the GGOS requirements of 1 mm dec^{-1}. On average, stations seem to move upwards when the empirical mapping functions were used, and slightly in the nadir direction when the empirical meteorological model was used. These features are indicative of rates in the datum perturbation parameters. Nevertheless, the velocity uncertainty claimed by the latest ITRFs is in this order of magnitude for several stations. However, all GFZ-PT parameters feature a robustly estimated linear trend that in principle should prevent spurious secular motion. Moreover, mismodelling atmospheric refraction should have an amplified impact on shorter time series. Therefore, discrete mapping functions (coefficients as time series) should be preferred over analytical ones such as GFZ-PT and GPT3 (as well as its predecessors).

The results presented in Fig. 6.2.3, Fig. 6.2.4, and Fig. 6.2.5 suggest that poor modelling of the atmospheric delay decrease with increasing elevation introduces factitious seasonal variations in the height coordinate component. In almost a quarter of the network (27 % of the GNSS stations), an artificial signal whose amplitude exceeds 1 mm in the S_a frequency is detected. In 16 % of the stations an S_{sa} signal with an amplitude larger than 1 mm could be discerned. The zenith non-hydrostatic delay series estimated from an adjustment where slightly incorrect zenith delays were supplied a priori will feature artificial variations, which from the one hand reduce the corruption of the station coordinates, but on the other hand dilute the quality of the tropospheric parameters.

After the major seasonal variations were removed from the reduced coordinate time series — scenarios (ii) to (iv) minus (i) — the WRMS of the post-fit residuals was calculated. On average, the WRMS is 2.5 mm for the solution where the GFZ-PT mapping function was used, and 1.5 mm for the solution where pressure from GFZ-PT was used.

From the results of the GNSS simulations presented in this section, it is apparent that while ignoring to account for synoptic variations in d_h^z does not impact the station coordinates appreciably because the estimated d_{nh}^z absorbs the largest part of the difference, ignoring to account for high-frequency variations in the mapping function coefficients contaminates the station coordinates considerably, posing an obstacle in meeting GGOS goals.

In a VLBI session, given the coordinate estimates of two stations that have participated in at least one scan together, and the block of the covariance matrix of unknowns that refers to these six parameters, the baseline length and the uncertainty thereof is computed. It is important not to ignore the covariances as the baseline length precision will erroneously appear better (at the 1 mm level), and will inescapably lead to drawing invalid conclusions regarding the statistical significance of e.g., two series of baseline lengths. After the baseline lengths for all possible pairs are formed for all sessions, the time series thereof are analyzed in a least-squares framework. Given the time series of a baseline length $\{b\}_{i=1}^{N}$, a line is fitted to each segment (determined by abrupt position changes mainly induced by earthquakes and hardware changes), and the WRMS scatter of the post-fit residuals is assessed. The WRMS computation requires the residuals (v_{b_i}), and the uncertainties thereof ($\sigma_{v_{b_i}}$), and reads as follows

$$\mathrm{WRMS} = \sqrt{\sum_{i=1}^{N} \frac{v_{b_i}^2}{\sigma_{v_{b_i}}^2} \left(\sum_{i=1}^{N} \frac{1}{\sigma_{v_{b_i}}^2} \right)^{-1}} \,. \tag{6.2.1}$$

Seasonal variations are implicitly included should the WRMS be calculated following (6.2.1). Of course, instead of a straight-line, a sinusoid can also be fitted, thus reducing the WRMS. However,

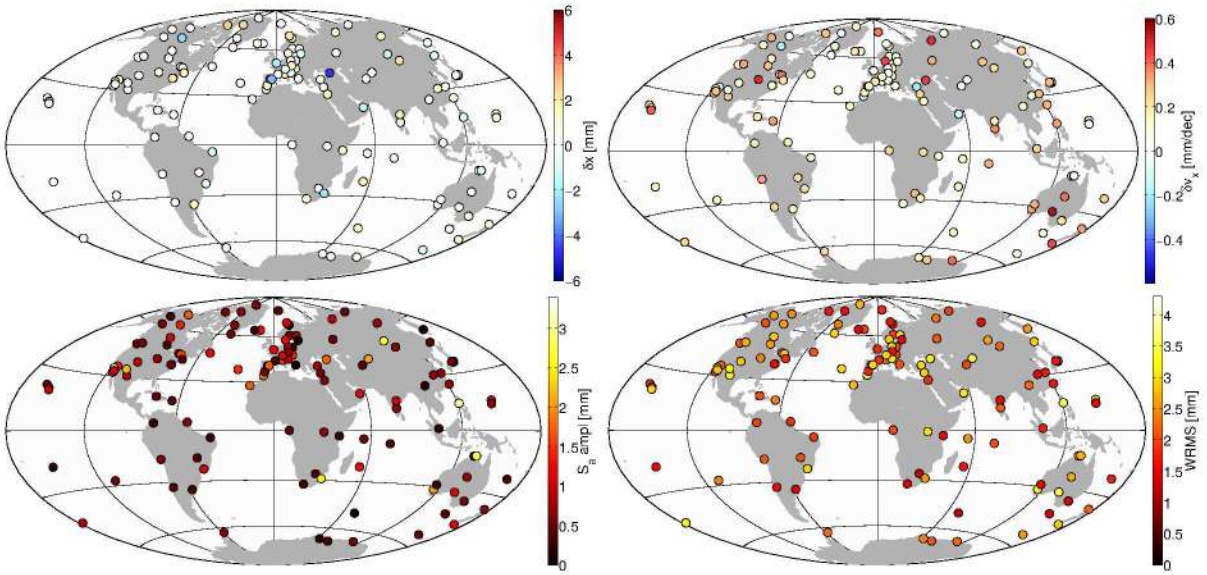


Figure 6.2.3: The average displacement bias (upper left), the spurious linear velocity (upper right), the S_a amplitude (lower left), and the WRMS (lower right) of the radial station coordinate relative errors stemming from alternating the mapping functions to GFZ-PT.

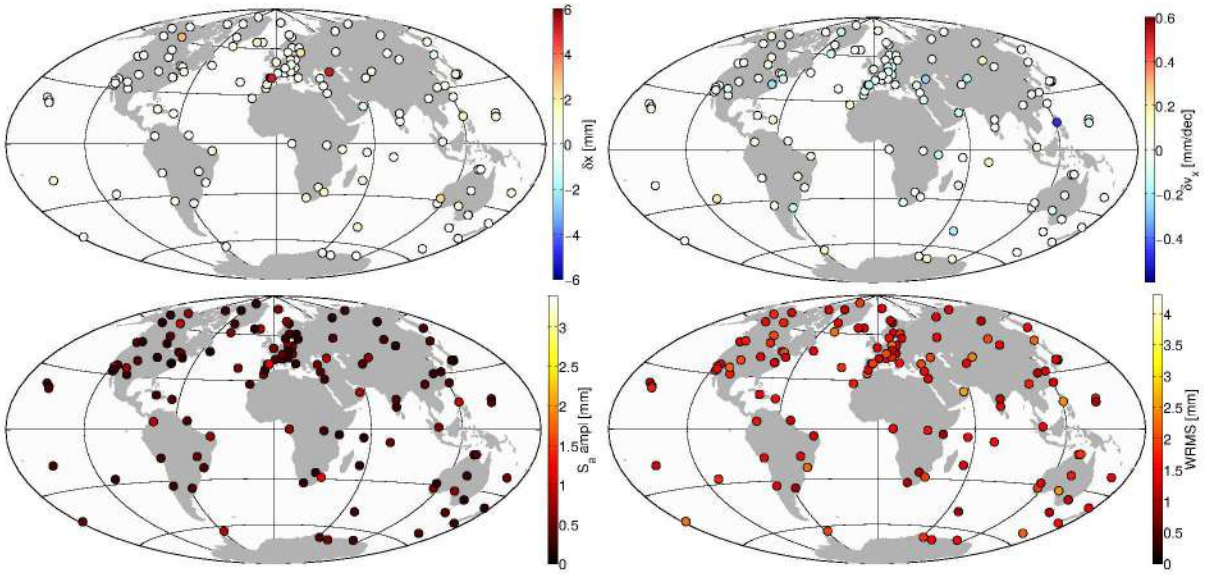


Figure 6.2.4: The average displacement bias (upper left), the spurious linear velocity (upper right), the S_a amplitude (lower left), and the WRMS (lower right) of the radial station coordinate relative errors stemming from alternating the meteorological to GFZ-PT.

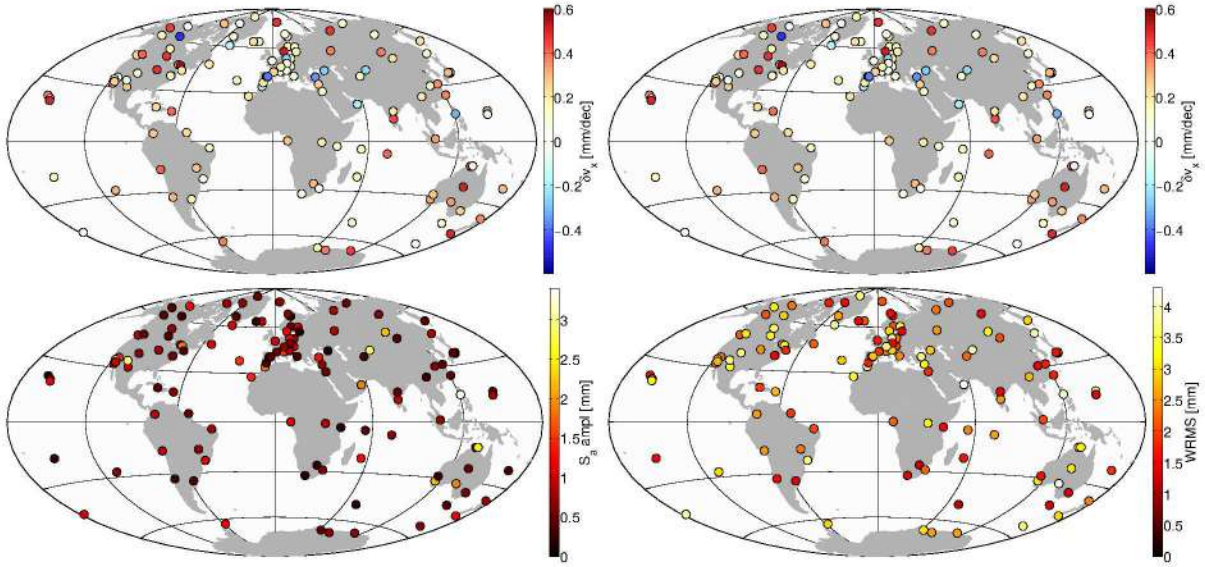


Figure 6.2.5: The average displacement bias (upper left), the spurious linear velocity (upper right), the S_a amplitude (lower left), and the WRMS (lower right) of the radial station coordinate relative errors stemming from alternating both the mapping functions and meteorological data to GFZ-PT.

in this case WRMS estimates from different solutions will not be comparable as they will refer to different functional models, assuming that the seasonals are not identical. An interesting feature of the WRMS of baseline lengths is its almost quadratic decay as a function of baseline length. To assess the overall impact of a change in VLBI processing, the following fitting ansatz (e.g., MacMillan and Ma, 1994) is commonly employed as the observation equation

$$\mathrm{WRMS}(b) = \sqrt{A^2 + (Bb)^2}. \tag{6.2.2}$$

Due to Earth's curvature, VLBI measurements from baselines longer than $R\sqrt{2}$ are typically carried out at lower elevation angles; these angles decrease on average with increasing baseline length. The B estimates serve as a quality indicator of low-elevation reduced observations, which is directly dependent upon the success with which elevation-dependent systematic and random effects were reduced, and in turn related to the fidelity of the mapping functions utilized in the analysis of the group delays. Of course there are other effects that contribute to the fact that the time series of longer baselines feature more scatter compared with shorter baselines, the most predominant of which is source structure (Anderson and Xu, 2018).

Following the aforementioned procedure, the baseline length repeatability coefficients (A, and B) for all VLBI solutions were calculated. Alternating both hydrostatic and non-hydrostatic mapping functions in VLBI data analysis between PMF and VMF1 does not yield a statistically significant difference in these parameters (improvement at the 1 % level), whereas employing PMF instead of GFZ-PT yields an improvement in A by 20 %, and an improvement in B by 2 %. All three, the PMF, the VMF1, and the GFZ-PT are already of very good quality, the differences are not very large. However, the quality of the a priori d_h^z is more important in this regard. Changing the source of meteorological data from raw to homogenized in situ, yields an improvement in A by 9 %, and in B by 3 %. Opting to use ERAinML over GFZ-PT yields an improvement in A by 26 %, and in B by 2 %. The differences in the baseline length repeatability between a solution where homogenized in situ meteorological data were used, and ERAinML are negligible. The latter provides proof that if no in situ meteorological data are available, or there

is a doubt about the quality thereof, ERAinML may be used without degrading the solution whatsoever. An account of these findings is provided in Balidakis et al. (2018c).

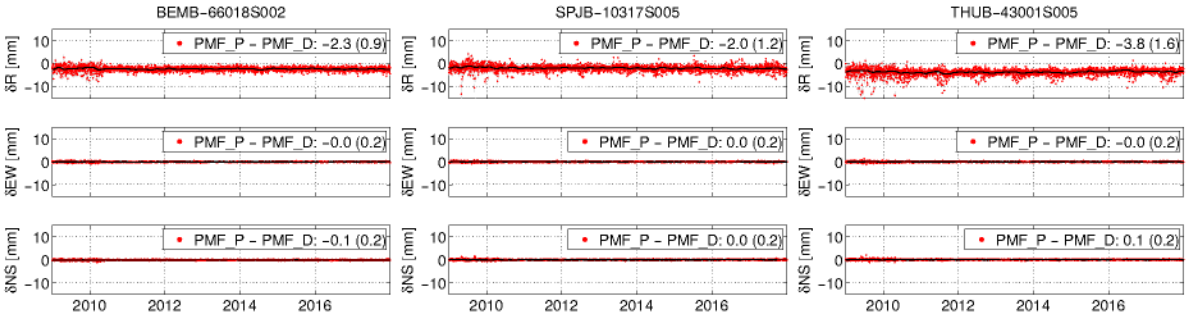


Figure 6.2.6: Topocentric coordinate differences between a DORIS solution where a DORIS-tailored PMF was used, and a DORIS solutions where a GPS-tailored PMF was used. The stations shown are Belgrano (left), Ny-Ålesund (middle), and Thule (right).

Due to the increased ray-bending for DORIS observations, compared to VLBI and GNSS, a VLBI- or GNSS-tailored mapping function is inappropriate, as it induces elevation-dependent errors that cannot be compensated by station-based parameters. Based on the simulations carried out herein with FGST, employing a VLBI- or GPS-tailored mapping function to reduce DORIS observations induces a 2 mm height bias, on average. Figure 6.2.6 attests to this statement by illustrating the coordinate differences for the DORIS beacons with the largest number of observations (cf. Fig. 2.4.3).

6.3 Impact on station network

To assess the extent to which improving the atmospheric refraction model impacts on the implied reference frame, a number of session-wise conformal Bursa-Wolf (or Helmert) transformations have been carried out between the different VLBI (real group delays, `VieVS@GFZ`), and GNSS solutions (simulated ranges, FGST). An account of the VLBI-related results may be found in Balidakis et al. (2018c). All VLBI coordinate transformations were carried out with respect to the VLBI solution where the PMF and homogenized in situ data were used. GNSS transformations were carried out with respect to the GNSS solution where no systematic errors were simulated.

Alternating the mapping functions and the pressure utilized to compute the a priori zenith delay does not introduce significant translations or rotations. The translation bias is in all cases below the 0.1 mm level, with a scatter that does not exceed 0.9 mm. The rotations' bias is also at the 0.1 mm level, with a scatter below 0.7 mm for all pairs. As far as the differential scale factor is concerned, no significant bias appears between the VLBI solutions. However, the scatter is considerably larger than in the time series of the other similarity transformation parameters. Changing the mapping functions between PMF and VMF1, induces a scatter in the scale time series at the level of 1.1 mm. Erroneous in situ meteorological data are responsible for an 1.3 mm scale scatter, whereas utilizing ERAinML instead of homogenized in situ data yields a WRMS of 1.2 mm. Employing the empirical meteorological model GFZ-PT introduces a scatter of 1.8 mm. In previous work (Balidakis et al., 2016) meteorological data extracted from the surface of MERRA2 were used — for a trial run — to calculate the zenith hydrostatic delay. The scale between that solution and the solution where the homogenized in situ meteorological data were used features a WRMS at the level of 7 mm, thus rendering apparent that raw surface

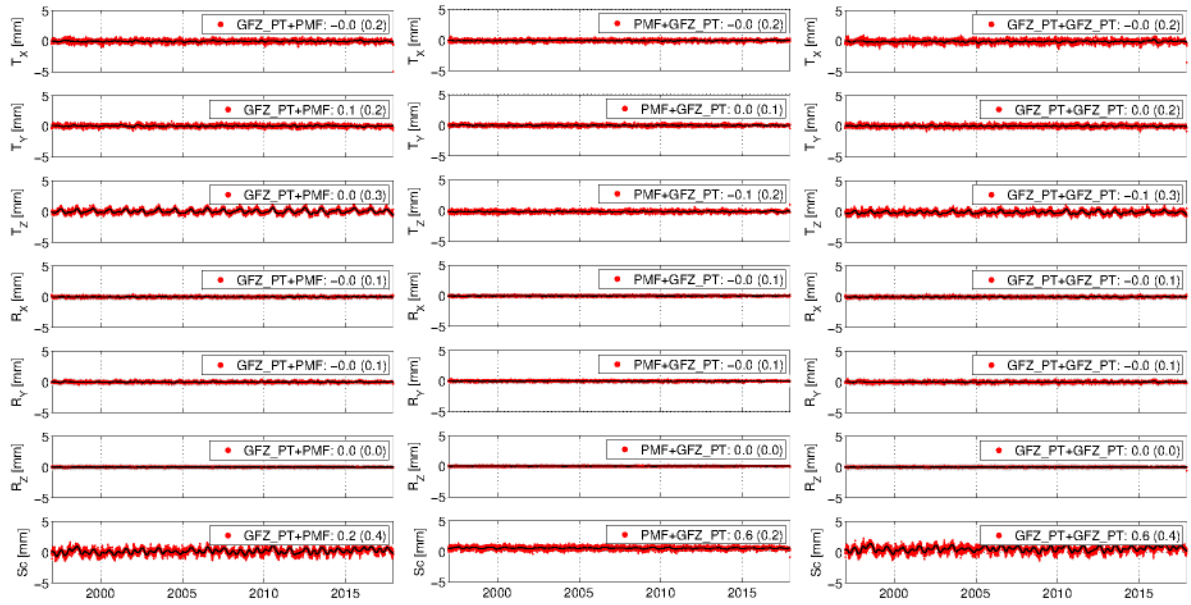


Figure 6.3.1: The time series of a 7-parameter similarity transformation between the ensemble mean of the solution where GFZ-PT served as mapping functions (left), the solution where GFZ-PT was used to calculate the d_h^z (middle), and the solution where GFZ-PT was used for mf_h, mf_{nh}, and d_h^z (right), with respect to the GNSS solution where no systematic errors where simulated. In the legend of these graphs, the average offset appears, as well as the WRMS of a straight-line fit, enclosed in parenthesis.

meteorological data should not be used (unless they are calibrated for the height difference). At this point, it is important to mention that all these differences are small in comparison to the datum perturbation parameters estimated from a similarity transformation between any of the VLBI solutions prepared herein and ITRF2014, where a 3.7 mm scale bias is detected, as well as a WRMS of 2.5 mm. Neither alternating the mapping function nor the a priori zenith delay induces statistically significant rates in the datum perturbation parameters.

The impact of varying the mapping functions and the meteorological data on the station network was also assessed in the framework of GNSS simulations with FGST. The results do not reveal offsets in any similarity parameters except for the scale when d_{nh}^z from GFZ-PT is applied. Then the bias slightly exceeds the 0.5 mm level. The WRMS of all Helmert parameters is below the 1 mm level. The largest scatter is detected in the time series of the translation in the X coordinate component as well as the differential scale factor. The inflated noise in T_X is due to the interhemispheric imbalance of the network based on which the observations were simulated. The noise in the scale is expected because the quality of mapping functions and zenith delays predominantly affect the radial coordinate component. Figure 6.3.1 illustrates the aforementioned time series for the three different scenarios.

The results from the GNSS simulations are in large part transferable to DORIS, with the difference that the noise would be amplified due to fewer observations.

Should VLBI- or GNSS-tailored mapping functions be used in DORIS data analysis, a small height bias (2 mm) is detected. This station-dependent error manifest as a bias in almost all similarity transformation parameters, and in particular the scale (2.2 mm), as well as T_Z (1.3 mm) and R_Z (81 µas). Figure 6.3.2 illustrates the time series of the parameters estimated from the Helmert transformation. In addition to the bias and the large scatter in the parameters, an offset in the time series at epoch 2010 can also be discerned. This offset, which is accompanied by an increase in the precision of the station coordinates and the datum perturbation parameters,

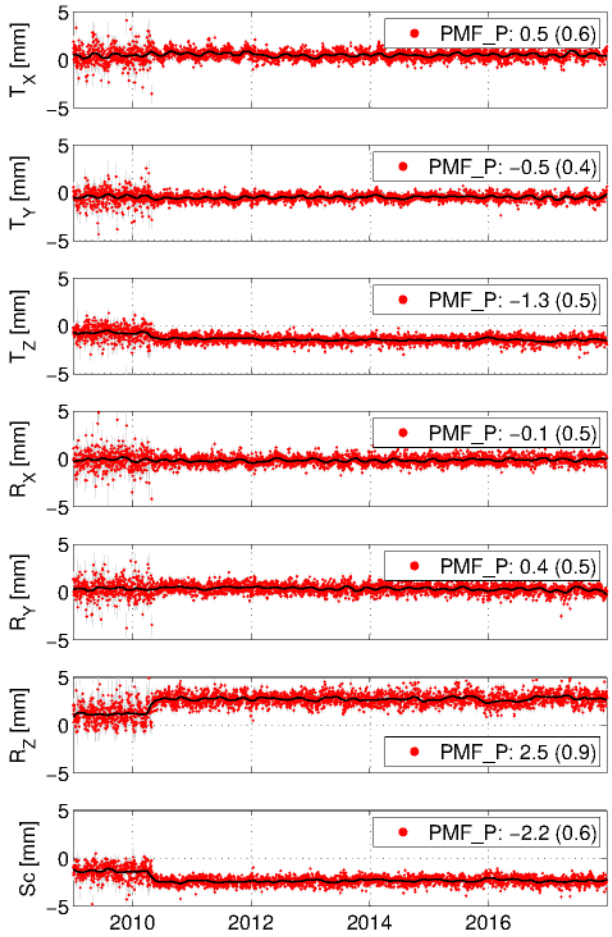


Figure 6.3.2: The datum perturbation parameters from a 7-parameter Helmert transformation between DORIS solutions where a VLBI-, and a DORIS-tailored mapping function was used to model the delay decay with increasing elevation angle. The offset and scatter of the related time series are shown in the legend.

stems from the inclusion of Cryosat-2 and HY-2A in the simulation and ensuing analysis carried out herein. The fact that both missions have an orbital altitude below 1000 km (717 km for Cryosat-2) results in a large mapping function discrepancy, thus highlighting errors induced by employing mapping functions tailored for VLBI in DORIS data analysis. This suggests that part of the differences in datum-defining parameters between single-mission DORIS solutions may also be attributed to inappropriate (not orbital-altitude-tailored) mapping functions/factors.

6.4 Impact on Earth orientation parameters

Atmospheric delay modeling mainly affects the estimated station coordinates — therefore the baseline lengths and the implied TRF too, the clock function, and the residual tropospheric delay parameters (d^z_{nh} and gradient components). Nevertheless, due to the fact that corrections to the radio source positions as well as corrections to the EOPs are estimated in a common adjustment, the quality of the atmospheric delay model will affect these parameters as well. Furthermore, the estimation of Earth orientation is overparameterized from a strictly mathematical viewpoint as five angles are set up to describe — in essence — three rotations. To determine the extent of

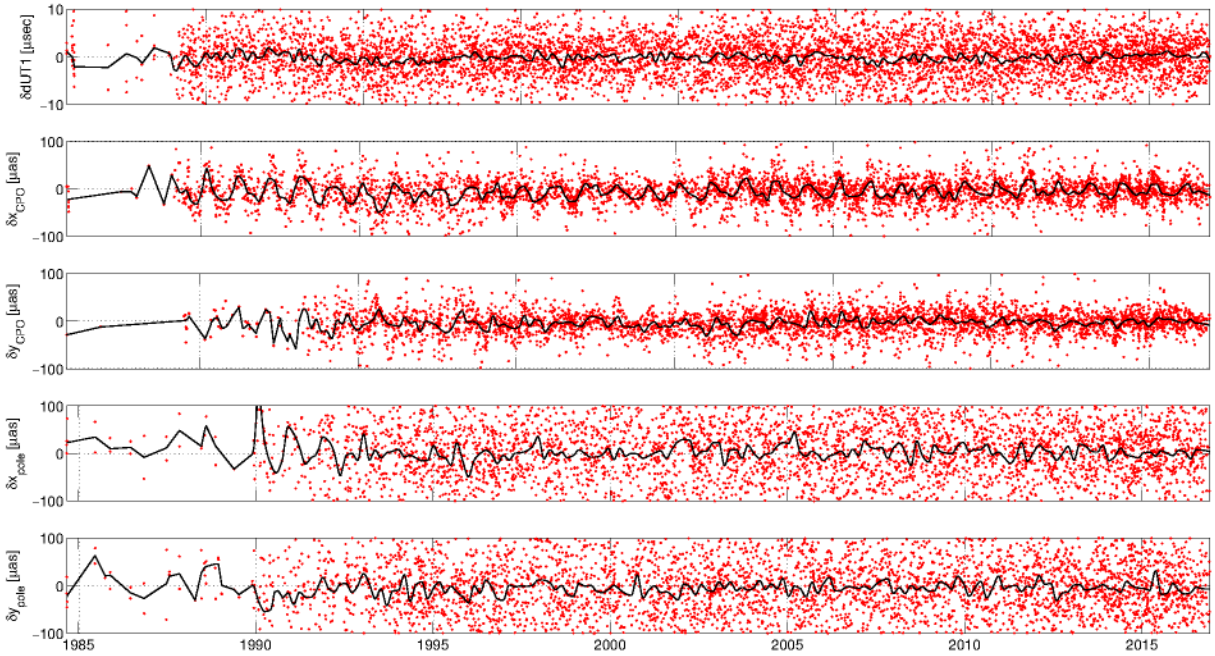


Figure 6.4.2: The differences in the EOPs estimated in VLBI data analysis employing the PMF developed herein and VMF1. The differences are shown in red, and the running median in black.

this dependence, the correlation matrix was studied. The element of the correlation matrix $\mathbf{R}$ that is derived from the invertible normal equation matrix (NNT and NNR applied already) of the e.g., VLBI adjustment, and expresses the correlation between parameters i and j reads

$$R_{ij} = \frac{Q_{ij}}{\sqrt{Q_{ii}Q_{jj}}}, \tag{6.4.1}$$

where $\mathbf{Q} = \mathbf{N}^{-1}$ denotes the inverse of the normal equation matrix (cofactor matrix of the estimated parameters). Figure 6.4.1 depicts the correlations between EOPs and station coordinate corrections. The correlation between corrections in the nutation offsets (x_{CPO} and y_{CPO}) and the station coordinates is on average below 20 %, over all stations that participated in IVS rapid turnaround sessions (2002–2018). The correlations between station coordinates and dUT1 are slightly larger, typically below 45 %. Polar motion variations are even more correlated with station coordinates. Better network geometry improves the decorrelation between EOP and station coordinates, thus yielding more precise EOP corrections.

In the following, EOP changes induced by varying (i) the mapping function between VMF1 (IERS standard) and PMF (this work), as well as (ii) between PMF and GFZ-PT (a seasonal fit to PMF) are assessed. Afterwards, the impact of alternating the pressure, effectively d_h^z is also assessed. For the latter three scenarios were evaluate: (i) in situ pressure, as recorded for the barometer co-located with the VLBI station, (ii) the empirical model GFZ-PT (cf. Sec. 4.3), (iii) series rigorously extracted from the model levels of ERA Interim (cf. Sec. 3.3), (iv) in situ data after they were homogenized (cf. Sec. 3.3.2).

As for the EOP there is no reference to compare with (when they are estimated based on real measurements), only relative errors can be studied. However, since the solution where PMF was used in addition to homogenized in situ meteorological records yields slightly better baseline length repeatability, it serves as a reference.

Alternating the mapping function, few systematics are induced in the estimated EOPs. First, the long-term offsets between the solution where VMF1 (GFZ-PT) was utilized with respect to the solution where PMF was used, are compared. The bias, PMF minus VMF1 (PMF minus GFZ-PT), in dUT1 is 0.1 µs (0.2 µs), in the Celestial pole offsets it is −4.0 µas (0.6 µas) and −2.3 µas (−0.2 µas) for the x_{CPO} and y_{CPO}, respectively. The largest biases are found in polar motion; 11.0 µas (−8.6 µas) for x_p and −6.4 µas (2.3 µas) y_p. It is rather unexpected that an empirical model induces less bias than VMF1, considering that both VMF1 and PMF account for weather variability, and are forced from similar data sets (ECMWF operational analysis and ERA Interim, respectively). EOP differences between the PMF and VMF1 solutions are shown in Fig. 6.4.2. To better comprehend these discrepancies, the seasonal component thereof was estimated within a weighted least-squares adjustment. Table 6.4.1 shows the seasonal amplitudes, as well as the uncertainties thereof, together with the WRMS of the post-fit residuals. The most prominent differences are found in polar motion, where the S_a amplitude is around 8 µas for both components (VMF1), and around 2 µas for GFZ-PT. The scatter between PMF and GFZ-PT is ≈ 15 µas, and surprisingly ≈ 30 µas between PMF and VMF1. The annual variations in x_{CPO} and y_{CPO} between VMF1 and PMF can probably be attributed to the use of a priori gradients (1st and 2nd order) with loose absolute constraints in the latter solution. To identify the source of this discrepancies, the atmospheric delay correction differences between VMF1 and PMF were studied. The relative differences between VMF1, PMF, and ray-traced delays from the VLBI group at GSFC[2] spanning the period 2000–2016, show a better agreement between PMF and GSFC in terms of systematics and scatter for symmetric mapping factors, zenith delays, and asymmetric delays, e.g., cf. Fig. 4 from Balidakis et al. (2018c). Noise aside, it was found that for some stations, the coordinates employed in the ray-tracing procedure were slightly different from the actual ones that were used for the computation of PMF. Consistent differences in the zenith delays at the 1–5 mm level can be attributed to different underlying NWMs, refractivity expressions, or numerical integration approaches. Nevertheless, almost all Australian stations as well as some others feature biases in the zenith delays that cannot be ascribed to any of the aforementioned causes; `YARRA12M` (70 mm in d_h^z), `KATH12M` (40 mm in d_h^z), `HOBART12` (6 mm in d_h^z), and `WESTFORD` (13 mm in d_h^z). Beside these cases, there are a number of stations whose coordinates changed slightly throughout the years, yielding differences in the zenith delays at the level of 5 mm (e.g., Nikolaidou et al., 2018a,b). However, since VMF1 is an operational service such changes are to be expected, but should be taken care of for reprocessing campaigns.

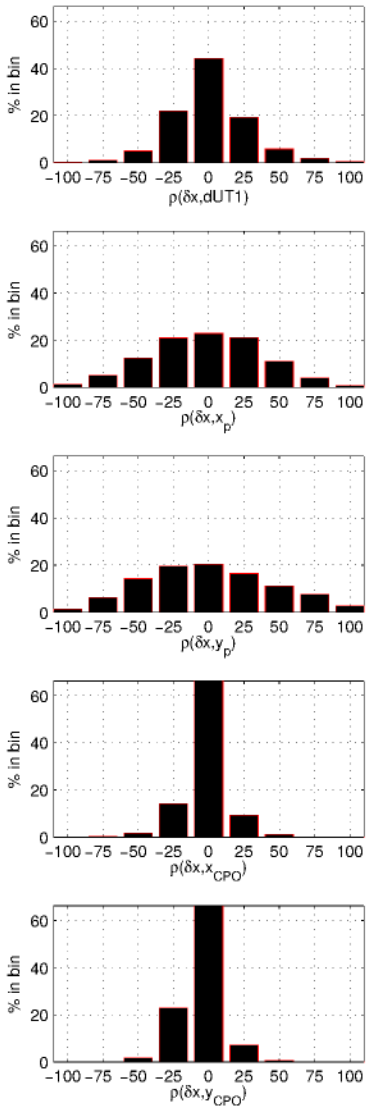


Figure 6.4.1: The correlation between EOPs and station coordinates in least-squares adjustments with `VieVS@GFZ` (all IVS-R1 and IVS-R4 spanning the period 2002–2018), where EOPs and station coordinates are set up as single offsets per station.

[2]Service https://vlbi.gsfc.nasa.gov/services/tropodelays/tropodelays/ no longer updated.

Table 6.4.1: Seasonal amplitudes and WRMS of the post-fit residuals of the EOP differences stemming from alternating the mapping functions (PMF, VMF1, and GFZ-PT), and the meteorological data used for the computation of d_h^z (raw in situ, GFZ-PT, ERAinML, and homogenized in situ), at the observation equation level in VLBI data analysis (IVS non-intensive sessions spanning the period 1979–2018).

	EOP	S_a	σ_{S_a}	S_{sa}	$\sigma_{S_{sa}}$	S_{ta}	$\sigma_{S_{ta}}$	WRMS
PMF vs. VMF1	δdUT1 [µs]	0.42	0.06	0.14	0.05	0.03	0.05	1.68
	δdX [µas]	12.23	0.27	7.62	0.28	1.11	0.27	9.37
	δdY [µas]	5.83	0.31	7.05	0.30	1.45	0.31	10.93
	δx_p [µas]	8.96	1.29	3.39	1.22	3.93	1.21	29.52
	δy_p [µas]	7.64	1.32	1.16	1.22	2.32	1.24	29.28
PMF vs. GFZ-PT	δdUT1 [µs]	0.08	0.04	0.10	0.04	0.17	0.04	1.02
	δdX [µas]	0.49	0.28	0.48	0.28	0.56	0.28	7.47
	δdY [µas]	0.98	0.28	0.53	0.28	0.48	0.28	7.53
	δx_p [µas]	2.29	0.79	3.07	0.80	2.95	0.78	15.57
	δy_p [µas]	0.87	0.85	1.27	0.84	1.33	0.85	13.92
homogenized vs. raw in situ	δdUT1 [µs]	0.29	0.11	0.27	0.10	0.21	0.10	3.34
	δdX [µas]	17.31	1.62	7.37	1.67	1.69	1.65	49.51
	δdY [µas]	10.72	1.44	9.77	1.44	4.04	1.45	48.30
	δx_p [µas]	5.10	2.09	7.38	2.21	3.78	2.16	53.70
	δy_p [µas]	5.08	2.08	6.17	2.15	8.67	2.09	50.51
homogenized vs. ERAinML	δdUT1 [µs]	0.02	0.02	0.01	0.02	0.01	0.02	0.41
	δdX [µas]	0.73	0.11	0.21	0.11	0.32	0.11	3.44
	δdY [µas]	0.86	0.11	0.36	0.11	0.05	0.11	3.51
	δx_p [µas]	0.47	0.26	0.56	0.24	0.70	0.24	4.77
	δy_p [µas]	0.52	0.24	1.07	0.26	0.62	0.27	5.46
ERAinML vs. GFZ-PT	δdUT1 [µs]	0.09	0.02	0.07	0.02	0.03	0.02	0.60
	δdX [µas]	1.01	0.13	0.56	0.13	0.51	0.13	3.75
	δdY [µas]	0.48	0.13	0.36	0.12	0.32	0.12	3.76
	δx_p [µas]	0.80	0.40	0.83	0.39	0.32	0.37	6.59
	δy_p [µas]	0.76	0.43	0.38	0.45	1.05	0.45	8.15

The analysis of the complete IVS history (1979–2018) reveals no substantial systematic EOP offsets induced by varying the source of meteorological data between GFZ-PT, ERAinML, and homogenized in situ. For the EOP vector $\begin{bmatrix} dUT1 & x_{CPO} & y_{CPO} & x_p & y_p \end{bmatrix}^\top$, the offsets induced by varying the meteorological data between homogenized in situ and ERAinML are $\begin{bmatrix} 0.0\,\mu s & 0.3\,\mu as & -0.6\,\mu as & 1.3\,\mu as & -1.0\,\mu as \end{bmatrix}^\top$, and the offsets induced by varying the meteorological data between ERAinML and GFZ-PT are below the 0.1 µs and 0.1 µas level, as shown in Fig. 6.4.3. The lack of considerable systematics between the three aforementioned solutions suggests that if solely EOPs are to be studied, these models may be used interchangeably. However, to avoid a scatter increase in the Celestial pole offsets by $\approx 4\,\mu as$, and in polar motion by $\approx 6\,\mu as$, homogenized in situ data should be preferred when available.

The largest disagreement between EOP estimated from solutions where the a priori zenith delay was varied, was detected in changing between raw (GPT2 as backup if e.g., the pressure entry in the NGS was `-999.000`) and homogenized in situ meteorological data. While the offsets are not very large — except for 14.1 µas in x_{CPO} — the scatter in the differences is (cf. Fig. 6.4.4).

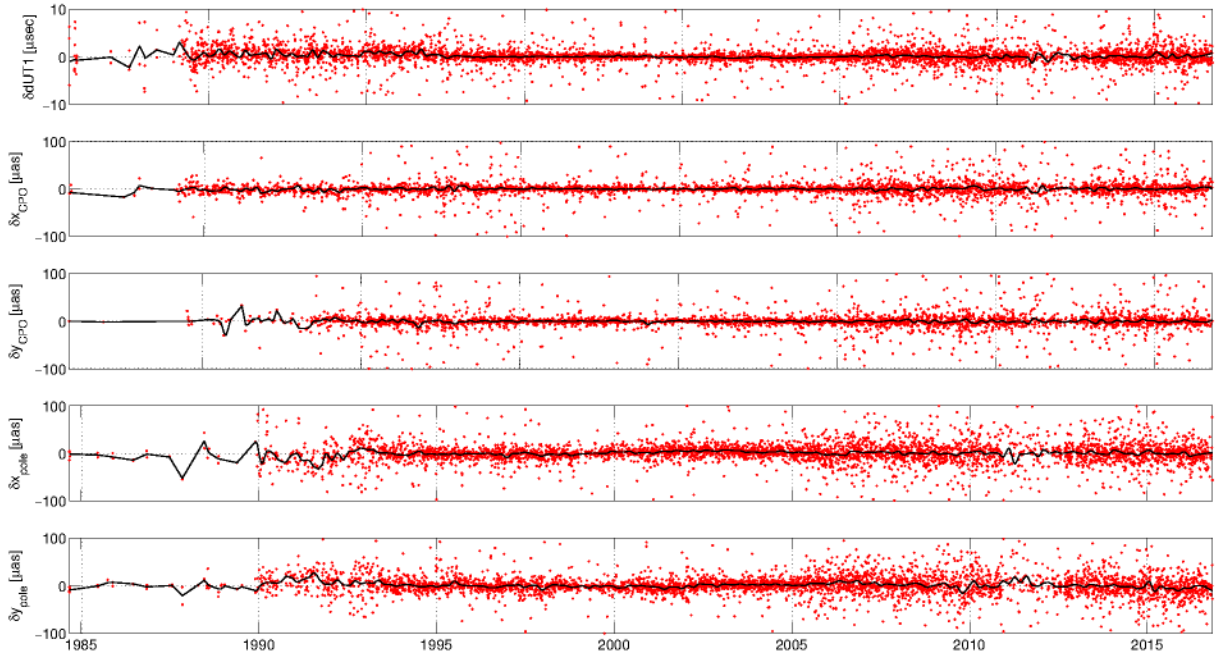


Figure 6.4.3: The differences in the EOPs estimated in VLBI data analysis employing the homogenized in situ meteorological data and ERAinML. The differences are painted red, and the running median in black.

This scatter stems from both systematic variations (seasonal signals) and random variations. Table 6.4.1 shows that in the polar motion differences there is a 7 µas annual signal as well as 9 µas semi-annual and ter-annual signals. The trajectory of the Celestial pole also experiences spurious seasonal variations should the raw in situ meteorological data be used: 20 µas (S_a), 12 µas (S_{sa}), and 4 µas (S_{ta}). The scatter is also relatively large compared to all other scenarios, exceeding 50 µas for the terrestrial and Celestial pole motion. The difference $UT1 - UTC$ displays a very large scatter as well (3 µs).

The results outlined in Table 6.4.1 suggest that the quality of the meteorological data employed to compute the a priori zenith delays, as well as the mapping functions in VLBI data analysis, is a far greater concern in EOP estimation than station displacement induced by mass transport within Earth's fluid envelope. In view of VGOS, employing inhomogeneous meteorological data (series with several offsets and outliers) is going to pose an immovable obstacle in estimating EOPs with an accuracy of 1 µs and 15 µas.

Introducing the a priori gradient components developed herein at the observation level in SLR data analysis reduces the polar motion bias with respect to the IERS 14 C04 (IAU2000A) series by 90 % and 63 % for x_p, and y_p, respectively — confirmed by M. Drożdżewski and K. Sośnica employing Bernese v5.3, within a collaborative work (Drożdżewski et al., 2019).

6.5 Impact on integrated water vapour trends

The fact that microwave space geodetic techniques can accurately sense long-term water vapour variation has been proven manyfold. For a review, the interested reader is referred to e.g., Haas et al. (2003); Heinkelmann et al. (2007); Nilsson and Elgered (2008); Alshawaf et al. (2017); Balidakis et al. (2018c); Alshawaf et al. (2018) and the references therein. Motivated from the facts that (i) introducing changes in the a priori, the deterministic, and the stochastic

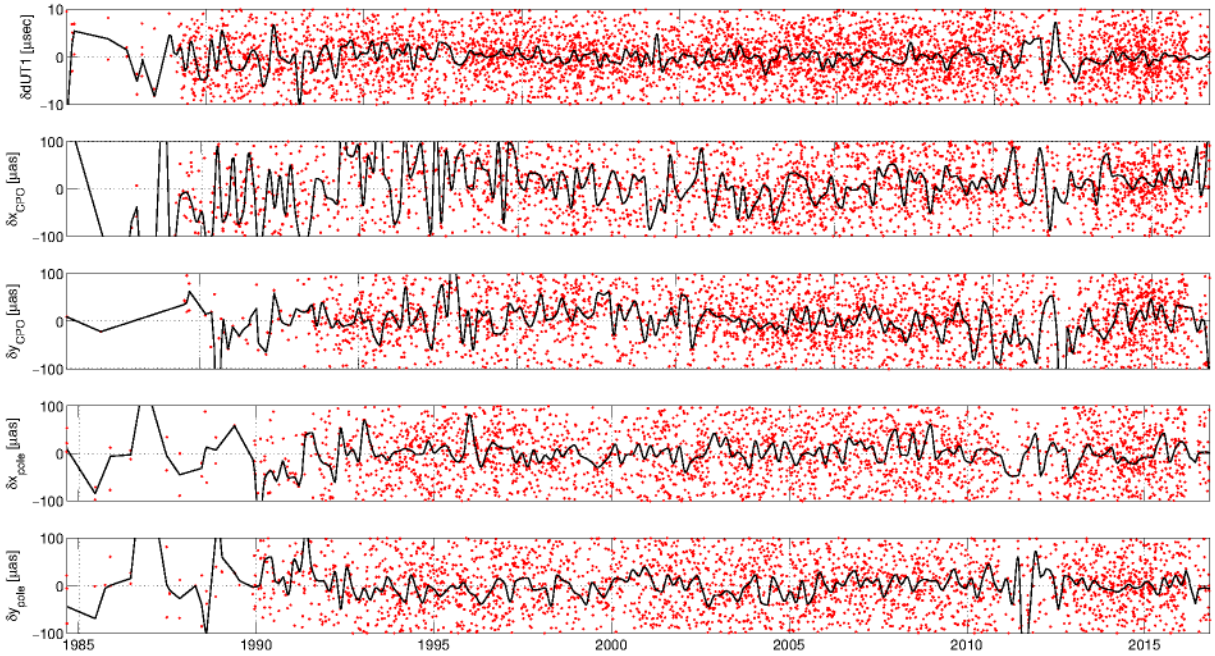


Figure 6.4.4: The differences in the EOPs estimated in VLBI data analysis employing the homogenized and raw in situ meteorological data. The differences are in red and the running median in black.

model that describe atmospheric delay variations in the vicinity of a station in the space geodetic data analysis will affect all parameters constituting the parameter space in a least-squares adjustment to an extent dictated by the a posteriori covariance matrix, and (ii) monitoring integrated water vapour (retrieved by the estimated zenith non-hydrostatic delays and the so-called water vapour-weighted mean temperature) is crucial for a whole host of meteorological applications, long-term integrated water vapour (IWV) and gradient rates from both real and simulated GNSS and VLBI observations were assessed. Some of these investigated are outlined in Alshawaf et al. (2017); Balidakis et al. (2018c,d); Alshawaf et al. (2018). In this section, a brief comparison of IWV trends from the analysis of real VLBI (`VieVS@GFZ`) and GPS (`EPOS.P8`) observations is presented, followed by a more comprehensive analysis of IWV and gradient component rates from simulated VLBI and multi-GNSS observations (FGST).

An in-depth comparison of IWV trends at sites where VLBI radio telescopes are co-located with at least one GPS receiver is presented in Balidakis et al. (2018c), and will not be repeated herein. It is important to note that while a relatively good agreement (in 75 % of the stations the relative errors are not statistically significant) was proven between VLBI, GPS, and ERA Interim, the limited number of stations studied therein prompts a follow-up study to ascertain the results. Figure 6.5.1 illustrates the linear IWV trends estimated at all sites where a VLBI and a GPS receiver observed for more than 10 years. To make the comparison rigorously, atmospheric ties (cf. Sec. 4.4) were applied to the d^z_{nh} from GPS, so that they refer to the position of the VLBI station. However, since the actual IWV trend is not known neither which of the three approaches considered therein to obtain it is more reliable, it is impossible to conclude on the actual accuracy of the estimates, and therefore only relative errors can be examined. Moreover, a gradient trend comparison could not be carried out as for the 2nd TIGA reprocessing BS98 was employed to model the elevation dependence of the asymmetric delays, whereas for the VLBI reprocessing the CH97 gradient mapping function was always used (cf. Sec. 4.2.3). Kačmařík et al. (2019) demonstrates differences stemming from the gradient mapping function choice.

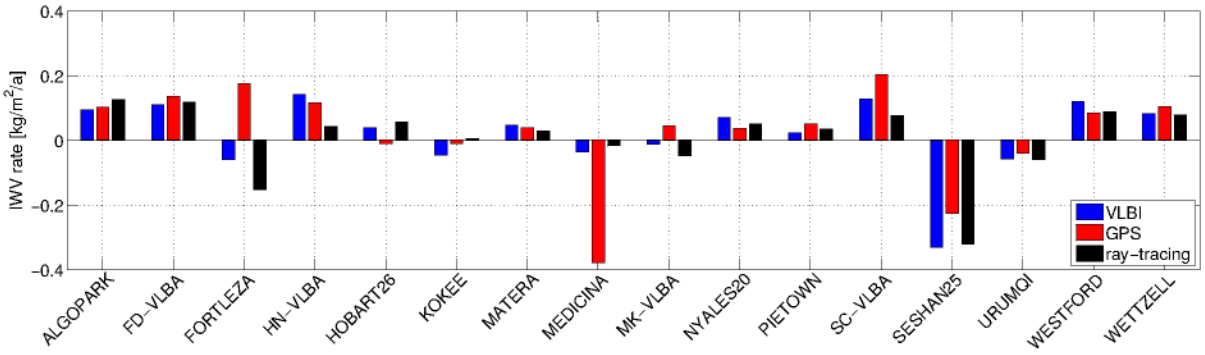


Figure 6.5.1: IWV trends estimated from real VLBI and GPS observations employing `VieVS@GFZ`, `EPOS.P8`, and ray-tracing. For the trend estimation, the three different time series (for every station) were synchronized.

Due to the fact that not all differences between the real VLBI- and GPS-derived IWV trends could be explained, a simulation study was carried out (Balidakis et al., 2018d), in an attempt to explain the role of the observation geometry and accuracy in the observed IWV trend differences. In all cases, atmospheric delays were simulated based on ERA-Interim-derived technique-specific ray-traced delays ("observed" vector). In terms of the "computed" vector, four solutions were processed:

- ☐ correct mapping functions, and correct a priori zenith delays,
- ☐ correct mapping functions, and wrong a priori zenith delays,
- ☐ wrong mapping functions, and correct a priori zenith delays, and
- ☐ wrong mapping functions, and wrong a priori zenith delays.

"Correct" denotes the geodetic solutions where effects were reduced based on consistent PMFs. For the scenarios denoted by "wrong", only the seasonal harmonics of GFZ-PT were used for the retrieval while ray-traced delays were used to simulate the related observations (all cases). For this study, 20 years of multi-GNSS observations (1997–2018), and 17 years of VLBI observations (2002–2018) were simulated based on the final orbits from GFZ Potsdam and the IVS schedules for the rapid turnaround sessions, respectively. Figure 6.5.3 illustrates the d^z_{nh} for different modelling scenarios, as well as employing GPS-only observations as opposed to multi-GNSS observations. It is apparent that employing measurements from more systems reduces the scatter around the ensemble mean, with small impact on its value whatsoever. A single day for `POTS` is also shown where the a priori d^z_h was supplied from GFZ-PT in lieu of numerical integration in the model levels of ERA Interim. While there is almost no increase in the scatter, the solution is biased. Linear atmospheric gradient components from a GPS-only solution, and a multi-GNSS solutions are illustrated in Fig. 6.5.2. It is clear that processing the observations of more navigation systems substantially reduces the noise about the ensemble mean, thus yielding a benefit for atmospheric monitoring.

Afterwards, d^z_{nh} from all VLBI and GNSS solutions were converted to IWV employing consistent refractivity constants with those employed in the ray-tracing, and T_m from numerical integration, cf. (4.3.1). Two sets of IWV series were generated: the first set featured IWV calculated from the direct d^z_{nh} output of FGST (biased for the solutions were the a priori delays were modelled with GFZ-PT), and the second featured adjusted d^z_{nh} series. To obtain the latter (labeled "adjusted" in the related figure), correct (PMF-derived) d^z_h were subtracted from the

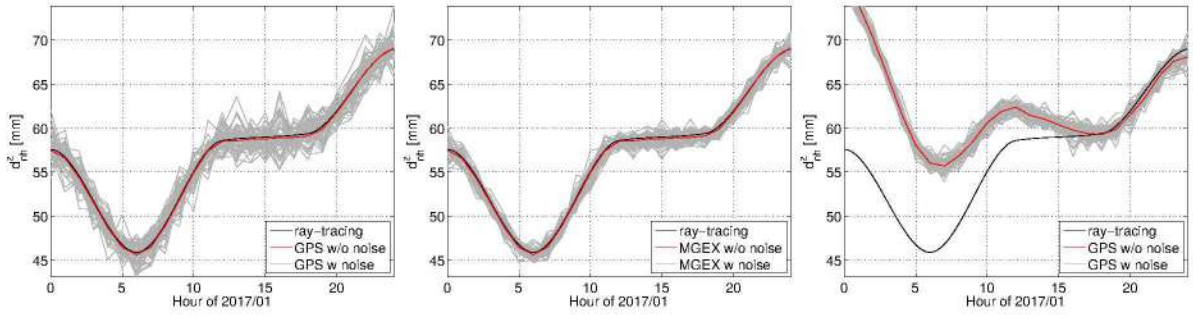


Figure 6.5.3: Zenith non-hydrostatic delay estimated from simulated GNSS observation with FGST at POTS. The d^z_{nh} from numerical integration in the model levels of ERA Interim is displayed in black, the estimates from the individual ensemble members are shown in gray, and the ensemble mean is shown in red. On the left shown is a series of solutions where no systematic errors were introduced, and only GPS observations were utilized. The solutions from multi-GNSS observations are in the middle, and on the right are GPS solutions where the a priori d^z_h stem from GFZ-PT.

zenith total delays. Thereupon, the linear rates of the IWV, G_{NS}, and G_{EW} time series were calculated employing an iterative weighted least-squares adjustment where seasonal variations were also estimated, and the temporal correlations were modelled in a data-driven Hirvonen covariance function.

The differences between IWV trends estimated from simulated VLBI observations, and those estimated from numerical integration in ERA Interim are presented in Fig. 6.5.4. The large differences in the IWV trends from the solutions where a reduced version of GFZ-PT was utilized to compute the a priori d^z_h, between the upper and the lower panel can be partly attributed to linear trends in the d^z_h that were not considered in the "wrong" scenarios. This feature in consistent between the GNSS and VLBI simulations. After statistical analysis, it is found that in 60 % (75 %) of the VLBI (GNSS) stations, the combination of erroneous a priori d^z_h (most probably due to wrong pressure series) and erroneous mapping functions distort the IWV trends statistically significantly, if not corrected a posteriori. If the d^z_{nh} series are adjusted after the adjustment, only in 27 % (18 %) of the VLBI (GNSS) stations are the

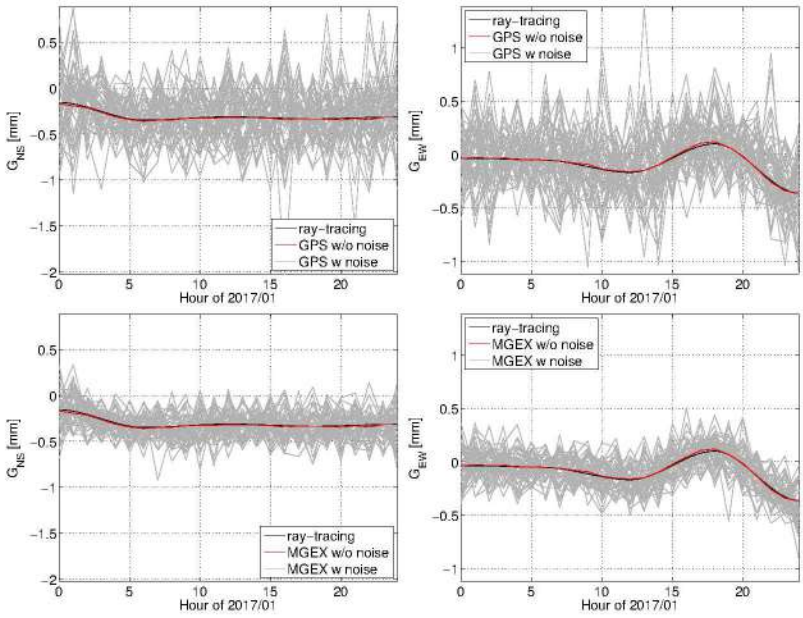


Figure 6.5.2: Linear atmospheric gradients estimated from simulated GNSS observation with FGST at POTS. Gradients from ray-tracing are displayed in black, the estimates from the individual ensemble members are shown in gray, and the ensemble mean is shown in red. On the left, the G_{NS} are presented, and on the right lie the G_{EW}. On the upper row are the GPS-only solutions, and on the lower row are the multi-GNSS solutions.

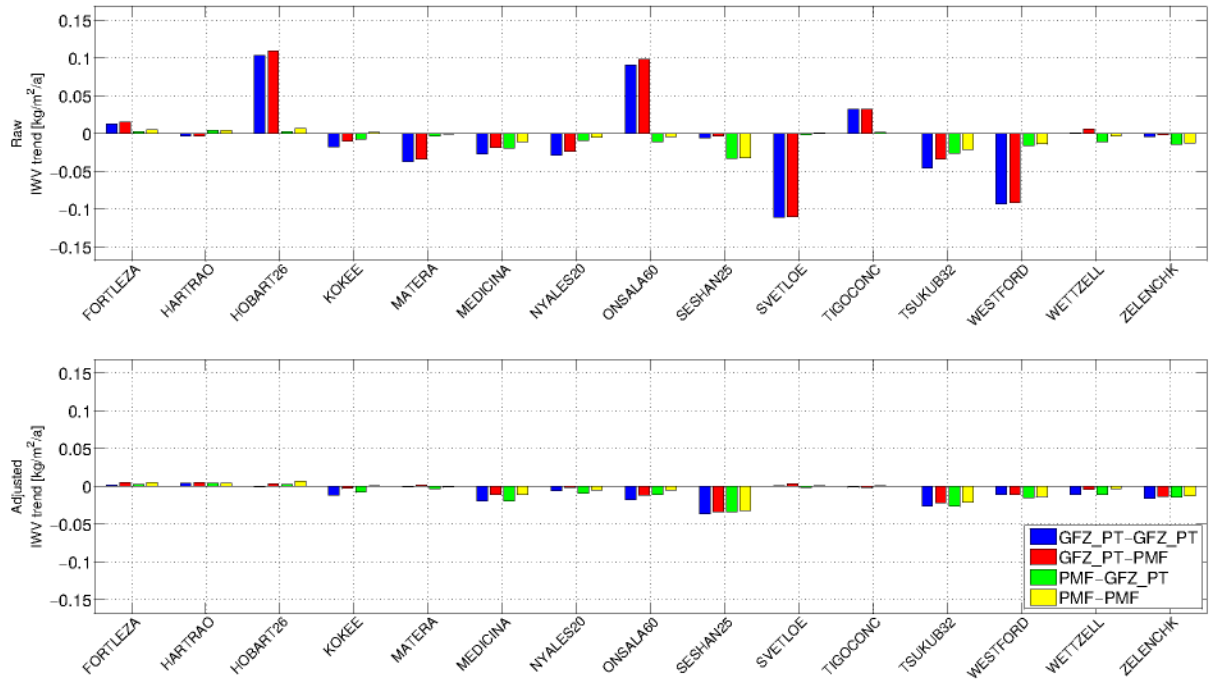


Figure 6.5.4: Deviations of linear IWV rates from simulated VLBI observations with respect to IWV from numerical integration in ERA Interim, for stations with more than 10 years of observations. The upper panel shows the trends estimated by converting the d^z_{nh} output of FGST directly to IWV, and the lower panel shows the trends estimated after correcting for the erroneous d^z_h. In the legend, first appears the name of the model for the a priori delay and then the mapping function.

differences statistically significant. If the mapping function is correct but the a priori d^z_h is not, 67 % (67 %) of the VLBI (GNSS) stations experience significant differences. However, should the d^z_h be adjusted, these figures reduce to below 4 % for both techniques. If the mapping function is wrong and the a priori d^z_h is not, then 20 % (12 %) of the VLBI (GNSS) stations have significant differences. Note that the aforementioned percentages of GNSS and VLBI stations should not be intercompared strictly due to the very small VLBI sample (# stations) size.

The differences between gradients estimated in the VLBI simulations are shown in Fig. 6.5.5. The very large relative trend errors at Hartebeesthoek and Concepción are due to the fact that in the early 2000s, there were so few VLBI radio telescopes in the Southern Hemisphere, that in turn very few observations were scheduled towards southern radio sources, and therefore the skyplots of the stations are almost empty in their southern part. Figure 6.5.6 provides proof for this statement, and also shows the difference in the observation geometry within a decade. To verify that these systematics are not a manifestation of random errors, a single simulation run was carried without applying noise (no turbulence, no clocks, no thermal noise), ergo $\mathbf{y^b} - \mathbf{y^0} = \mathbf{0}$. Since, the results illustrated in Fig. 6.5.7 do not paint a different picture compared to Fig. 6.5.5, the trend differences are real. Studying Table. 6.5.1 that quantifies the number of VLBI and GNSS stations with statistically significant gradient trend differences, the following conclusions are drawn: (i) G_{EW} temporal rates can be more accurately estimated than G_{NS} rates in both VLBI and GNSS, (ii) a larger portion of the GNSS network can recover accurate G_{EW} gradients compared to the VLBI network, and (iii) gradient rates are not affected by the tropospheric parameterization as much as the IWV rates. Systematic errors in the gradient trends could be indicative of systematics in the lateral station velocity components, and will be studied in a future work.

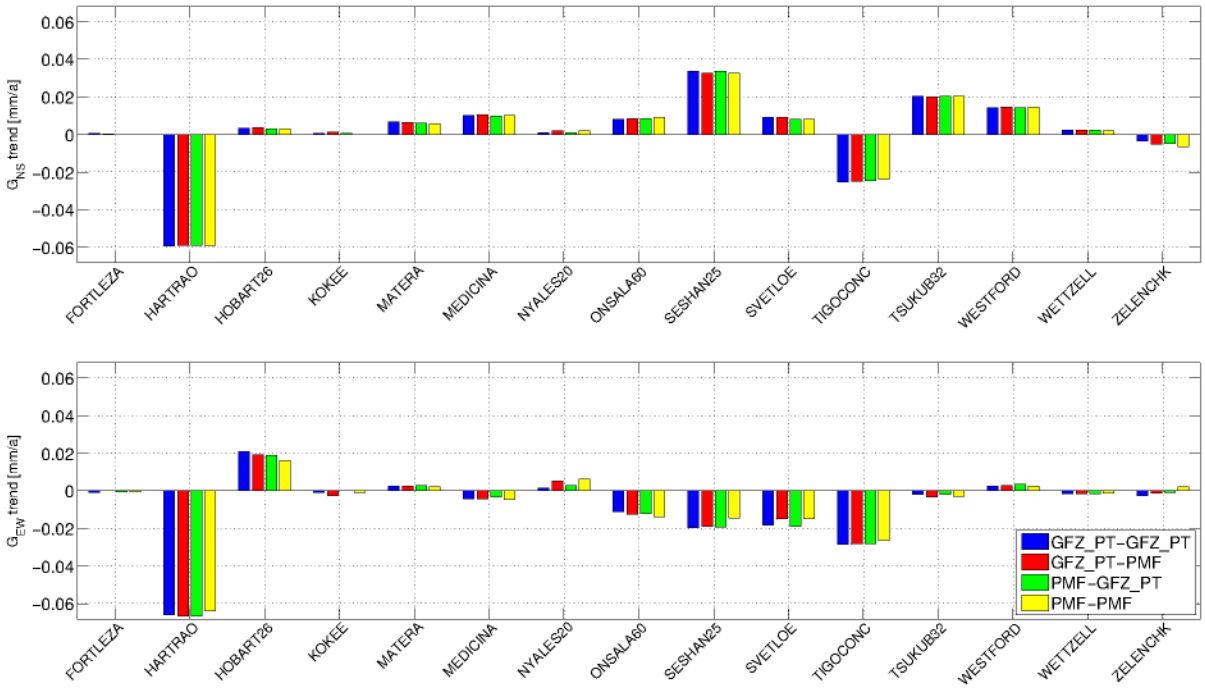


Figure 6.5.5: Deviations of linear G_{NS} and G_{EW} rates from simulated VLBI observations (FGST) with respect to ray-traced gradients in ERA Interim, for stations with more than 10 years of observations.

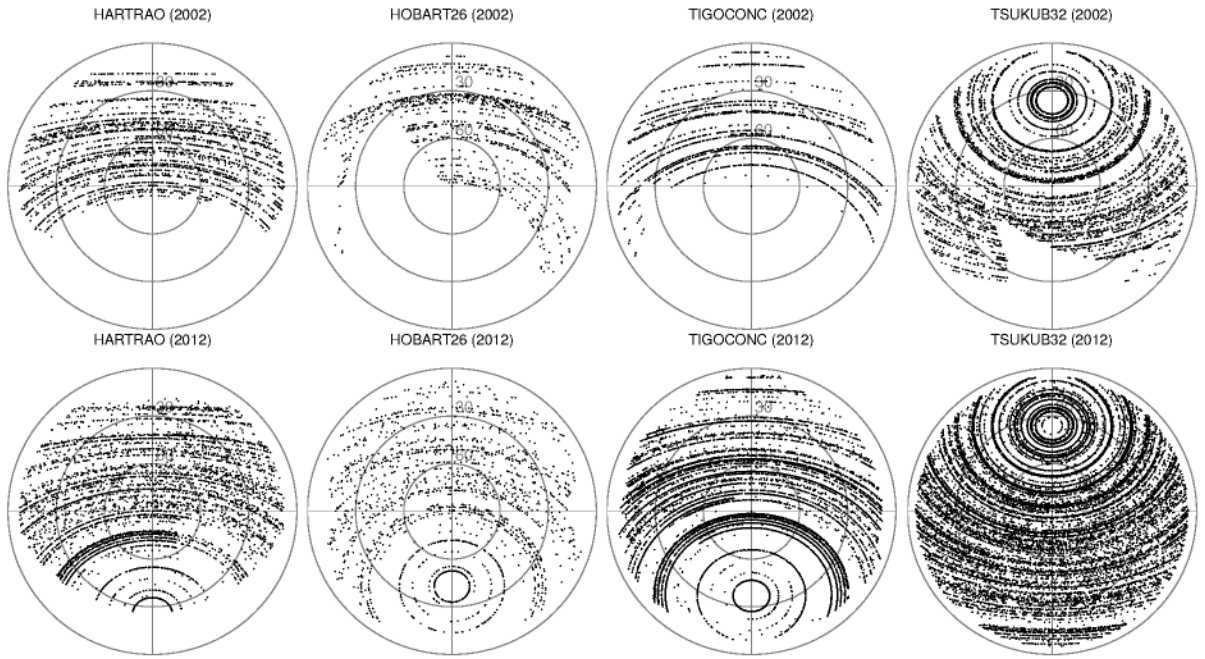


Figure 6.5.6: From left to right, the observation geometry during 2002 (upper row), and 2012 (lower row), for `HARTRAO`, `HOBART26`, `TIGOCONC`, and `TSUKUB32` is presented. Note the improvement of the azimuthally uneven observation distribution over one decade.

Table 6.5.1: The portion [%] of the VLBI (R) and GNSS (P) station networks where the gradient component linear temporal rates show statistically significant deviations with respect to ray-traced gradients. In the description row, first appears the a priori zenith delay source, and then the mapping function name.

		GFZ-PT & GFZ-PT	GFZ-PT & PMF	PMF & GFZ-PT	PMF & PMF
$\delta\frac{\partial G_{NS}}{\partial t}$	R	66.7	66.7	66.7	60.0
	P	52.3	52.3	53.0	51.5
$\delta\frac{\partial G_{EW}}{\partial t}$	R	40.0	46.7	40.0	33.3
	P	15.4	16.9	16.2	14.6

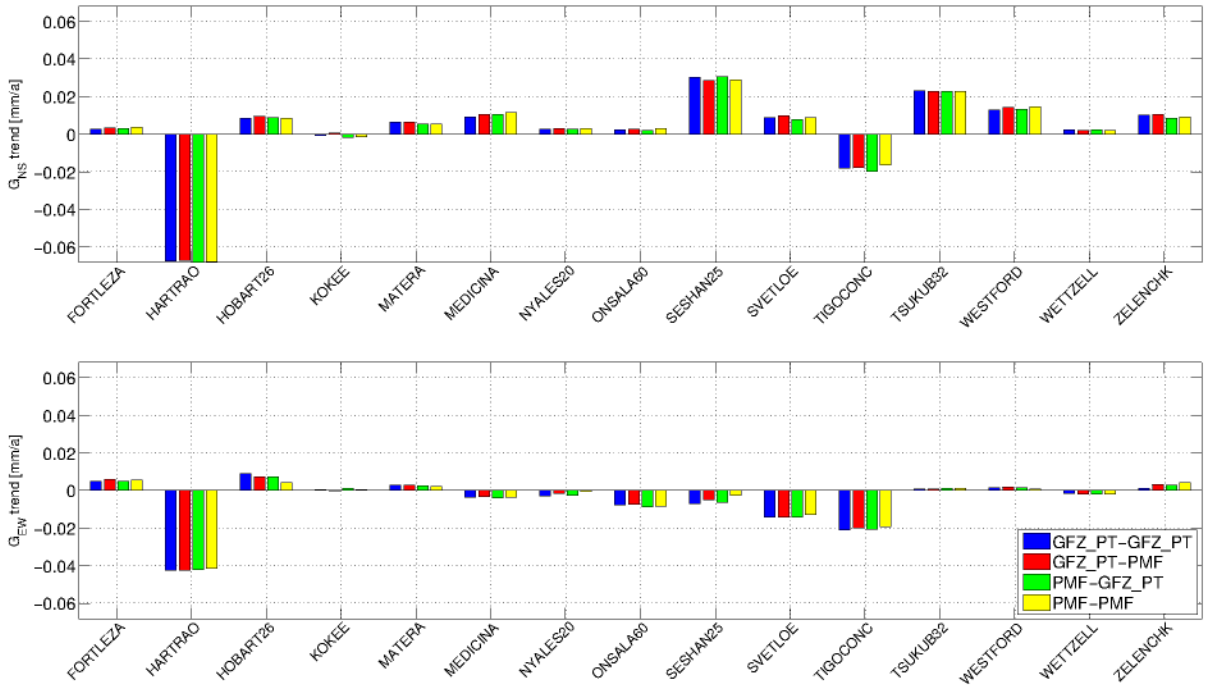


Figure 6.5.7: Deviations of linear G_{NS} and G_{EW} rates from simulated VLBI observations (FGST) with respect to ray-traced gradients in ERA Interim, for stations with more than 10 years of observations. In this simulation run, no noise was applied to **b**.

Last but not least, it was also assessed whether VLBI or GNSS is the better suited to probe climate change (in terms of long IWV and gradient trends). For the comparison to be meaningful, atmospheric ties were applied for all parameters (zenith non-hydrostatic delays, and linear horizontal gradients) consistently to the developments presented in Sec. 4.4. Figure 6.5.8 presents the IWV trends from VLBI, GNSS, and ERA Interim (reference), from synchronized series. From the results, it seems that VLBI is more appropriate for the task at hand, mainly due to the fact that much fewer clock-related parameters need to be estimated, and that no elevation-dependent weighting strategy was adopted in analyzing the simulated VLBI observations, thus facilitating the decorrelation between height, clock, and d^z_{nh}. Nevertheless, only at one GNSS station (`TSKB`, co-located with `TSUKUB32`) are the IWV rates significantly different with respect to those estimated from VLBI and numerical integration in ERA Interim. Figure 6.5.8 presents the gradient component trends. It is found that both G_{NS} and G_{EW} trends can be more accurately recovered from GNSS, compared to VLBI observations. In particular, for G_{NS}, in 62 % of the

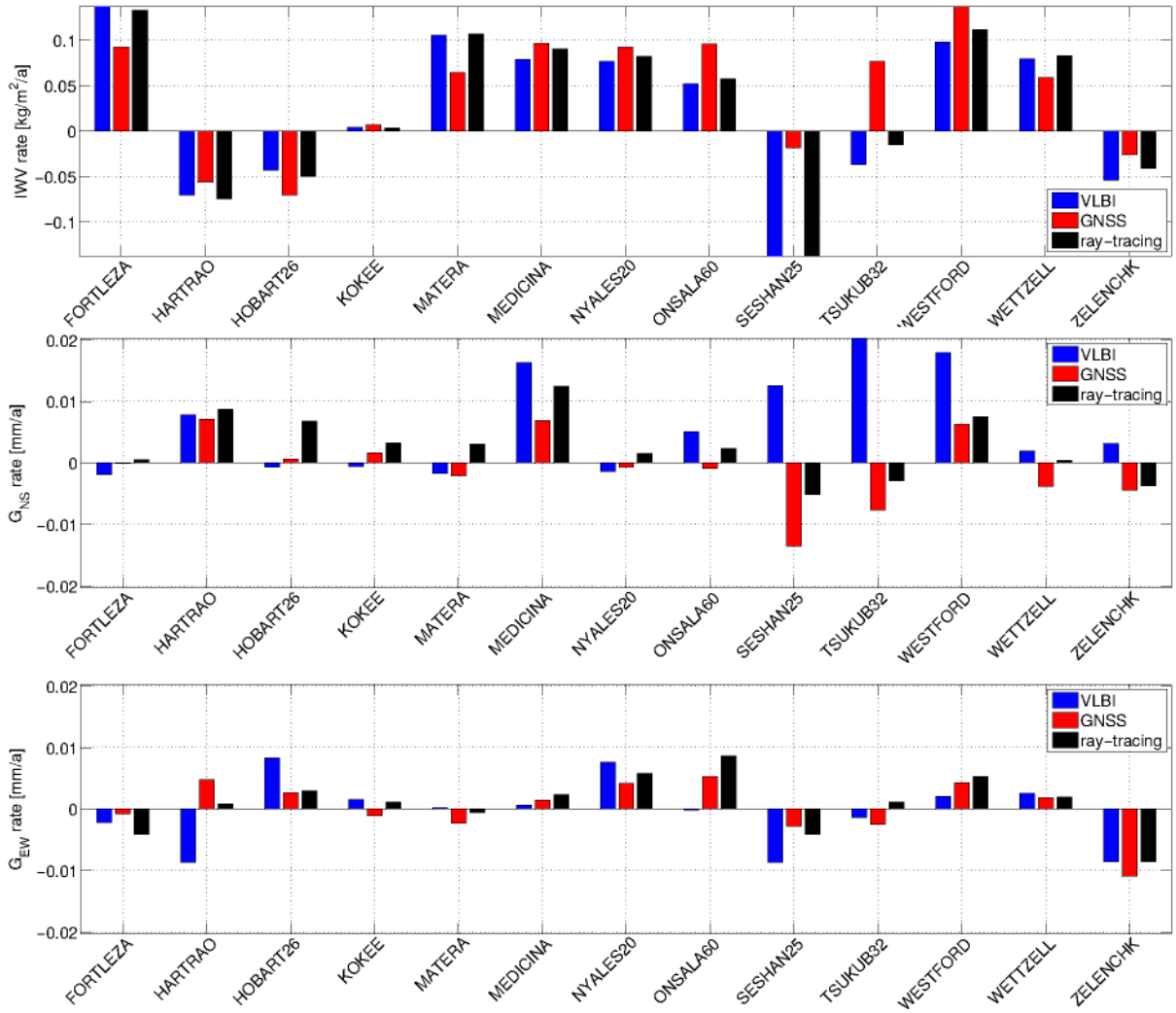


Figure 6.5.8: IWV (1st row) and gradient component (2nd and 3rd row) trends estimated from simulated VLBI and GNSS observations employing FGST, and ray-tracing. For the trend estimation, the three different time series (for every station) were synchronized.

VLBI stations the trends are statistically significant, compared to 39 % of the GNSS stations. G_{EW} trends are more accurately recovered from the simulated GNSS measurements; statistically significant differences in 15 % of the stations, whereas 31 % of the VLBI stations yield trends that differ appreciably from the ray-traced gradients. Comparing GNSS with VLBI directly shows a moderate agreement; 54 % for G_{NS}, and 69 % for G_{EW}. The fact that GNSS-derived gradient trends are better is due to the fact that the GNSS observation geometry does not depend on the network size as much as it does in VLBI. The difference between GPS-only with multi-GNSS lies solely in the reduction of the noise in the time series, not the reduction of systematics whatsoever. However, as the number of VLBI stations that operate in the Southern Hemisphere increases, it is expected that the edge GNSS has over VLBI, in this regard, will cease to exist in the future.

7 Application of geophysical loading models to space geodetic data analysis

This chapter is dedicated to the presentation of the effect of applying the geophysical loading models developed and presented in Chapter 5 in the space geodetic data analysis. The displacement models were applied either to the observation equations thus alternating mainly the related reduced observations vector, or directly at the station coordinates estimated from a processing where the loading displacements' influence was neglected. While the former is more rigorous — station motion also affects parameters other than the station coordinates, e.g., EOP — to get a rough estimate of the repercussions on the station coordinates should erroneous or no modelling at all be used, the second was applied additionally. Testing displacement models in such a manner is conditional upon accepting the premise that phenomena acting on station coordinates do not affect other parameters, and the modelled displacements are without error.

With the exception of VLBI data analysis, all other geodetic analysis (SLR, GNSS, and DORIS) carried out herein was performed employing observations simulated utilizing FGST (cf. Sec. 2.6), and processed with an own software. Observed interferometric group delays were analyzed employing the GFZ version (Nilsson et al., 2015b) of the Vienna VLBI software VieVS (Böhm et al., 2011; Böhm et al., 2018), hereinafter `VieVS@GFZ`. In the geodetic analysis GFZ-PT (cf. Sec. 4.3) served as ersatz atmospheric refraction model, and EGLM (cf. Sec. 5.5) served as ersatz geophysical displacement model. Other than the modelling of tropospheric refraction and geophysical loading displacement, the geodetic processing abides by the latest IERS Conventions (Petit and Luzum, 2010), and updates thereof. In geodetic VLBI data analysis observations between short (local) baselines e.g., at Wettzell, Hobart, and Hartebeesthoek, are not included in the adjustment. The rational behind rejecting a priori these measurements lies in the fact that the injected phase calibration tones obstruct the correlation process. While this can be treated by applying band-rejection filters, the so-called notch filters, it is not a standard in data generated in the IVS framework as of yet. The VLBI processing is not consistent throughout the years, and under no circumstances should it be. For instance, in early sessions, the estimation of gradients is either not possible or significantly degrades the solution. These cases have been identified by studying the observation geometry of every station that participated in every session. The treatment applied was either imposing of heavy absolute constraints on gradients estimated from ray-tracing in ERA Interim refractivity fields (Sec. 4.2.2), or simply introducing ray-traced gradients as additional observations in the related adjustment.

There are very few studies where loading models have been applied to more than one technique (e.g., Roggenbuck et al., 2017), and even fewer studies where models where developed and tested in a single work. In Chapter 7, an attempt is made to understand how geophysical loading components impact the analysis of space geodetic observations, at different levels (observation equation, and parameter). In Sec. 7.1 the influence of mass transport on station displacements is studied. Loading models are applied to all space geodetic techniques at the parameter level (real data), and at the observation equation level (real and simulated measurements). In Sec. 7.2 the extent to which the implied reference frame of all four space geodetic techniques is distorted is assessed. The penultimate section of this chapter (Sec. 7.3) deals with how station displace-

ments induced by geophysically-excited loading manifest into variations in all Earth orientation parameters. For the latter, 24-hour-long global sessions as well as one-hour-long single-baseline sessions — the so-called Intensives — have been analyzed. In the last section (Sec. 7.4), the impact of mass redistribution on satellite orbits is discussed.

7.1 Impact on station coordinates

In this section, the impact of accounting for non-tidal geophysical loading in geodetic data analysis, on station coordinates is assessed. Regarding the application of loading models, the outcome of three scenarios is presented herein; applying the related model at: (i) the parameter level, that is, directly adding loading displacements to the coordinates estimated in the geodetic adjustment of real observations where no non-tidal loading models had been applied, (ii) the observation equation level in an adjustment of observations simulated following Sec. 2.6, and (iii) the observation equation level in an adjustment of real observations. For all cases, the isomorphic reference frame of preference is the center of mass of the Earth system as defined by Blewitt (2003) as in the inversion of the NEQs of the different techniques, discrete Tisserand conditions were imposed with respect to e.g., ITRF2008. In addition, the following assumption was made: the uncertainty of simulated loading displacements is constant in space and time. For the case where loading displacements are applied a posteriori, the official contributions of IVS (Bachmann et al., 2016), ILRS (Luceri and Pavlis, 2016), IGS (Rebischung et al., 2016), and IDS (Moreaux et al., 2016) to different realizations of the latest terrestrial reference system, namely ITRF2014 (Altamimi et al., 2016), DTRF2014 (Seitz et al., 2016), and JTRF2014 (Abbondanza et al., 2017), were used as well. The reason for choosing to work with the combined solutions of all four techniques for ITRF2014 stems from their being publicly available, being a product of homogeneous reprocessing, and being extensively tested. Loading displacements were applied to the estimated coordinates from all four techniques directly (parameter level), averaged over the interval each estimate refers to. The related documentation states that no non-tidal modelling was considered neither at the NEQ (similar to the observation equation) level, nor at the parameter level, hence adding the loading displacements to the estimated coordinates is sound.

Since one purpose of this work is to better understand and therefore be able to reproduce geophysical loading signals based on non-geodetic observations (NWM data), a model is considered successful if it can describe part of the variability of the station position vector. In essence, upon application of these models some systematic features such as the annual amplitude or the bi-weekly variation related to high/low pressure systems should attenuate in magnitude. So, reduced magnitude in seasonal signals as well as reduced WRMS are indicators that the loading models perform well. Nevertheless, it is possible that while the loading model at a site is accurate, seasonal amplitudes increase. In such cases, poor model performance can be ascribed either to the incomplete modelling strategy and inaccurate NWM data, or to effects that are anti-correlated with non-tidal displacements and were not considered at the observation equation level, e.g., atmospheric delays.

To assess whether a displacement model improves or not the coordinate time series at a station, all segments of the individual time series were identified first. This task was facilitated by ingesting information on the segments already identified in the framework of the realization of the latest TRF, ITRF2014. In essence, offsets, secular and post-seismic deformation signals were reduced from the coordinate time series of all four techniques so that quasi zero-mean series remained. In the vast majority of cases applying the related `ITRF2014-*-TRF.SNX`, `ITRF2014-soln-*.snx`, and `ITRF2014-psd-*.snx` was sufficient. Nevertheless, there were a num-

ber of cases where it was not sufficient, e.g., GGAO7108, OHIGGINS, and SINTOTU3, to name a few. Subsequently, geophysical loading models developed in Chapter 5 were applied, that is, interpolated at the observations' epochs of the individual techniques, and then averaged over the course of the length of each solution (e.g., daily for GNSS and weekly for SLR). The following five scenarios were assessed:

- NTAL alone,
- NTOL alone,
- CWSL alone,
- NTAL+CWSL, and
- NTAL+NTOL+CWSL.

The latter is hereinafter labeled as accumulated non-tidal geophysical loading (ANGL), and consists of the individual non-tidal contributions of the atmosphere, the oceans and the hydrology being linearly superposed. Thereupon, amplitude- and phase-locked seasonals (neither amplitude nor phase were set up as variable in time) were estimated together with the residual offsets, velocities, and the WRMS of the post-fit residuals in weighted least-squared adjustments.

Although the application of loading models at the parameter level was carried out consistently across the techniques, the performance of the models varies considerably. This discrepancy is predicated upon the fact that while all geodetic markers are fixed to the ground and should experience similar displacement at co-location sites, technique-specific issues induce an impediment in this regard. Such effects include but are not limited to the thermal and gravitational deformation of VLBI radio telescopes, mismodelled non-gravitational satellite accelerations, and spurious signals that coincide with the satellite orbital period — as well as overtones thereof — of the observed satellites. The impact of applying discrete loading models directly on VLBI station coordinates is shown in Table 7.1.1. No loading model combination scenario yields an overall improvement in terms of seasonal amplitude and WRMS of the post-fit residuals reduction, of both the station coordinates (topocentric) and baseline lengths. This is rather unexpected since applying exactly the same models at the observation equation level yields a clear improvement in the vast majority of radio telescopes (cf. Fig. 7.1.1 and Fig. 7.1.3). Table 7.1.2 shows the percentage of SLR stations where applying certain scenarios of combining loading models yields a reduced PSD in major frequencies, that translates to lower seasonal amplitudes. More than 73 % of the SLR stations experience a statistically significant improvement in terms annual amplitude in the radial coordinate component, for all scenarios assessed herein. The best performing scenario is the one where the combined effect of NTAL and CWSL was reduced from the SLR station coordinates. In all scenarios more than half of the stations' radial coordinate component obtains a benefit from the application of non-tidal loading models, at the major seasonal frequencies. Applying loading models to DORIS coordinate series yields an overall improvement, but not for all frequencies and loading model combination scenarios. Table 7.1.3 shows that the best performing model is the combination of NTAL and CWSL, which reduces the WRMS in 67 % of the stations and the S_a amplitude in 72 % of the stations. The reason why all model combinations perform poorly in reducing the ter-annual North-South displacement amplitude is unclear and will be investigated in a follow-on study. The majority of GNSS stations benefit from accounting for non-tidal deformation, especially in the radial direction; in all cases radial S_a amplitudes reduce on average, and for the combination of NTAL and CWSL this reaches 63 % of the stations (cf. Table 7.1.4). Discrepancies between displacement series derived from loading models

Table 7.1.1: The percentage of VLBI stations that contributed to ITRF2014 where there is a statistically significant seasonal amplitude (S_a, S_{sa}, S_{ta}) and a WRMS reduction (improvement) upon applying discrete loading models (NTAL, NTOL, and CWSL) developed in Chapter 5 using ERA Interim data. R, EW, and NS denote the radial, East-West, and North-South topocentric coordinate component, respectively.

Loading models	S_a [%]			S_{sa} [%]			S_{ta} [%]			WRMS [%]
	R	EW	NS	R	EW	NS	R	EW	NS	
NTAL	31.7	36.5	20.6	47.6	41.3	34.9	47.6	47.6	42.9	31.7
NTOL	54.0	25.4	31.7	42.9	33.3	27.0	57.1	47.6	41.3	34.9
CWSL	28.6	22.2	36.5	49.2	38.1	38.1	50.8	49.2	44.4	25.4
NTAL+CWSL	27.0	12.7	4.8	44.4	39.7	31.7	38.1	42.9	46.0	20.6
NTAL+NTOL+CWSL	28.6	11.1	14.3	38.1	23.8	27.0	38.1	41.3	46.0	19.0

Table 7.1.2: The percentage of SLR stations that contributed to ITRF2014 where there is a statistically significant seasonal amplitude (S_a, S_{sa}, S_{ta}) and a WRMS reduction (improvement) upon applying discrete loading models (NTAL, NTOL, and CWSL) developed in Chapter 5 using ERA Interim data. R, EW, and NS denote the radial, East-West, and North-South topocentric coordinate component, respectively.

Loading models	S_a [%]			S_{sa} [%]			S_{ta} [%]			WRMS [%]
	R	EW	NS	R	EW	NS	R	EW	NS	
NTAL	81.4	39.0	57.6	69.5	50.8	42.4	59.3	50.8	76.3	76.3
NTOL	62.7	33.9	32.2	55.9	49.2	37.3	52.5	44.1	76.3	59.3
CWSL	72.9	30.5	40.7	57.6	35.6	57.6	44.1	55.9	76.3	67.8
NTAL+CWSL	88.1	32.2	45.8	64.4	49.2	52.5	59.3	55.9	76.3	72.9
NTAL+NTOL+CWSL	86.4	27.1	35.6	59.3	44.1	50.8	52.5	47.5	74.6	72.9

or GRACE and GNSS may be attributed to erroneous NWM data, network effects, as well as shortcomings in modelling of geodetic measurements such as the non-conservative accelerations on the space vehicles, e.g., solar radiation pressure or Earth's albedo (e.g., Horwath et al., 2010). Under the subset of stations where a statistically significant improvement was not achieved, may fall stations where either a relatively small improvement was accomplished or a deterioration. Illustrations of the station networks are shown in Chapter 2. Tables 7.1.1–7.1.4 tabulate results of the application of loading displacements to station coordinates obtained from the analysis of real observations (the official contribution of the individual space geodetic techniques to ITRF2014).

While for GNSS, SLR, and DORIS applying discrete geophysical loading models a posteriori seems to yield a general improvement in terms of S_a amplitude, and WRMS of the post-fit residuals, the promising results are not shared by the VLBI station time series. A potential explanation is that unlike the aforementioned satellite techniques, VLBI sessions feature a relatively poor station network. In point of fact only in 12.4 % of all non-intensive sessions organized in the framework of IVS, are there more than ten radio telescopes with "good" observations (based on `vgosDB` data spanning the period 1979–2019). On average, geodetic VLBI sessions feature six radio telescopes. However, the observing networks tend to get larger (on average nine stations for 2019). The small number of radio telescopes that participate in the minimum constraints has a heavy impact on the values of the estimated station coordinates, albeit not distorting the internal geometry, e.g., baseline lengths (e.g., Sillard and Boucher, 2001; Kotsakis, 2018). To further justify why applying non-tidal loading displacements to VLBI station coordinate estimates a posteriori, both the total discrete geophysical loading model and the EGLM were applied at

Table 7.1.3: The percentage of DORIS stations that contributed to ITRF2014 where there is a statistically significant seasonal amplitude (S_a, S_{sa}, S_{ta}) and a WRMS reduction (improvement) upon applying discrete loading models (NTAL, NTOL, and CWSL) developed in Chapter 5 using ERA Interim data. R, EW, and NS denote the radial, East-West, and North-South topocentric coordinate component, respectively.

Loading models	S_a [%]			S_{sa} [%]			S_{ta} [%]			WRMS [%]
	R	EW	NS	R	EW	NS	R	EW	NS	
NTAL	60.0	48.5	55.4	50.8	53.8	43.1	62.3	50.0	6.9	70.8
NTOL	52.3	52.3	52.3	57.7	48.5	57.7	60.8	49.2	6.2	60.8
CWSL	66.9	52.3	42.3	53.1	38.5	42.3	50.8	55.4	6.9	61.5
NTAL+CWSL	73.1	47.7	48.5	53.8	38.5	37.7	55.4	52.3	6.9	68.5
NTAL+NTOL+CWSL	59.2	50.8	48.5	53.8	43.1	45.4	60.0	57.7	6.9	65.4

Table 7.1.4: The percentage of GNSS stations that contributed to ITRF2014 where there is a statistically significant seasonal amplitude (S_a, S_{sa}, S_{ta}) and a WRMS reduction (improvement) upon applying discrete loading models (NTAL, NTOL, and CWSL) developed in Chapter 5 using ERA Interim data. R, EW, and NS denote the radial, East-West, and North-South topocentric coordinate component, respectively.

Loading models	S_a [%]			S_{sa} [%]			S_{ta} [%]			WRMS [%]
	R	EW	NS	R	EW	NS	R	EW	NS	
NTAL	61.5	22.5	9.9	51.2	29.8	15.2	54.1	20.7	32.7	71.4
NTOL	59.7	25.5	47.6	48.9	34.5	50.6	51.6	38.1	43.4	49.2
CWSL	57.9	11.6	22.9	40.0	33.2	11.4	45.6	33.4	42.2	53.4
NTAL+CWSL	62.4	4.8	3.5	48.3	33.8	6.5	51.0	17.0	26.4	66.8
NTAL+NTOL+CWSL	53.5	2.5	10.7	45.2	25.6	7.0	45.8	20.3	31.0	53.0

the observation equation level in geodetic VLBI data analysis employing `VieVS@GFZ`. In the following, the results of analyzing real group delays is assessed. It will be shown that the applying either EGLM, or the discrete model is beneficial for geodetic VLBI data analysis.

First, an assessment of the impact of the loading models on the estimated time series takes place. Applying the fully fledged EGLM (atmosphere, oceans, and hydrology) at the observation equation level in lieu of no non-tidal loading model, reduces the S_a, S_{sa}, and S_{ta} amplitude in 82 %, 41 %, and 54 % of the VLBI stations, respectively. Comparing the amplitude of the height series of solutions estimated where the accumulated geophysical loading displacement model was applied at the observation equation level, and no non-tidal loading model was applied, there is a slightly better reduction compared to EGLM; the S_a, S_{sa}, and S_{ta} amplitudes were reduced in 82 %, 54 %, and 54 % of the VLBI stations. The largest improvement in terms of annual amplitude reduction was achieved in Katherine; 3.3 mm for EGLM, and 4 mm for the discrete model. In `HART15M` (Hartebeesthoek) both models did not perform well; amplitude increase of 1.6 mm for EGLM, and 2 mm for the discrete model. Nevertheless, the fact that there is an improvement at the co-located VLBI station `HARTRAO` (1.2 mm for EGLM, and 1.8 mm), prompts that the poor performance of the models derived herein could be result of the interplay of other effects that are not yet understood in VLBI data analysis, or of impurities in the mass anomaly fields. In addition, due to the fact that in the modelling of hydrological loading only transient water mass transport has been considered — to the author's knowledge no relevant information is provided by any NWM regarding mass redistribution at depths below 3 m — a disagreement between the motion of a geodetic sensor and the prediction of its displacement stemming from hydrological

mass transport could be attributed to effects such as the poroelastic uplift induced by aquifer recharge (e.g., Milliner et al., 2018). This assumption can be confirmed by studying the seasonal signals at other co-located stations such as those at Hobart, where the S_a amplitude differences are as large as 8 mm, regardless of the non-tidal loading treatment applied. Figure 7.1.1 shows the amplitudes of the major seasonal signals in the height component of the most important VLBI stations that participated in IVS-R1 and IVS-R4 sessions. The power spectral density (PSD) of the coordinate series was calculated as well. Figure 7.1.2 demonstrates that there is a significant decrease in the S_a PSD in almost all cases, whereas such a statement does not always hold for higher frequencies. As far as the height repeatability is concerned, EGLM yields an improvement in 73 % of the stations, and the discrete model yields an improvement in 82 % of the stations. The related WRMS per solution are illustrated in Fig. 7.1.3.

Besides inducing changes on the amplitude of the major seasonal signals, accounting for non-tidal loading deformation at the observation equation level induces changes in the phase of the signals as well. While the differences comparing the phase of coordinate series after applying EGLM or the discrete non-tidal model are relatively small, the differences between applying any non-tidal model and not is much larger. The annual phase does not change sign between EGLM and the discrete non-tidal model (except for Ny-Ålesund where the related amplitudes are quite small already), and the differences are at the level of 4°, on average. On the contrary, applying or not a non-tidal loading model yields phase differences so large that the annual phase sign changes in 27 % of the stations that have participated in IVS rapid turnaround sessions (`FORTLEZA`, `HOBART26`, `KATH12M`, `NYALES20`, `SVETLOE`, `ZELENCHK`). The phase of annual overtones is affected much more by applying non-tidal loading models in an absolute sense, but statistical significance of the related differences varies widely across the stations.

Non-secular VLBI station displacement variations in the horizontal plane are on average three times smaller than those in the radial component. However, the horizontal displacement series experience seasonal variations as large as 2.1 mm in the North-South, and 3.9 mm in the East-West component (`HART15M`). In the lateral plane, EGLM and the discrete model are slightly less effective in reducing the seasonal signals as they are in the radial component. In particular, in the North-South coordinate component, the annual, semi-annual, and ter-annual amplitude is reduced in only 73 %, 36 %, and 59 % of the stations for EGLM, and 82 %, 64 %, and 41 % of the stations for the discrete model, respectively. In the East-West component, no clear improvement is visible either; only in 59 % (64 %), 59 % (64 %), and 68 % (73 %) of the stations does the S_a, S_{sa}, and S_{ta} decrease, if the EGLM (discrete model) is applied at the observation equation level, respectively. The lateral coordinate repeatability (WRMS of the post-fit residuals) is improved in only 68 % of the stations for EGLM and 73 % for the discrete model. Accounting for non-tidal loading can reduce the S_a as much as 1.4 mm (`HART15M`) in the North-South direction, and 0.9 mm (`FORTLEZA`) in the East-West direction. As far as the phase of the related series is concerned, there are seven stations where the phase of the displacement series in the horizontal plane changes sign (`BADARY`, `KATH12M`, `KOKEE`, `MATERA`, `NYALES20`, `SESHAN25`, and `TSUKUB32`).

Since mass conservation was enforced during the model development stage (cf. Chapter 5), and long wavelength variations in the geophysical loading displacement series were filtered prior to application in VLBI data analysis, no spurious secular signals should contaminate the VLBI group delays, thus no station velocity changes are expected. The latter holds should long enough data sets be employed for the related computations; 2–3 years of reasonably continuous data suffice (e.g., Blewitt and Lavallée, 2002). Except for the East-West coordinate component of Kokee, no statistically significant velocity difference was found ($-5.0\,\mathrm{mm\,dec^{-1}}$ if no non-tidal loading is considered, and $-1.1\,\mathrm{mm\,dec^{-1}}$ for the discrete model, with an uncertainty of $1.2\,\mathrm{mm\,dec^{-1}}$).

Due to the fact that there might be either natural phenomena that act upon geodetic ob-

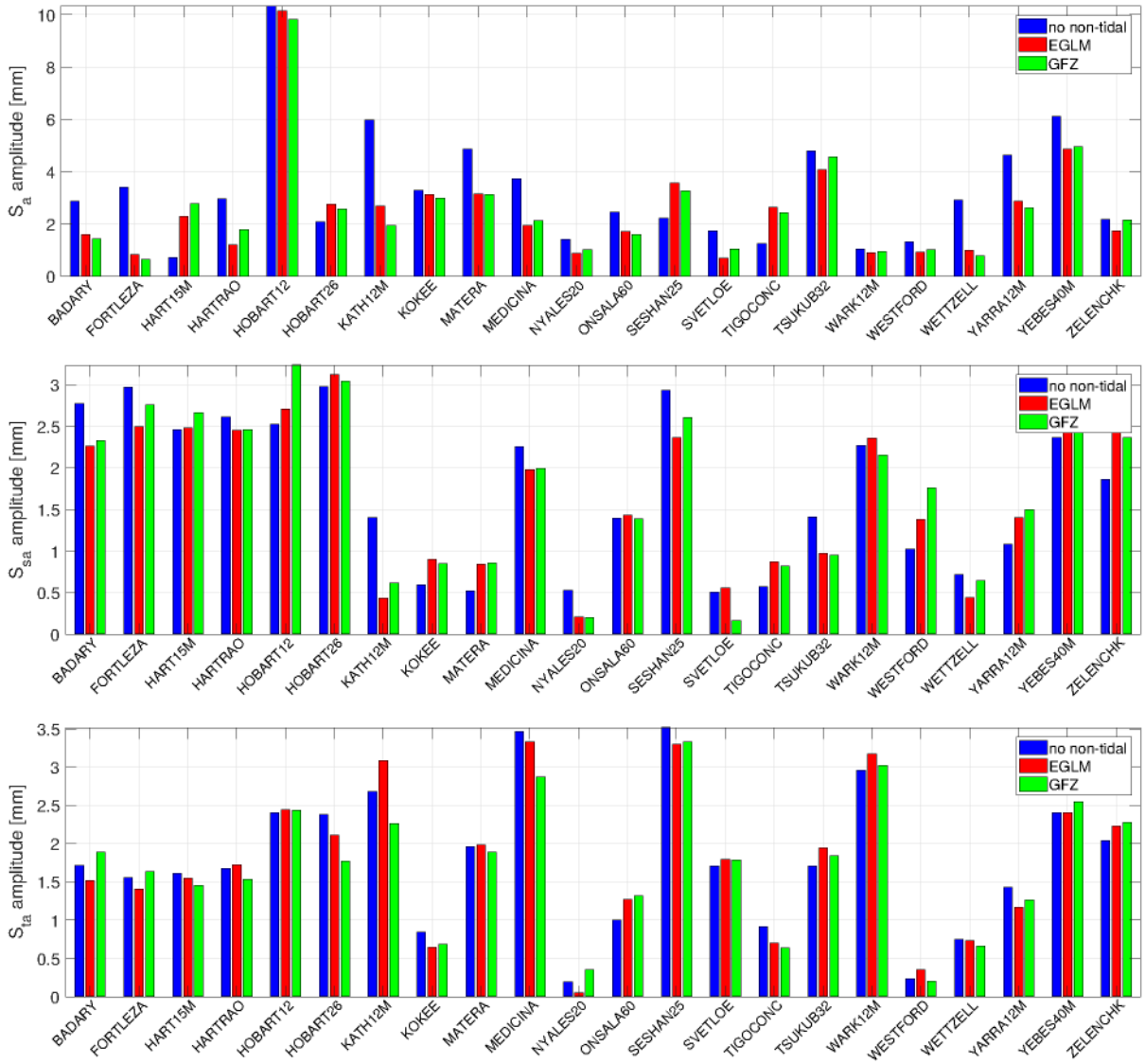


Figure 7.1.1: The S_a (1st row), S_{sa} (2nd row), and S_{ta} (3rd row) amplitudes of station displacements in the radial coordinate component after applying no non-tidal displacement models (blue), the fully fledged EGLM (red), and the discrete series of detrended accumulated geophysical loading (green), at the observation equation level.

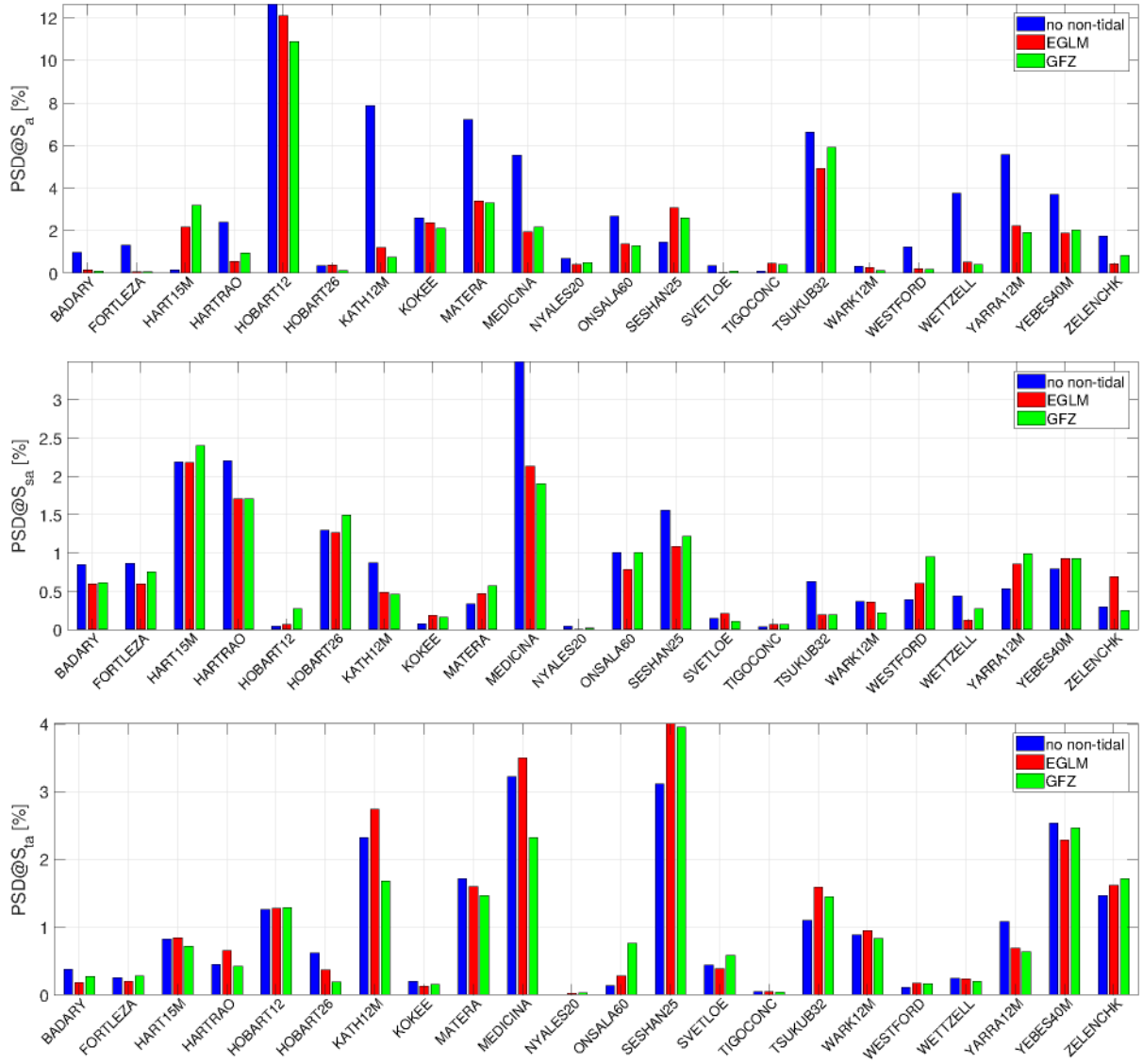


Figure 7.1.2: The normalized PSD at the S_a (1st row), S_{sa} (2nd row), and S_{ta} (3rd row) frequency of radial station displacements after applying no non-tidal displacement models (blue), the fully fledged EGLM (red), and the discrete series of detrended accumulated geophysical loading (green), at the observation equation level.

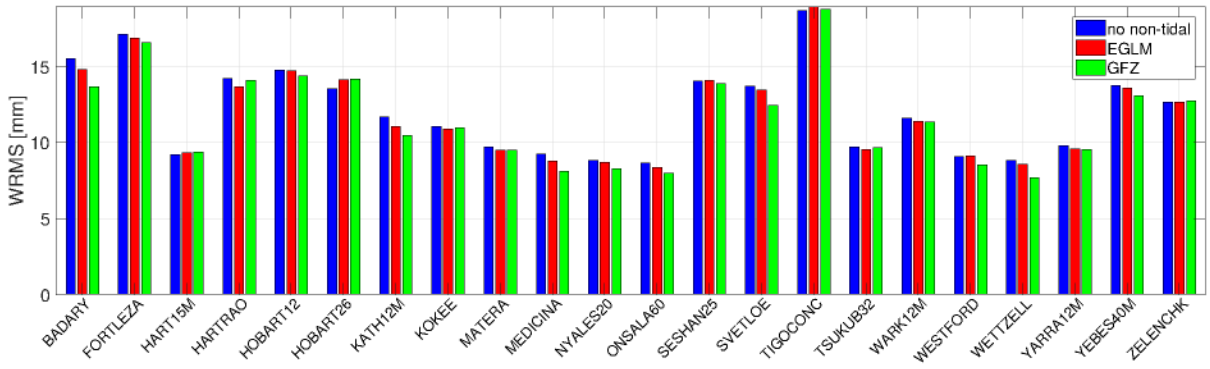


Figure 7.1.3: The station height repeatability (seasonals removed) after applying no non-tidal displacement models (blue), the fully fledged EGLM (red), and the discrete series of detrended accumulated geophysical loading (green), at the observation equation level.

servations unbeknownst to state-of-the-art geodetic analysis while being anti-correlated with geophysical loading, or there are still effects in VLBI's processing chain that are not yet understood, or both, analyzing simulated observations facilitates the understanding of how geophysical loading affects geodetic parameters, void of effects that are not understood.

Utilizing FGST (cf. Sec. 2.6), VLBI observations were simulated based on the schedules of sessions carried out in the framework of IVS and QUASAR. The observations were simulated based on quasar-tailored ray-traced delays in hourly ERA5 refractivity tensors, non-tidal geophysical loading induced by mass transport within the atmosphere, the oceans, and the continental hydrology, and noise; random walk plus integrated random walk for the clocks, turbulence model for the troposphere (Nilsson and Haas, 2010), and station-dependent white noise. Since in this chapter the focus is placed on loading, modelling atmospheric refraction is carried out with a VLBI-tailored PMF — thus no systematic error is introduced from mismodelling the troposphere — and residual zenith delays and horizontal gradients are estimated at all stations. The station coordinates — estimated sessionwise — between a solution where non-tidal loading was reduced at the observation equation level, and another where it was ignored were compared. Neglecting to model non-tidal loading is responsible for a large scatter in the station coordinates, especially the stations' height (cf. Fig. 7.1.4). From the simulations carried out herein, no statistically significant bias in the station coordinates was identified. Comparing the S_a amplitudes illustrated in Fig. 7.1.4 with those shown in Fig. 7.1.1, two issues are apparent: (i) the fact that co-located stations often do not participate in the same sessions, or the observations thereof span different periods should not yield large differences in the estimated harmonics, and (ii) the fact the station coordinate amplitudes differ considerably in some stations (real vs. simulated observations) could be indicative of effects that are either not considered in the MC simulations, are not understood well enough in the analysis of the real observations, or are to an extent anticorrelated with other unknown/unmodeled effects.

Employing FGST (cf. Sec. 2.6), laser ranges were simulated to Ajisai, LAGEOS 1 and 2, Etalon 1 and 2, LARES, Larets, Stella, and Starlette from all SLR stations that contributed to ITRF2014, employing ray-traced delays (tailored for the laser frequency at each station, as well as the orbital altitude of the different satellites), loading displacements, and cloud cover tensors, all calculated consistently from hourly ERA5 data. It was assumed that potential ranges to satellites are not carried out only due to clouds or the fact that a satellite (within the subset of choice) with higher priority had to be observed at the same time. In a first solution, NTAL was simulated but not modelled — simply put, simulations were carried out where the loading signals

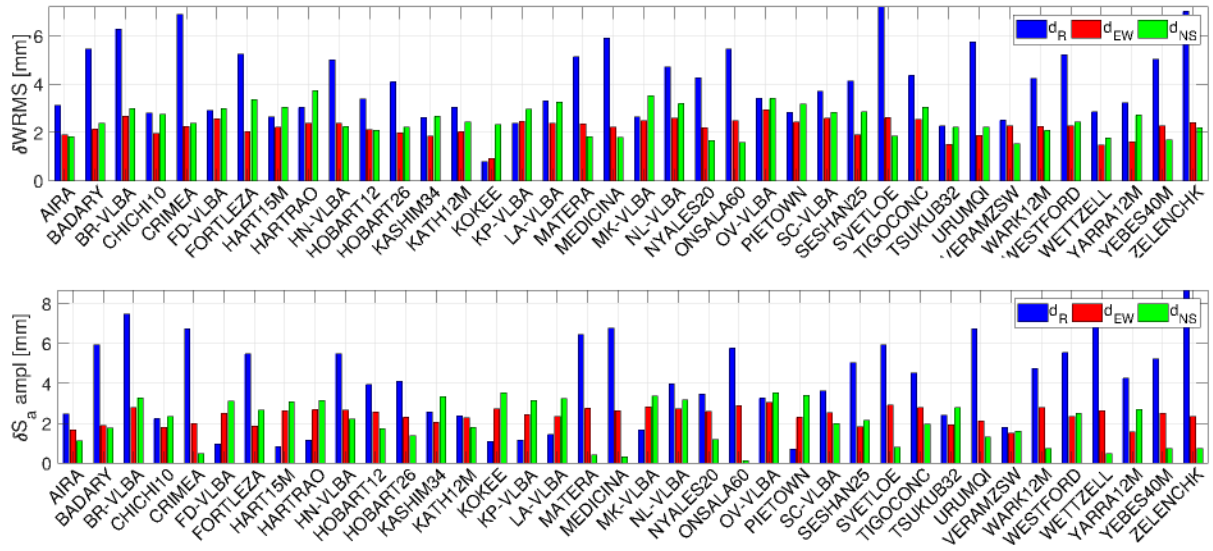


Figure 7.1.4: The portion of WRMS (upper panel) and S_a amplitude (lower panel) in the VLBI station coordinates that is solely attributed to neglecting to model non-tidal loading deformation at the observation equation level, based on simulated observations (cf. Sec. 2.6). The scatter in the radial, North-South, and East-West coordinate component is shown in blue, red, and green, respectively.

were included in the "observed" vector but not in the computed, a common practice in SLR data analysis. Figure 7.1.5 illustrates the temporal average of the spurious displacements induced by this omission averaged over 50 ensemble members. While these offsets do not correlate with any of the average cloud cover temporal averages, they induce artificial offsets mainly in the height component that in certain cases exceed 1 mm. In only two stations, namely Metsähovi (Finland) and Svetloe (Russia), spurious velocities are introduced in the radial component that exceed 1 mm dec^{-1}. Except for a noise amplification in all coordinate components, repeating the same experiment not accounting for atmospheric asymmetry does not introduce additional systematic effects. Excluding ranges to all satellites save for LAGEOS and Etalon, does not introduce any statistically significant offsets in the ensemble average with respect to utilizing ranges to all 9 satellites. From Fig. 7.1.5, it is apparent that modelling atmospheric asymmetry is far more important than accounting for non-tidal atmospheric pressure loading.

For the next experiment, instead of average cloud fields, the instantaneous (hourly) cloud tensors were used. Figure 7.1.6 illustrates the bias induced by the not only due to the omission of modelling non-tidal loading, but also due to the reduced number of observations under cloudy conditions. While no clear cloud-dependent pattern can be discerned, simulating laser ranges based on instantaneous cloud tensors in lieu of average cloud fields causes statistically significant differences in the station coordinates.

To sum up, simulating NTAL but not reducing it in the geodetic adjustment induces seasonal variations and increased scatter in all coordinate components. Comparing the modelled displacements to those obtained from the geodetic adjustment, the annual height amplitudes of the latter are slightly overestimated in 76 % of the SLR stations, below the 1 mm level. The corresponding phase differences do not exceed 10° in 90 % of the stations. In more than 85 % of the cases, the WRMS of the post-residuals is smaller than the variations in the geophysical models. Applying any superimposition of NTAL and NTOL with CWSL models yields similar results; the S_a amplitudes are underestimated in 83 % of the cases in the radial component, and 61 % of the cases in the lateral component. The phase differences are in almost all cases below

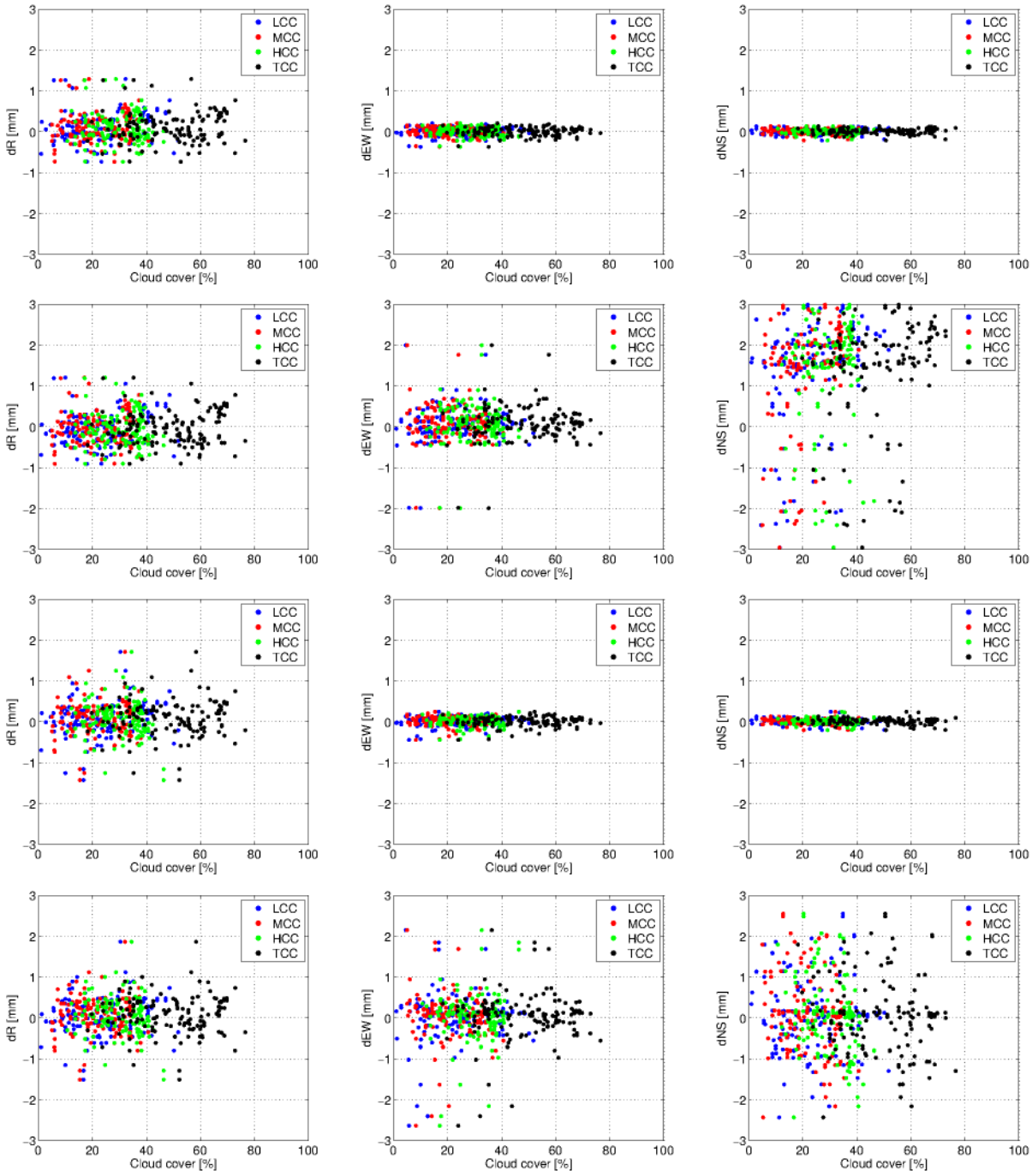


Figure 7.1.5: The coordinate bias in the radial (1st column), East-West (2nd column), and North-South (3rd column) component, induced by neglecting to model NTAL at the observation equation level in SLR data analysis, for all stations that are part of ITRF2014. The 1st row shows the bias when only noise is injected in the observations and NTAL is not modelled. The 2nd row shows the bias when in addition to noise, the atmospheric asymmetry is not modelled nor estimated either. Rows 3rd and 4th display the difference between the solutions on the first two rows and the respective ones where the correct NTAL model was applied at the observation level. In the legend, LCC, MCC, HCC, and TCC denote the low, medium, high, and total cloud cover aloft the stations.

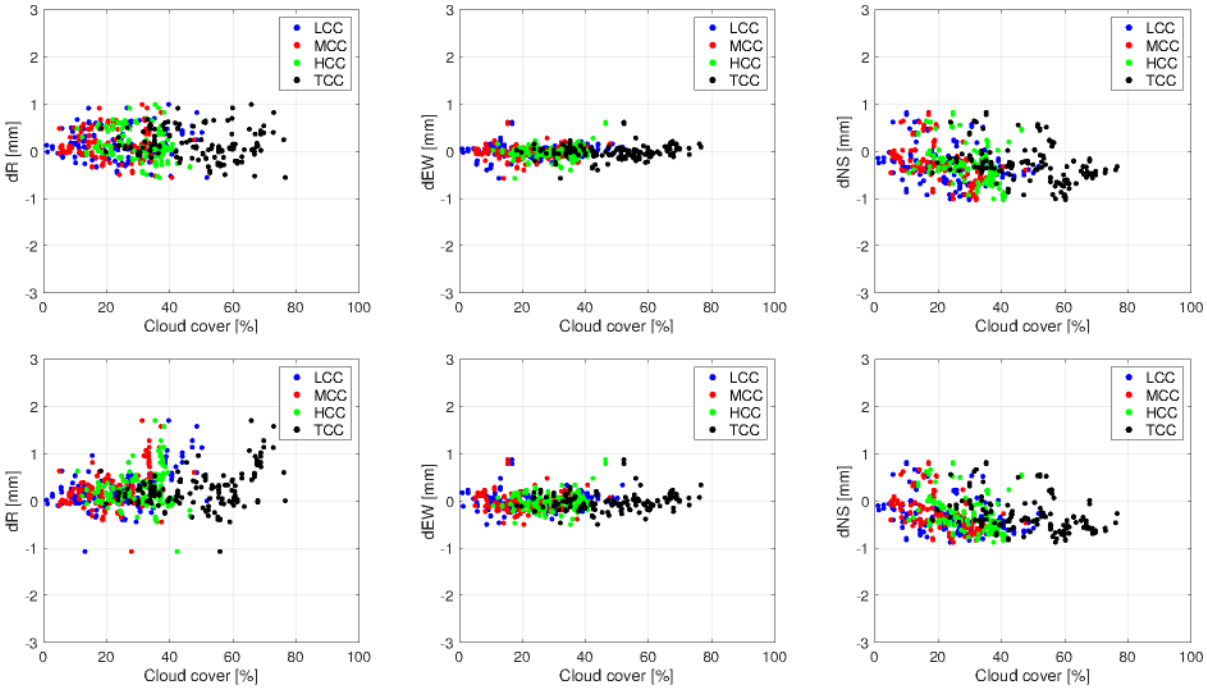


Figure 7.1.6: The coordinate bias in the radial (1st column), East-West (2nd column), and North-South (3rd column) component, induced by neglecting to model NTAL (1st row) or ANGL (2nd row) at the observation equation level in SLR data analysis, for all stations whose data were assimilated into ITRF2014. For the simulation of the related observations, hourly cloud tensors from ERA5 have been utilized. In the legend, LCC, MCC, HCC, and TCC denote the low, medium, high, and total cloud cover aloft the stations.

5°. Such a good agreement is due to the fact that neither clock function nor tropospheric parameters are estimated in SLR analysis, thus rendering SLR a suitable tool to monitor deformation induced by non-tidal mass transport within Earth's fluid envelope. The bias introduced by not accounting for any combination of non-tidal loading models (so long as the mass is implicitly conserved, cf. Sec. 5.1) is at the 0.1 mm level in the horizontal plane, and usually below 0.3 mm in the height component. There are stations (Zelenchukskaya (12351S002-1889) and Santiago de Cuba (40701S001-1953)) where an offset larger than 1 mm is introduced. As far as the station velocities are concerned, lateral velocity differences do not exceed 0.3 mm dec^{-1} except for Kunming and Greenbelt, and vertical velocity discrepancies are relatively larger and can reach 0.9 mm dec^{-1} for San Juan, for NTAL. That relative velocity error introduced is close to the GGOS requirements of 1 mm dec^{-1} (e.g., Gross et al., 2009). For the scenarios where hydrological loading was simulated but not reduced at the observation level, the differences are much larger; 22 % of the cases the vertical velocity difference is too large to satisfy the GGOS requirements, and the average relative horizontal velocity error is 0.4 mm dec^{-1}. As the formal error of these velocity estimates ranges from 0.1 to 0.2 mm dec^{-1} and stems from a 50 member ensemble, it is safe to say that the differences are statistically significant. In Fig. 7.1.7 the coordinate time series from the simulated observations at Wettzell are depicted.

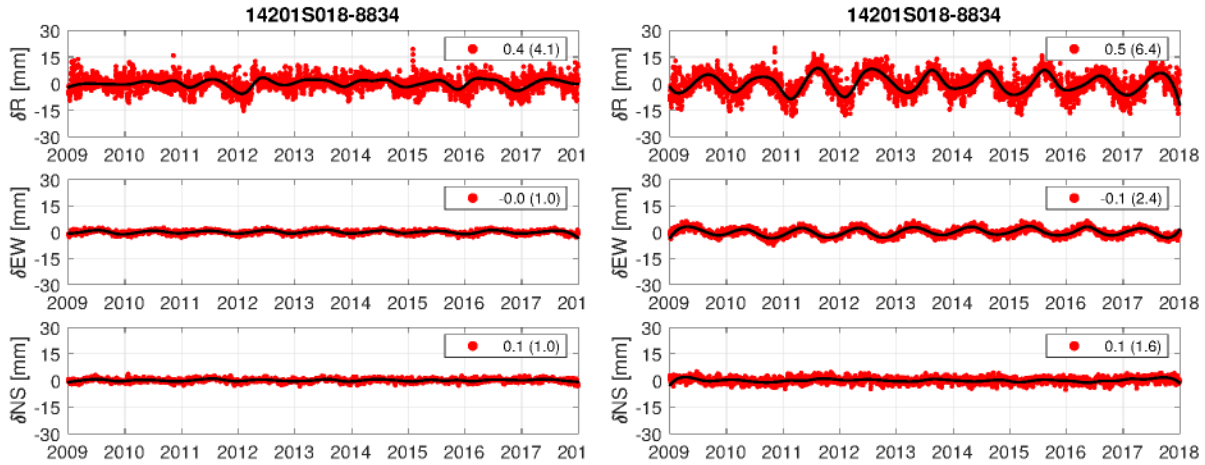


Figure 7.1.7: Station coordinate residuals (from simulated observations) obtained when non-tidal geophysical loading displacements at Wettzell are not modelled. The displacements due to NTAL (left) and ANGL (right) are shown in red. In black shown is the three-month moving median. The long-term average and scatter are shown in the legend.

7.2 Impact on the station network

To assess the impact of not accounting for displacements due to geophysical loading at the reduction of space geodetic measurements on the station network (implied reference frame), several series of 3D 7- and 14-parameter similarity transformations were performed. The so-called Helmert transformations, were carried out for different scenarios. For the cases where the loading displacements were applied at the parameter level (utilizing the services' contribution to ITRF2014), five sets of displacement series were utilized based on one or more geophysical loading components (atmosphere, oceans, and continental hydrology), cf. Sec. 7.1. Thereupon, five series of Helmert transformation parameters were estimated between the original solutions and the set of coordinates obtained by displacing them by the loading models developed herein. For the cases where the loading models developed in Chapter 5 were applied at the observation equation level (for both simulated and real observations), the same assessment approach was followed.

Given the station coordinates estimated by analyzing a global station network with parameterization A, and B, $\mathbf{X_A}$ and $\mathbf{X_B}$, respectively, the L_2-norm estimate of the Helmert (or Bursa-Wolf) transformation between them reads (e.g., Sillard and Boucher, 2001; Kotsakis et al., 2014)

$$\begin{aligned} \hat{\boldsymbol{\theta}} &= \mathbf{C}_{\hat{\theta}}\mathbf{A}^{\top}\left(\mathbf{C}_{\mathbf{X_A}}+\mathbf{C}_{\mathbf{X_B}}\right)^{-1}\left(\mathbf{X_A}-\mathbf{X_B}\right), \\ \mathbf{C}_{\hat{\theta}} &= \left(\mathbf{A}^{\top}\left(\mathbf{C}_{\mathbf{X_A}}+\mathbf{C}_{\mathbf{X_B}}\right)^{-1}\mathbf{A}\right)^{-1}, \end{aligned} \tag{7.2.1}$$

where the Euclidean similarity parameters $\hat{\boldsymbol{\theta}}$ set up are a translation ($\mathbf{T}=\begin{bmatrix}T_X & T_Y & T_Z\end{bmatrix}^{\top}$), a rotation matrix ($[\begin{bmatrix}R_X & R_Y & R_Z\end{bmatrix}^{\top}\times]$), and a differential scale factor D. $\mathbf{A}$ denotes the design matrix whose form is affected by the number of parameters set up. The stochastic character of $\mathbf{A}$ is neglected owing to its marginal contribution to $\hat{\boldsymbol{\theta}}$ (e.g., Schaffrin and Felus, 2008). The station coordinate block of the covariance matrices of the two different solutions are denoted by $\mathbf{C}_{\mathbf{X_A}}$ and $\mathbf{C}_{\mathbf{X_B}}$, respectively, and the covariance matrix of the datum perturbation parameters is denoted by $\mathbf{C}_{\hat{\theta}}$. Being estimated in a single adjustment, the elements of the related NEQs corresponding

to coordinate components of different stations are to a certain extent correlated. Thus, fully-populated covariance matrices have been used in (7.2.1). While there are other approaches to perform the similarity transformations, such as employing quaternions (Mercan et al., 2018), there is no utility in adopting anything other that (7.2.1) for the task at hand.

First, the impact of applying loading corrections a posteriori on the different station networks was assessed. The impact of loading displacements on the different networks differs mainly as a function of the station spatial distribution and number (158 for VLBI, 142 for SLR, 1410 for GNSS, and 186 for DORIS), as well as the temporal resolution of the station coordinate estimation process. For instance, Fig. 7.2.1 shows the estimated differential scale factor for all four networks for the fifth loading combination case (NTAL+NTOL+CWSL). In the Appendix, Fig. B.0.1 to Fig. B.0.4 display the scale time series for all other cases. While there is almost no long-term bias or trend in the time series, the scatter differs substantially. Examining the related graphs reveals that CWSL yields clear seasonal variations in the datum parameters, whereas NTOL contributes mainly to the noise. NTAL induces strong seasonal signals (up to 2 mm in T_Z of SLR) together with a noise amplification (more than 1 mm in the scale of VLBI). All VLBI and GNSS solutions stem from a reanalysis spanning 24 hours, whereas the SLR and DORIS solutions utilize 7-day arcs. Note that for the period 1983–1992 ranges only to LAGEOS 1 have been used (for ITRF2014), hence coordinates were estimated on a biweekly basis (15-day arcs). The time resolution of the solutions can to an extend explain the significantly larger scatter in VLBI and GNSS. Compared to coordinate time series from GNSS data analysis, VLBI solutions are noisier as a result of significantly smaller networks as well as the network turnaround between VLBI sessions. In point of fact, for the ITRF2014 contributions, the size of the GNSS network can be two orders of magnitude larger. The excellent spatial distribution of the DORIS ground network renders its stability practically impervious to geophysical loading displacements, provided the total mass is conserved (at least implicitly). Nevertheless, this statement does not hold for the station coordinate series (cf. Sec. 7.1).

To quantify the signal characteristics, offsets, trends, and amplitude- and phase-locked seasonals of $\hat{\theta}_j$, $j = [1, 7]$ were estimated in a least-squares adjustment where an empirical Hirvonen covariance function was employed to account for the inherent temporal correlations, cf. (4.3.5). Figure 7.2.2 displays the S_a amplitude and phase of all possible scenarios for the translation in the Z direction and scale, as well as the WRMS of the post-fit residuals. In almost all similarity transformation parameters, the largest amplitudes as well as the largest WRMS of the post-fit residuals is found in VLBI. The reason for that is the fairly limited ground network, as well as the fact that session-wise solutions (daily) are utilized, with an ever-changing station network. To assess whether there is an explanation other than those postulated above, based on the NEQs in the VLBI SINEX files, biweekly and monthly global solutions were created (not shown here). The phase does not change considerably, but the S_a amplitude is reduced at the levels of the SLR amplitudes. Assessing the phase of the scale series (cf. Fig. 7.2.2), there seems to be a large disagreement for the NTAL solutions, that cannot be attributed solely to the small amplitude because the NTOL solutions display smaller amplitudes but the scale does not show such a variation.

By and large, T_Z is related to the so-called degree-one deformation (cf. Fig. 5.1.4 and Fig. 5.1.5). The phase for T_Z is fairly stable across the techniques, with the exception of applying NTOL to the GNSS network. This is probably due to the fact that NTOL-induced systematic variations are rather small, hence the precise phase estimation is hindered. The S_a T_Z amplitude is the largest for SLR almost in all cases. This is mainly due to the lack of tracking stations in polar regions, contrary to VLBI. The $\mathbf{T}$ series obtained herein (not shown) are in agreement with Fig. 5.2.4 of Glaser (2014) and Fig. 3 of Glaser et al. (2015), as well as (Männel and Rothacher,

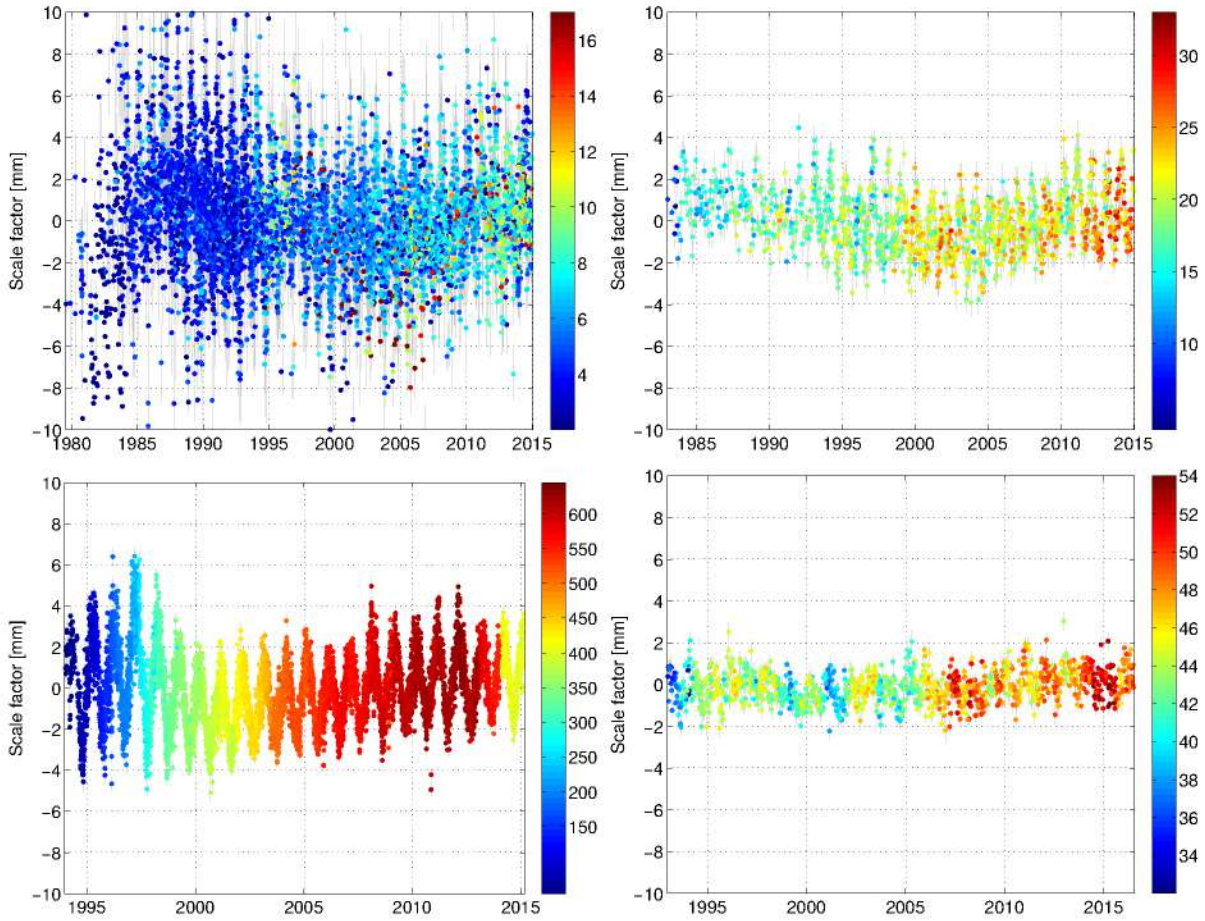


Figure 7.2.1: The impact of the combined effect of non-tidal atmospheric pressure loading, non-tidal ocean loading and continental water storage loading on the scale of the implied reference frame of the networks of IVS (upper-left), ILRS (upper-right), IGS (lower-left) and IDS (lower-right). The colorbars indicate the number of stations.

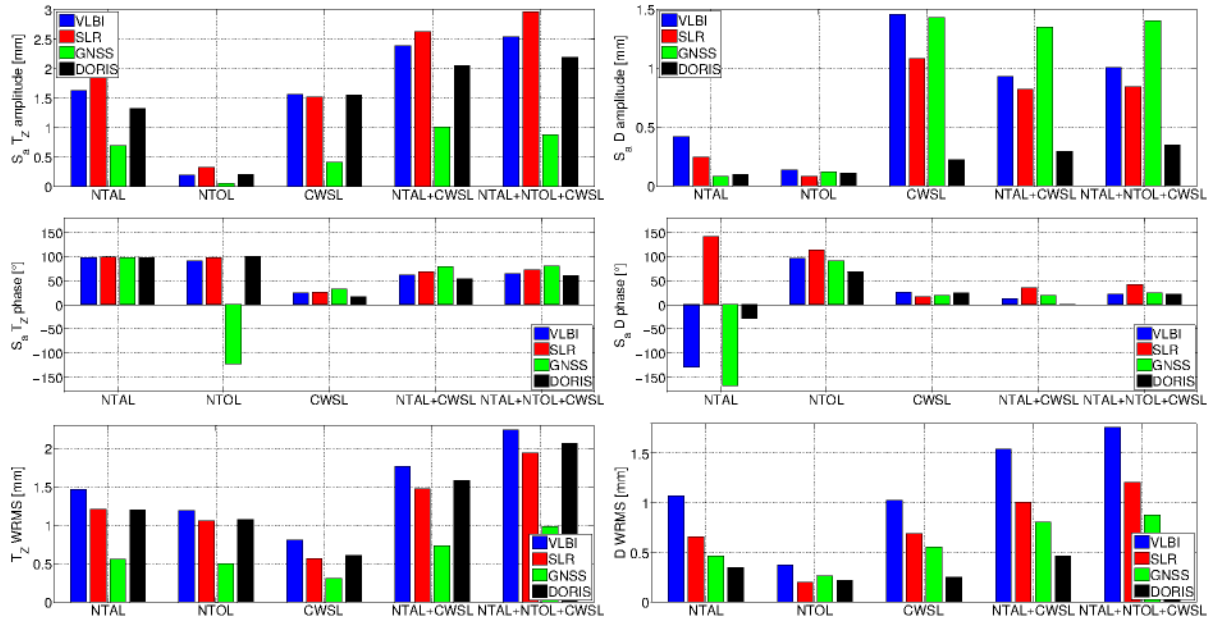


Figure 7.2.2: The annual amplitude and phase of T_Z and the differential scale factor from the application of loading models at the parameter level, as well as the scatter of the post-fit residuals. Note the varying vertical axis limits.

2017). For a quantitative assessment of the $\hat{\boldsymbol{\theta}}$ signals, the interested reader is referred to Table B.0.1 to Table B.0.5, in the Appendix.

There is a wealth of information on the temporal variations in amplitude and phase variation, that remains unexploited should only two parameters per frequency be estimated (amplitude and phase). Some of these variations are artificial (due to mismodelling geophysical fluid dynamics, changes in the tracking network, or changes on the observed targets), and others are real e.g., El Niño-like effects. To this end, in Balidakis et al. (2019) a different approach of approximating loading effects analytically was explored: amplitude and phase modulation of the related time series. The amplitude and phase are estimated as continuous PWLFs at quarterly intervals with the caveat that Tikhonov regularization should applied to the least-squares solution (personal communication with M. Chatzinikos) as this is an ill-posed problem in the sense of Hadamard. As phase variations are slightly larger than amplitude variations, a different interval may be set for the PWLFs.

Applying the total discrete geophysical loading model and EGLM (after the removal of the secular trends) at the group delays in VLBI data analysis (observation equation level), has an effect similar to applying the related loading models a posteriori, on the implied frame. All datum perturbation parameters experience seasonal signals, as well as a scatter. Figure 7.2.3 illustrates the differential scale factor, employing only the stations that participated in the NNT and NNR condition equations — in essence all stations with the exception of those that have experienced large Earthquakes i.e., Tsukuba and TIGO at Concepcion. Including these in the estimation of the similarity parameters (of course accounting for fully populated variance-covariance matrix) does not yield a statistically significant change, although the differences can be as large as 1.5 mm. Should only the VLBI stations that constitute an earlier frame e.g., ITRF2008, be used, the differences would be much larger as the size of the observation network would be reduced to a third in many cases (fewer Russian and Australian stations). Table B.0.5 shows the WRMS of the session-wise 7-parameter Helmert transformation between the aforementioned solutions.

As geophysical loading affects other parameters in addition to station coordinates, in the next

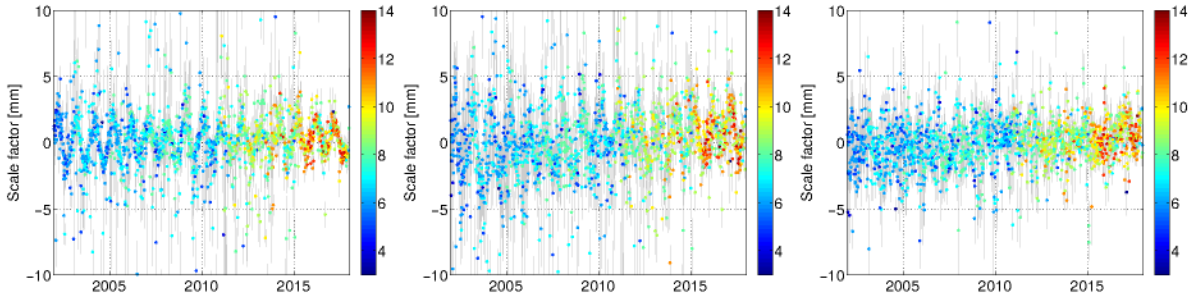


Figure 7.2.3: The differential scale factor between VLBI station coordinates estimated employing `VieVS@GFZ`. Shown from left to right are the scale for (i) no non-tidal vs. discrete, (ii) no non-tidal vs. EGLM, and (iii) EGLM vs. discrete loading model.

Table 7.2.1: WRMS of the session-wise Helmert transformation parameters between VLBI solutions obtained employing `VieVS@GFZ` to analyze all the IVS rapid turnaround sessions, where no non-tidal loading, the EGLM, and the discrete loading model was applied at the observation equation level.

	T_X [mm]	T_Y [mm]	T_Z [mm]	R_X [mm]	R_Y [mm]	R_Z [mm]	D [mm]
no non-tidal vs. discrete	1.0	1.5	1.4	1.3	0.7	0.8	2.6
no non-tidal vs. EGLM	1.3	2.1	1.6	2.5	1.1	0.9	3.1
EGLM vs. discrete	2.9	1.1	2.0	1.9	2.8	1.4	1.8

experiment the loading effect on the related observations was simulated, but was not modelled in the ensuing parameter adjustment. In SLR data analysis, such a setup allows to assess the impact of the reduced amount of observations under cloudy weather conditions.

In SLR data analysis, not accounting for NTAL or ANGL induces artificial geocenter motion with an S_a amplitude of 2.2 mm and 3.9 mm, respectively (cf. Table B.0.1 and Table B.0.5). Omitting to model non-tidal loading displacements induces seasonal variations on the scale of the implied frame as large as 0.7 mm for NTAL and 1.4 mm for ANGL. The impact on the rotation is much smaller, well below the 1 mm level. Figure 7.2.4 illustrates the time series of the related Helmert transformation parameters. Comparing these estimates with those tabulated in Table B.0.1 and Table B.0.5, it is clear that the application of loading models at the parameter level and the observation equation (or NEQ) level is quite different because loading information leaks into other parameters in the latter case. For instance, while the elements of **T** appear larger for the parameter level case, seasonal scale variations are smaller. Nevertheless, the phase of the translations and the scale are in a very good agreement (usually below 10°). The phase of the **R** series can differ largely (e.g., 30° for R_X for the ANGL case). These differences could be attributed — to a certain extend — to the 140 station network considered for the SLR simulations carried out herein as opposed to the combined ILRS solution where it is rather rare that more than 30 stations contribute to a weekly solution.

Comparing Fig. 7.2.4 to Fig. 7.2.5, it is apparent that the approach selected to simulate the cloud cover induces significant changes on the implied SLR reference frame. If potential observations are rejected based on a random function, sites with high TCC will have fewer observations than stations with low TCC, but all coordinate estimates will be normally distributed in time. On the other hand, accounting for instantaneous cloud cover will result in the same reduction in the number of observations, but the remaining observations will not be evenly distributed across meteorological conditions. This feature results in a small offset in the geocenter coordinates (0.75 mm) as well as a small scale bias (0.7 mm).

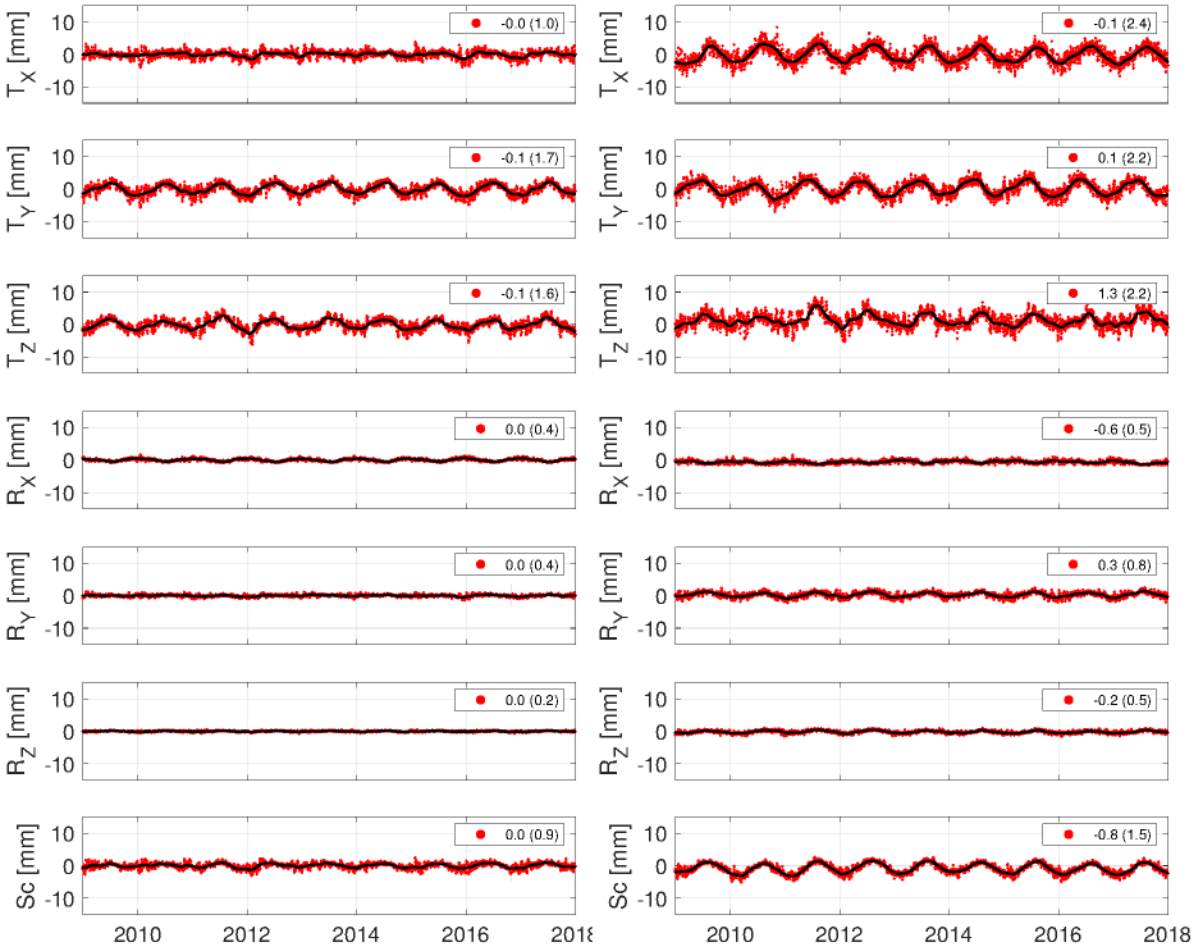


Figure 7.2.4: The impact of not applying NTAL (left) and ANGL (right) on the implied reference frame realized by SLR observations, expressed in terms of Helmert transformation parameters. Laser ranges were simulated based on the *temporal average* of the cloud cover atop each station. In the legend, the long-term average and the scatter of the related series is illustrated.

7.3 Impact on Earth orientation parameters

The accuracy and precision of EOPs estimated by geodetic networks largely depend upon the station distribution, as well as the measurement accuracy. For instance, Malkin (2009) demonstrated that the EOP quality obtained by geodetic VLBI data analysis is directly related to the baseline vectors (length and orientation), as well as the number thereof, which — to an extent — can be quantified by the volume V of the observing network of at least four stations, and can be approximated by a power law $\sigma_{EOP} = \alpha V^{\beta}$, where α and β are empirically determined constants. Based on all IVS rapid turnaround sessions that were analyzed in this work, it was found that the accuracy of $UT1 - UTC$ improves much faster with increasing network volume ($\beta = -0.288$) compared with the celestial pole coordinates (-0.354, -0.321), and terrestrial pole coordinates (-0.405, -0.442). The VLBI network polyhedron ranges in volume from $0.027\,\mathrm{Mm}^3$ (`08DEC23XE`) to $507.731\,\mathrm{Mm}^3$ (`14MAY27XA`). Therefore it is apparent that to obtain highly accurate EOPs, ramified networks must be employed. In particular, long North-South baselines

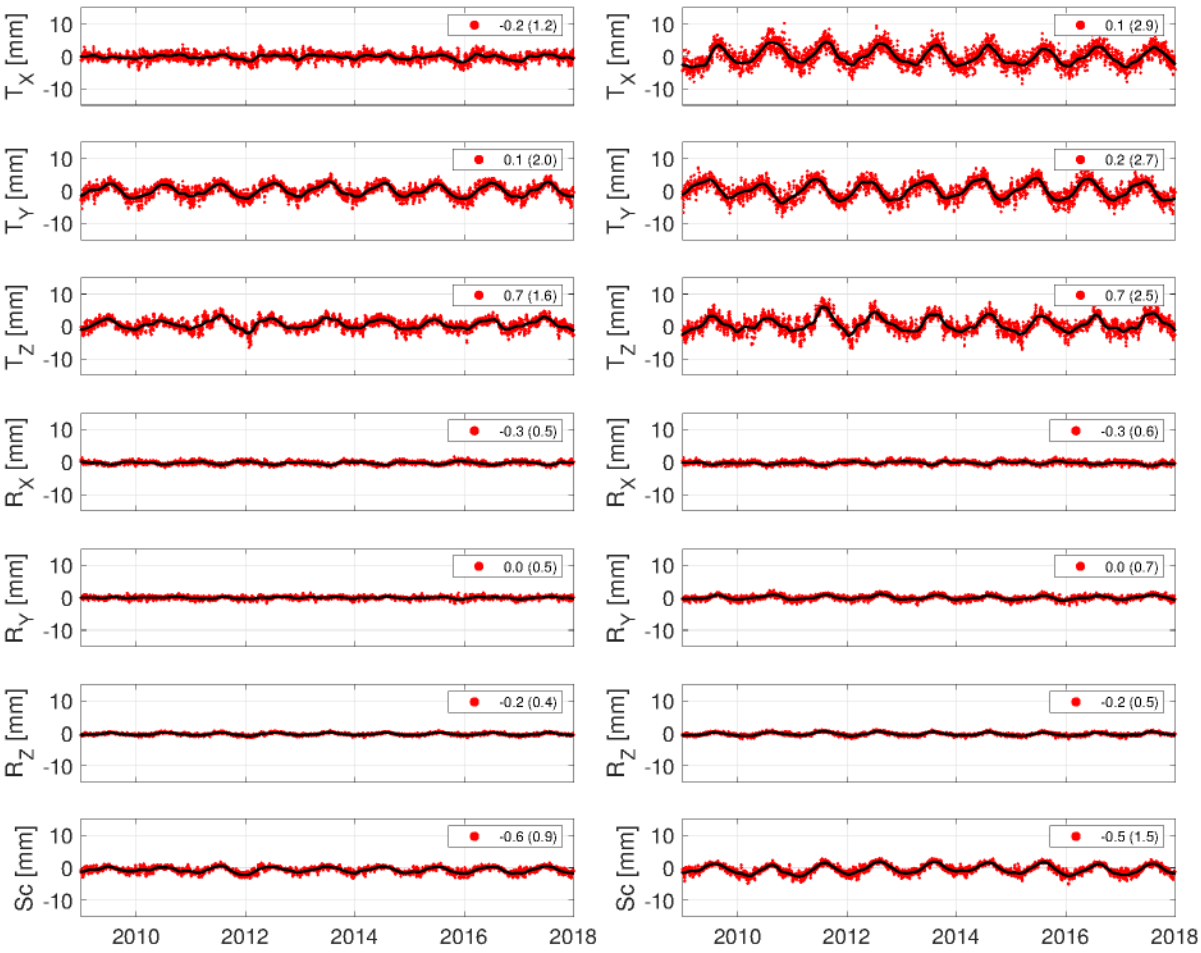


Figure 7.2.5: The impact of not applying NTAL (left) and ANGL (right) on the implied reference frame realized by SLR observations, expressed in terms of Helmert transformation parameters. Laser ranges were simulated based on *hourly* cloud cover tensors. In the legend, the long-term average and the scatter of the related series is shown.

increase the sensitivity to polar motion, and long East-West baselines increase the sensitivity to $UT1 - UTC$. There are certainly other parameters that affect EOP quality, most of which can be tuned during scheduling, such as the data recording rate and the source selection strategy. In this work, to evaluate the impact of geophysical loading models on Earth orientation, only global VLBI networks have been chosen. The impact of non-tidal crustal deformation on $UT1 - UTC$ from the so-called Intensive VLBI sessions is briefly discussed herein and in more detail in Balidakis et al. (2019).

In this section the results of applying two non-tidal geophysical loading models at the observation equation level in VLBI data analysis with `VieVS@GFZ` are presented; the discrete model (sum of NTAL and CWSL from ERA5, and NTOL from Mog2D-G), and the empirical geophysical loading model EGLM (cf. Sec, 5.5).

By and large, EOP determined from VLBI should not be affected by applying or not non-tidal loading deformation models to station coordinates, from a statistical viewpoint. The fact that polar motion and LOD remain unaffected has also been confirmed in the analysis of GNSS

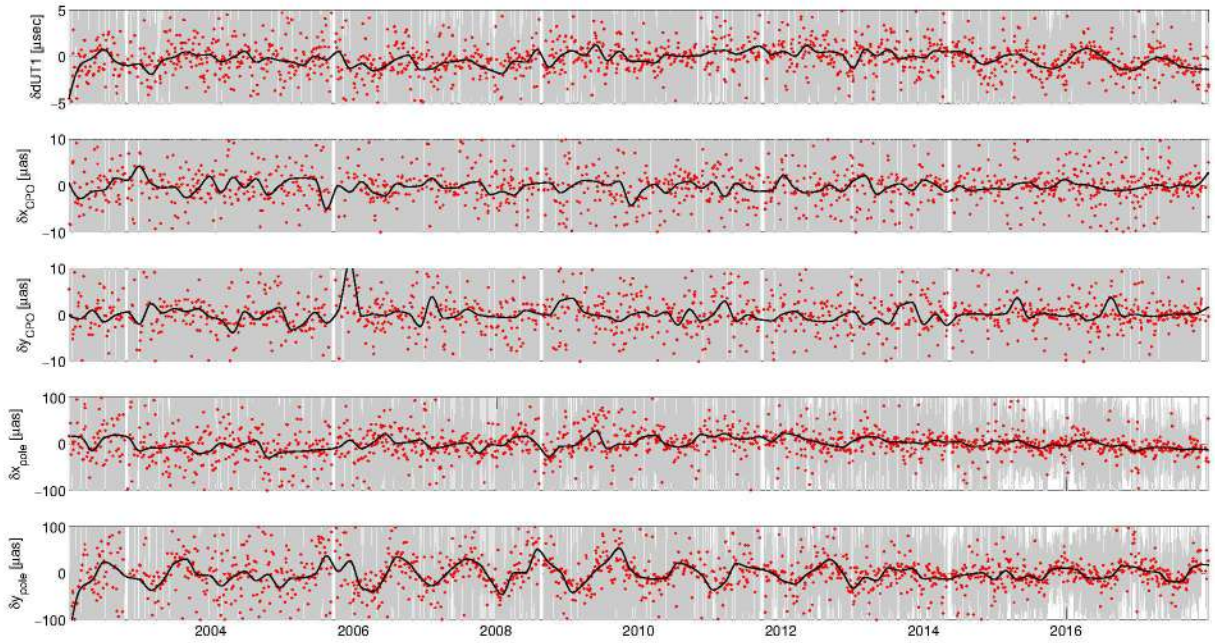


Figure 7.3.1: The impact of the *combined effect of NTAL, NTOL and CWSL* on EOPs estimated in VLBI data analysis. The differences between the EOPs obtained employing non-tidal loading and those obtained applying no non-tidal loading models (red), the formal errors thereof (gray), and the 60-day running median (black).

observations from a global network (collaboration with B. Männel). Figure 7.3.1 illustrates the differences between EOP estimated applying the discrete model, and not applying a non-tidal model, from the analysis of all rapid turnaround IVS sessions (2002–2018) with `VieVS@GFZ`. All EOP differences exhibit noisy seasonal variations (cf. Table 7.3.1). Similar results have been obtained by applying the EGLM at the observation level in VLBI data analysis (cf. Fig. 7.3.2). The largest systematic difference is observed in polar motion, and especially in y_p, where annual signal of the differences reaches an amplitude of 8 µas for the discrete model, and 6 µas for EGLM. The polar motion residuals also exhibit the largest scatter, in all cases above 10 µas. In both polar motion components, the impact of non-tidal geophysical loading exceeds 100 µs for several sessions. The EOP differences between applying the discrete model and EGLM are illustrated in Fig. 7.3.3, and do not exhibit neither the large seasonals nor the scatter observed in the previous cases (no non-tidal vs. EGLM and no non-tidal vs. discrete). Nevertheless, the fact that EGLM cannot capture synoptic variations, excites EOP variations in all parts of the power spectrum, some of which manifest into annual signals (e.g., for y_p).

The main reason why EOPs are not significantly affected by neglecting to model non-tidal geophysical loading is that estimating corrections to the station coordinates absorbs a large portion of the non-tidal geophysical loading signal. However, should no station coordinates be set up as unknowns in the geodetic adjustment, neglecting loading will introduce spurious variations to the zenith delays and the EOPs. Even in this case, no bias is introduced because the long-term variation is absorbed by the clock offset, and some of the high-frequency variations are recognized as short-term H-maser instabilities. Nevertheless, the physical meaning of the estimated parameters will be fudged.

As of this writing the publication latency with which group/phase delays and the temporal rates thereof from 24-hour VLBI experiments, is a fortnight, on average. It is clear that for

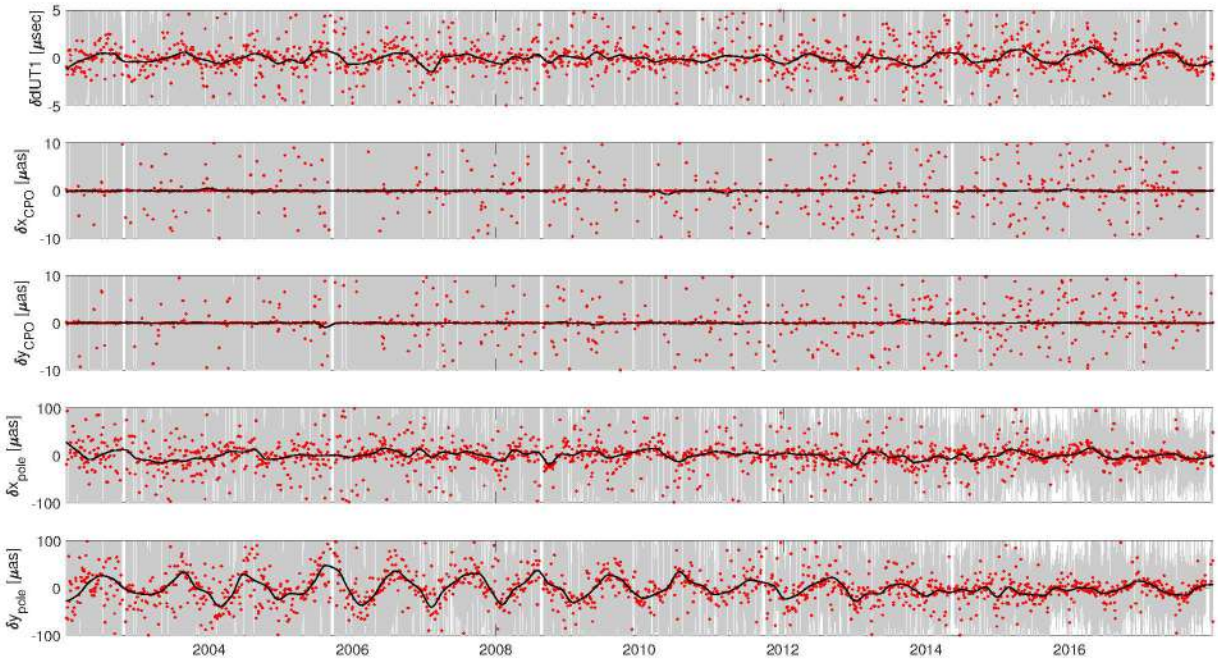


Figure 7.3.2: The impact of *EGLM* on EOPs estimated in VLBI data analysis. The differences between the EOPs obtained employing EGLM and those obtained applying no non-tidal loading models (red), the formal errors thereof (gray), and the 60-day running median (black).

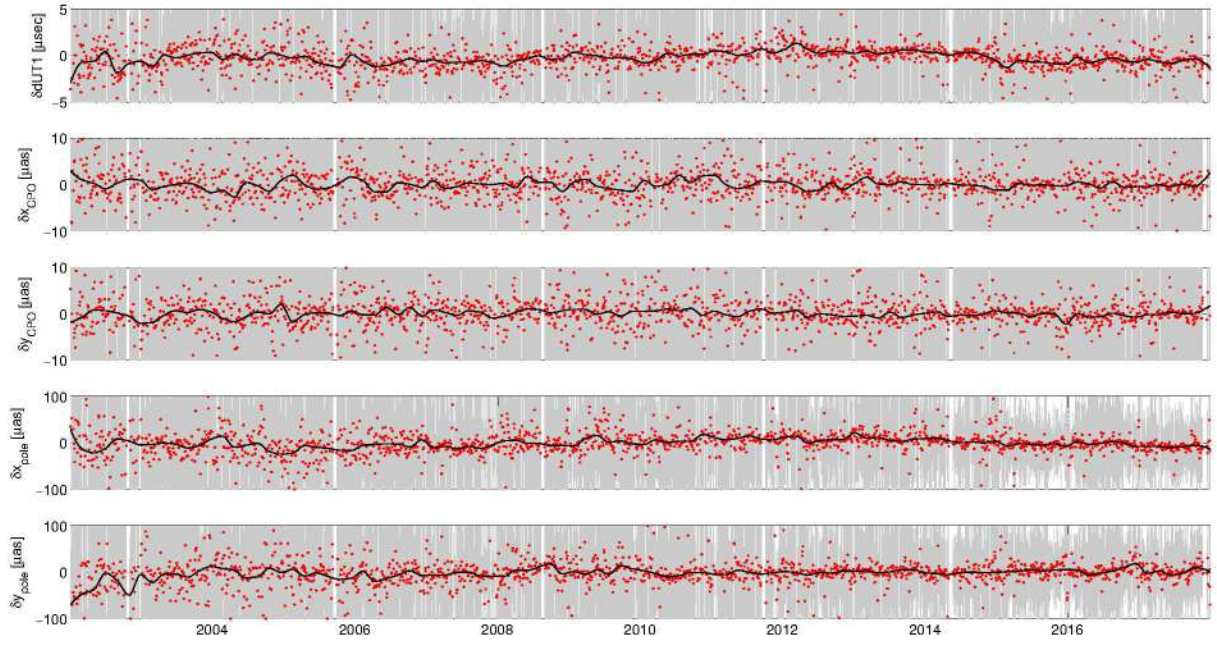


Figure 7.3.3: The differences in the EOPs estimated in VLBI data analysis employing discretized loading series developed herein and EGLM. The differences (red), the formal errors thereof (gray), and the 60-day running median (black).

Table 7.3.1: Seasonal amplitudes and WRMS of the post-fit residuals of the EOP differences between applying the discrete loading model or EGLM, and not applying any non-tidal loading model, at the observation equation level in VLBI data analysis (IVS rapid turnaround sessions spanning the period 2002–2018).

	EOP	S_a	σ_{S_a}	S_{sa}	$\sigma_{S_{sa}}$	S_{ta}	$\sigma_{S_{ta}}$	WRMS
no non-tidal vs. EGLM	δdUT1 [µs]	0.38	0.03	0.07	0.03	0.07	0.03	0.82
	δdX [µas]	1.28	0.31	0.97	0.30	0.77	0.30	8.94
	δdY [µas]	1.13	0.27	0.30	0.27	1.25	0.27	8.05
	δx_p [µas]	3.58	0.41	0.77	0.40	1.96	0.41	10.28
	δy_p [µas]	6.08	0.48	0.47	0.48	0.77	0.49	12.85
no non-tidal vs. discrete	δdUT1 [µs]	0.44	0.03	0.22	0.03	0.06	0.03	1.14
	δdX [µas]	0.66	0.25	0.38	0.24	0.80	0.24	7.54
	δdY [µas]	0.90	0.25	0.30	0.25	1.11	0.25	7.72
	δx_p [µas]	3.83	0.49	1.25	0.48	1.63	0.49	12.93
	δy_p [µas]	7.97	0.57	1.02	0.56	2.23	0.57	15.68
EGLM vs. discrete	δdUT1 [µs]	0.03	0.02	0.10	0.02	0.03	0.02	0.80
	δdX [µas]	0.18	0.06	0.09	0.05	0.20	0.06	1.76
	δdY [µas]	0.07	0.05	0.26	0.05	0.09	0.05	1.80
	δx_p [µas]	0.78	0.29	0.43	0.29	1.58	0.29	8.93
	δy_p [µas]	2.35	0.30	1.36	0.29	1.44	0.30	8.88

time-critical applications such as real-time positioning where accurate $UT1 - UTC$ information is imperative, these data sets cannot be utilized. In addition, only three 24-hour sessions, on average, are organized on a weekly basis by the IVS. To this end, different types of sessions are organized to allow for low latency and more frequent $UT1 - UTC$ updates, the so-called Intensives (INT). These sessions usually feature a single baseline interferometer that observes for one hour. Afterwards, within a couple of hours the data have already been correlated, and the geodetic adjustment has already been performed. Due to this special setup, no station nor source coordinates can be estimated, therefore any mismodelled station motion will be absorbed by other parameters. Usually, only $UT1 - UTC$, troposphere (residual zenith delays and occasionally linear horizontal gradient components), and a clock function (usually a two-state model) are estimated. Therefore, accurate $UT1 - UTC$ estimation is highly dependent upon the a priori models, as there is no capability for accounting for erroneous models by setting up parameters. To this end, source coordinates need to be accurately known — this is why only sources with fairly small structure are scheduled for these experiments, polar motion and celestial pole offsets need to be known precisely, atmospheric refraction has to be modelled appropriately, and of course the driving mechanisms of station displacements (tidal and non-tidal) must be understood.

As of this writing, there are three types of publicly available IVS Intensives:

- ☐ IVS-INT1, 65 % of all Intensives, featuring the baseline Kokee-Wettzell (10 357.4 km, $\delta\lambda = 172.5°$)
- ☐ IVS-INT2, 19 % of all Intensives, featuring the baseline Tsukuba-Wettzell (8445.0 km, $\delta\lambda = 127.2°$), and
- ☐ IVS-INT3, 4 % of all Intensives, featuring the triangle Ny-Ålesund-Tsukuba-Wettzell.

Currently, Ishioka observes in lieu of Tsukuba, and sometimes more than one radio telescopes

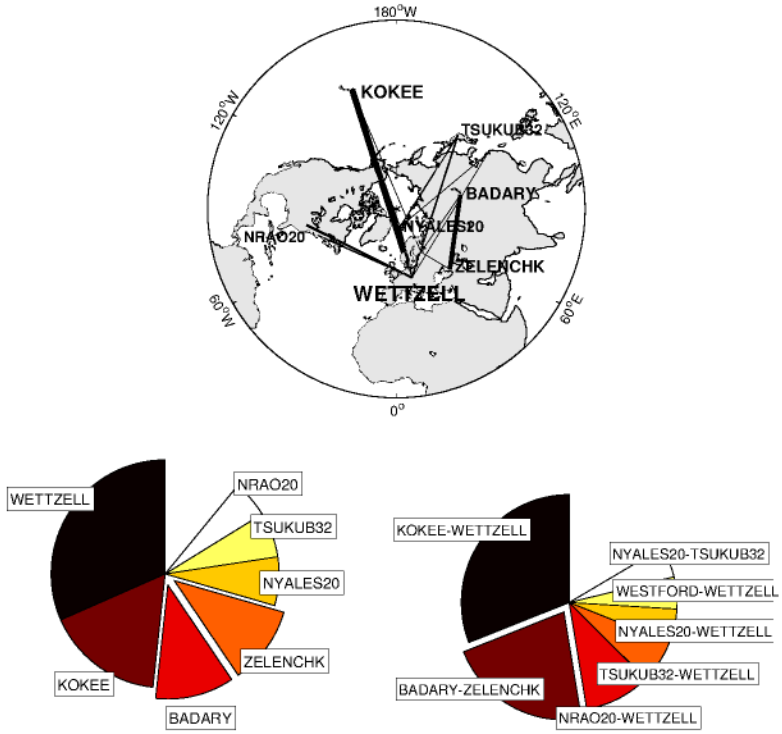


Figure 7.3.4: VLBI stations that participated in most IVS and QUASAR Intensive VLBI sessions. In the upper row, stations that appear in larger font have participated in more Intensives; baselines drawn employing wider lines have been observed more during Intensives. Shown are the stations (lower left) and baselines (lower right) that have the largest number of observations.

at Wettzell participate[1]. There are other publicly available Intensive sessions in addition to the aforementioned, such as those carried out between Wettzell, `MK-VLBA`, and `PIETOWN` (`XW`), as well as those carried out between `AGGO` and Wettzell (`INT9`). Figure 7.3.4 illustrates the stations and baselines that participated in most Intensives.

There is a number of Intensive VLBI sessions that is observed outside the framework of IVS such as the Russian network Badary-Svetloe-Zelenchukskaya (suffix `XT`). Observations were carried out on a weekly basis prior to June 2012, and on a daily basis ever since. For the period 2009–2017, 94 % of the sessions feature the single 4404.8 km-long interferometer Badary-Zelenchukskaya ($\delta\lambda = 60.7°$).

Due to the fact that INT sessions take place at the same time every day (e.g., around 18:30 for INT1), $UT1 - UTC$ estimation is prone to mismodelled tidal effects such as tidal atmospheric pressure loading. Figure 7.3.5 displays the tidal loading at the VLBI stations that participate in most Intensive session, according to simulations carried out at GFZ (Dill and Dobslaw, 2013), and at the GGFC (recommended by the IERS). All Intensives were analyzed varying the tidal atmospheric pressure loading model, but no statistically significant differences were identified.

The landscape is slightly different when non-tidal loading models were applied in the analysis of Intensives. Unlike the 24-hour analysis presented in this chapter, the Intensives were analyzed with the Kalman filter module of `VieVS@GFZ` (Nilsson et al., 2015b, 2017b). This choice was deliberate — over a batch least-squares adjustment — for within the Kalman filter and smoother, the treatment of atmospheric asymmetry in the form of gradients is facilitated, with the epochwise estimation of linear gradient components that are loosely constrained to gradients stemming from

[1] `ftp://cddis.gsfc.nasa.gov/pub/vlbi/ivscontrol/master??-int.txt`

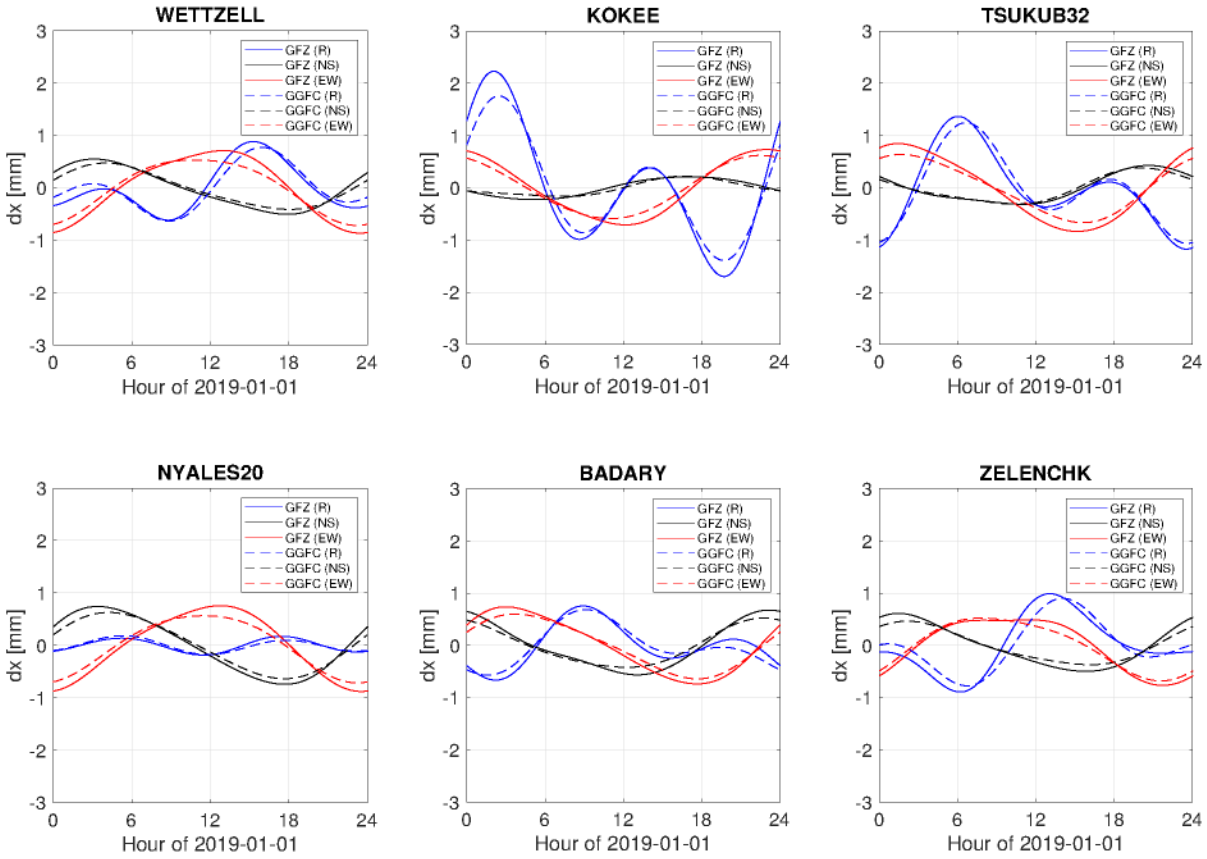


Figure 7.3.5: Tidal atmospheric pressure loading at Wettzell (upper left), Kokee Park (upper middle), Tsukuba (upper right), Ny-Ålesund (lower left), Badary (lower middle), and Zelenchukskaya (lower right), on 2019-01-01. The displacements shown have been simulated by GFZ (solid line), and GGFC (dashed line), for the radial (blue), North-South (black), and East-West (red) coordinate component, in the CM frame.

ray-tracing in ERA5. All sessions in the IVS[2] and QUASAR[3] archive that were identified as Intensive have been analyzed; in total, 9530 IVS Intensives and 2301 Russian Intensives. From the estimated dUT1 series, the seasonal harmonics have been estimated by a weighted least-squares adjustment. Some of the estimated parameters (amplitudes, and WRMS of the post-fit residuals) are tabulated in Table 7.3.2. It is apparent that the session type, and therefore the orientation of the baseline (for the single baseline interferometers), and the area of the ellipsoidal triangle (occasionally polyhedron), largely affects the quality of the estimated dUT1, as well as the sensitivity thereof to mismodelling of mass transport. Note that the stations participating at these sessions are subject to change, that is, not all INT1 sessions feature the Wettzell-Kokee baseline alone. By and large, the QUASAR Intensives seem to be more sensitive to non-tidal geophysical loading; dUT1 differences between applying or not the discrete model at the observation equation level yields S_a variations as large as 4.2 µs for the Russian Intensives, but only 0.6 µs for the INT1 sessions that feature one of the largest baselines. However, as

[2] https://vlbi.gsfc.nasa.gov/output/vgosDB_IVS/
[3] ftp://quasar.ipa.nw.ru/pub/EOS/IAA/ngs/

Table 7.3.2: Seasonal amplitudes and WRMS of the post-fit residuals of the dUT1 differences [µs] between applying the discrete loading model or EGLM, and not applying any non-tidal loading model, at the observation equation level in VLBI data analysis of Intensive sessions.

	Session type	S_a	σ_{S_a}	S_{sa}	$\sigma_{S_{sa}}$	S_{ta}	$\sigma_{S_{ta}}$	WRMS
no non-tidal vs. EGLM	INT1	0.66	0.01	0.10	0.01	0.07	0.01	0.20
	INT2	0.49	0.01	0.19	0.01	0.07	0.01	0.28
	INT3	0.70	0.02	0.20	0.02	0.03	0.02	0.26
	QUASAR	2.31	0.03	0.56	0.03	0.42	0.03	0.83
no non-tidal vs. discrete	INT1	0.56	0.02	0.12	0.02	0.07	0.02	0.82
	INT2	2.12	0.08	0.62	0.08	0.36	0.08	1.83
	INT3	2.55	0.13	0.50	0.13	0.32	0.13	1.75
	QUASAR	4.16	0.10	1.17	0.10	0.96	0.10	3.10
EGLM vs. discrete	INT1	0.38	0.02	0.23	0.02	0.00	0.02	0.77
	INT2	1.87	0.08	0.45	0.08	0.30	0.08	1.80
	INT3	2.22	0.12	0.35	0.13	0.34	0.13	1.73
	QUASAR	3.17	0.10	0.72	0.10	0.52	0.10	2.98

the average uncertainty of the dUT1 estimated from the analysis with `VieVS@GFZ` is 10 µs, 8 µs, 7 µs, and 23 µs for INT1, INT2, INT3, and QUASAR Intensives, respectively, dUT1 variations induced by non-tidal loading are below the noise floor, and cannot be characterized as statistically significant — the average dUT1 uncertainty from modern global VLBI sessions is usually below 5 µs. Furthermore, since very small non-tidal displacements are expected during the course of an Intensive session (typically one hour long), the influence of non-tidal loading degenerates (approximately) to a bias. The loading-induced bias in the baseline length will be — to an extent — compensated by the baseline clock offset that has to be set up in the parameter space of the analysis of Intensives.

While for the current accuracy level non-tidal loading does not seem to yield statistically significant differences, in the framework of VGOS, where the coveted polar motion and $UT1 - UTC$ accuracy is 75 µas and 7 µs, respectively (for the ultra-rapid VLBI products), and 15 µas 1 µs, respectively (for the final VLBI products), non-tidal loading will be more important than it is as of this writing (e.g., Nothnagel et al., 2016).

7.4 Impact on satellite orbits

The impact of mass redistribution within Earth's fluid envelope on satellite orbits is briefly discussed. It was not assessed in the framework of this thesis. Non-tidal geophysical loading mainly induces mm-level seasonal signals on satellite orbits. Loading-induced satellite coordinate errors stem from not modelling (i) the real displacements caused by the gravitational potential differences, and (ii) the artificial displacements caused by ignoring loading on ground stations. According to (e.g., Dach et al., 2011; Sośnica et al., 2013; Männel et al., 2019), these variations can reach 5 mm, and for GNSS affect mainly the Z-component (S_a amplitudes up to 4 mm). Männel et al. (2019) noted that the estimated satellite coordinate differences between accounting or not for non-tidal loading at the observation equation level have similar spectral characteristics with the degree-1 mass loading deformation coefficients. Due to the fact that neither the Keplerian elements nor satellite coordinates are usually included in SINEX files, it is no possible

to account for loading-induced orbit errors at the parameter level (Dach et al., 2011). The latter highlights the need to apply for non-tidal geophysical loading at the observation equation level in the analysis of satellite-based techniques.

8 Summary, conclusions and outlook

In this final installment of the thesis, a recapitulation of the major results is carried out. The impetus of the work conducted herein was to address the impact of signal delay induced by atmospheric refraction, and crustal deformation induced by geophysical loading in the analysis of space geodetic observations. Section 8.1 recounts the main achievements, and Sec. 8.2 provides the main conclusions that can be drawn from this work. Section 8.2.1 provides recommendations to the IAG services involved in the realization of the Global Geodetic Reference System. On a final note, plans for future research are also presented (Sec, 8.3).

8.1 Recapitulation

In the framework of this dissertation, a number of topics has been investigated, namely:

- ☐ the atmospheric refraction of microwave and optical signals, and the differences thereof;
- ☐ the crustal deformation induced by mass redistribution within Earth's fluid envelope including the atmosphere, the oceans, and the continental hydrology;
- ☐ the simulation of VLBI, SLR, GNSS, and DORIS observations within a Monte Carlo framework, employing for the deterministic part ray-traced delays, geophysical loading displacements, cloud cover, and for the stochastic part an atmospheric turbulence model for the small scale refractivity fluctuations, random walks to characterize the stability of frequency standards, and white noise;
- ☐ the analysis of real and simulated space geodetic observations employing `VieVS@GFZ` and Fast Geodetic Simulation Tool (FGST), respectively, where some of the atmospheric refraction and geophysical loading models were implemented.

Software has been developed ad hoc, capable of simulating observations of all space geodetic techniques. FGST can simulate clock stability as 1-, 2-, 3-, state model, turbulent atmospheric refraction based on ray-traced delays, as well as the thermal noise of receiver and transmitter — wherever applicable. In addition to its capability of consistently simulating all four space geodetic techniques, an edge of FGST over similar developments is its ability to simulate the probability of SLR observations taking place accepting the premise that thick clouds impede laser observations. In contrast to the time- and space-invariant SLR station performance assumed heretofore, in this work the integrated cloud fraction from the 5th generation NWM ERA5 was considered to determine the probability of laser ranges (later normal points) being considered as useful observations in the SLR geodetic adjustment. FGST has two modules: (i) weighted least-squares, batch processing and (ii) Kalman filter and smoother, recursive processing.

A major portion of the thesis was devoted to the development of atmospheric refraction models for all space geodetic techniques that currently contribute to the realization of terrestrial reference systems. Ray-tracing was instrumental in investigating a number of effects such as ray-bending, that render employing VLBI-tailored delay models to other space geodetic techniques

causative of systematic biases that eventually hinder the proper reduction of space geodetic observations. Some aspects that are often overlooked in the design of a ray-tracing system such as the radius of curvature, the orbital altitude, and ray path deviations induced by ionospheric refraction were treated in full rigor. In addition, the derivation of the position operator of the underlying refractivity tensors, as well as the refractivity itself was slightly revised to accommodate non-ideal gas behavior. Based on these developments several mapping functions were derived, namely the Potsdam and Berlin mapping functions, as well as the empirical model GFZ-PT. These mapping functions are tailored for the individual frequencies, and the orbital altitudes of the different systems' components. The relations amongst atmospheric refraction for the different observing systems (VLBI, SLR, GNSS, and DORIS), the so-called atmospheric ties were comprehensively investigated.

On a tangent, a method for homogenizing meteorological observations recorded in the vicinity of geodetic stations based on the penalized maximal t-test was presented, as well as a method for obtaining reliable atmospheric corrections in the absence of in situ meteorological measurements from the model levels of NWMs. At the time of writing, all VLBI and SLR stations are equipped with precise meteorological sensors. While there is a number of GNSS and DORIS sensors that enjoy this commodity, this does not apply globally. However, these sensors often suffer from calibration issues, that will — if not treated at the instrument or the analysis level — contaminate the geodetic results, and predominantly the station coordinates and the atmospheric delays.

A scrupulous treatment of modelling displacements induced by mass transport within Earth's fluid envelope has been presented. Several modelling aspects have been evaluated within the framework of employing load Green's kernels assuming an elastic response to all loading excitations, such as oceans response to atmospheric forcing, and the Earth model on which the load Love numbers are based. A number of geophysical fluid mass anomaly sources (atmosphere, ocean, and hydrology) have been used, such as ECMWF's ERA Interim and ERA5, Mog2D-G, and GRACE. Some of the models developed herein were compared against state-of-the-art models available by established services such as from GFZ Sec. 1.3 (R. Dill and H. Dobslaw), Astrogeo (L. Petrov), Université de Strasbourg (J.-P. Boy), and University of Luxembourg (T. van Dam). The development of the ersatz geophysical loading model (EGLM), which is conceptually similar to the atmospheric model GFZ-PT has also been performed.

Some of the atmospheric refraction models developed herein were evaluated within the analysis of real VLBI observations, as well as simulated observations, for all four space geodetic techniques. A framework for dealing with undetected impurities in the meteorological data recorded at SLR stations, as well as with atmospheric azimuthal asymmetry on the laser ranges has been developed. The impact of alternating (i) the mapping functions amongst PMF, VMF1, and GFZ-PT, and (ii) the barometric pressure amongst raw and homogenized in situ series rigorously extracted from the model levels of ERA Interim, and GFZ-PT, on VLBI data analysis estimates was also presented. In particular, the series of the station coordinates (in the topocentric system), the baseline lengths, the datum perturbation parameters, and the Earth orientation parameters was assessed. As reliable integrated water vapour monitoring is crucial for climate change studies, special focus was placed on the derivation of the long-term trends thereof from real and simulated VLBI and multi-GNSS observations. The impact of alternating the mapping functions and the meteorological data on station coordinates and the implied reference frame was also assessed in the analysis of simulated GNSS and DORIS measurements.

The influence of some of the geophysical loading models developed in this work on the estimated parameters, was assessed at the observation equation and parameter level. The evaluation was performed with real (VieVS@GFZ) and simulated (FGST) observations, for all four space geodetic techniques. For the investigations where models were applied a posteriori, the contri-

butions of IVS, ILRS, IGS, and IDS to ITRF2014 were used. Special focus was placed on the EOPs retrieved from different VLBI sessions (IVS-R1, IVS-R4, INT1, INT2, INT3, and Russian Intensives), and the extend to which they are affected by non-tidal loading deformation of the observing network (or of only one baseline).

Last but not least, the multi-technique combination with local and atmospheric ties was investigated. The input data used were (i) reduced VLBI, SLR, GNSS, and DORIS normal equation systems (station coordinates, zenith delays, and atmospheric gradient components) generated employing FGST, and (ii) atmospheric ties from ray-tracing. However the results of these investigations (Balidakis et al., 2018b,a) were not included in here since this would obscure the main thread of the analysis.

8.2 Conclusions and recommendations

In the adjustment of space geodetic observations, setting up the partial derivatives e.g., for residual zenith delays, only yields the parameters of intent in an acceptable precision provided they are resolvable by the observation geometry and that no systematic errors remain unaccounted in the functional model. All developments in this work were towards a better understanding of the systematic effects induced by atmospheric refraction and geophysical loading on the parameters estimated by space geodetic techniques. This was achieved by developing models for these effects and applying them in the analysis of real and simulated geodetic measurements. In the following, some of the major results obtained in this work are outlined. The interested reader is referred to the respective chapters for details.

The quality of meteorological observations obtained in the vicinity of geodetic stations should be guaranteed, prior to their applying for the calculation of the a priori zenith delays (all four techniques), and for the thermal deformation. In addition to the VLBI antenna thermal deformation that was discussed herein, all space geodetic techniques are subject to thermal deformation effects, but probably to a lesser extent; geodetic monuments and the surrounding bedrock thereof expand and contract due to temperature changes, as well as changes in the incoming solar radiation (e.g., Haas et al., 2013). To do so, an approach was proposed involving a maximal likelihood estimator and data from the model levels of an accurate NWM. It was found that meteorological parameters extracted from the surface field should not be used in the analysis of space geodetic observations because of the limited representativeness of state-of-the-art NWMs. The proposed method to obtain pressure, temperature, and relative humidity was successful, because the differences of the meteorological parameter series with respect to in situ observations, as well as several NWMs are typically without a bias. Therefore, it is concluded that in the absence of reliable in situ measurements, meteorological data rigorously extracted from the model levels of state-of-the-art NWMs should be used instead of empirical models such as GFZ-PT as they can capture synoptic scale weather events that closed form models will be limited to do.

A series of mapping functions were developed in this work. The Potsdam mapping functions (project initiated by F. Zus), the Berlin mapping functions, and GFZ-PT are some of the developments done in this work. It was found that under severe weather events, the linear approximation of the azimuthal delay variations does not hold, in particular for the non-hydrostatic delay component. To this end, non-linear terms were included in the atmospheric asymmetry ansatz. The precision of the result is such that employing ray-traced delays in lieu of PMF together with 2nd order gradient components yields differences below the noise floor provided by the NWM. Site-dependent gradient mapping function coefficients were estimated for an equiangular grid of 1°, from a "global" solution of almost four decades of ERA Interim data. Employing these gradient mapping function coefficients instead of a constant improves the precision of the

analytical form, only marginally. Furthermore, spurious features (artificial asymmetries in e.g., Mariana Trench) discernible in the gradient component fields provided from Vienna (e.g., GPT3) are not present in the developments carried out in this work. These artefacts are attributed to the fact that gravity anomalies were consided in the derivation of the position tensor where the refraction index tensor refers to.

A fair part of this work focused on the atmospheric ties. Regarding the inter-technique comparison of mapping functions, an important result is that given a direction (elevation and azimuth), the mapping factor for SLR will be smaller than the mapping factors for VLBI and GNSS, which will be smaller than the mapping factors for DORIS. DORIS-tailored mapping functions differ for VLBI-tailored mapping functions for two reasons: ray-bending and ionosphere. The gradients obtained from the VLBI, GNSS, or DORIS ray-tracing setup may be used interchangeably. Unlike microwave gradients, optical gradients are very smooth, both spatially and temporally as they are marginally affected by water vapour variations. Therefore, scaling microwave gradients to obtain optical gradients is a mistake. Another important result regarding gradient components, both linear and non-linear, is that they decrease in absolute value with increasing height. Regarding the optical mapping functions and gradients, it was found that both mapping factors and gradients decrease with increasing frequency, in an absolute sense. It was proven that both hydrostatic and non-hydrostatic mapping factors depend on the height of the receiver and transmitter, a fact previously ignored.

A number of developments was suggested to improve the quality of atmospheric, non-tidal oceanic and hydrological loading displacements. Some of the most important is the use of mass anomaly fields for an orography that is more finely resolved than the one provided by the NWM of choice, by rigorously extracting the relevant parameters from the model levels of NWMs. Alternating the Earth model based on which the load Love numbers are calculated has a marginal effect on atmospheric loading. However, the isomorphic reference frame based on which the loading displacements are computed has a very large impact, displacing stations up to 5 mm depending on whether the center of mass or the center of figure is considered (degree-one surface load coefficients). The inverse barometer assumption was slightly modified, so that it is applied to individual large basins such as the Caspian Sea. The differences with respect to applying the inverse barometer assumption only to the global ocean were below the accuracy of the mass anomaly fields. From all modelling options, the ocean response to atmospheric forcing is the most impactful, especially for stations with close proximity to the ocean. The difference between adopting the inverse barometer hypothesis and assuming a dynamic atmospheric response exceeds e.g., 5 mm for Onsala. Assuming a dynamic atmospheric response, thus considering wind effects in addition to barometric pressure variations, in the calculation of atmospheric pressure loading, is identical to the sum of atmospheric and non-tidal ocean loading. Hydrological loading was simulated based on — among else — mass anomaly fields from ERA5, GLDAS, WaterGAP, and GRACE data. The loading displacements are starkly different. One of the main reasons identified is the simulation of groundwater, which in models such as ERA5 does not take place whatsoever at the time of writing. Moreover, some suggestions were made to render the computationally heavy global convolution more efficient, without loss of accuracy, when the computation of geophysical loading displacements over the entire globe is sought.

Two empirical models were derived in this thesis: GFZ-PT and EGLM. Given the station coordinates, the observing frequency, and the orbital altitude, GFZ-PT returns a number of parameters relevant for the computation of atmospheric refraction corrections (e.g., mapping function coefficients, gradients components of 1st and 2nd order, zenith delays), as well as other meteorological parameters (pressure, temperature, relative humidity, water vapour-weighted mean temperature, and integrated water vapour). GFZ-PT features robustly estimated linear rates as

well as annual, semi-annual, ter-annual, diurnal, semi-diurnal, and ter-diurnal harmonics for all parameters. GFZ-PT is driven from ERA Interim (low frequencies) and ERA5 (high frequencies) data. Given a location and an epoch, EGLM returns displacements due to non-tidal atmospheric loading, non-tidal ocean loading, and continental water storage loading, in a topocentric system. Unlike GFZ-PT, EGLM does not feature high-frequency displacements, but only harmonics at the annual, semi-annual, ter-annual, and 5-year mark. EGLM also provides a linear trend that may or may not be true, despite being precise. EGLM was forced from 39 years of equiangular 0.5° displacement fields from GFZ Sec. 1.3 (R. Dill and H. Dobslaw), that are consistently derived. Furthermore, EGLM provides the two-sample Allan standard deviation that characterizes the noise of the post-fit residuals, and is very useful for terrestrial reference frame estimation with a Kalman filter. Both are grid- and station-based (for efficiency) and have been tested successfully in VLBI data analysis with VieVS@GFZ. Unquestionably, if access to the discrete series of coefficients is granted (PMF and GFZ loading displacements), they should be preferred over these analytical models. However, both GFZ-PT and EGLM are reliable backup models.

All meteorological records of VLBI and SLR observations that were found online were homogenized based on rigorously extracted meteorological series from ERA Interim. Consistent offsets, jumps, and drifts were detected in the vast majority of stations, and were corrected. The homogenized meteorological series were applied to the adjustment of real group delays (VieVS@GFZ), and laser ranges to LAGEOS-1, and -2 (using EPOS-OC, by R. König, GFZ Sec. 1.2). Utilizing homogenized data in VLBI data analysis, reduces the scatter of the height time series as well as the baseline lengths (baseline length repeatability), and ensures the estimated zenith non-hydrostatic delays are physically meaningful (no negative values, and better agreement of the long-term trends thereof with trends from co-located GNSS stations and NWMs). As far as the analysis of real SLR data is concerned, it is work under progress together with R. König; an excerpt of this work is that a pressure bias detected at Wettzell is responsible for discrepancies in the velocity vector of the station.

Some mapping function developments were applied in the analysis of VLBI and SLR data analysis. Due to the fact that VLBI observes targets at much lower elevation angles than SLR, treating mapping function imperfections is more important in VLBI data analysis. This feature of SLR observation geometry renders employing ray-traced delays in lieu of mapping functions with linear and non-linear gradient components not necessary. The analysis with VieVS@GFZ provides proof that PMF yields improvements in terms of baseline length repeatability with respect to the IERS standard VMF1. In SLR analysis, so long as the temperature inserted in the IERS standard FCULa mapping function is adequately accurate, no statistically significant differences are discernible in the geodetic results. The last statement was confirmed also by R. König and K. Sośnica[1] (Bernese v5.3) who validated the optical PMF computed in the framework of this thesis. However, an improvement is found when a priori PMF gradients are supplied in SLR data analysis and residual gradient components are estimated in terms of Earth rotation — reduction of bias with respect to VLBI and GNSS.

According to pressure and cloud fraction fields from ERA5 and MODIS, the at first intuitive that thick cloud cover is related with low pressure, does not hold, in general. Studying the correlation between non-tidal atmospheric loading displacements (developed herein as well as from other established providers) and cloud cover fields, both from ERA5, reveals no clear linear correlation, thus suggesting that the Blue-Sky effect is not solely responsible for the scale discrepancies between the weather-dependent SLR and the all-weather (mostly) VLBI. According to the results presented herein, the scale bias induced by the weather-dependence of SLR, is no

[1]Wrocław University of Environmental and Life Sciences

larger than 1 mm, on average. However, there is another atmospheric effect that is not considered in the analysis of laser ranges: atmospheric asymmetry. According to the results obtained in this work, neglecting to model atmospheric gradients in SLR analysis or even to set them up as unknowns in the least-squares adjustment, induces a virtual polewards motion of all stations as large as 4 mm, thus introducing a scale bias in the implied reference frame at least 1.5 mm. This can be explained by the fact that the atmosphere is on average thicker at the equator, given an elevation angle the atmospheric delay of ranges towards the nearest pole will be slighly smaller than the corresponding delay towards the equator; this effect is not considered when utilizing symmetric (over azimuth) mapping functions. To circumvent such spurious effects, either a priori gradients should be supplied, or gradient components should be estimated based on the laser ranges themselves. However, the sparsity or SLR normal points especially under cloudy conditions impedes the latter, therefore optical gradients may be estimated at daily intervals or longer, as they do not exhibit the rapid fluctuations microwave gradients do. Utilizing meteorological data from uncalibrated sensors (or sensors for which there is no information regarding the relative position thereof with respect to the reference point of the laser telescope) induces biases in the height component that are proportional to the size of the bias. Therefore, either the quality of meteorological data (mainly barometric pressure) should be checked, or station-dependent residual zenith atmospheric delays be estimated in the SLR adjustment. Moreover, neglecting to model displacements due to non-tidal loading and atmospheric asymmetry induces spurious geocenter motion as large as 2 mm predominantly along the Z-axis, due to the uneven interhemispheric distribution of the SLR station network, which is imperative to avoide for the definition of the origin of modern TRFs stems solely from SLR. Therefore, it is recommended that at least non-tidal atmospheric pressure loading be applied at the observation equation or normal equation level, and that gradients are either estimated from the laser ranges themselves or be introduced a priori from ray-tracing.

Currently the mapping functions used for the analysis of DORIS observations are calculated on a setup tailored for VLBI. However, owing to the fact that all satellites that comprise the DORIS system orbit fairly low (below 1400 km), the ray-bending effects are much smaller than for VLBI and GNSS. Failing to account for these discrepancies, inexorably results in a height bias at the level of 2 mm, which in turn induces issues in the datum definition in that there is an offset in the implied origin (1.5 mm), the rotation, as well as the scale (2.2 mm). The discrepancies in the datum perturbation parameters other than the network scale are manifestations of the imperfect station network and the imbalance between the number of observations with latitude stemming from the orbits' characteristics. Ergo, if stations are simulated in e.g., a reduced Gaussian grid, and the experiment carried out herein is repeated (change between mapping funtions for VLBI and DORIS), only a scale bias will be visible. Regarding the ray-bending, the same applies for laser observations to LEOs, but on account of the fact that SLR typically is not allowed to observe below 10°, mapping function errors are not as devastating as for the microwave techniques.

IWV trends from the analysis of decade-long real data of VLBI and GPS have been robustly estimated and compared with ERA Interim (Balidakis et al., 2018c). Motivated from the lack of a reference based on which IWV quality may be evaluated, VLBI and GNSS observations were simulated based on ray-traced delays. The results indicate that employing erroneous meteorological data to calculate the a priori zenith delay can be compensated almost completely following the approach suggested in Balidakis et al. (2018c). However, the influence of erroneous mapping functions cannot be removed neither from the estimated station coordinates, nor from the derived IWV series and the trends thereof. It was also found that the varying observation geometry of VLBI at stations located in the Southern Hemisphere (mainly) is devastating for the quality of the estimated gradient component trends. On the grounds that the atmospheric gra-

dient components are correlated with the corrections in the lateral coordinate component, these spurious gradient trends are also indicative of impurities in the estimated station velocities.

From all the non-tidal geophysical loading models developed in this work, only the results of two being applied at the observation level were shown herein: The "discrete" model is the sum of non-tidal atmospheric loading forced from ERA5, non-tidal ocean loading forced from Mog2D-G, and continental water storage loading from ERA5. The other model was EGLM. It was shown that in almost all cases the repeatability of the height series, as well as the harmonic response of the station coordinates at the main seasonal frequencies was improved. An interesting feature that was found was that some co-located VLBI stations (e.g., at Hobart and at Hartebeesthoek) experience largely different harmonic motion. The scale series estimated from a 7-parameter Helmert transformation between applying or not non-tidal loading at the observation equation level in VLBI data analysis have a WRMS around 3 mm.

Non-tidal loading displacements were also applied (in different combinations of NTAL, NTOL, and CWSL) at the parameter level (directly at the station coordinates) to the contributions of IVS, ILRS, IGS, and IDS. On average, the S_a amplitude as well as the WRMS of the post-fit residuals from a least-squares harmonic fit on these time series, improves on average for all combinations, for all techniques except for VLBI. The success of the non-tidal models varies considerably across the techniques, a fact that indicates that the seasonal variations in the time series of the services' contribution to ITRF2014 are a manifestation of other unmodeled effects, in addition to non-tidal loading, such as thermal bedrock expansion and antenna thermal deformation (for VLBI). Afterwards, 7-parameter Helmert transformations were performed between the original series, and those obtained after applying the loading models developed herein. The results support that the technique whose network is mostly affected by neglecting non-tidal loading displacements is VLBI, and the one that is least affected is DORIS. Of course this is expected as the VLBI station network typically consists of no more than twelve stations and the coordinates are estimated on 24-hour basis, whereas in DORIS the station network typically consists of no less than 45 stations and the data thereof are used to produce weekly solutions. Combining VLBI sessions into weekly "global" solutions also reduces the impact of loading effects on the implied TRF. The harmonic coefficients of the Helmert transformation parameter series from the different models and the different techniques were estimated and intercompared. In addition to differences in the amplitude, differences in the phase of the related signals were also detected, especially in T_Z which is related to the degree-one surface deformation. These discrepancies are mainly attributed to the network geometry.

The results obtained from the VLBI analysis performed in this work provide proof that EOPs are marginally affected by geophysical loading. This was confirmed by analyzing non-intensive sessions and Intensive sessions. It was hoped that due to the fact that station coordinates are not estimated in the analysis of Intensive sessions, the modelling error will propagate in the dUT1 estimation. It was found that due to the fact that non-tidal loading variation within the course of an Intensive (one hour) are like a baseline offset, the largest part of the loading signal is absorbed by the constant baseline clock term. The differences in all EOP (relative errors) are well below the accuracy capabilities of the modern VLBI system. However, these differences will become relevant in the framework of VGOS. Employing erroneous a priori zenith delays poses a far greater concern as inhomogeneous meteorological observations induce spurious variations of 50 µs in the components of the terrestrial and celestial pole.

8.2.1 Recommendations to relevant IAG services

The results obtained in this thesis can contribute to significant improvements in the analysis of space geodetic techniques. In the following, the author provides a final wrap-up leading to recommendations to the IAG services involved in the realization of the Global Geodetic Reference System.

International DORIS Service (IDS). If observations at elevations below 7° are to be utilized, mapping functions tailored for VLBI may not be applied (e.g., Niell mapping function, or VMF3), as this oversight potentially induces large height- and eventually scale-related biases that depend on the average orbital altitude. Satellite-specific mapping functions should be preferred instead, or an orbital altitude correction scheme be adopted. While performing ray-tracing to derive the related atmospheric delay corrections, the contribution of the ionosphere to the refraction index should be accounted. As the low frequencies employed by the DORIS system render the ray-trajectory deviations (including or not the influence of the ionosphere) non-negligible, they induce artificial features coherent mainly with electron density aloft each site. Non-tidal geophysical loading models should be applied at the observation equation level, because they reduce the amplitude of seasonal harmonics of station position vectors, as well as the time series scatter thereof. However, caution should be exercised so that consistent models for station-specific (loading displacement) and satellite-specific (the so-called atmosphere and ocean de-aliasing products) corrections are applied. Moreover, since the estimation of atmospheric delay gradients is not feasible under poor observation geometry, in such cases gradients derived from a ray-tracing procedure similar to the one described above should be used instead. That is, tight absolute constraints may be imposed with respect to gradients from ray-tracing in accurate NWMs.

International GNSS Service (IGS). A considerable number of GNSS stations are equipped with meteorological sensors whose data are not employed as of yet. Upon calibration, in situ meteorological data should be used in geodetic data analysis. If not available or found unsuitable, meteorological data from weather models should be used instead. For real-time applications data from high-resolution weather forecasts should be preferred in the absence of reliable in situ meteorological data. In all cases, the use of empirical models should be avoided as they are by definition inferior to weather model data. So long as low-elevation observations are heavily down-weighed, advances in the quality of mapping functions and gradients will not affect the geodetic results considerable. Therefore, as no statistically significant difference between a VLBI- and a GNSS-tailored mapping function is to be expected, under these circumstances VLBI-tailored mapping functions may continue to be used. For GNSS meteorology applications, the water vapor-weighted mean temperature should be derived from state-of-the-art weather model 3D fields instead of regression formulas employing surface temperature. Non-tidal geophysical loading models should be applied to reduce GNSS observations because by doing so seasonal amplitudes and scatter are reduced. Due to the large number of instrumental changes (in comparison to the other geodetic techniques mentioned in this section), applying non-tidal loading models will facilitate the detection of breakpoints and reduce the required observing time (typically three years) to obtain a reliable tectonic velocity. Moreover, so long as Keplerian elements of the related satellite orbits are typically pre-eliminated and are thus not included in the related `SINEX` files, it is not possible to account for the impact of non-tidal loading on satellite orbits at any stage later than the observation equations. Therefore, if the application of non-tidal loading to satellite-based techniques is intended, it should be carried out at the observation equation level.

International Laser Ranging Service (ILRS). In SLR/LLR data analysis, no atmospheric

delay parameters are usually estimated, which implies that modelling shortcomings propagate to other parameters, mainly the station coordinates, as well as other parameters such as the range biases. Since it is difficult to estimate gradients from the laser observations, it is recommended to use a priori gradients from weather models as by doing so a lateral station coordinate bias pointing opposite from the average atmospheric gradient vector is avoided, as well as an artificial bias in the SLR scale and Z-component translation. The application of gradients is encouraged in LLR as there is a very limited elevation-azimuth range for all possible lunar targets (`apollo11`, `apollo14`, `apollo15`, `luna17`, and `luna21`), thus introducing spurious biases. The meteorological sensors in all SLR stations should be homogenized as erroneous pressure records result in height and velocity biases. As no laser observations are carried out at low elevation angles, SLR will probably not benefit appreciably from more accurate mapping functions. In the current setting (no low elevation observations and no estimation of residual atmospheric delays), mapping function separation to hydrostatic and non-hydrostatic (or dry and wet) is unnecessary. The application of non-tidal loading models improves SLR coordinate solutions, as the Blue-Sky effect is treated, thus is recommended. In simulation studies for new SLR observatories, the time-dependent 3D cloud cover (or at least site-specific long-term average) should be considered as otherwise conclusions will be unrealistic and unreliable.

International VLBI Service for Geodesy and Astrometry (IVS). As the VLBI archive includes a considerable number of low elevation observations, VLBI probably benefits the most from advanced mapping functions, and is also susceptible to elevation-dependent modelling errors (e.g., gravitational and thermal deformation of radio telescopes). A consensus should be reached on the use of meteorological data as the IVS meteorological database is rife with inhomogeneities (mainly jumps and outliers). If not, data from weather models should be used instead, as there is no considerable difference because of the high quality of the state-of-the-art weather models. Due to the fact that the observation geometry in sessions where the station network is limited (e.g., Intensives, regional, K-band, and early era), employing a priori gradients from ray-tracing in weather models should be considered in lieu of estimating gradients from the group delays. While the application of non-tidal atmospheric pressure loading is accepted in the VLBI community, strides should be made towards accounting for displacements induced by mass variations of the entire fluid envelope, that is including oceans and continental hydrology. Applying or not non-tidal loading models affects the estimation of Earth orientation parameters; however, the induced differences are not statistically significant for the present-day system, they will be for VGOS, thus non-tidal loading should be accounted at the observation equation level, and not as late as the parameter level.

Meteorological data. It is recommended to utilize in situ meteorological observations provided (i) sensors are calibrated, and (ii) the relative position between the reference points of the meteorological sensor and the geodetic instrument is known at all times and taken into account. If there is either no co-located meteorological sensor, or the sensor is not calibrated, or the vector between meteorological sensor and geodetic instrument is not known to the cm-level, meteorological data from the model (or pressure) levels of state-of-the-art high spatio-temporal resolution NWMs (e.g., ERA5 and MERRA2) may be applied instead. For time-critical applications, high-resolution, short-term weather forecasts (e.g., GFS) should be preferred over empirical models (e.g., GPT3 or GFZ-PT), as the latter cannot capture synoptic weather changes. The author maintains a database of homogenized meteorological data (pressure, temperature, humidity) necessary for geodetic processing for the geodetic VLBI, GNSS, SLR, and DORIS systems. For sites without a meteorological sensor, the database contains meteorological data rigorously extracted from the model levels of ERA5.

8.3 Future research

Provided solid theoretical background, atmospheric refraction and geophysical loading models can only be as good as the underlying NWMs. Since the models derived herein are precise, the related corrections will only get better, so long as the related NWMs become more accurate.

A consistent pressure bias (2 hPa) was detected in all stations that comprize the VLBA. It would be illuminating to assess its influence on parameters that are derived simultaneously for other VLBI networks, such as in CONT17.

Reduced ray-bending with decreasing orbital altitude could have implications to differential VLBI (D-VLBI) in the scenario that the observing schedule suggests alternating observations between low Earth orbiting satellites and quasars (e.g., Anderson et al., 2018). The results acquired from the DORIS simulations justify an assessment. Similar to DORIS, the modelling errors will contaminate other parameters in addition to the stations' height due to imperfect observation geometry.

In some cases (large non-linear atmospheric refraction asymmetries), a fixed term in the gradient mapping function expansion does not capture correctly the elevation dependence of the asymmetric delay. A remedy to that is the estimation of a station- and time-dependent coefficient, as was already presented in this work. However, due to the fact that the gradient components are very much correlated with the value of this coefficient, the time series of the gradient components are inhomogeneous, and in addition comparisons between different sites become a fairly intricate problem. To this end, further investigations towards a scientifically sound and at the same time efficient solution will be carried out.

At the time of writing, the fully fledged PMF (including non-linear azimuthal variations) driven from ECMWF operational analysis (IFS-Cy45r1, 9 km) is the standard component of the VLBI analysis software VieVS@GFZ, for operational purposes, and a PMF derived from ERA5 data may be used for reprocessing projects. Due to the fact that the online detection of inhomogeneities is extremely difficult as the expected offsets are usually smaller than the scatter of the differences between in situ measurements and data rigorously extracted from state-of-the-art NWMs, the concept of total mapping functions will be explored driven from hourly data (or even sub-hourly from an own run with the Weather Research and Forecasting model, WRF). When total mapping functions are considered a single site-and-weather-dependent obliquity factor is used to project both hydrostatic and non-hydrostatic zenith delays to the direction of each observation; thus, any relatively small errors in the a priori delays should be completely absorbed by the residual tropospheric parameter estimates. The proof of that concept is provided in the analysis of simulated SLR data with a bias.

While small-scale loads unresolvable by GRACE/GRACE-FO can be obtained from mass anomalies from NWMs, most state-of-the-art NWMs provide information only up to the depth of 3 m, which may be obtained by GRACE data. Therefore, the accuracy of loading displacements would increase with the assimilation of GRACE and GRACE-FO data into hydrological models (e.g., Karegar et al., 2018), which is still at an experimental phase. An issue where recently light was cast upon is the proper georeferencing of water mass that lies within river channels that is partly skewed due to the finite representativeness or the underlying models (Dill et al., 2018). Addressing this issue would definitely improve the fidelity of the simulated continental water storage loading displacements. Moreover, phase differences between the ITRF2014 time series analyzed and non-tidal deformation suggest that a purely elastic Earth model might not be a sound approximation due to spatial variations of the upper-mantle rheology. Therefore, performing the global convolution sum utilizing load Love numbers for an anisotropic viscoelastic Earth model (e.g., Pagiatakis, 1990) might be capable of producing non-tidal models with a better

agreement to the observed station position variations.

In the framework of VGOS, to achieve the coveted increase in the number of observations by an order of magnitude, the VLBI scan duration will be considerably shorter compared to what is carried out heretofore. This aspect will inescapably highlight the impact of atmospheric turbulence on the related observations. Coupled with the smaller SNR mainly due to the smaller size of the observing radio telescopes, VLBI data analysis would benefit from a proper treatment of the stochastic variability of the measurements. It is intended that the experience obtained during this work dealing with atmospheric refraction put to use for the derivation of site- and time-dependent atmospheric turbulence parameters.

A review of the deterministic model of space geodetic techniques that rely on clock stability reveals that the current way of estimating clock parameters is responsible for on the one hand absorbing portion of unmodeled station-dependent biases, but on the other hand masking important information about the station movement and the water vapour distribution aloft the stations, among else. The fact that the nominal active Hydrogen maser stability and the high-frequency clock function variations differ considerably in the vast majority of stations prompt further investigations in this direction.

It has been shown that not properly accounting for geophysical loading, azimuthal atmospheric asymmetries, and the zenith delay are capable of inducing a scale bias in SLR data analysis. However, these effects cannot explain the 1.374 ppb bias in ITRF2014. Other elevation dependent effects in VLBI may stem from the gravitational deformation (e.g., Nothnagel et al., 2019; Lösler et al., 2019), for which no treatment is applied in most stations whatsoever, so far.

Bibliography

Abbondanza, C., Chin, T. M., Gross, R. S., Heflin, M. B., Parker, J. W., Soja, B. S., van Dam, T., and Wu, X. (2017). JTRF2014, the JPL Kalman filter and smoother realization of the International Terrestrial Reference System. *J. Geophys. Res.*, 122(10):8474–8510.

Alexandersson, H. (1986). A homogeneity test applied to precipitation data. *J. Climatol.*, 6(6):661–675.

Alizadeh, M. M., Wijaya, D. D., Hobiger, T., Weber, R., and Schuh, H. (2013). *Ionospheric Effects on Microwave Signals*, pages 35–71. Springer Berlin Heidelberg, Berlin, Heidelberg.

Alshawaf, F., Balidakis, K., Dick, G., Heise, S., and Wickert, J. (2017). Estimating trends in atmospheric water vapor and temperature time series over Germany. *Atmos. Meas. Tech.*, 10(9):3117–3132.

Alshawaf, F., Zus, F., Balidakis, K., Deng, Z., Hoseini, M., Dick, G., and Wickert, J. (2018). On the Statistical Significance of Climatic Trends Estimated From GPS Tropospheric Time Series. *J. Geophys. Res.*, 123(19):10,967–10,990.

Altamimi, Z., Rebischung, P., Métivier, L., and Collilieux, X. (2016). ITRF2014: A new release of the International Terrestrial Reference Frame modeling nonlinear station motions. *J. Geophys. Res.*, 121(8):6109–6131. 2016JB013098.

Amante, C. and Eakins, B. (2009). ETOPO1 1 Arc-Minute Global Relief Model: Procedures, Data Sources and Analysis. *Technical Memorandum NESDIS NGDC-24. National Geophysical Data Center, NOAA.*

Anderson, J. M., Beyerle, G., Glaser, S., Liu, L., Männel, B., Nilsson, T., Heinkelmann, R., and Schuh, H. (2018). Simulations of VLBI observations of a geodetic satellite providing co-location in space. *J. Geod.*, 92(9):1023–1046.

Anderson, J. M. and Xu, M. H. (2018). Source Structure and Measurement Noise Are as Important as All Other Residual Sources in Geodetic VLBI Combined. *J. Geophys. Res.*, 123(11):10,162–10,190.

Aparicio, J. M., Deblonde, G., Garand, L., and Laroche, S. (2009). Signature of the atmospheric compressibility factor in COSMIC, CHAMP, and GRACE radio occultation data. *J. Geophys. Res.*, 114(D16). D16114.

Aparicio, J. M. and Laroche, S. (2011). An evaluation of the expression of the atmospheric refractivity for GPS signals. *J. Geophys. Res.*, 116(D11). D11104.

Appleby, G., Rodríguez, J., and Altamimi, Z. (2016). Assessment of the accuracy of global geodetic satellite laser ranging observations and estimated impact on ITRF scale: estimation of systematic errors in LAGEOS observations 1993–2014. *J. Geod.*, 90(12):1371–1388.

Arabelos, D. and Tziavos, I. (2007). *Introduction to the Gravity Field of the Earth.* Editions ZITI.

Askne, J. and Nordius, H. (1987). Estimation of tropospheric delay for microwaves from surface weather data. *Radio Sci.*, 22(3):379–386.

Bachmann, S., Thaller, D., Roggenbuck, O., Lösler, M., and Messerschmitt, L. (2016). IVS contribution to ITRF2014. *J. Geod.*, 90(7):631–654.

Balidakis, K., Dobslaw, H., Glaser, S., Dill, R., Nilsson, T., and Schuh, H. (submitted 2019). Impact of Non-Tidal Loading on dUT1 Estimates from VLBI Intensive Sessions. *J. Geod.*

Balidakis, K., Glaser, S., Karbon, M., Soja, B., Nilsson, T., Lu, C., Anderson, J., Liu, L., Mora-Diaz, J., Raposo-Pulido, V., Xu, M., Heinkelmann, R., and Schuh, H. (2015a). The effect of meteorological data on atmospheric pressure loading corrections in VLBI data analysis. Geophys. Res. Abstr. Vol. 17, EGU2015-993, EGU General Assembly 2015.

Balidakis, K., Glaser, S., Zus, F., Nilsson, T., and Schuh, H. (2018a). Combination of space geodetic techniques with atmospheric and local ties. A simulation study. Geophys. Res. Abstr. Vol. 21, EGU2019-1509, EGU General Assembly 2019.

Balidakis, K., Glaser, S., Zus, F., and Schuh, H. (2018b). Combination of space geodetic techniques with atmospheric and local ties; a simulation study. Geodätische Woche, Frankfurt.

Balidakis, K., Heinkelmann, R., Lu, C., Soja, B., Karbon, M., Nilsson, T., Glaser, S., Mora-Diaz, J., Anderson, J., Liu, L., Raposo-Pulido, V., Xu, M., and Schuh, H. (2015b). Homogenization of atmospheric pressure time series recorded at VLBI stations using a segmentation LASSO approach. Geophys. Res. Abstr. Vol. 17, EGU2015-979, EGU General Assembly 2015.

Balidakis, K., Heinkelmann, R., Phogat, A., Soja, B., Glaser, S., Nilsson, T., Karbon, M., and Schuh, H. (2016). On the impact of inhomogeneities in meteorological data on VLBI data analysis. In Behrend, D., Baver, K., and Armstrong, K., editors, *Proceedings, 9th IVS General Meeting "New Horizons with VGOS"*, pages 356–360.

Balidakis, K., Nilsson, T., Zus, F., Glaser, S., Heinkelmann, R., Deng, Z., and Schuh, H. (2018c). Estimating integrated water vapour trends from VLBI, GPS and numerical weather models: sensitivity to tropospheric parameterization. *J. Geophys. Res. Atmos.*, 123(12):6356–6372.

Balidakis, K., Zus, F., Glaser, S., Nilsson, T., Alshawaf, F., Dick, G., and Schuh, H. (2018d). How precisely can we monitor climate signals with GNSS and VLBI? A simulation study. Geophys. Res. Abstr. Vol. 20, EGU2018-1477, EGU General Assembly 2018.

Balidakis, K., Zus, F., Glaser, S., Nilsson, T., and Schuh, H. (submitted). Inter- and Intra-technique atmospheric ties for Space Geodesy. *J. Geophys. Res. Atmos.*

Bar-Sever, Y. E., Kroger, P. M., and Borjesson, J. A. (1998). Estimating horizontal gradients of tropospheric path delay with a single GPS receiver. *J. Geophys. Res.*, 103(B3):5019–5035.

Bassiri, S. and Hajj, G. (1993). Higher-order ionospheric effects on the global positioning system observables and means of modeling them. *Man. Geod.*, 18:280–289.

Berrisford, P., Kållberg, P., Kobayashi, S., Dee, D., Uppala, S., Simmons, A. J., Poli, P., and Sato, H. (2011). Atmospheric conservation properties in ERA-Interim. *Q. J. Royal Meteorol. Soc.*, 137(659):1381–1399.

Bertin, K., Collilieux, X., Lebarbier, E., and Meza, C. (2017). Semi-parametric segmentation of multiple series using a DP-Lasso strategy. *J. Stat. Comput. Simul.*, 87(6):1255–1268.

Bevis, M., Brown, A., and Kendrick, E. (2013). Devising stable geometrical reference frames for use in geodetic studies of vertical crustal motion. *J. Geod.*, 87(4):311–321.

Bevis, M., Businger, S., Chiswell, S., Herring, T. A., Anthes, R. A., Rocken, C., and Ware, R. H. (1994). GPS meteorology: Mapping zenith wet delays onto precipitable water. *J. Appl. Meteor.*, 33(3):379–386.

Beyerle, G. (2008). Carrier phase wind-up in GPS reflectometry. *GPS Solut.*, 13(3):191.

Bilitza, D., Altadill, D., Truhlik, V., Shubin, V., Galkin, I., Reinisch, B., and Huang, X. (2017). International Reference Ionosphere 2016: From ionospheric climate to real-time weather predictions. *Space Weather*, 15(2):418–429.

Blewitt, G. (2003). Self-consistency in reference frames, geocenter definition, and surface loading of the solid Earth. *J. Geophys. Res.*, 108(B2):2103.

Blewitt, G., Kreemer, C., Hammond, W. C., and Gazeaux, J. (2016). MIDAS robust trend estimator for accurate GPS station velocities without step detection. *J. Geophys. Res.*, 121(3):2054–2068. 2015JB012552.

Blewitt, G. and Lavallée, D. (2002). Effect of annual signals on geodetic velocity. *J. Geophys. Res.*, 107(B7):ETG 9–1–ETG 9–11.

Blewitt, G., Lavallée, D., Clarke, P., and Nurutdinov, K. (2001). A New Global Mode of Earth Deformation: Seasonal Cycle Detected. *Science*, 294:2342–2345.

Bloßfeld, M., Rudenko, S., Kehm, A., Panafidina, N., Müller, H., Angermann, D., Hugentobler, U., and Seitz, M. (2018). Consistent estimation of geodetic parameters from SLR satellite constellation measurements. *J. Geod.*, 92(9):1003–1021.

Bock, D., Noomen, R., and Scherneck, H.-G. (2005). Atmospheric pressure loading displacement of SLR stations. *J. Geodyn.*, 39:247–266.

Boehm, J., Heinkelmann, R., Mendes Cerveira, P. J., Pany, A., and Schuh, H. (2009). Atmospheric loading corrections at the observation level in VLBI analysis. *J. Geod.*, 83(11):1107.

Boehm, J., Heinkelmann, R., and Schuh, H. (2007). Short note: A global model of pressure and temperature for geodetic applications. *J. Geod.*, 81(10):679–683.

Boehm, J. and Schuh, H. (2004). Vienna mapping functions in VLBI analyses. *Geophys. Res. Lett.*, 31:L01603.

Boehm, J., Werl, B., and Schuh, H. (2006). Troposphere mapping functions for GPS and very long baseline interferometry from European Centre for Medium-Range Weather Forecasts operational analysis data. *J. Geophys. Res.*, 111:B02406.

Böhm, J. (2004). *Troposphärische Laufzeitverzögerungen in der VLBI.* PhD thesis, Vermessung und Geoinformation, Technische Universität Wien, Wien, Österreich. Geowissenschaftliche Mitteilungen 68, 70 pp.

Böhm, J., Böhm, S., Boisits, J., Girdiuk, A., Gruber, J., Hellerschmied, A., Krásná, H., Landskron, D., Madzak, M., Mayer, D., McCallum, J., McCallum, L., Schartner, M., and Teke, K. (2018). Vienna VLBI and Satellite Software (VieVS) for Geodesy and Astrometry. *Publ. Astron. Soc. Pac.*, 130(986):044503.

Böhm, J., Böhm, S., Nilsson, T., Pany, A., Plank, L., Spicakova, H., Teke, K., and Schuh, H. (2011). The New Vienna VLBI Software VieVS. In *Geodesy for Planet Earth*, pages 1007–1011. Springer Berlin Heidelberg.

Böhm, J., Ess, M., and Schuh, H. (2005). Asymmetric mapping functions for CONT02 from ECMWF. *EVGA Working Meetings*, No. 17:64–68.

Böhm, J., Möller, G., Schindelegger, M., Pain, G., and Weber, R. (2015). Development of an improved empirical model for slant delays in the troposphere (GPT2w). *GPS Solut.*, 19(3):433–441.

Böhm, J., Salstein, D., Alizadeh, M. M., and Wijaya, D. D. (2013a). *Geodetic and Atmospheric Background*, pages 1–33. Springer Berlin Heidelberg, Berlin, Heidelberg.

Böhm, J., Urquhart, L., Steigenberger, P., Heinkelmann, R., Nafisi, V., and Schuh, H. (2013b). A priori gradients in the analysis of space geodetic observations. In Altamimi, Z. and Collilieux, X., editors, *Reference Frames for Applications in Geosciences*, pages 105–109, Berlin, Heidelberg. Springer Berlin Heidelberg.

Born, M. and Wolf, E. (1999). *Principles of Optics*. Cambridge University Press, 7 edition.

Boy, J.-P., Gegout, P., and Hinderer, J. (2002). Reduction of surface gravity data from global atmospheric pressure loading. *Geophys. J. Int.*, 149(2):534–545.

Boy, J.-P. and Lyard, F. (2008). High-frequency non-tidal ocean loading effects on surface gravity measurements. *Geophys. J. Int.*, 175(1):35–45.

Brunner, F. K. and Gu, M. (1991). An improved model for the dual frequency ionospheric correction of GPS observations. *Manuscr. Geod.*, 16(3):205–214.

Brunner, F. K. and Rüeger, J. M. (1992). Theory of the local scale parameter method for EDM. *Bull. Geod.*, 66(4):355.

Budden, K. (1985). The propagation of radio waves: The theory of radio waves of low power in the ionosphere and magnetosphere, cambridge univ. *Press, Cambridge, UK.*

Capitaine, N. (2000). Definition of the celestial ephemeris pole and the celestial ephemeris origin. *International Astronomical Union Colloquium*, 180:153–163.

Capitaine, N., Wallace, P. T., and McCarthy, D. D. (2003). Expressions to implement the IAU 2000 definition of UT1. *A&A*, 406(3):1135–1149.

Carrère, L. and Lyard, F. (2003). Modeling the barotropic response of the global ocean to atmospheric wind and pressure forcing - comparisons with observations. *Geophys. Res. Lett.*, 30(6):n/a–n/a. 1275.

Chaffee, J. W. (1987). Relating the Allan Variance to the Diffusion Coefficients of a Linear Stochastic Differential Equation Model for Precision Oscillators. In *41st Annual Symposium on Frequency Control*, pages 112–115.

Chambers, D. P. and Bonin, J. A. (2012). Evaluation of Release-05 GRACE time-variable gravity coefficients over the ocean. *Ocean Sci.*, 8(5):859–868.

Chapman, S. and Lindzen, R. S. (1969). *Atmospheric Tides*. Springer Netherlands.

Charlot, P. (1990). Radio-source structure in astrometric and geodetic very long baseline interferometry. *Astron. J.*, 99.

Chen, G. and Herring, T. A. (1997). Effects of atmospheric azimuthal asymmetry on the analysis of space geodetic data. *J. Geophys. Res.*, 102(B9):20489–20502.

Ciddor, P. (1996). Refractive index of air: new equations for the visible and near infrared. *Appl. Opt.*, 35(9):1566–1573.

Ciddor, P. and Hill, R. (1999). Refractive Index of Air. 2. Group Index. *Appl. Opt.*, 38(9):1663–1667.

Clarke, P. J., Lavallée, D. A., Blewitt, G., van Dam, T. M., and Wahr, J. M. (2005). Effect of gravitational consistency and mass conservation on seasonal surface mass loading models. *Geophys. Res. Lett.*, 32(8). L08306.

Combrinck, L. (2010). *Sciences of Geodesy – I*, chapter Satellite Laser Ranging, pages 301–338. Springer Berlin Heidelberg.

Corey, B. (2012). Calibration systems: noise, phase, and cable. IVS VLBI2010 Workshop on Technical Specifications, Bad Kötzting/Wettzell (Germany).

Dach, R., Böhm, J., Lutz, S., Steigenberger, P., and Beutler, G. (2011). Evaluation of the impact of atmospheric pressure loading modeling on GNSS data analysis. *J. Geod.*, 85(2):75–91.

Dach, R., Lutz, S., Walser, P., and Fridez, P., editors (2015). *Bernese GNSS Software Version 5.2.* Astronomical Institute, University of Bern, Switzerland.

Davis, J. L., Elgered, G., Niell, A. E., and Kuehn, C. E. (1993). Ground-based measurement of gradients in the "wet" radio refractivity of air. *Radio Sci.*, 28(6):1003–1018.

Degnan, J. J. (2013). *Millimeter Accuracy Satellite Laser Ranging: a Review*, pages 133–162. American Geophysical Union (AGU).

Deng, Z., Fritsche, M., Nischan, T., and Bradke, M. (2016). Multi-GNSS Ultra Rapid Orbit-, Clock- & EOP-Product Series. *GFZ Data Services.*

Dermanis, A. (2004). The rank deficiency in estimation theory and the definition of reference systems. In Sansò, F., editor, *V Hotine-Marussi Symposium on Mathematical Geodesy*, pages 145–156, Berlin, Heidelberg. Springer Berlin Heidelberg.

Dermanis, D. (1987). *Adjustment of Observations and Estimation Theory, Volume 2.* Editions ZITI.

Dill, R. (2008). *Hydrological model LSDM for operational Earth rotation and gravity field variations.* Deutsches GeoForschungsZentrum. Scientific Technical Report STR 08/09.

Dill, R. and Dobslaw, H. (2013). Numerical simulations of global-scale high-resolution hydrological crustal deformations. *J. Geophys. Res.*, 118(9):5008–5017.

Dill, R., Klemann, V., and Dobslaw, H. (2018). Relocation of river storage from global hydrological models to geo-referenced river channels for improved load-induced surface displacements. *J. Geophys. Res.*, 123(8):7151–7164.

Dill, R., Klemann, V., Martinec, Z., and Tesauro, M. (2015). Applying local green's functions to study the influence of the crustal structure on hydrological loading displacements. *J. Geodyn.*, 88(Supplement C):14 – 22.

Dobslaw, H. (2016). Homogenizing surface pressure time-series from operational numerical weather prediction models for geodetic applications. *J Geod Scie*, 6(1).

Dobslaw, H., Bergmann-Wolf, I., Dill, R., Poropat, L., and Flechtner, F. (2017a). Product Description Document for AOD1B Release 06, Rev. 6.1. [Available at ftp://isdcftp.gfz-potsdam.de/grace/DOCUMENTS/Level-1/].

Dobslaw, H., Bergmann-Wolf, I., Dill, R., Poropat, L., Thomas, M., Dahle, C., Esselborn, S., Kö nig, R., and Flechtner, F. (2017b). A new high-resolution model of non-tidal atmosphere and ocean mass variability for de-aliasing of satellite gravity observations: AOD1B RL06. *Geophys J Int*, 211(1):263–269.

Dobslaw, H., Dill, R., Grötzsch, A., Brzeziński, A., and Thomas, M. (2010). Seasonal polar motion excitation from numerical models of atmosphere, ocean, and continental hydrosphere. *J. Geophys. Res. Solid Earth*, 115(B10).

Dobslaw, H., Flechtner, F., Bergmann-Wolf, I., Dahle, C., Dill, R., Esselborn, S., Sasgen, I., and Thomas, M. (2013). Simulating high-frequency atmosphere-ocean mass variability for dealiasing of satellite gravity observations: AOD1B RL05. *J. Geophys. Res. Oceans*, 118(7):3704–3711.

Dobslaw, H. and Thomas, M. (2007). Simulation and observation of global ocean mass anomalies. *J. Geophys. Res. Oceans*, 112(C5). C05040.

Döll, P., Müller, S. H., Schuh, C., Portmann, F. T., and Eicker, A. (2014). Global scale assessment of groundwater depletion and related groundwater abstractions: Combining hydrological modeling with information from well observations and GRACE satellites. *Water Resour. Res.*, 50(7):5698–5720.

Doodson, A. T. (1921). The Harmonic Development of the Tide-Generating Potential. *Proceedings of the Royal Society of London. Series A, Containing Papers of a Mathematical and Physical Character*, 100(704):305–329.

Drożdżewski, M. and Sośnica, K. (2018). Satellite laser ranging as a tool for the recovery of tropospheric gradients. *Atmospheric Res.*, 212:33 – 42.

Drożdżewski, M., Sośnica, K., Zus, F., and Balidakis, K. (2019). Troposphere delay modeling with horizontal gradients for satellite laser ranging. *J. Geod.*

Dziewonski, A. and Anderson, D. (1981). Preliminary reference Earth model. *Phys. Earth Plan. Int.*, 25(4):297–356.

ECMWF (2016). *IFS Documentation CY43R3.* ECMWF. Operational implementation: 11 July 2017.

ECMWF (2017). *Part II: Data Assimilation.* IFS Documentation. ECMWF.

ECMWF (2017). *Part III: Dynamics and Numerical Procedures.* IFS Documentation. ECMWF.

Eriksson, D. and MacMillan, D. S. (2014). Continental hydrology loading observed by VLBI measurements. *J. Geod.*, 88(7):675–690.

Eriksson, D., MacMillan, D. S., and Gipson, J. M. (2014). Tropospheric delay ray tracing applied in VLBI analysis. *J. Geophys. Res. Solid Earth*, 119(12):9156–9170.

Exertier, P., Belli, A., Samain, E., Meng, W., Zhang, H., Tang, K., Schlicht, A., Schreiber, U., Hugentobler, U., Procházka, I., Sun, X., McGarry, J. F., Mao, D., and Neumann, A. (2018). Time and laser ranging: a window of opportunity for geodesy, navigation, and metrology. *J. Geod.*

Farrell, W. (1972). Deformation of the Earth by Surface Loads. *Rev. Geophys. Space Phys.*, 10(3):761–797.

Fey, A. L., Gordon, D., Jacobs, C. S., Ma, C., Gaume, R. A., Arias, E. F., Bianco, G., Boboltz, D. A., Böckmann, S., Bolotin, S., Charlot, P., Collioud, A., Engelhardt, G., Gipson, J., Gontier, A.-M., Heinkelmann, R., Kurdubov, S., Lambert, S., Lytvyn, S., MacMillan, D. S., Malkin, Z., Nothnagel, A., Ojha, R., Skurikhina, E., Sokolova, J., Souchay, J., Sovers, O. J., Tesmer, V., Titov, O., Wang, G., and Zharov, V. (2015). The second realization of the international celestial reference frame by very long baseline interferometry. *Astron. J.*, 150(2):58.

Foelsche, U. (1999). *Tropospheric water vapor imaging by combination of ground-based and spaceborne GNSS sounding data.* PhD thesis. Wissenschaftlicher Bericht No. 10, 164 pp, Institut für Meteorologie und Geophysik, Karl-Franzens-Universität Graz, Austria.

Förste, C., Bruinsma, S., Abrikosov, O., Lemoine, J.-M., Marty, J. C., Flechtner, F., Balmino, G., Barthelmes, F., and Biancale, R. (2014). EIGEN-6C4 the latest combined global gravity field model including GOCE data up to degree and order 2190 of GFZ Potsdam and GRGS Toulouse.

Fritsche, M., Dietrich, R., Knöfel, C., Rülke, A., Vey, S., Rothacher, M., and Steigenberger, P. (2005). Impact of higher-order ionospheric terms on GPS estimates. *Geophys. Res. Lett.*, 32:L23311.

Fritsche, M., Dietrich, R., Rülke, A., Rothacher, M., and Steigenberger, P. (2009). Low-degree earth deformation from reprocessed GPS observations. *GPS Solut.*, 14(2):165–175.

Fritsche, M., Döll, P., and Dietrich, R. (2012). Global-scale validation of model-based load deformation of the Earth's crust from continental watermass and atmospheric pressure variations using GPS. *J. Geodyn.*, 59-60:133–142.

Fujita, T. T. (1986). *Mesoscale Classifications: Their History and Their Application to Forecasting*, pages 18–35. American Meteorological Society, Boston, MA.

Fukumori, I. (2002). A Partitioned Kalman Filter and Smoother. *Mon. Weather Rev*, 130(5):1370–1383.

Fukumori, I., Raghunath, R., and Fu, L.-L. (1998). Nature of global large-scale sea level variability in relation to atmospheric forcing: A modeling study. *J. Geophys. Res. Oceans*, 103(C3):5493–5512.

Fukushima, T. (2012). Numerical computation of spherical harmonics of arbitrary degree and order by extending exponent of floating point numbers. *J. Geod.*, 86(4):271–285.

Gardner, C. S. (1976). Effects of horizontal refractivity gradients on the accuracy of laser ranging to satellites. *Radio Sci.*, 11(12):1037–1044.

Gegout, P., Biancale, R., and Soudarin, L. (2011). Adaptive mapping functions to the azimuthal anisotropy of the neutral atmosphere. *J. Geod.*, 85(10):661–677.

Gelaro, R., McCarty, W., Suárez, M. J., Todling, R., Molod, A., Takacs, L., Randles, C. A., Darmenov, A., Bosilovich, M. G., Reichle, R., Wargan, K., Coy, L., Cullather, R., Draper, C., Akella, S., Buchard, V., Conaty, A., da Silva, A. M., Gu, W., Kim, G.-K., Koster, R., Lucchesi, R., Merkova, D., Nielsen, J. E., Partyka, G., Pawson, S., Putman, W., Rienecker, M., Schubert, S. D., Sienkiewicz, M., and Zhao, B. (2017). The Modern-Era Retrospective Analysis for Research and Applications, Version 2 (MERRA-2). *J. Clim.*, 30(14):5419–5454.

Gelb, A. (1974). *Applied Optimal Estimation*. The MIT Press.

Geleyn, J. and Hollingsworth, A. (1979). An economical analytical method for the computation of the interaction between scattering and line absorption of radiation. *Beitr. Phys. Atmos*, 52:1–16.

Ghaderpour, E. and Pagiatakis, S. D. (2017). Least-Squares Wavelet Analysis of Unequally Spaced and Non-stationary Time Series and Its Applications. *Math. Geosci.*, 49(7):819–844.

Giorgi, G., Schmidt, T., Trainotti, C., Calvo, R. M., Fuchs, C., Hoque, M., Berdermann, J., Furthner, J., Günther, C., Schuldt, T., Sanjuan, J., Gohlke, M., Oswald, M., Braxmaier, C., Balidakis, K., Dick, G., Flechtner, F., Ge, M., Glaser, S., König, R., Michalak, G., Murböck, M., Semmling, M., and Schuh, H. (2019). Advanced Technologies for Satellite Navigation and Geodesy. *Adv. Space Res.*, 64(6):1256 – 1273.

Glaser, S. (2014). *On the optimization of the combination strategy of different geodetic satellite techniques to realize a global terrestrial reference system (in German)*. PhD thesis, TU Dresden.

Glaser, S., Ampatzidis, D., König, R., Nilsson, T., Heinkelmann, R., Flechtner, F., and Schuh, H. (2017a). *Simulation of VLBI Observations to Determine a Global TRF for GGOS*, pages 1–7. Springer Berlin Heidelberg, Berlin, Heidelberg.

Glaser, S., Fritsche, M., Sośnica, K., Rodríguez-Solano, C. J., Wang, K., Dach, R., Hugentobler, U., Rothacher, M., and Dietrich, R. (2015). A consistent combination of GNSS and SLR with minimum constraints. *J. Geod.*, 89(12):1165–1180.

Glaser, S., König, R., Ampatzidis, D., Nilsson, T., Heinkelmann, R., Flechtner, F., and Schuh, H. (2017b). A global terrestrial reference frame from simulated VLBI and SLR data in view of GGOS. *J. Geod.*, 91(7):723–733.

Glaser, S., König, R., Neumayer, K. H., Balidakis, K., and Schuh, H. (2019). Future SLR station networks in the framework of simulated multi-technique terrestrial reference frames. *J. Geod.*

Glaser, S., König, R., Neumayer, K. H., Nilsson, T., Heinkelmann, R., Flechtner, F., and Schuh, H. (2018). On the impact of local ties on the datum realization of global terrestrial reference frames. *J. Geod.*, 93(5):655–667.

Gödel, M., Schmidt, T. D., and Furthner, J. (2017). Kalman filter approaches for a mixed clock ensemble. In *2017 Joint Conference of the European Frequency and Time Forum and IEEE International Frequency Control Symposium (EFTF/IFCS)*, pages 666–672.

Greatbatch, R. J. (1994). A note on the representation of steric sea level in models that conserve volume rather than mass. *J. Geophys. Res. Oceans*, 99(C6):12767–12771.

Greenhall, C. A. (2011). Reduced kalman filters for clock ensembles. In *2011 Joint Conference of the IEEE International Frequency Control and the European Frequency and Time Forum (FCS) Proceedings*, pages 1–5.

Gross, R., Beutler, G., and Plag, H.-P. (2009). *Global Geodetic Observing System: Meeting the Requirements of a Global Society on a Changing Planet in 2020*, chapter Integrated scientific and societal user requirements and functional specifications for the GGOS, pages 209–224. Springer Berlin Heidelberg, Berlin, Heidelberg.

Guier, W. H. and Weiffenbach, G. C. (1960). A Satellite Doppler Navigation System. *Proceedings of the IRE*, 48(4):507–516.

Guo, J. Y., Li, Y. B., Huang, Y., Deng, H. T., Xu, S. Q., and Ning, J. S. (2004). Green's function of the deformation of the Earth as a result of atmospheric loading. *Geophys. J. Int.*, 159(1):53–68.

Haas, R., Bergstrand, S., and Lehner, W. (2013). Evaluation of gnss monument stability. In Altamimi, Z. and Collilieux, X., editors, *Reference Frames for Applications in Geosciences*, pages 45–50, Berlin, Heidelberg. Springer Berlin Heidelberg.

Haas, R., Elgered, G., Gradinarsky, L., and Johansson, J. (2003). Assessing long term trends in the atmospheric water vapor content by combining data from VLBI, GPS, radiosondes and microwave radiometry. In Schwegmann, W. and Thorandt, V., editors, *Proceedings, 16th Working Meeting On EVGA, BKG, Frankfurt, Germany*, pages 279–288.

Haas, R., Ning, T., and Elgered, G. (2010). Observation of long term trends in the amount of atmospheric water vapor by space geodesy and remote sensing techniques. In *2010 IEEE International Geoscience and Remote Sensing Symposium*, pages 2944–2947.

Halsig, S., Artz, T., Iddink, A., and Nothnagel, A. (2016). Using an atmospheric turbulence model for the stochastic model of geodetic VLBI data analysis. *Earth Planets Space*, 68(1):106.

Halsig, S., Bertarini, A., Haas, R., Iddink, A., Kodet, J., Kronschnabl, G., Neidhardt, A., Nothnagel, A., Plötz, C., and Schüler, T. (2018). Atmospheric refraction and system stability investigations in short-baseline VLBI observations. *J. Geod.*, 93(4):593–614.

Hasegawa, S. and Stokesberry, D. P. (1975). Automatic digital microwave hygrometer. *Rev. Sci. Instrum.*, 46(7):867–873.

Hawarey, M., Hobiger, T., and Schuh, H. (2005). Effects of the 2nd order ionospheric terms on VLBI measurements. *Geophys. Res. Lett.*, 32(11).

Healy, S. B. (2011). Refractivity coefficients used in the assimilation of GPS radio occultation measurements. *J. Geophys. Res.*, 116(D1). D01106.

Heinkelmann, R. (2013). VLBI Geodesy: Observations, Analysis and Results. In Jin, S., editor, *Geodetic Sciences*, chapter 3. IntechOpen, Rijeka.

Heinkelmann, R., Balidakis, K., Phogat, A., Lu, C., Mora-Diaz, J. A., Nilsson, T., and Schuh, H. (2018). Effects of Meteorological Input Data on the VLBI Station Coordinates, Network Scale, and EOP. In Freymueller, J. T. and Sánchez, L., editors, *International Symposium on Earth and Environmental Sciences for Future Generations*, pages 195–202, Cham. Springer International Publishing.

Heinkelmann, R., Boehm, J., Schuh, H., Bolotin, S., Engelhardt, G., MacMillan, D. S., Negusini, M., Skurikhina, E., Tesmer, V., and Titov, O. (2007). Combination of long time-series of troposphere zenith delays observed by VLBI. *J. Geod.*, 81(6):483–501.

Herring, T. (1992). Modelling atmospheric delays in the analysis of space geodetic data. In *Symposium on Refraction of Transatmospheric Signals in Geodesy*, number 36, pages 157–164. Netherlands Geodetic Commission Series.

Herring, T. A., Davis, J. L., and Shapiro, I. I. (1990). Geodesy by radio interferometry: The application of Kalman Filtering to the analysis of very long baseline interferometry data. *J. Geophys. Res.*, 95(B8):12561–12581.

Hinteregger, H. F., Shapiro, I. I., Robertson, D. S., Knight, C. A., Ergas, R. A., Whitney, A. R., Rogers, A. E. E., Moran, J. M., Clark, T. A., and Burke, B. F. (1972). Precision Geodesy via Radio Interferometry. *Science*, 178(4059):396–398.

Hirvonen, R. (1962). *On the Statistical Analysis of Gravity Anomalies.* Annales Academiae Scientiarum Fennicae/A. Ohio State University Research Foundation.

Hofmann-Wellenhof, B. and Moritz, H. (2006). *Physical geodesy (Second, corrected edition).*

Holmes, S. A. and Featherstone, W. E. (2002). A unified approach to the Clenshaw summation and the recursive computation of very high degree and order normalised associated Legendre functions. *J. Geod.*, 76(5):279–299.

Hoque, M. M. and Jakowski, N. (2007). Higher order ionospheric effects in precise GNSS positioning. *J. Geod.*, 81(4):259–268.

Horwath, M., Rülke, A., Fritsche, M., and Dietrich, R. (2010). *Mass Variation Signals in GRACE Products and in Crustal Deformations from GPS: A Comparison*, pages 399–406. Springer Berlin Heidelberg, Berlin, Heidelberg.

Hulley, G. and Pavlis, E. (2007). A ray-tracing technique for improving Satellite Laser Ranging atmospheric delay corrections, including the effects of horizontal refractivity gradients. *J. Geophys. Res. Solid Earth*, 112(B6):B06417.

Jekeli, C. (2016). *Geometric Reference Systems in Geodesy.* Division of Geodetic Science School of Earth Sciences, Ohio State University, 2016 edition.

Jungclaus, J. H., Fischer, N., Haak, H., Lohmann, K., Marotzke, J., Matei, D., Mikolajewicz, U., Notz, D., and von Storch, J. S. (2013). Characteristics of the ocean simulations in the Max Planck Institute Ocean Model (MPIOM) the ocean component of the MPI-Earth system model. *J. Adv. Model. Earth Syst.*, 5(2):422–446.

Kalman, R. E. (1960). A new approach to linear filtering and prediction problems. *ASME J. Basic. Eng.*

Kalnay, E., Kanamitsu, M., Kistler, R., Collins, W., Deaven, D., Gandin, L., Iredell, M., Saha, S., White, G., Woollen, J., Zhu, Y., Leetmaa, A., Reynolds, R., Chelliah, M., Ebisuzaki, W., Higgins, W., Janowiak, J., Mo, K. C., Ropelewski, C., Wang, J., Jenne, R., and Joseph, D. (1996). The NCEP/NCAR 40-Year Reanalysis Project. *Bull. Amer. Meteor. Soc.*, 77(3):437–471.

Kanamitsu, M., Ebisuzaki, W., Woollen, J., Yang, S.-K., Hnilo, J. J., Fiorino, M., and Potter, G. L. (2002). NCEP-DOE AMIP-II Reanalysis (R-2). *Bull. Amer. Meteor. Soc.*, 83(11):1631–1644.

Karegar, M. A., Dixon, T. H., Kusche, J., and Chambers, D. P. (2018). A New Hybrid Method for Estimating Hydrologically Induced Vertical Deformation From GRACE and a Hydrological Model: An Example From Central North America. *J. Adv. Model. Earth Syst.*, 10(5):1196–1217.

Kashcheyev, A., Nava, B., and Radicella, S. M. (2012). Estimation of higher order ionospheric errors in GNSS positioning using a realistic 3D electron density model. *Radio Sci.*, 47(4).

Kačmařík, M., Douša, J., Zus, F., Václavovic, P., Balidakis, K., Dick, G., and Wickert, J. (2019). Sensitivity of GNSS tropospheric gradients to processing options. *Ann. Geophys.*, 37(3):429–446.

Kennett, B. L. N. and Engdahl, E. R. (1991). Traveltimes for global earthquake location and phase identification. *Geophys. J. Int.*, 105(2):429–465.

Kennett, B. L. N., Engdahl, E. R., and Buland, R. (1995). Constraints on seismic velocities in the earth from traveltimes. *Geophys. J. Int.*, 122(1):108–124.

Killick, R., Fearnhead, P., and Eckley, I. A. (2012). Optimal Detection of Changepoints With a Linear Computational Cost. *J. Am. Stat. Assoc.*, 107(500):1590–1598.

Kiuchi, H., Hama, S., Amagai, J., Yoshino, T., and Imae, M. (1997). Instrumental delay calibration with zero baseline interferometry for VLBI time comparison. *IEE Proceedings - Science, Measurement and Technology*, 144(4):181–188.

Koch, K.-R. (1997). *Parameterschätzung und Hypothesentests in linearen Modellen.* Ferd. Dümmler Verlag, Bonn, 3 edition.

Koenig, R., Balidakis, K., Neumayer, H., and Zus, F. (2018). Can we impeove the atmospheric delay corrections for satellite laser ranging? PSD.1-0015-18, COSPAR 2018. Pasadena, USA.

Kondo, T. and Takefuji, K. (2016). An algorithm of wideband bandwidth synthesis for geodetic VLBI. *Radio Sci.*, 51(10):1686–1702.

Kotsakis, C. (2005). On the trade-off between model expansion, model shrinking, and parameter estimation accuracy in least-squares data analysis. *J. Geod*, 79(8):460–466.

Kotsakis, C. (2007). A covariance-adaptive approach for regularized inversion in linear models. *Geophys. J. Int.*, 171(2):509–522.

Kotsakis, C. (2013). Generalized inner constraints for geodetic network densification problems. *J. Geod.*, 87(7):661–673.

Kotsakis, C. (2016). *Reference Station Weighting and Frame Optimality in Minimally Constrained Networks*, pages 221–226. Springer International Publishing, Cham.

Kotsakis, C. (2018). *Datum Definition and Minimal Constraints*, pages 1–6. Springer International Publishing, Cham.

Kotsakis, C., Vatalis, A., and Sansò, F. (2014). On the importance of intra-frame and inter-frame covariances in frame transformation theory. *J. Geod.*, 88(12):1187–1201.

Kravtsov, Y. A. and Orlov, Y. I. (1981). Boundaries of geometrical optics applicability and related problems. *Radio Sci.*, 16(6):975–978.

Krügel, M., Thaller, D., Tesmer, V., Rothacher, M., Angermann, D., and Schmid, R. (2007). Tropospheric parameters: combination studies based on homogeneous VLBI and GPS data. *J. Geod.*, 81(6):515–527.

Kustowski, B., Ekström, G., and Dziewoński, A. M. (2008). Anisotropic shear-wave velocity structure of the Earth's mantle: A global model. *J. Geophys. Res.*, 113(B6). B06306.

Lagler, K., Schindelegger, M., Böhm, J., Krásná, H., and Nilsson, T. (2013). GPT2: Empirical slant delay model for radio space geodetic techniques. *Geophys. Res. Lett.*, 40(6):1069–1073.

Landskron, D. and Böhm, J. (2018a). Refined discrete and empirical horizontal gradients in VLBI analysis. *J. Geod.*

Landskron, D. and Böhm, J. (2018b). VMF3/GPT3: refined discrete and empirical troposphere mapping functions. *J. Geod.*, 92(4):349–360.

Landskron, D., Hofmeister, A., and Böhm, J. (2017). *Refined Tropospheric Delay Models for CONT11*, pages 65–69. Springer International Publishing, Cham.

Lanzante, J. R. (1996). Resistant, robust and non-parametric techniques for the analysis of climate data: theory and examples, including applications to historical radiosonde station data. *Int. J. Climatol.*, 16(11):1197–1226.

Laske, G., Masters, G., Ma, Z., and Pasyanos, M. (2013). Update on CRUST1.0 - A 1-degree Global Model of Earth's Crust. [Available at https://igppweb.ucsd.edu/~gabi/crust1.html].

Laske, G., Masters, G., and Reif, C. (2012). CRUST 2.0: A New Global Crustal Model at 2x2 Degrees. [Available at https://igppweb.ucsd.edu/~gabi/crust2.html].

Leandro, R., Santos, M., and B. Langley, R. (2006). UNB Neutral Atmosphere Models: Development and Performance. *Proceedings of the 2006 National Technical Meeting of The Institute of Navigation*, 2:564–573.

Leick, A., Rapoport, L., and Tatarnikov, D. (2015). *GPS Satellite Surveying*. John Wiley & Sons, Inc.

Lemoine, F. and Schrama, E. (2016). Preface-Scientific applications of DORIS in space geodesy. *Adv. Space Res.*, 58(12):2477–2478. Scientific Applications of DORIS in Space Geodesy.

Leßmann, L. and Möller, J. (2018). Analysis of non-tidal ocean loading for gravitational potential observations in northern Europe. *J. Geodyn.*, 119:23–28.

Lieske, H., Lederle, T., Fricke, W., and Morando, B. (1977). Expression for the precession quantities based upon the IAU (1976) system of astronomical constants. *Astron. Astrophys.*, 58.

Lösler, M., Haas, R., Eschelbach, C., and Greiwe, A. (2019). Gravitational deformation of ring-focus antennas for VGOS: first investigations at the Onsala twin telescopes project. *J. Geod.*

Luceri, V. and Pavlis, E. (2016). The ILRS contribution to ITRF2014. [Available at http://itrf.ign.fr/ITRF_solutions/2014/doc/ILRS-ITRF2014-description.pdf].

Lynch, D. R. and Gray, W. G. (1979). A wave equation model for finite element tidal computations. *Comput. Fluids*, 7(3):207 – 228.

MacMillan, D. (1995a). Atmospheric gradients from very long baseline interferometry observations. *Geophys. Res. Lett.*, 22(9):1041–1044.

MacMillan, D. S. (1995b). Atmospheric gradients from very long baseline interferometry observations. *Geophys. Res. Lett.*, 22(9):1041–1044.

MacMillan, D. S. and Gipson, J. M. (1994). Atmospheric pressure loading parameters from very long baseline interferometry observations. *J. Geophys. Res.: Solid Earth*, 99(B9):18081–18087.

MacMillan, D. S. and Ma, C. (1994). Evaluation of very long baseline interferometry atmospheric modeling improvements. *J. Geophys. Res.*, 99(B1):637–651.

MacMillan, D. S. and Ma, C. (1997). Atmospheric gradients and the VLBI terrestrial and celestial reference frames. *Geophys. Res. Lett.*, 24(4):453–456.

Maiman, T. H. (1960). Stimulated optical radiation in ruby. *Nature*, 187(4736):493–494.

Malkin, Z. (2009). On comparison of the Earth orientation parameters obtained from different VLBI networks and observing programs. *J. Geod.*, 83(6):547–556.

Männel, B., Dobslaw, H., Dill, R., Glaser, S., Balidakis, K., Thomas, M., and Schuh, H. (2019). Correcting surface loading at the observation level: impact on global GNSS and VLBI station networks. *J. Geod.*

Männel, B. and Rothacher, M. (2017). Geocenter variations derived from a combined processing of LEO- and ground-based GPS observations. *J. Geod.*, 91(8):933–944.

Marini, J. (1972). Correction of satellite tracking data for an arbitrary tropospheric profile. *Radio Sci.*, 7(2):223–231.

Marini, J. and Murray, C. (1973). Correction of laser range tracking data for atmospheric refraction at elevations above 10 degrees. Technical report, Goddard Space Flight Center.

Masoumi, S., McClusky, S., Koulali, A., and Tregoning, P. (2017). A directional model of tropospheric horizontal gradients in Global Positioning System and its application for particular weather scenarios. *J. Geophys. Res. Atmos.*, 122(8):4401–4425. 2016JD026184.

Matveenko, L. I., Kardashev, N. S., and Sholomitskii, G. B. (1965). Large base-line radio interferometers. *Soviet Radiophysics*, 8(4):461–463.

McGarry, J. F., Hoffman, E. D., Degnan, J. J., Cheek, J. W., Clarke, C. B., Diegel, I. F., Donovan, H. L., Horvath, J. E., Marzouk, M., Nelson, A. R., Patterson, D. S., Ricklefs, R. L., Shappirio, M. D., Wetzel, S. L., and Zagwodzki, T. W. (2018). NASA's satellite laser ranging systems for the twenty-first century. *J. Geod.*

Mendes, V. and Pavlis, E. (2004). High-accuracy zenith delay prediction at optical wavelengths. *Geophys. Res. Lett.*, 31:L14602.

Mendes, V., Prates, G., Pavlis, E., Pavlis, D., and Langley, R. (2002). Improved mapping functions for atmospheric refraction correction in SLR. *Geophys. Res. Lett.*, 29(10):53–1–53–4.

Mendes, V. B. (1999). *Modeling the neutral-atmosphere propagation delay in radiometric space techniques.* PhD thesis, Department of Geodesy and Geomatics Engineering, University of New Brunswick, Fredericton, New Brunswick, Canada. Technical Report No. 199, 353 pp.

Menemenlis, D., Hill, C., Adcrocft, A., Campin, J.-M., Cheng, B., Ciotti, B., Fukumori, I., Heimbach, P., Henze, C., Köhl, A., Lee, T., Stammer, D., Taft, J., and Zhang, J. (2005). NASA supercomputer improves prospects for ocean climate research. *Eos. Trans. AGU*, 86(9):89–96.

Mercan, H., Akyilmaz, O., and Aydin, C. (2018). Solution of the weighted symmetric similarity transformations based on quaternions. *J. Geod.*, 92(10):1113–1130.

Merkowitz, S. M., Bolotin, S., Elosegui, P., Esper, J., Gipson, J., Hilliard, L., Himwich, E., Hoffman, E. D., Lakins, D. D., Lamb, R. C., Lemoine, F. G., Long, J. L., McGarry, J. F., MacMillan, D. S., Michael, B. P., Noll, C., Pavlis, E. C., Pearlman, M. R., Ruszczyk, C., Shappirio, M. D., and Stowers, D. A. (2018). Modernizing and expanding the NASA Space Geodesy Network to meet future geodetic requirements. *J. Geod.*

Milliner, C., Materna, K., Bürgmann, R., Fu, Y., Moore, A. W., Bekaert, D., Adhikari, S., and Argus, D. F. (2018). Tracking the weight of Hurricane Harvey's stormwater using GPS data. *Sci. Adv.*, 4(9).

Milly, P. C. D. and Shmakin, A. B. (2002). Global Modeling of Land Water and Energy Balances. Part I: The Land Dynamics (LaD) Model. *J. Hydrometeor.*, 3(3):283–299.

Moreaux, G., Lemoine, F. G., Capdeville, H., Kuzin, S., Otten, M., Štěpánek, P., Willis, P., and Ferrage, P. (2016). The International DORIS Service contribution to the 2014 realization of the International Terrestrial Reference Frame. *Adv. Space Res.*, 58(12):2479 – 2504. Scientific Applications of DORIS in Space Geodesy.

Mysen, E. (2017). On the equivalence of Kalman filtering and least-squares estimation. *J. Geod.*, 91(1):41–52.

Napier, P. J., Bagri, D. S., Clark, B. G., Rogers, A. E. E., Romney, J. D., Thompson, A. R., and Walker, R. C. (1994). The Very Long Baseline Array. *Proc. IEEE*, 82(5):658–672.

Niell, A. (1996). Global mapping functions for the atmosphere delay at radio wavelengths. *J. Geophys. Res.*, 101(B2):3227–3246.

Niell, A. (2001). Preliminary evaluation of atmospheric mapping functions based on numerical weather models. *Physics and Chemistry of the Earth, Part A: Solid Earth and Geodesy*, 26(6):475 – 480. Proceedings of the First COST Action 716 Workshop Towards Operational GPS Meteorology and the Second Network Workshop of the International GPS Service (IGS).

Niell, A., Barrett, J., Burns, A., Cappallo, R., Corey, B., Derome, M., Eckert, C., Elosegui, P., McWhirter, R., Poirier, M., Rajagopalan, G., Rogers, A., Ruszczyk, C., SooHoo, J., Titus, M., Whitney, A., Behrend, D., Bolotin, S., Gipson, J., Gordon, D., Himwich, E., and Petrachenko, B. (2018). Demonstration of a Broadband Very Long Baseline Interferometer System: A New Instrument for High-Precision Space Geodesy. *Radio Sci.*, 53(10):1269–1291.

Niell, A. E., Coster, A. J., Solheim, F. S., Mendes, V. B., Toor, P. C., Langley, R. B., and Upham, C. A. (2001). Comparison of Measurements of Atmospheric Wet Delay by Radiosonde, Water Vapor Radiometer, GPS, and VLBI. *J. Atmospheric Ocean. Technol.*, 18(6):830–850.

Nikolaidou, T., Balidakis, K., Nievinski, F., Santos, M., and Schuh, H. (2018a). Impact of different NWM-derived mapping functions on VLBI and GPS analysis. *Earth Planets Space*, 70(1):95.

Nikolaidou, T., Nievinski, F., Balidakis, K., Schuh, H., and Santos, M. (2018b). PPP without troposphere estimation: Impact assessment of regional versus global numerical weather models and delay parametrization. In *International Association of Geodesy Symposia*. Springer Berlin Heidelberg.

Nilsson, T., Böhm, J., Wijaya, D. D., Tresch, A., Nafisi, V., and Schuh, H. (2013). *Path Delays in the Neutral Atmosphere*, pages 73–136. Springer Berlin Heidelberg, Berlin, Heidelberg.

Nilsson, T., Davis, J. L., and Hill, E. M. (2009). Using ground-based GPS to characterize atmospheric turbulence. *Geophys. Res. Lett.*, 36(16).

Nilsson, T. and Elgered, G. (2008). Long-term trends in the atmospheric water vapor content estimated from ground-based GPS data. *J. Geophys. Res. Atmos*, 113(D19). D19101.

Nilsson, T. and Haas, R. (2008). Modeling tropospheric delays with atmospheric turbulence models. In Finkelstein, A. and Behrend, D., editors, *Measuring the future, Proceedings of the 5th IVS General Meeting, Institute of Applied Astronomy RAS 2008, Nauka, ISBN 978-5-02-025332-2*, pages 361–370.

Nilsson, T. and Haas, R. (2010). Impact of atmospheric turbulence on geodetic very long baseline interferometry. *J. Geophys. Res.*, 115(B3).

Nilsson, T., Haas, R., and Elgered, G. (2007). Simulations of atmospheric path delays using turbulence models. In Böhm, J., Pany, A., and Schuh, H., editors, *Proceedings of the 18th European VLBI for Geodesy and Astrometry Work Meeting, 12–13 April 2007, edited by J. Böhm, A. Pany, H. Schuh, Geowissenschaftliche Mitteilungen, Heft Nr. 79, Schriftreihe der Studienrichtung Vermessung und Geoinformation, Technische Universität Wien, ISSN 1811-8380, p. 175-180*, pages 175–180.

Nilsson, T., Karbon, M., Soja, B., Heinkelmann, R., Lu, C., and Schuh, H. (2015a). Atmospheric modeling for co-located VLBI antennas and twin telescopes. *J. Geod.*, 89(7):655–665.

Nilsson, T., Mora-Diaz, J. A., Raposo-Pulido, V., Heinkelmann, R., Karbon, M., Liu, L., Lu, C., Xu, B. S. M., and Schuh, H. (2017a). Antenna Axis Offsets and Their Impact on VLBI Derived Reference Frames. In van Dam, T., editor, *REFAG 2014*, pages 53–58, Cham. Springer International Publishing.

Nilsson, T., Soja, B., Balidakis, K., Karbon, M., Heinkelmann, R., Deng, Z., and Schuh, H. (2017b). Improving the modeling of the atmospheric delay in the data analysis of the Intensive VLBI sessions and the impact on the UT1 estimates. *J. Geod.*, 91(7):857–866.

Nilsson, T., Soja, B., Karbon, M., Heinkelmann, R., and Schuh, H. (2015b). Application of Kalman filtering in VLBI data analysis. *Earth Planets Space*, 67(1):136.

Nothnagel, A. (2019). *Very Long Baseline Interferometry*, pages 1–58. Springer Berlin Heidelberg, Berlin, Heidelberg.

Nothnagel, A., Behrend, D., Bertarini, A., Charlot, P., Combrinck, L., Gipson, J., Himwich, E., Haas, R., Ipatov, A., Kawabata, R., Lovell, J., Ma, C., Niell, A., Petrachenko, B., Schüler, T., and Wang, G. (2016). Strategic Plan of the IVS for the Period 2016-2025. In *IVS2016GM Proceedings: "New Horizons with VGOS", Eds. Dirk Behrend, Karen D. Baver, Kyla L. Armstrong, NASA/CP-2016-219016, p. 3-14 - 13-19 March 2016 South Africa*, pages 3–14, Johannesburg , South Africa.

Nothnagel, A. et al. (2015). The IVS data input to ITRF2014, International VLBI Service for Geodesy and Astrometry, GFZ Data Services.

Nothnagel, A., Holst, C., and Haas, R. (2019). A VLBI delay model for gravitational deformations of the Onsala 20m radio telescope and the impact on its global coordinates. *J. Geod.*

Nothnagel, A., Nilsson, T., and Schuh, H. (2018). Very Long Baseline Interferometry: Dependencies on Frequency Stability. *Space Sci. Rev.*, 214(3):66.

Oueslati, B. and Bellon, G. (2013). Convective Entrainment and Large-Scale Organization of Tropical Precipitation: Sensitivity of the CNRM-CM5 Hierarchy of Models. *J. Clim.*, 26(9):2931–2946.

Owens, J. C. (1967). Optical refractive index of air: Dependence on pressure, temperature and composition. *Appl. Opt.*, 6(1):51–59.

Pagiatakis, S. and Peidou, A. (2019). Demystifying the origin of stripes in GRACE mission gravity field models. Geophys. Res. Abstr. Vol. 21, EGU2019-14247, EGU General Assembly 2019.

Pagiatakis, S. D. (1990). The response of a realistic earth to ocean tide loading. *Geophys. J. Int.*, 103(2):541–560.

Pany, A., Böhm, J., MacMillan, D., Schuh, H., Nilsson, T., and Wresnik, J. (2011). Monte Carlo simulations of the impact of troposphere, clock and measurement errors on the repeatability of VLBI positions. *J. Geod.*, 85(1):39–50.

Parker, T. E. (1999). Environmental factors and hydrogen maser frequency stability. *IEEE Trans. Ultrason., Ferroelectr., Freq. Control*, 46(3):745–751.

Pearlman, M. R., Noll, C. E., Pavlis, E. C., Lemoine, F. G., Combrink, L., Degnan, J. J., Kirchner, G., and Schreiber, U. (2019). The ILRS: approaching 20 years and planning for the future. *J. Geod.*

Petit, G. and Luzum, B., editors (2010). *IERS Conventions (2010)*, volume 36 of *IERS Technical Note*. Verlag des Bundesamts für Kartographie und Geodäsie, Frankfurt am Main.

Petrachenko, B., Niell, A., Behrend, D., Corey, B., Boehm, J., Charlot, P., Collioud, A., Gipson, J., Haas, R., Hobiger, T., Koyama, Y., MacMillan, D., Malkin, Z., Nilsson, T., Pany, A., Tuccari, G., Whitney, A., and Wresnik, J. (2009). Design Aspects of the VLBI2010 System. Progress Report of the IVS VLBI2010 Committee, June 2009. NASA/TM-2009-214180, 2009, 62 pages.

Petrov, L. (2000). Instrumental Errors of Geodetic VLBI. In Vandenberg, N. R. and Baver, K. D., editors, *International VLBI Service for Geodesy and Astrometry 2000 General Meeting Proceedings*, pages 230–235.

Petrov, L. (2017). *The International Mass Loading Service*, pages 79–83. Springer International Publishing, Cham.

Petrov, L. and Boy, J.-P. (2004). Study of the atmospheric pressure loading signal in very long baseline interferometry observations. *J. Geophys. Res.*, 109:B03405.

Petrov, L., Gordon, D., Gipson, J., MacMillan, D., Ma, C., Fomalont, E., Walker, R. C., and Carabajal, C. (2009). Precise geodesy with the Very Long Baseline Array. *J. Geod.*, 83(9):859–876.

Petrov, L. and Ma, C. (2003). Study of harmonic site position variations determined by very long baseline interferometry. *J. Geophys. Res.*, 108(B4).

Picard, A., Davis, R. S., and Fujii, M. G. K. (2008). Revised formula for the density of moist air (CIPM-2007). *Metrologia*, 45(2):149.

Plank, L., Lovell, J. E. J., McCallum, J. N., Mayer, D., Reynolds, C., Quick, J., Weston, S., Titov, O., Shabala, S. S., Böhm, J., Natusch, T., Nickola, M., and Gulyaev, S. (2017). The AUSTRAL VLBI observing program. *J. Geod.*, 91(7):803–817.

Pollet, A., Coulot, D., Bock, O., and Nahmani, S. (2014). Comparison of individual and combined zenith tropospheric delay estimations during CONT08 campaign. *J. Geod*, 88(11):1095–1112.

Powers, J. G., Klemp, J. B., Skamarock, W. C., Davis, C. A., Dudhia, J., Gill, D. O., Coen, J. L., Gochis, D. J., Ahmadov, R., Peckham, S. E., Grell, G. A., Michalakes, J., Trahan, S., Benjamin, S. G., Alexander, C. R., Dimego, G. J., Wang, W., Schwartz, C. S., Romine, G. S., Liu, Z., Snyder, C., Chen, F., Barlage, M. J., Yu, W., and Duda, M. G. (2017). The Weather Research and Forecasting Model: Overview, System Efforts, and Future Directions. *Bull. Amer. Meteor. Soc.*, 98(8):1717–1737.

Rabbel, W. and Schuh, H. (1986). The influence of atmospheric loading on VLBI-experiments. *Journal of Geophysics Zeitschrift Geophysik*, 59:164–170.

Ray, R. and Ponte, R. (2003). Barometric tides from ECMWF operational analyses. *Ann. Geophys.*, 21(8):1897–1910.

Rebischung, P., Altamimi, Z., Ray, J., and Garayt, B. (2016). The IGS contribution to ITRF2014. *J. Geod.*, 90(7):611–630.

Rienecker, M., Suarez, M., Todling, R., Bacmeister, J., Takacs, L., Liu, H.-C., Sienkiewicz, W., Koster, R., Gelaro, R., Stajner, I., and Nielsen, E. (2008). The GEOS Data Assimilation System - Documentation of Versions 5.0.1, 5.1.0, and 5.2.0., NASA/TM-2008-104606. [Available at http://gmao.gsfc.nasa.gov/pubs/docs/tm27.pdf].

Rodell, M., Famiglietti, J. S., Wiese, D. N., Reager, J. T., Beaudoing, H. K., Landerer, F. W., and Lo, M.-H. (2018). Emerging trends in global freshwater availability. *Nature*, 557(7707):651–659.

Rodell, M., Houser, P. R., Jambor, U., Gottschalck, J., Mitchell, K., Meng, C.-J., Arsenault, K., Cosgrove, B., Radakovich, J., Bosilovich, M., Entin, J. K., Walker, J. P., Lohmann, D., and Toll, D. (2004). The global land data assimilation system. *Bulletin of the American Meteorological Society*, 85(3):381–394.

Rogers, A. E. E. (1970). Very Long Baseline Interferometry with Large Effective Bandwidth for Phase-Delay Measurements. *Radio Sci.*, 5(10):1239–1247.

Roggenbuck, O., Thaller, D., Engelhardt, G., Franke, S., Dach, R., and Steigenberger, P. (2017). Loading-Induced Deformation Due to Atmosphere, Ocean and Hydrology: Model Comparisons and the Impact on Global SLR, VLBI and GNSS Solutions. In van Dam, T., editor, *REFAG 2014*, pages 71–77, Cham. Springer International Publishing.

Rothacher, M., Angermann, D., Artz, T., Bosch, W., Drewes, H., Gerstl, M., Kelm, R., König, D., König, R., Meisel, B., Müller, H., Nothnagel, A., Panafidina, N., Richter, B., Rudenko, S., Schwegmann, W., Seitz, M., Steigenberger, P., Tesmer, S., Tesmer, V., and Thaller, D. (2011). GGOS-D: homogeneous reprocessing and rigorous combination of space geodetic observations. *J. Geod.*, 85(10):679–705.

Rothacher, M., Beutler, G., Herring, T. A., and Weber, R. (1999). Estimation of nutation using the Global Positioning System. *J. Geophys. Res.*, 104(B3):4835–4859.

Rothacher, M., Springer, T., Schaer, S., and Beutler, G. (1997). Processing Strategies for Regional GPS Networks. In *IAG General Assembly, Rio de Janeiro*, Berlin, Heidelberg, New York. Springer.

Rousseeuw, P. J. and Leroy, A. M. (2005). *Multiple Regression*, pages 75–157. John Wiley and Sons, Inc.

Rowlands, D. D., Luthcke, S. B., Klosko, S. M., Lemoine, F. G. R., Chinn, D. S., McCarthy, J. J., Cox, C. M., and Anderson, O. B. (2005). Resolving mass flux at high spatial and temporal resolution using GRACE intersatellite measurements. *Geophys. Res. Lett.*, 32(4).

Rüeger, J. (2002). Refractive index formulae for electronic distance measurement with radio and millimeter waves [Available at http://www.sage.unsw.edu.au/about/school_pubs/pdfrep/s68.pdf].

Saastamoinen, J. (1972). *Atmospheric Correction for the Troposphere and Stratosphere in Radio Ranging Satellites*, pages 247–251. American Geophysical Union (AGU).

Saastamoinen, J. (1973). Contribution to the theory of atmospheric refraction. *B. Geod.*, 107(1):13–34.

Sakazaki, T. and Hamilton, K. (2017). Physical processes controlling the tide in the tropical lower atmosphere investigated using a comprehensive numerical model. *J. Atmos. Sci.*, 74(8):2467–2487.

Salzberg, I. M. (1967). Mathematical relationships of the MFOD ANTENNA axes. Technical Report NASA-TM-X-55956, X-553-67-213, NASA Goddard Space Flight Center, Greenbelt, MD, United States.

Schaffrin, B. (1985). Aspects of network design. In Grafarend, E. W. and Sansò, F., editors, *Optimization and Design of Geodetic Networks*, pages 548–597, Berlin, Heidelberg. Springer Berlin Heidelberg.

Schaffrin, B. and Felus, Y. (2008). Multivariate total least – squares adjustment for empirical affine transformations. In *International Association of Geodesy Symposia*, pages 238–242. Springer Berlin Heidelberg.

Schindelegger, M., Böhm, S., Böhm, J., and Schuh, H. (2013). *Atmospheric Effects on Earth Rotation*, pages 181–231. Springer Berlin Heidelberg, Berlin, Heidelberg.

Schönberg, I. J. (1946). Contributions to the problem of approximation of equidistant data by analytic functions: Part A: On the problem of smoothing of graduation. a first class of analytic approximation formulae. *Q. Appl. Math*, 4(1):45–99.

Schreiber, K. U. and Kodet, J. (2017). The application of coherent local time for optical time transfer and the quantification of systematic errors in satellite laser ranging. *Space Sci. Rev.*, 214(1):22.

Schuh, H. (1987). *Die Radiointerferometrie auf langen Basen zur Bestimmung von Punktverschiebungen und Erdrotationsparametern*. PhD thesis, Rheinische Friedrich-Wilhelms-Universität zu Bonn.

Schuh, H. and Behrend, D. (2012). VLBI: A fascinating technique for geodesy and astrometry. *J Geodyn*, 61:68 – 80.

Schuh, H. and Böhm, J. (2013). *Very Long Baseline Interferometry for Geodesy and Astrometry*, pages 339–376. Springer Berlin Heidelberg, Berlin, Heidelberg.

Schüler, T. (2014). The TropGrid2 standard tropospheric correction model. *GPS Solut.*, 18(1):123–131.

Seeber, G. (2003). *Satellite Geodesy.* Walter de Gruyter, Berlin – New York, 2 edition.

Seitz, M., Bloßfeld, M., Angermann, D., Schmid, R., Gerstl, M., and Seitz, F. (2016). The new DGFI-TUM realization of the ITRS: DTRF2014 (data).

Sherwood, S. C., Roca, R., Weckwerth, T. M., and Andronova, N. G. (2010). Tropospheric water vapor, convection, and climate. *Rev. Geophys.*, 48(2).

Siebert, M. (1961). Atmospheric tides. volume 7 of *Adv. Geophys.*, pages 105 – 187. Elsevier.

Sillard, P. and Boucher, C. (2001). A review of algebraic constraints in terrestrial reference frame datum definition. *J. Geod.*, 75(2-3):63–73.

Simmons, A. J. and Burridge, D. M. (1981). An Energy and Angular-Momentum Conserving Vertical Finite-Difference Scheme and Hybrid Vertical Coordinates. *Mon. Wea. Rev.*, 109(4):758–766.

Smith, E. K. and Weintraub, S. (1953). The constants in the equation for atmospheric refractive index at radio frequencies. *Proceedings of the IRE*, 41(8):1035–1037.

Sneeuw, N. (1994). Global spherical harmonic analysis by least-squares and numerical quadrature methods in historical perspective. *Geophys. J. Int.*, 118(3):707–716.

Soja, B. (2016). *Anwendung eines Kalman-Filters in der Auswertung von VLBI-Daten.* PhD thesis, Technische Universität Wien.

Soja, B., Gross, R. S., Abbondanza, C., Chin, T. M., Heflin, M. B., Parker, J. W., Wu, X., Balidakis, K., Nilsson, T., Glaser, S., Karbon, M., Heinkelmann, R., and Schuh, H. (2018). Application of time-variable process noise in terrestrial reference frames determined from VLBI data. *Adv. Space Res.*, 61(9):2418 – 2425.

Soja, B., Nilsson, T., Balidakis, K., Glaser, S., Heinkelmann, R., and Schuh, H. (2016). Determination of a terrestrial reference frame via Kalman filtering of very long baseline interferometry data. *J. Geod.*, 90(12):1311–1327.

Somigliana, C. (1929). Teoria generale del campo gravitazionale dell' ellissoide di rotazione. *Mem. Soc. Astron. Ital.*, 4:541–599.

Sośnica, K., Thaller, D., Dach, R., Jäggi, A., and Beutler, G. (2013). Impact of loading displacements on SLR-derived parameters and on the consistency between GNSS and SLR results. *J. Geod.*, pages 1–19.

Sovers, O. and Jacobs, C. (1994). Observation model and parameter partials for the JPL VLBI parameter estimation software MODEST, NASA-CR-197328. Technical report.

Sovers, O. J., Fanselow, J. L., and Jacobs, C. S. (1998). Astrometry and geodesy with radio interferometry: experiments, models, results. *Rev. Mod. Phys.*, 70:1393–1454.

Suess, M. and Matsakis, D. (2011). Simulation of future GPS clock scenarios with two composite clocks. In *2011 Joint Conference of the IEEE International Frequency Control and the European Frequency and Time Forum (FCS) Proceedings*, pages 1–6.

Sun, J. (2013). *VLBI scheduling strategies with respect to VLBI2010.* PhD thesis, Department of Geodesy and Geoinformation.

Tahmoush, D. A. and Rogers, A. E. E. (2000). Correcting atmospheric path variations in millimeter wavelength very long baseline interferometry using a scanning water vapor spectrometer. *Radio Sci.*, 35(5):1241–1251.

Takahashi, F., Kondo, T., Takahashi, Y., and Koyama, Y. (2000). *Very Long Baseline Interferometer (Wave Summit Course).* Ohmsha, Ltd.

Tatarskiĭ, V. (1971). *Effects of the Turbulent Atmosphere on Wave Propagation.*

Tesauro, M., Audet, P., Kaban, M. K., Bürgmann, R., and Cloetingh, S. (2012). The effective elastic thickness of the continental lithosphere: Comparison between rheological and inverse approaches. *Geochem. Geophys.*, 13(9). Q09001.

Teunissen, P. J. and Montenbruck, O. E. (2017). *Springer handbook of global navigation satellite systems.* Cham, Switzerland: Springer, 2017.

Thaller, D. (2008). *Inter-technique combination based on homogeneous normal equation systems including station coordinates, Earth orientation and troposphere parameters.* Deutsches GeoForschungsZentrum. Scientific Technical Report STR 08/15.

Thayer, G. (1974). An improved equation for the radio refractive index of air. *Radio Sci.*, 9(10):803–807.

Thébault, E., Finlay, C. C., Beggan, C. D., Alken, P., Aubert, J., Barrois, O., Bertrand, F., Bondar, T., Boness, A., Brocco, L., Canet, E., Chambodut, A., Chulliat, A., Coïsson, P., Civet, F., Du, A., Fournier, A., Fratter, I., Gillet, N., Hamilton, B., Hamoudi, M., Hulot, G., Jager, T., Korte, M., Kuang, W., Lalanne, X., Langlais, B., Léger, J.-M., Lesur, V., Lowes, F. J., Macmillan, S., Mandea, M., Manoj, C., Maus, S., Olsen, N., Petrov, V., Ridley, V., Rother, M., Sabaka, T. J., Saturnino, D., Schachtschneider, R., Sirol, O., Tangborn, A., Thomson, A., Tøffner-Clausen, L., Vigneron, P., Wardinski, I., and Zvereva, T. (2015). International geomagnetic reference field: the 12th generation. *Earth Planets Space*, 67(1):79.

Thomas, M. (2002). *Ozeanisch induzierte Erdrotationsschwankungen: Ergebnisse eines Simultanmodells für Zirkulation und ephemeridische Gezeiten im Weltozean.* PhD thesis, Staats- und Universitätsbibliothek Hamburg.

Tibshirani, R. (1996). Regression shrinkage and selection via the lasso. *J. R. Stat. So.c Series B Stat. Methodol.*, 58(1):267–288.

Titov, O., Lambert, S. B., and Gontier, A.-M. (2011). VLBI measurement of the secular aberration drift. *A&A*, 529:A91.

Titov, O. and Schuh, H. (2000). Short periods in Earth rotation seen in VLBI data analysed by the least-squares collocation method. *IERS Technical Note*, 28:33–41.

Tregoning, P. and Herring, T. A. (2006). Impact of a priori zenith hydrostatic delay errors on GPS estimates of station heights and zenith total delays. *Geophys. Res. Lett.*, 33(23).

Tregoning, P. and van Dam, T. (2005a). Atmospheric pressure loading corrections applied to GPS data at the observation level. *Geophys. Res. Lett.*, 32:L22310.

Tregoning, P. and van Dam, T. (2005b). Effects of atmospheric pressure loading and seven-parameter transformations on estimates of geocenter motion and station heights from space geodetic observations. *J. Geophys. Res.*, 110:B03408.

Treuhaft, R. and Lanyi, G. (1987). The effect of the dynamic wet troposphere on radio interferometric measurements. *Radio Sci.*, 22(2):251–265.

van Dam, T., Altamimi, Z., Collilieux, X., and Ray, J. (2010). Topographically induced height errors in predicted atmospheric loading effects. *J. Geophys. Res.*, 115(B7):n/a–n/a. B07415.

van Dam, T., Blewitt, G., and Heflin, M. (1994). Atmospheric pressure loading effects on Global Positioning System coordinate determinations. *J. Geophys. Res.*, 99(B12):23,939–23,950.

van Dam, T., Collilieux, X., Wuite, J., Altamimi, Z., and Ray, J. (2012). Nontidal ocean loading: amplitudes and potential effects in GPS height time series. *J. Geod.*, 86(11):1043–1057.

van Dam, T. and Herring, T. (1994). Detection of atmospheric pressure loading using very long baseline interferometry measurements. *J. Geophys. Res.*, 99:4505–4518.

van Dam, T., Plag, H.-P., Francis, O., and Gegout, P. (2003). GGFC Special Bureau for Loading: Current Status and Plans. In Richter, B., Schwegmann, W., and Dick, W., editors, *Proceedings of the IERS Workshop on Combination Research and Global Geophysical Fluids*, volume 30 of *IERS Technical Note*, pages 180–198.

van Dam, T. and Wahr, J. (1987). Displacements of the Earth's Surface due to Atmospheric Loading: Effect on Gravity and Baseline Measurements. *J. Geophys. Res.*, 92:1281–1286.

van den Dool, H., Saha, S., Schemm, J., and Huang, J. (1997). A temporal interpolation method to obtain hourly atmospheric surface pressure tides in Reanalysis 1979 – 1995. *J. Geophys. Res.*, 102(D18):22,013–22,024.

Veis, G. (1960). Geodetic Uses of Artificial Satellites. *Smithsonian Contributions to Astrophysics*, 3:95.

Vey, S., Dietrich, R., Fritsche, M., Rülke, A., Steigenberger, P., and Rothacher, M. (2009). On the homogeneity and interpretation of precipitable water time series derived from global GPS observations. *J. Geophys. Res.*, 114(D10).

Wade, C. M. (1970). Precise Positions of Radio Sources. *Astrophys. J.*, 162:381.

Wang, H., Xiang, L., Jia, L., Jiang, L., Wang, Z., Hu, B., and Gao, P. (2012). Load Love numbers and Green's functions for elastic Earth models PREM, iasp91, ak135, and modified models with refined crustal structure from Crust 2.0. *Comput. Geosci.*, 49(Supplement C):190 – 199.

Wang, X. L., Wen, Q. H., and Wu, Y. (2007). Penalized Maximal t Test for Detecting Undocumented Mean Change in Climate Data Series. *J. Appl. Meteorol. Climatol.*, 46(6):916–931.

Watkins, M. M., Wiese, D. N., Yuan, D., Boening, C., and Landerer, F. W. (2015). Improved methods for observing Earth's time variable mass distribution with GRACE using spherical cap mascons. *J. Geophys. Res. Solid Earth*, 120(4):2648–2671.

Wheelon, A. D. (2001). *Electromagnetic Scintillation: Geometrical Optics (Vol 1)*. Cambridge University Press.

Wijaya, D. D. (2010). *Atmospheric correction formulae for space geodetic techniques*. PhD thesis, Graz University of Technology, Institute of Engineering Geodesy and Measurements Systems, Graz, Austria.

Wijaya, D. D. and Brunner, F. K. (2011). Atmospheric range correction for two-frequency SLR measurements. *J. Geod.*, 85(9):623–635.

Wilhelm, H. and Zürn, W. (1984). *2.5.1.6 Harmonic development*, pages 268–278. Springer Berlin Heidelberg, Berlin, Heidelberg.

Williams, S. (2008). CATS: GPS coordinate time series analysis software. *GPS Solut.*, 12(2):147–153.

Williams, S. D. P. and Penna, N. T. (2011). Non-tidal ocean loading effects on geodetic GPS heights. *Geophys. Res. Lett.*, 38(9). L09314.

Wresnik, J., Haas, R., Boehm, J., and Schuh, H. (2007). Modeling thermal deformation of VLBI antennas with a new temperature model. *J. Geod.*, 81(6):423–431.

Wu, X., Ray, J., and van Dam, T. (2012). Geocenter motion and its geodetic and geophysical implications. *J. Geodyn.*, 58:44–61.

Wunsch, C., Heimbach, P., Ponte, R. M., Fukumori, I., and the ECCO-GODAE Consortium Members (2009). The Global General Circulation of the Ocean Estimated by the ECCO-Consortium. *Oceanography*, 22.

Wunsch, C. and Stammer, D. (1997). Atmospheric loading and the oceanic "inverted barometer" effect. *Rev. Geophys.*, 35(1):79–107.

Xu, M. H., Heinkelmann, R., Anderson, J. M., Mora-Diaz, J., Schuh, H., and Wang, G. L. (2016). The Source Structure of 0642+449 Detected from the CONT14 Observations. *Astron. J.*, 152(5):151.

Yan, H. (1996). A New Expression for Astronomical Refraction. *Astron. J.*, 112:1312.

Zhou, F., Li, X., Li, W., Chen, W., Dong, D., Wickert, J., and Schuh, H. (2017). The Impact of Estimating High-Resolution Tropospheric Gradients on Multi-GNSS Precise Positioning. *Sensors*, 17(4).

Zumberge, J. F., Heflin, M., Jefferson, D., Watkins, M. M., and Webb, F. (1997). Precise point positioning for the efficient and robust analysis of GPS data from large networks. *J. Geophys. Res.*, 102(B3):5005–5017.

Zus, F., Bender, M., Deng, Z., Dick, G., Heise, S., Shang-Guan, M., and Wickert, J. (2012). A methodology to compute GPS slant total delays in a numerical weather model. *Radio Sci.*, 47(2). RS2018.

Zus, F., Deng, Z., Heise, S., and Wickert, J. (2017a). Ionospheric mapping functions based on electron density fields. *GPS Solut.*, 21(3):873–885.

Zus, F., Deng, Z., and Wickert, J. (2017b). The impact of higher-order ionospheric effects on estimated tropospheric parameters in Precise Point Positioning. *Radio Sci.*, 52(8):963–971.

Zus, F., Dick, G., Douša, J., Heise, S., and Wickert, J. (2014). The rapid and precise computation of GPS slant total delays and mapping factors utilizing a numerical weather model. *Radio Sci.*, 49(3):207–216.

Zus, F., Dick, G., Dousa, J., and Wickert, J. (2015a). Systematic errors of mapping functions which are based on the VMF1 concept. *GPS Solut*, 19(2):277–286.

Zus, F., Dick, G., Heise, S., and Wickert, J. (2015b). A forward operator and its adjoint for GPS slant total delays. *Radio Sci.*, 50(5):393–405. 2014RS005584.

Zus, F., Douša, J., Kačmařík, M., Václavovic, P., Dick, G., and Wickert, J. (2018). Estimating the Impact of Global Navigation Satellite System Horizontal Delay Gradients in Variational Data Assimilation. *Remote Sens.*, 11(1):41.

Appendix

A Components of EGLM

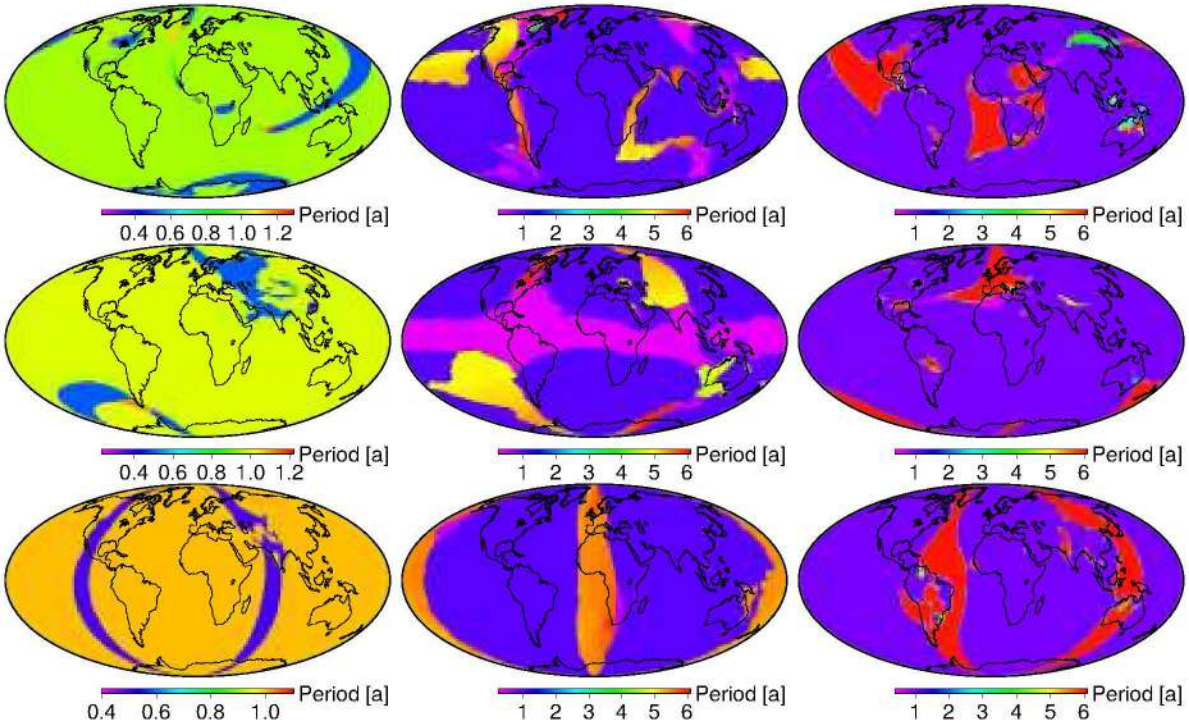


Figure A.0.1: The period at which the PSD from simulated displacements induced by NTAL (left), NTOL (middle), CWSL (right), in the radial (1st row), North-South (2nd row), and East-West (3rd row) coordinate component is maximized. Note the different color scales.

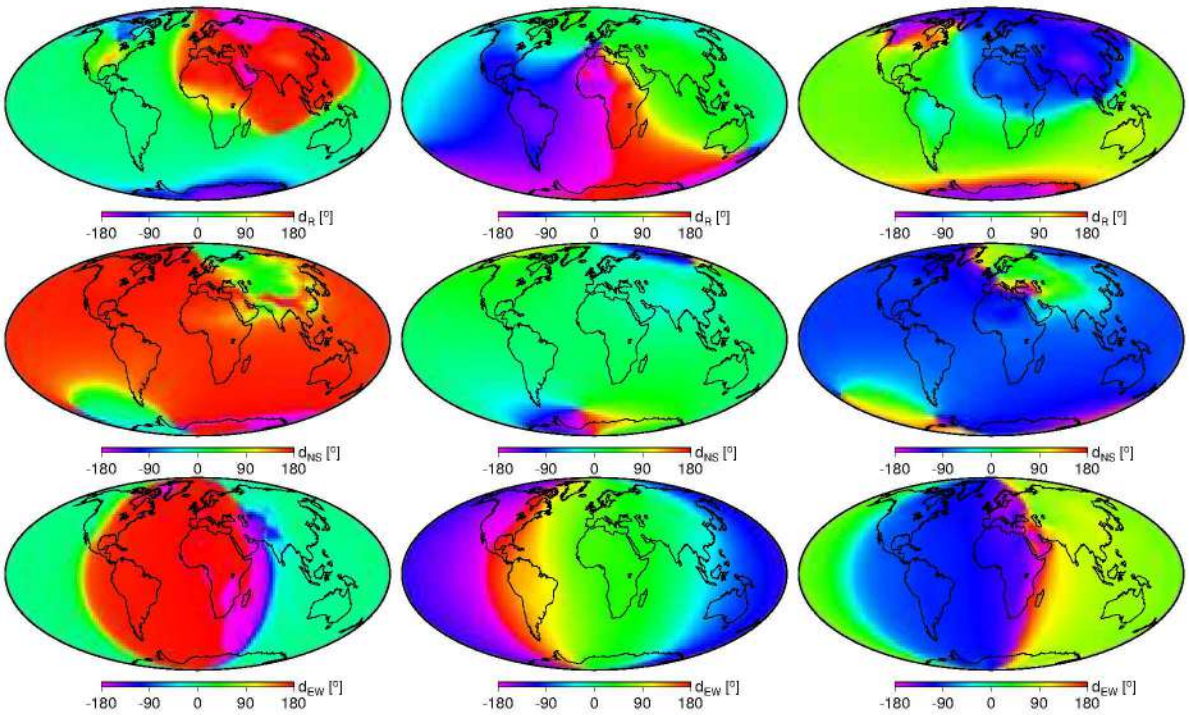


Figure A.0.2: The phase of the simulated displacements induced by NTAL at S_a (1st column), S_{sa} (2nd column), and S_{ta} (3rd column) frequencies, at the radial (1st row), North-South (2nd row) and East-West (3rd row) coordinate component.

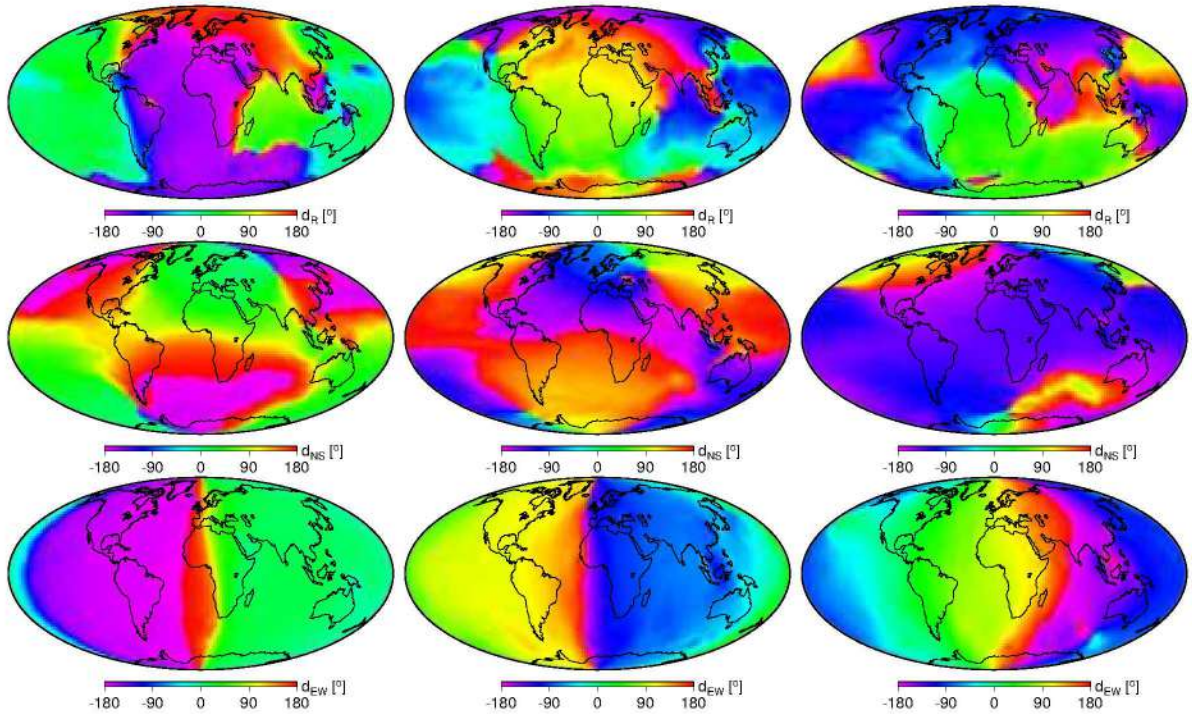


Figure A.0.3: The phase of the simulated displacements induced by NTOL at S_a (1st column), S_{sa} (2nd column), and S_{ta} (3rd column) frequencies, at the radial (1st row), North-South (2nd row) and East-West (3rd row) coordinate component.

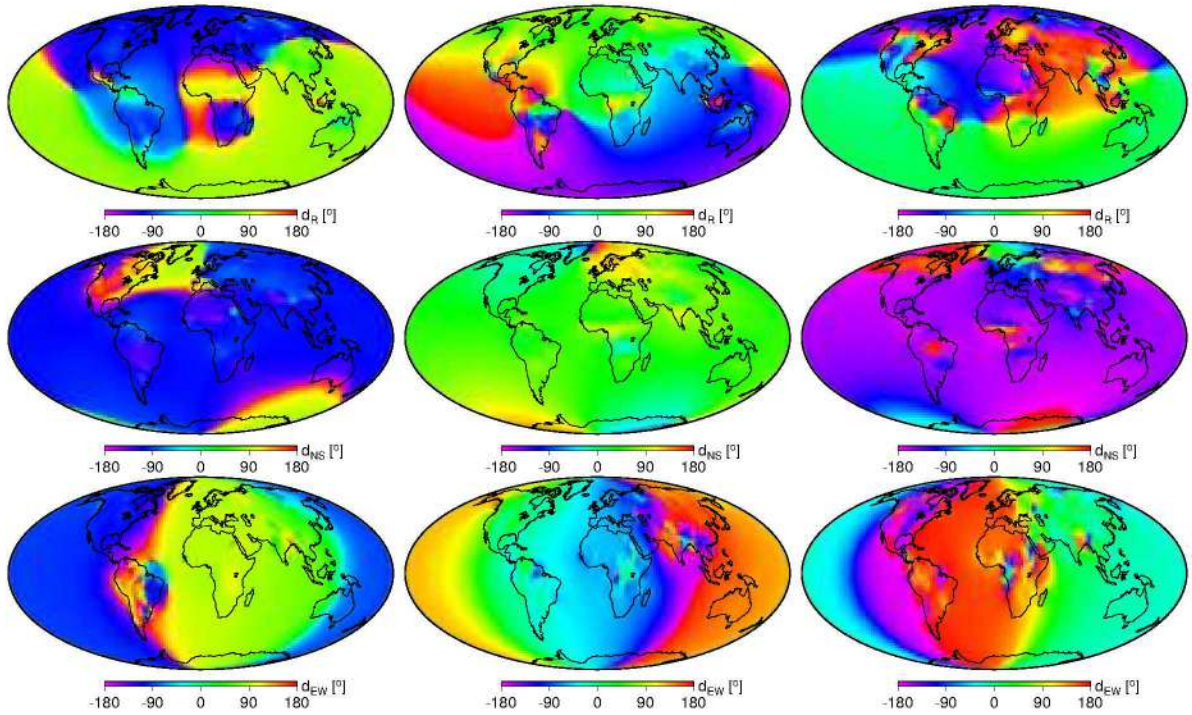


Figure A.0.4: The phase of the simulated displacements induced by CWSL at S_a (1st column), S_{sa} (2nd column), and S_{ta} (3rd column) frequencies, at the radial (1st row), North-South (2nd row) and East-West (3rd row) coordinate component.

B Impact of loading displacements on TRFs

The following graphs illustrate the time series of the differential scale factor between the official contribution of the IVS, ILRS, IGS, and IDS to ITRF2014 and applying the geophysical loading models developed in Chapter 5 at the parameter level. The scale estimates stem from (7.2.1).

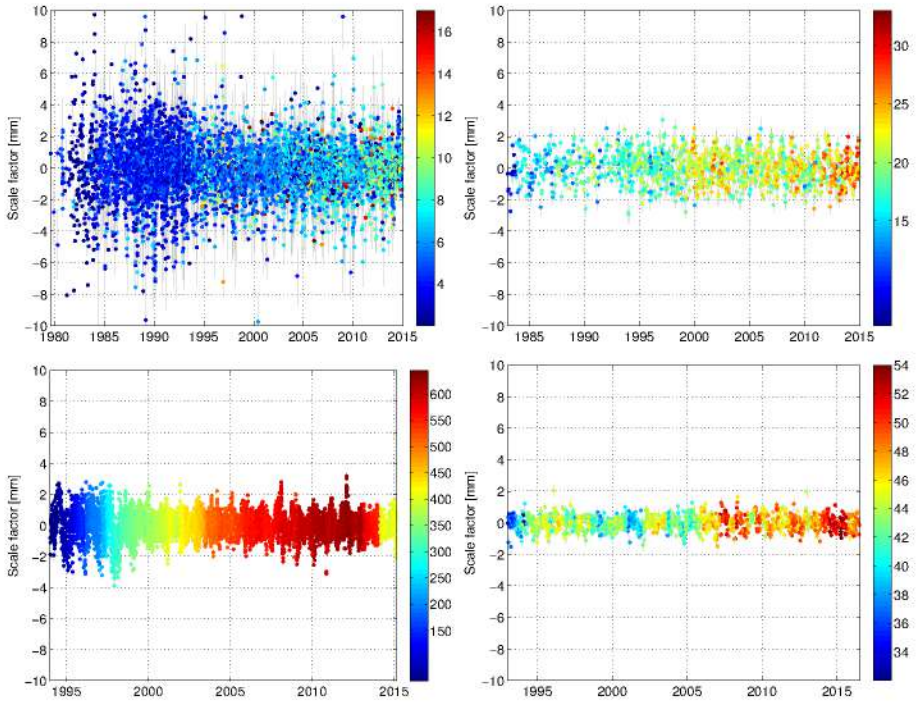


Figure B.0.1: The impact of non-tidal atmospheric pressure loading effects on the scale of the implied reference frame of the networks of IVS (upper-left), ILRS (upper-right), IGS (lower-left) and IDS (lower-right). The colorbars indicate the number of stations.

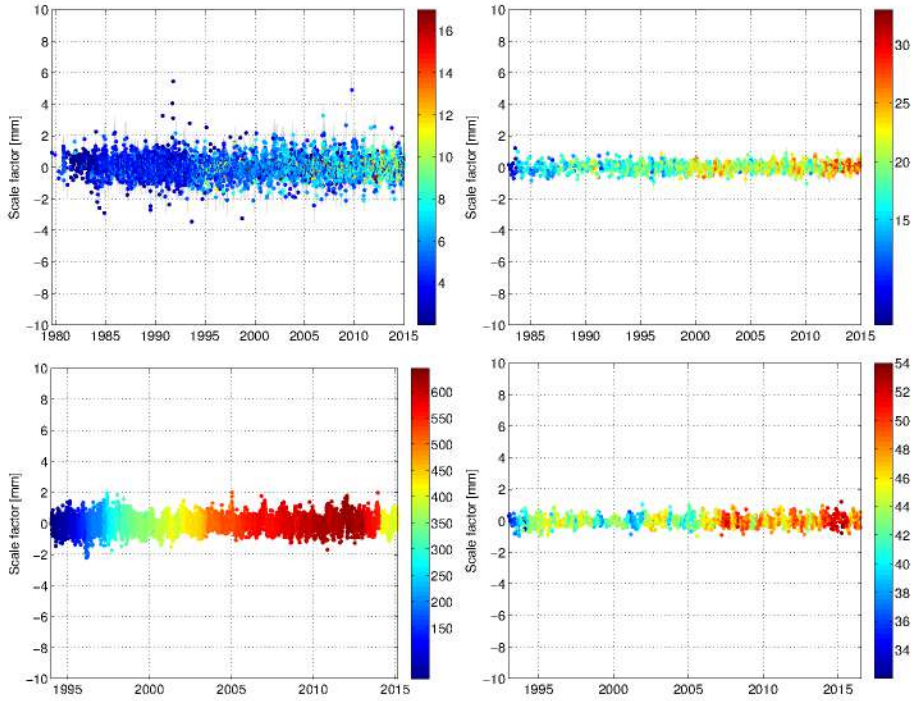


Figure B.0.2: The impact of non-tidal ocean loading effects on the scale of the implied reference frame of the networks of IVS (upper-left), ILRS (upper-right), IGS (lower-left) and IDS (lower-right). The colorbars indicate the number of stations.

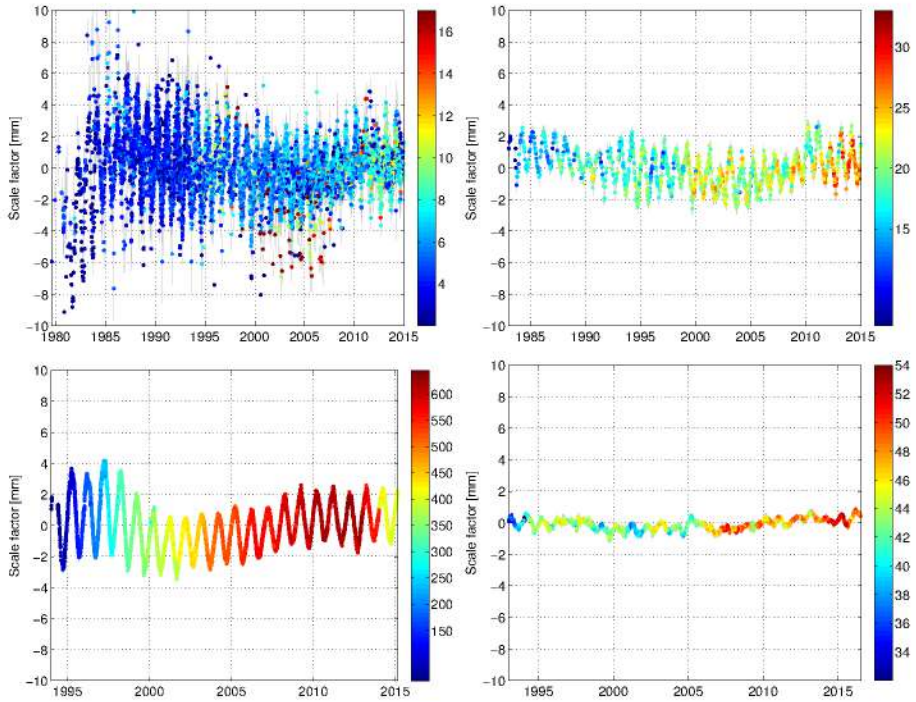


Figure B.0.3: The impact of continental water storage loading effects on the scale of the implied reference frame of the networks of IVS (upper-left), ILRS (upper-right), IGS (lower-left) and IDS (lower-right). The colorbars indicate the number of stations.

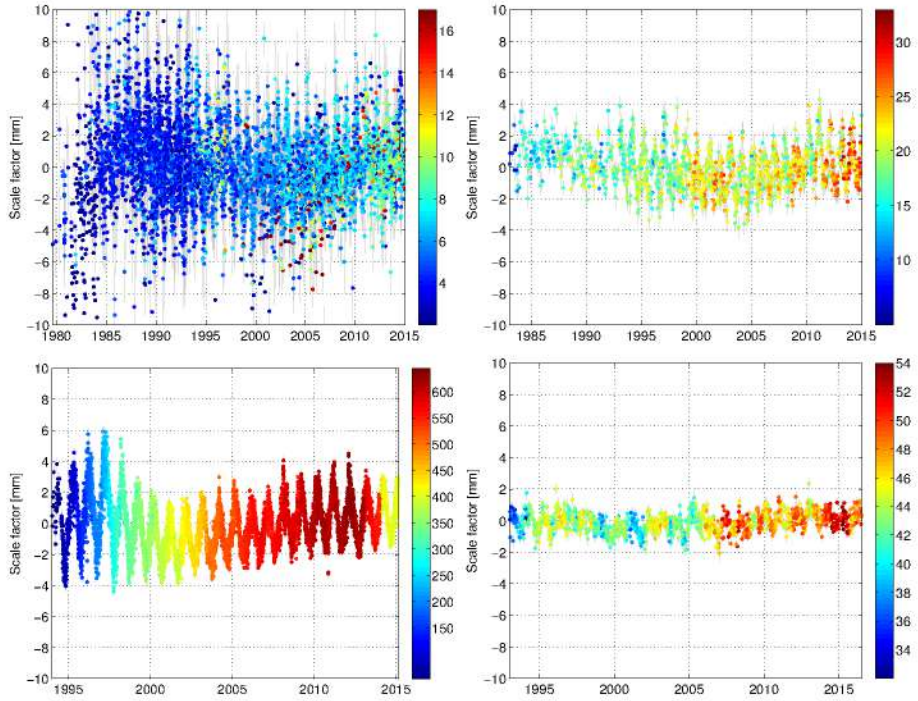


Figure B.0.4: The impact of the combined effect of non-tidal atmospheric pressure loading and continental water storage loading on the scale of the implied reference frame of the networks of IVS (upper-left), ILRS (upper-right), IGS (lower-left) and IDS (lower-right). The colorbars indicate the number of stations.

The following tables present the estimates of the Helmert transformation (7.2.1) between the official contribution of the IVS, ILRS, IGS, and IDS to ITRF2014 and applying the geophysical loading models developed in Chapter 5 at the parameter level.

Table B.0.1: The bias, temporal rate, scatter, annual amplitude and phase, as well as the WRMS of the post-fit residuals from the estimates of the 7- and 14-parameter similarity transformations employing the *NTAL* model developed in Chapter 5, and the station coordinates and the covariance matrices thereof assimilated into ITRF2014. Standard SINEX notation was used: R for VLBI, L for SLR, P for GNSS, and D for DORIS.

$\hat{\boldsymbol{\theta}}$		Bias [mm]	Rate [mm dec^{-1}]	Scatter [mm]	S_a amplitude [mm]	S_a phase [°]	WRMS [mm]
T_X	R	-0.1	-0.1	3.2	0.6	99.6	1.2
	L	-0.1	-0.0	1.8	0.5	95.9	1.0
	P	0.0	-0.0	0.1	0.0	176.9	0.1
	D	-0.1	-0.0	0.8	0.4	102.1	0.6
T_Y	R	-0.2	-0.1	3.5	1.6	90.7	1.4
	L	-0.1	0.0	1.9	1.6	86.1	1.0
	P	-0.0	0.0	0.1	0.0	91.2	0.1
	D	-0.1	0.0	1.5	1.5	90.8	0.8
T_Z	R	-0.1	-0.1	3.2	1.6	97.7	1.5
	L	-0.1	-0.0	2.0	1.9	98.9	1.2
	P	-0.0	-0.0	1.1	0.7	97.3	0.6
	D	-0.1	-0.0	1.8	1.3	97.9	1.2
R_X	R	0.0	0.1	3.5	0.3	-106.0	1.2
	L	0.0	0.0	0.5	0.4	-91.8	0.3
	P	0.0	-0.0	0.1	0.1	-84.2	0.1
	D	0.0	-0.0	0.1	0.1	-89.3	0.1
R_Y	R	-0.0	-0.0	2.9	0.1	111.0	0.9
	L	0.1	0.0	0.8	0.0	-91.6	0.5
	P	-0.0	-0.0	0.1	0.0	111.7	0.1
	D	-0.0	-0.0	0.1	0.0	84.3	0.1
R_Z	R	0.0	0.0	2.1	0.0	139.8	0.7
	L	0.0	0.0	0.4	0.2	-79.0	0.3
	P	0.0	-0.0	0.3	0.2	-87.1	0.1
	D	0.0	-0.0	0.1	0.0	101.5	0.1
D	R	0.1	-0.1	1.8	0.4	-129.7	1.1
	L	0.0	-0.1	1.0	0.2	141.2	0.7
	P	-0.1	-0.0	0.8	0.1	-167.3	0.5
	D	-0.0	0.0	0.5	0.1	-29.0	0.3

Table B.0.2: The bias, temporal rate, scatter, annual amplitude and phase, as well as the WRMS of the post-fit residuals from the estimates of the 7- and 14-parameter similarity transformations employing the *NTOL* model developed in Chapter 5, and the station coordinates and the covariance matrices thereof assimilated into ITRF2014. Standard SINEX notation was used: R for VLBI, L for SLR, P for GNSS, and D for DORIS.

$\hat{\boldsymbol{\theta}}$		Bias [mm]	Rate [mm dec^{-1}]	Scatter [mm]	S_a amplitude [mm]	S_a phase [°]	WRMS [mm]
T_X	R	0.0	0.1	2.3	1.0	78.2	1.5
	L	-0.0	0.1	1.9	1.1	66.6	1.3
	P	0.0	-0.0	0.2	0.0	70.8	0.1
	D	0.1	-0.1	1.7	0.7	72.9	1.3
T_Y	R	0.0	-0.0	1.6	0.3	102.2	1.1
	L	0.1	-0.1	1.2	0.3	90.9	1.0
	P	0.0	0.0	0.1	0.0	-50.5	0.1
	D	0.0	-0.1	1.2	0.2	107.9	1.0
T_Z	R	-0.0	0.1	1.6	0.2	90.8	1.2
	L	-0.0	0.2	1.1	0.3	97.9	1.1
	P	0.0	0.0	0.8	0.0	-122.5	0.5
	D	0.0	0.3	1.3	0.2	99.9	1.1
R_X	R	0.0	0.0	1.2	0.1	-110.9	0.6
	L	0.0	0.0	0.2	0.1	-127.5	0.1
	P	-0.0	0.0	0.1	0.0	-93.8	0.1
	D	0.0	0.0	0.1	0.0	-79.0	0.0
R_Y	R	0.0	-0.0	1.2	0.1	60.6	0.7
	L	-0.0	-0.0	0.4	0.1	70.2	0.2
	P	0.0	-0.0	0.2	0.0	78.4	0.1
	D	-0.0	-0.0	0.1	0.0	-141.1	0.0
R_Z	R	-0.0	0.0	0.7	0.1	82.3	0.5
	L	0.0	0.0	0.2	0.0	-74.0	0.1
	P	-0.0	0.0	0.5	0.0	-61.2	0.2
	D	-0.0	0.0	0.1	0.0	51.7	0.0
D	R	-0.0	0.0	0.6	0.1	95.6	0.4
	L	-0.1	0.0	0.3	0.1	112.9	0.2
	P	-0.0	0.1	0.5	0.1	90.5	0.3
	D	-0.0	0.0	0.3	0.1	67.8	0.2

Table B.0.3: The bias, temporal rate, scatter, annual amplitude and phase, as well as the WRMS of the post-fit residuals from the estimates of the 7- and 14-parameter similarity transformations employing the *CWSL* model developed in Chapter 5, and the station coordinates and the covariance matrices thereof assimilated into ITRF2014. Standard SINEX notation was used: R for VLBI, L for SLR, P for GNSS, and D for DORIS.

$\hat{\boldsymbol{\theta}}$		Bias [mm]	Rate [mm dec^{-1}]	Scatter [mm]	S_a amplitude [mm]	S_a phase [°]	WRMS [mm]
T_X	R	-0.3	0.3	3.1	1.8	17.3	1.0
	L	-0.1	0.5	2.1	2.4	24.1	1.0
	P	0.0	-0.0	0.1	0.0	-44.6	0.1
	D	0.2	-0.1	1.2	1.2	15.7	0.8
T_Y	R	-0.1	0.1	3.3	1.0	169.3	1.3
	L	0.1	-0.0	1.9	1.8	-178.0	1.2
	P	-0.0	0.0	0.1	0.0	13.6	0.1
	D	0.1	-0.1	1.5	1.5	178.3	1.0
T_Z	R	-0.1	-0.1	2.9	1.6	24.1	0.8
	L	-0.0	-0.2	1.3	1.5	25.5	0.6
	P	-0.1	0.0	0.5	0.4	33.1	0.3
	D	-0.2	-0.1	1.3	1.5	16.9	0.6
R_X	R	-0.0	-0.2	3.0	0.5	-152.6	1.1
	L	-0.1	0.0	0.4	0.0	73.9	0.3
	P	0.0	0.0	0.1	0.0	-153.8	0.1
	D	0.0	-0.0	0.1	0.0	-131.6	0.1
R_Y	R	-0.0	0.2	2.5	0.4	7.7	0.8
	L	0.0	0.2	0.7	0.7	29.0	0.4
	P	-0.0	0.0	0.2	0.2	11.6	0.1
	D	-0.0	0.0	0.1	0.0	171.7	0.1
R_Z	R	0.1	0.1	1.7	0.2	6.7	0.6
	L	-0.0	0.1	0.4	0.2	-42.6	0.3
	P	-0.1	0.2	0.4	0.3	-2.0	0.2
	D	0.0	-0.0	0.1	0.0	18.0	0.1
D	R	0.0	-0.1	2.1	1.5	26.0	1.0
	L	-0.4	-0.0	1.1	1.1	16.0	0.7
	P	-0.2	0.5	1.5	1.4	19.0	0.6
	D	-0.1	0.2	0.3	0.2	25.1	0.3

Table B.0.4: The bias, temporal rate, scatter, annual amplitude and phase, as well as the WRMS of the post-fit residuals from the estimates of the 7- and 14-parameter similarity transformations employing the *NTAL and CWSL* models developed in Chapter 5, and the station coordinates and the covariance matrices thereof assimilated into ITRF2014. Standard SINEX notation was used: R for VLBI, L for SLR, P for GNSS, and D for DORIS.

$\hat{\boldsymbol{\theta}}$		Bias [mm]	Rate [mm dec^{-1}]	Scatter [mm]	S_a amplitude [mm]	S_a phase [°]	WRMS [mm]
T_X	R	-0.3	0.2	4.5	1.9	33.5	1.4
	L	-0.2	0.5	2.8	2.3	36.2	1.6
	P	0.0	-0.0	0.2	0.0	-63.7	0.1
	D	0.2	-0.1	1.4	1.3	36.5	1.0
T_Y	R	-0.2	-0.1	5.0	2.3	121.2	1.8
	L	-0.1	0.0	2.6	2.4	138.4	1.5
	P	-0.0	0.0	0.2	0.1	51.6	0.1
	D	-0.1	-0.2	2.2	2.3	134.0	1.2
T_Z	R	-0.1	-0.2	4.9	2.4	62.3	1.8
	L	0.1	-0.2	2.6	2.6	68.1	1.5
	P	-0.1	0.0	1.3	1.0	78.9	0.7
	D	0.0	-0.0	2.3	2.1	53.3	1.6
R_X	R	-0.0	-0.1	4.7	0.6	-109.8	1.1
	L	-0.1	0.0	0.6	0.3	-81.1	0.4
	P	0.0	0.0	0.2	0.1	-108.4	0.1
	D	0.0	-0.0	0.1	0.1	-96.4	0.1
R_Y	R	-0.0	0.1	3.7	0.4	23.3	1.1
	L	-0.0	0.2	1.0	0.5	26.1	0.7
	P	-0.0	0.0	0.2	0.2	20.5	0.1
	D	-0.0	0.0	0.1	0.0	121.8	0.1
R_Z	R	0.1	0.1	2.4	0.2	19.1	0.9
	L	0.0	0.1	0.6	0.3	-55.8	0.4
	P	-0.1	0.2	0.5	0.4	-36.3	0.3
	D	0.0	-0.0	0.1	0.1	50.6	0.1
D	R	-0.0	-0.1	2.7	0.9	12.2	1.5
	L	-0.4	-0.2	1.4	0.8	35.3	1.0
	P	-0.3	0.5	1.6	1.3	19.2	0.8
	D	-0.1	0.2	0.6	0.3	0.3	0.5

Table B.0.5: The bias, temporal rate, scatter, annual amplitude and phase, as well as the WRMS of the post-fit residuals from the estimates of the 7- and 14-parameter similarity transformations employing the *NTAL, NTOL, and CWSL* models developed in Chapter 5, and the station coordinates and the covariance matrices thereof assimilated into ITRF2014. Standard SINEX notation was used: R for VLBI, L for SLR, P for GNSS, and D for DORIS.

$\hat{\boldsymbol{\theta}}$		Bias [mm]	Rate [mm dec^{-1}]	Scatter [mm]	S_a amplitude [mm]	S_a phase [°]	WRMS [mm]
T_X	R	-0.2	0.3	5.5	2.5	48.0	2.4
	L	-0.1	0.6	3.8	3.2	47.8	2.4
	P	0.0	-0.0	0.3	0.0	55.3	0.2
	D	0.3	-0.1	2.5	2.0	53.7	1.9
T_Y	R	-0.1	-0.1	5.6	2.5	120.4	2.2
	L	0.1	-0.0	2.9	2.7	133.7	1.9
	P	-0.0	0.0	0.3	0.1	51.9	0.1
	D	0.0	-0.4	2.6	2.5	130.8	1.7
T_Z	R	-0.1	-0.0	5.2	2.5	63.8	2.2
	L	0.1	-0.1	3.0	3.0	72.7	1.9
	P	-0.1	0.0	1.5	0.9	80.3	1.0
	D	0.1	0.3	2.8	2.2	60.1	2.1
R_X	R	-0.0	-0.1	5.1	0.6	-108.0	1.2
	L	-0.0	0.0	0.6	0.4	-90.2	0.5
	P	0.0	0.0	0.3	0.1	-105.2	0.1
	D	0.0	-0.0	0.2	0.1	-96.2	0.1
R_Y	R	-0.0	0.1	4.0	0.4	24.2	1.3
	L	-0.0	0.2	1.2	0.7	36.6	0.7
	P	-0.0	0.0	0.3	0.2	30.8	0.2
	D	-0.0	0.0	0.1	0.0	124.4	0.1
R_Z	R	0.0	0.1	2.7	0.2	32.3	0.9
	L	0.0	0.2	0.7	0.4	-57.1	0.5
	P	-0.1	0.3	0.8	0.4	-38.0	0.4
	D	0.0	-0.0	0.2	0.1	50.3	0.1
D	R	-0.0	-0.1	2.8	1.0	22.0	1.8
	L	-0.4	-0.2	1.4	0.8	42.4	1.2
	P	-0.2	0.6	1.7	1.4	24.7	0.9
	D	-0.1	0.2	0.7	0.3	21.6	0.6